

Advanced Structured Materials

Andreas Öchsner  
Holm Altenbach *Editors*

# Properties and Characterization of Modern Materials

 Springer

# **Advanced Structured Materials**

Volume 33

## **Series editors**

Andreas Öchsner, Southport Queensland, Australia

Lucas F.M. da Silva, Porto, Portugal

Holm Altenbach, Magdeburg, Germany

More information about this series at <http://www.springer.com/series/8611>

Andreas Öchsner · Holm Altenbach  
Editors

# Properties and Characterization of Modern Materials

 Springer



*Editors*

Andreas Öchsner  
Griffith University  
Southport, QLD  
Australia

Holm Altenbach  
IFME  
Otto-von-Guericke-University Magdeburg  
Magdeburg, Saxony-Anhalt  
Germany

ISSN 1869-8433

Advanced Structured Materials

ISBN 978-981-10-1601-1

DOI 10.1007/978-981-10-1602-8

ISSN 1869-8441 (electronic)

ISBN 978-981-10-1602-8 (eBook)

Library of Congress Control Number: 2016943428

© Springer Science+Business Media Singapore 2017

This work is subject to copyright. All rights are reserved by the Publisher, whether the whole or part of the material is concerned, specifically the rights of translation, reprinting, reuse of illustrations, recitation, broadcasting, reproduction on microfilms or in any other physical way, and transmission or information storage and retrieval, electronic adaptation, computer software, or by similar or dissimilar methodology now known or hereafter developed.

The use of general descriptive names, registered names, trademarks, service marks, etc. in this publication does not imply, even in the absence of a specific statement, that such names are exempt from the relevant protective laws and regulations and therefore free for general use.

The publisher, the authors and the editors are safe to assume that the advice and information in this book are believed to be true and accurate at the date of publication. Neither the publisher nor the authors or the editors give a warranty, express or implied, with respect to the material contained herein or for any errors or omissions that may have been made.

Printed on acid-free paper

This Springer imprint is published by Springer Nature

The registered company is Springer Science+Business Media Singapore Pte Ltd.

# Preface

The success of materials in technical applications as well as their safety during operation depends on robust characterization and/or prediction methods which provide reliable material properties. This becomes more and more important because engineering materials are used closer and closer to their limit to increase the performance of any machines and structures. To increase the engineering value of a material, components are designed under the consideration of their multi-physical properties and functions which requires a much more comprehensive investigation and characterization of these materials. The materials covered in this monograph range from metal-based groups such as lightweight alloys and advanced high-strength steels to modern titanium alloys. Furthermore, a wide range of polymers and composite materials (e.g., with micro- and nanoparticles or fibers) is covered. The properties that are covered range from classical mechanical characterization related, for example, to wear, creep, fatigue, and crack growth over specific surface properties to dielectric and electrochemical values. As in all fields of modern engineering, the process is many times accompanied by numerical simulation and optimization.

The 9th International Conference on Advanced Computational Engineering and Experimenting, ACE-X 2015, was held in Munich, Germany, from 29 June to 2 July, 2015, with a strong focus on computational based and supported engineering. This conference served as an excellent platform for the engineering community to meet with each other and to exchange the latest ideas. This volume contains 34 revised and extended research articles written by experienced researchers participating in the conference. Well-known experts present their research on metallic and polymer-based materials.

The organizers and editors wish to thank all the authors for their participation and cooperation which made this volume possible. Finally, we would like to thank the team of Springer Verlag, especially Dr. Christoph Baumann, for the excellent cooperation during the preparation of this volume.

Southport, Australia  
Magdeburg, Germany  
April 2016

Andreas Öchsner  
Holm Altenbach

# Contents

<b>Options for Nanoreinforced Cast Al–Si Alloys with TiO<sub>2</sub> Nanoparticles</b> . . . . .	1
A.Y. Shash, I.S. El-Mahallawi and A.E. Amer	
<b>Mechanical Properties and Wear Resistance of Semisolid Cast Al<sub>2</sub>O<sub>3</sub> Nano Reinforced Hypo and Hyper-eutectic Al–Si Composites</b> . . . . .	13
I.S. El-Mahallawi and A.Y. Shash	
<b>Simulation of a Crack Emanating from a Microvoid in Cement of a Reconstructed Acetabulum</b> . . . . .	31
B. Serier, L. Zouambi, M.M. Bouziane, S. Benbarek and B. Bachir Bouiadjra	
<b>Analysis of the Optical Properties of PVP/ZnO Composite Nanofibers</b> . . . . .	43
Wiktor Matysiak, Tomasz Tański and Marta Zaborowska	
<b>Multiobjective Optimization of Dielectric Material’s Selection in Marine Environment</b> . . . . .	51
I. Kuzmanić, I. Vujović and J. Šoda	
<b>Metallurgical Quality Assessment of Modified Zn–Al–Cu Alloys</b> . . . . .	63
Krupiński Mariusz, Krupińska Beata, Karkoszka Tatiana, Borek Wojciech and Babilas Rafał	
<b>Fatigue Test of the Inconel Alloy 718 Under Three Point Bending Load at Low Frequency</b> . . . . .	75
J. Belan, L. Hurtalová, A. Vaško, E. Tillová and M. Chalupová	
<b>Development of a Finite Element Program for Determining Mat Pressure in the Canning Process of a Catalytic Converter</b> . . . . .	85
S.J. Chu and Y.D. Lee	

<b>Evolution of Droplet Impact on Dry Surfaces with Different Surface Characteristics . . . . .</b>	99
Cheng-Hsiung Kuo and Yao-Tsyn Wang	
<b>Numerical Optimization in Ropeway Planning . . . . .</b>	113
H. Thaler, M. Wenin, J. Brunner, D. Reiterer, M.L. Bertotti, G. Modanese and E. Oberhuber	
<b>The Finite Volume Diffusion Method on Nonmatched Polygonal Meshes Suited for the Lagrangian Slide Lines Calculation . . . . .</b>	125
Xuezhe Liu, Zhong Lin and Ruili Wang	
<b>Effect of Defects and Electric Field on Stress-Induced Motion of 90° Domain Wall in PbTiO<sub>3</sub>: A Molecular Dynamics Study . . . . .</b>	135
Yoshitaka Umeno and Atsushi Kubo	
<b>Ce,Tb-Doped Y<sub>2</sub>SiO<sub>5</sub> Phosphor Luminescence Emissions Modeling and Simulation . . . . .</b>	145
D. Cervantes, D.L. Flores, E. Gutiérrez and M.A. Chacón	
<b>Extended Characterization of the Hardening and Failure Behavior of Advanced High Strength Steels at Dynamic Compression Load. . . . .</b>	157
Markus Grillenberger and Martin Schagerl	
<b>High Temperature Mechanical Behavior of Plasma-Nitrided Inconel 625 Superalloy . . . . .</b>	167
M.M. Oliveira, A.A. Couto, R. Baldan, D.A.P. Reis, J. Vatauvuk, J.C. Vendramim, N.B. Lima and A.G. Reis	
<b>Thermal Properties of Sandwiches for Applications in Transportation . . . . .</b>	179
Pavel Košťial, Vladimír Rusnák, Svetozár Malinarič, Zora Jančíková, Jan Valíček and Marta Harničárová	
<b>Evaluation of Creep Resistance and Superficial Study of Titanium Alloy Treated by PIII-N . . . . .</b>	185
S. Zepka, D.A.P. Reis, M.M. Silva, M. Ueda, A.A. Couto and A.G. Reis	
<b>Properties of WE43 Metal Matrix Composites Reinforced with SiC Particles . . . . .</b>	197
B. Dybowski, T. Rzychoń, B. Chmiela and A. Gryc	
<b>Primary Dendrite ARM Spacing Effects upon Mechanical Properties of an AL-3Wt%CU-1Wt%LI Alloy . . . . .</b>	215
G.A. Santos, P.R. Goulart, A.A. Couto and A. Garcia	
<b>The Influence of Heat Treatment on the Microstructure and Mechanical Properties of the Mg-7Sn-1Si Magnesium Alloy . . . . .</b>	231
T. Rzychoń and B. Dybowski	

**Volume Changes of Cement Composite Based on Steel Slag During Thermal Load** . . . . . 245  
 V. Šimíček, V. Václavík, T. Kubín, T. Dvorský, A. Břenek, J. Valíček, M. Kušnerová, M. Harničárová and L. Gola

**Magnetic Alloys Design Using Multi-objective Optimization** . . . . . 261  
 R. Jha, G.S. Dulikravich, M.J. Colaço, M. Fan, J. Schwartz and C.C. Koch

**Basic Evaluation Technology Development of Battery Installation Safety for Electric Vehicles** . . . . . 285  
 Kee Joo Kim, Young-Cheol Lee and Jun-Hyub Park

**Study of the Electrochemical Properties of 316LVM Steel with TiO<sub>2</sub> Layer Deposited by Means of the ALD Method** . . . . . 297  
 M. Basiaga, W. Walke, M. Staszuk and W. Kajzer

**Design and Development of a Simplified Wear Simulator for Total Knee Replacement (TKR) Based on Pin-Disc Machine** . . . . . 309  
 R. Rodríguez-Martínez, G. Urriolagoitia-Sosa, C. Torres San Miguel, L.H. Hernández-Gómez, J.A. Beltrán-Fernández and B. Romero-Ángeles

**Elaboration and Modeling of Water Molecule Sensitive Layers Deposited from Hexamethyldisiloxane** . . . . . 315  
 Noubel Guermat

**Synthesis and Characterization of Cu<sub>2</sub>ZnSnS<sub>4</sub> Absorber Layers by Ultrasonic Spray Pyrolysis** . . . . . 325  
 W. Daranfed, M.S. Aida, N. Attaf, J. Bougdira and H. Rinnert

**Fault Tolerance Methodology for Micro-volume Deposit System** . . . . . 333  
 Luis Yépez-Pérez, Rogelio Bustamante-Bello, Ricardo A. Ramírez-Mendoza and Jorge de J. Lozoya-Santos

**Electromagnetic Compatibility Aspects of Wind Turbine Analysis and Design** . . . . . 345  
 D. Poljak and D. Čavka

**Customization and Numerical Simulation of a Cranial Distractor Using Computed Axial Tomography (CAT)** . . . . . 371  
 J.A. Beltrán-Fernández, J. Martínez-Paredes, M. González-Rebattú, L.H. Hernández-Gómez and O. Ruíz-Muñoz

**Prediction of In-Service NBR Properties by TG-IR After Storage in Mineral Oil** . . . . . 399  
 Tobias Föster

<b>Structural Integrity Analysis of a BWR Core Shroud with an Irregular Distribution of Cracks: Limit Load Analysis . . . . .</b>	<b>413</b>
Pablo Ruiz-López, Luis H. Hernández-Gómez, Guillermo Urriolagoitia-Calderón, María L. Serrano-Ramírez, Arturo Ocampo-Ramirez, Juan A. Beltrán-Fernández and Guillermo Urriolagoitia-Sosa	
<b>Numerical Evaluation of the Structural Integrity Exhibited by a TiO<sub>2</sub> Thin Solid Film Doped with Au. . . . .</b>	<b>429</b>
D. Fernández-Valdés, L.H. Hernández-Gómez, M. Trejo-Valdéz, C. Torres-Torres, J.A. Beltrán-Fernández, N.M. León-Lugo and G. Urriolagoitia-Calderón	
<b>State of the Art Thermal Barrier Coating (TBC) Materials and TBC Failure Mechanisms . . . . .</b>	<b>441</b>
Abdullah Cahit Karaoglanli, Kadir Mert Doleker and Yasin Ozgurluk	

# Options for Nanoreinforced Cast Al–Si Alloys with TiO<sub>2</sub> Nanoparticles

A.Y. Shash, I.S. El-Mahallawi and A.E. Amer

**Abstract** This study presents a new concept of refining and enhancing the properties of cast aluminium alloys by adding nanoparticles. In this work the effect of adding titanium dioxide (TiO<sub>2</sub>) nano-particles (40 nm) to the aluminum cast alloy A356 as a base metal matrix was investigated. Titanium dioxide nano-powders were stirred into the A356 matrix with different fraction ratios ranging from (0, 1, 2, 3, 4, 5 %) by weight at variable stirring speeds ranging from (270, 800, 1500, 2150 rpm) in both the semisolid (600 °C) and liquid state (700 °C) using a constant stirring time of one minute. The cast microstructure exhibited change of grains from dendritic to spherical shape when increasing stirring speed. The fracture surface showed the presence of nanoparticles at the interdendritic spacing of the fracture surface and was confirmed with EDXS analysis of these particles. The results of the study showed that the mechanical properties (strength, elongation and hardness) for the nanoreinforced castings using TiO<sub>2</sub> were enhanced for the castings made in the semi-solid state (600 °C) with 3 % weight% of TiO<sub>2</sub> at 1500 rpm stirring speed.

**Keywords** Nanoreinforced castings · Semisolid casting · Hypoeutectic aluminium alloys

---

A.Y. Shash (✉)  
Mechanical Design and Production Department, Cairo University,  
Giza, Egypt  
e-mail: ahmed.shash@cu.edu.eg

I.S. El-Mahallawi  
Mining Petroleum and Metallurgical Engineering Department, Cairo University,  
Giza, Egypt  
e-mail: ielmahallawi@bue.edu.eg

A.E. Amer  
Mechanical Design and Production Department, Beni-Suef University,  
Beni Suef, Egypt  
e-mail: aeid958@yahoo.com



## 1 Introduction

Al–Si alloys are used for several automotive applications and for various applications in the aerospace industry due to their outstanding properties such as high castability, abrasion resistance and excellent strength to weight ratio. The Al–Si alloys in particular are greatly known for their rapidly advancing influence in the aircraft, aerospace and automotive industries. Intensive efforts were made to understand the modifications of these alloys caused by adding Na, Sr or Sb [1–4]. The addition of certain elements, such as calcium, sodium, strontium, and antimony, to hypoeutectic aluminum-silicon alloys results in a finer lamellar or fibrous eutectic network [4]. Gruzleski et al. [2] discussed the techniques commonly used in the foundry, and showed that the addition of P to the melt results in modified hypereutectic Al–Si alloys, with both coarse and unmodified eutectic silicon surrounding the refined primary silicon. Though Na and Sr are used to achieve refinement of the eutectic silicon, a combined effect does not happen at the same time with P due to chemical incompatibility of phosphorus with the other modifying chemicals such as strontium and sodium. This has been explained [2] to result from the formation of strontium phosphide or sodium phosphide upon the addition of strontium or sodium to phosphorus pre-refined alloys. Other investigations have shown that adding rare earth elements would result in modification and refinement of the primary and eutectic silicon particles [5, 6].

The mechanical properties of the A356 alloy, not only, depend on the dendritic structures, but also on the sizes and morphologies of the eutectic Si particles [7, 8]. The eutectic Si of untreated A356 presents a coarse plate-like structure, which will deteriorate the mechanical properties (especially the ductility) of the alloy. While, the mechanical properties of the hypereutectic Al–Si alloys are highly affected by the morphology, size, and distribution of both primary Si particles (PSPs) and eutectic silicon. The morphology of silicon particles is dependent on the solidification rate; as under normal casting conditions PSPs are very coarse and show star-like and other irregular shapes. Therefore, to improve the mechanical properties of the hypo and hypereutectic Al–Si alloys, size, distribution, and the morphology of PSPs and eutectic silicon should be controlled, as well as the refining of the aluminium dendrites [2, 3].

The use of ceramic particles to improve the yield and ultimate strength (UTS) of cast Al alloys has been considered by many researchers [9–15]. Prospects of using nanoparticles as refining and reinforcement agents to gain improved performance of Al–Si cast alloys by adding  $\text{Al}_2\text{O}_3$  and  $\text{TiO}_2$  particles have gained significant interest recently [16–22].

Rohatgi et al. [11] have predicted the significant role of producing Al–Si ceramic composites for bearings, pistons, cylinder liners, etc. leading to savings in material and energy. Previous trials to modify the structure and enhance the mechanical properties of A356 via reinforcement with ceramic micro-sized particles, such as  $\text{Al}_2\text{O}_3$  [12], SiC [13, 14] and TiC [15] did not result a breakthrough in casting modification, though a small number of engineering cast products entered the market [23].

It has been shown that enhanced as-cast properties of Al–Si alloys are obtained by treating the melt with nano-sized particles [16–22]. Introducing Al<sub>2</sub>O<sub>3</sub> nanoparticles to the (A356) cast alloy in the semi-solid state with mechanical stirring has a beneficial effect on improving strength–ductility relationship in these alloys [16, 17]. This is attributed to the modification of the dendritic columnar structure into a smaller and equiaxed globular grain arrangement, resulting from semi-solid casting conditions. Moreover, the enhanced viscosity of the semi-solid processing would serve to improve the ceramic particle/melt wettability and entrap or capture the reinforcement material physically. The addition of ceramic particles to aluminium alloys raises the viscosity very quickly [24] providing suitable conditions for particle capture. Moreover the Al<sub>2</sub>O<sub>3</sub> nanoparticles possess appropriate properties that are compatible with the Al alloy’s relatively high thermal conductivity and thermal expansion coefficients that affect its role as a nanodispersion for reinforcement in the Al alloy matrix [16–19].

For most applications, a homogeneous distribution of the particles is desirable in order to maximize the mechanical properties. In order to achieve a good homogeneous distribution of the particles in the matrix, the process parameters related with the stir casting method must be considered, the stirring speed and stirring time are key parameters. There is some debate in the literature about the appropriate stirring speeds, while one study [25] has investigated stirring speeds within the range of 500, 600 and 700 rpm and the stirring times in the range of 5, 10 and 15 min, another study [26] has used higher stirring speeds in the range 1000–1500 rpm.

Haizhi [23] has presented an overview of Al–Si based alloys for engine applications where it was shown that fatigue failure and wear caused by surface delamination are the most important causes for failure or end of life of engine parts. The main causes according to the analysis presented by Haizhi Ye [23] are the size and shapes (morphology) of the Primary Si Particles (PSPs). Also, these materials have low specific gravity that makes their properties particularly superior in strength and modulus to many traditional engineering materials. Therefore, the aim of this work is to compare the effect of adding three different nanoparticles as reinforcements (Al<sub>2</sub>O<sub>3</sub>, TiO<sub>2</sub> and ZrO<sub>2</sub>) on the microstructure, the mechanical properties and the wear behavior of A356 aluminum alloy cast from the semi-solid state, in order to evaluate the options for using nanoparticles dispersion for the production of semi-solid cast A356 alloy with improved properties.

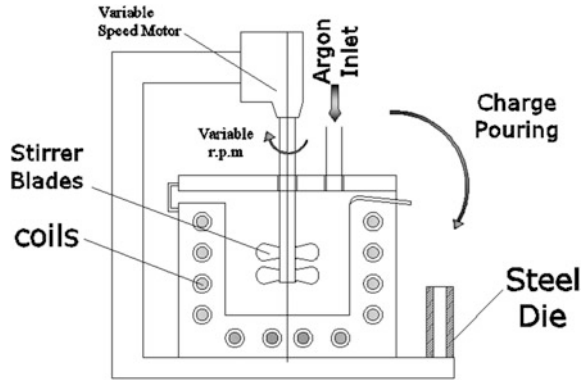
## 2 Experimental Work

### 2.1 Material Preparation

Titanium dioxide (TiO<sub>2</sub>) ceramic particles of 40 nm particle size were added as reinforcement materials to the A356 alloy with the chemical composition illustrated in Table 1. A charge of 1 kg of aluminum alloy A356 was placed in a crucible furnace, and then heated to the required temperature (640 °C). The addition of the

**Table 1** Chemical composition (in wt%) of A356 cast Al–Si

Alloy	Chemical composition (wt%)							
	Al	Si	Mg	Fe	Cu	Pb	Zn	Mn
A356	Bal.	7.44	0.3	0.27	0.02	0.022	0.01	Nil

**Fig. 1** Furnace used for preparing the castings

nanoparticles was made either at 710 °C or 640 °C in the liquid or semisolid state, respectively, by direct immersion of small packages of TiO<sub>2</sub> nanoparticles wrapped in aluminum foil with simultaneous mechanical stirring of the melt. The melting and casting conditions are fully presented in previous works [16–18]. In the case of the liquid state, the melt was brought to 700 °C when the addition was made, then stirred and poured. While in the case of the semisolid state, the temperature of the melt was brought down to 600 °C before pouring. The nanoparticles were added, while the melt was stirred mechanically at varied stirring speeds of (270, 800, 1500, 2150 rpm), and using the melting unit illustrated in Fig. 1. The stirring was carried out mechanically using a four blade impeller. The TiO<sub>2</sub> nanoparticles were pre-heated to 400 °C, to avoid entering the sintering stage. After completion of stirring and mixing, the alloys were poured in preheated steel moulds at 300 °C. Table 2 summarizes the different casting conditions used in this work.

**Table 2** Casting conditions used in this work

No.	TiO <sub>2</sub> weight%	Temperature (°C)	Stirring speed (rpm)
1	0	600	1500
2	1	600	1500
3	2	600	1500
4	3	600	1500
5	5	600	1500
6	3	600	270
7	3	600	800
8	3	600	2150
9	3	700	1500

## **2.2 Mechanical Testing**

The mechanical properties, mainly tensile strength, ductility, and hardness were determined in the as-cast conditions for the investigated material. The tensile tests were conducted on round tension test specimens of diameter 5.02 mm and gauge length 25.2 mm using a universal testing machine according to DIN 50125. The hardness tests were conducted on Rockwell hardness testing machine using a ( $\frac{1}{16}$ ) diameter hardened steel ball and a 62.5 kg applied load.

## **2.3 Microstructure and SEM Analysis**

The microstructure examination was carried out using a OLYMPUS DP12 optical metallurgical microscope equipped with a high-resolution digital camera for investigating the microstructure. The surface topography and fracture characteristics were studied using Scanning Electron Microscope (SEM) to understand the fracture mechanism and to detect the favorable sites for particle incorporation by using JSM-5410 Scanning Electron Microscope with a high-resolution of 3.5 nm, equipped with an energy dispersive X-ray spectrometer (EDXS).

## **2.4 Wear Test for the TiO<sub>2</sub> Nanoreinforced Alloy**

A PLINT TE 79 Multi Axial Tribometer Machine was used for measuring the friction force; friction coefficient and wear rate for the manufactured materials. A standard specimen with diameter of 8 and 20 mm length as a computerized Pin on disc machine used for friction & wear testing of materials is loaded vertically downwards onto the horizontal disc. The wear tests were then performed for the A356 cast material with the following parameters: velocity = 0.8 m/s, time = 1200 s and load = 10 N. The differences in the weight of the samples were taken as an indication of the wear resistance of the material.

# **3 Results and Discussion**

## **3.1 Mechanical Properties**

### **3.1.1 Effect of Nanoparticles Addition**

Figure 2 presents the mechanical properties (ultimate tensile strength (UTS), elongation% and hardness) of the produced castings with TiO<sub>2</sub> nanoparticles reinforcement.

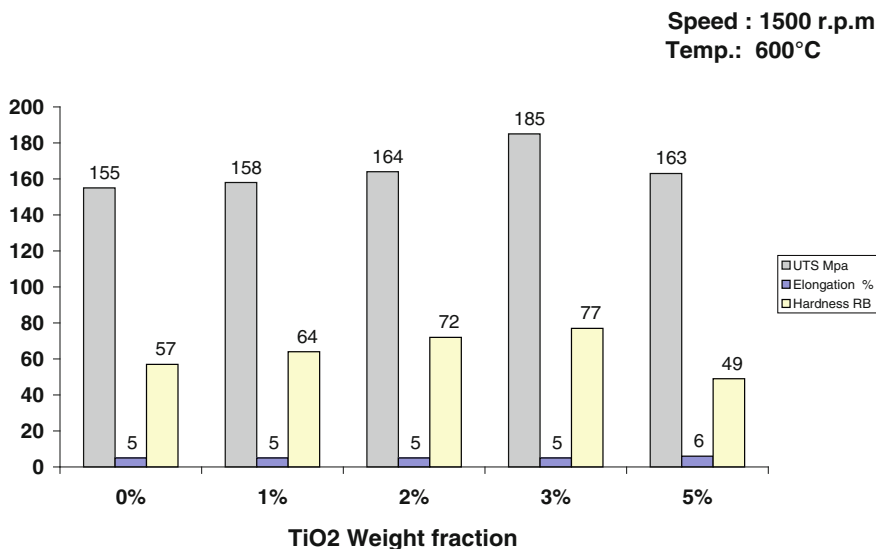


**Fig. 2** The effect of TiO<sub>2</sub> nanoparticles% on the UTS, hardness and ductility using 1500 rpm stirring speed at semi-solid state (600 °C)

Figure 2 shows that as the weight% of the TiO<sub>2</sub> nanoparticles increases up to 3 %, the UTS increases until reaching 185 MPa. Beyond this weight%, the UTS decreases with increase in the wt% of the TiO<sub>2</sub> nanoparticles. The ductility reaches its maximum with 3 wt% TiO<sub>2</sub> nanoparticles added, and then drops to a minimum value with 5 wt% TiO<sub>2</sub> nanoparticles added. The hardness reaches its minimum value of 49 HRB with the addition of 5 wt% TiO<sub>2</sub> nanoparticles, which means that the material becomes softer and this is supported by the drop in the strength.

The previous results show that the inclusion of 2–3 wt% nanoparticles increases the tensile strength of the nanoreinforced A356 alloy, as well as its ductility. Beyond this limit all properties drop. The observed increase in the strength of the A356 nanoreinforced alloys suggests a misfit effect in the lattice parameter of the matrix phase. This would be a result of cooling induced changes caused by the difference between the coefficients of thermal expansion between the primary phase (Al or Si) and the nanoparticles), resulting in an increase in the hardness of the first. The coefficients of thermal expansion are: ( $22.2 \times 10^{-6}$  m/m K for Al,  $3 \times 10^{-6}$  m/m K for Si,  $9 \times 10^{-6}$  m/m K for TiO<sub>2</sub> nanoparticles). Additionally, enhanced dislocation generation and reduced sub grain size owing to the presence of the nanoparticles may be contributing to the increased hardness of the aluminum phase. The increase in the hardness is also due not only to the mismatch in thermal expansion, but also the mismatch in elastic moduli of the nanoparticles. The addition of the nanoparticles also results in a constraint in the plastic flow of the matrix. The matrix could flow only with the movement of the nanoparticles or over the particles during plastic deformation. The matrix gets constrained considerably to

the plastic deformation because of smaller inter-particle distance and this results in higher degree of improvement in the flow stress.

Rapid quenching from the melt or solid state reaction have been identified as processing routes for obtaining nanostructured materials leading to two phase nanostructures, however, it is highly desirable to obtain such nanostructures directly in bulk form, e.g. through casting [27]. The current work focuses on the properties of nanodispersed A356 alloys obtained by rheocasting, which is a challenging production method for producing nanodispersed alloys. The potential for nanodispersed materials for being a high-tech material has been explored [28, 29] and it has been shown that the addition of nano-oxides results in improvements in the hardness, the tensile strength and the ductility of stir cast aluminium. This has been explained by the tendency of the oxide nanoparticles to agglomerate on the grain boundaries in columnar structures, whereas these oxide nanoparticles are more likely to disperse uniformly along the equiaxed structures resulting from stirring.

### 3.1.2 Effect of Stirring Speed

Figure 3 shows that as the stirring speed of nano TiO<sub>2</sub> reinforced casting increases to 1500 rpm, the UTS increases to reach 185 MPa. Beyond this stirring speed, the UTS decreases as the stirring speed increases possibly due to increase in internal

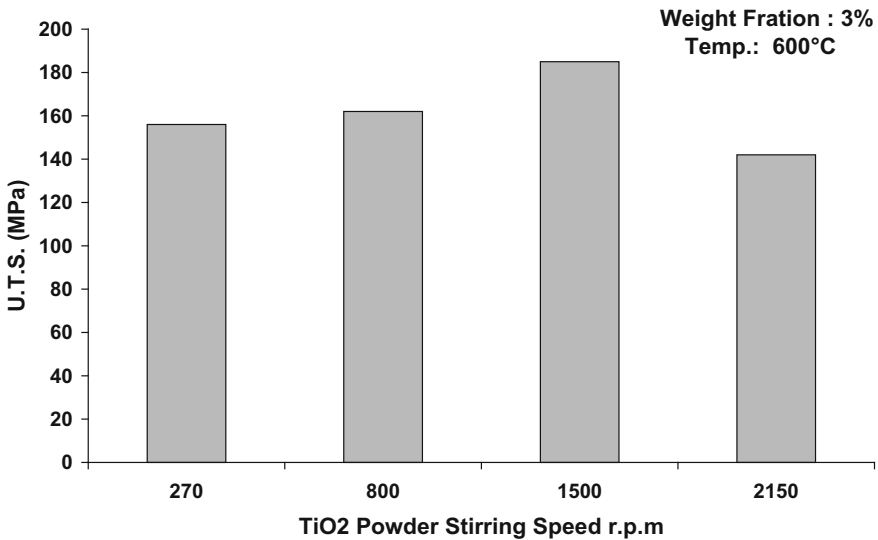


**Fig. 3** The effect of stirring speed on the UTS of 3 wt% TiO<sub>2</sub> nanoreinforced alloy at 600 °C

porosity [18] and cooling of the semi-solid slurry, as explained before. When increasing stirring speed beyond 850 rpm the ductility starts to increase. The ductility increases slightly at the stirring speed of 1500 rpm. At 2150 rpm stirring speed, the ductility reaches its minimum value; possibly due to the high porosity [18] content created in the composite. Again, the hardness at this stirring speed decreases after reaching its maximum value at 1500 rpm.

### 3.1.3 Effect of Casting Temperature

From Fig. 4, it is clear that the UTS reaches the maximum value for the semi-solid casting at 600 °C. As explained before, the beneficial role of the semi-solid state (mushy zone) in obtaining homogeneous distribution of the nanoparticles in the A356 matrix leads to better reinforcement of the matrix. The good reinforcement leads to higher UTS and higher ductility with a high hardness.

The improved strength and ductility exhibited by the nano-composites fabricated by the semi-solid method over that fabricated by liquid metallurgy (700 °C) method may be attributed to the high effective viscosity of the metal slurry that prevents particles from settling, floating, or agglomerating. This leads to better distribution of the ceramic phase and hence better mechanical properties.

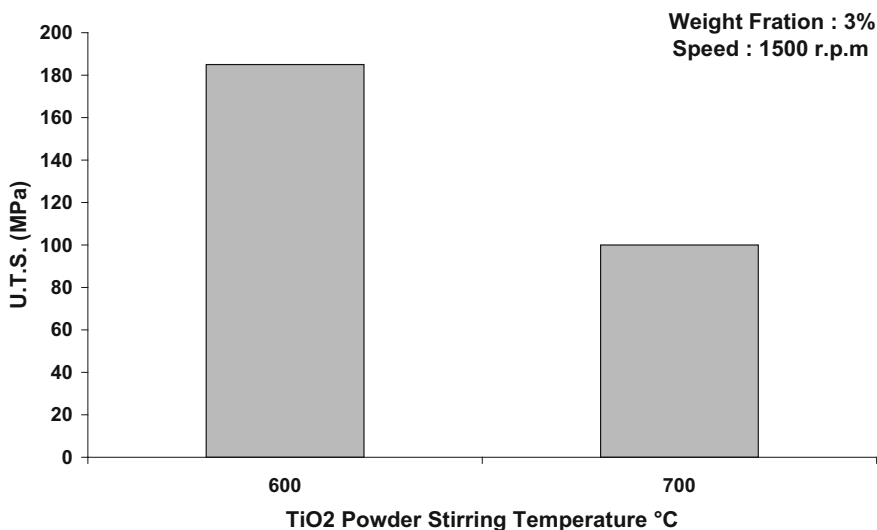
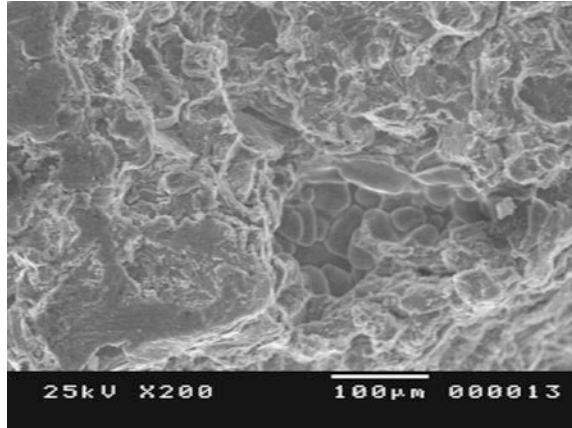


**Fig. 4** The effect of stirring temperature on the UTS of MMC with 3 wt% fraction of TiO<sub>2</sub> nano particles at 1500 rpm stirring speed

**Fig. 5** The (SEM) of the fracture surface specimen reinforced with 3 wt% TiO<sub>2</sub> nanoparticles



### 3.2 Microstructural Evolution

Figure 5 illustrates the brittle fracture surface of the specimen of the A356 alloy reinforced with 3 wt% TiO<sub>2</sub> which showed the optimum mechanical properties. It was difficult to detect TiO<sub>2</sub> nanoparticles; possibly due to the absence of agglomerated particles which could appear clearly.

### 3.3 Wear Test Results

The average-wear results of A356 samples reinforced with 0, 1, 2, 3 and 5 weight% TiO<sub>2</sub> nanoparticles are shown in Table 3. It can be seen from Table 3 that the addition of 1 weight% of nanoparticles resulted in a significant drop in friction coefficient, unaccompanied by any improvement in terms of weight loss. Increasing nanoparticles up to 5 % resulted in deterioration in wear resistance in terms of friction coefficient and weight loss, as also included from a previous research work [29, 30].

**Table 3** The average wear results of A356 samples reinforced with 0, 1, 2, 3 and 5 weight% TiO<sub>2</sub> nanopowder

Sample no.	Additions	Weight loss (mg)	Friction coefficient
1	A356	3.6	0.38
2	A356 + 1 % TiO <sub>2</sub>	4.0	0.36
3	A356 + 2 % TiO <sub>2</sub>	4.2	0.39
4	A356 + 3 % TiO <sub>2</sub>	4.6	0.41
5	A356 + 5 % TiO <sub>2</sub>	5.1	0.44



The results show that the addition of 1 weight% nanoparticles did not produce a significant change in the wear resistance of the hypo-eutectic alloy A356, though there was a reduction in the friction coefficient. The fact that the wear resistance deteriorated after adding 2, 3 and 5 weight% nanoparticles (though the hardness and strength increased) may be attributed to microstructural effects as well as the high load used in the test [30, 31].

## 4 Conclusion

- The castings made by adding nano-sized dispersoids using the semi-solid route exhibited better mechanical properties when compared with those prepared by liquid metallurgy route.
- The stirring speed has a significant effect on the mechanical properties of the nano-dispersed castings. Increasing stirring speed to more than 1500 rpm causes a reduction in the tensile strength. The alloy stirred with 1500 rpm exhibits the highest tensile strength and elongation%.
- The A356 matrix alloy reinforced with 3 % weight of  $\text{TiO}_2$  at the conditions of 1500 rpm stirring speed at the semi solid state temperature 600 °C has the highest mechanical properties.
- Analysis using scanning electron microscopy (SEM) at high magnification shows evidence for the possibility of incorporating and entrapping nano-sized particles within the interdendritic interface developing during the solidification of the dispersed alloys.
- The introduction of varying amounts of nanosized particles to the A356 alloy did not produce a significant change on the wear resistance of the tested hypo-eutectic alloy A356 material with 1 % nanoparticles and resulted in deterioration after adding 2, 3 and 5 % nanoparticles, though a drop in the friction coefficient occurred at 1 % addition.

**Acknowledgement** The authors would like to acknowledge the role of late Prof. Dr.-Ing. Y. Shash the head of Mechanical Design and Production Dept., Faculty of Engineering, Cairo University who advised and supported this work at its early stages.

## References

1. Kashyap K, Muralli S, Raman K, Murthy K (1993) Casting and heat treatment variables of Al-7Si-Mg alloy. *Mater Sci Technol* 9:189–203
2. Gruzleski E, Closset B (1990) The treatment of liquid Aluminium-Silicon alloys. AFS, Des Plaines, Illinois, pp 107–126
3. Cacers C (2000) Microstructure effects on the strength-ductility relationship of Al-7Si-Mg casting alloys. *Mater Sci Forum* 331:223–228

4. Rooy E (1992) ASM metals handbook, vol 15. Aluminum and aluminum alloys, Aluminum Company of America
5. Weixi S, Bo G, Tu G, Li S, Hao Y, Yu F (2010) Effect of neodymium on primary silicon and mechanical properties of hypereutectic Al-15 %Si alloy. *J Rare Earths*, vol 28. Spec. Issue, pp 367–370
6. Chen C, Liu Z, Ren B, Wang M, Weng Y, Liu Z (2007) Influences of complex modification of P and RE on microstructure and mechanical properties of hypereutectic Al-20Si alloy. *Trans Nonferrous Met SOCC China* 17:301–306
7. Dahle AK, Nogita K, McDonald SD, Dinnis C, Lu L (2005) Eutectic modification and microstructure development in Al–Si Alloys. *Mater Sci Eng A* 413–414:243–248
8. Cruz KS, Meza ES, Fernandes FAP, Quaresma JMV, Casteletti LC, Garcia A (2010) Dendritic arm spacing affecting mechanical properties and wear behavior of Al–Sn and Al–Si alloys directionally solidified under unsteady-state conditions. *Metall Mater Trans A* 41:972–984
9. Mehrabian R, Riek R, Flemings M (1974) Preparation and casting of metal-particulate non-metal composites. *Metall Trans* 5A:1899–1905
10. Eliasson J, Sandstorm R (1995) Applications of aluminium matrix composites. Part 1. In: Newaz GM, Neber-Aeschbacherand H, Wohlbier FH (eds). *Trans. Tech. publications, Switzerland*, pp 3–36
11. Rohatgi K, Asthana R, Das S (1986) Solidification, structure and properties of cast metal-ceramic particle composites. *Int Metals Rev* 31(3):115–139
12. Singh J, Alpas AT (1995) Elevated temperature wear of Al6061 and Al6061 20 % Al<sub>2</sub>O<sub>3</sub>. *Scripta Metall Mater* 32:1099–1105
13. Seyed Reihani SM (2006) Processing of squeeze cast Al6061–30vol% SiC composites and their characterization. *Mater Des* 27:216–222
14. Amir Khanlou S, Niroumand B (2011) Development of Al356/SiCp cast composites by injection of SiCp containing composite powders. *Mater Des* 32:1895–1902
15. Jerome S, Ravisankar B, Kumar Mahato P, Natarajan S (2010) Synthesis and evaluation of mechanical and high temperature tribological properties of in-situ Al–TiC composites. *Tribol Int* 43:2029–2036
16. El Mahallawi I, Egenfeld K, Kouta F, Hussein A, Mahmoud T, Rashad R, Shash A, Abou-AL-Hassan W (2008) Synthesis and characterization of new cast A356/ (Al<sub>2</sub>O<sub>3</sub>)p metal matrix nano- composites. In: *Proceedings of the 2nd multifunctional nanocomposites & nanomaterials: international conference& exhibition MN2008*, 11–13 Jan 2008, Cairo Egypt. Copyright © 2008 by ASME
17. El-Mahallawi I, Shash Y, Egenfeld K, Mahmoud T, Rashad R, Shash A, El Saeed M (2010) Influence of nano-dispersions on strength ductility properties of semi-solid cast A356 Al alloy. *Mater Sci Technol* 26(10):1226–1231
18. El-Mahallawi I, Abdelkader H, Yousef L, Amer A, Mayer J, Schwedt A (2012) Influence of Al<sub>2</sub>O<sub>3</sub> nanodispersions on microstructure features and mechanical properties of cast and T6 heat-treated Al Si hypoeutectic alloys. *Mater Sci Eng A* 556:76–87
19. El Mahallawi I, Shash Y, Rashad R, Abdelaziz M, Mayer J, Schwedt A (2014) Hardness and wear behavior of semi-solid cast A390 alloy reinforced with Al<sub>2</sub>O<sub>3</sub> and TiO<sub>2</sub> nanoparticles. *Arab J Sci Eng* 39:5171–5184
20. Mazahery A, Baharvandi HR, Abdizadeh H (2009) Development of high performance A356-nano Al<sub>2</sub>O<sub>3</sub> composites. *Mater Sci Eng A* 518:23–27
21. Sajjadi S, Ezatpour H, Beygi H (2011) Comparison of microstructure and mechanical properties of A356 aluminum alloy/Al<sub>2</sub>O<sub>3</sub> composites fabricated by stir and compo-casting processes. *Mater Sci Eng A* 528:8765–8771
22. Choi H, Konishi H, Li X (2012) Al<sub>2</sub>O<sub>3</sub> nanoparticles induced simultaneous refinement and modification of primary and eutectic Si particles in hypereutectic Al–20Si alloy. *Mater Sci Eng A* 541:159–165
23. Haizhi Y (2003) An overview of the development of Al-Si-alloy based material for engine applications. *J Mater Eng Perform JMEPEG* 12:288–297
24. Chawla K (2006) *Metal matrix composites*. Springer, Berlin

25. Balasivanandha Prabu S (2006) Influence of stirring speed and stirring time on distribution of particles in cast MMC. *J Mater Process Technol* 171:268–273
26. Shash A (2007) M. Sc. Thesis on “Effect of processing parameters on the mechanical characteristics of A356/(Al<sub>2</sub>O<sub>3</sub>)p cast metal matrix nano-composites (MMNCs)”, Cairo University
27. Koch C (2002) Nanostructured materials processing, properties and potential applications, pp 423–526
28. Kim G, Hong S, Lee M, Kim S, Ioka I, Kim B, Kim I (2010) Effect of oxide dispersion on dendritic grain growth characteristics of cast aluminum alloy. *Mater Trans* 51(10):1951–1957
29. Fadavi Boostani A, Tahamtan S, Jiang Z, Wei D, Yazdani S, Azari Khosroshahi R, Taherzadeh Mousavian R, Xu J, Zhang X, Gong D (2014) Enhanced tensile properties of aluminium matrix composites reinforced with graphene encapsulated SiC nanoparticles. *Composites: Part A*, Available online 14 October 2014
30. Shash Ahmed Y, Amer Amer E, El-Saeed Moataz (2015) Influence of Al<sub>2</sub>O<sub>3</sub> nano-dispersions on mechanical and wear resistance properties of semisolid cast A356 Al alloy, mechanical and materials engineering of modern structure and component design. *J Adv Struct Mater* 70: 13–24 (Springer International Publishing)
31. El-Mahallawi I, Shash A, Amer A (2015) Nanoreinforced cast Al-Si alloys with Al<sub>2</sub>O<sub>3</sub>, TiO<sub>2</sub> and ZrO<sub>2</sub> nanoparticles. *J Metals* 5(2):802–821

# Mechanical Properties and Wear Resistance of Semisolid Cast Al<sub>2</sub>O<sub>3</sub> Nano Reinforced Hypo and Hyper-eutectic Al–Si Composites

I.S. El-Mahallawi and A.Y. Shash

**Abstract** The present investigation studies the prospects of using nanoparticles as reinforcement ceramic powders to gain improved performance of hypo and hyper eutectic Al cast alloys. A series of castings were prepared using A356 and A390 as the matrix alloy and alumina nano-powder in 40 nm size as the reinforcement. The nanoparticles were added to the molten slurries with stirring with different fraction ratios ranging from (0, 1, 2 and 4 wt%) in the mushy zone using a constant stirring time for one minute. To evaluate the results, the alloys were further characterized by various tribological and mechanical characterization methods. The results showed higher strength values with improved ductility compared to the monolithic alloys under the same casting conditions. The results also showed improvement in the wear resistance of the nano-reinforced alloys. The scanning electron microscopy of the fracture surface and the wear surface revealed the presence of nanoparticles in the interdendritic spacing and this confirmed with EDX analysis of these particles. The data obtained from the experimental work in this study together with previous published work by the authors were statistically analyzed using analysis of variance (ANOVA) to define the significant factors on both ultimate tensile strength and ductility and their level of confidence, using the orthogonal array L8. Response surface methodology (RSM) was used to build a model relating the type of matrix and nanoparticles addition to the ultimate tensile strength (UTS). The results have shown that the percent of the nanoparticles additions have a significant effect on the tensile properties of the alloys.

**Keywords** Nano-metal matrix composites • Al<sub>2</sub>O<sub>3</sub> nano-powders • Wear resistance • Mushy zone • Mechanical stirring

---

I.S. El-Mahallawi  
Metallurgical Engineering Department, Faculty of Engineering, Cairo University,  
Giza, Egypt  
e-mail: ielmahallawi@bue.edu.eg

A.Y. Shash (✉)  
Mechanical Design and Production Department, Faculty of Engineering,  
Cairo University, Giza, Egypt  
e-mail: ahmed.shash@cu.edu.eg

## 1 Introduction

Composite materials are emerging chiefly in response to unprecedented demands from technology due to rapidly advancing activities in aircrafts, aerospace and automotive industries. These materials have low specific weight that makes their properties particularly superior in strength and modulus to many traditional engineering materials such as metals. Composite structures have shown universally savings of at least 20 % over metal counterparts and a lower operational and maintenance cost [1]. Aluminum based alloys and metal matrix composites (MMCs) exhibit attractive tribological and mechanical properties such as high specific modulus, good strength, long fatigue life, superior wear resistance and improved thermal stability, which allow these alloys to have numerous applications in the aerospace, automobile and military industries. The released data on the service life of composite structures shows that they maintain dimensional integrity, resist fatigue loading and are easily maintainable and repairable. Composites will continue to find new applications, but the large scale growth in the marketplace for these materials will require less costly processing methods and the prospect of recycling [2] will have to be solved [3].

As a result of intensive studies into the fundamental nature of materials and better understanding of their structure property relationship, it has become possible to develop new nanodispersed composite materials with improved physical and mechanical properties [4–8]. These new materials include high performance composites such as polymer matrix composites (PMCs), ceramic matrix composites (CMCs) and metal matrix composites (MMCs). Continuous advancements have led to the use of composite materials in more and more diversified applications. The importance of composites as engineering materials is reflected by the fact that out of over 1600 engineering materials available in the market today more than 200 are composites [6].

The challenge with manufacturing composite materials occurs in obtaining homogeneous distributions of the secondary phase which is usually a ceramic material. For most applications, a homogeneous distribution of the particles is desirable in order to maximize the mechanical properties [5, 7]. The manufacturing method also represents a challenge where researchers used both casting and powder metallurgy methods. Mechanical stir casting is a practical and economic method that has been used by researchers and industry to produce MMCs [4–8]. In order to achieve a good homogeneous distribution of a particle in the matrix, the process parameters related with the stir casting method were studied [4, 5, 7, 8]. The influence of stirring speed and stirring time on the distribution of the particles in MMCs has been investigated and Prabu [9] has recommended stirring speeds in the range of 500–700 rpm and the stirring times taken in the range 5–15 min.

Evidence of significant enhancement in strength and other properties of Al–Si cast alloys by incorporating nanoparticles have been recently presented, for example El-Mahallawi et al. [4–13] have shown that introducing  $\text{Al}_2\text{O}_3$  nano-ceramic particles to A356 and A390 alloys cast in the semi-solid state with

mechanical stirring has a beneficial effect on optimizing the strength–ductility relationship in these alloys. Mazahery et al. [10] used stir casting with a modified treatment for the added particles and have also shown significant improvement in hardness, 0.2 % yield strength, UTS and ductility of (A356) alloy. Rohatgi et al. [11] have predicted the significant role of producing Al–Si ceramic composites for bearings, pistons, cylinder liners, etc. leading to savings in materials and energy. Strengthening in nanostructured material is owed to having an appreciable fraction of their atoms in defect environments such as grain or interface boundaries [14].

Though previous studies have claimed enhanced mechanical properties for the rheocast and nanodispersed alloys relative to those produced by reinforcing with micro particles and conventional casting techniques [4–13], little work is done on evaluating the performance of these alloys related to real life applications [8, 15]. Therefore the aim of this research work is to evaluate the influence of the Al<sub>2</sub>O<sub>3</sub> nano particles dispersion on the mechanical and tribological properties of the A356 and A390 aluminum alloys cast in the semisolid state.

## 2 Experimental Procedures

The experimental work carried out through this scientific study consists of the following three stages:

- (a) Production of the new NMMC alloys.
- (b) Identification of the mechanical and wear resistance properties.
- (c) Characterization of the new material.

### 2.1 Materials Produced

The hypoeutectic alloy A356 and the hypereutectic A390 alloy were used as a base metal for the produced material having the following chemical composition illustrated in Table 1. The material used for reinforcement was 1, 2, and 4 % by weight Al<sub>2</sub>O<sub>3</sub> ceramic nano-particles with constant particle size of 40 nm, (provided by Nano-Tech Egypt), the description of which is given in Table 2.

**Table 1** Chemical composition (in wt%) of A356 cast Al–Si

Alloy	Chemical Composition (wt%)								
	Al	Si	Mg	Fe	Cu	Pb	Ti	Zn	Mn
A356	Bal.	7.44	0.3	0.27	0.02	0.022	–	0.01	Nil
A390	Bal.	17	0.45	0.5	4.5	–	0.2	0.1	0.1

**Table 2** Properties of Al<sub>2</sub>O<sub>3</sub> reinforcement powders

Reinforcement	$\gamma$ -Al <sub>2</sub> O <sub>3</sub>
Density (solid) (g/cm <sup>3</sup> )	3.95
Crystal structure	FCC
Appearance	White solid
Young's Modulus (GPa)	380
Average size (nm)	40
Melting point	2054 °C

## 2.2 Casting and Composite Manufacturing

### 2.2.1 Melting Furnace

An electric resistance furnace was designed and constructed for approaching this research work for preparing the NMMCs. It consists of a lift out ceramic crucible up to 5 kg, heating system, and is connected to a stirring mechanism with 3000 rpm max. rotating speed motor and adjustable height with a control unit up to 1200 °C connected to a thermocouple for controlling the stirring temperature as illustrated in Fig. 1.

### 2.3 Melting Methodology and Approach

A charge of 0.5 kg of the A356 alloy was introduced to the crucible and heated up to the melting temperature (640 °C). The melt was degassed and shielded with argon before pouring after reaching the liquid state to prevent oxidation of the molten metal. The melt was subsequently brought down to the semi-solid state by around 605 °C and hence the Al<sub>2</sub>O<sub>3</sub> nano- powders were preheated to 700 °C and then added to the melt simultaneously with mechanical stirring for 1 min at 1500 rpm. The fabrication conditions of the composites prepared in this

**Fig. 1** Schematic apparatus used for preparing the NMMCs

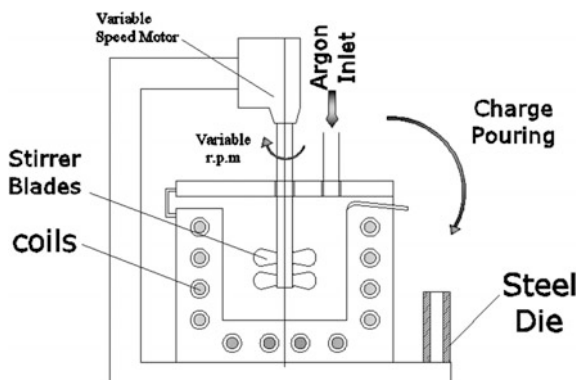


**Table 3** List of produced alloys and fabrication conditions

Melt No.	Additions	Stirring (rpm)	Pouring Temp. (semi-solid) (°C)
Melt 1	A356	1500	605
Melt 2	A356 + 1 % Al <sub>2</sub> O <sub>3</sub>	1500	605
Melt 3	A356 + 2 % Al <sub>2</sub> O <sub>3</sub>	1500	605
Melt 4	A356 + 4 % Al <sub>2</sub> O <sub>3</sub>	1500	605
Melt 5	A390	1000	660
Melt 6	A390 + 2 %	Al <sub>2</sub> O <sub>3</sub>	660

investigation are summarized in Table 3. Cast samples were poured in the prepared mould without additions and with additions of the different investigated Al<sub>2</sub>O<sub>3</sub> percentage.

Similarly, 3 kg charge of the hypereutectic base alloy was introduced to the crucible and heated up to above the melting temperature (730 °C). After reaching the liquid state the melt was degassed with either argon or hexachlorethane degasser tablet, to get rid of gases. After degassing the melt was brought down to 660 °C, and poured. 2 % Al<sub>2</sub>O<sub>3</sub> nanoparticles were prepared in packages of aluminium foil and preheated to about 600 °C, added at 660 °C, stirred for 1 min and poured. The packets were added to the melt through the opening in the top of the furnace one packet after the other, simultaneously with mechanical stirring for 1 min at 1000 rpm.

## 2.4 Mechanical Properties

Mechanical properties, mainly tensile strength, ductility, hardness and wear resistance were determined in the as-cast conditions for the investigated NMMC samples.

### 2.4.1 Tensile Test

The tensile tests were conducted on round tension test specimens of diameter 5.02 mm and gage length 25.2 mm using a universal testing machine according to DIN 50125. The elongation percent and ultimate tensile strength were calculated. The results were based on the average of three samples taken from each melt.

### 2.4.2 Hardness Test

The overall hardness of the A356 composite was measured by a Rockwell hardness testing machine, using a  $\left(\frac{1}{16}\right)''$  diameter hardened steel ball and a 62.5 kg applied load.



As for the A390 composite material, a Brinell hardness testing machine using 2.5 mm diameter hardened steel ball and 1839 N applied load was used. The reported results are the average of three reading for each case.

### **2.4.3 Wear Test**

A PLINT TE 79 multi axis tribometer machine was used for measuring the friction force; friction coefficient and wear rate for NMMC manufactured materials. In which a standard specimen with diameter of 8 mm and 20 mm length as a computerized pin on disc machine used for Friction and wear testing of materials is loaded vertically downwards onto the horizontal disc. The wear tests were then performed for the A356 composite material with the following parameters: velocity = 0.8 m/s, time = 1200 s and load = 10 N. The differences in the weight of the samples were taken as an indication of the wear resistance of the material.

The wear test conditions for the A390 composite material is presented elsewhere [7].

## **2.5 Material Characterization**

### **2.5.1 Microstructural Study**

Representative sections from the cast samples were cut into 3 pieces: the 1st from the top, the 2nd from the middle and the 3rd from the bottom. Samples were wet grounded on a rotating disc using silicon carbide abrasive discs of increasing fineness (120, 180, 220, 320, 400, 600, 800, 1000 and 1200 grit). Then they were polished using 10  $\mu\text{m}$  alumina paste.

### **2.5.2 Optical Microscopy (OM)**

The microstructure examination was carried out using an OLYMPUS DP12 optical metallurgical microscope, equipped with a high resolution digital camera for microstructural investigations.

### **2.5.3 Scanning Electron Microscopy (SEM)**

The surface topography and fracture characteristics were studied using SEM to understand the fracture mechanism and also to detect the favorable sites for particle incorporation in the Gemeinschaftslabor fuer Metallographie, RWTH-Aachen University by using a JSM-5410 and JSM-7000F FEG-SEM. Both microscopes are high-performance multipurpose SEM with a high-resolution of 3.5 nm, and EDXS

(energy dispersive X-ray spectrometer), with automated features including auto focus/auto stigmator, and automatic contrast and brightness. The EDS expands the function from morphological observation to multi-purpose high-resolution elemental analysis.

### 2.6 Statistical Analysis

Statistical analysis by using ANOVA was used to find the significant factor affecting on tensile strength. The data used was based on the experimental data obtained from this work, in addition to previous work by the authors [4–8]. Material type (Si content), pouring temperature and nanoparticles percent were the factors used in the orthogonal array L8 and the ultimate tensile strength (UTS) and the elongation % were the response.

## 3 Results

### 3.1 Mechanical Properties of the NMMC

Figures 2 and 3 illustrate the mechanical properties (tensile strength, elongation% and hardness) of the produced castings with reinforced Al<sub>2</sub>O<sub>3</sub> nanoparticles in A356 and A390 metal matrix, respectively.

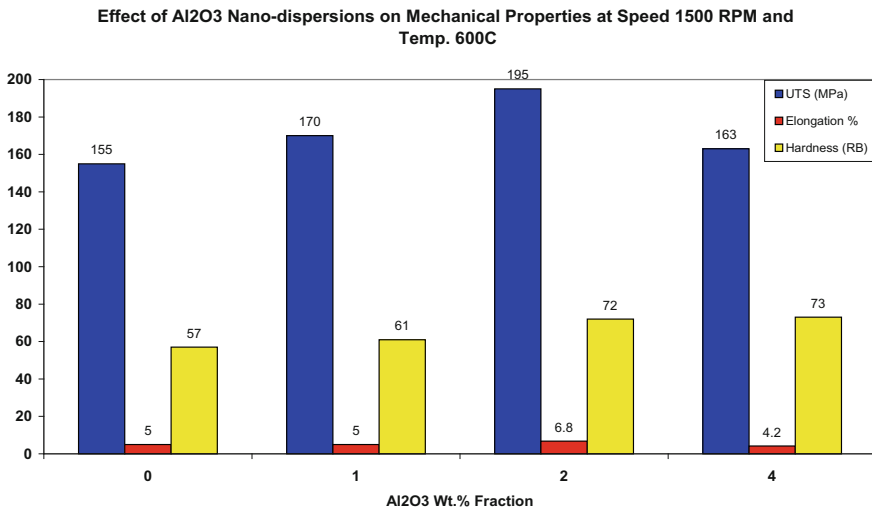


**Fig. 2** The effect of wt% fraction of Al<sub>2</sub>O<sub>3</sub> nano-powders in A356 on the UTS, elongation % and Hardness of MMC at 1500 rpm stirring speed at semi-solid state (600 °C)

**Effect of Al<sub>2</sub>O<sub>3</sub> Nano-dispersions on Mechanical Properties at speed 1000 RPM and Temp. 660C**

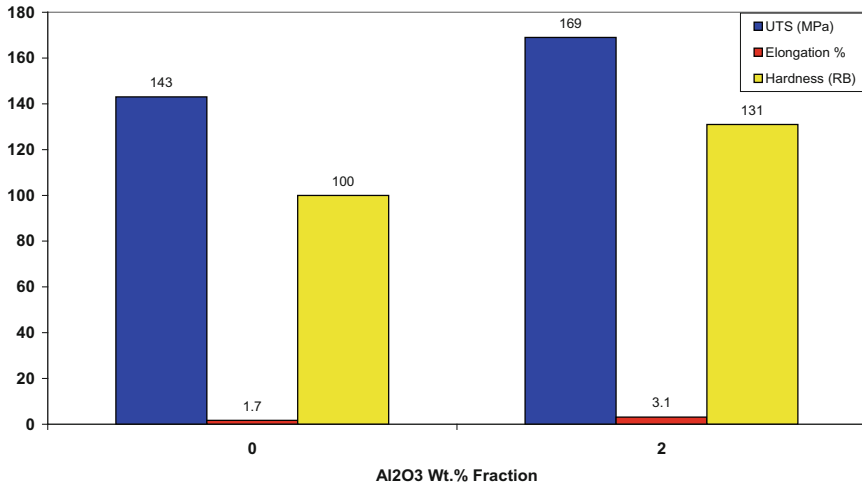


**Fig. 3** The effect of 2 wt% of Al<sub>2</sub>O<sub>3</sub> nano-powders in A390 on the UTS, elongation % and Hardness of MMC at 1000 rpm stirring speed at semi-solid state (660 °C)

It is shown in Fig. 2 that as the fraction of Al<sub>2</sub>O<sub>3</sub> nanopowder (wt%) increases, up to a value of 2 wt% of Al<sub>2</sub>O<sub>3</sub>, the UTS increases reaching 195 MPa. Beyond this weight fraction, the UTS decreases as the wt% increases. As shown in Fig. 2, increasing the weight fraction of Al<sub>2</sub>O<sub>3</sub> has no visible effect on ductility until reaching 1 wt%, then with increasing the wt% beyond 1 wt% the ductility increases. The ductility of NMMC increases by about 40 % at 2 wt% of Al<sub>2</sub>O<sub>3</sub> nanoparticles. At 4 wt% fraction, the ductility reaches its minimum values; probably due to the agglomeration of the dispersed particles in the NMMC, while its hardness at this weight fraction increases by about 30 % as shown in Fig. 2. The presence of the ceramic agglomerates increases the hardness of the alloys and hence, reduces the ductility of the composites in comparison with the matrix alloy.

The enhanced strength properties along with good ductility which are observed in these alloys (with 1 and 2 wt% nanoparticles) probably originate from the fine distribution of globular particles in an A356 matrix on a nanometer scale, where the globular particles act as strength bearing components, while the A356 matrix supplies ductility. The existence of a crystalline approximant phase at the interface between the particles and the FCC Al matrix improves interfacial bonding between the different phases, leading to the combination of high strength and good ductility without failure at the interface [13].

Similar results were obtained for the A390 composite alloy where an increase of 18 % occurred in the tensile strength and 82 % in the ductility and 31 % in the hardness after adding 2 wt% nanoparticles.

The observed increase in the hardness of the A356 and A390 nano-reinforced alloys suggests a misfit effect in the lattice parameter of the matrix phase, due to cooling induced changes caused by the difference between the coefficients of thermal expansion between the primary phase (Al or Si) and the nanoparticles: ( $3 \times 10^{-6}$  m/m K, for Si and  $5.4 \times 10^{-6}$  for  $Al_2O_3$  nanoparticles), resulting in an increase in the hardness of the first. Additionally, enhanced dislocation generation and reduced sub grain size owing to the presence of the nanoparticles may be contributing to the increased hardness for the aluminium phase.

### 3.2 Statistical Analysis

ANOVA technique was applied on the responses to find the factors (f) and compare it with the tabulated values at the levels of confidence (90, 95, and 99 %). Response surface methodology (RSM) is the technique used to build models to correlate the responses and factors. Table 4 shows the orthogonal array L8 that was used to apply the ANOVA technique.

The obtained results showed that nano-reinforcement is significant at 99 %. The silicon content (type of alloy) is significant at 95 %.

The Anova analysis has shown that the following equations may be used to predict the mechanical properties of nano-reinforced AlSi alloys:

$$UTS = UTS \text{ (monolithic alloy)} + 14 \times \text{Nano\%} - 0.57 \text{ stirring temp} + 0.0383 \times (\text{Si} * \text{semi-solid temp})$$

$$\text{Elongation \%} = \text{Elongation \% (monolithic alloy)} + 0.5812 \times \text{Nano\%} - 0.0561 \times \text{semisolid temp} + 0.0042 \times (\text{Si} * \text{semi-solid temp})$$

Figure 4 shows the comparison between the UTS and elongation % predicted by these equations and the measured values for the experimental alloys prepared in this work.

### 3.3 Microstructure Study

Figure 5a, b shows the optical microstructure of the base matrix A356 alloys reinforced with 2 wt% fraction of  $Al_2O_3$  nano-powder. Also, the optical microstructure

**Table 4** Factors levels for ANOVA Analysis

Factor	Level 1	Level 2
Si%	0	2
Nanoparticle%	0	2
Semi-solid pouring temp	0	2

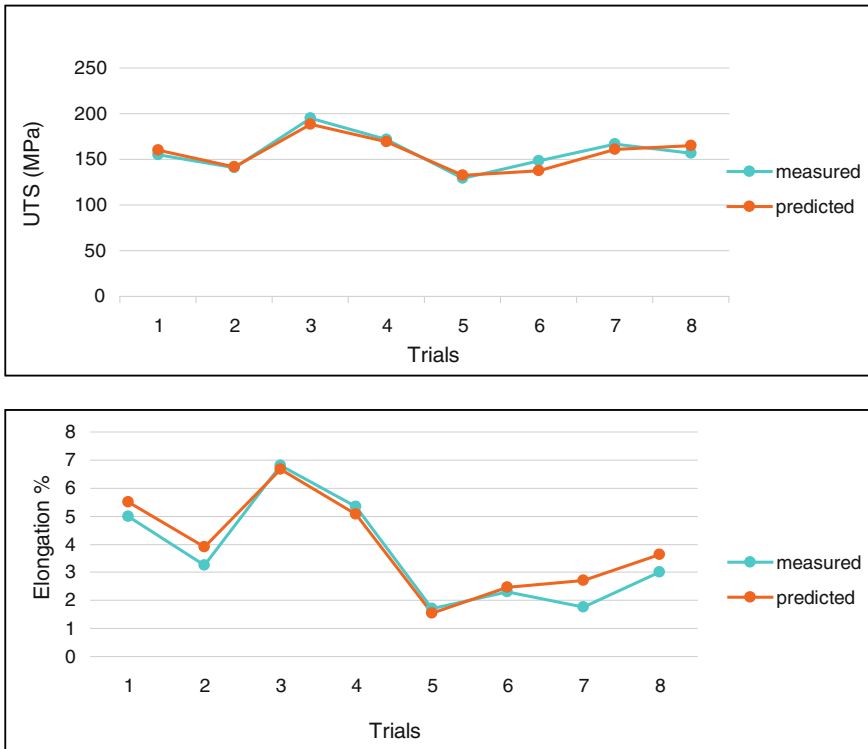


**Fig. 4** Comparison between measured and predicted data for UTS and Elongation %

of the base matrix A390 alloys reinforced with 2 wt% fraction of  $\text{Al}_2\text{O}_3$  nano-powder is shown in Fig. 6a, b. The microstructures of the two castings show that the phases in A356 are uniformly distributed consisting of primary aluminium and eutectic structure, whereas it includes primary Si particles too in the A390 composite material. It also shows clearly a morphological change in the microstructures. In the base matrix sample, the microstructure is dendritic whereas in the other rheocast samples, some of the primary dendrites change to globular structures due to mechanical stirring.

As the structure contains good amount of eutectic phases it should give a range of mechanical properties when mechanical stirring processed [7, 14]. This was clear in the mechanical properties of alloys reinforced with nano-powder using mechanical stirring. It was also observed from the metallographic pictures and applying image analyzer technique that by increasing the stirring speed and the quantity of nano-dispersions, the eutectic phases would decrease by around 10 %.

The SEM illustrated in Figs. 7 and 8 show a typical fracture surface for a specimen reinforced with 2 wt% fraction of  $\text{Al}_2\text{O}_3$  in A356 and A390, respectively. The fracture surface shows a mixture of dendrites and globular structures. Agglomerated nanoparticles also appear. The agglomeration could happen by the

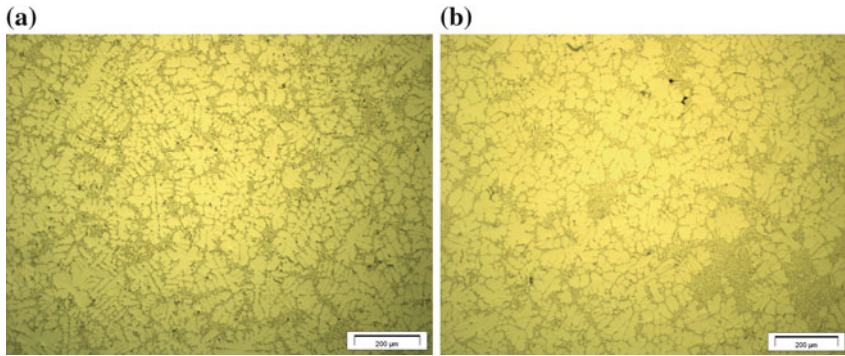


**Fig. 5** The optical microstructure of **a** Base matrix A356 alloys **b** Reinforced with 2 wt% fraction of Al<sub>2</sub>O<sub>3</sub> nano-powders

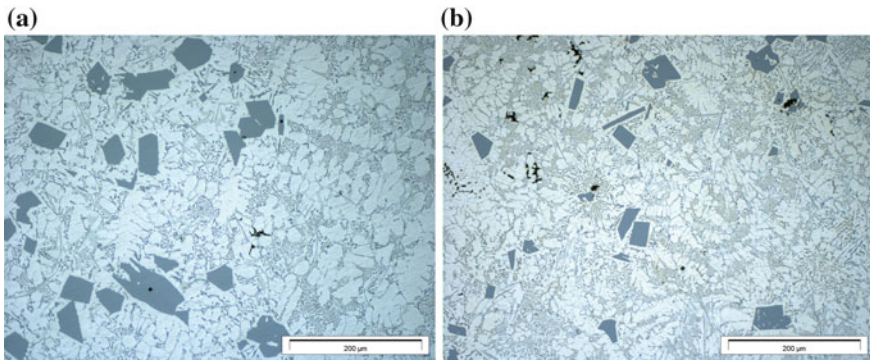


**Fig. 6** The optical microstructure of **a** Base matrix A390 alloys **b** Reinforced with 2 wt% fraction of Al<sub>2</sub>O<sub>3</sub> nano-powders

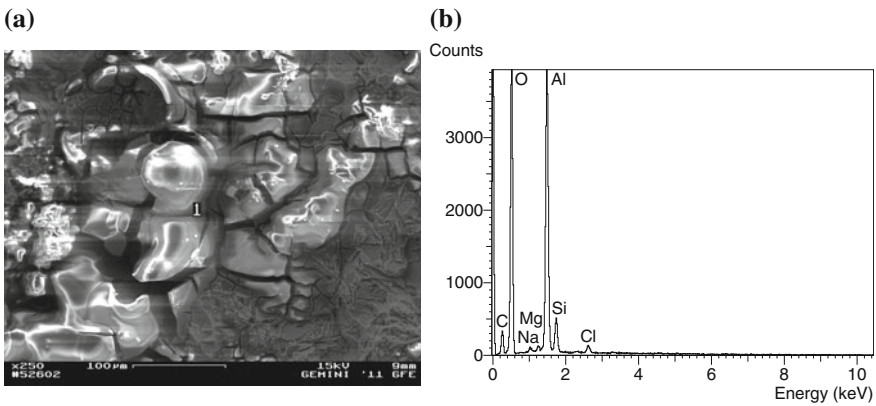


**Fig. 7** **a** SEM of the fracture surface A356 specimen reinforced with 2 %wt fraction of Al<sub>2</sub>O<sub>3</sub> nano-powder. **b** EDX of Al<sub>2</sub>O<sub>3</sub> agglomerated particles

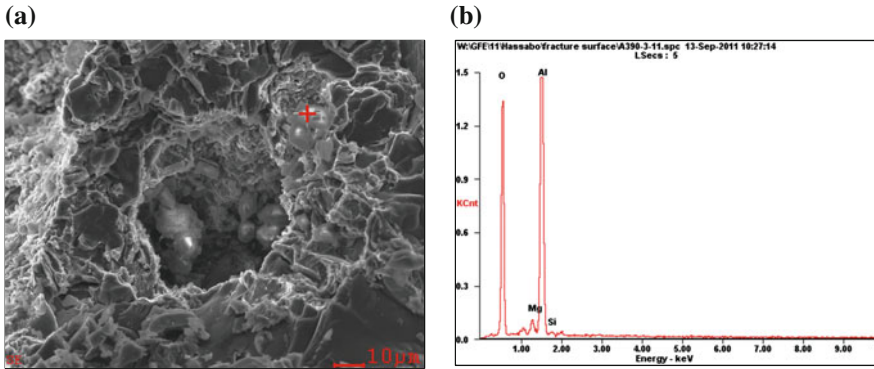


**Fig. 8** a SEM of the fracture surface A390 specimen reinforced with 2 %wt fraction of  $\text{Al}_2\text{O}_3$  nano-powder. b EDX of  $\text{Al}_2\text{O}_3$  agglomerated particles

**Table 5** Specified analysis of the EDX of  $\text{Al}_2\text{O}_3$  agglomerated particles

Label	Range (keV)	Gross	Net	Total %
O Ka	0.407–0.668	5459	3149	38.1
Al Ka	1.327–1.628	5942	4222	51.1
Si Ka	1.648–1.888	2347	891	10.8

particles reinforced inside the matrix during the melting stage. Moreover, these agglomerated particles were not homogeneously distributed inside the matrix.  $\text{Al}_2\text{O}_3$  agglomerated particles have a size less than  $1 \mu\text{m}$  attached in the interdendritic space for the A356 composite alloy and bonded to the primary Si particles for the A390 composite alloy. The EDX analysis shown in Figs. 7b and 8b, has evidently confirmed that these are  $\text{Al}_2\text{O}_3$  particles though a strong reflection from the matrix was inevitable. The specified analysis of the EDX and the percentage of O, Al and S are illustrated in Table 5. It is clear that the high percentage of the oxygen and aluminum, confirms the presence of  $\text{Al}_2\text{O}_3$  nano-powders in the matrix.

The fracture surface of the nano-dispersed hypereutectic alloys agrees with previous findings [13] and shows that the major mechanism of fracture is the breakage of the faceted Si particles and the debonding at the interfaces between Al phase and Si particles, where the crack crosses the cleavage planes in the primary Si particles round with the eutectic Al and Si regions. The nano-particles adhere themselves to the primary Si particles in several locations (whereas in the case of the hypoeutectic alloy A356 they were found in interdendritic locations). This is explained in view of the solidification effective mechanisms for both cases where dendrite growth in the process of solidification tends not to include the impurity into the crystal, but to push the oxide nano-particles and the impurity into the residual melt [16]. On the other side, in the case of equiaxed structures a part of remained

**Table 6** Average wear results of A356 samples reinforced with 0, 1, 2 and 4 wt% Al<sub>2</sub>O<sub>3</sub> nanopowder

Sample no.	Additions	Weight loss (mg)	Friction coefficient
1	A356	3.9	0.4
2	A356 + 1 % Al <sub>2</sub> O <sub>3</sub>	4.0	0.361
3	A356 + 2 % Al <sub>2</sub> O <sub>3</sub>	4.5	0.385
4	A356 + 4 % Al <sub>2</sub> O <sub>3</sub>	5.5	0.430

liquid including oxide nano-particles is blocked inside the grain attaching themselves to the primary silicon particles [8, 16].

### 3.4 Results of Wear Test

The average wear results of A356 samples reinforced with 0, 1, 2 and 4 wt% Al<sub>2</sub>O<sub>3</sub> nanoparticles are shown in Table 6. It can be seen from Table 6 that the addition of 1 % nanoparticles resulted in a significant drop in the friction coefficient, unaccompanied with any improvement in terms of weight loss. Increasing nanoparticles up to 4 % resulted in a deterioration in the wear resistance in terms of friction coefficient and weight loss.

The results show that the addition of 1 % nano-particles did not produce a significant change on the wear resistance of the hypo-eutectic alloy A356, though there was a reduction in the friction coefficient. The fact that the wear resistance deteriorated after adding 2 and 4 % nanoparticles (though the hardness and strength increased) may be attributed to microstructural effects as well as the high load used in the test. Previous work by the authors on A390 alloy [7] has shown that the wear resistance of nano reinforced A390 was enhanced compared to monolithic A390 alloy, which has been attributed to higher hardness resulting from refinement in microstructural constituents. The main wear mechanism observed [7] was delamination and tearing. Other work [15] has reported enhancement in the wear resistance of A356 rheocast alloy compared to those obtained by conventional casting, which has been attributed to the equiaxed structure obtained by rheocasting. The main wear mechanism was found to be ploughing at small stresses and mixed ploughing and delamination at high stresses. However, no data has been found to evaluate the wear performance of the rheocast nanodispersed A356 alloy.

The samples subjected to wear tests have been examined using SEM. Figure 9a, b shows clearly the Al<sub>2</sub>O<sub>3</sub> nano-particles distributed on the surface of samples with 1 and 4 wt% Al<sub>2</sub>O<sub>3</sub> addition subjected to wear, respectively. The figure also shows that the dominant wear mechanism was a combination of adhesion and delamination mechanisms, similar to findings in a previous work for hypereutectic AlSi alloy A390 [7].



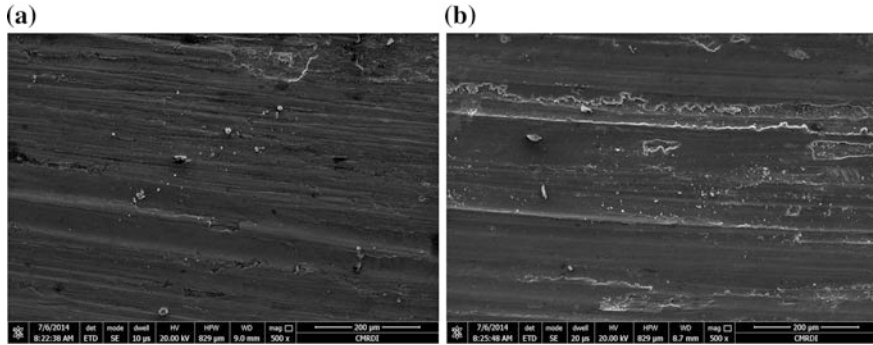


**Fig. 9** SEM image for wear surface of **a** 1wt%  $\text{Al}_2\text{O}_3$  and **b** 2 wt%  $\text{Al}_2\text{O}_3$  nano-particles

The nano-composites manufactured using the semi-solid route exhibited better mechanical properties when compared with those prepared by the liquid metallurgy route. Also, a high mixing speed is required in order to obtain a good distribution of the particles reinforced and to introduce it inside the matrix as introducing the reinforced  $\text{Al}_2\text{O}_3$  particles to the A356 matrix in the semi solid state is difficult due to the higher density of the matrix at this state, in which the alloys stirred with 1500 rpm exhibits the best tensile strength and elongation.

The A356 matrix alloy reinforced with 2 wt% fraction of  $\text{Al}_2\text{O}_3$  nano-powder has the best tensile strength properties at conditions of 1500 rpm stirring speed at semi solid state temperature 600 °C. The wear resistance increases as the weight percentage of the reinforced nano-particles increases. The wear resistance results were evidently confirmed by increasing the hardness and decreasing the friction coefficient values as the wt% of the nano-dispersions increases.

In the base matrix sample without stirring, the microstructure is dendritic whereas in the other rheocast samples, the primary dendrites are fragmented due to mechanical stirring which explains the improvement in the mechanical properties. Analysis using both scanning electron microscope and high magnification shows evidence for the possibility of incorporating and entrapping nano-sized particles within the interdendritic interface developing during the solidification of the dispersed alloys.

## 4 Discussions

Rapid quenching from the melt or solid state reaction have been identified as processing routes for obtaining nanostructured materials leading to two phase nanostructures, however, it is highly desirable to obtain such nanostructures directly in bulk form, e.g. through casting [14]. The current work focuses on the properties of nanodispersed A356 and A390 alloys obtained by rheocasting, which is a

challenging production method for producing nanodispersed alloys. The potential for nanodispersed materials for being high-tech material has been explored [16] and it has been shown that the addition of nano oxides results in the improvement in both the hardness and the tensile strength of stir cast aluminium, which has been explained by the tendency of oxide nanoparticles to agglomerate at the grain boundaries in the columnar structures, whereas these oxide nanoparticles are uniformly dispersed in the equiaxed structure resulting from stirring.

The difference between the wear performance of the nanodispersed hypo and hyper eutectic alloys (reported in this work) may be explained by the effect of the nano particles additions on both alloys. The addition of nanoparticles promotes the formation of the  $\alpha$ -Al phase and has been attributed to the improved nucleation of Si particles and depletion of Si element near the Si particles [8, 17]. This would produce a deterioration effect on the wear resistance of the hypo-eutectic alloys, whereas the effect would be less significant on the hyper-eutectic alloys, since the morphology of the Si particles and the shape of the  $\alpha$ -Al, as well as the morphology of the eutectic Si have a major contribution. It has been stated [17] that the cracks easily initiate inside the brittle primary Si or eutectic Si, and then propagate through boundaries with  $\alpha$ -Al phase, thus the change in the Si morphology (according to restricted nucleation and growth theory of modification), and the crystalline appearance of the  $\alpha$ -Al phase would improve the wear resistance for the hyper-eutectic alloys [8]. Also, the addition of nanoparticles to the hypereutectic alloys has been shown to produce a refining effect on the primary silicon particles, which has been attributed to increasing the nucleation sites [17] or inducing a thermal sub-cooling effect.

It has been shown [4–8] that nanodispersed aluminium alloys have refined microstructural constituents (Al dendrites, interlamellar spacing and primary Si particles) compared to their monolithic counterparts. The mechanical strength of crystalline metals or alloys is largely controlled by the grain size “d”. The well known empirical Hall–Petch equation relates the yield strength “ $\sigma_y$ ” to the average grain size “d” according to  $\sigma_y = \sigma_0 + k d^{-1/2}$ . Where  $\sigma_0$  is the friction stress and k is a constant. A similar relation exists between the hardness and the grain size. Consequently, reducing “d” to the nanometer regime increases the strength considerably. However, the limits of the conventional description of yielding and of new mechanisms that may occur at these small dimensions need to be explored and studied in much more detail [14].

Nanodispersed cast structures carry both natures of composites and refined structures. It is important at this stage to understand the active strengthening mechanisms in these materials as this will be the key to develop new structures.

The known models addressing the incorporation of particles into a solidifying matrix have been identified [18] to be: (i) the kinetic models based on the interaction between the velocity of the solid/liquid interface and the velocity of the particle, (ii) the thermodynamic models which are closely related to classical heterogeneous nucleation theory and (iii) the models based on the ratio of the thermophysical properties of the particles and the melt. A good correlation among all three models [19] has integrated many of the effective parameters and has

suggested that there are three possible pathways for nanoparticle capture: viscous capture, Brownian capture and spontaneous capture. Viscous capture occurs under conditions of extremely high cooling rates or increased viscosity of the melt. Brownian capture is likely to occur when the nanoparticles have slightly lower Hamaker constants than the melt. Spontaneous capture was proposed as the most favorable for nanoparticle capture during solidification of metal melt, the key being to select or design/fabricate suitable nanoparticles that offer a higher Hamaker constant than that of the liquid metal [19]. However, the problem with these models is that they consider capturing of the nanoparticles but ignore strengthening mechanisms for the proposed matrix/reinforcement combinations.

This work and other work have shown that adding nanoparticles to metal matrix composites (A356 and A390 in this case) has significant potential of enhancing both strength and ductility. The addition of ceramic particles to aluminium alloys raises the viscosity very quickly [20] providing suitable conditions for particle capture, moreover the  $\text{Al}_2\text{O}_3$  nanoparticles have been shown to possess appropriate properties that are compatible with the Al alloy, namely relatively high thermal conductivity and thermal expansion coefficients that affects its role as a nanodispersion for reinforcement in the Al alloy matrix [4–8]. It has been shown [20, 21] that in eutectic and hypereutectic matrix alloys, such as Al-Si, particle capture take place for all growth conditions, whereas, in hypoeutectic Al alloy systems, where a non-planar solid-liquid interface is typically present, particle pushing takes place. The classical theory for strengthening in dispersed structures forming composites [17, 20, 21] is based on the dislocation motion being constrained by the precipitates and dispersoid particles. These particles form coherency strains and dislocation networks around them, leading to a misfit between the particles and the matrix which causes the hardness and strength to increase. The usual drop in ductility associated with increase in strength is explained by the fact that dislocations move on specific slip planes under the action of a shear stress. If the slip plane has obstacles penetrating it, e.g., precipitates or dispersoids, a dislocation moving on this slip plane must interact with these obstacles. The high volume fraction of interfacial regions offered by the nanodispersion causes the improvement in ductility where grain boundary sliding becomes the major deformation mechanism [14].

## 5 Conclusion

1. The introduction of 2 % nano-sized particles leads to an increase in the hardness of the A356 alloy from about 57 HB to 72 RB, the tensile strength from 155 to 195 MPa, and the elongation% from 5 to 6.8 %; and the increase in the tensile strength of A390 alloy from 143 to 169 and the elongation % from 1.7 to 3.1 and the hardness from 100 to 131 HB.
2. The addition of nano particles promote the formation of Al phase and decrease in the amount of eutectic structure.

3. The introduction of varying amounts of nano-sized particles to the A356 alloy did not produce a significant change on the wear resistance of the tested hypo-eutectic alloy A356 material with 1 % nanoparticles and resulted deterioration after adding 2 and 4 % nanoparticles, though a drop in the friction coefficient occurred at 1 % addition [17]. While, the wear resistance of nano reinforced A390 was enhanced compared to monolithic A390 alloy after adding 1 % nanoparticles. This behavior is attributed to microstructural effects in both alloys, where nano additions promote Al phase formation for the hypoeutectic alloys, whereas their refining effect is more pronounced for the hypereutectic alloys.
4. It is possible to predict the UTS and elongation % of nanodispersed composite materials using equations developed by ANOVA analysis. These equations show that nanoparticles addition up to 2 % and the semisolid pouring temperature are the main controlling parameters.
5. Nanoparticles are pushed to interdendritic locations during the solidification of hypoeutectic AlSi alloys systems, and tend to adhere to primary Si particles during the solidification of hypereutectic alloys.

**Acknowledgement** The authors would like to acknowledge the role of late Prof. Dr.-Ing. Y. Shash the head of Mechanical Design and Production Dept., Faculty of Engineering, Cairo University who advised and supported this work at its early stages. Great thanks go also for Dr. M. El-Saeed, Eng. M. Hassabo and Eng. A. Abdel-Fatah for offering data to this scientific work.

## References

1. Dhingra A (1986) Metal replacement by composite. JOM 38(03):17
2. Mehrabian R, Riek R, Flemings M (1974) Preparation and casting of metal-particulate non-metal composites. Metall Trans 5A:1899–1905
3. Eliasson J, Sandstorm R (1995) Applications of aluminium matrix composites. Part 1, Newaz GM, Neber-Aeschbacherand H, Wohlbiel FH (eds). Trans. Tech. publications, Switzerland, pp 3–36
4. El-Mahallawi I, Eigenfeld K, Kouta F, Hussein A, Mahmoud T, Rashad R, Shash A, Abou-AL-Hassan W (2008) Synthesis and characterization of new cast A356/ (Al<sub>2</sub>O<sub>3</sub>) p metal matrix nano- composites. In: Proceedings of the 2nd multifunctional nanocomposites & nanomaterials: international conference& exhibition MN2008, 11–13 Jan 2008, Cairo Egypt. Copyright © by ASME
5. El-Mahallawi I, Shash Y, Eigenfeld K, Mahmoud T, Rashad R, Shash A, El Saeed M (2010) “Influence of nano-dispersions on strength ductility properties of semi-solid cast A356 Al alloy. Mater Sci Technol 26(10):1226–1231
6. El-Mahallawi I, Abdelkader H, Yousef L, Amer A, Mayer J, Schwedt A (2012) Influence of Al<sub>2</sub>O<sub>3</sub> nano-dispersions on microstructure features and mechanical properties of cast and T6 heat-treated AlSi hypoeutectic alloys. Mater Sci Eng A A556:76–82
7. El Mahallawi I, Shash Y, Rashad R, Abdelaziz M, Mayer J, Schwedt A (2014) Hardness and wear behaviour of semi-solid cast A390 alloy reinforced with Al<sub>2</sub>O<sub>3</sub> and TiO<sub>2</sub> nanoparticles. Arab J Sci Eng 39(6):5171–5184
8. El Mahallawi I, Othman O, Abdelaziz M, Raed H, Abd El-Fatah T, Ali S (2014) Understanding the role of nanodispersions on the properties of A390 hyper-eutectic Al-Si cast alloy. TMS Light Metals 1361–1365

9. Prabu S (2006) Influence of stirring speed and stirring time on distribution of particles in cast MMC. *J Mater Process Technol* 171:268–273
10. Mazahery A, Baharvandi H, Abdizadeh H (2009) Development of high performance A356-nano Al<sub>2</sub>O<sub>3</sub> composites. *Mater Sci Eng A* 518:23–27
11. Rohatgi K, Asthana R, Das S (1986) Solidification, structure and properties of cast metal-ceramic particle composites. *Int Metals Rev* 31(3):115–139
12. Zhao J, Wu S (2010) Microstructure and mechanical properties of rheo-diecasted A390 alloy. *Trans Nonferrous Met Soc China* 20:754–757
13. Choi H, Konishi H, Li X (2012) Al<sub>2</sub>O<sub>3</sub> nanoparticles induced simultaneous refinement and modification of primary and eutectic Si particles in hypereutectic Al–20Si alloy. *Mater Sci Eng A* 541:159–165
14. Koch C (2002) Nanostructured materials processing, properties and potential applications, pp 423–526
15. Dey A, Poddar P, Singh K, Sahoo K (2006) Mechanical and wear properties of rheocast and conventional gravity die cast A356 alloy. *Mater Sci Eng A* 435–436:521–529
16. Kim G, Hong S, Lee M, Kim S, Ioka I, Kim B, Kim I (2010) Effect of oxide dispersion on dendritic grain growth characteristics of cast aluminum alloy. *Mater Trans* 51(10):1951–1957
17. El-Mahallawi I, Shash A, Amer A (2015) Nanoreinforced cast Al-Si alloys with Al<sub>2</sub>O<sub>3</sub>, TiO<sub>2</sub> and ZrO<sub>2</sub> nanoparticles. *J Metals* 5(2):802–821
18. Boostani A, Tahamtan S, Jiang Z, Wei D, Yazdani S, Azari Khosroshahi R, Taherzadeh Mousavian R, Xu J, Zhang X, Gong D (2014) Enhanced tensile properties of aluminium matrix composites reinforced with graphene encapsulated SiC nanoparticles. *Composites: Part A*
19. Xu J, Chen L, Choi H, Li X (2012) Theoretical study and pathways for nanoparticle capture during solidification of metal melt. *J Phys Condensed Matter* 24:255304 (10 pp)
20. Chawla K (2006) METAL MATRIX COMPOSITES. Springer, Berlin
21. Shash A, Amer A, El-Saeed M (2015) “Influence of Al<sub>2</sub>O<sub>3</sub> nano-dispersions on mechanical and wear resistance properties of semisolid cast A356 Al alloy”, mechanical and materials engineering of modern structure and component design. *J Adv Struct Mater* 70:13–24 (Springer International Publishing)

# Simulation of a Crack Emanating from a Microvoid in Cement of a Reconstructed Acetabulum

**B. Serier, L. Zouambi, M.M. Bouziane, S. Benbarek and B. Bachir Bouiadjra**

**Abstract** In this study, the finite element method is used to analyse the crack behaviour emanating from a microvoid and the effects of the crack-microvoid and crack-crack interactions according to the crack locations in the cement of the reconstructed acetabulum by computing the stress intensity factor (SIF) at the crack tip. We selected one load case corresponding to the stem axis position of  $50^\circ$  which reflects the squatting activity. We show that the failure mode of these cracks (opening and shearing) depends on the orientation of the crack and its size. The crack initiated along the cement thickness propagates essentially in mode I. The initiated crack in the cement ( $90^\circ$ ) propagates in mode II and the crack inclined with  $45^\circ$  propagates in mixed mode. We also show that the crack propagation kinetics depend on the presence of the microdefects in the propagation crack path. This behaviour leads to the fracture of the cement and the loosening of the prosthesis.

**Keywords** Bone cement · Microvoid · Crack · Stress intensity factor · Interaction

---

B. Serier (✉) · L. Zouambi · S. Benbarek · B. Bachir Bouiadjra  
LMPM, Mechanical Engineering Department, University of Sidi Bel Abbes,  
BP89, Sidi Bel Abbes 22000, Algeria  
e-mail: serielem@yahoo.fr

L. Zouambi  
e-mail: zouambileila@yahoo.com

S. Benbarek  
e-mail: sma\_benbarek@yahoo.fr

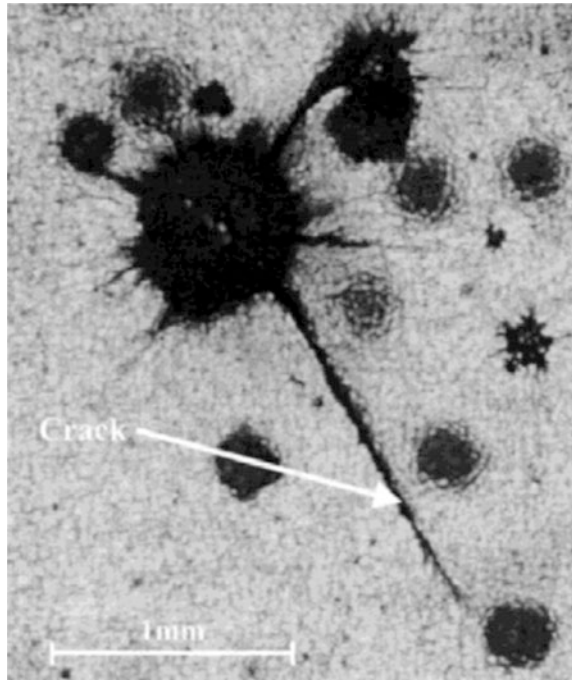
B. Bachir Bouiadjra  
e-mail: bachirbou@yahoo.fr

M.M. Bouziane  
Department of Mechanical Engineering, University of Masacra, BP305,  
Route de Mamounia Masacra, Algeria  
e-mail: agk\_bouziane@yahoo.fr

## 1 Introduction

The bone cement is a determining factor of arthroplasty. It must ensure both its three fundamental functions of transmission of antibiotics, good adhesion implant-cement-bone and good load transfer bone-implant [1, 2]. It therefore determines the performance, reliability and durability of cemented total hip arthroplasty. It is the main cause of loosening. Indeed, porosity is a characteristic that we do not control. If the porosity is a support of local broadcasting, especially for the antibiotics and antimetotics, it presents a risk of priming, by the notch effect, and the propagation of cracks. These cracks promote the interconnection of pores (Fig. 1) [3]. Several works have shown that the presence of microvoids in the bone cement can lead to loosening of the total hip arthroplasty [1–7]. These defects are thus, the site of stress concentration; the level reaches or exceeds the local tensile strength of cement [3–14]. In this study, the finite element method was used to analyse the behaviour of cracks emanating from microvoids according to the patient's activity, localization of porosity, orientation of the cracks and the crack-microvoid and crack-crack interactions. This behaviour was analysed by computing the stress intensity factor.

**Fig. 1** Cracks observed experimentally in the orthopaedic cement [3]



## 2 Materials and Methods

In this bi-dimensional finite element method (FEM) analysis of a right side pelvic bone, Fig. 2 shows the assignment of different elements of the acetabulum prosthesis. Fitting in is imposed on the pubic symphysis. Zero displacement is imposed along the axis ( $x = 0$ ) on the sacroiliac joint [1, 2] (Fig. 2). We selected load cases corresponding to the stem axis position equivalent to  $50^\circ$  which reflects the squatting activity with an average body's weight of 70 kg [7].

Table 1 contains the materials properties of cement, cup and all different regions of the acetabulum bone [15]. This geometrical model was taken from our previous studies [1, 2].

The microvoid diameter in the cement is in the order of  $100 \mu\text{m}$ . The mesh around the crack tip is very refined (Fig. 3). The finite element code Abaqus 6.11 was used to analyse the effect of microdefects in the cement [16].

**Fig. 2** Geometrical model and boundary conditions

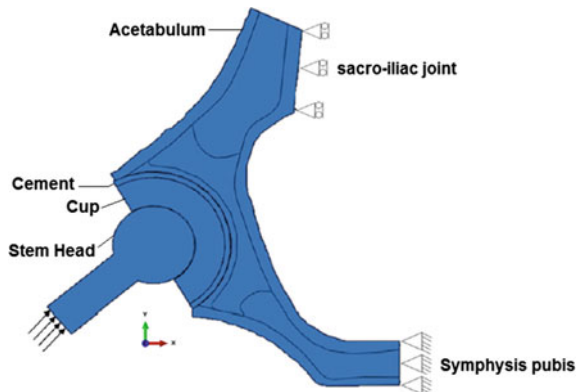
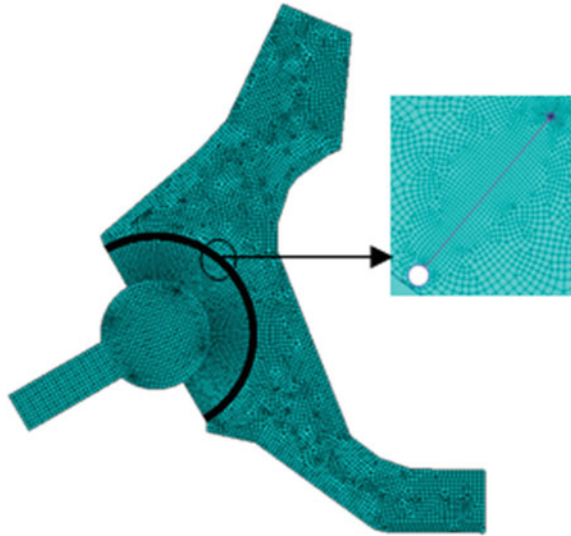


**Table 1** Materials properties [15]

Materials	Young's modulus E (MPa)	Poisson's ratio ( $\nu$ )
Cortical bone	17,000	0.3
Spongious bone	1–132	0.2
Sub-chondral bone	2000	0.3
Cement (PMMA)	2300	0.3
Cup (UHMWPE)	700	0.3
Titane alloy	210,000	0.3



Fig. 3 Mesh model



### 3 Results

The behaviour of the crack emanating from the microvoids was analysed by computing the stress intensity factor (SIF) at the crack tip according to the microvoid localization, crack orientation and their size and the crack-microvoid and crack-crack interaction in the cement of reconstructed acetabulum [1, 2, 7] (Fig. 4).

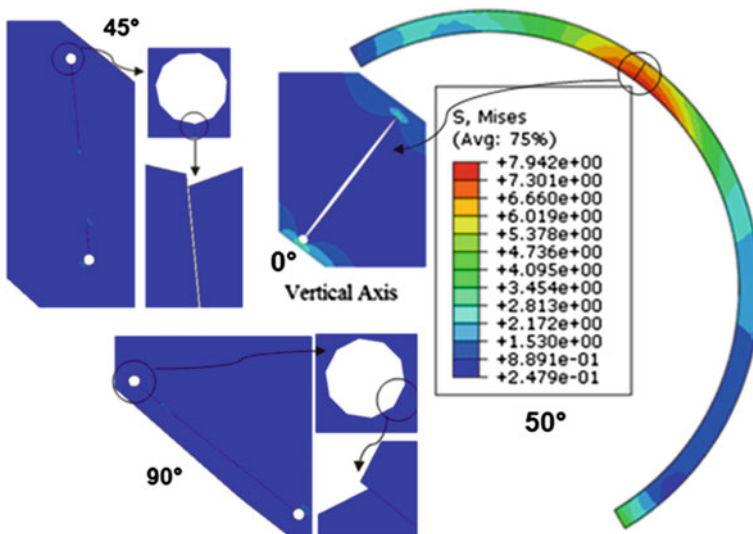


Fig. 4 Representation of the stress concentration site and the vertical axis in the bone cement

### 3.1 Crack Emanating from the Microvoid

The behaviour of a crack emanating from microvoids in the orthopaedic cement is analysed according to its size and its propagation direction towards the bone and the cup. In the first step, crack is localized in close proximity to the cement/bone interface noted here (CB) and develops towards the cement/cup interface noted (CC). Figure 5 presents the behaviour of these cracks which propagate along the thickness of the cement and the effect of the interfaces. Indeed, a crack propagates more easily to the cup. This behaviour is defined by the variation of the curve  $K_I = f(a)$ .

### 3.2 Interaction Effect

In Fig. 5, the results allow to analyse the behaviour of a crack localized in close proximity to the cement/bone interface and propagating along the thickness of the cement to a located microvoid in vicinity of the cement/cup interface. Figure 6a, b shows that the presence of a microvoid in the growth direction of crack accelerates its propagation kinetic. This behaviour is observed by the augmentation of SIF in modes I and II (Fig. 6a, b).

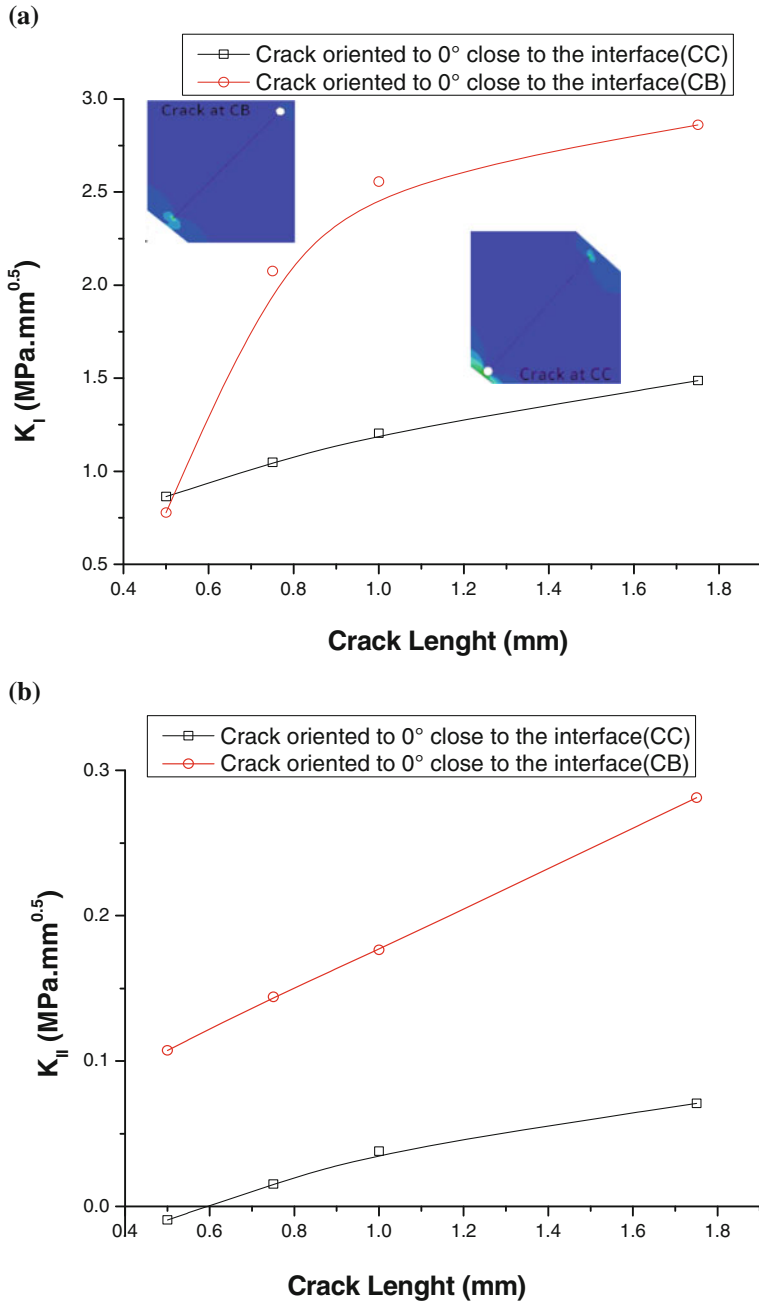
### 3.3 The Orientation Effect

The cracks emanating from microvoids localized in close proximity to the cement/bone interface (CB) were initiated along the thickness of the cement (defined as  $0^\circ$  direction) along its length (defined by a  $90^\circ$  direction) and between these two directions (defined by  $45^\circ$ ). The initiation of the cracks was on the right and left sides of the microvoid. This study analyses the behaviour of these cracks which are propagating in the direction of microdefects (microvoid, fixed crack emanating from another microvoid and a mobile crack emanating from another microvoid).

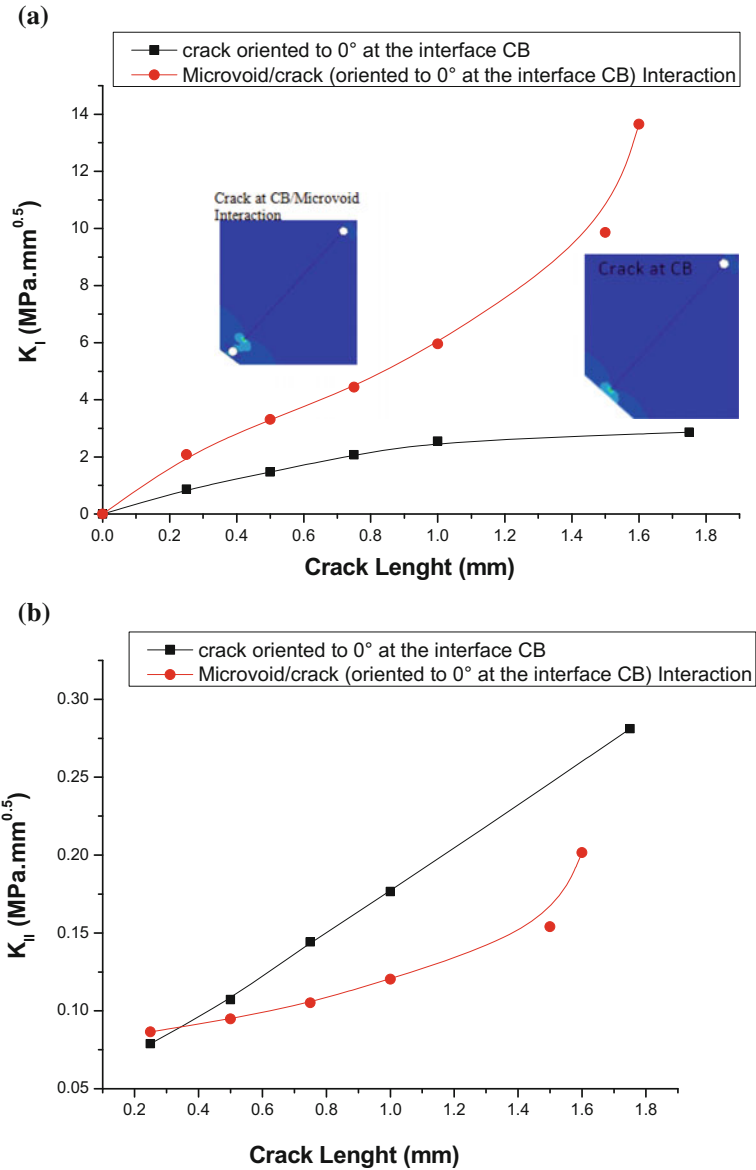
#### 3.3.1 Mobile Crack (CB) Oriented-Microvoid Interaction

Figure 7a, b illustrates the variation of SIF in mode I and II resulting from a mobile crack at the cement/bone interface (CB) propagating to a microvoid according to the mobile crack length and orientation. We note that the crack initiated along the cement thickness ( $0^\circ$ ) propagates essentially in mode I. The crack oriented along the cement ( $90^\circ$ ) propagates in mode II and the crack oriented at  $45^\circ$  propagates in mixed mode.

Whatever the orientation of the crack and the failure mode, the presence of the microvoid accelerates the kinetic of the crack propagation (Fig. 7a, b). The effect of



**Fig. 5** Nature of the interface effect (CC, CB) on the SIF (crack orientation of 0°): **a** mode I, **b** mode II



**Fig. 6** Effect of the presence of a microvoid on the direction of propagation of a crack emanating from another microvoid: **a** mode I, **b** mode II

the crack-microvoid interaction is dominant when defects are located very close to each other. Such behaviour promotes the interconnection of these two microvoids experimentally observed [3].

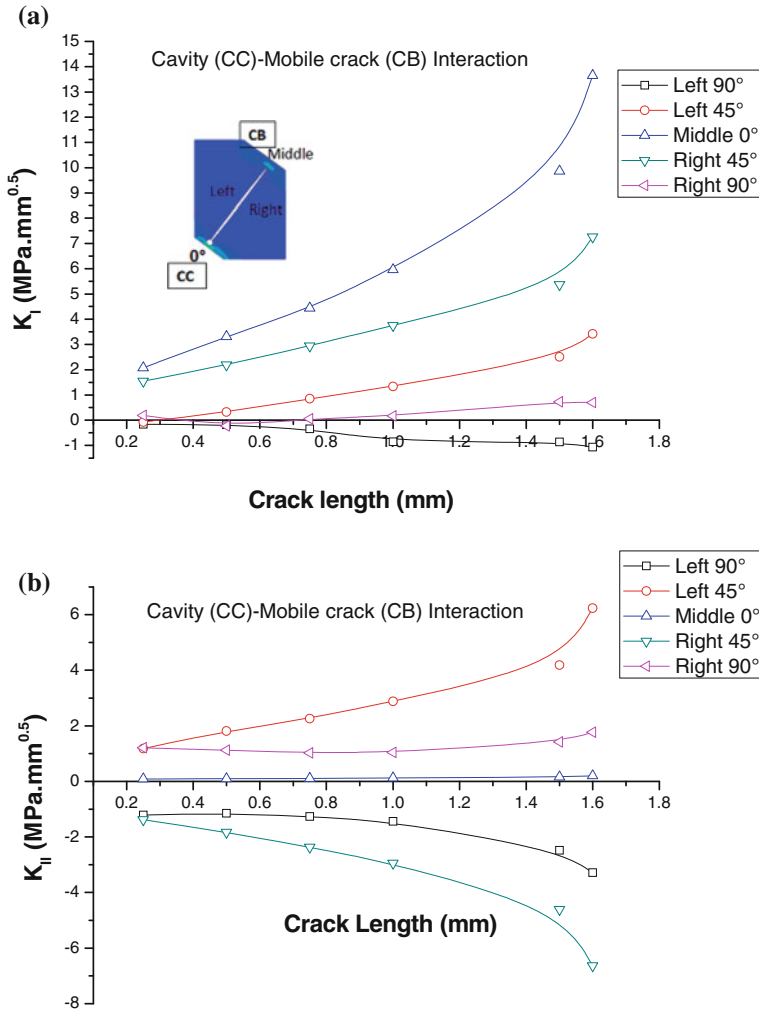
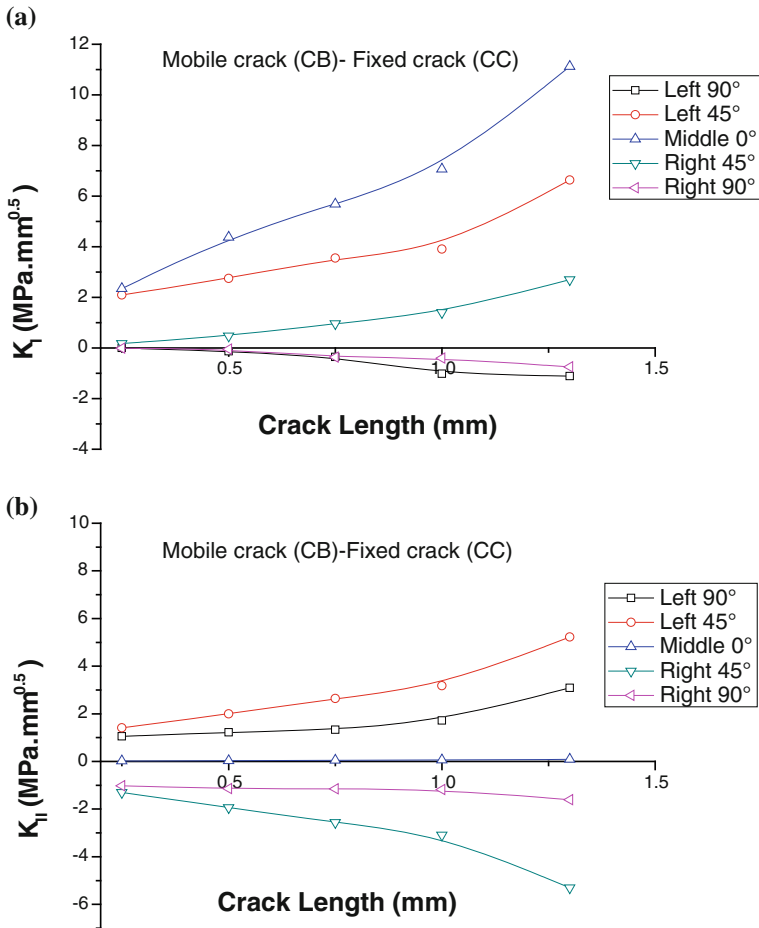


Fig. 7 Variation of the SIF in mode I (a) and II (b) according to the orientation of the crack (microvoid-crack interaction)

Our results show that the values of the SIF in mode I are most significant when the cracks are initiated in the right side of the microvoid.

### 3.3.2 Mobile Crack Oriented-Fixed Crack Interaction

The behaviour of cracks initiated in 0°, 45°, and 90° orientation related to the microvoid is analysed. These cracks propagate in the direction of another fixed crack from another microvoid. The variation of SIF in modes I and II according to



**Fig. 8** Variation of the SIF in mode I (a) and II (b) according to the orientation of the crack (mobile crack-fixed crack interaction)

the size of the mobile crack is illustrated in Fig. 8. We show that these criteria of failure increase slowly and then quickly when the mobile crack front approaches that of the fixed crack. This behaviour leads to coalescence of these two cracks (Fig. 8a, b) and thus the interconnection of the two microvoids.

Compared with the results of Fig. 7a, b and for the same size of the crack, the SIF resulting from such cracks is much more important.

Compared with the results of Fig. 7a, b, the stress intensity factor resulting from the mobile crack tip is more significant at 45° starting on the left side. It is in this part of the surgical cement compared to the microvoid that the effect of fixed crack-mobile crack interaction is paramount.

### 3.3.3 Mobile Crack—Mobile Crack Interaction

In this section, the behaviour of the oriented mobile crack, emanating from the microvoid and initiated at the cement/bone (CB) interface which propagates in the direction of another mobile crack emanating from a second microvoid is analysed. Figure 9a, b illustrates the variations of SIF in modes I and II at the crack tip of the mobile crack localized in close proximity to the (CB) interface, according to its

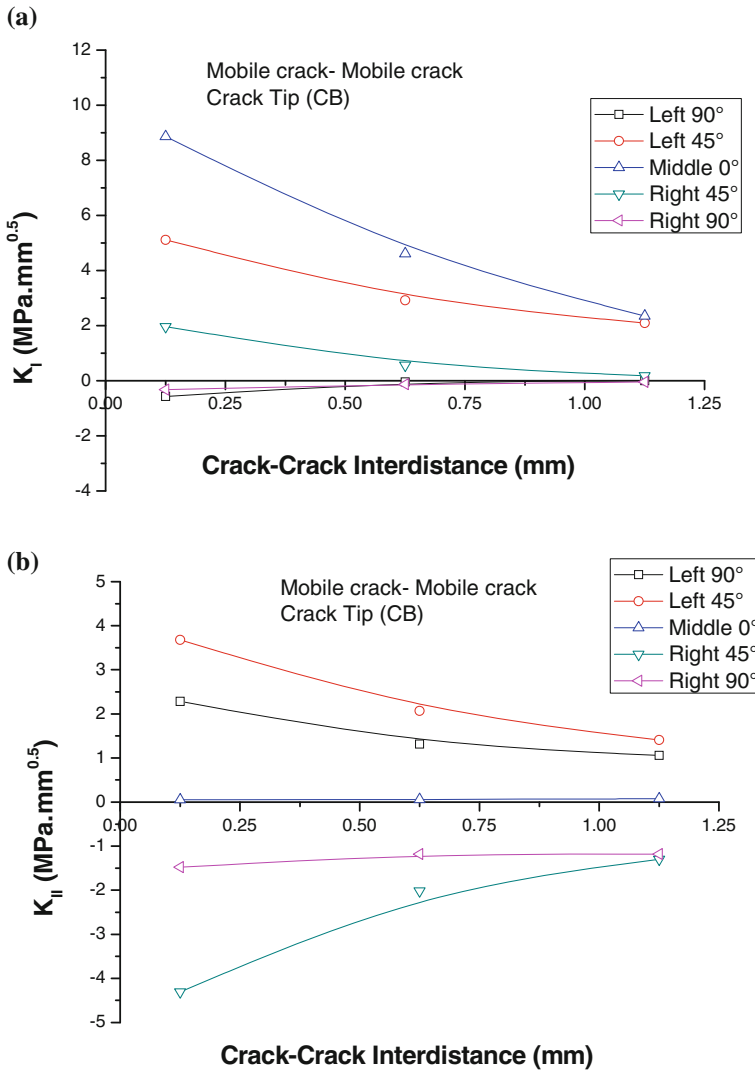


**Fig. 9** Variation of the SIF in modes I and II in crack tip CB depending on the orientation of the crack (mobile crack-mobile crack interaction)

orientation and the separating interdistance to the second crack. We note that the value of the SIF increases when the distance between the two cracks decreases.

Our results show that, when compared to the previous case, the effect of mobile crack-mobile crack interaction promotes instability of short cracks. Indeed, the size of the subcritical crack is greatly reduced (about three times) when it is located in close vicinity of another crack of the same length.

It is the interaction of stress fields highly concentrated at the two crack tips that is responsible for this significant increase of SIF. This increase greatly accelerates the kinetics of propagation of the two cracking defects which promotes their coalescence and leads to the interconnection of the two microvoids. This behaviour may explain other cases of interaction studied in this work; like crack-microvoid and mobile crack-mobile crack interactions.

We show that the crack-microvoid, fixed crack-mobile crack and mobile crack-mobile crack interaction effects promote the instability of short cracks by reducing the subcritical defects. This instability is defined by the evolution marked, characterized by a steep slope in the curve  $K = f$  (interdistance crack-crack) of the SIF at the mobile crack tip. This behaviour increases the risk of interconnecting microvoids by the coalescence phenomena of the two mobile cracks.

## 4 Conclusion

The results obtained in this study show that:

- The stress intensity factor of a crack emanating from a microvoid depends on the location of this micro-defect and the interface;
- The mode of propagation of a crack emanating from the microvoid on the priming site: the crack initiated along the cement thickness ( $0^\circ$ ) propagates essentially in mode I. The crack oriented along the cement ( $90^\circ$ ) propagates in mode II and a crack oriented at  $45^\circ$  propagates in mixed mode;
- Whatever the mode of failure and orientation of cracks emanating from a microvoid, the stress intensity factor is even more important when the defects are closer.

The quick increase of this factor leads to the interconnection of these two cracks and thus their coalescence;

- The effect of crack-microvoid interactions depends on the site of crack initiation oriented at  $45^\circ$ . Indeed, the SIF values in mode I are more significant when the cracks are initiated at the right side of the microvoid in the cement.
- The resulting SIF from mobile crack/fixed crack interaction is more important than that resulting from the microvoid/mobile crack interaction;
- The stress intensity factor resulting from the mobile crack tip, at  $45^\circ$  started on the left side, is more significant. It is in this part of the surgical cement compared



to the microvoid that the effect of fixed crack -mobile crack interaction is paramount.

- The Interaction mobile crack-mobile crack leads to a reduction of subcritical defect size. The short cracks are more dangerous when they are located in the vicinity of each other.

## References

1. Zouambi L, Serier B, Fekirini H et al (2013) Effect of cavity-cavity interaction on the stress amplitude in orthopaedic cement. *J Biomat Nanobiotech* 4:30–36
2. Zouambi L, Serier B, Benamara N (2014) Effect of cavity-defects interaction on the mechanical behavior of the bone cement. *Adv Mater Res* 3(1):271–281
3. Murphy BP, Prendergast PJ (2001) The relationship between stress, porosity, and non-linear damage accumulation in acrylic bone cement. *Inc J Biomed Mater Res* 59:646–654
4. Benbarek S, Bachir Bouiadjra B, Achour T et al (2007) Finite element analysis of the behaviour of crack emanating from microvoid in cement of reconstructed acetabulum. *Mater Sci Eng A* 457:385–391
5. Bhambrik SK, Gilbertson LN (1995) Micromechanisms of fatigue crack initiation and propagation in bone cements. *J Biomed Mater Res* 29:233–237
6. Bouziane MM, Bachir Bouiadjra B, Benbarek S et al (2010) Finite element analysis of the behaviour of microvoids in the cement mantle of cemented hip stem: static and dynamic analysis. *Mater Des* 31:545–550
7. Benbarek S, Bachir Bouiadjra B, Bouziane MM et al (2013) Numerical analysis of the crack growth path in the cement mantle of the reconstructed acetabulum. *Mater Sci Eng C* 33:543–549
8. Grégoire D, Maigre H, Combescure A (2007) Simulation de la propagation dynamique de fissure sous chargement mixte et comparaisons expérimentales, 8ème Colloque National en Calcul des Structures
9. Nguyen NC, Maloney WJ, Dauskardt RH (1997) Reliability of PMMA bone cement fixation: fracture and crack-growth behaviour. *J Mater Sci Mater Med* 8:473–483
10. Fineberg J, Gross SP, Marder M et al (1991) Instability in dynamic fracture. *Phys Rev Lett* 67(4):457–460
11. Fineberg J, Gross SP, Marder M et al (1992) Instability in the propagation of fast cracks. *Phys Rev B* 45(10):5146–5154
12. Melin S (1983) Why do cracks avoid each other? *Inter J Fract* 23(1):37–45
13. Sharon E, Fineberg J (1996) Microbranching instability and the dynamic fracture of brittle materials. *Phys Rev B* 54(10):7128–7139
14. Oshkour AA, Davoodi MM, Abu Osman NA et al (2013) Finite element analysis of circumferential crack behavior in cement femoral prosthesis interface. *Mater Des* 49:96–102
15. Foucat D (2003) Effets de la présence d'un grillage métallique au sein du ciment de scellement des cupules des prothèses totales de hanches: Etude mécanique et thermique. Université de strasbourg, Thèse de doctorat
16. ABAQUS Inc (2011) Abaqus Ver 6-11, User Guide. Cornell University, Ithaca

# Analysis of the Optical Properties of PVP/ZnO Composite Nanofibers

Wiktor Matysiak, Tomasz Tański and Marta Zaborowska

**Abstract** The aim of this study was to produce nanocomposites polymer fibers, with the participation of the reinforcing phase in the form of ZnO nanoparticles with a matrix of polyvinylpyrrolidone (PVP), made by electrospinning. Furthermore, examining the impact of the concentration of reinforcing phase on the optical properties of the obtained composites nanofibers. The morphology of nanofibers was examined by atomic force microscope and it showed that the applied process parameters gave the polymer fiber mats PVP from 10 % solution PVP/EtOH and composites PVP/ZnO from 10 % solution, wherein the concentration by weight of the used reinforcing phase was as follow: 5 and 10 %. To improve the influence of the concentration by weight of the used reinforcing phase on the optical properties, the spectroscopy UV-Vis has been used.

**Keywords** Nanofibers · Polymer composite nanofibers · PVP/ZnO · Electrospinning methods · Optical properties

---

W. Matysiak · T. Tański (✉) · M. Zaborowska  
Department of Materials Processing Technology, Management and Technology in Materials,  
Institute of Engineering Materials and Biomaterials, Silesian University of Technology,  
Konarskiego 18a Str., 44-100 Gliwice, Poland  
e-mail: tomasz.tanski@polsl.pl

W. Matysiak  
e-mail: wiktormatysiak@polsl.pl

M. Zaborowska  
e-mail: martakzaborowska@gmail.com

T. Tański  
Center for Nanotechnology, Silesian University of Technology,  
Konarskiego 18a Str., 44-100 Gliwice, Poland

## 1 Introduction

Zinc oxide due to its physical properties, which include a wide-direct band gap of 3.37 eV and a large excitation binding energy (60 meV), is widely used for the manufacture of gas sensors [1, 2], solar cells [3], LEDs [4], transistors [5] and cosmetics [6]. The current developments in the field of nanotechnology allow for the production of innovative nanocomposites based on polymers reinforced ceramic nanostructures, including nanoparticles ZnO. A distinctive feature of the composite materials produced is significant improvement in physical properties in respect of the polymer matrix and the reinforcing phase [7].

It has been shown that collagen hydrogel reinforced ZnO nanoparticles having superior strength and mechanical properties than natural collagen, therefore revealing no toxicity due to low release rate of ZnO<sup>2+</sup>. It is possible to use the hydrogel composite PVP/ZnO as a carrier of drugs in the human body, owing to biocompatibility with the human cornea [8].

Composites PVP/ZnO are also used in medicine as transporters of drugs to tumor cells in the treatment of leukemia. Complex used in drug delivery system consist of nanocomposites PVP/ZnO and daunorubicin on the surface of the composites, which is attached by means of phenol groups. Ready sets are used as carries of drugs to infected tumor cells [9]. The polymers may also be used as surfactants relative to zinc oxide nanoparticles. In such situation it is not necessary to use organic solvents, which allows to use this type of composites PVP/ZnO in cosmetics without the risk to harm the body. Using this method cause a further reduction in release of toxic gases into the atmosphere. The resulting ZnO by co-precipitation has a hexagonal structure and smaller grain, by which it can be used for electrodes in lithium-ion batteries or adsorbents, thanks to the improvement of morphology of microstructures and surface [10]. However, the most important is, that zinc oxide on the polymer matrix has higher absorption than a pure zinc oxide, therefore it has higher ability to absorb UV radiation [6]. Another use of precipitation methods are luminescent sensors, due to the emission of light at a wavelength of 420 and 495 nm [11]. Multilayered nanodiscs from poly (vinylpyrrolidone) and sodium lauryl sulfate (SDS) also can be produced by hydrothermal method. Those nanodiscs can be used as sensors for detecting the formaldehyde, which is organic compound harmful for human body [12]. ZnO particles as nanofillers in polymers play a dual role; on the one hand these are capable to absorb UV radiation, on the other—those are catalytically active nanoparticles which are rapidly photooxidation degrading leading to heterogeneous nanocomposite structure. It is noted, that degradation is only limited to surface layers of the nanocomposites, since the presence of zinc oxide nanoparticles limits the penetration of the light inside the structure. Therefore there is no photooxidation process throughout the nanocomposite structure. This process depends on the concentration of ZnO particles in the polymer solution and it is not possible to determine, which effect—UV radiation absorption or photooxidation—will decide on nanocomposites reinforced zinc oxide properties [13].

## 2 Materials and Methods

In order to prepare the solutions, the following were used: poly(vinylpyrrolidone) (PVP), purity of 99 %, Mw = 1,300,000 g/mol. The reinforcing phase were nanoparticles of zinc oxide. The solvent was ethanol (EtOH), purity of 99.8 %. The final products were the solutions of PVP/EtOH/ZnO nanoparticles at a concentration of 10 % by weight, with 0, 5 and 10 % concentration of ZnO by weight. In order to break the agglomerates of zinc oxide nanoparticles, the measuring amount of reinforcing phase was added to ethanol and so prepared solutions were subjected to sonification for 15 min. Directly after the sonification process, the solution was added with the measuring amount of polymer and subjected to mixing using a magnetic mixer for 3 h in room temperature. Immediately after mixing, the solution was placed in a pump device, which was the sterile syringe. The polymer nanofibers was obtained using the electrospinning method from the solution using the device FLOW—Nanotechnology Solutions Electrospinner 2.2.0-500. The used process parameters are shown in Table 1.

In order to identify the morphology of the obtained nanofibers the atomic force microscope was used (AFM), by PARK Systems. In order to identify the optical properties of fibrous polymer and composite mats, absorbance spectra versus wavelength obtained using spectrophotometer UV/VIS Evolution 220 by Thermo-Scientific, computer controlled was measured. The wavelength of 190–1100 nm fell perpendicular on the sample.

## 3 Results

### 3.1 Morphology Analysis

In order to analyze the morphology of the produced nanocomposites PVP/ZnO examination was performed using atomic force microscope (AFM) in a non-contact mode. Image analysis of the surface topography of polymeric fibrous mats PVP and composites PVP/ZnO showed that fiber diameter for each sample was approx. 4  $\mu\text{m}$  (Fig. 1). Preliminary observation of fiber diameters allows to determine, that fiber diameter decrease below 4  $\mu\text{m}$  with increasing concentration of ZnO nanoparticles

**Table 1** The parameters of the fibers production process

The electrospinning process parameters			
Name sample	The distance between the electrodes (cm)	The potential difference between the electrodes (kV)	The solution flow rate (ml/h)
Sample no 1	15	20	1.5
Sample no 2	12.5	20	3.5
Sample no 3	12.5	20	3.5

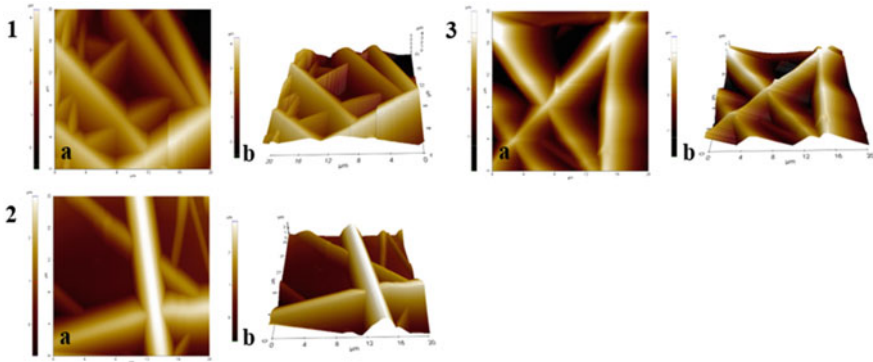


**Fig. 1** Morphology of AFM images: (a) view from above on the obtained fibrous mats, (b) 2D image of the fibers; 1 sample no 1 with the concentration of 10 % PVP, 2 sample no 2 with the concentration of 5 % ZnO in relation to 10 % PVP, 3 sample no 3 with the concentration of 10 % ZnO in relation to 10 % PVP

in relation to polymer. It is planned by the authors the ability to analyze received composite fibrous mats using a scanning electron microscope (SEM) for more accurate analysis of the morphology of the obtained materials and using the backscattered electron mode, analyze the nanoparticles dispersion of the reinforcing phase in the whole volume of the polymer fibrous mat.

### 3.2 UV-Vis Spectra Analysis

Studies of the optical properties of the obtained fibrous polymer and composite mats was made using UV-Vis spectroscopy (Fig. 2). Analysis of the absorption spectrum as a function of the wavelength falling radiation on the sample showed that the sharp absorption edge for the PVP polymer fibers falls at 290 nm wavelength, while the maximum of the absorption corresponds to the waves of 260 nm, which is in agreement in results presented in Abdelghany et al. [14]. The analysis of the absorption spectrum for pure ZnO nanopowder revealed, that the reinforcing phase is characterized by the lowest absorption rate, compared to the used polymer and resulting composite materials, wherein the absorption blurred edge of the absorption peak fall at 360 nm wavelength, while the absorption maximum falls at 340 nm wavelength, which is confirmed with the results obtained for pure ZnO nanopowder presented in Yuliah et al. [15]. After the addition of zinc oxide to PVP polymer solution, in order to obtain nanocomposite fiber mats, the absorption spectrum changed and remain the resultant spectra of pure ZnO nanopowder and PVP fibers [6]. The difference graph of the absorption spectra results from the morphology of the examined materials, pure ZnO powder is one-dimensional structure, while the composite nanofibers are three-dimensional structures [16]. The

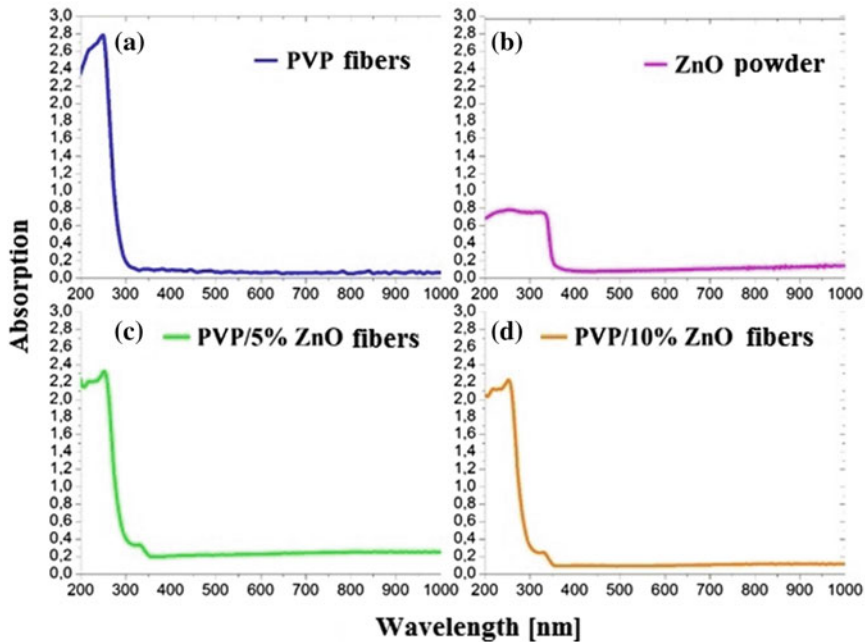


**Fig. 2** The absorption spectrum as a function of the wavelength: (a) for PVP fibers, (b) for pure ZnO nanopowder, (c) for PVP fibers with the concentration of 5 % by weight of ZnO, (d) for PVP fibers with the concentration of 10 % by weight of ZnO

addition of the ZnO nanoparticles results in a decrease in absorption of the resulted composite fibers as compared to the fibers made from polymer solution. For a composite material containing concentration of nanoparticles of 5 % in relation to polymer, an absorption edge was determined at a wavelength of 300 nm, while there were two absorption peaks that falls at 220 and 250 nm wavelengths. Probably the first absorption maximum correspond to waves of 220 nm derived from the reinforcing phase, however the absorption rate is lower. Similar results were obtained for PVP fibers at concentration of 10 % by weight of ZnO, however the absorption rate is lower than the maximum absorbance value for the obtained fibers at concentration 5 % by weight of ZnO, which is due to the greater mass fraction of the applied reinforcing phase.

## 4 Conclusion

The paper describes a method of making nanocomposites fiber mats using electrospinning from the solution technique. The applied method allows to obtain a polymer fibers PVP and composite fibers PVP/ZnO with the concentration by

weight of nanoparticles: 5 and 10 %, whose diameter was approx. 4  $\mu\text{m}$ , which was confirmed by AFM analysis of the surface. Depending on the concentration of ZnO nanoparticles in respect to PVP, the diameter was changed. The increase in proportion of the reinforcing phase resulted in decrease in diameter of the fibers. Analysis of the absorption spectra in the wavelength function showed a decrease of absorption with increase of the concentration of ZnO in respect to PVP.

**Acknowledgments** Project was funded by the National Science Centre, Poland based on the decision number 2014/15/B/ST8/04767

## References

1. Hassan HS, Kashyout AB, Morsi I, Nasser AAA, Ali I (2014) Synthesis, characterization and fabrication of gas sensor devices using ZnO and ZnO. *Benisuef Univ J Basic Appl Sci* 3:216–221 (In: *Nanomaterials*)
2. Tański T, Matysiak W, Markovičová L, Florek-Szotowicz N, Snopiński S, Krzemiński Ł, Wiśniowski M (2015) Analysis of the morphology and properties of PAN/Bi<sub>2</sub>O<sub>3</sub> composite nanomaterials produced by electrospraying method. *J Achievements Mater Manuf Eng* 73 (2):176–184
3. Hu G, Guo W, Yu R, Yang X, Zhou R, Pan C, Wang ZL (2016) Enhanced performances of flexible ZnO/perovskite solar cells by piezo-phototronic effect. *Nano Energy* 23:27–33
4. Özgür Ü, Alivov YI, Liu C, Teke A, Reshchikov MA, Doğan S, Avrutin V, Cho S-J, Morkoç H (2005) A comprehensive review of ZnO materials and devices. *J Appl Phys* 98:041301
5. Vidor FF, Meyers T, Wirth GI, Hilleringmann U (2016) ZnO nanoparticle thin-film transistors on flexible substrate using spray-coating technique. *Microelectron Eng* 159:155–158
6. Yu ZJ, Kumar MR, Sun DL, Wang LT, Hong RY (2016) Large scale production of hexagonal ZnO nanoparticles using PVP as a surfactant. *Mater Lett* 166:284–287
7. Olejnik M (2008) Nanokompozyty polimerowe—rola nanododatków, Instytut Technologii Bezpieczeństwa “Moratex”, Łódź, [http://www.moratex.eu/pliki/tww/2008\\_12/06\\_1-2\\_2008.pdf](http://www.moratex.eu/pliki/tww/2008_12/06_1-2_2008.pdf). Accessed 19 June 2016
8. Lian J, Agban Y, Cheong S, Kuchel RP, Raudsepp A, Williams MAK, Rupenthal ID, Henning A, Tilley RD, Holmes G, Prabakar S (2016) ZnO/PVP nanoparticles induce gelation in type I collagen. *Eur Polym J* 75:399–405
9. Hariharan R, Senthilkumar S, Suganthi A, Rajarajan M (2013) Synthesis and characterization of daunorubicin modified ZnO/PVP nanorods and its photodynamic action. *J Photochem Photobiol A Chem* 252:107–115
10. Kim JH, Choon Choi W, Young Kim H, Kang Y, Park Y-K (2005) Preparation of mono-dispersed mixed metal oxide micro hollow spheres by homogeneous precipitation in a micro precipitator. *Powder Technol* 153(3):166–175
11. Singla ML, Shafeeq MM, Kumar M (2009) Optical characterization of ZnO nanoparticles capped with various surfactants. *J Lumin* 129:434–438
12. Hussain S, Liu T, Aslam N, Kashif M, Cao S, Rashad M, Zhang Y, Zeng W, Javed MS (2015) Polymer-assisted co-axial multi-layered circular ZnO nanodisks. *Mater Lett* 152:260–263
13. Bussière P-O, Peyroux J, Chadeyron G, Therias S (2013) Influence of functional nanoparticles on the photostability of polymer materials: recent progress and further applications. *Polym Degrad Stab* 98:2411–2418
14. Abdelghany AM, Abdelrazek EM, Badr SI, Morsi MA (2016) Effect of gamma-irradiation on (PEO/PVP)/Au nanocomposite: materials for electrochemical and optical applications. *Mater Design* 97:532–543

15. Yuliah Y, Bahtiar FA, Siregar RE (2016) The optical band gap investigation of PVP-capped ZnO nanoparticles synthesized by sol-gel method. In: AIP Conference Proceedings, vol 1712, p 050018
16. Ravichandran S, Ramalingam G (2013) Synthesis, optical and morphological studies for Sol-Gel derived ZnO/PVP one dimensional nano-composite. J NanoSci NanoTechnol 1 (2):39-43



# Multiobjective Optimization of Dielectric Material's Selection in Marine Environment

I. Kuzmanić, I. Vujović and J. Šoda

**Abstract** In this paper, a multiobjective approach to the optimal material's selection for dielectrics in marine environment is proposed. The starting point is the definition of the Pareto optimal criteria for the material selection. The proposed method is visualized and the proposed algorithm is explained step by step. The dielectric material is identified from the lookup table by the relative permittivity. Dominant dependences are simulated through the influence to the relative permittivity.

**Keywords** Complex relative dielectric constant · Pareto optimization · Visualization · Partial discharge current · Capacity

## 1 Introduction

Marine environments present a demanding ambient for electrical insulation materials or dielectrics in general. Dielectric materials play a vital role not just in insulation, but also in optical communications (fiber optic materials), LCDs, and similar applications. The demanding environment can cause electrofracture of the materials. Even when an ambient is not as demanding, there are a lot of cases where the insulator's surface becomes contaminated by e.g. moisture, pollutants deposition, dust, salt spraying, etc. The contaminated surface develops sufficient surface conductance to enable discharge between parts of the electric circuit even below the

---

I. Kuzmanić (✉) · I. Vujović · J. Šoda  
Faculty of Maritime Studies, University of Split, Zrinsko-Frankopanska 38,  
21000 Split, Croatia  
e-mail: ikuzman@pfst.hr

I. Vujović  
e-mail: ivujovic@pfst.hr

J. Šoda  
e-mail: jsoda@pfst.hr

material's breakdown strength [1–4]. Therefore surface tracking occurs. This mechanism can also lead to insulator aging [5, 6].

This paper is organized as follows. The second section overviews references relevant to this field of research. The third section considers the influential parameters and explains the multiobjective approach to the topic. The fourth section presents steps of the proposed algorithm for dielectric material selection. The final section presents conclusions.

## 2 Literature Overview

Dielectrics' performance is greatly influenced by various parameters, which are mainly determined by an application. In our area of research, maritime traffic is of interest. So, it was important to find out, which influential factors to dielectrics' properties are important in maritime applications. Firstly, it can be seen that quite different pieces of equipment and machinery are used aboard ships. Hence, some factors could be important in one application and others in another application aboard. Based on different research studies [7–15], we selected the three most important factors that influence dielectrics' performance. Such influences can be introduced through different manners, so we selected to model the influence through the relative complex dielectric constant (permittivity). The three dominant factors that influence the dielectric constant are identified in [7, 8] as temperature, frequency and moisture. Works in [9, 10] do not model such an influence through the relative dielectric constant. Research in [11] deals with ecological aspects—finding an oil spill by radar and the influence of the change in surface dielectric constant to the radar reflectance. Since we are interested in the electrical and electronic equipment aboard ships, it was not of vital interest to our research. The research in [12] deals with molecular dynamics simulation, but only with water, which could be a part of electrical components. Research in [13] deals with a dielectric breakdown, which is introduced through an equivalent capacitor in the cable insulate. This is of interest to the aboard applications. Findings in [14] resulted in the conclusion that the real part of relative permittivity does not show significant changes due to salinity, but only to moisture. However, an imaginary part increases when there is no salinity and decreases when there is salinity. The covered frequency range was 1–4 GHz. This influence is important in satellite communications, but not in electro-energy transmissions aboard the ship. Similar research was performed in [15]. In the case of high voltage, the assessment of partial discharges gives important information in the reliability analysis of the high voltage equipment [16]. Therefore the authors developed a simulation model to investigate this influence.

The multiobjective approach can be found in many references covering different applications [17–21]. Material selection was a topic in [21], but not concerning dielectric or marine applications.

It is obvious, that the data sets would be large and therefore it is important to find a tool for handling such an amount of data. Therefore the tensor approach should be used. An example of tensor usage in large datasets is given in [22]. An example of designing new materials based on physical properties was presented as a case study. A data set contained a small set of melting point measurements in function of the concentrations of several different materials. A question arises if such a methodology can be used for dielectric material selection for specific applications, for instance considering the influence of various environments, such as marine, space, desert, polar, high-pressure conditions etc.

A novel approach to optimal dielectric selection is presented in [23]. It is based on theory of sets.

### 3 Theoretical Approach

This type of problems arises in many engineering/science fields due to the fact that some problems cannot be optimized considering only one scalar metric. Generally, such problems can be defined as in Definition 3.1 [17].

**Definition 3.1** A multiobjective approach is defined by maximizing the objective vector:

$$\underset{x}{\text{maximize}} \ g(x) = [g_1(x), g_2(x), \dots, g_M(x)]^T, \quad (1)$$

where  $x \in \mathcal{X}$ , and  $M$  is a number of objectives.

Generally speaking, the problem can be defined as finding the extreme value.

Considering a model of a void in the insulator [4, 16], our problem of minimizing effects of dominant factors to the reliability can be seen as minimizing the partial discharge (denoted as PD) current through the equivalent capacitor circuit. If the phenomenon is extensive, then the PD current can become a breakdown current.

The natural course of action is to recalculate the capacity for each parameter change and to use the so called Pareto approach to find an optimal solution. The optimal solution should lead to a material in the database with such a relative permittivity. By applying the famous Ohm's law for the part of the circuit and the expression for reactance of the capacitor, it can be easily seen that we should maximize the function, which has the approximate equation:

$$\frac{1}{i(\theta, T, \omega)} \approx C(\theta, T, \omega) \quad (2)$$

where  $C$  is the capacitance of a void in the dielectric material considered,  $i$  the PD current,  $\theta$  the volumetric percentage of a moisture,  $T$  the temperature and  $\omega$  the cycling frequency.

The objective is obtained by setting partial differentiates to zero:

$$\frac{\partial C}{\partial \theta} = 0, \quad \frac{\partial C}{\partial T} = 0, \quad \frac{\partial C}{\partial \omega} = 0 \quad (3)$$

It is not highly likely that the solutions for all dependences in (3) will coincide. Therefore the boundary conditions of tolerances should be added and evaluated in order to find an intersection for all three conditions in the range of tolerances for the relative dielectric constant. Then, the materials are chosen by the unified  $\varepsilon$  at the operating temperature, which is not so straight-forward as it seems. For example, capacitance does not depend only on temperature, since materials can compress or extend in some or all dimensions due to the temperature influence and dimensions are also responsible for the total value of the capacitance.

So, as it was described there is a question of a multiobjective formulation for the proposed problem.

The same problem can be defined by applying several approaches. In this paper, we decided to follow a multiobjective approach. We will extend the problem formulation in finding an optimal dielectric material for maritime applications in dependence on the operating conditions and boundary tolerances. This means that we need to obtain strait lines of dependences around the operating point, which should be parallel to the x-axis. Then, the partial derivatives would be equal to zero.

**Definition 3.2** Selection of the dielectric material for the specific application can be performed by maximization of the goal that the breakdown does not occur in the specified operating conditions, including the range of possible variations of the conditions.

**Definition 3.3** The goal in Definition 3.2 is obtained by setting the partial derivatives of the relative dielectric constant dependences to the dominant factors to zero. The optimal solution is obtained by minimizing the vector:  $[\frac{\partial \varepsilon_r}{\partial \theta}, \frac{\partial \varepsilon_r}{\partial T}, \frac{\partial \varepsilon_r}{\partial \omega}]^T$ . Hence, there are three objectives, which must be fulfilled to find an optimal solution:

$$\frac{\partial \varepsilon_r}{\partial \theta} = 0, \quad \frac{\partial \varepsilon_r}{\partial T} = 0, \quad \frac{\partial \varepsilon_r}{\partial \omega} = 0.$$

We will derive the equations for all three objectives.

### 3.1 Frequency Dependence

A usual approach to address the problem of frequency dependence is to apply Debye's equation, which can be in generalized in the form [1, 7, 8]:

$$\varepsilon_r = \varepsilon_{r\infty} + \frac{\varepsilon_{rDC} - \varepsilon_{r\infty}}{[1 + (j\omega\tau)^\alpha]^\beta} \quad (4)$$

However, due to simplicity, we will assume that the materials for selection obey the classic Debye's equation. By separating the real and the imaginary part, we obtain:

$$\varepsilon_r = \varepsilon_{r\infty} + \frac{\varepsilon_{rDC} - \varepsilon_{r\infty}}{1 + (j\omega\tau)} \cdot \frac{1 - (j\omega\tau)}{1 - (j\omega\tau)} = \varepsilon_{r\infty} + \frac{(\varepsilon_{rDC} - \varepsilon_{r\infty}) \cdot (1 - j\omega\tau)}{1 + (\omega\tau)^2}$$

$$\frac{\partial \varepsilon_r}{\partial \omega} = \frac{(1 + (\omega\tau)^2)((\varepsilon_{rDC} - \varepsilon_{r\infty}) \cdot (-j\tau)) - (\varepsilon_{rDC} - \varepsilon_{r\infty}) \cdot (1 - j\omega\tau) \cdot 2(\omega\tau)\tau}{(1 + (\omega\tau)^2)^2}$$

Solving for zero, we obtain:

$$(1 + (\omega\tau)^2) \cdot (-j) - (1 - j\omega\tau) \cdot 2(\omega\tau) = 0$$

$$\omega_1 = \frac{1}{\tau}, \omega_2 = 0$$

This is only a simple solution for the electronic type of polarization. It can be seen that the ideal solution depends on the relaxation time of the material and only one frequency is the ideal solution.

### 3.2 Moisture Dependence

There are two types of moisture, which could be considered: gas moisture from the environmental atmosphere and water molecules which penetrated the material's structure in the manufacturing process or during operation time. A ship's environment is full of unwanted moisture, with the addition of salt. Mostly, researchers were investigating the relationship between the relative dielectric constant and volumetric moisture in different soil classes. There are no explicit studies considering the moisture content within the product's material.

Let us assume that soil dependences are the same as in the product's material. In such a case, moisture can be modeled as [24]:

$$\theta = a \pm b \cdot \varepsilon_r ( + c \cdot \varepsilon_r^2 \pm d \cdot \varepsilon_r^3 ) \quad (5)$$

For a simple linear model, we can derive:

$$\begin{aligned}\theta - a &= -b \cdot \varepsilon_r \\ \varepsilon_r &= \frac{a - \theta}{b} \\ \frac{\partial \varepsilon_r}{\partial \theta} &= -\frac{1}{b}\end{aligned}$$

So, there is no optimal solution, unless  $b$  tends to infinity, which is not realistic. Fortunately, there are materials with cubic dependence. It is possible to obtain the result if it satisfies the result:

$$\frac{\partial \varepsilon_r}{\partial \theta} = \frac{1}{-b + 2c\varepsilon_r - 3d\varepsilon_r^2} \rightarrow 0$$

which is satisfied only if  $b$ ,  $c$  or  $d$  tends to infinity.

The relation between the moisture content in the atmosphere and physical parameters of a leaf should be defined experimentally and in X-band (satellite communications and satellite radar surveillance applications) these are [25]:

$$\begin{aligned}\text{Re}(\varepsilon_r) &= a \cdot e^{b\theta} - c \\ \frac{\partial \text{Re}(\varepsilon_r)}{\partial \theta} &= ab \cdot e^{b\theta} = 0\end{aligned}$$

which means that  $a$  or  $b$  should be 0 or  $b$  should tend to  $-\infty$ . All of these conditions are not realistic.

$$\begin{aligned}\text{Im}(\varepsilon_r) &= d \cdot e^{e\theta} - f \\ \frac{\partial \text{Im}(\varepsilon_r)}{\partial \theta} &= de \cdot e^{e\theta} = 0\end{aligned}$$

which could be satisfied only if  $d$  or  $e$  are 0 or  $e$  should tend to  $-\infty$ , which is also not realistic.

### 3.3 Temperature Dependence

In classic materials, it can be observed that electronic and ionic polarization is weakly temperature dependent, while dipolar orientational polarization is strongly dependant [1]. It is observed that the relative dielectric constant (permittivity)

decreases with temperature. Dipolar orientational polarization is of interest in MHz or lower frequencies (not in satellite communications, but in the range of some marine communication frequencies). Dipolar orientational polarization is normally exhibited by polar liquids and gases and solids with structures such as in glasses.

Temperature dependence of the relative permittivity is often considered as a two-variable function of temperature and frequency. For example, a temperature dependence of the relative permittivity of PET at 1 kHz can be approximated by the function (calculation performed for this paper by authors):

$$\text{Re}(\varepsilon_r) = 0.14 \cdot \tanh(T - 140) + 2.75 \quad (6)$$

which is interpolated by the measurement points:

$T = [50, 100, 150, 200]$  and  $\text{Re}(\varepsilon_r) = [2.6, 2.680766, 2.87692, 2.884612]$ . After 230 °C, the experimental curve increases exponentially, which is not modeled in this simplified case. The condition for the temperature dependence should be:

$$\frac{\partial \varepsilon_r}{\partial T} = 0.14 \cdot \frac{1}{\cosh^2(T - 140)} \quad (7)$$

or the general case for such types of materials:

$$\text{Re}(\varepsilon_r) = sc \cdot \tanh(T - shf) + DC \quad (8)$$

$$\frac{\partial \text{Re}(\varepsilon_r)}{\partial T} = sc \cdot \frac{1}{\cosh^2(T - shf)} \quad (9)$$

where  $sc$  is a scaling constant,  $shf$  the shifting parameter, and  $DC$  the offset from the horizontal axis.

It can be seen that the conclusion is non-encouraging again. Namely, the hyperbolic cosine function cannot become zero. Also, the reciprocal value of the square of the hyperbolic cosine function cannot become zero. Hence, the scale determines the pick at the inflection point, the offset has no influence in the first derivation. However, the value of the real part of the relative permittivity is  $5.9 \times 10^{-73}$  at 57 °C, which could be considered zero. So, actually, the solution can be anything except a small temperature range in the proximity of the inflection point.

The analytic representation of the dependence is shown in relation to the experimental measurement points for PET in Fig. 1a.

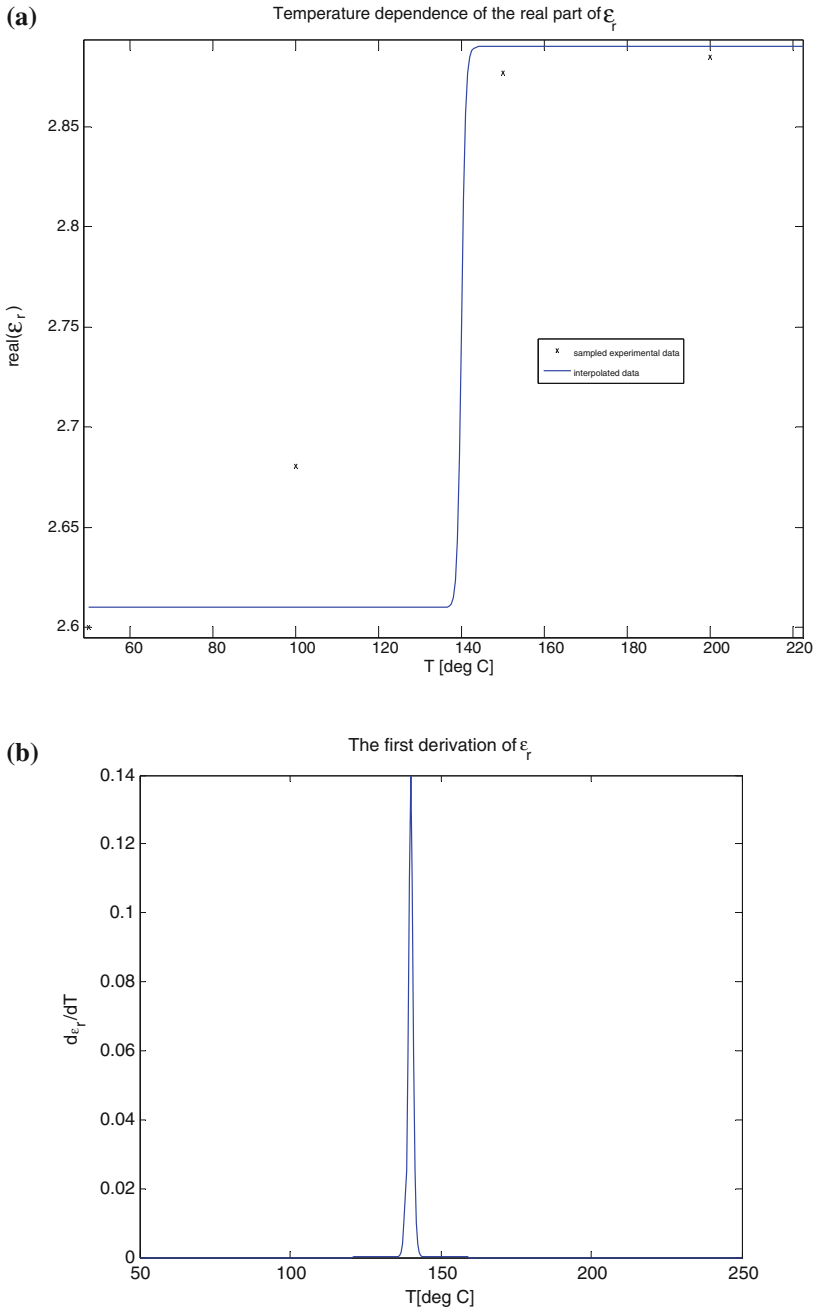


**Fig. 1** Temperature dependence of: **a** the real part of the relative permittivity, **b** the first derivation



## 4 Proposed Solution

A trivial solution of the problem defined in Eq. (3) is to design a material with no dependences to the considered parameters. Materials can be temperature-independent, frequency independent or moisture-independent in some limited range. Therefore, a multiobjective approach can lead to a finding material which is not dependent of important factors in the operating ranges of frequency, temperature and moisture. Unfortunately, most of the materials are not dependent on temperature at one frequency range, and most of them are hygroscopic. Some materials can be formed to be moisture-independent by impregnation with oils, compound masses, or similar. Due to variety of dielectric applications, such trivial solutions cannot hold in many real cases. Therefore, the multiobjective approach is necessary in the generalized case.

Sections 3.1, 3.2 and 3.3 illustrate the complexity of the problem. It is shown that, in many cases, it is not possible to find any analytical solution at all, not to mention an optimal solution. Firstly, it is not possible to include all types of the polarization in a single integrated analytic expression. Secondly, it is not possible to evaluate in the same way all types of materials. Therefore, it is necessary to establish an alternative, non-analytic method of finding the optimal material for some application.

In order to do this, it is obvious that numeric data and fitting will be of vital importance, due to the fact that it is not possible to obtain experimental or analytical data for every possible change. Therefore, the pre-algorithm steps should be (in the case of a non-trivial solution):

Firstly, it is necessary to identify dependences that are of importance for the specific application. In the case of the marine environment, the dominant factors are temperature, frequency and moisture [7, 8].

Next, a data collection process should be performed. In this phase, a data of dependences are collected for all materials that are of interest. This process includes data about the type of polarization, dependence on frequency, moisture, and temperature for the entire range of interest (in our case of marine applications). Data can be obtained experimentally or from references, published data, etc. The collected data forms the lookup table, which is used to select the optimal material. Every material is represented by its relative dielectric constant for every triple of the dependences (for example, a value of the relative permittivity of some material for specific temperature, moisture and frequency).

Figure 2 illustrates an example of the proposed algorithm operation: based on the desired ranges, a volume (slice) in the figure is found. The relative dielectric constant corresponding to the found volume slice is input to the lookup table. The optimal material is identified from the table.

After these preliminary steps, an algorithm for the material's selection can be performed.

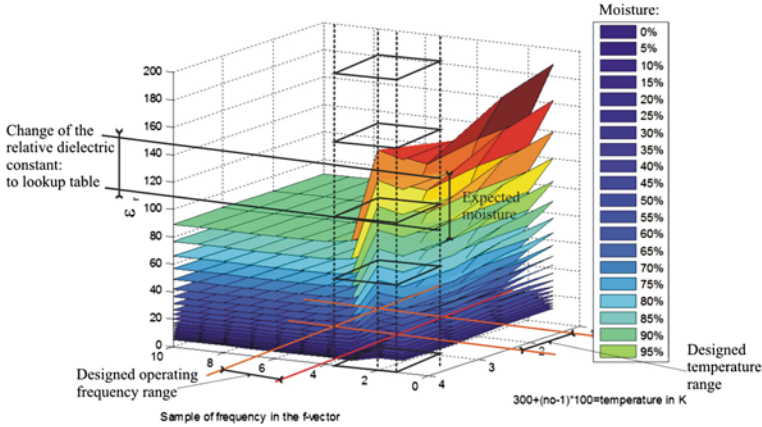


**Fig. 2** Visualization of the multiobjective approach: designed temperature and frequency range and expected moisture for material selection based on relative dielectric constant

#### Algorithm 4.1 (Multiobjective Selection of Dielectrics)

- Step 1: Input the design frequency and temperature range and the expected moisture content.
- Step 2: Calculate the first order partial derivate by temperature, frequency and moisture.
- Step 3: Find the intersection of the solution for all three dependences. If there is the answer go to step 8.
- Step 4: Extend solution to desired ranges around the operating point and find the intersectional slice in the 4D tensor  $(\omega, T, \theta, \epsilon_r)$ . If there is the intersection go to step 8.
- Step 5: Reduce 4D tensor to 3D by removing the least significant dependence.
- Step 6: Find the intersectional slice in the obtained 3D tensor. If there is the intersection, go to step 8.
- Step 7: If there is no the intersection set of data for the 3D tensor, exit algorithm with failure message. Conclusion is that there is no optimal material in the known set of data. Data should be updated with a new class of materials or a novel material should be developed.
- Step 8: If there is more than one material that satisfies intersection criteria, ask for additional selection criterion (price, availability, standards, etc.).
- Step 9: Perform the additional selection criteria and present the final result on the material's selection. The material is identified from the lookup table (dielectric constant vs materials name).

It has to be noticed that algorithm does not include research in methods for handling multidimensional tensors or search method for the lookup table (step 9). Therefore, one can select it arbitrarily.

## 5 Conclusions

In this paper, a multiobjective approach to the optimal material's selection for dielectrics in marine environments is proposed. The first idea was to make an easy dielectric material selection by visualization of the dominant factors for the dielectric's properties. In the research, we found out that a simulation can be performed through capacity of the equivalent model of the partial discharge. Change of the relative dielectric constant should be introduced through the change in the capacity.

Finally, we selected dominant factors and proposed an algorithm for the material's selection based on a multiobjective approach and an optimization, which could be described in an essence as the Pareto optimization. We considered parameters that we found important for marine environments. A similar approach could be used for other applications simply by addressing different dominant dependencies.

## References

1. Kasap SO (2006) Principles of electronic materials and devices. McGraw Hill, New York
2. Singh N, Debdas S, Chauhan R (2013) Simulation & experimental study of partial discharge in insulating materials for high voltage power equipments. *Int J Sci Eng Res.* 4:1677–1684
3. Kavitha D, Alex N, Nambiar TNP (2013) Classification and study on factors affecting partial discharge in cable insulation. *J Electr Syst* 2013:346–354
4. Sabat A (2011) Simulation of partial discharge in high voltage power equipment. MSc Thesis, National Institute of Technology, Rourkela, India
5. Pethrick RA, Banks WM, Brodesser M (2014) Ageing of thermoplastic umbilical hose materials used in a marine environment I—Polyethylene. *P I Mech Eng L MDA.* doi:10.1177/1464420713482827
6. Pethrick RA, Banks WM, Brodesser M (2014) Ageing of thermoplastic umbilical hose materials used in a marine environment II—Nylon. *P I Mech Eng L MDA.* doi:10.1177/1464420713482828
7. Vujović I, Kulenović Z, Vujović Kežić S (2014) Proposal of new method for dielectric materials selection in ship system applications. *Naše More* 61:28–32
8. Vujović I, Kuzmanić I, Kulenović Z (2014) Dielectric materials' selection for marine applications. Lambert Academic Publishing, Berlin
9. Cheng YM, Ku H, Snook C, Baddeley D (2004) Impact strength of vinyl ester composites cured by microwave irradiation: preliminary results. *P I Mech Eng L MDA.* doi:10.1177/146442070421800495
10. David-West OS, Banks WM, Pethrick RA (2011) A study of the effect of strain rate and temperature on the characteristics of quasi-unidirectional natural fibre reinforced composites. *P I Mech Eng L MDA.* doi:10.1177/0954420711404635
11. Yang CS, Park SM, Oh Y, Ouchi K (2013) An analysis of the radar backscatter from oil-covered sea surfaces using moment method and Monte-Carlo simulation: preliminary results. *Acta Oceanol Sin.* doi:10.1007/s13131-013-0267-7
12. Gereben O, Pusztai L (2009) On the accurate calculation of the dielectric constant and the diffusion coefficient from molecular dynamics simulations: the case of SPC/E water. <http://arxiv.org/ftp/arxiv/papers/1009/1009.5958.pdf>. Accessed 24 Feb 2015

13. Heidari M, Nekoubin A (2014) Performance improvement of photovoltaic systems through harmonics elimination of system and minimizing of THD. *Res J Recent Sci* 3:53–57
14. Lasne Y, Paillou P, Ruffié G, Serradilla C, Demontoux F, Freeman A, Farr T, McDonald K, Chapman B, Malézieux JM (2008) Effect of salinity on the dielectric properties of geological materials: implication for soil moisture detection by means of remote sensing. *IEEE T Geosci Remote* 46:1674–1688
15. Li YY, Zhao K, Ren JH, Ding YL, Wu LL (2014) Analysis of the dielectric constant of saline-alkali soils and the effect on radar backscattering coefficient: a case study of soda alkaline saline soils in western Jilin province using RADARSAT-2 data. *Sci World J*. doi:[10.1155/2014/563015](https://doi.org/10.1155/2014/563015)
16. Gopinath S, Sathiyasekar K (2014) Simulation of partial discharges in solid dielectric material: a study on PD magnitudes to the parallel and perpendicular axis of a cylindrical cavity. *Int J Eng Tech* 6:1786–1792
17. Björnson E, Jorswieck E, Debbah M, Ottersten B (2014) Multiobjective signal processing optimization—the way to balance conflicting metrics in 5G systems. *IEEE Sig Proc Mag*. doi:[10.1109/MSP.2014.2330661](https://doi.org/10.1109/MSP.2014.2330661)
18. Lampinen J (2000) Multiobjective nonlinear Pareto-optimization, a pre-investigation report. Lappeenranta University of Technology, Laboratory of Information Processing
19. Bentley PJ, Wakefield JP (1997) Finding acceptable Pareto-optimal solutions using multiobjective genetic algorithms. In: Chawdhry PK, Roy R, Pant RK (eds) *Soft computing in engineering design and manufacturing*. Springer, London
20. Caramia M, Dell’Olmo P (2008) Multi-objective management in freight logistics, increasing capacity, service level and safety with optimization algorithms. Springer, Berlin
21. Tang X, Bassir DH, Zhang W (2011) Shape, sizing optimization and material selection based on mixed variables and genetic algorithm. *Optim Eng*. doi:[10.1007/s11081-010-9125-z](https://doi.org/10.1007/s11081-010-9125-z)
22. Vervliet N, Debals O, Sorber L, De Lathauwer L (2014) Breaking the curse of dimensionality using decomposition of incomplete tensors. *IEEE Sig Proc Mag*. doi:[10.1109/MSP.2014.2329429](https://doi.org/10.1109/MSP.2014.2329429)
23. Vujović I, Kulenović Z, Kuzmanić I (2015) New algorithm for optimal dielectric material selection in marine environment. *Brodogradnja* 66:39–48
24. Kaiser DR, Reinert DJ, Reichert JM, Minella JPG (2010) Dielectric constant obtained from TDR and volumetric moisture of soils in Southern Brazil. *Rev Bras Ciênc Solo* 34:649–658
25. Helhel S, Colak B, Özen S (2007) Measurement of dielectric constant of thin leaves by moisture content at 4 mm band. *Prog Electromagn Res Lett* 7:183–191

# Metallurgical Quality Assessment of Modified Zn–Al–Cu Alloys

Krupiński Mariusz, Krupińska Beata, Karkoszka Tatiana, Borek Wojciech and Babilas Rafał

**Abstract** Zinc casting alloys are characterised by good technological and mechanical properties. The main problems connected with zinc casting alloying technology is creation of a coarse-grained, dendritic structure in the slowly solidifying castings. As a result of occurrence of dendritic micro segregation effects and structural instability the differentiation of properties can be observed. For the quality improvement of the liquid metal, which after casting in mould will assure the configuration of the required casting structure and guarantee good and stable properties, the modification operations are used. In the paper the influence of the chemical modification of Zn–Al–Cu casting alloys on the chosen properties (corrosion resistance, wear resistance, hardness) and the structure of zinc casting alloys have been researched. The results of the assessment of the alloy, both: in the in-state and after the modification state have been analysed with the application of quality assessment methods, particularly the statistical tools. The usage of control charts of variables reflecting the measurable properties of the Zn–Al–Cu–Sr and Zn–Al–Cu–Ti–B alloys have made the complex assessment possible. The modified alloys have been produced by the adding the modified Sr and Ti–B in the range between 0,1 and 1 % to the aluminium master alloy and casting to the metal casting dies.

**Keywords** Zinc alloy · Microstructure · Thermo derivative analysis · Crystallisation kinetics · Quality methods · Control charts

---

K. Mariusz · K. Beata (✉) · K. Tatiana · B. Wojciech · B. Rafał  
Institute of Engineering Materials and Biomaterials, Silesian University of Technology,  
Konarskiego St. 18a, 44-100 Gliwice, Poland  
e-mail: beata.krupinska@polsl.pl

K. Mariusz  
e-mail: mariusz.krupinski@polsl.pl

K. Tatiana  
e-mail: tatiana.karkoszka@polsl.pl

B. Wojciech  
e-mail: wojciech.borek@polsl.pl

B. Rafał  
e-mail: rafal.babilas@polsl.pl

## 1 Introduction

The advancement of technology forces the application of modern engineering materials of increasingly better utility properties. Due to increasing market competition, one expects the quality of products and the effectiveness of the production process to increase. This leads to a search for such solutions regarding the realised processes, which on one hand will allow for ensuring better, fulfilling the clients' expectations utility features, and on the other hand, will allow for cost limitation. There is an obvious need to apply such tools, which in a complex way will allow for limiting the risk of not fulfilling the requirements stated by the clients and the producers. Surely enough, on the first stage the vital thing is to check if the new processes give the chance for ensuring the stable conditions during the production time [1–5].

Zn–Al–Cu cast alloys are characterised by good technological features, the main problem in the production technology of these alloys is the susceptibility to gassing and oxidation as well as creating an inhomogeneous thick-grained structure [1, 3, 6–9].

Zinc cast alloys are in the possession of similar features to Al or Cu cast alloys. The differences are connected with the lower temperature of melting and higher density [2].

In order to shape the features of the Zn–Al–Cu cast alloys, one should implement the modifiers, which in turn give to the liquid alloys the properties allowing for obtaining the modified structure in the solid state. The effectiveness of the modification is estimated mainly by the analysis of the obtained mechanical and utility properties as well as the level of the structure fragmentation. For the estimation of the modified Zn–Al–Cu alloys one may also apply the analysis of the cooling curve, the basis of which was developed by W. Long. The structure obtained in the modified Zn–Al–Cu alloys highly depends on the cooling rate [1–3].

In order to improve the mechanical properties of the cast alloys, apart from the heat treatment, one may also apply the modification operation, which causes the change within the morphology and diminishes the inter-phase  $\alpha + \beta$  eutectic distance as well as the fragmentation of the micro-structure. Due to the reasons mentioned above, various modifiers are applied [1–3].

Nowadays, one applies the modification by strontium and antimony, since they are long-term-activity modifiers. The effect of strontium activity is still maintained after numerous re-meltings of alloy, which in turn enables the modified alloys to already be manufactured in the steel mills. For the modification of the cast alloys, rare earth elements are increasingly being used [1–3, 7].

The Zn alloys, especially those with high Al concentration, are prone to casting shrinkage, which may be eliminated by implementation of the following casting additions: Sr, Ca, Li, Na, Be; in this case, the following additions are meaningless: Ti, Zr, Sb, B and the rare earth elements. The good castability as well as the filling of the mould are decreased by the rare earth elements, which as Titanium cause susceptibility to hot-cracking [2, 3].

Properly run chemical modifications as well as application of the right cooling of the moulds lead to the improvement of the utility and quality of the produced moulds. Therefore, the knowledge concerning: the changeability of the mould's structure simultaneously with the change of cooling rate or change of the chemical content towards adding the modifiers to the liquid metal, is of high significance [3, 8–11].

In the result of this research, concerning the influence of the addition of rare earth elements, one has stated that they cause the following: the deoxidating process during melting in the open furnace, the fragmentation of the micro-structure as a result of implementing plenty of crystallisation nuclei and finally the hardening of the precipitation. Addition of the rare earth elements enables the application of the material within the elements working in the increased temperature, since it causes the improvement of the mechanical properties in the increased temperature range (above 300 °C) [3, 8–11].

## 2 Materials and Experimental Procedure

For statement of the interdependence between the chemical composition and the structure of the Zn–Al–Cu zinc cast alloy modified Sr and Ti–B, see Table 1. The casts were made in the resistance furnace with chamote—graphite crucibles. During the procedure the protective atmosphere was used in form of argon. The alloys were cast into metal moulds.

In order to determine the relationship between the crystallization kinetics of the alloy, and the chemical composition, microstructure and properties of the zinc alloy, the casting were further modified with cerium and the following tests were performed:

- thermo-derivative analysis of the investigated Zn alloys tested before and after modification with different cooling rates in the temperature range of  $T_{\text{Liq}}$  and  $T_{\text{Sol}}$   $0.09 \text{ } ^\circ\text{C s}^{-1}$  as well as  $0.13 \text{ } ^\circ\text{C s}^{-1}$ . Study of the effects of cerium addition was performed by means of a crystallization process simulation with UMSA using cylindrical specimens melted in a graphite crucible. For temperature measurement a chromel-alumel thermocouple of the K type was applied with a reaction time of 250 ms,
- macrostructure by light microscopy,
- wear resistance testing with the ball on plate method. The tribological test consisted of the following steps: changeover the tribotester for testing the wear

**Table 1** Chemical composition of Zn–Al–Cu zinc alloy

	Mass concentration of the element, in % mass,					
	Al	Cu	Ti	B	Sr	Zn
Zn–Al–Cu–Sr (A)	8.25	0.76	–	–	0.13	rest
Zn–Al–Cu–Ti–B (D)	8.96	0.94	0.04	0.012	–	rest

resistance in a reciprocating mode “ball on plate”, attachment of the sample to the device table, setting the previously selected parameters (load, speed of linear movement of the sample, the wear distance setting, read-out frequency of the coefficient of friction) on the basis of experimental tests, performing the test, measurement of the wear resistance on the cross-section of the sample and determination of the mechanical cross-sectional area, performance of the final report,

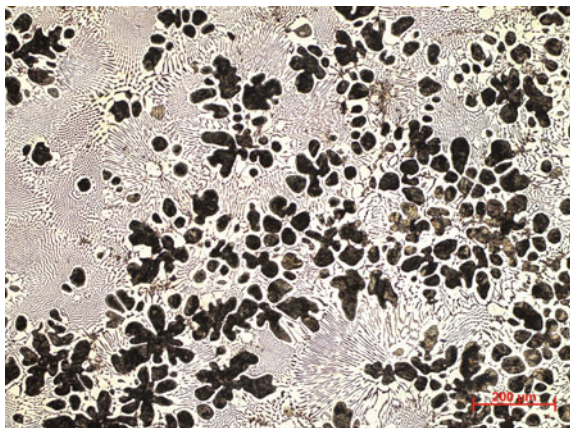
- corrosion resistance. The corrosion resistance investigations in salt spray were carried out according to the guidelines contained in ISO 9227:2006: Corrosion tests in artificial atmospheres—Salt spray tests. Before testing, the samples were weighed. Corrosion resistance test have consisted of the following steps in a salt spray test: preparation of 5 % saline solution, setting the samples at the angle of  $15^\circ$  in a salt spray chamber, starting a test images after 2, 6, 24, 48 and 96 h, drying the samples after test, cleaning the samples with rinsing water and a re-drying in an air stream,
- assessment of the stability of the realised processes of Zn–Al–Cu alloy modifications with application of X bar and R bar control charts for different properties of Zn–Al–Cu, Zn–Al–Cu–Sr and Zn–Al–Cu–Ti–B alloys. Variables were obtained by collecting the samples after the modification process. The samples had the same sample size in the assessment of the specific properties (corrosion resistance, hardness, wearability). On every chart both the central line and upper and lower control limits statistically identified were marked. The charts were used to identify occurrences of assignable causes in the situation, when a plot point is outside the chart’s control limits or there is a trend in points.

### 3 Results and Discussion

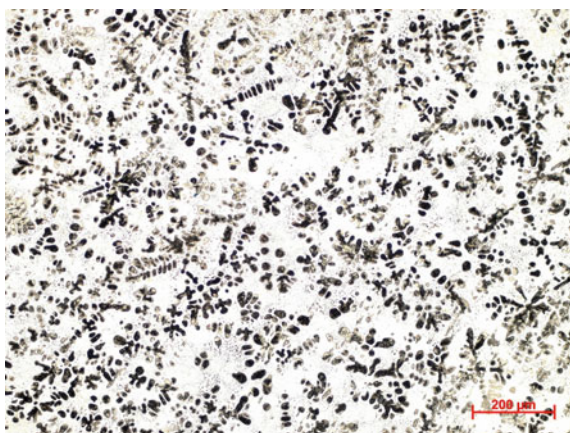
The results of the metallographic research, carried out with the usage of an optical microscope, have proved that the cast zinc-aluminium-copper alloys are of the  $\alpha'$  solid solution character, posing the precipitation of aluminium and eutectic grains  $\alpha' + \eta$ , morphology of which depends on the mass concentration of the modifiers or the alloy additions represented by Sr, Ti–B. The micro-structure of the Zn–Al–Cu alloy is characterised by globular precipitations of the  $\alpha'$  phase (Fig. 1). Modification of the Zn–Al–Cu alloy with strontium causes the change within the morphology of the  $\alpha'$  precipitations, which obtain the dendritic shape (Fig. 2). Modification of Ti–B does not cause changes in the morphology of the eutectic phase. However, it causes the fragmentation of the  $\alpha'$  phase precipitations as well as the  $\alpha' + \eta$  eutectic phase (Fig. 3).



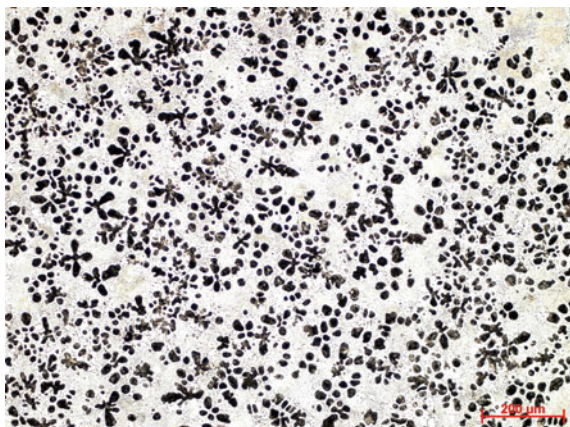
**Fig. 1** Microstructure of the Zn–Al–Cu alloy cooled at the rate of  $0.09\text{ }^{\circ}\text{C}\cdot\text{s}^{-1}$



**Fig. 2** Microstructure of the Zn–Al–Cu–Sr alloy cooled at the rate of  $0.09\text{ }^{\circ}\text{C}\cdot\text{s}^{-1}$



**Fig. 3** Microstructure of the Zn–Al–Cu–Ti–B alloy cooled at the rate of  $0.09\text{ }^{\circ}\text{C}\cdot\text{s}^{-1}$



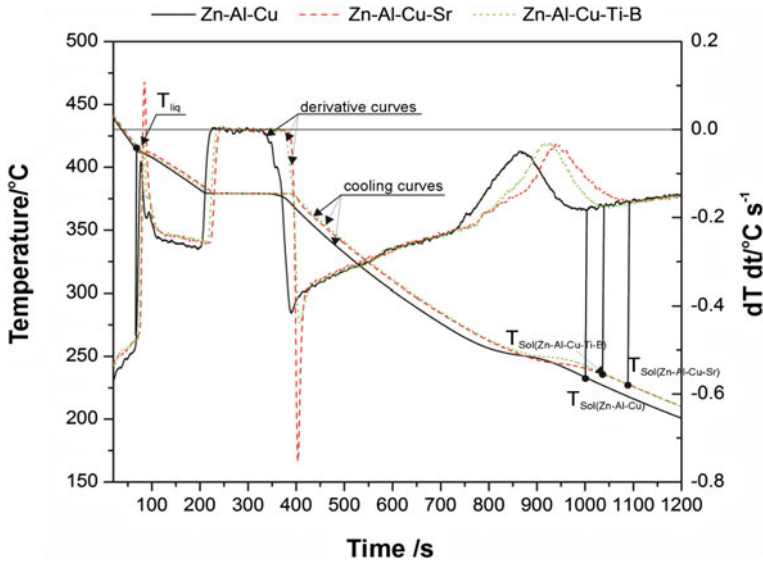


**Fig. 4** Cooling curves and derivative curves for alloys: Zn–Al–Cu, Zn–Al–Cu–Sr and Zn–Al–Cu–Ti–B cooled with the rate of  $0.2\text{ }^{\circ}\text{C}\cdot\text{s}^{-1}$

Modification of the analysed zinc alloys with strontium, titanium as well as boron is synonymous to the partial modification of the microstructure, also the  $\alpha' + \eta$  eutectic, what has been proven by the metallographic research and the changes are shown on the diagrams of the thermo derivative analysis (Fig. 4).

The conducted research of corrosion resistance have indicated its increase only in the Sr modified sample. The research hasn't proven the increase of corrosion resistance of the Ti–B modified alloy (Fig. 5).

In Zn–Al–Cu alloys modified both with Sr and Ti–B one has observed the increase of hardness in comparison with the original alloy (Fig. 6).

Wear resistance research has revealed wear resistance improvement both in Sr and Ti–B modified alloys (Fig. 7).

To analyse if the processes of Zn–Al–Cu alloys modification can fulfil the stability conditions even in the laboratory conditions the X bar and range charts have been prepared, for both the Zn–Al–Cu–Sr and Zn–Al–Cu–Ti–B alloys. In both cases variables have reflected the results of corrosion resistance, hardness and wearability resistance measurements. For preparation of quality control charts it was necessary to calculate: central line, upper control line and lower control line for X bar chart as well as central line and upper control line for range chart.

For the application of the X bar and range charts and the assessment of process stability based on corrosion measurement of the Zn–Al–Cu–Sr alloy (Fig. 8) in the

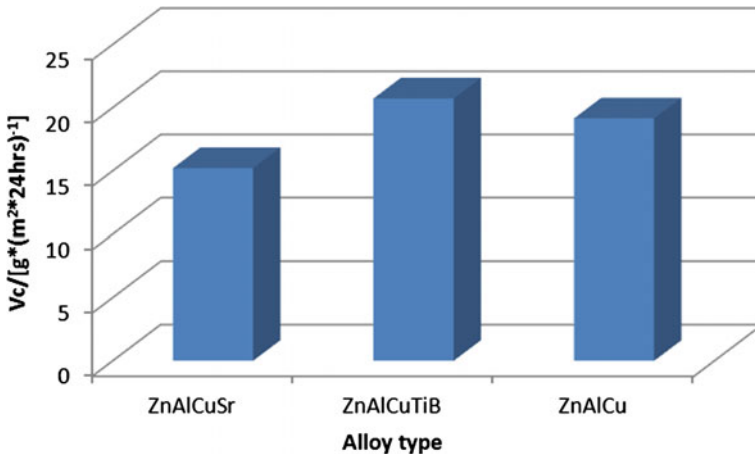


Fig. 5 Corrosion measurement results of the investigated Zn–Al–Cu alloys

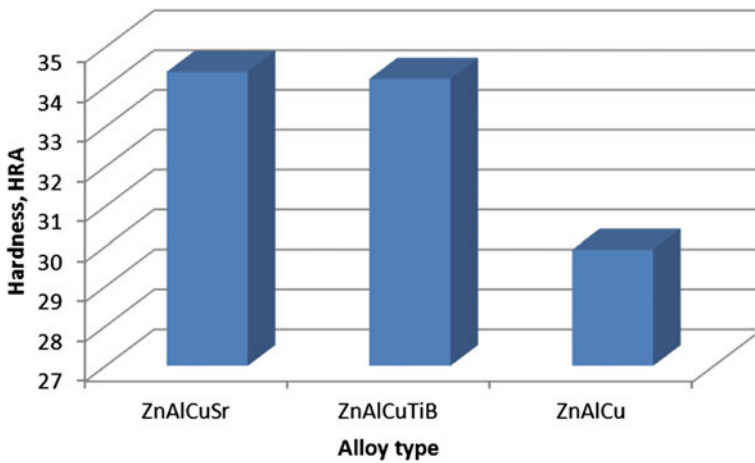


Fig. 6 Hardness measurement results of the investigated Zn–Al–Cu alloys

laboratory conditions one has calculated the following values: central line for X bar chart (CL = 15.02), upper control line for X bar chart (UCL = 15.24), lower control line for X bar chart (LCL = 14.79), central line for range chart (CL = 0.12), upper control line for range chart (UCL = 0.39).

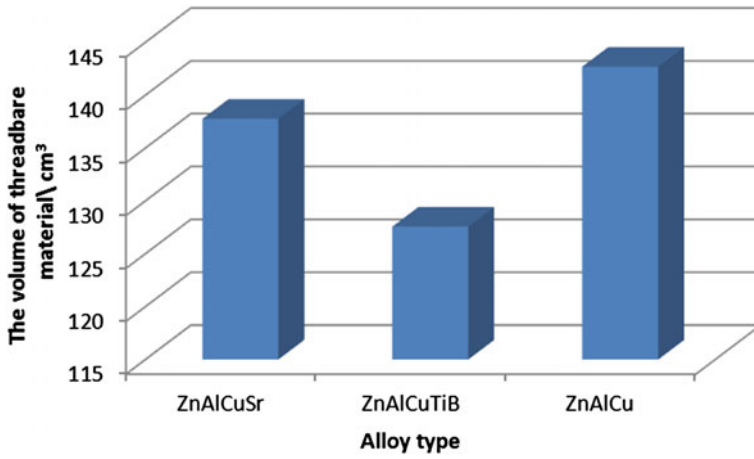


Fig. 7 Hardness measurement results of the investigated Zn–Al–Cu alloys

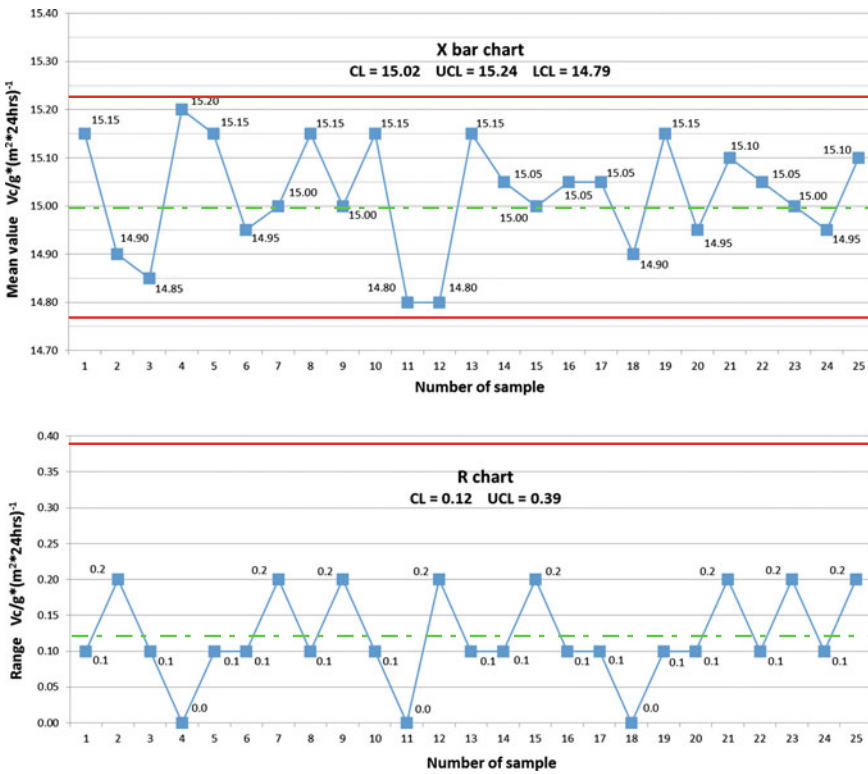


Fig. 8 X bar and R control charts for corrosion resistance of Zn–Al–Cu–Sr alloy

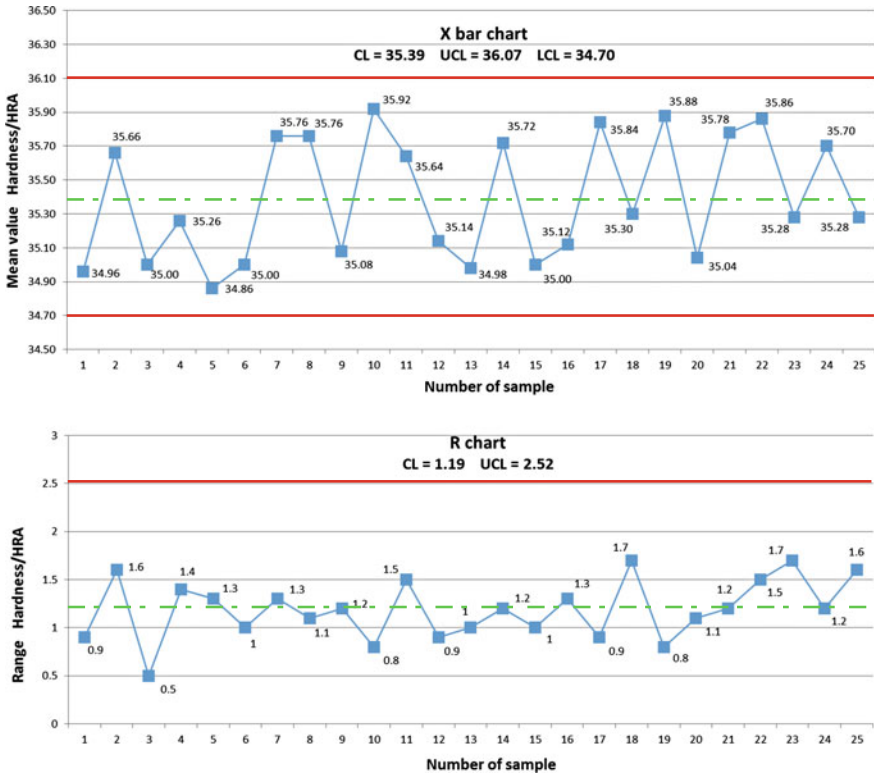


Fig. 9 X bar and R control charts for hardness of Zn–Al–Cu–Sr alloy

The application of the X bar and range charts and the assessment of process stability based on hardness measurement of the Zn–Al–Cu–Sr alloy (Fig. 9) in the laboratory conditions has required the calculation of the following values: central line for X bar chart (CL = 35.39), upper control line for X bar chart (UCL = 36.07), lower control line for X bar chart (LCL = 34.70), central line for range chart (CL = 1.19), upper control line for range chart (UCL = 2.52).

To assess the process stability based on the hardness measurement of the Zn–Al–Cu–Sr alloy (Fig. 10) in the laboratory conditions one has calculated the following values: central line for X bar chart (CL = 137.76), upper control line for X bar chart (UCL = 145.73), lower control line for X bar chart (LCL = 129.79), central line for range chart (CL = 4.24), upper control line for range chart (UCL = 13.85).

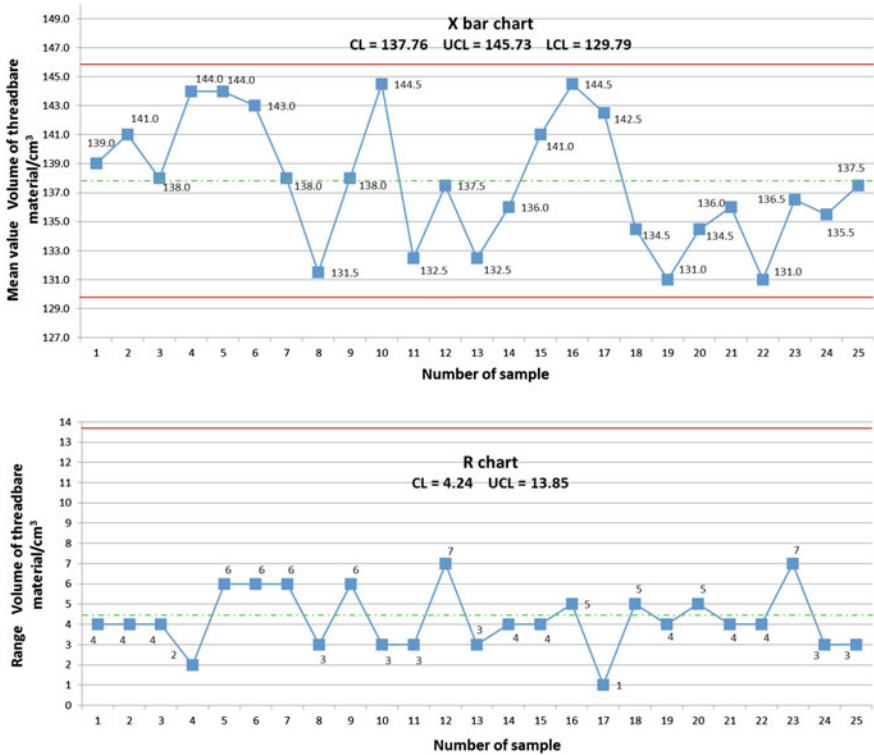


Fig. 10 X bar and R control charts for wearability of Zn-Al-Cu-Sr alloy

### 4 Conclusion

Changes in the  $\alpha$  phase (Al) morphology of the cast zinc alloy can be the effect of the modification of the alloy with strontium. It is caused by the changes in crystallization kinetics. The base for heterogeneous nucleation of the alloy in this case is aluminium.

A confirmation of these changes is the shape of the cooling curve of the modified alloy in comparison with the original one. The increase of hardness of investigated alloy of about 7 % is the result of the addition of strontium. In areas out of the heat centre, where a shrinkage cavity pipe occurs, the new alloys are also characterized by low porosity. The microstructure of the mould gets more uniform without segregation of its compounds, when the shrinkage cavity pipe reaches the outside form of the melting system.

Furthermore, modification process of Zn-Al-Cu alloys—with formation of Zn-Al-Cu-Sr and Zn-Al-Cu-Ti-B alloys—realised and verified in the laboratory conditions can be defined as a stable one. Potential variables are of natural character

and there are no variations resulting from special causes. Basing on the analysis' results it can be stated that modification process—realised according to the planned suggested parameters—can assure the fulfilment of specified requirements made to the modified Zn–Al–Cu alloys even in the laboratory conditions.

## References

1. Krajewski W (1999) Research of phase transformation in high-alu-minium zinc foundry alloys modified by Ti addition. *Prakt Metallogr—Pract Metallography* 30:9–11
2. Górny Z, Sobczak J (2005) Non-ferrous metals based novel materials in foundry practice. ZA-PIS, Cracow
3. Krajewski W (2000) DTA examinations of the solidification course of medium-aluminium zinc alloys modified with Ti. *Metall Foundry Eng* 26(2):143–147
4. Karkoszka T, Soković M (2014) Risk based on quality, environmental and occupational safety in heat treatment processes. *Metallurgy* 53:545–548
5. Karkoszka T (2013) Risk in fulfilling the quality, environmental and occupational safety requirements. Śląsk, Katowice
6. Osorio WR, Garcia A (2002) Modeling dendritic structure and mechanical properties of Zn-Al alloys as a function of solidification conditions. *Mater Sci Eng* 325:103–111
7. Zhu YH (2001) Phase transformations of eutectoid Zn-Al alloys. *J Mater Sci* 36:3973–3980
8. Dobrzański LA, Krupiński M, Labisz K, Krupińska B, Grajcar A (2010) Phases and structure characteristics of the near eutectic Al–Si–Cu alloy using derivative thermo analysis. *Mater Sci Forum* 638:475–480
9. Krupiński M, Krupińska B, Labisz K, Rdzawski Z, Borek W (2014) Influence of cooling rate on crystallisation kinetics on microstructure of cast zinc alloys. *J Therm Anal Calorim* 118 (2):1361–1367
10. Krupiński M, Krupińska B, Rdzawski Z, Labisz K, Tański T (2015) Additives and thermal treatment influence on microstructure of nonferrous alloys. *J Therm Anal Calorim* 120 (3):1573–1583
11. Krupińska B (2015) Structure and Properties of Zn–Al–Cu Alloys with Alloying Additives. *Mech Mater Eng Mod Struct Compon Des, Adv Structured Mater* 70:341–349

# Fatigue Test of the Inconel Alloy 718 Under Three Point Bending Load at Low Frequency

J. Belan, L. Hurtalová, A. Vaško, E. Tillová and M. Chalupová

**Abstract** Inconel alloy 718 is a high-strength, corrosion-resistant, and hardenable Ni–Cr alloy with good tensile, fatigue, creep, and rupture strength which has resulted in its usage in a wide range of applications. It is used at temperatures ranging from –250 up to 705 °C. The main areas of application are the aircraft industry, as well as the space industry. Turbine-engine components experience significant fluctuations in stress and temperature during their repeated takeoff-cruise-landing cycles. These cycles can result in localized, small, plastic strains. Thus low-cycle, low-frequency fatigue is of interest to engine design. Engine vibrations and airflow between the stages of the turbine can also result in high-cycle fatigue with rapid cycle accumulation in airfoils at much higher frequencies, in the kHz range. This article deals with fatigue test of the IN 718 alloy under three point bending load at low frequency. Most of the fatigue tests for this alloy have been previously done under rotation bending loading, with the aim of comparing the results achieved in fatigue crack initiation and crack propagation. SEM microstructure and fractography analyses have also been carried out in this regard.

**Keywords** Inconel alloy 718 · Fatigue test · Three point bending · S-N curve · SEM fractography

---

J. Belan (✉) · L. Hurtalová · A. Vaško · E. Tillová · M. Chalupová  
Faculty of Mechanical Engineering, Department of Materials Engineering,  
University of Žilina, Univerzitná 8215/1, 01026 Žilina, Slovakia  
e-mail: juraj.belan@fstroj.uniza.sk

L. Hurtalová  
e-mail: lenka.hurtalova@fstroj.uniza.sk

A. Vaško  
e-mail: alan.vasko@fstroj.uniza.sk

E. Tillová  
e-mail: eva.tilova@fstroj.uniza.sk

M. Chalupová  
e-mail: maria.chalupova@fstroj.uniza.sk



## 1 Introduction

This alloy was developed in the 1960s when the former Fe-based superalloys evolved towards Ni-based superalloys. Alloy 718 contains both Fe and Ni alloyed with some Al and Ti, though the most important addition is the refractory element Nb. The strength of the alloy 718 comes from coherent solid-state precipitates, which are for a small part  $\gamma'$ -Ni<sub>3</sub>Al but mostly  $\gamma''$ -Ni<sub>3</sub>Nb precipitates [1–6]. The major strengthening phases in the alloy 718 are the  $\gamma''$  and  $\gamma'$  phases which produce coherency strains in the  $\gamma$  matrix. The  $\gamma''$  phase is considered to be the main strengthening phase and has a DO<sub>22</sub> BCT crystal structure, while the  $\gamma'$  phase is a FCC ordered phase with a L1<sub>2</sub> crystal structure. The strengthening phases  $\gamma''$  and  $\gamma'$  contain 3 atoms of Ni, while the  $\gamma''$  phase is richer in Nb, while the  $\gamma'$  phase is richer in Al.

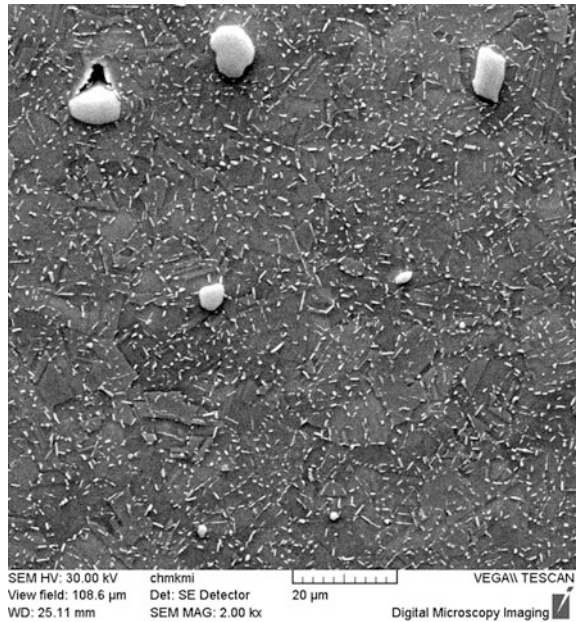
The  $\gamma''$  and  $\gamma'$  phases have unique morphologies. The  $\gamma'$  phase precipitates as round particles with size less than 200 Å, and continues to be round in shape when it coalesces at higher temperatures. The  $\gamma''$  phase rather takes the shape of a disk with a length of 5–6 times its thickness; however, when the  $\gamma''$  phase precipitates at very low temperatures, a TEM is necessary to resolve its shape. The  $\gamma''$  phase continues to grow in the disk shape at higher heat treatment temperatures or exposures. Some studies [7] have indicated that the  $\gamma''$  and  $\gamma'$  phases grow in a sandwich-like morphology indicating a co-precipitation of the phases.

Because the  $\gamma''/\gamma'$  phases grow with higher temperatures and long time exposures at low temperatures, a transition of  $\gamma'$  to  $\gamma''$  to delta phase occurs slowly at lower temperatures, but the reaction occurs faster or sooner at higher temperatures. Recent data [7] has indicated that the  $\gamma''$  phase is the least stable phase and the transition goes through  $\gamma''$  phase to delta phase and finally  $\gamma'$  phase.

The delta phase found in alloy 718 is incoherent with the  $\gamma$  and has an orthorhombic crystal structure. The delta phase is found mostly as plates growing on the (111) planes or nucleating on the grain boundaries, and is associated with loss of strength as well as loss of fatigue lifetime in this alloy. The delta phase in the grain boundaries is used to control the grain size in wrought materials and seems to also be important for notch ductility [7]. Figure 1 shows a typical microstructure of the wrought alloy 718. The microstructure consists of light grey blocks of carbides and fine lenticular and lamellar particles of delta phase (Ni<sub>3</sub>Nb) distributed in the FCC matrix, with grain size approximately 10  $\mu$ m and a few deformation twins.

During the past few decades, extensive investigations have been made on the low-cycle fatigue (LCF) and high-cycle fatigue (HCF) properties of IN718, such as the effect of temperature on the cyclic stress-strain response and LCF life associated with the deformation of microstructures [8–10], the factors (temperature, environment, and loading parameters, etc.) influencing fatigue crack growth [11–13], the creep-fatigue oxidation interactions [13, 14], the mechanism-based modelling of fatigue life prediction [15], etc. Nowadays, the very high-cycle fatigue (VHCF) properties of high-strength metals have become more and more significant, ever since the finding of fatigue failure beyond 10<sup>7</sup> cycles in high-strength steels [16]. The subsequent studies on many ferroalloys [17, 18] prove that the conventional

**Fig. 1** The typical wrought INCONEL alloy 718 microstructure, SEM, etch. Kallings



fatigue limit in HCF disappears in the VHCF regime and there is a transition of fatigue crack initiation from the surface to the internal defects at around  $10^6$ – $10^7$  cycles [19]. Furthermore, it is recognized that the gigacycle fatigue failure of high strength steels is preferentially initiated from interior inclusions, giving the appearance of a fish-eye [17, 18].

Compared to the comprehensive investigation and understanding of the VHCF properties of steels [19, 20] and Al-alloys [21], few studies exist on nickel-based superalloys, e.g. IN718 superalloy [22].

Yan et al. [22] performed a rotary bending fatigue test on IN718 and found that it did not show gigacycle fatigue failure at room temperature, but did at 500 °C. However, another study [23], under ultrasonic frequency, revealed that fatigue fracture of IN718 occurred between  $10^7$  and  $10^8$  cycles. As the experimental work suggests, it is still disputable whether this superalloy under practical loading would show VHCF or not. Furthermore, it is known that the fatigue crack initiation process becomes increasingly important with the extension of fatigue life.

In this study, the HCF properties of the IN718 superalloy were investigated under a three point flexure fatigue test at the average frequency  $f = 143$ – $151$  Hz and at room temperature. With the help of a scanning electron microscope (SEM), fractography analyses were performed to disclose the fracture features of samples in different life ranges. And finally the comparisons of ultrasonic push-pull fatigue test results to the three point flexure fatigue test results are given. Also the initiation and propagation of fatigue crack at various conditions of loading is discussed.

## 2 Experimental Materials and Methods

The material used in this study is a Ni-based superalloy INCONEL 718 with a chemical composition (in wt%) shown in Table 1.

The material was heat treated, according to the supplier's BIBUS Ltd. (CZ) material sheet, at 980 °C/1 h AC (air cooled) and heating at 720 °C/8 h followed FC (furnace cooled) (50 °C per hour) to temperature 620 °C holding time 8 h and air cooled. The achieved mechanical properties of the material with grain size ASTM 12 are in Table 2.

The experimental material for the three point flexure fatigue test was machined down into a simple blocky shape as reported in the schematic drawing (see Fig. 2). Also, for the calculation of the maximum bending stress, we used the formula (1):

$$\sigma_{omax} = \frac{3 \times F \times L}{2 \times b \times h^2} \text{ MPa} \quad (1)$$

where  $\sigma_{omax}$  is the maximum bending stress (MPa),  $F$  is the dynamic load (N),  $L$  is the distance of supports (mm),  $b$  is the specimens width (mm), and  $h$  is the sample height (mm).

The three point flexure fatigue test was carried out on testing machine ZWICK/ROELL Amsler 150 HFP 5100 at room temperature with a static pre-load  $F_{static} = -15$  kN (this value may be considered as  $F_{medium}$  when dynamic load changes from maximum to minimum around this  $F_{medium}$ ) and dynamic force  $F_{dynamic}$  varies from 6.31 up to 12.8 kN. The value of  $2 \times 10^7$  cycles was set as a reference and when the sample had reached this value without breaking, the so-called run-out, that bending stress was considered as the fatigue lifetime limit. The frequency of fatigue tests was approximately  $f = 150$  Hz. The S-N curve was

**Table 1** Chemical composition (in wt%) of INCONEL alloy 718

	C	Si	Mn	Al	Co	Cr	Mo	Nb	Ni	Ta	Ti
Btm	0.026	0.08	0.07	0.56	0.14	19.30	2.98	5.27	53.29	<0.01	0.95
Top	0.026	0.09	0.07	0.57	0.14	19.31	2.99	5.30	53.32	<0.01	0.96
Max	0.08	0.35	0.35	0.8	1.00	21.00	3.30	5.50	55.0	0.05	1.15

Fe content is the remainder

**Table 2** Mechanical properties of INCONEL alloy 718 as received, according to BIBUS Ltd. material sheet

Temp. (°C)	Rp 0.2 (MPa)	Rm (MPa)	Elongation A (%)	Reduced area Z (%)	HBW 10/3000	$\sigma_{T/649}$ (MPa)	Rupture life (h)	A (%) creep
20	1213	1549	21.3	33.3	429	–	–	–
649	986	1123	22.6	68.0	–	689	26.8	45.7

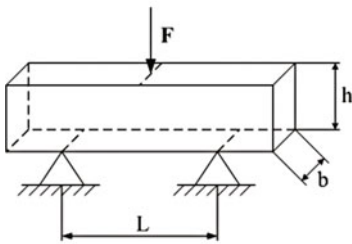


**Fig. 2** A schematic drawing of the experimental sample dimensions for the three-point flexure  $\sigma_{\text{max}}$  calculation and setting of the fatigue test

plotted from the measured values, which gives the relation between the maximum bending stress  $\sigma_{\text{max}}$  and the number of cycles  $N_f$ .

Fractography analysis of broken samples was also carried out. For fractography analysis we used the scanning electron microscope TESCAN Vega II LMU. All fractography analyses were carried out in order to describe mechanisms of fatigue crack initiation, fatigue crack propagation and final static fracture of the samples.

### 3 Results and Discussion

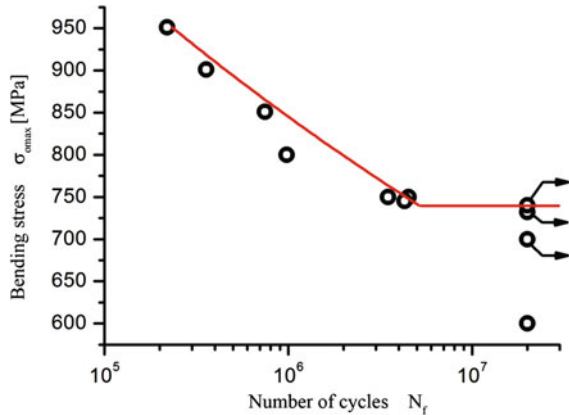
For low-frequency fatigue testing we used 10 samples with simple blocky shape as seen in Fig. 2. Figure 3 shows the S-N curve of IN718 obtained from the three-point flexure fatigue tests at room temperature with a frequency of 150 Hz under the load ratio of  $R = 0.11$ . Obtained results were approximated using Eq. (2), which is Basquin’s formula for the S-N presentation and approximation. This approach was also used for other materials [24].

$$\sigma_a = 2591 \times N_f^{-0.0811} \tag{2}$$

where  $\sigma_f' = 2591$  is the coefficient of fatigue strength, and  $-0.0811 = b$  is the lifetime curve exponent.

It is clearly seen from the measured S-N curve that the fatigue life increases with decreasing stress amplitude and the S-N curve appears to continuously decline as

**Fig. 3** The S-N curve for three-point flexure fatigue test of the Inconel alloy 718 with run-outs after reaching  $2 \times 10^7$  cycles

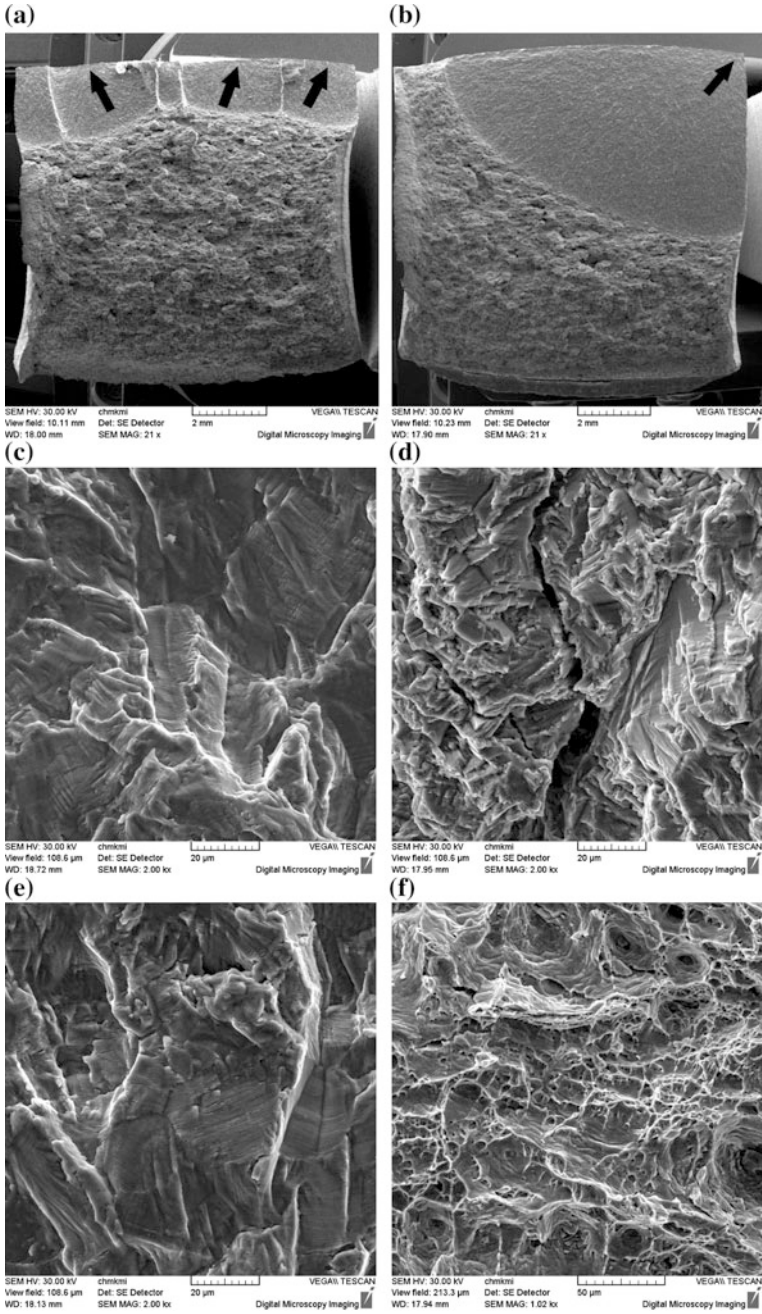


the life extends. The limit number of cycles— $2 \times 10^7$  (20,000,078)—was reached at the maximum bending stress  $\sigma_{\text{omax}} = 740$  MPa. Accordingly, fatigue lifetime stress obtained using a different testing method—ultrasonic push-pull loading with  $R = -1$  [25]—increases this factor by two fold higher (push-pull fatigue lifetime of about 386 MPa compared to three-point flexure fatigue lifetime of 740 MPa at the same number of cycles). Of course, these values may only roughly be compared because of different frequency of test and different mechanisms of loading.

From the three-point flexure fatigue tested samples we selected two samples as representatives for SEM observation to examine the fractured surface. Figure 4 shows an overall view of the fractured surfaces at different stress levels. Initiation sites are marked by an arrow. As a confirmation of the facts published in [26] at high stress levels as shown in Fig. 4a, fatigue cracks initiated from multiple initiation sites and resulted in a very small tensile final fracture area. With decreasing stress levels, the number of initiation sites decreases, as shown in Fig. 4b, controlled by the crystallographic slip at surface grains and, the static tensile final fracture area enlarges. This result is in good correlation with the results obtained at different fatigue loadings—ultrasonic push-pull and rotation bending loading. Fracture due to a single fatigue crack occurs in samples with longer fatigue life. Regardless of how high or low the stress levels are, all fatigue cracks initiate on free surfaces without a significant oxide or extrusion presence, even the presence of fish-eye commonly occurring in high frequency fatigue testing. After initiation, the fatigue crack propagates with transcrystalline mechanisms with typical striations, indicating the stable crack propagation as reported in Fig. 4c–d. The fatigue crack propagation mechanism is the same as in other fatigue loading (ultrasonic push-pull or rotation bending).

At higher stress levels, as shown in Fig. 4d–e, a major fatigue crack was generated and a few secondary cracks have appeared perpendicular to the main fatigue crack propagation, and probably situated at grain boundaries.

Figure 4f shows the change in the micro-mechanism of fractures from typical fatigue crack propagation and classical transcrystalline ductile dimpled fracture



◀ **Fig. 4** SEM micrographs for fractography analysis of Inconel alloy 718 after three-point flexure fatigue test. An overall view of the fatigue crack initiation sites **a**  $\sigma_{\max} = 900$  MPa,  $N_f = 3.578 \times 10^5$ ; **b**  $\sigma_{\max} = 750$  MPa,  $N_f = 4.52 \times 10^6$ . Fatigue crack propagation: **c** striation occurrence at  $\sigma_{\max} = 800$  MPa,  $N_f = 9.79 \times 10^5$ , **d** major fatigue crack at  $\sigma_{\max} = 850$  MPa,  $N_f = 7.49 \times 10^5$  and **e** formation of secondary crack at  $\sigma_{\max} = 850$  MPa,  $N_f = 7.49 \times 10^5$ , **f** the static fracture area with ductile dimple morphology

mechanism in the tensile final fatigue region. There is also a possibility to observe fractured NbC primary carbides. However, most of them are totally crushed, which confirms the fact about ductile mechanism of breaking in this region—pulling up the dimples till one massive crack occurs and causes the fracture.

## 4 Conclusions

The nickel-based superalloy INCONEL 718 is a well known material used for high temperature applications especially in the manufacturing of aero jet turbine discs. Many authors have carried out fatigue tests with rotation bending loading at room or elevated temperatures. Results of three-point bending fatigue tests are original and unique from this point of view. The three-point bending fatigue test was carried out at up to  $\approx 2 \times 10^7$  cycles at room temperature. From fatigue testing, we obtained the following conclusions:

- Initiation of a fatigue crack is on a free surface without any oxide, carbide or other extrusion presence, or even fish-eye presence. At higher levels of stress, initiation occurs at multiple sites and with decreasing stress the initiation sites decrease to one single site. This is in good correlation with the results achieved by other authors who have carried out fatigue tests with different mechanisms of loading.
- Fatigue crack propagation is achieved via a transcrystalline mechanism with typical striation, and at higher stress levels the major crack forms together with small secondary cracks that are perpendicular to the crack propagation direction. The area of static tensile overload is characterised by ductile dimple morphology.

Fractography analysis shows a quite similar fatigue behaviour of this Inconel alloy 718 at three-point bending load and rotation bending load, even with high frequency ultrasonic push-pull loading. The only differences are in the form of initiation sites, which of course depends on the loading regime, and obtained different fatigue lifetime limits, where at three-point bending the fatigue lifetime is two times longer compared to ultrasonic push-pull loading at the same number of cycles.

**Acknowledgments** This work has been supported by Scientific Grant Agency of Ministry of Education of The Slovak Republic and the Slovak Academy of Sciences, No. 1/0533/15, No. 044ŽU-4/2014 and project EU ITMS 26110230117.

## References

1. Paulonis DF, Oblak JM, Duvall DS (1969) Precipitation in nickel-base alloy 718. *Trans ASM* 62(3):611–622
2. Kirman I, Warrington DH (1970) The precipitation of Ni<sub>3</sub>Nb phases in a Ni-Fe-Cr-Nb alloy. *Metall Trans* 1(10):2667–2675
3. Cozar R, Pineau A (1973) Morphology of  $\gamma'$  and  $\gamma''$  precipitates and thermal stability of Inconel 718 type alloys. *Metall Trans* 4(1):47–59
4. Oblak JM, Paulonis DF, Duvall DS (1974) Coherency strengthening in Ni base alloys hardened by DO<sub>22</sub>  $\gamma'$  precipitates. *Metall Trans* 5(1):143–153
5. Sundaraman M, Mukhopadhyay P, Banerjee S (1992) Some aspects of the precipitation of metastable intermetallic phases in INCONEL 718. *Metall Trans A* 23(7):2015–2028
6. Slama C, Servant C, Cizeron G (1997) Aging of the Inconel 718 alloy between 500 and 750 °C. *J Mater Res* 12(9):2298–2316
7. Radavich JF (1989) The physical metallurgy of cast and wrought alloy 718. In: Loria EA (ed) *Superalloy 718—metallurgy and applications*, The Minerals, Metals & Materials Society
8. Fournier D, Pineau A (1977) Low cycle fatigue behavior of Inconel 718 at 298 K and 823 K. *Metall Mater Trans A* 8(7):1095–1105
9. Reger M, Remy L (1988) High-temperature, low-cycle fatigue of IN100 superalloy influence of frequency and environment at high-temperatures. *Mater Sci Eng A* 101:55–63
10. Reger M, Remy L (1988) High-temperature, low-cycle fatigue of IN100 superalloy influence of temperature on the low-cycle fatigue behavior. *Mater Sci Eng A* 101:47–54
11. Bache MR, Evans WJ, Hardy MC (1999) The effects of environment and loading waveform on fatigue crack growth in IN718. *Int J Fatigue* 21(1):69–77
12. Remy L, Alam A, Haddar N, Köster A, Marchal N (2007) Growth of small cracks and prediction of lifetime in high-temperature alloys. *Mater Sci Eng A* 468–470:40–50
13. Leo Prakash DG, Walsh MJ, Maclachlan D, Korsunsky AM (2009) Crack growth micro-mechanisms in the IN718 alloy under the combined influence of fatigue, creep and oxidation. *Int J Fatigue* 31(11–12):1966–1977
14. Pineau A (1989) Mechanisms of creep-fatigue interactions. In: Moura-Branco C, Guerra Rosa L (eds) *Advances in fatigue science and technology*. Kluwer Academic, Dordrecht
15. Alexandre F, Deyber S, Pineau A (2004) Modelling the optimum grain size on the low cycle fatigue life of a Ni based superalloy in the presence of two possible crack initiation sites. *Scripta Mater* 50(1):25–30
16. Masuda C, Tanaka Y (1986) Relationship between fatigue strength and hardness for high strength steels. *Trans Jpn Soc Mech Eng Part A* 52(476):847–852
17. Murakami Y, Kawakami K, Duckworth WE (1991) Quantitative evaluation of effects of shape and size of artificially introduced alumina particles on the fatigue strength of 1.5Ni–Cr–Mo (En24) steel. *Int J Fatigue* 13(6):489–499
18. Sakai T, Sakai T, Okada K, Furuichi M, Nishikawa I, Sugeta A (2006) Construction of electronic factual database on very high cycle fatigue properties for structural metallic materials. *Int J Fatigue* 28(11):1486–1492
19. Sakai T, Sato Y, Oguma N (2002) Characteristic S-N properties of high-carbon-chromium-bearing steel under axial loading in long-life fatigue. *Fatigue Fract Eng Mater Struct* 25(8–9):765–773
20. Wang QY, Bathias C, Kawagoishi N, Chen Q (2002) Effect of inclusion on subsurface crack initiation and gigacycle fatigue strength. *Int J Fatigue* 24(12):1269–1274
21. Wang QY, Kawagoishi N, Chen Q (2006) Fatigue and fracture behaviour of structural Al-alloys up to very long life regimes. *Int J Fatigue* 28(11):1572–1576
22. Yan N, Kawagoishi N, Chen Q, Wang QY, Nishitani H, Kondo E (2003) Fatigue properties of inconel 718 in long life region at elevated temperature. *Key Engineering Materials*. doi:10.4028/www.scientific.net/KEM.243-244.321



23. Chen Q, Kawagoishi N, Wang QY, Yan N, Ono T, Hashiguchi G (2005) Small crack behaviour and fracture of nickel-based alloy under ultrasonic fatigue. *Int J Fatigue* 27 (10–12):1227–1232
24. Trško L, Bokůvka O, Guagliano M, Nový F, Hazlinger M (2013) Ultra long fatigue life of 50CrMo4 steel with strengthened surface by high energy shot peening. In: Alfirević I, Semenski D (eds) 30th Danubia-Adria symposium on advances in experimental mechanics. Croatian Society of Mechanics, Zagreb
25. Belan J (2015) High frequency fatigue test of in 718 alloy—microstructure and fractography evaluation. *Metalurgija—Metalurgy* 54(1):59–62
26. Ma XF, Duan Z, Shi HJ, Murai R, Yanagisawa E (2010) Fatigue and fracture behavior of nickel-based superalloy Inconel 718 up to the very high cycle regime. *J Zhejiang Univ Sci A (Applied Physics & Engineering)* 11(10):727–737

# Development of a Finite Element Program for Determining Mat Pressure in the Canning Process of a Catalytic Converter

S.J. Chu and Y.D. Lee

**Abstract** A catalytic converter in the automotive exhaust system, consists of a substrate in the center, a mat outside the substrate and a can outside the mat. Since the substrate is brittle, it is wrapped in mats and press-fitted into a can. If the mat pressure developed during the canning process is excessive, it might cause the fracture of the substrate. A finite element program for finding mat pressures on the substrate in the canning process was developed in Microsoft EXCEL. It is a user-friendly program with easy input and graphical output. By modeling the substrate, the mat and the can as simply as possible, fixing the number of elements and iterations and taking into account only a small part of the output radial distance changes in the current step to calculate the input pressure in the next step, the material nonlinear problem was solved successfully in Microsoft EXCEL. The solutions were compared to ABAQUS solutions and found to be accurate.

**Keywords** Catalytic converter · Substrate · Mat · Can · Hyperfoam · Finite element analysis

## Nomenclature

$a, b$	Semi major- and minor-axis
$F_x, F_y, M_z$	Forces and moment on a node
$g_t$	Target gap between a substrate and a can
$L$	Length of a beam element
$p_e$	Converted mat pressure on a substrate
$p_m$	Radial pressure on a mat
$X, Y, R$	Profiles of a mat
$r_1, r_2$	Profiles of a substrate

---

S.J. Chu (✉) · Y.D. Lee  
School of Mechanical Engineering, University of Ulsan, MuGeo-Dong,  
680-749 Nam-Gu, Ulsan, South Korea  
e-mail: sjchu@ulsan.ac.kr

Y.D. Lee  
e-mail: mablej@naver.com

$t$	Can thickness
$t_m$	Mat thickness
$u, v, \theta_z$	Translation and rotation of a can
$\epsilon$	Nominal radial strain of a mat
$\eta$	Error correction factor

## 1 Introduction

A catalytic converter is a vehicle emissions control device that converts toxic pollutants in exhaust gases to less toxic pollutants [1]. It consists of a substrate in the center, a mat outside the substrate and a can outside the mat as shown in Fig. 1. A substrate is a ceramic body with a number of small axial openings through which the exhaust gas passes. To increase the surface area exposed to the exhaust gas, the wall thickness of the openings were reduced. Then it is more likely that the substrate will be subjected to brittle fracture. Since the substrate is brittle, it is wrapped in a soft mat and inserted into a steel can. It is called canning.

The contact pressure on the substrate depends mainly on how much the mat is compressed between the substrate and the can. If the contact pressure is too low, the substrate would slide, hit the can and be damaged when the car is in severe acceleration or deceleration. On the contrary, if the contact pressure is too high, the substrate would be damaged due to the contact pressure itself.



Fig. 1 Substrate, mat and can in a catalytic converter

It is important to know the contact pressure on the substrate in the canning process. Kyoung [2] predicted the mat pressure distribution either in the canning process or under operation conditions using commercial software. He assumed that the mat material follows the hyperfoam model.

Instead of using commercial software, a small finite element analysis can be carried out in Microsoft EXCEL. Its matrix manipulation capability enables it to carry out the analysis. Several authors [3–7] used EXCEL to solve finite element problems. Using EXCEL to solve such problems is shown to be common when teaching the FEM to students. Because the finite element program in EXCEL cannot be fully-flexible, only very small number of elements was used in their applications. The first author of this paper was interested in the finite element analysis using EXCEL and published a book on it [8]. In this paper, a finite element program was developed in EXCEL and the mat pressure distribution in the canning process was predicted. It was a rather large-size problem for the program and furthermore the iteration process to get a converged solution was required.

## 2 Finite Element Analysis

A finite element program for finding the contact pressure on the substrate in canning of a catalytic converter was developed in EXCEL. It is a user-friendly program with easy input and graphical output. To check the accuracy of our solution, it was compared with the solution computed in ABAQUS.

### 2.1 Geometry of the Substrate Outer Surface

The substrate is of circular or oval section. The profile of an oval section is constructed from two circular arcs shown in Fig. 2. The first arc with its center at  $(x_1, 0)$  and radius  $r_1$  subtends an angle  $\theta_1$ . The second arc with center at  $(0, y_2)$  and radius  $r_2$  subtends an angle  $\theta_2$ .

The semi-major and minor axes of an oval section are

$$a = x_1 + r_1 \tag{1}$$

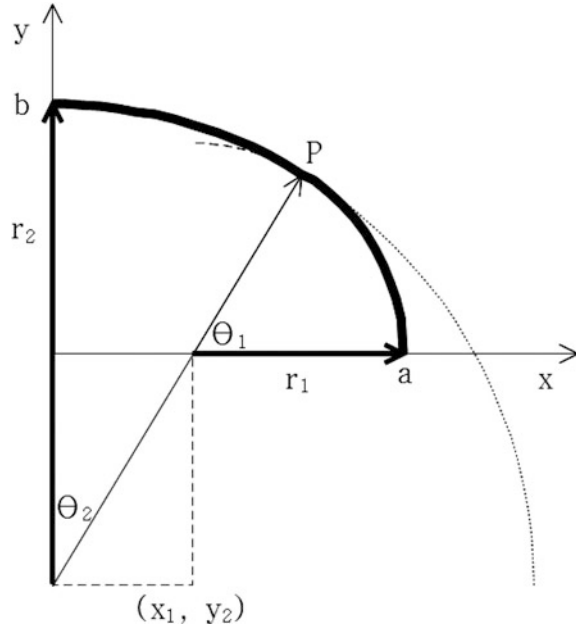
$$b = y_2 + r_2 \tag{2}$$

Note that  $y_2$  is negative.

The sum of the subtended angles is

$$\theta_1 + \theta_2 = 90^\circ \tag{3}$$

**Fig. 2** Creation of an oval section by combining two arcs



The horizontal and vertical distances from the origin to the point P where the two arcs are connected are

$$x_1 + r_1 \cos\theta_1 = r_2 \sin\theta_2 \quad (4)$$

$$r_1 \sin\theta_1 = r_2 \cos\theta_2 + y_2 \quad (5)$$

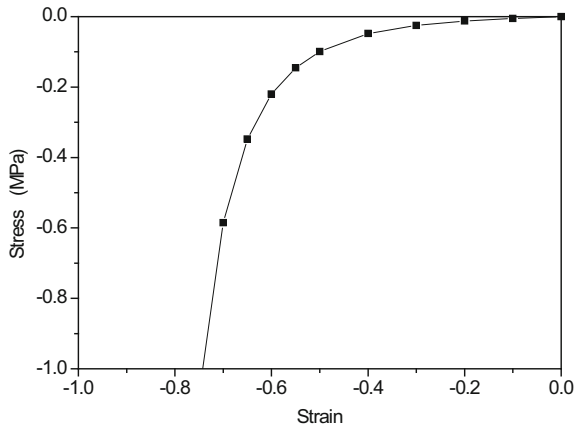
We have five Eqs. (1)–(5) with eight unknowns. Three of eight unknowns should be given to determine all unknowns.

## 2.2 *Finite Element Modeling of the Substrate, Mat and Can*

A finite element program was developed in EXCEL. Using matrix multiplication, matrix transverse and matrix inverse functions in EXCEL, we can construct a finite element equation and solve it. Due to difficulties in creating fully-automatic program in EXCEL, however, it is difficult to develop a program for a large-sized problem and even more difficult to develop a non-linear program.

The problem should be idealized as far as possible to be solved in EXCEL. Noting that the material of a substrate is softer than the steel but sufficiently hard compared to the material of a mat, the substrate can be idealized as being rigid. Then it is not necessary to model the substrate itself. Only the profile of a substrate

**Fig. 3** Nonlinear compression behavior of a mat



is needed to calculate the gap between the substrate outer surface and the can inner surface.

The material of a mat shows a material nonlinearity as shown in Fig. 3. We found that it was not needed to model the mat. Only the mat pressure was calculated from the gap between the substrate and can and applied on the can inner surface.

The can was assumed to be 2-dimensional and can resist both bending and membrane stresses. It was modeled as a beam.

It is not easy to develop a flexible, i.e. being able to adapting itself to different number of elements or different number of iterations, program in EXCEL. Therefore we conveniently fixed the number of elements and the number of iterations. In this way, a dedicated special finite element program using 35 elements and 20 iterations was developed.

### 2.3 Finite Element Procedures

- (a) Input  $a, b$  and  $x_1$ . Calculate  $y_2, r_1, r_2, \theta_1$  and  $\theta_2$  sequentially.

$$y_2 = b - r_2 \tag{6}$$

$$r_1 = a - x_1 \tag{7}$$

$$r_2 = \frac{(a^2 + b^2 - 2ar_1)}{2(b - r_1)} \tag{8}$$

$$\theta_1 = \cos^{-1} \frac{x_1}{r_2 - r_1} \tag{9}$$

**Table 1** Input mechanical properties and dimensions

Can	E	206 GPa
	$\nu$	0.28
	$t$	1.5 mm
Mat	$\mu_1, \alpha_1$	0.705e-3, 11.412
	$\mu_2, \alpha_2$	1.186e-6, 25.000
	$\mu_3, \alpha_3$	1.511e-3, -2.183
	$t_m$	10.6 mm
	$g_t$	3.8 mm
Substrate	E	11.8 GPa
	$\nu$	0.29
	$a$	40.00 mm
	$b$	28.50 mm
	$r_1$	24.09 mm

$$\theta_2 = \frac{\pi}{2} - \theta_1 \tag{10}$$

(b) Input  $t_m$  and  $g_t$ . Calculate  $\epsilon$ .

$$\epsilon = \frac{g_t}{t_m} - 1 \tag{11}$$

(c) Input  $\mu_i$  and  $\alpha_i$ , i.e. coefficients and exponents in Ogden hyperfoam model. The values are listed in Table 1. Calculate  $p_m$ .

$$p_m = \frac{2}{1 + \epsilon} \sum_{i=1}^N \frac{\mu_i}{\alpha_i} [(1 + \epsilon)^{\alpha_i} - 1] \tag{12}$$

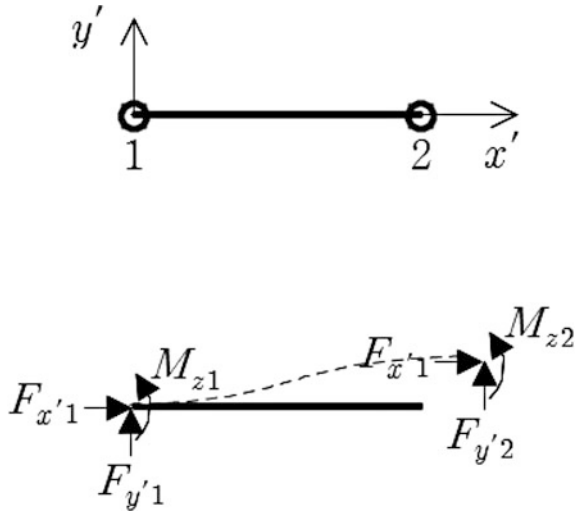
(d) Determine the number of elements in each arc so that the element size in each arc similar to each other. In this way, the first arc is equally divided into 19 elements and the second arc into 16 elements. Nodes #17–#35 are on the first arc and node #1–#17 are on the second arc.

$$\frac{N_2}{N_1} \approx \frac{r_2 \theta_2}{r_1 \theta_1} \tag{13}$$

(e) Model the can as a 2-dimensional beam. Construct element stiffness matrices and assemble them.

The beam is of rectangular cross section with a unit width and thickness  $t$ . The sectional area and second moment of inertia are

**Fig. 4** Forces and moment on a beam element



$$A = t \tag{14}$$

$$I_z = t^3/12 \tag{15}$$

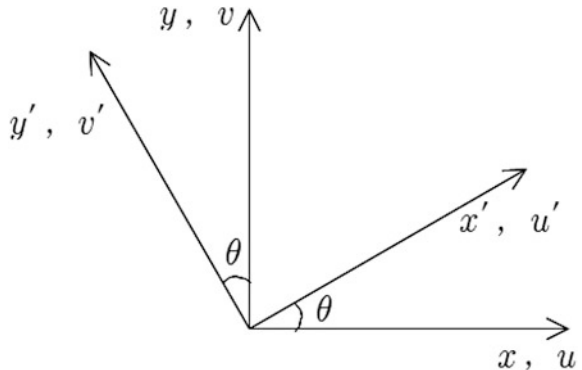
The beam in Fig. 4 can resist uniform tension and compression as well as bending. The element stiffness matrix in local coordinate system is

$$\frac{EI_z}{L^3} \begin{bmatrix} \alpha & 0 & 0 & -\alpha & 0 & 0 \\ 0 & 12 & 6L & 0 & -12 & 6L \\ 0 & 6L & 4L^2 & 0 & -6L & 4L^2 \\ -\alpha & 0 & 0 & \alpha & 0 & 0 \\ 0 & -12 & -6L & 0 & 12 & -6L \\ 0 & 6L & 4L^2 & 0 & -6L & 4L^2 \end{bmatrix} \begin{Bmatrix} u'_1 \\ v'_1 \\ \theta_{z1} \\ u'_2 \\ v'_2 \\ \theta_{z2} \end{Bmatrix} = \begin{Bmatrix} F_{x1} \\ F_{y1} \\ M_{z1} \\ F_{x2} \\ F_{y2} \\ M_{z2} \end{Bmatrix} \tag{16}$$

where  $\alpha = AL^2/I_z$ . Note that the nodes are on the mid-surface of the can.

Converting it into global coordinate system in Fig. 5

**Fig. 5** Global and local coordinate system





$$\frac{EI_z}{L^3} \begin{bmatrix} c & -s & 0 & 0 & 0 & 0 \\ s & c & 0 & 0 & 0 & 0 \\ 0 & 0 & 1 & 0 & 0 & 0 \\ 0 & 0 & 0 & c & -s & 0 \\ 0 & 0 & 0 & s & c & 0 \\ 0 & 0 & 0 & 0 & 0 & 1 \end{bmatrix} \begin{bmatrix} \alpha & 0 & 0 & -\alpha & 0 & 0 \\ 0 & 12 & 6L & 0 & -12 & 6L \\ 0 & 6L & 4L^2 & 0 & -6L & 4L^2 \\ -\alpha & 0 & 0 & \alpha & 0 & 0 \\ 0 & -12 & -6L & 0 & 12 & -6L \\ 0 & 6L & 4L^2 & 0 & -6L & 4L^2 \end{bmatrix} \quad (17)$$

$$\begin{bmatrix} c & s & 0 & 0 & 0 & 0 \\ -s & c & 0 & 0 & 0 & 0 \\ 0 & 0 & 1 & 0 & 0 & 0 \\ 0 & 0 & 0 & c & s & 0 \\ 0 & 0 & 0 & -s & c & 0 \\ 0 & 0 & 0 & 0 & 0 & 1 \end{bmatrix} \begin{Bmatrix} u_1 \\ v_1 \\ \theta_{z1} \\ u_2 \\ v_2 \\ \theta_{z2} \end{Bmatrix} = \begin{Bmatrix} F_{x1} \\ F_{y1} \\ M_{z1} \\ F_{x2} \\ F_{y2} \\ M_{z2} \end{Bmatrix}$$

where  $c = \cos \theta$ ,  $s = \sin \theta$ .

The force vector is

$$\begin{Bmatrix} F_{x1} \\ F_{y1} \\ M_{z1} \\ F_{x2} \\ F_{y2} \\ M_{z2} \end{Bmatrix} = p_m \frac{L}{2} \begin{Bmatrix} -\sin \theta \\ \cos \theta \\ 0 \\ -\sin \theta \\ \cos \theta \\ 0 \end{Bmatrix} \quad (18)$$

The global finite element equations are constructed by assembling them.

$$[K]\{u\} = \{f\} \quad (19)$$

The equations can be solved by multiplying the inverse matrix  $[K]^{-1}$  on both sides.

$$\{u\} = [K]^{-1}\{f\} \quad (20)$$

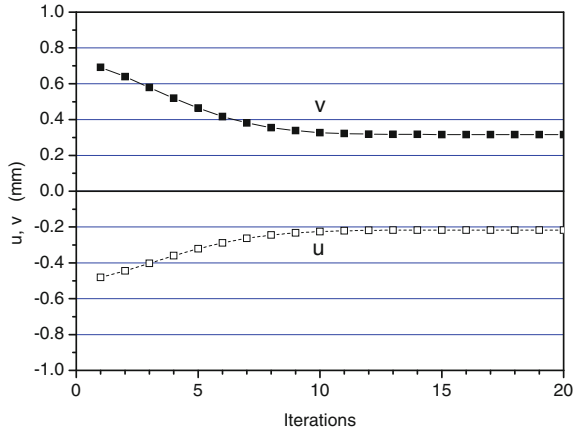
- (f) The gap between the substrate and the can changed due to the deformation of the can.

The radial distance to the mat—can interface in the radial direction toward node  $i$  is

$$R_i^* = \sqrt{\left[ (r_1 + g_i) \cos \frac{(36-i)\theta_1}{N_1} + u_i \right]^2 + \left[ (r_1 + g_i) \sin \frac{(36-i)\theta_1}{N_1} + v_i \right]^2} \quad (20a)$$

( $i = 17 - 36$ )

**Fig. 6** Converged horizontal and vertical displacements at nodes on  $y = 0$  and  $x = 0$



$$R_i^* = \sqrt{\left[ (r_2 + g_t) \sin \frac{(i-1)\theta_2}{N_2} + u_i \right]^2 + \left[ (r_2 + g_t) \cos \frac{(i-1)\theta_2}{N_2} + v_i \right]^2} \quad (i = 1 - 17) \quad (20b)$$

If we took the whole change into account in calculating new mat pressures, the iteration might not converge. Only a small part  $\eta$  of the radial distance change should be taken into account to avoid diverging. In the first iteration, a very small  $\eta$  was used and after that increased gradually to accelerate the convergence. For example,  $\eta = 0.06 - 0.48$  was used in the iteration shown in Fig. 6. The deformed shape from the converged displacements was plotted in Fig. 7.

$$R_i = (1 - \eta)R_{i-1} + \eta R_i^* \quad (21)$$

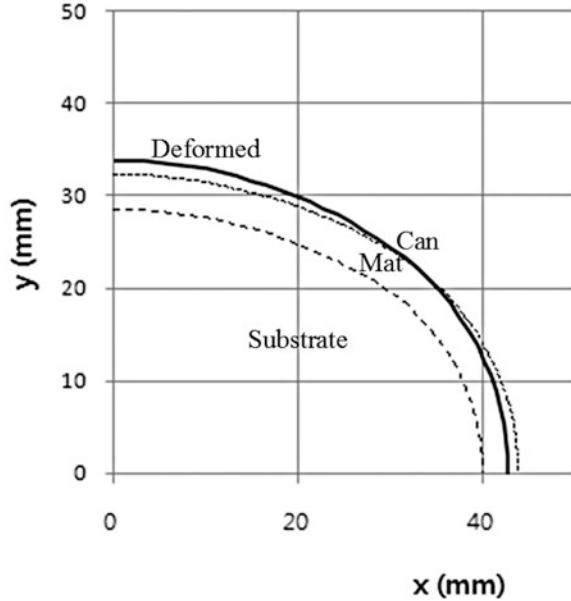
(g) Determine new  $\epsilon$ .

$$\epsilon = \frac{R_i - r_i}{t_m} - 1 \quad (22)$$

Repeat step (c)–(g) until the iteration number 20 is reached.

The deformed can surface was drawn together with the undeformed can surface and the substrate outer surface in Fig. 7. The can deformation is amplified by a factor of 5.

**Fig. 7** Deformed shape of a can (deformation amplification factor 5)



## 2.4 Comparison with ABAQUS Solution

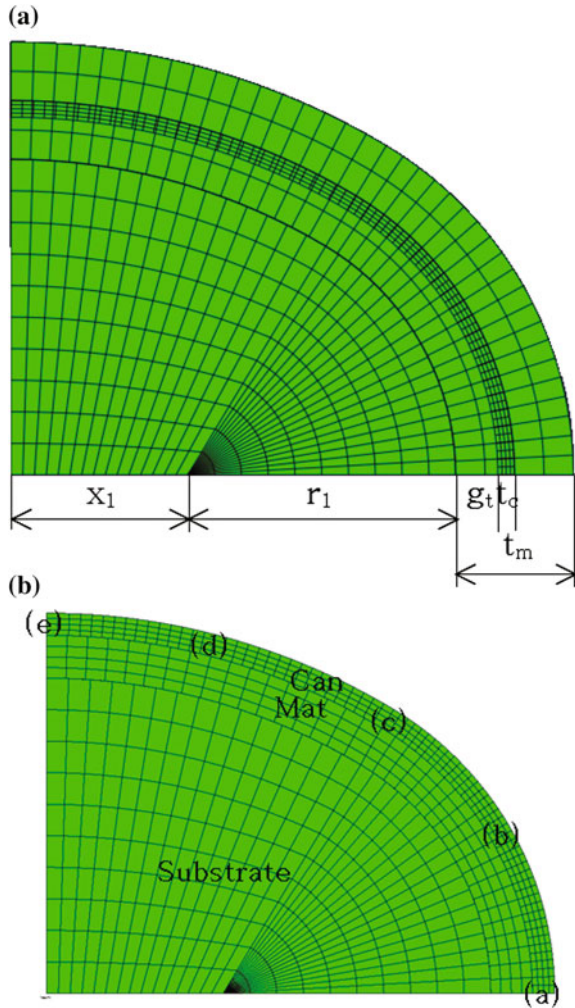
Using ABAQUS, the substrate and mat as well as the can were modeled with plane strain elements as shown in Fig. 8a. Note that nearly half the undeformed mat is outside the can at the beginning. Contact at the substrate—mat interface and at the mat—can interface were activated. Furthermore, at the mat—can interface shrink fit was activated [9, 10]. The shrink-fitted mat inside the can is shown in Fig. 8b.

To check the effect of mesh refinement, both a coarse mesh and a fine mesh were created. In the coarse mesh shown in Fig. 8, the can was divided into  $72 * 4$  elements while in the fine mesh it was divided into  $144 * 8$  elements.

The displacements at the selected five points (a)–(e) on the can mid-surface were compared to the solution given by our program. The displacements fell in the region  $u \leq 0$  and  $v \geq 0$  as shown in Fig. 9. See the deformed shape in Fig. 7. The can tends to become more circular due to the mat pressure. It is interesting to note that the displacements became closer to the solution given by our program as the mesh was refined. Note that the more efficient beam elements were used in our program while the plane strain elements were used in ABAQUS.

To see the pressure distribution, the minimum principal stress was plotted in Fig. 10. Along the mat—can interface, the mat pressure had its minimum at  $x = 0$  and the maximum at  $y = 0$ . In the radial direction, the mat pressure decreased as the radial distance increased. It is interesting to note that the pressure became closer to the solution given by our program as the mesh was refined. The mat pressures by our program in Fig. 11 were on the mat—can interface.

**Fig. 8** Coarse mesh created in ABAQUS



Let's consider the equilibrium of radial forces on the mat element neglecting the tangential forces in Fig. 12. It is found that the mat pressure is inversely proportional to the radial distance. Since the mat pressure on the substrate is the most important pressure, the pressures in the mat were converted to the pressure on the substrate.

Along the first and second arc, respectively

$$p_e = pr/r_1 \quad \text{and} \quad p_e = pr/r_2 \tag{23}$$

As shown in Fig. 13, the equivalent pressure, i.e. the converted pressures on the substrate were nearly constant. It tells us that the inverse proportionality holds

**Fig. 9** Comparison of displacement components at five selected nodes

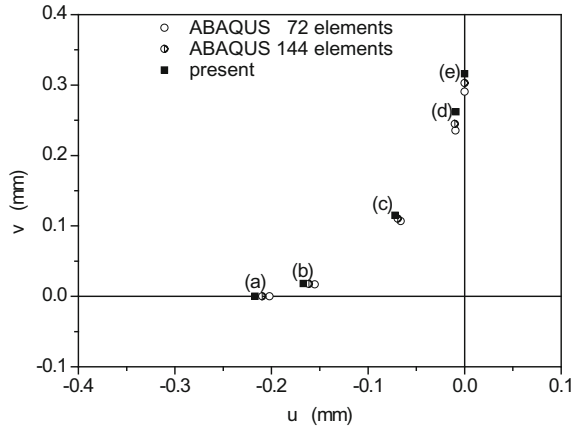


**Fig. 10** Contour plot of the minimum principal stress in ABAQUS

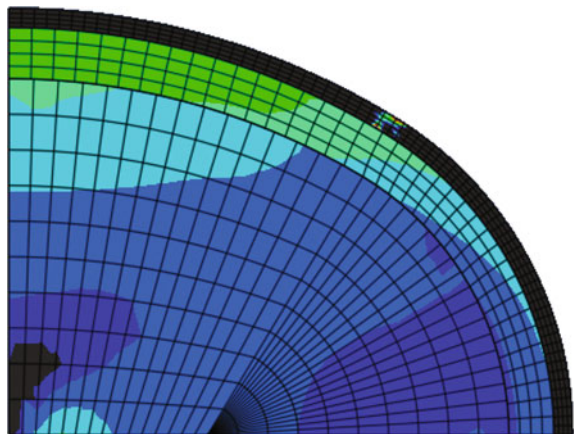


**Fig. 11** Comparison of mat pressure versus radial distance along  $x = 0$  and  $y = 0$

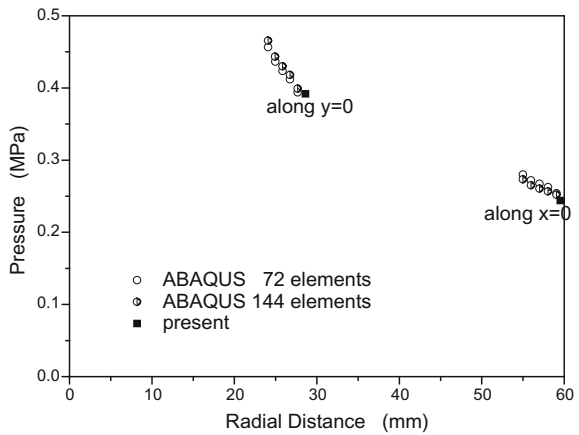


**Fig. 12** Equilibrium of radial forces on the mat element

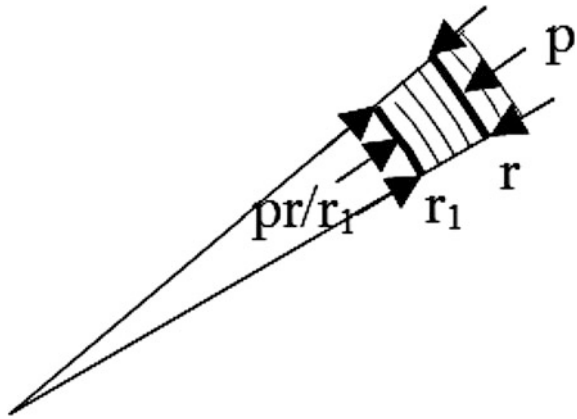
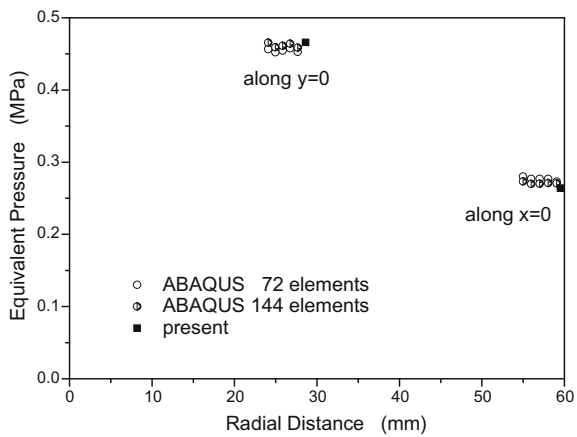


**Fig. 13** Comparison of equivalent pressure, i.e. converted mat pressure on the substrate



between the mat pressure and the radial distance. It is interesting to note that the equivalent pressures became also closer to the solution given by our program as the mesh was refined.

### 3 Conclusions

A finite element program for finding mat pressures on the substrate in canning of a catalytic converter was developed on Microsoft EXCEL. It is a user-friendly program with easy input and graphical output. By modeling the substrate, mat and can as simply as possible, fixing the number of elements and iterations and taking only a small part of the output radial distance change in the current step into account to

calculate the input pressure in the next step, the material nonlinear problem was solved successfully.

To check the accuracy of our program's solution, the same problem was modeled more realistically and solved using ABAQUS. To check the effect of mesh refinement in the ABAQUS mode, both a coarse mesh and a fine mesh were used. Both the can displacements and the mat pressures were in good agreement with our program solution. Furthermore, as the mesh was refined, the ABAQUS solution approached our program's solution. Hence the accuracy of our program solution was confirmed.

It was determined that the mat pressure is inversely proportional to the radial distance from each arc center. The pressure on the substrate outer surface can be determined from the pressure on the can inner surface by the inverse proportionality.

## References

1. <https://en.wikipedia.org/>
2. Kyoung WM (2002) Intumescent mat modeling for the pressure distribution prediction of the catalytic converter system. In: KSME materials and fracture proceeding, pp 295–392
3. McDermott C (2003) Inside Finite Elements for Outsiders
4. The K, Morgan L (2005) The application of EXCEL in teaching finite element analysis to final year engineering students. In: Proceedings of the 2005 ASEE/A aeE 4th global colloquium on engineering education
5. Siswanto WA, Darmawan AS (2012) Teaching finite element method of structural line elements assisted by open source freemat. Res J Appl Sci Eng Technol 4:1277–1286
6. Alonso-Marroquin F (2013) Finite element modeling for civil engineering
7. Campbell R Finite element structural analysis on an EXCEL spreadsheet. In: An online continuing education provider for professional engineers
8. Chu SJ (2005) Finite element analysis using Microsoft EXCEL. UOU Press
9. ABAQUS 6.10 Benchmarks Manual 3.1.5
10. ABAQUS 6.10 Keywords Reference Manual

# Evolution of Droplet Impact on Dry Surfaces with Different Surface Characteristics

Cheng-Hsiung Kuo and Yao-Tsyn Wang

**Abstract** The temporal variations of the spreading diameter, in relation to the dynamic contact angle, are measured by a high speed camera while the droplet impacts onto dry solid surfaces of different surface characteristics. Immediately after impingement at high impact Reynolds numbers, there always exists a thin lamella already attached to the surface, leading to an acute initial contact angle. The dynamic contact angle increases dramatically and attains a maximum value before the maximum spreading diameter is reached. The dynamic contact angle decreases substantially toward the end of the receding stage; and will experience large fluctuation if the rebounding and the oscillating stages exist. The contact angle will eventually approach the equilibrium contact angle after completely wetted on the surfaces. During the kinematics stage, the spreading speeds are proportional to  $(t^*)^{-0.5}$ . The spreading speed experiences a rapid and continuous deceleration and may be related to the non-regular variations of the dynamic contact angle before the maximum spreading diameter is reached. The receding speeds of the liquid film depend strongly on the surface characters. The more hydrophobic the surface is, the higher the receding speed of the liquid film.

**Keywords** Hydrophobic · Droplet · Dynamic contact angle · Spreading · Receding · Wetting speeds

---

C.-H. Kuo (✉) · Y.-T. Wang  
Department of Mechanical Engineering, National Chung Hsing University,  
No. 250 Kuo-Kuang Road, 402 Taichung, Taiwan  
e-mail: chkuo@dragon.nchu.edu.tw

Y.-T. Wang  
e-mail: James5210@yahoo.com.tw



## 1 Introduction

Because of the fundamental problems of how the droplet will deposit on the dry surfaces, numerous quantitative knowledge of the evolution process is required for practical applications. For instance, the ink-jet printing, the thin film forming and coating, the spray cooling, the cleaning and deposition of the spraying process as well as the atomization for fire extinguishment are all relevant to industrial applications. Drop impact on the dry surfaces exhibits very diversified deforming patterns and varieties of the evolution stage were observed because of differing amounts of initial kinetic energy, different surface textures, roughness, wettability, and so on [1–4]. It is difficult to develop a universal relationship between the deformed patterns and the parameters after impingement.

In the beginning, the investigators focused largely on the qualitative descriptions of the phenomenon and summarized many important non-dimensional parameters that influence most of the evolution of the impact droplet at various situations. Pasandideh-Fard et al. [5] proposed a model for a droplet deformed into a cylindrical disk with the assumptions of volume and energy conservation. Their results agreed well with many experimental results, but do not fit well with those for droplets with low impact velocity or large contact angle. Numerical modeling of Fukai et al. [6] and Mao et al. [4] simulated the dynamic process of the deformed droplet during the impingement. In 2001, Kim and Chen [3] employed a model of truncated sphere to predict the spreading and the recoiling processes of the deformed droplet. They concluded that, at small Ohnesorge numbers, the cylinder model is appropriate for predicting the dynamics of the recoiling process. Recently, Park et al. [7] proposed a cap model for the deformed droplet with cap profiles. In cases of low impact velocity and high Reynolds and Weber numbers, their results agreed quite well with the experimental results. In 2004, Clanet et al. [8] found that the maximum non-dimensional diameter can be simply related to the power of the Weber number,  $D^* = 0.91(We)^{1/4}$ , for droplets impacting onto a superhydrophobic surface. In addition to the Weber number, Scheller and Bousfield [9] further provided an empirical relation for the maximum spreading diameter in terms of the Ohnesorge number (Oh),  $D^* = 0.6(We/Oh)^{1/6}$ , suitable for the cases without recoiling.

Some experimental studies were also performed to quantify the evolution of a liquid droplet impact on the dry surfaces to provide some physicochemical viewpoints from engineering aspects [7, 10–13]. In 2002, Rioboo et al. [10] and Sikalo et al. [13] concluded that the similarity in the temporal variations of the non-dimensional diameter is obtained in the kinematics stage, with a simple scaling to the speed and drop diameter before impact. They also verified, using high resolution digital photography, that in the pure wetting stage, the diameter increases proportionally to  $(t^*)^{1/10}$ , demonstrated by Tanner [14]. In 2004, Roux and Cooper-White [12] investigated the evolution of the water droplet impact onto a glass surface. Particular attention is given to the dynamics of the contact angle and its relevance to the maximum spreading diameter. Furthermore, they pointed out

that the model based purely on energy conservation is inadequate because the different shape of the droplet during deformation will determine their outcomes.

To reveal the relevant mechanism controlling the dynamics of the evolution processes (e.g., the spreading, the receding and the possible rebounding as well as the wetting processes), the variations of the contact angle during the entire process should be known. Wang et al. [15] studied the dynamic contact angle by comparing the model with a precursor film and the experimental results. They found that the dynamics of the wetting process depends strongly upon the surface properties; however, it is independent of the composition or species of the liquid. More recently, Roisman et al. [11] developed a new algorithm for modelling the apparent dynamic contact angle at low Weber numbers. The numerical simulation imposed the contact angle of Kistler’s relation [16] on the contact line as a boundary condition, and the results were found to agree well with the experimental data. They also pointed out that accurate modelling of the dynamic contact angle is still a challenging problem.

In this study, the temporal variations of the spreading diameter and the dynamic contact angle are measured during the evolution of the droplet impacting onto three surfaces of different surface characters. Further, the temporal variations of the spreading, the receding and the wetting speeds in relation to the fluid and the surface properties were studied to get an in-depth understanding of the evolution process.

## 2 Experimental System and Techniques

### 2.1 Material

The water droplet (distilled water) and three solid surfaces (smooth glass, silicon wafer and DVD disk) were employed in this study. During the experiments, the temperature was maintained at  $25 \pm 1.5$  °C. The static equilibrium contact angles of the water droplet on these surfaces and the non-dimensional parameters are shown in Table 1. The droplet is generated by the pipettes manufactured by LEADER BIOTECH (Model L100) with a minimum scale of 10  $\mu$ l and full scale of 100  $\mu$ l. The droplet size can be precisely controlled by carefully feeding the liquid

**Table 1** The static contact angle of the water on dry surfaces of glass, silicon wafer and DVD disk

Water droplet			
Surfaces	$\theta_{sc}$ (SD)		
Glass	11 ( $\pm$ 1.0)	Reynolds number	4650
Silicon wafer	56 ( $\pm$ 3.2)	Weber number	98.7
DVD	86 ( $\pm$ 3.0)		

The unit of  $\theta_{sc}$  is in degree, and SD stands for the standard deviation

through the pipettes. The impact velocity is controlled by releasing the droplet freely from a specific height above the surfaces.

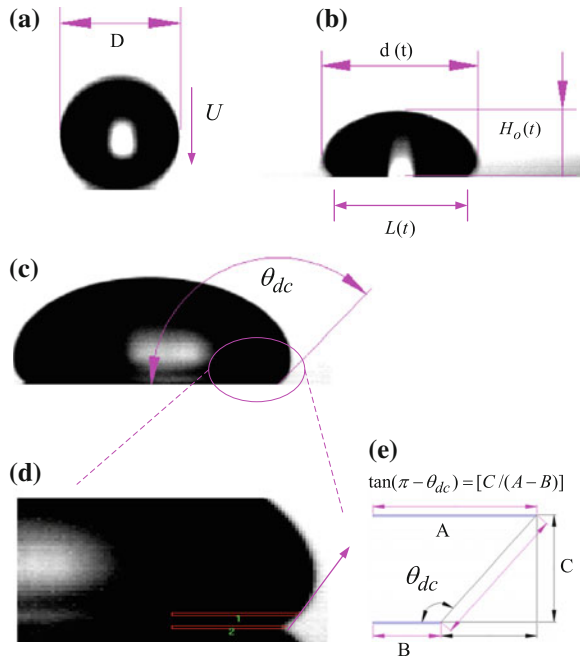
## 2.2 *Image Acquisition System*

The images were recorded in black and white by a high-speed CMOS camera (Redlake) with a full spatial resolution of  $512 \times 512$  pixels at a framing rate of 5000. To acquire the image of the deformed droplet, the camera was aligned horizontally with the frontal view. The optical axis of the camera is normal to the median plane where the deformed droplet resides. Several fields of view are employed to achieve enough spatial resolution for different targets. For example, for the acquisition of the maximum spreading diameter of the deformed droplet, a field of view about  $15 \text{ mm} \times 15 \text{ mm}$  is selected with a resolution of  $29 \text{ }\mu\text{m}/\text{pixel}$ . This resolution is also employed for the measurement of the apparent dynamic contact angle within the localized magnified region. All experiments are repeated at least five times for each experimental condition. Over several experimental runs, the maximum standard deviation of the measured diameter and the central height are 2.3, 0.7 % of the droplet diameter, respectively. The consistency of the experimental results further confirms the repeatability of controlling the experimental conditions, such as the size, the impact velocity of the droplet and the surface characters, and so on.

## 2.3 *Drop Size and Impact Velocity Measurements*

Before impingement, the sizes of the droplets are determined from several successive nearly spherical images. Since the actual shapes of the droplet are not perfectly spherical for free falling droplets at each experimental run, an equivalent diameter  $D = (D_h^2 D_v)^{1/3}$  is employed to represent the size of the droplet before impacting onto dry surfaces [12]. Here  $D_v$  and  $D_h$  denote the maximum lengths in both the vertical and the horizontal axes. Based on fifteen experimental tests, the measured equivalent diameter has a ratio  $D_v/D_h = 1.01 \pm 0.02$ , indicating that the droplet is nearly spherical before impingement. In this study, the diameter of the falling droplet is maintained at  $D = 3 \text{ mm} \pm 0.07 \text{ mm}$ . The averaged impact velocities are calculated by  $U = \Delta y/\Delta t$  from the displacements ( $\Delta y$ ) of the centroids of several successive images. The impact velocity 1.5 m/s is employed, with a deviation of  $\pm 0.01 \text{ m/s}$ ; and the corresponding Reynolds number is 4650. Hereafter in this study, the equivalent diameter and averaged velocity are denoted as the diameter  $D$  and the impact velocity  $U$  before impingement, indicated in Fig. 1a. The spreading diameter  $d(t)$  and the contact diameter  $L(t)$  are defined in Fig. 1b.

**Fig. 1** Schematics of the parameters employed **a** diameter and velocity of droplet before impacting on the surface; **b** the spreading diameter  $d(t)$ , the contact diameter  $L(t)$  of the droplet; **c** the dynamic contact angle of the deformed droplet. **d** Enlarged view of (c); **e** geometric representation for calculating the dynamic contact angle



### 2.4 Dynamic Contact Angle Measurements

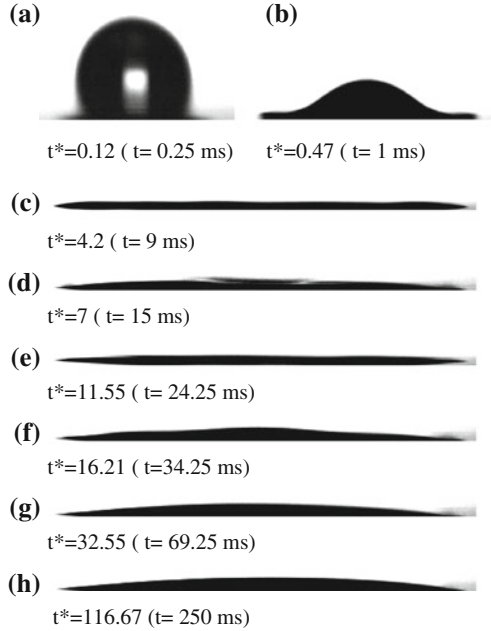
In this study, the dynamic contact angle is determined experimentally using the image system captured by the high speed camera. This apparent contact angle is termed as the dynamic contact angle hereafter and is defined in Fig. 1c; the algorithm to calculate the dynamic contact angle is illustrated in Fig. 1d. The distance C is selected to be five pixels upward from the contact surface so that the calculated contact angles will change smoothly and reasonably.

## 3 Results and Discussions

### 3.1 Water Droplet Impinging onto Glass Surface

Figure 2 illustrates the deforming images of a water droplet impact onto a dry smooth glass surface. Before impact onto the surface, the velocity and the diameter are 1.55 m/s and 3 mm and corresponds to  $Re = 4650$  and  $We = 98.7$ . Immediately after the impingement, a very thin lamella is clearly visible near the contact line (see Fig. 2a). At this moment, this lamella is already attached to the solid surface; meanwhile, the remaining part of the droplet deforms into a truncated sphere (see Fig. 2a). As time continues, the central height of the droplet decreases and the

**Fig. 2** Deforming patterns of the water droplet impact onto the glass surface. The pictures are not in the same scale

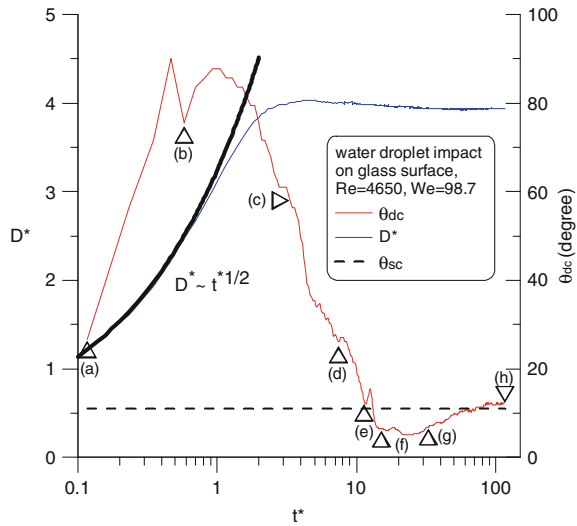


diameter expands rapidly in the radial direction, forming a shape of hat (see Fig. 2b). Similar deformation patterns were found in Roux and Cooper-White [12] at very close impact conditions. The central height of the droplet continues to decrease; and the diameter of the deformed droplet soon reaches the maximum diameter, forming a liquid film on the glass surface (see Fig. 2c, d) and a shallow cavity with little dimple in the central region (see Fig. 2e). In Fig. 2f, the central height of the deformed droplet recovers slightly. Between instants (c) and (f) ( $4 \leq t^* \leq 16$ ), the spreading diameters decreases very mildly, indicating an insignificant receding process. For  $t^* > 40$ , the diameter is observed to increase with a very small increasing rate. This is called the purely wetting stage of the deformed droplet.

The non-dimensional spreading diameter ( $D^*$ ) and the associated dynamic contact angle during the evolution process are illustrated in Fig. 3 in semi-log scale. The instants, (a), (b) and so on, indicated in each plot correspond to the pictures in Fig. 2. During the kinematics stage, based on the mass conservation of the impacting droplet, the variation of the spreading diameter is shown as Eq. (1)

$$D^* = \{4^*[1 - (1 - t^*)^3]/3(1 - t^*)\}^{1/2} \quad (1)$$

**Fig. 3** Evolution of the spreading diameter  $D^*$  and the dynamic contact angles  $\theta_{dc}$  of the water droplet impact onto dry smooth glass surface. The thicker lines in 4a denote the functions of  $D^* \sim (t^*)^{1/2}$  and  $t^* = tU/D$



As  $t^* \ll 1$ , Eq. (1) can be simplified as Eq. (2)

$$D^* = [4t^*]^{1/2} \tag{2}$$

In Fig. 3a, the spreading diameter increases rapidly during the kinematics stage ( $0 \leq t^* \leq 0.4$ ). As indicated by the heavy line in Fig. 3a, the variation of spreading diameter is proportional to  $(t^*)^{1/2}$  within this stage as indicated in Eq. (2). The measured spreading diameter fits this relation quite well during the kinematics stage. During the spreading stages ( $0.4 \leq t^* \leq 3 \sim 4$ ), the spreading diameter starts to deviate from the heavy line and continues to increase until it reaches a maximum ( $D^* = 4$ ) near the instant (c) in Fig. 3a. This maximal value is about the same as those experimentally obtained by Roux and Cooper-White [12] and the prediction by Pasandideh-Fard et al. [5] at close impact condition. Then, the diameter decreases very slowly, corresponding to the insignificant receding process.

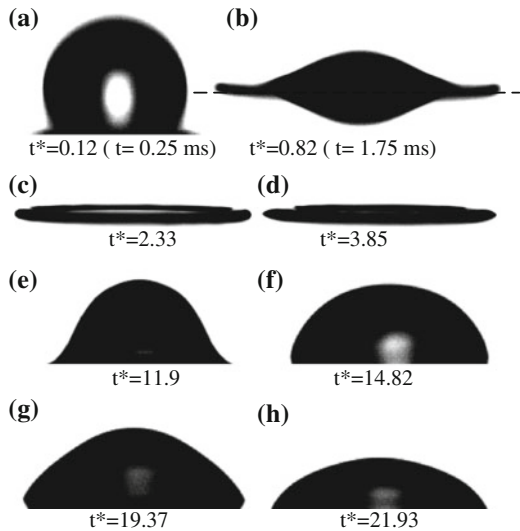
The variation of the dynamic contact angle during the evolution process is also illustrated in Fig. 3. Immediately after impingement onto the glass surface, the initial contact angle is an acute angle because the lamella has already attached to the wall in Fig. 2a. Between the instants (a) and (b), an accumulation of fluid mass near the leading-edge is clearly observed; and the contact angle increases rapidly to a local maximum value around  $90^\circ$  before the instant (b). This is probably because the spreading velocity of the leading-edge is higher than the contact line velocity. The contact angle experiences abrupt changes between two local maxima about the instant (b) before the spreading diameter reaches the maximum. As will be seen in the later section, this fluctuation in the contact angle may be related to the significant deceleration of spreading speed of the liquid film.

Although the receding process is mild and insignificant, the leading-edge of the liquid thin continues to become thinner; and the contact angle decreases very quickly and monotonously. The receding stage ends around the instants (f) and (g) within which the contact angle reaches a minimum. Beyond the instant (g), the spreading liquid film starts the wetting process. During the wetting stage, the spreading diameter continues to increase at a very slow rate; meanwhile, the contact angle increases gradually and approaches the value of static contact angle (see Table 1). At the instant (h), the liquid film is completely spread and stays almost in equilibrium with the glass surface. Similar variations of the dynamic contact angle can be found in Pasandideh-Fard et al. [5].

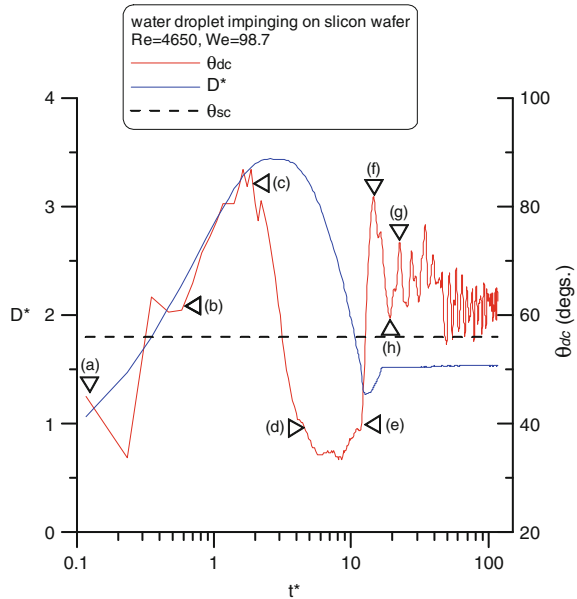
### 3.2 Water Droplet Impinging onto Silicon Wafer

Figure 4 shows the sequential pictures of the droplet impact onto the surface of a silicon wafer. When a water droplet of the same size is placed stationarily on the silicon wafer, the static (or equilibrium) contact angle is measured to be  $56^\circ$  (see Table 1). Obviously, in Fig. 4, the complete evolution process includes the kinematics (Fig. 4a), the spreading (Figs. 4b–c), and the receding (Fig. 4d–e), the rebounding and oscillating (Fig. 4f–h). The non-dimensional spreading diameter of the droplet is illustrated in Fig. 4a, b, respectively. The spreading diameter ( $D^*$ ) increases rapidly within the kinematic and the spreading stages until the maximum diameter ( $D^* = 3.4$ ) is reached. Then, the spreading diameter of the deformed droplet decreases substantially until it reaches a minimum value around the instant (e). During this time elapse, the droplet experiences an apparent receding process.

**Fig. 4** Deforming patterns of the water droplet impact onto the surface of silicon wafer. Note that the Reynolds and the Weber numbers of the droplet before impingement are  $Re = 4650$  and  $We = 98.7$ , respectively. The pictures are not in the same scale



**Fig. 5** Evolution of the spreading diameter  $D^*$  and the dynamic contact angles  $\theta_{dc}$  of the water droplet impact onto the surface of silicon wafer



Between the instants (e) and (h) in Fig. 4b, the deformed droplet undergoes a rebounding and oscillation process; and the diameter expands slightly in the radial direction. For  $t^* > 15$ , the diameter of the droplet remains nearly constant around  $D^* = 1.5$ .

The variation of the dynamic contact angle is also depicted in Fig. 5 in relation to the spreading diameter. Immediately after impingement, the contact angle also starts from an acute angle of about  $45^\circ$  which is evident by the existence of a thin lamella in Fig. 4a. This angle further decreases to a smallest value due to continuous thinning of the lamella. The contact angle increases largely to about  $60^\circ$  at the instant (b) when the spreading liquid film accumulates some mass at the leading edge. Between the instants (b) and (c), the central region of the droplet continues to deform from a cap profile to a central cavity with a visible crater at the leading-edge of the spreading liquid film (Fig. 4b–c). In Fig. 4c, the upward and outward curved leading-edge of the liquid film is a clear evidence of increasing contact angle from the instants (b) to (c). In this case, the maximum spreading diameter and contact angle are  $D^* = 3.4$  and  $90^\circ$ , respectively. During the receding stage, the spreading diameter decreases substantially and the associated contact angle reduces monotonously until a minimum value is reached. Within this stage, the decrease of the dynamic contact angle is primarily caused by the competition between the viscous dissipation and the surface tension of the liquid film. Between the instants (d) and (e), the change in the contact angle is associated with the onset of rebounding of the deformed droplet. For  $t^* > 15$ , the fluctuation of the contact angle is associated with the oscillating stage following the rebounding of droplet. At the end of the



oscillating stage, the fluctuating amplitudes of the contact angle and the central height diminish; and the purely wetting stage begins. Finally, the fluctuating contact angle tends to approach the value slightly larger than the equilibrium contact angle (about  $60^\circ$ ).

### 3.3 Water Droplet Impinging onto DVD Disk

The static (or equilibrium) contact angle of the water droplet on the surface of a DVD disk is measured to be  $86^\circ$  (see Table 1). In Fig. 6, the evolution process includes: the kinematics (Fig. 6a), the spreading (Figs. 6b, c), and the receding (Fig. 6d, e), the rebounding and the oscillating (Fig. 6e–h). For the water droplet impacting onto the surface of a DVD disk, the temporal variations of the non-dimensional spreading diameter and the contact angle are illustrated simultaneously in Fig. 7. Similar variation trends of  $D^*$  are observed in Fig. 7a; however, the rebounding and oscillating characters are pronounced. The maximum and the minimum spreading diameters ( $D^*$ ) are 3.1 and 0.8, respectively; and the final stabilized spreading diameters reaches about 1.3.

**Fig. 6** Deforming patterns of the water droplet impact onto the DVD surface. The pictures are not in the same scale

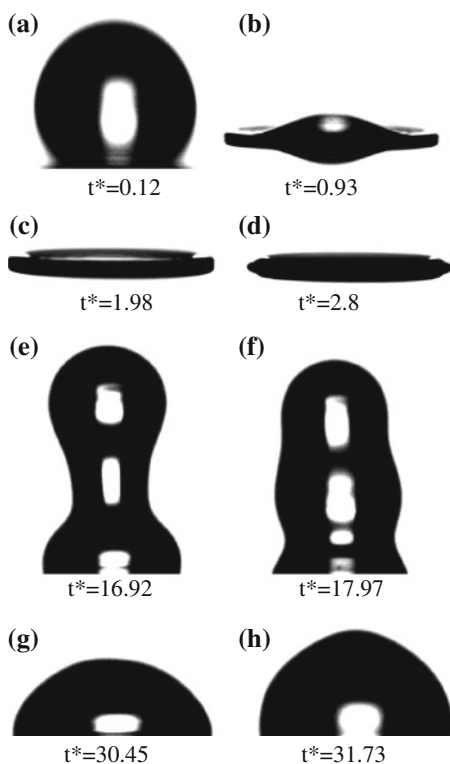
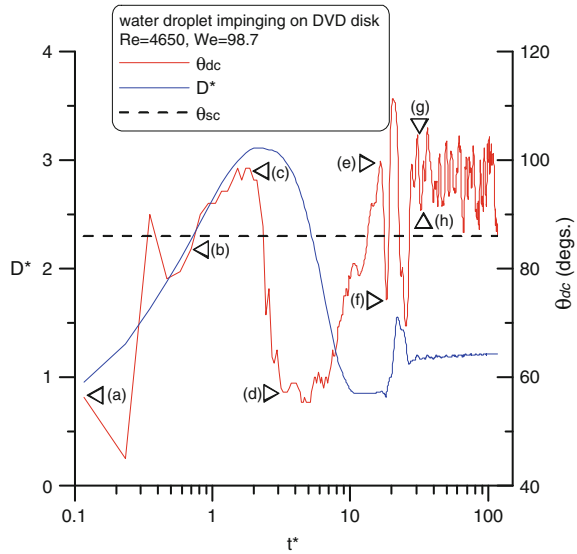


**Fig. 7** Evolution of the spreading diameter  $D^*$  and the dynamic contact angles  $\theta_{dc}$  of the deformed water droplet impact onto DVD disk. The dimensionless time is defined as  $t^* = tU/D$

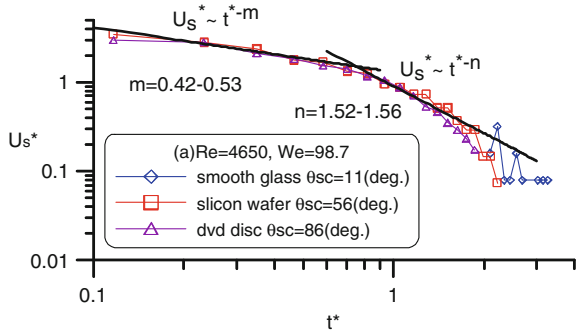


The contact angle evolution shows a similar trend as that in Fig. 5. The initial contact angle is also acute because of the existence of the thin lamella (Fig. 7a) immediately after the droplet impingement. Within the kinematics and the spreading stages ( $t^* \leq 3$ ), significant changes of the contact angle are also observed. This complicated behaviour is probably caused by the competitions (or imbalances) between the inertial, viscous dissipation and the surface tension of the deformed droplet. Similarly, during the receding stage, the contact angle decreases rapidly and monotonously until the instant (d). Between the instants (d) and (e), the contact angle increases largely to an obtuse angle and begins to oscillate with large amplitude and a mean value larger than the equilibrium one ( $86^\circ$ ). This corresponds to the process of significant rebounding and oscillating stages (Fig. 7e–g). At the end of the sampling interval ( $t^* \leq 3$ ), the oscillation still exists, indicating that a much longer time elapse is needed to reach the purely wetting stage.

### 3.4 Spreading Speeds

Figure 8 illustrates the temporal variations of the spreading speed of the water droplet along surfaces of different surface characters during the kinematic and the spreading stages ( $0.1 \leq t^* \leq 3.5$ ). The spreading speed is calculated by the time derivative of  $D^*$  shown in Figs. 3, 5 and 7, and is normalized by the impacting speed  $U$ . In Fig. 8a, the magnitudes of the spreading speed initially start around a value  $U_s^* = 3.5$ , experience monotonous decrease, and eventually approach zero when the maximum spreading diameters are reached. The variation of the spreading

**Fig. 8** Temporal variations of the spreading speed during the kinematics and the spreading stages

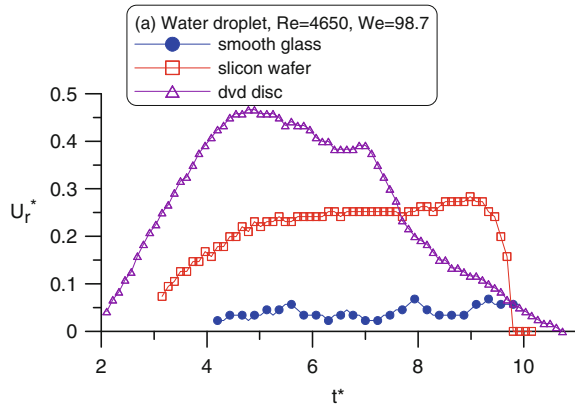


speed can be expressed as a functional relation of time with varying negative powers. In other words, within the time interval  $0.1 \leq t^* \leq 0.5$ , the variations of the spreading speeds fit quite well with the curve of  $(t^*)^{-0.48}$ . Since the spreading speed equals the time derivative of the spreading diameter, the functional dependence of  $(t^*)^{-0.5}$  within  $0.1 \leq t^* \leq 0.5$  is reasonable because the spreading diameter grows in proportion to  $(t^*)^{0.5}$  during the kinematics stage (the heavy line in Fig. 3a). In the time interval  $0.5 \leq t^* \leq 1$ , the spreading speed experiences a rapid and continuous deceleration. Although the strict hydrodynamic analysis at the fluid/solid interface (or dynamic contact angle) is still an open question, the rapid and continuous deceleration of the spreading speed may be related to the non-regular variations of the dynamic contact angle within almost the same time interval in Figs. 3, 5 and 7. Near the end of the spreading stage ( $1 \leq t^* \leq 3$ ), the spreading speed varies in proportion to  $(t^*)^{-1.9}$ . Figure 8a also reveals that the functional dependence of the temporal variations of the spreading speed is nearly independent of the surface characteristics (hydrophilic or hydrophobic).

### 3.5 Receding Speed

In Fig. 9, the non-dimensional receding speed during the receding stage ( $2 \leq t^* \leq 10$ ) is calculated in the same way as that for the spreading speed. For the water droplet impinging on surfaces of different surface characters (hydrophilic or hydrophobic) at the same Reynolds numbers, the variations of the receding speed are quite different in both the magnitudes and the variation trends. At this Reynolds number, the receding speed is the largest at about  $U_r^* = 0.4$  along the surface of the DVD disk, the second along the silicon wafer and the smallest along the glass surface. Clearly, the more hydrophobic the surface is, the higher the receding speed. Along the surface of the DVD disk, the large receding speed withdraws the deformed liquid film more quickly. This leads to a substantial decrease of the dynamic contact angle from the obtuse to the acute angles within the receding stage. Besides, the large receding speed recoils the liquid film and refills the cavity in the

**Fig. 9** Temporal variations of the receding speed during the receding stage. The receding speeds are also normalized by the impact velocity of the droplet



central region more efficiently. This process restores large amount of energy for the pronounced rebounding and oscillating processes. The receding process is a phenomenon relating to an imbalance between the surface tension and the viscous dissipation of the liquid film along the solid surface. The viscous dissipation depends strongly on the hydrophobic or hydrophilic characters of the solid surface studied. Therefore, the receding speed is strongly dependent upon the surface characters in Fig. 9.

### 4 Conclusions

During the evolution of the droplet impact onto the dry surface, the temporal variations of the spreading diameter and the central height, in conjunction with the apparent dynamic contact angle, are measured experimentally by a high speed camera.

Immediately after impingement of the water droplet at high Reynolds numbers, there exists a thin lamella already attached to the surface and thus the initial contact angles are acute angles. The dynamic contact angle increases rapidly but non-regularly while the diameter spreads in the radial direction. The non-regular patterns may be caused by the rapid and continuous deceleration of the spreading speed while transits from the kinematics and the spreading stages. The dynamic contact angle increases and attains a maximum value before the maximum spreading diameter is reached. While the spreading diameter reaches the maximum, the dynamic contact angle decreases substantially toward the end of the receding stage. The dynamic contact angle will experience large fluctuations if the rebounding and the oscillating stages exist. Eventually, the contact angle will approach the equilibrium contact angle if the sampling time is long enough.

The spreading speed experiences a rapid and continuous deceleration and the functional relation follows a negative power of  $t^*$ , varying from  $-0.5$  to  $-2.0$ , while

the spreading liquid film transits from the kinematics to the spreading stages. Within the receding stages, the receding speeds of the liquid film depend strongly on the surface characters. The more hydrophobic is the surface, the higher the receding speed of the liquid film.

**Acknowledgements** The authors appreciate the financial supports from the Ministry of Science and Technology, Taiwan for the project under grant no. NSC-102-2221-E-005-032-MY3.

## References

1. Yarin AL (2006) *Annu Rev Fluid Mech* 38:159
2. Chandra S, Avedisian CT (1991) *Proc R Soc London A* 432:13
3. Kim HY, Chun JH (2001) *Phys Fluids Ser A* 13:643
4. Mao T, Kuhn DCS, Honghi T (1997) *AIChE J* 43:2169
5. Pasandideh-Fard M, Qiao YM, Chandra S, Mostaghimi J (1996) *Phys Fluids* 8:650
6. Fukai J, Tanaka M, Miyatake O (1998) *J Chem Eng Jpn* 31:456
7. Park H, Carr W, Zhu J, Morris JF (2003) *AIChE J* 49:2461
8. Clanet C, Beguin C, Richard D, Quere D (2004) *J Fluid Mech* 517:199
9. Scheller BJ, Bousfield DW (1995) *AIChE J* 41:1357
10. Rioboo R, Marengo M, Tropea C (2002) *Exp Fluids* 33:112
11. Roisman IV, Opfer L, Tropea C, Raessi M, Mostaghimi J, Chandra S (2008) *Colloids Surf A* 332:183
12. Roux DCD, Cooper-White JJ (2004) *J Colloid Interface Sci* 277:424
13. Sikalo S, Marengo M, Tropea C, Ganic EN (2002) *Exp Thermal Fluid Sci* 25:503
14. Tanner LH, *J Phys D* 179, 12:1473
15. Wang X, Peng X, Duan Y, Wang B (2007) *Chin J Chem Eng* 15:730
16. Kistler SF (1993) *Hydrodynamics of wetting*. In: Berg JC (ed) Marcel Dekker, New York

# Numerical Optimization in Ropeway Planning

H. Thaler, M. Wenin, J. Brunner, D. Reiterer, M.L. Bertotti,  
G. Modanese and E. Oberhuber

**Abstract** Planning a cable railway is a complex task. One has to take into account many aspects and an optimal solution is not well defined. The calculation of the cable configurations for given support positions, cable pretension and cable types however is rather formalizable and presents a direct problem. In this research work we study the first steps to solve the inverse problem: computation of optimal support positions for a given support cable type and cable car mass. We define an appropriate cost functional (objective function) with several constraints and use numerical minimization strategies to obtain optimal solutions.

**Keywords** Cable railway · Optimization · Numerical cable support computation

---

H. Thaler · M. Wenin (✉)  
CPE Lana, Weingartnerstr. 28, 39011 Lana, Italy  
e-mail: markus.wenin@cphysics.com

H. Thaler  
e-mail: helmuth.thaler@cphysics.com

J. Brunner · D. Reiterer  
IDM Südtirol / Alto Adige, Siemensstr. 19, 39100 Bolzano, BZ, Italy  
e-mail: johannes.brunner@idm-suedtirol.com

D. Reiterer  
e-mail: daniel.reiterer@idm-suedtirol.com

M.L. Bertotti · G. Modanese  
Free University of Bozen–Bolzano, piazza Università 5, 39100 Bolzano, BZ, Italy  
e-mail: MariaLetizia.Bertotti@unibz.it

G. Modanese  
e-mail: Giovanni.Modanese@unibz.it

E. Oberhuber  
IMO Algund, Weingartnerstr. 42, 39033 Algund, Italy  
e-mail: erwin.oberhuber@hotmail.com

## 1 Introduction

The simulation of technical systems is typically a direct problem. The evolution equations for the system (usually differential equations) and the initial/boundary conditions are known. An appropriate solver gives us the (unique) state of the system to a later time. For the field of cable ropeways the solver consists of a program, which allows the computation of the various cable configurations, when the cable car is moving: support/hauling cable geometry, midspan catenary sags, the forces on the supports etc. [1, 2]. The equations of motion of classical mechanics and elasticity theory are the basis for this task [3]. Model parameters such as support positions, cable types, etc. usually are selected by the engineer and are input quantities.

A new, large research field for applied mathematics as well as engineering and physics is opening when inverse problems are considered. Inverse problems are typical, for example, in scattering theory, where from the incident and scattered waves one has to deduce the scattering potential (e.g. in applications of nuclear physics or nondestructive testing of steel by ultrasound [4, 5]). In the context of a cable railway inverse problems arise when one looks for an algorithm, which determines the model parameters autonomously [6]. For example, where are the best positions of the supports for a ropeway, when a mountain profile is given? Or which cable type and pretension is optimal? There are many questions, and the first of all is how we define a good solution and distinguish it from a bad solution.

The overview in Fig. 1 gives an impression of the several planning steps of a cable railway. The choice of the cable path is influenced by many requirements and standards, as well as restrictions. In this work we address the particular problem to find the optimal support positions for a cable railway. We define an appropriate cost functional and constraints. We use global and local optimization techniques to identify the optimal coordinates of a given constant number of supports. For this purpose we use two different models. When one searches a local minimum of a function, then a relatively small number of function evaluations are sufficient to find the solution. In this case we can use a sophisticated program to compute all quantities needed to evaluate the cost functional and the constraints. For each iteration step in the minimization procedure we are able to evaluate a complete ride of the cable car from valley to the mountain station (which takes less than a minute on a PC). Global optimization requires much more computational effort. To obtain a tractable model, we introduce suitable approximations for the determination of the cable car trajectory. In particular, we assume that the support cable is spanned with a counterweight in the valley station. This assumption drastically simplifies the computation of the support cable configurations [7]. Further simplifications were done:

- The movement of the cable car is assumed quasi-static (corresponding to the standards [8]).
- We neglect temperature effects. We work with one reference temperature only.

- We neglect the problem of the hauling cable (in particular its distance from the ground).
- Important questions about cable oscillations and their minimization are ignored [9].

## 2 Approximate Cable Curve and Cable Car Trajectory

The function to describe an inelastic cable in a gravitational field, the catenary, is well known [10]. For cable railway applications the elasticity must be taken into account, for small strains the “elastic catenary” in a  $x$ - $y$  coordinate system is given [11] by

$$y = \bar{a} \cosh\left(\frac{x - \bar{x}_m}{\bar{a}}\right) - \bar{c} - \frac{1}{2} \frac{g \rho_L}{\mathcal{E}A} \bar{a}^2 \sinh^2\left(\frac{x - \bar{x}_m}{\bar{a}}\right). \quad (1)$$

In this expression  $g$  is the earth acceleration,  $\rho_L$  the linear mass density (kg/m),  $\mathcal{E}$  the isothermal modulus of elasticity and  $A$  the cross section of the cable, respectively. The three parameters  $\bar{a}, \bar{x}_m, \bar{c}$  determine the cable curve uniquely and are fixed by appropriate boundary conditions. From Eq. (1) one deduces a parabola approximation for the empty cable [7]. Apart from this approximation the determination of the point load trajectory depends on the boundaries of the support cable. If the support cable is spanned with a weight, the problem is statically determined. In the other case, where the cable is held fixed at the end points, the problem is statically undetermined and a solution requires principles from elasticity theory [12]. The numerical computation of the cable configurations and the catenary sag of the point load, the forces on the supports etc. in this case is very time-consuming, which makes it difficult to use global optimization. So, in order to obtain results we also use a crude approximation for the computation of the point load trajectory and the empty cable configuration (see Fig. 2).

Let  $T_0$  be the gravitational force of the counterweight, and let  $m$  be the mass of the point load. We consider one span only with cartesian coordinates of the supports  $X_1, Y_1$  and  $X_2, Y_2$ . The mid-span catenary sag of a point-loaded cable is given<sup>1</sup> by

$$f_m = \frac{2mg + \rho_L g l}{(T_0 + \rho_L g y_m) \cos(\gamma)} \frac{l}{8}, \quad (2)$$

---

<sup>1</sup>The point load is sitting on the middle of the span.



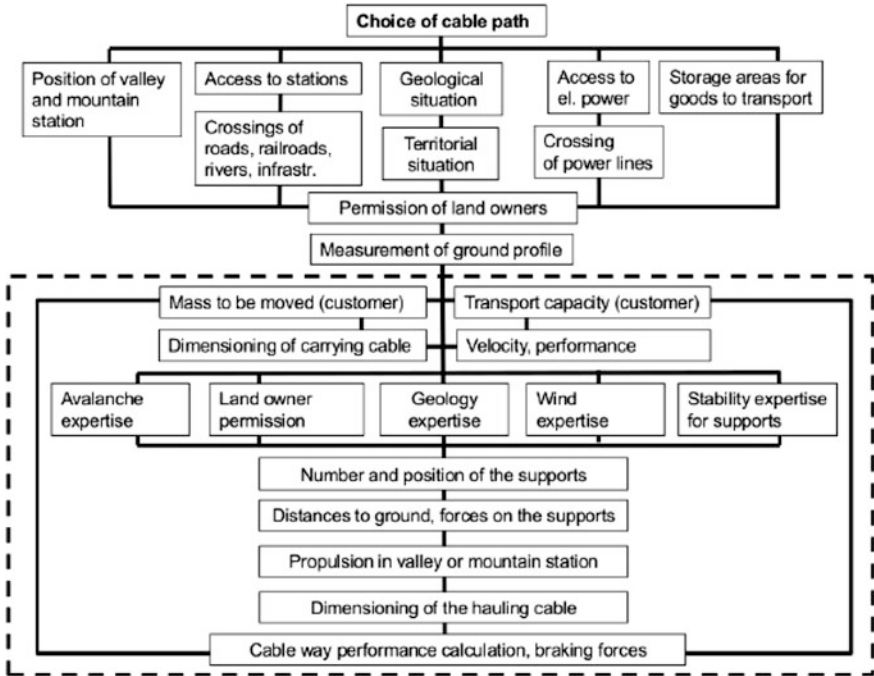


Fig. 1 Planning of a cable railway: aspects of the planning steps

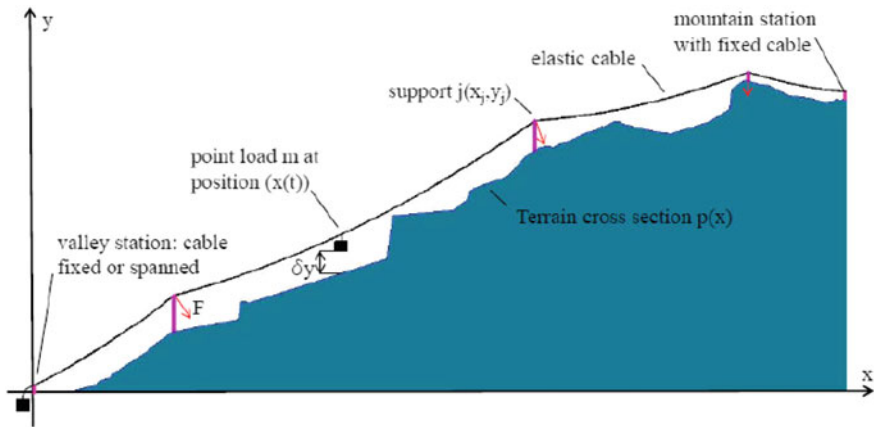


Fig. 2 Mechanical model used in our numerical simulations

where we use the abbreviations

$$l = \sqrt{(X_2 - X_1)^2 + (Y_2 - Y_1)^2}, \quad \gamma = \arctan \Delta, \quad \Delta \equiv \frac{Y_2 - Y_1}{X_2 - X_1}. \quad (3)$$

$l$  denotes the length and  $\gamma$  the slope angle of the chord respectively.  $y_m = (Y_1 + Y_2)/2$  is the mean  $y$ -value of the span. Given the coordinates of both supports and  $f_m$  one can compute the trajectory of the point load using a parabola approximation (see the lower part of Fig. 6). We obtain for  $X_1 \leq x \leq X_2$ ,

$$f_2(X_1, Y_1; X_2, Y_2; x) = ax^2 + bx + c, \quad (4)$$

with

$$a = \frac{X_1(Y_m - Y_2) + X_2(Y_1 - Y_m) + X_m(Y_2 - Y_1)}{(X_1 - X_2)(X_1 - X_m)(X_2 - X_m)}, \quad (5)$$

$$b = \frac{X_m^2(Y_1 - Y_2) + X_1^2(Y_2 - Y_m) + X_2^2(Y_m - Y_1)}{(X_1 - X_2)(X_1 - X_m)(X_2 - X_m)}, \quad (6)$$

$$c = \frac{X_m[X_2(X_2 - X_m)Y_1 + X_1(X_m - X_1)Y_2] + X_1(X_1 - X_2)X_2Y_m}{(X_1 - X_2)(X_1 - X_m)(X_2 - X_m)}. \quad (7)$$

Here we have defined:

$$X_m = \frac{X_1 + X_2}{2}, \quad (8)$$

$$Y_m = \Delta \cdot (X_m - X_2) + Y_2 - f_m. \quad (9)$$

With these expressions the trace of the point load trajectory  $(x, f(x))$  as well as the empty cable curve (obtained by setting  $m = 0$  in Eq. (2)) are computable for an arbitrary number of supports. Using the step function  $\Theta(x) = 1, x > 0, \Theta(x) = 0, x < 0$ , one can write

$$f(x) = \sum_j f_2(X_j, Y_j; X_{j+1}, Y_{j+1}; x) \Theta(x - X_j) \Theta(-(x - X_{j+1})). \quad (10)$$

The sum runs over all support coordinates including the valley and mountain stations. All considerations are based on a quasi—static movement of the point load, so the time-dependent trajectory is  $(x_{\text{pl}}(t), f(x_{\text{pl}}(t)))$ , where  $x_{\text{pl}}(t)$  is the time-dependent  $x$ -coordinate of the point load.

### 3 Setup of the Optimization Strategy

The optimization strategy requires in general the definition of a cost functional which has to be minimized and several constraints. In our case, the definition of an appropriate cost functional  $J$  is a non-trivial task. More than one desirable target makes the selection of the best cost functional ambiguously (multiobjective optimization). It is important however to keep in mind that a mathematical algorithm should help to reduce the number of possible solutions (reduction of the dimension of the search space). Otherwise the algorithm is valueless. Here we use a minimal support height for a fixed support number, in order to increase stability against crippling. Questions about robustness of the obtained solutions are ignored at the moment [13]. When one searches the minimum of a function, the choice of the initial guess is an important question. When we use local optimization, we construct the starting points using the following strategy: The terrain profile given by satellite measurements is interpolated linearly. Start- and end position of the cableway coincide with the first and the last pair of coordinates. Starting with a middle height of the cable supports (averaged between a reasonable minimal and maximal value) a first algorithm looks for further necessary supports between the existing supports, using chord junctions and evaluating positions in the interpolated profile with too little distance from the chord or even situated above the chord choosing the position with the most critical distance  $d_{\text{crit}}$  first. Here  $d_{\text{crit}}$  is defined trough Eq. (12) with  $T_0 \rightarrow \infty$  and  $m = 0$  and is the first absolute minimum counted from the left. Considering a necessary minimal distance between the empty cable and the profile of the terrain and further the sag of the chosen cable due to its weight, elasticity and tension a second algorithm looks for further necessary support points choosing the position with the most critical distance first putting there the next support. A third algorithm simulates the movement of the cable car at full weight along the support cable considering a maximum of support height and cable tension in the valley station to look for further necessary supports. Afterwards the optimization process starts using the chosen support positions as initial values for local minimization (by variation of support coordinates  $X_j, Y_j$ ). Global optimization strategies usually do not require initial guesses but a closed region, which contains probably the optimal solution.<sup>2</sup>

#### 3.1 Cost Functional

First we define the mountain profile as a real function  $p(x)$ , where  $x \in I$ , and  $I = [0, X_{\text{max}}]$  is some interval.<sup>3</sup> We use the cost

---

<sup>2</sup>See for example Mathematica Documentation Center, or the MATLAB Documentation.

<sup>3</sup>We exclude here the case of an overhanged rock formation.

$$J = \sum_{j=1}^N h_j, \quad (11)$$

where  $h_j \equiv Y_j - p(X_j)$  is the height of the  $j$ -th support. The coordinates  $X_j$ ,  $Y_j$  are variational parameters,  $N$  is the number of supports. As first numerical studies have shown, this approach reflects an important part of what in reality is useful. In fact increase the critical crippling force with the height of the support, so it is advantageous to use supports so low as possible. We use Eq. (11) for both local/global optimization strategies.

### 3.2 Constraints

The optimal solution must fulfill several constraints. We denote these by  $C_0, C_1, \dots$ . Constraints can be defined through equalities or inequalities. Here the introduced constraints are written either as equalities  $C_j = 0$  or inequalities  $C_j \leq 0$  respectively.

The most important constraint is the distance “car–ground”  $\delta y_{\min}$ , which must be greater than a certain value (e.g.  $\delta y_{\min} = 5$  m) to avoid car–ground collisions. The first constraint  $C_0$  consequently reads

$$C_0 = \delta y_{\min} - \min_{x_{\text{pl}} \in I} [f(x_{\text{pl}}) - p(x_{\text{pl}})], \quad (12)$$

where  $x_{\text{pl}}$  is the point load position. The second constraint ensures that the support cable during the raid of the car does not leave the support (for a discussion of this point see [7, 8]). The cable—support force at the support no.  $j$  is denoted as<sup>4</sup>

$$\mathbf{F}^j(x_{\text{pl}}) = F_x^j(x_{\text{pl}})\mathbf{e}_x + F_y^j(x_{\text{pl}})\mathbf{e}_y. \quad (13)$$

The components  $F_x^j(x_{\text{pl}})$ ,  $F_y^j(x_{\text{pl}})$  obviously depend on the position of the point load. We are interested for the vertical component  $F_y^j(x_{\text{pl}})$ , which must be at least negative for all supports and all positions  $x_{\text{pl}}$ . Let us define the boundary value for  $F_y^j(x_{\text{pl}})$  with  $F_{y,\min}^j$ . So we have

$$F_y^j(x_{\text{pl}}) \leq F_{y,\min}^j, \quad \forall j, x_{\text{pl}}. \quad (14)$$

In realistic situations the values  $F_{y,\min}^j$  are not constant but depend on the positions of the supports. This is due to the wind—induced vertical forces, which

---

<sup>4</sup>As usual  $\mathbf{e}_x, \mathbf{e}_y$  are the canonical basis vectors.

must be taken into account when computing  $F_{y,\min}^j$  [14]. At the moment we neglect this fact and use a constant value for all supports. The constraints, corresponding to Eq. (14), are

$$C_j = \max_{x_{pl} \in I} \left[ F_y^j(x_{pl}) - F_{y,\min}^j \right], \quad j = 1, 2, \dots, N \quad (15)$$

For a support cable fixed at the ends of the line, the cable tension depends on the position of the point load and in particular the determination of the maximal cable tension  $T_{\max}$  requires some computational effort. On the other hand the situation is quite simple when one end of the cable is movable. If one neglects friction resistances on the support, the maximal cable tension is constant i.e. does not depend on the position of the point load. In any case the maximal cable tension must be in the save range regarding the minimal breaking tension  $T_{br}$ . This yields the constraint

$$C_{N+1} = \nu T_{\max} - T_{br}. \quad (16)$$

Usually one sets for the security factor  $\nu = 3.5$  for person transport ropeways.

## 4 Numerical Examples

In this section we present two numerical examples to demonstrate the theory given in the previous sections.

### 4.1 Case Study: Linear Profile

A linear mountain profile, (horizontal 1000 m, vertical 500 m, Fig. 3), is the simplest possible case to check the optimization strategy and the numerical results. We use the “*Differential Evolution*” algorithm to minimize Eq. (11) with constraint  $C_0 = 0$ . As Fig. 3 shows, the position of the support takes place in the first half of the profile ( $X < 500$  m). This is reasonable, because the cable tension grows with increasing height. So the first span has a greater mid-span catenary sag than the second one. The end–points of the line are held fixed at a height of 5 m. Figure 4 shows a similar result for a support cable fixed at both ends of the line. A global minimum for the support height exists, which can be found using standard local optimization techniques as “*Line search*” methods. Table 1 shows a summary of results for both types of boundary conditions: cable fixed at the end points and spanned with a counterweight. As expected, for a cable fixed at the endpoints, the supports are quite lower.

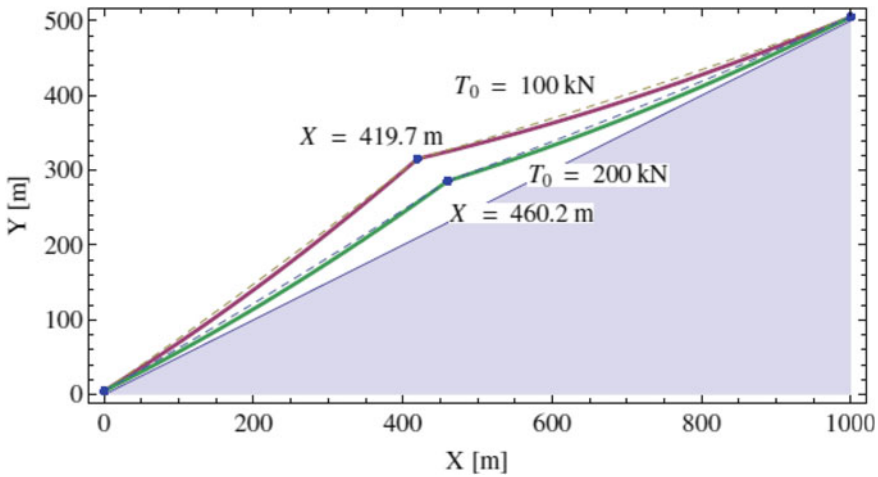


**Fig. 3** Results for a linear profile (slope 1/2) with 1 support. Two cases with different spanning weight  $T_0$  are shown: For  $T_0 = 100$  kN one obtains  $J \equiv h_1 = 105.5$  m and for  $T_0 = 200$  kN  $J = h_1 = 55.6$  m ( $\delta y_{\min} = 5$  m). *Dashed lines* indicate the empty cables. Cable parameters here and in all other figures: a locked coil rope with diameter 21 mm and a metallic cross section of  $301 \text{ mm}^2$  was used. The linear mass density is  $\rho_L = 2.53$  kg/m, the breaking tension  $T_{br} = 530$  kN, the mass of the point load is  $m = 1000$  kg respectively

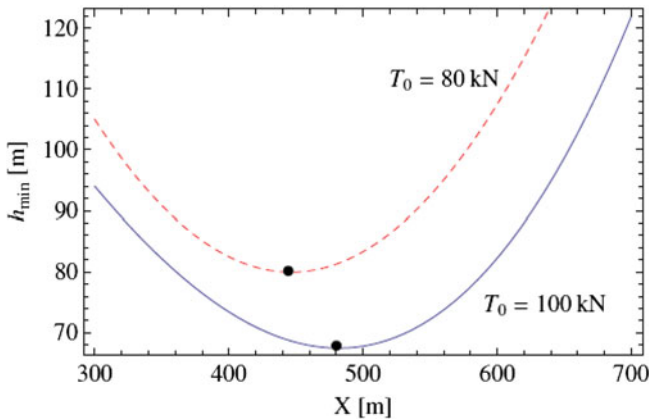


**Fig. 4** Plot of the minimal support height versus the support position for the linear profile and support cable fixed at the end points. The only constraint considered in this example is  $C_0 = 0$ , with  $\delta y_{\min} = 5$  m. The *red, dashed line* corresponds to  $T_0 = 80$  kN, the *solid, blue line* to  $T_0 = 100$  kN respectively. The global minimum of  $J$  in the latter case is  $h_{\min} \approx 68$  m at  $X \approx 480$  m. As expected the position of the minimum goes to the middle of the span for increasing tension  $T_0$

**Table 1** Optimal support positions and heights for a cable fixed at the end points and spanned with a counterweight  $T_0$ . Parameters as in Fig. 3

Bound. cond.	$T_0$ (kN)	100	150	200
End fix	$X_{\min}$ (m)	475	482.2	484.7
End fix	$h_{\min}$ (m)	63.3	49.1	40.3
Sp. weight	$X_{\min}$ (m)	419.7	446.9	460.2
Sp. weight	$h_{\min}$ (m)	105.5	72.2	55.6

### 4.2 Realistic Situation

The mountain profile is shown in the upper part of Fig. 5 (a plant in South tyrol). For the optimization procedure we have chosen the mass of the point load as  $m = 580$  kg, the cable type is as described in Fig. 3. The initial values for the support coordinates has been found by the algorithm—sequence discussed in the previous section. The cable is held fixed at both ends of the line and the positions of three supports are determined by minimization of Eq. (11) subjected to the constraints Eqs. (12), (15) and (16). The cable tension in the valley station is  $T_0 = 173$  kN. The maximal cable tension during the ride is  $T_{\max} = 192.6$  kN, occurring for  $x_{pl} \approx 700$  m. The constraint  $C_4$  is fulfilled for  $v = 3.1$  (Fig. 6).

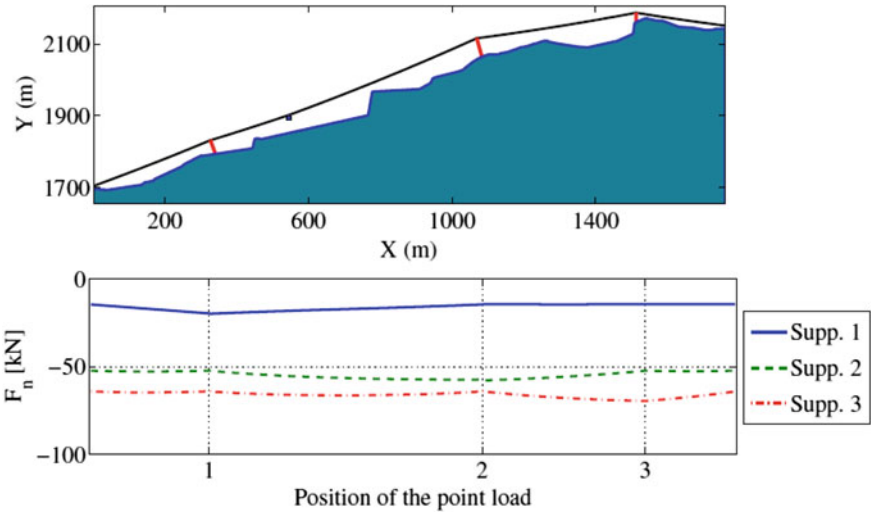


**Fig. 5** The upper panel shows the mountain profile and the optimal solution found by local optimization. The lower figure shows the normal forces (the magnitude of the force times the sign of the  $y$ -component) on the supports when the point load is moving. All forces are negative for all positions of the point load. The maximum value is about  $-15$  kN and occurs on the support no. 1 when the point load is near the mountain station. For the constraints  $C_1, C_2, C_3$  we have set  $F_{y,\min}^j = -5$  kN for all  $j$

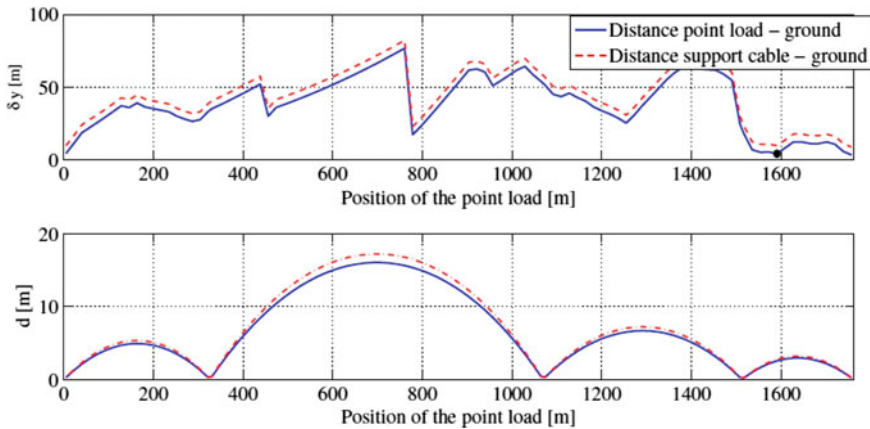


**Fig. 6** The *upper part* shows the support cable—ground distance during the ride. The minimum is indicated by a *black point* and is equal 5 m as required by the constraint  $C_0$ . The *lower panel* shows the distance  $d$  of the point load from the chord. The *blue line* corresponds to a certain reference temperature, for which the optimization was executed. To demonstrate the (important) effect of temperature we have also plotted the same distance for a temperature, which is 30 K higher. The maximum increase of  $d$  is about 1.2 m and occurs in the second span

## 5 Summary and Outlook

In this work we have presented first results of our research on optimization of cable railways. We have defined a cost functional and constraints to find out optimal support positions by an optimization procedure, where we have analyzed local and global optimization strategies. To check the validity of our approach we have tested a simple linear mountain profile. The results are reasonable and as expected from intuition. A second example, based on a real existing plant, shows reasonable results. The constraints regarding cable car-ground distance, support forces and allowed support cable tension are fulfilled. Further studies are needed to incorporate additional constraints and to ensure robustness of the solutions. Parallelization of the computations becomes essentially to reduce cpu-times.

**Acknowledgments** We wish to acknowledge the Amt für Forschung und Innovation des Landes Südtirol/Italy for financial support.

## References

1. Liedl S (1999) Bewegungen und Kräfte des Seilsystems und der Fahrzeuge von Seilschwebebahnen im Fahrbetrieb. Herbert Utz Verlag
2. Wenin M (2013) Rope: simulation of cable railways. <http://www.cphysics.com>
3. Schmutzer E (1989) Grundlagen der Theoretischen Physik Bd. 1. B.I. Wissenschaftsverlag



4. Achenbach J D (1973) Wave propagation in elastic solids. North-Holland Publishing Company
5. Rennert P, Schmiedl H (1995) Physik. B.I. Wissenschaftsverlag
6. Kazakoff AB (2012) Advances in engineering software for lift transportation systems. *J Theor Appl Mech* 42(1):3–22
7. Czitary E (1962) Seilschwebbahnen (2. erweit. Auflage). Springer, Wien
8. CEN-Norm (2015) Sicherheitsanforderungen für Seilbahnen für den Personenverkehr. Amtsblatt der EU C51
9. Volmer M (1999) Stochastische Schwingungen an ausgedehnten Seilfeldern und ihre Anwendung zur Spurweitenberechnung an Seilbahnen. <http://e-collection.library.ethz.ch/eserv/eth:23334/eth-23334-02.pdf>
10. Szabo I (1987) Geschichte der mechanischen Prinzipien (3. Auflage). Verlag Birkhäuser
11. Schell W (1880) Theorie der Bewegung und der Kräfte, II. Band. B. G. Teubner
12. Landau LD, Lifschitz EM (2010) Lehrbuch der Theoretischen Physik, Band VII, Elastizitätstheorie (7. Auflage). Verlag Harri Deutsch
13. Bertsimas D, Brown D, Caramanis C (2011) Theory and applications of robust optimization. *SIAM Rev* 53(3):464–501
14. Engel E, Löscher R (2003) Kritischer Seitenwind bei Zweiseil-Umlaufbahnen. <http://www.eiba.tuwien.ac.at/fileadmin/mediapool-eisenbahn/Diverse/Institutshefte/ih31.pdf>

# The Finite Volume Diffusion Method on Nonmatched Polygonal Meshes Suited for the Lagrangian Slide Lines Calculation

Xuezhe Liu, Zhong Lin and Ruili Wang

**Abstract** An efficient diffusion finite volume method on nonmatched polygonal meshes suited for fluid slide line calculation is proposed. The method manages the sliding meshes and the internal meshes unifying as arbitrary polygonal meshes, takes the hanging-nodes on slip-lines naturally as the nodes of the polygon, and constructs unified diffusion schemes with high accuracy and highly efficient solving algorithms. Furthermore, the radiation diffusion code on unstructured polygonal meshes has been developed and coupled with the hydrocode. Numerical results show the validity of the radiation diffusion computational method for Lagrangian slide lines calculation on nonmatched polygonal meshes.

**Keywords** Finite volume diffusion scheme · Nonmatched polygonal meshes · Lagrangian slide lines calculation

## 1 Introduction

In realistic physical simulations, people often face the problem of shear flow at material interfaces. If the materials move along each other but are tied to a single computational mesh without any sliding treatment, severe mesh distortions appear which can eventually caused the failure of the simulation. This problem is usually treated by introducing a slide line framework into the Lagrangian code. The introduction of slide lines is an old but fruitful idea that dates back to Wilkins [1] as a chapter in a book (reproduced in Chap. 5 of Wilkins [2]).

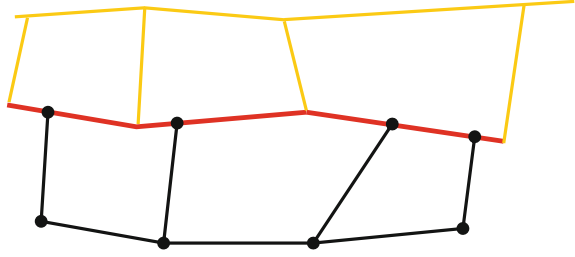
---

X. Liu (✉) · Z. Lin · R. Wang  
Institute of Applied Physics and Computational Mathematics,  
No. 2 Feng Hao East Road, Haidian District, Beijing 100094, China  
e-mail: liu\_xuezhe@iapcm.ac.cn

Z. Lin  
e-mail: lin\_zhong@iapcm.ac.cn

R. Wang  
e-mail: wang\_ruili@iapcm.ac.cn

**Fig. 1** A sample of nonmatched meshes with slide line



Suppose that there exist two different meshes interacting with each other through a common sliding line, one of them is specified as the master side defining the slide line shape, while the other -slave- side follows the slide line. Because of the different tangential-velocity component, the sliding treatment will cause non-matched meshes with arbitrary shapes (with hanging nodes), see Fig. 1.

If the diffusion solver is to be incorporated into a two-dimensional (2D) hydrodynamics code, the diffusion equation is solved on the hydrodynamic meshes, so it becomes a key issue whether the diffusion solver is suited with the nonmatched sliding meshes. Typically, slide line calculation requires special treatment due to the different mesh topology for the sliding meshes and the internal meshes, and this causes considerable difficulties for the design of diffusion schemes and iterative algorithms on such complex meshes, see reference [3, 4] and the reference cited there.

In this paper, we propose an efficient discretization method for solving diffusion equations on nonmatched meshes which has been caused by hydrodynamics slide lines calculation. The method manages the sliding meshes and the internal meshes unifying as arbitrary polygonal meshes, takes the hanging-nodes on slide lines naturally as the nodes of the polygon, and constructs unified diffusion schemes with high accuracy and highly efficient solving algorithms. The diffusion scheme on unstructured polygonal meshes has the advantages of easy coding and is quite promising for application in multi-dimensional radiation hydrodynamics codes.

## 2 Basic Equations

Let  $\Omega$  be an open bounded subset of  $R^2$  with  $\partial\Omega$  being its boundary. We consider the following nonlinear diffusion equations with Robin boundary condition:

$$\begin{aligned} \rho \frac{d\varepsilon}{dt} - \nabla \cdot (\kappa \nabla T) &= f, \\ T(x, r, 0) &= T^0, \\ \alpha \kappa \nabla T \cdot \mathbf{n} + \beta T &= g, \end{aligned} \tag{1}$$

where  $\rho$  is the mass density,  $\varepsilon = \varepsilon(\rho, T)$  is the mass-specific internal energy,  $t$  is the time,  $\kappa = \kappa(\rho, T)$  is the heat conduction coefficient,  $T$  is the temperature and  $f$  is the

volume-specific external energy sources.  $\mathbf{n}$  is the unit outward normal vector.  $\alpha, \beta, g$  are the given values as the function of the space coordinates  $(x, r)$ .

### 3 Construction of Diffusion Scheme on Nonmatched Polygonal Meshes

Let  $\Omega_h$  be a non-overlapping conformal partition of  $\Omega$  onto polygonal elements  $\Omega_i$ , we denote the cell and cell center by  $i$ , the node by  $\alpha$ , and the cell edge by  $\sigma$ , where  $i = 1, \dots, I$ , and  $I$  is the total number of the mesh cell. Denote  $A_i$  as the area of cell  $i$ ,  $L_{\sigma_j}$  as the length of the  $j$ -th edge  $\sigma_j$  of cell  $i$ ,  $d_{i,\sigma_j}, d_{i_j,\sigma_j}$  as the distance of  $\sigma_j$  and cell center  $i, i_j$  respectively,  $\theta$  as the angle between the line from  $i$  to  $i_j$  and edge  $\sigma_j$ ,  $\mathbf{n}_{i,\sigma_j}$  as the unit outward normal vector which points to cell  $i_j$  (see Fig. 2).

By integrating (1) over  $\Omega_i$  and using the Green formula, we obtain the following discretized finite volume diffusion scheme (more details in [5]):

$$m_i \frac{\varepsilon_i^{n+1} - \varepsilon_i^n}{\Delta t} + \sum_{j=1}^{l_i} F_{\sigma_j}^{n+1} S_{\sigma_j} = \nabla_i f_i^{n+1}, \tag{2}$$

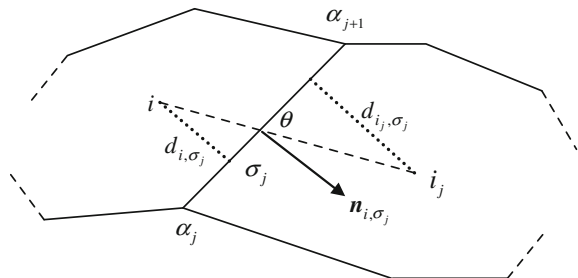
Where  $m_i$  is the mass of the cell  $i$ ,  $\Delta t$  is the time step,  $t^{n+1} = t^n + \Delta t$ ,  $l_i$  is the total number of the edges for cell  $i$ ,  $S_{\sigma_j}$  is the rotational area and  $\nabla_i$  is the rotational volume.  $F_{\sigma_j}$  is the discretized normal flux on edge  $\sigma_j$  in terms of cell-centered unknowns and node-unknowns:

$$F_{\sigma_j}^{n+1} = \begin{cases} -\kappa_{\sigma_j}^{n+1} \left[ \frac{T_{i_j}^{n+1} - T_i^{n+1}}{d_{i_j,\sigma_j} + d_{i,\sigma_j}} - D_{\sigma_j} \left( \frac{T_{\alpha_{j+1}}^{n+1} - T_{\alpha_j}^{n+1}}{L_{\sigma_j}} \right) \right], & \sigma_j - \text{internal edge} \\ -\kappa_i^{n+1} \frac{g_{\sigma_j} - \beta_{\sigma_j} T_i^{n+1}}{\alpha_{\sigma_j} \kappa_i^{n+1} + \beta_{\sigma_j} d_{i,\sigma_j}}, & \sigma_j - \text{boundary edge} \end{cases} \tag{3}$$

Where

$$\kappa_{\sigma_j}^{n+1} = \frac{d_{i_j,\sigma_j} + d_{i,\sigma_j}}{\frac{d_{i_j,\sigma_j}}{\kappa_{i_j}^{n+1}} + \frac{d_{i,\sigma_j}}{\kappa_i^{n+1}}}, \quad D_{\sigma_j} = \frac{(\mathbf{R}_{i_j} - \mathbf{R}_i) \cdot (\mathbf{R}_{\alpha_{j+1}} - \mathbf{R}_{\alpha_j})}{|\mathbf{R}_{i_j} - \mathbf{R}_i|} \cdot \frac{L_{\sigma_j}}{d_{i_j,\sigma_j} + d_{i,\sigma_j}}.$$

Fig. 2 Stencil of the diffusion scheme on polygonal meshes



$\kappa_{\sigma_j}$  is the harmonic mean of the  $\kappa$  on the adjacent meshes  $i$  and  $i_j$  of edge  $\sigma_j$ ,  $D_{\sigma_j}$  is the geometric quantity characterizing the mesh distortion, when the mesh is orthogonal,  $D_{\sigma_j}$  will be zero.

In order to obtain the normal flux approximation expressed in terms of cell-centered unknowns only, we should eliminate the terms associated with node unknowns, i.e.  $T_{\alpha_{j+1}}$  and  $T_{\alpha_j}$  in expression (3). It is usually approximated with the expression

$$T_{\alpha} = \frac{1}{\sum_{k=1}^{m_{\alpha}} \omega_{k,\alpha}} \sum_{k=1}^{m_{\alpha}} \omega_{k,\alpha} T_{i_k},$$

where  $m_{\alpha}$  is the total number of the adjacent cells for node  $\alpha$ ,  $T_{ij}$  is the temperature of the  $k$ -th adjacent cell  $i_k$ ,  $\omega_{k,\alpha}$  is the weight, see Fig. 3.

In [6], a highly accurate method of eliminating the cell node unknowns has been proposed on quadrilateral meshes based on Taylor expansion. We extend this approach to unstructured polygonal meshes, which is well suited for distorted nonmatched meshes.

The diffusion scheme on nonmatched polygonal meshes is fully implicit and should be solved by a nonlinear iteration method.  $\varepsilon$  is the nonlinear function of temperature  $T$ , it can be represented by the temperature:

$$\varepsilon_i^{n+1(s+1)} = \varepsilon_i^{n+1(s)} + \left(\frac{\partial \varepsilon}{\partial T}\right)^{n+1(s)} \left(T_i^{n+1(s+1)} - T_i^{n+1(s)}\right),$$

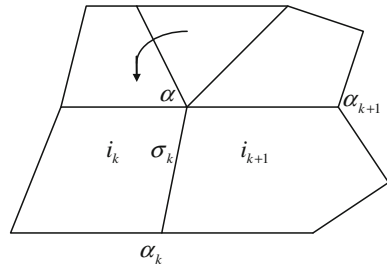
and  $\kappa$  is taken as the value of the last iterative step:

$$\kappa(\rho^{n+1}, T^{n+1}) \approx \kappa^{(s)} = \kappa(\rho^{n+1}, T^{(s)}).$$

Thus, we can obtain the linear systems which can be rewritten as the matrix form:

$$A\left(T^{n+1(s)}\right) T^{n+1(s+1)} = b\left(T^{n+1(s)}\right).$$

**Fig. 3** Adjacent cell of node  $\alpha$



The symmetric linear systems are solved by the conjugate gradient (CG) method, and the nonsymmetric linear systems are solved by the biconjugate gradient stabilized algorithm (BICGSTAB) (see [7]).

## 4 Numerical Tests

Now, we will present some numerical results to illustrate the behavior of the proposed finite volume scheme.

Let  $\Omega$  be the unit square, and let  $\partial\Omega_S$ ,  $\partial\Omega_E$ ,  $\partial\Omega_N$ ,  $\partial\Omega_W$  be the boundaries of  $\Omega$ . There is a nonmatched interface located around  $x = 0.5$  the mesh is independently generated by different methods on either side of the interface.

In our nonmatched grids we measure the mesh size approximately with the average size which is defined as:

$$h = \sqrt{\frac{S_\Omega}{I}},$$

where  $S_\Omega$  is the area of the whole computation domain and  $I$  is the sum of the cell number in all patches.

Note that an exact solution can be found for all our tests. Let  $\hat{T}_i^h$  be that exact solution at the centroid of the cell  $i$ .  $T_i^h$  is the numerical solution in the same cell. Then, the convergence rates can be estimated with the asymptotic errors using both the maximum norm

$$E_{\max}^h = \max_{i=1, \dots, I} |T_i^h - \hat{T}_i^h|,$$

and the mean-square norm

$$E_{L^2}^h = \sqrt{\sum_{i=1}^I (T_i^h - \hat{T}_i^h)^2 A_i}.$$

The asymptotic error is estimated by

$$E^h = Ch^q + O(h^{q+1}),$$

where  $q$  is the order of truncation error and the constant  $C$  is independent of  $h$ .

Calculations are performed on a sequence of grids with different values of  $h$ . For two grids with mesh size  $h_1$  and  $h_2$ , we denote the asymptotic error on these two

meshes with  $E_{h_1}$  and  $E_{h_2}$ , respectively. Then the order of convergence is evaluated using

$$q = \frac{\log\left(\frac{E^{h_1}}{E^{h_2}}\right)}{\log\left(\frac{h_1}{h_2}\right)}.$$

#### 4.1 Linear Diffusion Problem

We consider the following linear diffusion equation

$$\begin{aligned} T_t - \nabla \cdot \nabla T &= -2\pi^2 e^{-\pi^2 t} && \text{in } \Omega, \\ T &= e^{-\pi^2 t} (2 + \cos(\pi x) + \sin(\pi y)) && \text{on } \partial\Omega_S \cup \partial\Omega_N, \\ \nabla T \cdot \mathbf{n} &= 0 && \text{on } \partial\Omega_E \cup \partial\Omega_W, \\ T(x, 0) &= 2 + \cos(\pi x) + \sin(\pi y) && \text{on } \Omega. \end{aligned}$$

The exact solution for this problem is given by  $T = e^{-\pi^2 t} (2 + \cos(\pi x) + \sin(\pi y))$ .

We perform the calculation on a sequence of nonmatched polygonal meshes shown in Fig. 4, the numbers of cells are 158, 570, 2180 respectively. Figure 5 shows that the numerical solution is convergent to the exact solution as the mesh is further refined.

In addition the asymptotic error in the maximum norm and in the mean-square norm are displayed in the Fig. 6. The line labeled with 2nd order is also plotted to give the theoretical second convergence error. The results for our method show that it has almost a second order convergence rate in both the max and  $L_2$  norms on nonmatched polygonal meshes.

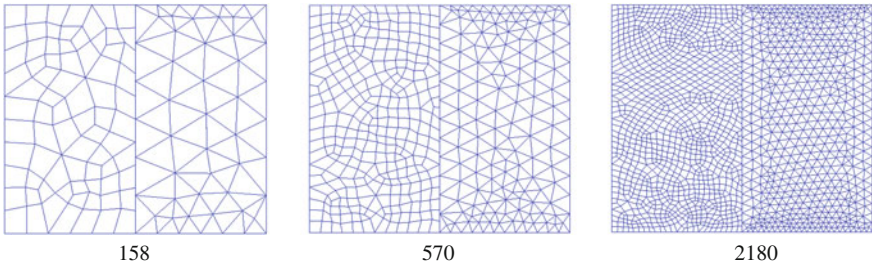


**Fig. 4** A sequence of nonmatched polygonal meshes

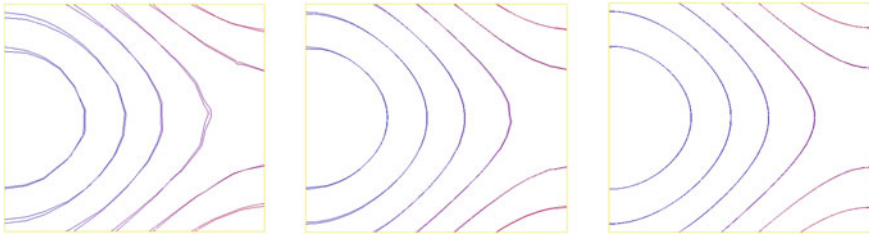
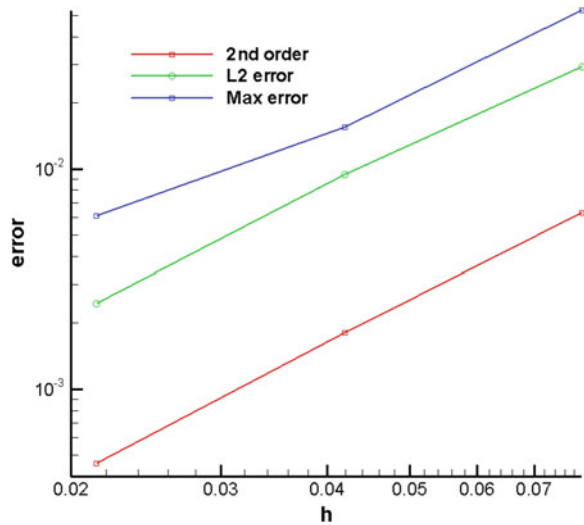


**Fig. 5** Contours of the numerical and exact solution for the linear problem

**Fig. 6** Asymptotic error in logarithmic scale for the linear problem



### 4.2 Nonlinear Diffusion Problem

Consider the following nonlinear problem

$$\begin{aligned}
 T_t - \nabla \cdot (\kappa \nabla T) &= f && \text{in } \Omega \\
 T(x, y, 0) &= T_0 && \text{on } \Omega \\
 T(x, y, t) &= g && \text{on } \partial\Omega
 \end{aligned}$$

The heat conduction coefficient is  $\kappa(T) = T^{7/5} + 1$ , and the nonlinear exact solution is given as  $T = e^t(2x^3 - 3x^2 + 2)(2y^3 - 3y^2 + 3)$ . The source term, Dirichlet boundary condition and the initial value of the temperature are given by the exact solution. We compute the solution until  $t = 0.1$ .

The asymptotic errors are evaluated on a sequence of nonmatched random meshes with three different resolutions. Specifically, there is a grid of  $10 \times 10$



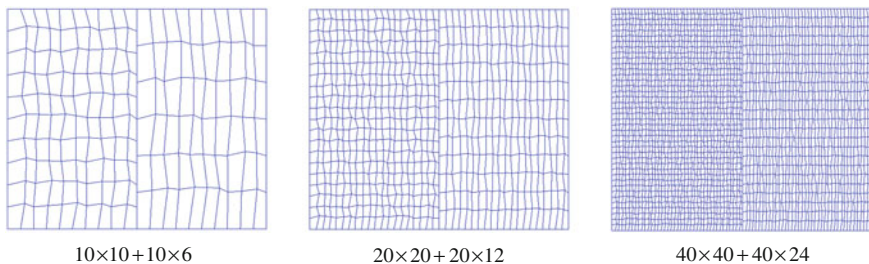


Fig. 7 A sequence of nonmatched random meshes

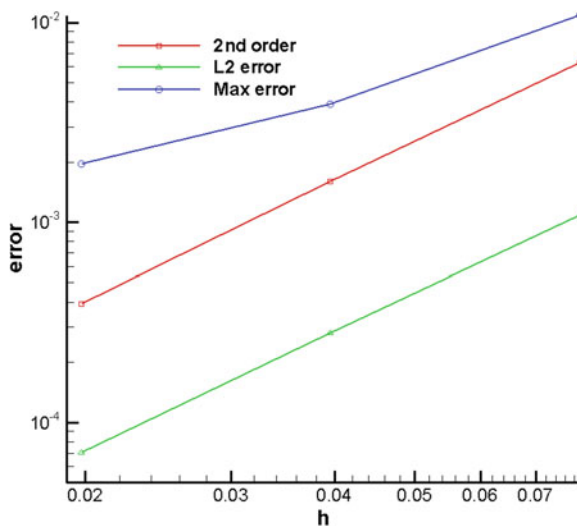


Fig. 8 Contours of the numerical and exact solution for nonlinear problem

(resp.  $20 \times 20$ ,  $40 \times 40$ ) cells on the left hand side of the sliding interface. And on the right-hand side is a grid of  $10 \times 6$  (resp.  $20 \times 12$ ,  $40 \times 24$ ) cells, see Fig. 7. It is shown in Fig. 8 that the numerical solution is convergent to the exact solution as the mesh is further refined.

In addition the asymptotic error in the maximum norm and in the mean-square norm are displayed in the Fig. 9. The line labeled with 2nd order is also plotted to

Fig. 9 Asymptotic error in logarithmic scale for the nonlinear problem



give the theoretical second convergence error. The results for our method show that it has almost a second order convergence rate in both the max and  $L_2$  norms on nonmatched polygonal meshes.

## 5 Conclusion

In this paper, we propose a finite volume diffusion method on nonmatched polygonal meshes caused by the fluid sliding computation. The diffusion scheme has some benefits:

- Cell center unknowns only
- Numerical flux has explicit physical meaning
- Numerical tests show the method has almost second order convergence for linear and nonlinear diffusion problems on distorted nonmatched meshes
- Suited for arbitrary polygonal meshes and easy to incorporated into a Lagrangian hydrodynamics code.

**Acknowledgment** This work was partially supported by the National Nature Science Foundation of China(11201035,11372051), and the Science and Technology Development Foundation of CAEP (2015B0202045).

## References

1. Wilkins ML (1963) Calculation of elastic-plastic flow. Technical report UCRL-7322. University Livermore, Lawrence Radiation Lab, California
2. Wilkins ML (1999) Computer simulation of dynamic phenomena. Springer, Scientific computation
3. Chang Lina, Yuan Guangwei (2009) Cell-centered finite volume methods with flexible stencils for diffusion equations on general nonconforming meshes. *Comput Methods Appl Mech Engrg* 198:1638–1646
4. Kuznetsov Y, Lipnikov K, Shashkov M (2004) The mimetic finite difference method on polygonal meshes for diffusion-type problems. *Comput Geosci* 8:301–324
5. Liu Xuezhe, Yunlong Yu, Wang Ruili, Lin Zhong (2010) A cell-centered finite volume scheme for discretizing diffusion equations on unstructured arbitrary polygonal meshes. *Numer Comput Comput Appl* 31(4):259–270 (in Chinese)
6. Sheng Zhiqiang, Yuan Guangwei (2008) A nine point scheme for the approximation of diffusion operators on distorted quadrilateral meshes. *SIAM J Sci Comput* 30:1341–1361
7. Saad Y (1996) *Iterative Method for Sparse Linear Systems*. PWS Publishing, New York

# Effect of Defects and Electric Field on Stress-Induced Motion of 90° Domain Wall in PbTiO<sub>3</sub>: A Molecular Dynamics Study

Yoshitaka Umeno and Atsushi Kubo

**Abstract** Perovskite ferroelectric crystals are common materials used for actuators utilizing their piezoelectricity. Perovskite materials generally contain ferroelectric domain walls (DWs), whose motion leads to domain switching. As the mobility of DWs is strongly related to the piezoelectric performance, it is essential to understand the mechanism of DW motion in detail. In this study we perform molecular dynamics (MD) simulations with a shell-model interatomic potential for the motion of a 90° DW in PbTiO<sub>3</sub>. The reliability of the employed potential has already been confirmed in terms of DW structure and mobility. We simulate the motion of DW induced by stress and investigate the effect of oxygen vacancies and external electric fields. Our simulations demonstrate that the critical shear stress of the motion of DWs having oxygen vacancies is much higher than that of clean DWs, representing the defect hindering domain switching. We also perform ‘multi-physics’ MD simulations, where the combined effect of mechanical stress and electric field is examined. The simulations demonstrate the effect of external electric fields on the stress-induced DW motion to reveal that the critical shear stress of DW motion strongly depends on the direction of the electric fields.

**Keywords** Molecular dynamics · Domain wall · PbTiO<sub>3</sub> · Deformation · Multi-physics

---

Y. Umeno (✉) · A. Kubo  
Institute of Industrial Science, The University of Tokyo, 4-6-1,  
Komaba, Meguro-Ku, Tokyo 153-8505, Japan  
e-mail: umeno@iis.u-tokyo.ac.jp

A. Kubo  
e-mail: kubo@ulab.iis.u-tokyo.ac.jp

## 1 Introduction

Some perovskites that possess spontaneous polarization at room temperature, e.g., lead titanate ( $\text{PbTiO}_3$ ) and barium titanate ( $\text{BaTiO}_3$ ), exhibit ferroelectricity and thus have various applications including sensors, actuators and random access memories (FeRAMs) [1–4]. In general such perovskites contain boundaries between uniformly polarized regions (domains), which are called domain walls (DWs). The motion of DWs induced by application of external stress or electric field causes domain switching. It is important to understand the mechanism of DW motion because the mobility of DWs is strongly related to the piezoelectric performance. For example, if DW motion is hindered for some reason, the response of the material to applied stress or electric field may become slow, resulting in poor device function.

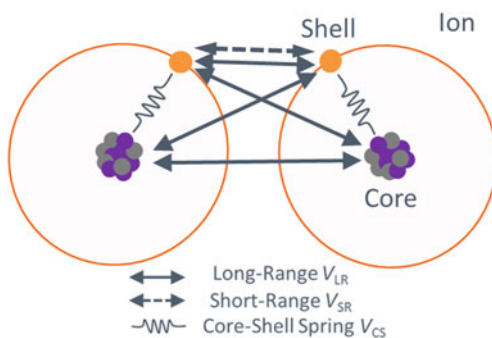
Some theoretical studies have been done to investigate DW properties at the atomistic scale. Shimada et al. [5] investigated stress-induced motion of  $90^\circ$  DW in  $\text{PbTiO}_3$  by the density functional theory (DFT). An empirical interatomic potential based on the shell-model was developed for  $\text{PbTiO}_3$  [6]. Kubo et al. [7, 8] performed classical molecular dynamics (MD) simulations using the shell model potential for  $\text{PbTiO}_3$ , and demonstrated that the MD simulation is applicable to stress-induced motion of  $90^\circ$  DW in  $\text{PbTiO}_3$ .

The aim of this study is to expand the approach in Refs. [7, 8] for deeper understanding of the behavior of DW motion. We deal with two issues; (a) the effect of oxygen vacancy defects, and (b) the effect of superimposed electric field and stress, on the motion of  $90^\circ$  DW in  $\text{PbTiO}_3$ .

## 2 Simulation Method

The shell model [9] describes ions and electrical polarization surrounding the ions by pairs of positively-charged particles (the core) and negatively-charged ones (the shell). Figure 1 schematically shows interactions between the cores and the shells.

**Fig. 1** Schematic of shell-model interatomic model



In the shell model, three types of interactions are considered; the long-range Coulomb interaction ( $V_{LR}$ ), the short-range repulsive interaction ( $V_{SR}$ ) and the core-shell spring ( $V_{CS}$ ), which are given in the following forms.

$$\begin{aligned}
 V_{LR}(r) &= \frac{q_i q_j}{4\pi\epsilon_0} \frac{1}{r} \\
 V_{SR}(r) &= \left\{ A \exp\left(-\frac{r}{\rho}\right) - \frac{C}{r^6} \right\} f_c(r) \\
 f_c(r) &= \begin{cases} 1 & (r < R_{C1}) \\ \frac{1}{2} \cos\left(\frac{\pi(r-R_{C1})}{2(R_{C2}-R_{C1})}\right) & (R_{C2} > r \geq R_{C1}) \\ 0 & (r \geq R_{C2}) \end{cases} \\
 V_{CS}(r) &= \frac{1}{2} k_2 r^2 + \frac{1}{24} k_4 r^4
 \end{aligned}$$

where  $q$ ,  $\epsilon_0$  and  $r$  denote the charge of the core or shell, the dielectric constant in vacuum and distance between two particles, respectively.  $A$ ,  $\rho$ ,  $C$ ,  $k_2$  and  $k_4$  are parameters.  $f_c(r)$  is an attenuation function to smoothly truncate the short-range interaction around the cut-off radii ( $R_{C2}$  and  $R_{C1}$ ). The polarization per volume in the  $\alpha(=x, y, z)$  directions is given by

$$P_\alpha = \sum_i (Z_i \xi_{i,\alpha} + Y_i \zeta_{i,\alpha}) / V$$

Where  $V$  is the volume,  $Z_i$  is the charge of the ion  $i$  (core and shell), and  $Y_i$  is that of the shell of the ion  $i$ .  $\xi_i$  is the displacement component of the core from the ideal lattice, and  $\zeta_i$  is the displacement of the shell from the core position. As shown above, the short-range interaction is described by the Buckingham type function. Coulomb interaction is calculated by the Ewald summation [10]. In this study we adopt the set of parameters developed for  $\text{PbTiO}_3$  by Shimada et al. [6].

Simulation models of  $90^\circ$  DW in  $\text{PbTiO}_3$  were set up as shown in Fig. 2. Atom positions are distorted to have charge polarization along  $\{100\}$  in different directions in the left half and the right half of the simulation box.  $N$  denotes the number of unit cells in the simulation box; the figure shows a model of  $N = 18$ . The boundaries are periodic in the  $x$ ,  $y$  and  $z$  directions, giving two DWs normal to the  $z$  direction in the box (center and edge). For the simulation of shear stress-induced DW motion, a shear strain  $\gamma_{zy}$  was applied to the simulation cell as shown in Fig. 2.  $\gamma_{zy}$  was increased stepwise until DW motion occurred. At each strain atoms were relaxed until all the forces on atoms become less than  $10^{-7}$  eV/Å. Normal stress components and shear stress components except  $\tau_{yz}(= \tau_{zy})$  were controlled to 0 MPa within the error of 10 and 1 MPa, respectively. Application of the electric field was simulated by imposing an extra Coulomb force ( $\mathbf{F}_{\text{ext}}$ ) on ions according to the external electric field ( $\mathbf{E}$ ); i.e.,  $\mathbf{F}_{\text{ext}} = \mathbf{E}q$ , where  $q$  is the charge of cores or shells.

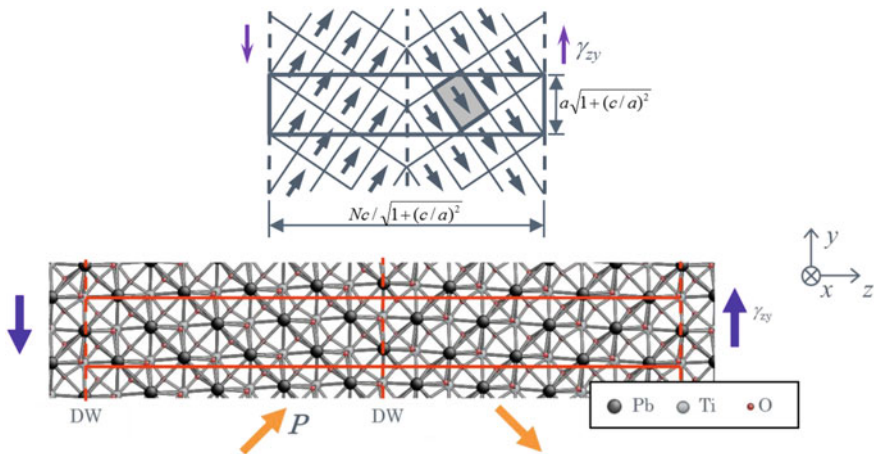


Fig. 2 Simulation model of 90° DW in PbTiO<sub>3</sub>

### 3 Motion of Domain Wall with Oxygen Vacancies

Before the simulation of DW motion, we calculated the total energy of the DW model with oxygen vacancies on different sites to determine the favorable site of the vacancy. To avoid interactions between periodic images of the vacancy, we expanded the simulation cell dimensions in the  $x$  and  $y$  directions to 11.1 and 7.72 Å, respectively. Figure 3 shows the vacancy sites examined in the calculation and the calculated energies are listed in Table 1. The site closest to the domain wall (Site 4) gives the lowest energy. We therefore choose this site of the oxygen vacancy in the following calculation of shear deformation.

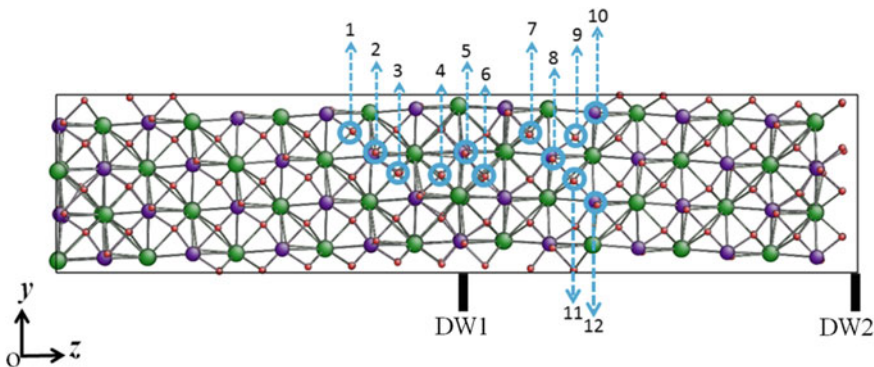
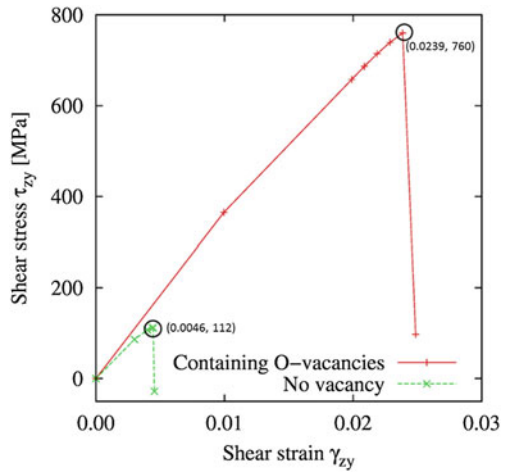


Fig. 3 Site of oxygen vacancy near DW

**Table 1** Total energy of DW model with vacancy

Vacancy site	Energy (eV)	Vacancy site	Energy (eV)
1	-10.55912	7	-10.55916
2	-10.55913	8	-10.55913
3	-10.55912	9	-10.55915
4	-10.55937	10	-10.55912
5	-10.55919	11	-10.55915
6	-10.55916	12	-10.55913

**Fig. 4** Stress-strain relationships of models with (green) and without (red) vacancies. Sharp drop of stress indicates DW motion



We then performed a MD simulation of DW motion induced by shear stress (strain). The obtained relationship between shear stress and shear strain is presented in Fig. 4. The figure also contains the result with a model without vacancies for comparison. It is found that the critical strain and stress of the model with oxygen vacancies are 4.2 and 5.8 times higher than those of the model without vacancies, respectively. This result demonstrates that the oxygen vacancies have a strong pinning effect on the DW motion. Snapshots of atoms before and after DW motion in the vacancy model are presented in Fig. 5, where one finds the motion of DW originally located at the edge of the simulation box (DW-2).

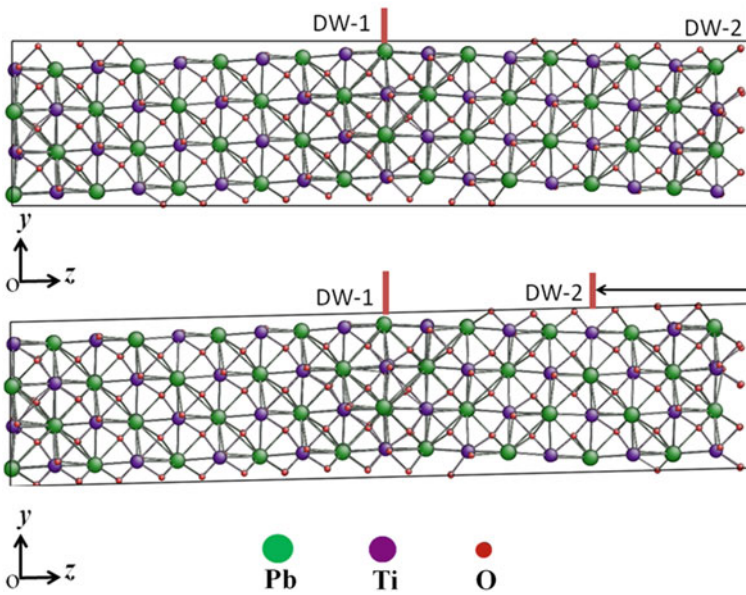


Fig. 5 Snapshots of atoms before and after DW motion in the vacancy model

## 4 Shear-Induced Domain Wall Motion Under Electric Field

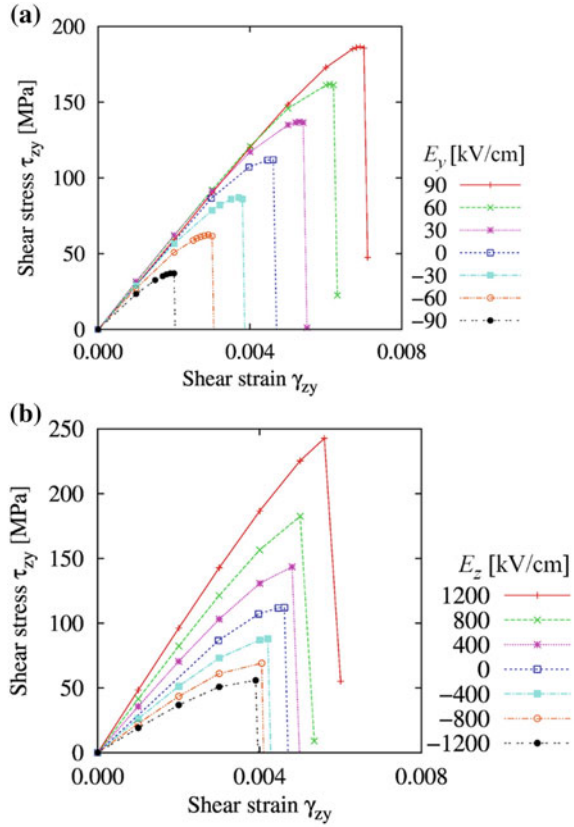
We performed MD simulations for the  $90^\circ$  DW model under superimposed electric field and shear strain. To obtain the critical stress and strain, we increased the shear strain until DW motion occurred under predetermined constant value of external electric field. Figure 6a shows stress-strain curves under electric field along the  $y$  direction (parallel to DW),  $E_y$ . Here we examined the value of the electric field within the range  $-90 \leq E_y \leq 90$  kV/cm. While the slopes near  $\gamma_{zy} = 0$  were nearly unchanged, the critical stress and strain were obviously affected by  $E_y$ . It is seen that the DW motion was facilitated by the electric field toward the  $-y$  direction.

Simulation results of stress-strain curves under electric field along the  $z$  direction (perpendicular to DW),  $E_z$ , are presented in Fig. 6b. Notice that the magnitude of  $E_z$  was set larger ( $-1200 \leq E_z \leq 1200$  kV/cm) than that of  $E_y$ . While we did observe the enhancement of DW motion by the application of the electric field toward the  $-z$  direction ( $E_z < 0$ ), the effect was much weaker than that of  $E_y$ . It should be also noted that the slopes of the stress-strain curves near  $\gamma_{zy} = 0$  were remarkably changed by the electric field perpendicular to the DW in contrast to the case of the electric field parallel to the DW.

The mechanism of the effect of the electric field on the DW motion is explained with the schematics in Fig. 7. The schematics show the case where the DW motion



**Fig. 6** Stress-strain curves under electric field **a** parallel and **b** perpendicular to DW



was enhanced by the electric field, i.e.,  $E_y < 0$  and  $E_z < 0$ . When the electric field toward the  $-y$  direction is applied, the electric field induces moments to charge polarizations counter-clockwise in both the left half and the right half of the simulation cell. As a result, the polarization in the left half is enhanced and that in the right half is suppressed, producing a driving force to the DW (DW in the center to the right and DW on the edges to the left). In contrast, the electric field toward the  $-z$  direction causes moments to charge polarizations in the different directions; clockwise in the left simulation cell and counter-clockwise in the right. This also works as a driving force to the DW because it tries to ‘flatten’ the polarization directions in both the sides of the cell, but the effect is much more modest than that in the previous case. The difference in the strength of the effect of the electric field can be understood by the above mentioned mechanisms that differ depending on the directional relationship between the electric field and the domain wall. This clarifies the strong anisotropy in the multi-physics aspect of the DW motion as a result of interplay between the electric field and the mechanical loading.

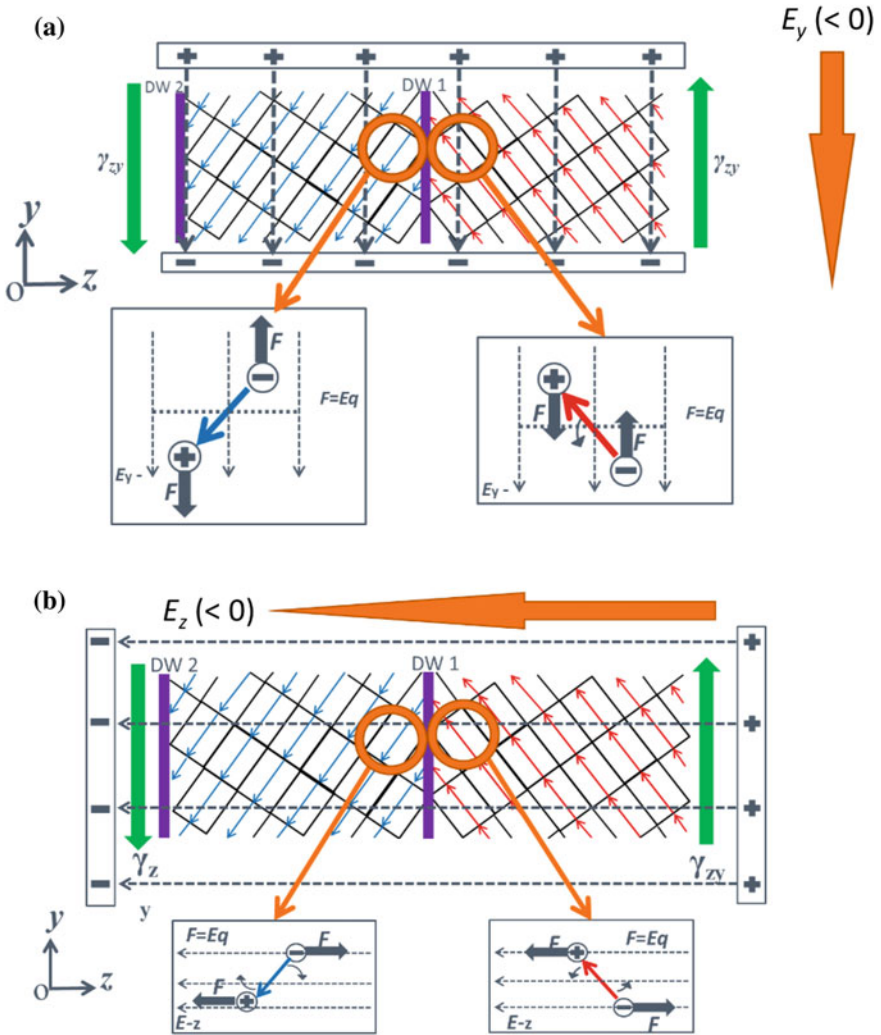


Fig. 7 Schematic illustrations explaining mechanism of enhancement of DW motion by electric field

## 5 Conclusion

To better understand the mechanism of domain switching in perovskites, we performed MD simulation of the motion of a  $90^\circ$  DW in  $\text{PbTiO}_3$  and investigated the effect of oxygen vacancies and external electric fields. It was demonstrated that the critical shear stress of the motion of DWs having oxygen vacancies is much higher than that of clean DWs, representing the defect hindering domain switching. Our

'multi-physics' MD simulations, where the combined effect of mechanical stress and electric field is examined, clarified the effect of external electric fields on the stress-induced DW motion. We revealed that the critical shear stress of DW motion strongly depends on the direction of the electric fields.

## References

1. Lines ME, Glass AM (1977) Principles and application of ferroelectrics and related materials. Clarendon, Oxford
2. Scott JF (2000) Ferroelectric memories. Springer, Berlin
3. Ramesh R (1997) Thin film ferroelectric materials and devices. Kluwer Academic, Boston
4. Auciello O, Scott JF, Ramesh R (1998) The Physics of Ferroelectric Memories. Phys Today. doi:[10.1063/1.882324](https://doi.org/10.1063/1.882324)
5. Shimada T, Umeno Y, Kitamura T (2008) Ab initio study of stress-induced domain wall switching in PbTiO<sub>3</sub>. Phys Rev B 77:094105
6. Shimada T, Wakahara K, Umeno Y, Kitamura T (2008) Shell model potential for PbTiO<sub>3</sub> and its applicability to surfaces and domain walls. J Phys: Condens Matter 20:325225
7. Kubo A, Umeno Y (2012) Atomistic model calculation of stress-induced domain wall instability in PbTiO<sub>3</sub> using shell model. J Solid Mech Mater Eng 6:90–98
8. Kubo A, Albina J-M, Umeno Y (2013) Atomistic study of stress-induced switching of 90-degree ferroelectric domain walls in PbTiO<sub>3</sub>: size, temperature, and structural effect. Modelling Simul Mater Sci Eng 21:065019
9. Dick BJ, Overhauser W (1958) Theory of the dielectric constants of alkali halide crystals. Phys Rev doi:[10.1103/PhysRev.112.90](https://doi.org/10.1103/PhysRev.112.90)
10. de Leeuw SW, Perram JW, Smith ER (1980) Simulation of electrostatic systems in periodic boundary conditions I. Lattice sums and dielectric constants. Proc Roy Soc London A373:27–56

# Ce,Tb-Doped $Y_2SiO_5$ Phosphor Luminescence Emissions Modeling and Simulation

D. Cervantes, D.L. Flores, E. Gutiérrez and M.A. Chacón

**Abstract** White light-emitting diodes offer the possibility of efficient, safe, and reliable solid-state lighting, and thus have various applications in artificial lighting. Reported white light-emitting phosphors usually contain rare-earth metals and are generally prepared by high-energy processes. The purpose of this research is the modeling and simulation of the molar percentages of cerium and terbium required to be incorporated into a yttrium silicate ( $Y_2SiO_5:Ce,Tb$ ) crystal structure for luminescent emission. The input data used for the modeling process comes from experiments with a set of molar concentrations of cerium and terbium ranging from 0.5 to 2%, and, from 1 to 6%, respectively; chromaticity coordinates are obtained from the photoluminescence spectra generated by the luminescent materials. With the information above, a simulation based on the proposed mathematical model was performed in order to obtain the approximation of the luminescent response of the molar concentrations whose experiments were not carried out in the laboratory. To demonstrate the results of the model and its simulation, a tool developed in the agent-based platform NetLogo is presented, which allows the user to observe the trend of the chromaticity coordinates for different molar percentages of cerium and cerium into yttrium silicate crystal structures.

**Keywords** Rare-earth phosphors materials · Chromaticity coordinates · Simulation · NetLogo

---

D. Cervantes · D.L. Flores (✉) · E. Gutiérrez · M.A. Chacón  
Autonomous University of Baja California, Ensenada, Mexico  
e-mail: dflores@uabc.edu.mx

D. Cervantes  
e-mail: dcervantes42@uabc.edu.mx

E. Gutiérrez  
e-mail: everardo.gutierrez@uabc.edu.mx

M.A. Chacón  
e-mail: marco.chacon@uabc.edu.mx

## 1 Introduction

In the last few decades there has been a great deal of interest in white light sources based on rare-earth doped phosphor materials due to their potential range of applications, for example, in the field of full color displays and solid state lighting. It is well known that white light is generated by an adequate blend of the three primary colors (such as red, green and blue). The selection of phosphor materials depends on the activation energy matching or the coupling of phosphor materials. In addition, it is necessary to increase the efficiency of white light-emitting solid state devices, so special attention has been paid lately to the development of new phosphors that can be activated in the range of long-UV ( $\lambda = 300\text{--}420$  nm) and/or blue radiation [1–3]. This consequently results in lower power consumption, which positively impacts the environment by reducing greenhouse gases emissions and the elimination of mercury in solid-state lamps production [4].

The use of one or two rare earth (RE) ions as color centers in the same crystalline host has been tested as an option for the development of new phosphor materials. Ce-doped  $\text{Y}_2\text{SiO}_5$  has proven to be an excellent blue-emitting phosphor, while Tb-doped  $\text{Y}_2\text{SiO}_5$  is appropriate for light emission in the green region [5, 6]. However, when both RE ions are incorporated in the same host matrix,  $\text{Ce}^{3+}$  becomes a blue broadband emitter with the ability of transferring energy from its lowest 5d levels to  $\text{Tb}^{3+}$  ions [1, 2, 7–9]. Due to this energy transfer it is possible to obtain both rare-earth emission simultaneously with only one excitation wavelength in the low energy region of UV radiation. Moreover, laboratory experiments can be complemented with computational tools, that is, from the first experimental results design laboratory experiments aimed to specific targets within the range possible results.

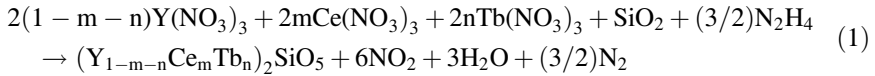
The present work analyses the chromaticity coordinates tendency of a series of cerium and terbium coactivated yttrium silicate phosphors with different rare-earth ions molar percentages. The chromaticity coordinates were determined using the emission spectra obtained by the photoluminescence technique and the CIE standard equations of primary colors with the uses of the NetLogo software to correlate the cerium and terbium molar percentages and then obtain the regression equation to design experiments with the optimum rare-earth ions molar percentages to reach the closest chromaticity coordinates with the D65 white light or to obtain specific chromaticity coordinates in the path of cerium and terbium simultaneous emission.

## 2 Experimental

The purpose of this work is to design experiments using computational resources and some experimental data obtained from luminescent properties of the system  $\text{Y}_2\text{SiO}_5:\text{Ce},\text{Tb}$  at different rare-earth molar percentages from 0.5 to 2 and from 1 to 6 for cerium and terbium ions, respectively. The goal is to reduce the number of laboratory experiments to achieve specific luminescent properties.

## 2.1 Synthesis of Cerium and Terbium Activated Yttrium Silicate, YSO:Ce,Tb

The synthesis of the YSO:Ce,Tb phosphor system was made by the pressure-assisted combustion synthesis (PACS) method [10, 11] according to the following chemical reaction:



Details of synthesis procedures were described in a previous publication in Cervantes et al. [12].

## 2.2 Characterization

Emission spectra were measured with a fluorescence spectrophotometer (PL, HITACHI f-7000) using 355 nm as excitation wavelength. Emission spectra data was used to determine the chromaticity coordinates through the NetLogo software and the design of a program that uses the CIE 1931 standard equations. The crystallographic structure of the nanoparticles was determined by X-ray diffraction (XRD, PHILIPS X' Pert) using Cu-K<sub>a</sub> radiation. Morphology images of the resulting powders were obtained by transmission electron microscopy (TEM, JEOL 2010).

## 3 Proposal Model

A simulation model is proposed as shown in Fig. 1; this figure depicts that the emission spectra that are provided to the simulation comes from experiments conducted in the laboratory described in [12]. Using our software simulation proposal in Netlogo, the chromaticity coordinates for each of the emission spectra of the materials were simulated and the values are shown in Table 1.

Once having the chromaticity coordinates, which according to CIE1931 (D65) are (0.3128, 0.329), the Euclidean distance to the coordinates of white light is calculated, with the data shown in Table 2.

With the values of the distances an equation multivariate linear regression obtained, where independent variables are the molar concentration of cerium and terbium and the dependent variable is the Euclidean distance. A linear least square approach was used as regression method, and its high level algorithms is as follows [13, 14]:

**Fig. 1** Proposal model diagram for rare-earth molar concentration simulation

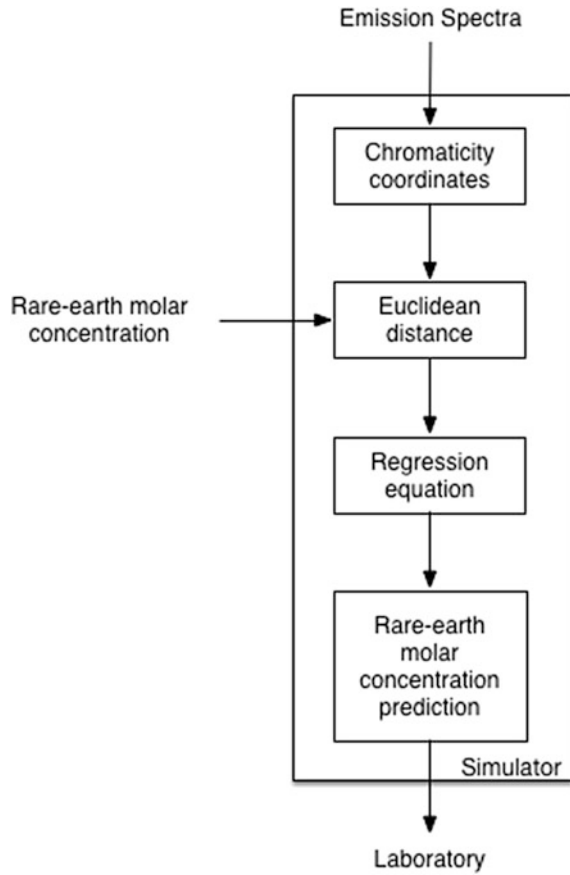


**Table 1** Chromaticity coordinates of each of nanomaterials

Name	Cerium (mol%)	Terbium (mol%)	Coord X (CIE1931)	Coord Y (CIE1931)
YSO0.5-3	0.5	3	0.2320	0.2656
YSO0.75-1	0.75	1	0.1793	0.1500
YSO0.75-2	0.75	2	0.2057	0.2143
YSO0.75-3	0.75	3	0.2312	0.2564
YSO0.75-3.5	0.75	3.5	0.2405	0.2929
YSO0.75-4	0.75	4	0.2440	0.3080
YSO0.75-4.96	0.75	4.96	0.2592	0.3407
YSO0.75-5	0.75	5	0.2585	0.3348
YSO0.75-6	0.75	6	0.2702	0.3631
YSO1-3	1	3	0.2323	0.2617
YSO2-3	2	3	0.2350	0.2802

**Table 2** Euclidean distance of each of the nanomaterials

Name	Euclidean distance
YSO0.5-3	0.102704430
YSO0.75-1	0.223300806
YSO0.75-2	0.156928328
YSO0.75-3	0.109221426
YSO0.75-3.5	0.080811509
YSO0.75-4	0.071933580
YSO0.75-4.96	0.054608882
YSO0.75-5	0.054862100
YSO0.75-6	0.054567115
YSO1-3	0.104926355
YSO2-3	0.091838336

**Algorithm 1. Regression with Linear Least Square**

*Input:* A set of  $m$  linear equations, each one with  $n$  independent variables and one dependent variable, given by the previous set of experiments.

*Step 1.* State each input equation as:  $f(x; \beta) = \beta_0 + \beta_1 x_1 + \dots + \beta_n x_n$ . Where each independent variable ( $x_1, x_2, \dots, x_n$ ) represent the used rare earths ions and the estimated  $f(x; \beta)$  values are given by results of the input experiments.

*Step 2.* Use quadratic minimization to find the coefficients  $\beta_0, \beta_1, \dots, \beta_n$  setting the system in matrix equation of the type  $Ax = b$  with the formula:  $(A^T A)\beta = A^T y$

*Step 3.* Calculate from previous formula the estimated slope and coefficients for independent variables and report them as output.

This algorithm gave as a result a set of coefficients, as shown in the following equation:

$$EuclDist = 0.233 - 0.0199 * Ce - 0.0330 * Tb \quad (2)$$

With the standard deviation is 0.0223565 and adjusted  $R^2$  is 80.7 %.

Also a multivariate quadratic regression was performed, which is shown in the following equation:

$$EuclDist = 0.316 - 0.00906 * Ce - 0.0943 * Tb + 0.00864 * Tb^2 \quad (3)$$

in this regression, the standard deviation is 0.00323709 and the adjusted  $R^2$  is 99.6 %.

Once these equations are obtained, a table with a series of experiments designed to perform in the laboratory as required by the expert can be generated. This set of suggested experimental values were calculated with a modified bisection search as follows [15]:

**Algorithm 2. Bisection Search**

*Input:* An interval  $[a, b]$  for one of the rare earths (cerium, terbium) and the factors  $c_1$  and  $c_2$  to calculate the cost function  $f = c_1 \text{ Cerium} + c_2 \text{ Terbium}$ .



Step 1. Calculate the middle point of the interval  $c = \frac{(a+b)}{2}$ .

Step 2. For each value  $a$ ,  $b$  and  $c$ , calculate the value for the dependent rare earth based on the linear equation given by the linear regression results.

Step 3. Calculate the cost function for  $(a, x_1)$ ,  $(b, x_2)$  and  $(c, x_3)$ , using  $a$ ,  $b$  and  $c$  as values for the independent rare earth and  $x_1$ ,  $x_2$  and  $x_3$  the calculated values in Step 2.

Step 4. If the convergence is satisfactory then return the pair  $(c, x_3)$  as proposed concentrations of rare earths to be tested experimentally and stop iterating.

Step 5. Replace either the lower or upper interval limit with  $c$  according with the cost function results, where our goal is to minimize it, and return to Step 1.

## 4 Results and Discussion

### 4.1 Emission Spectra and Crystalline Structure

The emission spectra of YSO:Ce,Tb nanopowders revealed the typical light emissions of the  $\text{Ce}^{3+}$  and  $\text{Tb}^{3+}$  ions (Fig. 2), revealing a broadband emission, located in the 380–475 nm wavelength range, which is generated by the 5d–4f

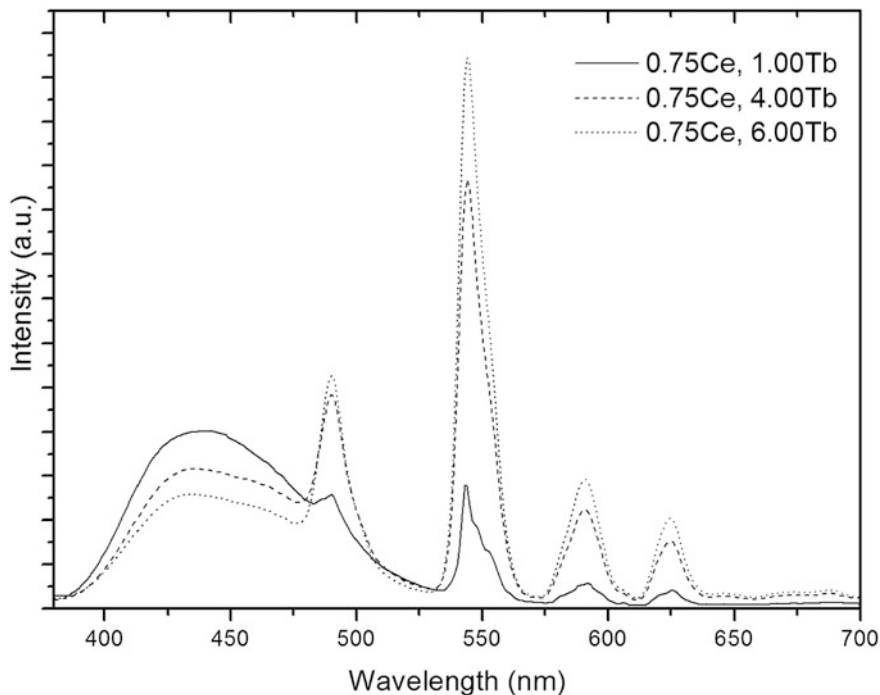


**Fig. 2** Photoluminescence emission spectra of  $\text{Y}_2\text{SiO}_5\text{:Ce,Tb}$  phosphors nanopowders

electronic transitions within the  $Ce^{3+}$  ions and a well-defined green emission located at 546 nm due to  $^5D_4-^7F_5$  transitions in the  $Tb^{3+}$  ions. The emission peaks observed at 490, 591 and 624 nm are also associated to  $^5D_4-^7F_6$ ,  $^5D_4-^7F_4$  and  $^5D_4-^7F_3$  transitions in  $Tb^{3+}$  ions, respectively. The chromaticity coordinates determined through emission spectra data show a linear trend that extends along the blue region to the green region in the CIE 1931 chromaticity coordinates diagram as a function of rare-earth ions molar percentages. These chromaticity coordinates were compared with chromaticity coordinates obtained by the color calculator software of the Osram Sylvania Company. Both sets of chromaticity coordinates had the same values. It is noteworthy that other authors have used Spectra Lux software to determine the chromaticity coordinates [16, 17]. Simultaneous emissions of  $Ce^{3+}$  and  $Tb^{3+}$  from YSO:Ce,Tb phosphors generates a light near to the chromaticity coordinates of D65 white-light. This light could get even closer to the D65 white light chromaticity coordinates with the addition of a red-emitting ion within the same host, or even more simple by mixing the YSO:Ce,Tb phosphor with a second phosphor compound, of red emission.

X-ray diffraction patterns (Fig. 3) of YSO:Ce,Tb nanopowders showed  $X1-Y_2SiO_5$  crystal phase (JCPDS 41-0004 card) and correspond to a monoclinic

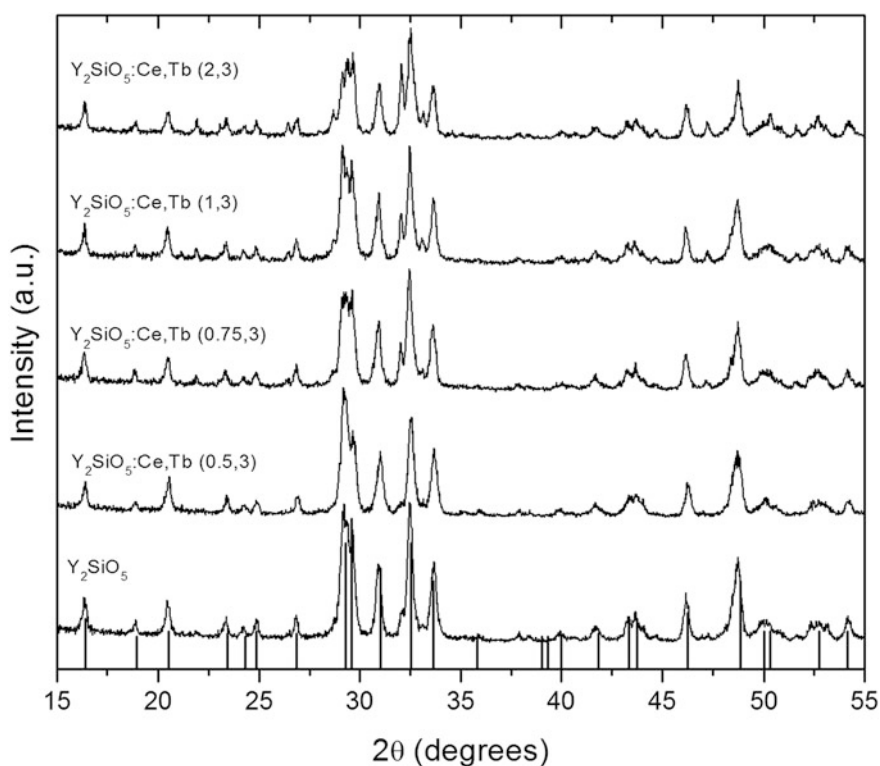


**Fig. 3** XRD patterns of YSO:Ce,Tb nanopowders at different rare-earth molar percentages compared with the JCPDS card 41-0004 for  $X1-Y_2SiO_5$  crystalline phase

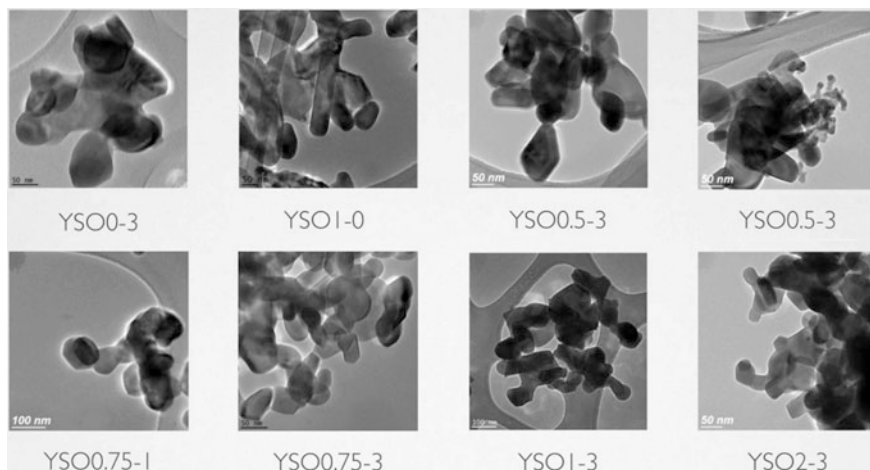


**Fig. 4** TEM images of YSO:Ce,Tb powders at different rare-earth ions molar percentages

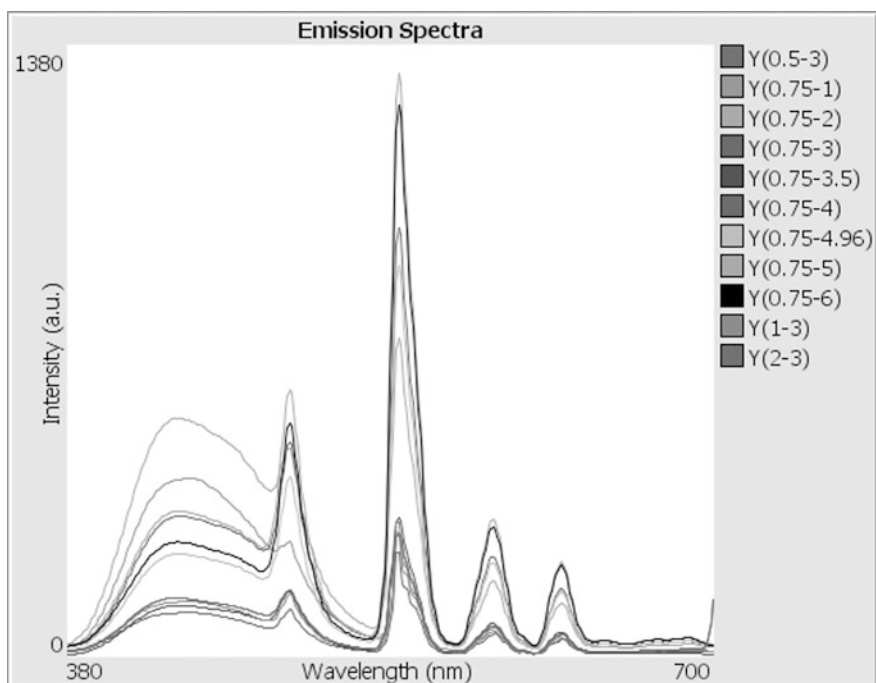


**Fig. 5** Emission spectra of the  $Y_2SiO_5:Ce,Tb$

system in accordance with the crystallographic phases found by other authors [18, 19]. The crystal structure was kept for the different rare-earth ions percentages. Figure 4 shows TEM images of YSO:Ce,Tb phosphors synthesized at different rare-earth ions molar percentages. Particles sizes of different samples were in the range from 30 to 100 nm.

## 4.2 An Agent-Based Platform for Data Analysis

A new tool was developed in an agent-based platform NetLogo, which allows the user to analyze the experimental data. Given a set of molar concentrations with their respective emission spectra, the platform allows visualizing emission spectra. It also calculates and shows on CIE 1931 chromaticity diagram the trend of the chromaticity coordinates for the different molar percentages of cerium and terbium.

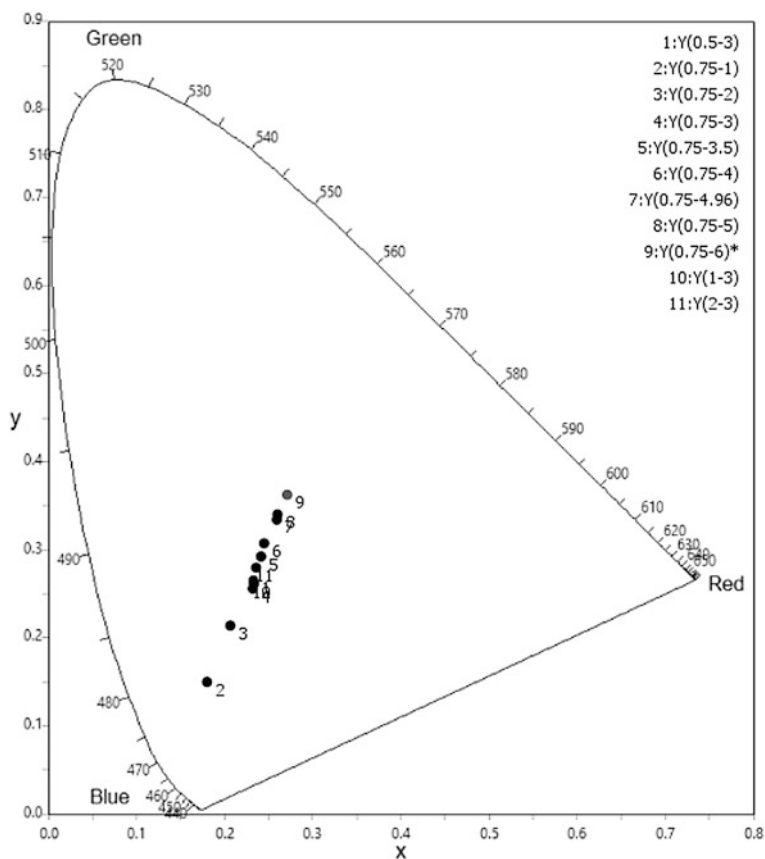


**Fig. 6** Chromaticity coordinates of  $Y_2SiO_5$  doped, on CIE 1931 chromaticity diagram

Figure 5 shows the emission spectra of the  $Y_2SiO_5:Ce,Tb$  doped as presented by the platform. The  $x, y$  color chromaticity coordinates of the  $Y_2SiO_5:Ce,Tb$  doped Yttrium Silicate have been determined and presented in Table 1 along with the  $x, y$  color chromaticity coordinates of the reported  $Y_2SiO_5$  doped systems. Figure 6 presents the location of the chromaticity coordinates of  $Y_2SiO_5$  doped on CIE 1931 chromaticity diagram. It is observed that, the chromaticity coordinates seem to have almost linear behavior.

The final analysis step allowed in the proposed platform gives the user some molar percentages as suggested for future experiments. First, Algorithm 1 is used to perform a linear regression over the input data, with molar concentrations and Euclidean distance as system variables. After that, Algorithm 2 allows to find some molar concentrations that minimize the cost function. This procedure needs to select the new concentrations without actually performing the experiments to calculate the chromaticity coordinates for each new combination. A function based on market costs was proposed as optimization criterion, the cerium concentration was multiplied by a weight of 0.14, while the terbium one by 0.86. Figure 7 shows the platform interface with the results for input data over  $Y_2SiO_5$  doped with cerium and terbium, while Table 3 shows the molar percentages proposed by the platform.

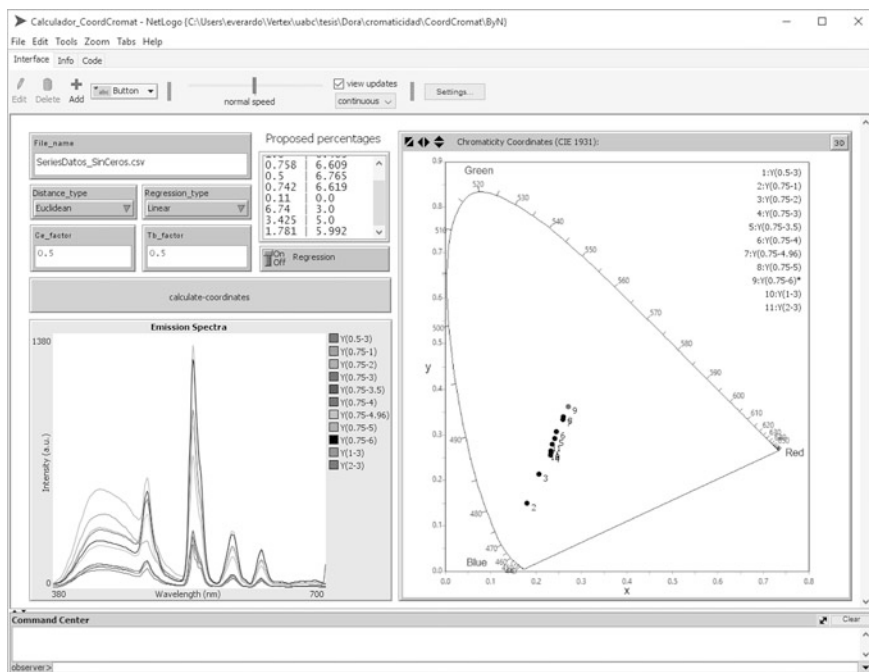


Fig. 7 NetLogo based platform interface

**Table 3** Molar percentages proposed by the platform

Cerium	Terbium
1.0	6.463
0.758	6.609
0.5	6.765
0.742	6.619
6.74	3.0
3.425	5.0
2.596	5.5

## 5 Conclusions

The simultaneous emission of cerium and terbium in the yttrium silicate, which produce white light, approaches the D65 light.

A model prediction molar percentage of rare earth cerium and terbium in the yttrium silicate was created for greater approximation to the D65 white light and decrease the number of experiments in the laboratory.

The graphical interface in NetLogo, which helps to display the emission spectra and chromaticity, coordinates of the experimental data jointly it, was developed.

The tool produces a list of molar concentrations of rare earth that binds the set of experiments performed in the laboratory.

**Acknowledgments** The authors are grateful to G.A. Hirata for their invaluable support, and to E. Aparicio and F. Ruiz for technical assistance.

## References

- Ballato J, Lewis JS III, Holloway P (1999) Display applications of rare-earth-doped materials. *MRS Bull.* doi:[10.1557/S0883769400053070](https://doi.org/10.1557/S0883769400053070)
- Gonzalez-Ortega JA, Tejeda EM, Perea N, Hirata GA, Bosze EJ, McKittrick J (2005) White light emission from rare earth activated yttrium silicate nanocrystalline powders and thin film. *J Opt Mater* 27:1221–1227
- Mingming X, Yunbei MA, Xixian L, Yao F, Tao J, Hong W, Xiaolong D (2014) Design and achieving of multicolor upconversion emission based on rare-earth doped tellurite. *J Rare Earths* 32:394–398
- Gouveia-Neto AS, Rios NPSM, Bueno LA (2012) Spectroscopic study and white-light simulation using praseodymium-doped fluorogermanate glass as single phosphor for white LEDs. *J Opt Mater* 35:126–129
- Shin SH, Jeon DY, Suh KS (2001) Emission band shift of the cathode luminescence of  $Y_2SiO_5$ :Ce phosphor affected by its activator concentration. *Jpn J Appl Phys* 1 40:4715–4719
- Choi YY, Sohn K, Park HD, Choi SY (2001) Luminescence and decay behaviors of Tb-doped yttrium silicate. *J Mater Res* 16:881–889
- Bosze EJ, Carver J, Singson S, McKittrick J, Hirata GA (2007) Long-ultraviolet-excited white-light emission in rare-earth-activated yttrium-oxyorthosilicate. *J Amer Cer Soc.* doi:[10.1111/j.1551-2916.2007.01809.x](https://doi.org/10.1111/j.1551-2916.2007.01809.x)

8. Ghosh P, Kar A, Patra A (2010) Energy transfer study between  $Ce^{3+}$  and  $Tb^{3+}$  ions in doped and core-shell sodium yttrium fluoride nanocrystals. *J Nanoscale* 2:1196–1202
9. Kar A, Patra A (2012) Impacts of core-shell structures on properties of lanthanide-based nanocrystals: crystal phase, lattice strain, downconversion, upconversion and energy transfer. *J Nanoscale* 4:3608–3619
10. García R, Hirata GA, McKittrick J (2001) New combustion synthesis technique for the production of  $(In_xGa_{1-x})_2O_3$  powders: hydrazine/metal nitrate method. *J Mater Res* 16:1059–1065
11. Hirata GA, Perea N, Tejada M, Gonzalez-Ortega JA, McKittrick J (2005) Luminescence study in Eu-doped aluminum oxide phosphors. *J Opt Mater* 27:1311–1315
12. Cervantes-Vásquez D, Contreras OE, Hirata GA (2013) Quantum efficiency of silica-coated rare-earth doped yttrium silicate. *J Lumin* 143:226–232
13. Lawson CL, Hanson RJ (1974) Solving least squares problems. Prentice-Hall, Englewood Cliffs
14. NIST/SEMATECH e-Handbook of Statistical Methods. <http://www.itl.nist.gov/div898/handbook/>. Accessed 01 July 2015
15. Burden RL, Faires JD (1985) Numerical analysis. Thomson, USA
16. Gomes J, Serra OA (2008) Cerium-based phosphors: blue luminescent properties for applications in optical displays. *J Mater Sci* 43:546–550
17. Maia AS, Stefani R, Kodaira CA, Felinto MCFC, Teotonio EES, Brito HF (2008) Luminescent nanoparticles of  $MgAl_2O_4:Eu, Dy$  prepared by citrate sol-gel method. *J Opt Mat* 31:440–444
18. Saha S, Chowdhury P, Patra A (2005) Luminescence of  $Ce^{3+}$  in  $Y_2SiO_5$  nanocrystals: role of crystal structure and crystal size. *J Phys Chem B* 109:2699–2702
19. Ghosh P, Sadhu S, Patra A (2006) Preparation and photoluminescence properties of  $Y_2SiO_5:Eu^{3+}$  nanocrystals. *J Phys Chem Chem Phys* 8:3242–3248

# Extended Characterization of the Hardening and Failure Behavior of Advanced High Strength Steels at Dynamic Compression Load

Markus Grillenberger and Martin Schagerl

**Abstract** Increasing requirements on energy efficiency and saving of resources, e.g. in the automotive industry, require the application of concepts of lightweight design. These concepts are based on design optimizations and the usage of high performance materials e.g. high stress steels. Caused by design optimizations, the stress level of materials, in particular at crash conditions, is increasing to nonlinear plastic ranges. To use the entire potential of high performance materials the knowledge about the behavior of these materials, especially in the nonlinear plastic range at crash conditions, is absolutely necessary. However, in order to lift the entire load potential of high stress steels, the latest material models are necessary. Therefore, the identification of specific material parameters e.g. strain rate sensitivity at compression load, is indispensable. This leads to the development of a test rig to extract even those needed specific material parameters. After defining boundary conditions for the test specimen geometry a general concept study took place to identify an optimized test rig concept. Next to the geometrical boundary conditions of the test specimen also the conditions for the test procedure itself have been defined. One main weakness of usual compression tests at high strain rate levels is the impact on the specimen surface (usually caused by falling weights) as it may cause deviations in the test results due to surface hardening. Furthermore, the idea to keep the plastic strain rate constant in the plastic strain range has to be implemented. These main tasks have been solved by developing a hydro mechanic cam shaft test rig with a special developed cam geometry. It allows compression of the specimen at different continuously variable strain rate levels without impact on the specimen at compression initiation and constant strain rate at every chosen strain rate level in the plastic range of the material. After manufacturing and assembling the test rig, a compression test was performed and compared to an existing material model of the tested material with good concordance. These results

---

M. Grillenberger (✉) · M. Schagerl  
Department of Constructional Lightweight Design,  
Johannes Kepler University Linz, Linz, Austria  
e-mail: markus.grillenberger@jku.at

M. Schagerl  
e-mail: martin.schagerl@jku.at



showed that this concept of the hydro mechanical cam shaft test rig is a relatively simple possibility to get information on material behavior at different strain rates and high deformation.

**Keywords** Material characterization • Compression test • Strain rate investigation • Advanced material testing

## 1 Introduction

### 1.1 Introduction

Simulation is one of the most important engineering tools. To get authoritative simulation results, knowledge of material behavior in the form of material models is required. An increasing number of these material models, operating with different parameters, make the enhancements on material testing in order to provide material parameters e.g. strain rate dependent flow curve, strain rate sensitivity and furthermore, necessary. Several test methods are available for the characterization of steel materials in terms of extracting material parameters. Every test method is afflicted with different advantages and disadvantages in terms of complexity and grade of extractable information. This article is dealing with a high dynamic compression test in order to get material information on strain rate dependent flow behavior and kinematic hardening effects of advanced high stress steels. For this a mechanical cam shaft test rig has been developed providing a defined dynamic load.

### 1.2 Formulation of the Problem

As mentioned in the introduction, simulation models need to be defined by material parameters. Most of common used material parameters were extracted out of tests at quasi statically conditions e.g. at the normalized tension test or a quasi-statically compression test (DIN 50106:1978-12). These tests are providing material data without information on material behavior at dynamic load conditions. The implementation of strain rate depended material behaviour is especially of interest for crash simulation. Therefore the focus lies at strain rates between 70 and 200 s<sup>-1</sup> where a Euro NCAP Front-Offset crash of a steel chassis with the target of room-, weight- and cost efficient transformation of kinetic energy into plastic work of the material is defined [1, p. 181]. To get material information at this strain rate level on one hand hydraulic testing machines (strain rate level <100 s<sup>-1</sup>) and on the other hand fall-weight test rigs (strain rate level >120 s<sup>-1</sup>) are common in use. Both testing concepts are coupled with similar problems. In general a very important issue in dynamic material testing is the need to provide measurement results at

constant strain rates. The fact that an increasing strain rate is shortening the testing time leads to the problem of the maximum controllable acceleration of hydro mechanical testing machines. Also the fall weight test rig has to deal with the restriction of non-constant strain rates during the test [1, p. 181]. Another problem, especially of fall weight test rigs is an occurring impact at the start of compression which may cause cold work hardening effects. Also, servo hydraulic testing machines have to deal with this problem usually when the strain rate is exceeding  $10 \text{ s}^{-1}$  because at this level a piston fore shot is necessary in order to reach the required piston velocity for the desired strain rate. After this, the development of a mechanical CAM test rig providing constant strain rate in the area of  $0.033\text{--}250 \text{ s}^{-1}$  without impact at begin of compression and constant logarithmic strain rate in the yield area of the tested material will be described.

### ***1.3 State of the Art—Cam Driven Compression Test Rigs***

Beside the mentioned servo hydraulic testing machines and fall-weight test rig concepts, the attempt of developing test rigs using a CAM shaft drive was done. According to the literature the first prototype of a CAM shaft drive test rig with the target of providing a constant strain rate was developed and published 1974 [2]. Based on a fly wheel driven CAM shaft (were the fly wheel will be powered up and is delivering the sufficient energy for deforming the specimen) a CAM geometry was designed in order to provide a constant strain rate. The disadvantage of this concept was that the cam shaft geometry was designed without consideration on the kinematic relationships of a CAM shaft drive which causes deviation in the resulting strain rate. Furthermore an impact at the beginning of the compression on the specimen is occurring (no smooth acceleration)

## **2 Test Rig Development**

### ***2.1 Requirement-Made Assumptions***

At the very beginning of the concept study for a high dynamic compression test rig, following assumptions have been made and requirements were defined.

- Range of performable strain rate:  $0.033\text{--}250 \text{ s}^{-1}$
- Achievement of the required strain rate before yielding of material
- Constant strain rate at yield strain area
- No impact at beginning of compression (smooth acceleration)
- Initial height of specimen: 1.4 mm

The range of the performable strain rate has been defined according to the deformation speed at crash conditions [3]. In order to reach the target according to the maximum strain rate of  $250 \text{ s}^{-1}$  using the velocity of a power unit (hydraulic cylinder) which is powering the test rig, the maximum height of the specimen was defined with 1.4 mm.

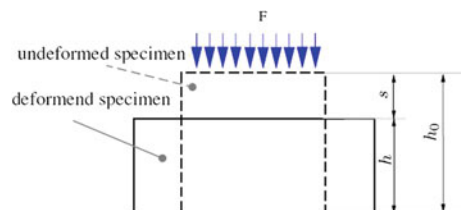
## 2.2 Main Concept

As already mentioned in Sect. 1, existing test devices like ram test rigs or hydraulic compression test rigs don't provide the material data of the defined requirements. Also existing CAM shaft test rigs will not deliver material behaviour at constant strain rates over the complete test duration without an impact at the beginning of deformation of the specimen. This leads to the need of developing a new mechanical CAM shaft test rig. The rig concept is based on a CAM shaft drive with a variable CAM geometry under consideration of the kinematic relationships of a CAM shaft drive. The CAM shaft is rolling against a pivot pin, connected to a stamp. According to the lobe and the set rotation speed the stamp is leaded against the specimen with a defined velocity profile, providing constant strain rate at every desired strain rate level. The advantages of this concept are, that on one hand the CAM geometry is designed in a way to provide constant strain rate without impact at the beginning of compression start, and on the other hand, every common power unit providing a constant velocity or rotations speed (hydraulic cylinder, servo electric motors) can be used for powering the test rig.

## 2.3 Displacement Function

Since the true strain rate has to be constant for a constant CAM rotation speed the displacement function must obey relations according to (1)–(5) where  $h_0$  is the initial specimen height,  $s$  the displacement function and  $\omega$  the rotation speed of the CAM shaft. Figure 1 shows the described parameters.

**Fig. 1** Specimen dimensions for displacement function



The definition of the logarithmic strain

$$\varepsilon(s) = \ln\left(\frac{h_0}{h_0 - s}\right) \tag{1}$$

and the derivative

$$\dot{\varepsilon} = \frac{d\varepsilon}{dt} = \frac{d\varepsilon ds}{ds dt} \rightarrow \dot{\varepsilon}(s) = v(s) \frac{1}{h_0 - s} \tag{2}$$

leads to the general mathematical description of the displacement for the constant strain rate.

$$s(t) = h_0 - e^{-\dot{\varepsilon}t - C} \tag{3}$$

According to the initial conditions  $s(t = 0) = 0$  the constant C is defined as  $C = -\ln(h_0)$ . The complete mathematical description of the displacement profile for constant strain rate is given by

$$s(t) = h_0 - e^{-\dot{\varepsilon}t} \tag{4}$$

Respectively with  $t = \frac{\phi}{\omega}$  depending on the CAM angle  $\phi$

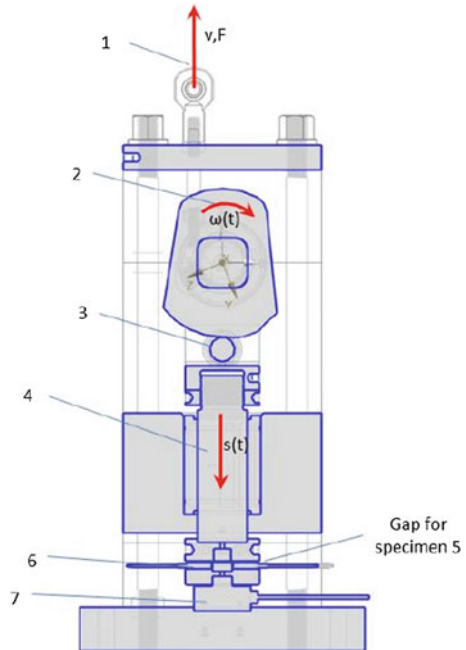
$$s(t) = h_0 - e^{-\dot{\varepsilon}\frac{\phi}{\omega}} \tag{5}$$

To avoid an impact at the beginning of the deformation the displacement function out of (5) has been adjusted by fitting in an additional function in the area of  $s(\phi) = 0$  to  $s(\phi)$  were the desired strain rate is archived. Out of this developed displacement function  $s(\phi)$ , and based on the kinematic relationships of a general CAM shaft drive a variable CAM geometry was derived fulfilling the mentioned requirements from Sect. 2.1.

### 2.4 Design and Functional Principle

The functional principle in general is explained according to Fig. 2. A tension device is connected to a hydraulic cylinder providing constant speed **1**. The connected hydraulic cylinder is pulling the tension device with constant speed which causes rotation with nearly constant angle velocity of the cam shaft **2** (definition of piston speed according required strain rate e.g. a piston speed of  $0.5 \text{ m s}^{-1}$  leads to a strain rate of  $250 \text{ s}^{-1}$ ). The developed geometry of the cam is rolling on a pivoted pin **3**, connected with a stamp **4** this stamp is leaded against a test specimen **5** driven by the CAM shaft, were the CAM geometry is defining the constant strain rate level. As mentioned, the strain rate level is defined by the set piston speed and

**Fig. 2** Compression test rig  
—functional principle



therefore completely adjustable variable. The specimen is also compressed without impact at the beginning of the test or rather at contact between stamp and specimen. To avoid deviations on constant strain rate value and impact at compression begin the length of the stamp is slightly adjustable to avoid gaps and clearances between CAM and pivot pin and further specimen and stamp. To make sure that the required piston speed is archived at compression begin there is an acceleration area set at the lobe before compression starts. The measurement of the force **6** and displacement **7** values is done very close to the specimen to avoid deviations in measurement results caused by stamp acceleration or vibrations.

## 2.5 Measurement Equipment

For recordings of the measured values the measurement equipment is placed close to the specimen to avoid influence of impact or vibrations on the measurement signals. For displacement measurements, two capacitive sensors are applied next to the specimen. The force will be measured by using a load cell connected with the specimen. In Fig. 3 the setting and positioning of the measurement equipment is shown.

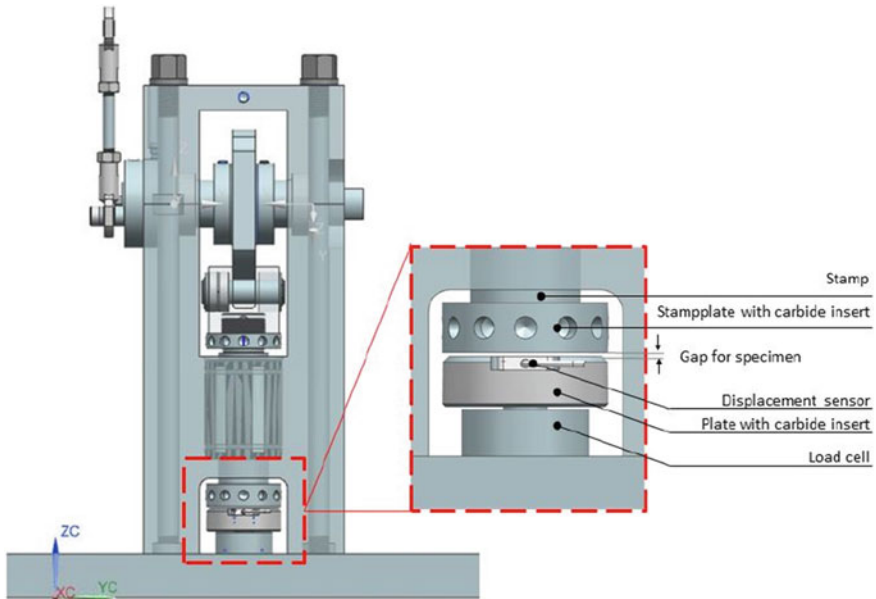


**Fig. 3** Measurement device

**Table 1** Performance data

Specimen height	max. 1.4 mm
Performable strain rate	0.033–250 s <sup>-1</sup>
Applicable compression load	max. 30 kN @ max. sampling rate of 4096 Hz
Resolution of displacement measurement device	0.002 mm @ max. sampling rate of 4096 Hz

### 2.6 Performance Data

See Table 1.

## 3 First Test Result

After manufacturing the test rig, the first tests took place. The hydro mechanical test rig was operated by a hydraulic cylinder with a max. load of 25 kN. Specimen, provided from the company Voestalpine in Linz, with measurements of 1.4 × 1.4 × 1.4 mm and manufactured by erosion from a 1.4 mm thick metal

sheet of defined strength, were tested. For the first test a slow speed ramp was chosen. The resulting strain rate was  $\dot{\varepsilon} = 2 \text{ s}^{-1}$ . The specimen was compressed to a final height of 0.6 mm means a logarithmic strain of 0.8. Figures 4 and 5 are showing the yield curve compared to the provided material model from the company Voestalpine. The comparison of the measurement results to the FEM model data in general showed good correlations. Deviations in the elastic area are visible. This deviation was caused by a slight clamping between force transducer and specimen plate due to eccentric positioning of the specimen. Considerations of the yield area of the tested material showed good accordance between measured result and the yield curve based on the material data up to a logarithmic strain of  $\varepsilon = 0.2$ . A strong deviation is visible at a strain level of 0.25 up to 0.8, caused by increasing of multiaxial stress ratio and increasing friction between the specimen and compression stamp. This friction causes an increase of force that cannot be clearly dedicated to the load necessary for compression only. A further challenge in extracting yield curves out of measurement data is the occurring specimen surface during deformation caused by friction. This analysis is a topic of further investigation. In a first step based on constant volume of the specimen, the surface was calculated depending on the grade of deformation and adapted by using an approximation factor created out of the measured surface at the end of compression.

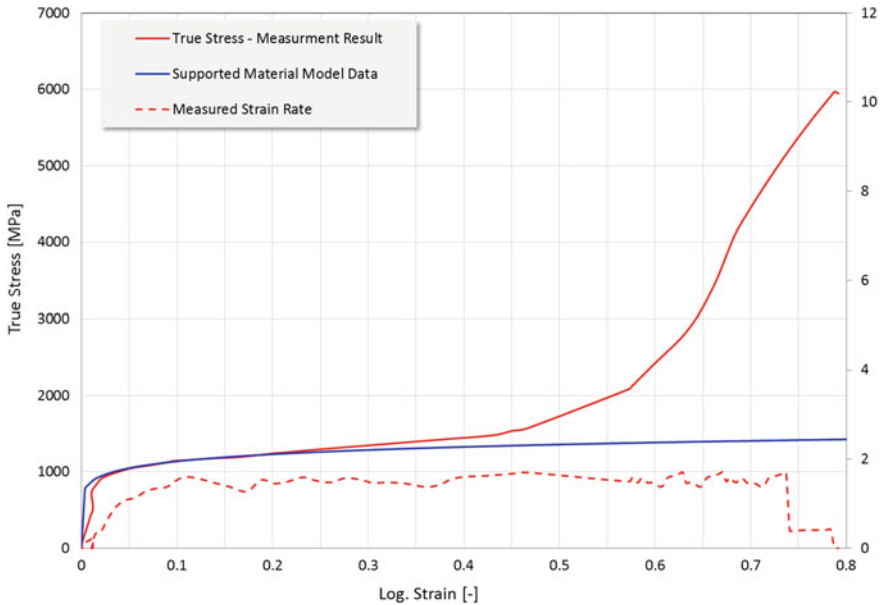


**Fig. 4** Complete yield curve

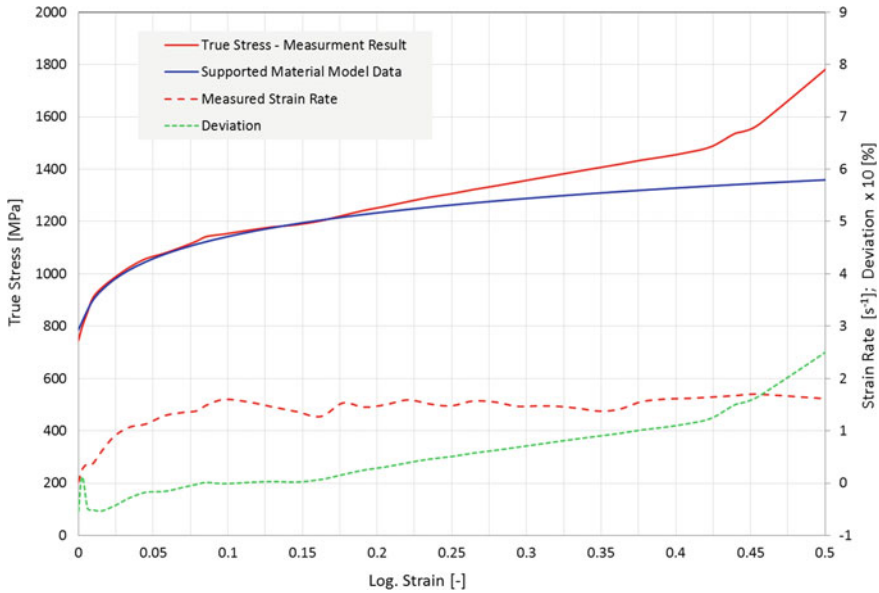


Fig. 5 Yield curve in area of plasticity

## 4 Conclusion

### 4.1 Hydro Mechanical Cam Shaft Test Rig

The developed hydro mechanical CAM shaft test rig for compression testing on metal materials presents a relatively simple possibility to get information on the material behaviour in the field of extended material characterization. The test rig is providing material data at dynamic compression loads at constant strain rate without impact at different strain rate levels up to  $\dot{\epsilon} = 250 \text{ s}^{-1}$ . The rig is equipped with very sensitive measurement equipment. The design keeps the measurement error as minimal as possible to support investigations on yield behavior and hardening effects of metallic materials with focus on the definition of additional parameters (strain rate sensitivity, hardening parameters) for FEM simulation models.

### 4.2 Test Result

First test results were performed at low strain rate level ( $\dot{\epsilon} = 2 \text{ s}^{-1}$ ). The test showed that the required target of achieving a constant strain rate level was met. The required strain rate was achieved shortly before yielding of the material started and also was nearly constant at the yield area of the tested material. Furthermore,



the results showed good correlation to the provided material data at the yield area up to a strain level of  $\varepsilon = 0.25$ , at a higher strain level strong deviation compared to the material model can be noticed. This deviation is cause for further investigation with the object on analysis on strain rate depended hardening effects and failure behaviour of AHSS steels at dynamic compression load

**Acknowledgments** The authors gratefully appreciate the technical support from our project partners Edwin Till and Christian Walch from the company Voestalpine, steel division in Linz. The technical support by Peter Mayrl is gratefully acknowledged. Particular thanks are due to Erich Humer for his support in design and testing the developed devices. This work has been supported by the Austrian COMET-K2 programme of the Linz Center of Mechatronics (LCM), and was funded by the Austrian federal government and the federal state of Upper Austria.

## References

1. Biermann H, Krüger L (2015) *Moderne Methoden der Werkstoffprüfung*. Wiley-VCH, Freiberg
2. Steward M (1974) Constant true strain rate compression: the cam plastometer. *Can Metall Q* 13 (3):503–509
3. Merklein M (2006) *Charakterisierung von Blechwerkstoffen für den Leichtbau*. Meisenbach, Bamberg

# High Temperature Mechanical Behavior of Plasma-Nitrided Inconel 625 Superalloy

M.M. Oliveira, A.A. Couto, R. Baldan, D.A.P. Reis,  
J. Vatavuk, J.C. Vendramim, N.B. Lima and A.G. Reis

**Abstract** INCONEL 625 nickel-based superalloys present limitations for use at temperatures above 600 °C. For this reason, protective coatings can be used as barriers to avoid both nucleation and crack propagation. The aim of this work is to evaluate the mechanical properties at high temperatures of non-nitrided and plasma-nitrided samples of the INCONEL 625 superalloy. The microstructural characterization of the nitrided layer was performed with the aid of optical

---

M.M. Oliveira (✉) · A.A. Couto · N.B. Lima · A.G. Reis  
Nuclear and Energy Research Institute, IPEN–CNEN/SP, São Paulo, SP, Brazil  
e-mail: mauromach@gmail.com

A.A. Couto  
e-mail: acouto@ipen.br

N.B. Lima  
e-mail: nblima@ipen.br

A.G. Reis  
e-mail: adriano.g.reis@hotmail.com

M.M. Oliveira  
Federal Institute of Education Science and Technology of São Paulo,  
São Paulo, SP, Brazil

R. Baldan  
Campus Experimental Itapeva, São Paulo State University—UNESP,  
São Paulo, SP, Brazil  
e-mail: renato@itapeva.unesp.br

D.A.P. Reis  
Federal University of São Paulo—UNIFESP, São José Dos Campos, SP, Brazil  
e-mail: danielireis@gmail.com

J. Vatavuk  
Mackenzie Presbyterian University, São Paulo, SP, Brazil  
e-mail: janvatavuk@uol.com.br

J.C. Vendramim  
Isoflama Heat Treatment, Indaiatuba, SP, Brazil  
e-mail: vendramim@isoflama.com.br

microscopy (OM) and X-ray diffraction (XRD). Tensile tests were performed between 600 and 1000 °C and deformation rates between 0.0002 and 0.002 s<sup>-1</sup>. The results have shown that nitrated sample present expanded fcc phase and chromium nitride (CrN) phases. Tensile tests showed that there was no significant difference in the yield strength and elongation between non-nitrated and plasma-nitrated samples at the same temperatures. Serrated stress-strain behavior was observed in the curves obtained at 600 and 700 °C, which was associated with the dynamic strain aging effect. At 600 °C, the increase in strain rate promoted an increase of the amplitude and oscillation frequency of the stress.

**Keywords** Inconel 625 · Plasma-nitriding · Superalloys · Mechanical properties

## 1 Introduction

Nickel-based superalloys generally present high mechanical properties, good creep, fatigue and corrosion resistance and are able to work at high temperatures. These properties are reached by the combination of a solid solution austenitic matrix ( $\gamma$  phase) with high volumetric fraction of coherent precipitates such as Ni(Ti, Nb, Ta)<sub>3</sub>Al, which is commonly known by gamma-prime phase. These materials are also present at up to 75 wt% of Ni and up to 30 wt% of Cr [1].

Inconel 625 is a nickel-chromium-molybdenum alloy with excellent oxidation resistance, outstanding strength and toughness from cryogenic to high temperatures. Alloy 625 also has exceptional fatigue resistance. The high amount of Cr (21 wt%), Mo (9 wt%) and Nb (4 wt%) increases the resistance of  $\gamma$  phase without the necessity of solution and aging heat-treatments [2]. It also promotes an increasing of up to 40 % for both yield and ultimate tensile strength at room temperature when compared with the 600 alloy, for the same elongation. At high temperatures (870 °C for example), the increasing of the mechanical properties of the alloy 625 is between 50 and 120 % higher than the alloy 600 [2, 3]. However, the  $\gamma$  phase presents MC and M<sub>6</sub>C carbides with high amounts of niobium and molybdenum.

This alloy also resists a wide range of severely corrosive environments and is especially resistant to pitting and crevice corrosion. Due to the outstanding corrosion resistance, this precipitation hardenable alloy is commonly used in chemical processing, aerospace and marine engineering, pollution-control equipments, and nuclear reactor applications.

Despite the notable progress in the development of the mechanical resistance at high temperatures of the Inconel alloys, limitations can occur when these alloys are used in temperatures higher than 600 °C. The Inconel 625 superalloy presents better weldability than many others nickel-base alloys. In spite of their otherwise excellent properties, Inconel 625 has poor wear characteristics. Thus, surface treatments can be used in order to improve the tribological behavior without affecting corrosion resistance [4].

Plasma nitriding has been traditionally used as a surface treatment for several nickel-based alloys to create protective coatings that can be used as barriers for both nucleation and crack propagation when these materials are applied for long time at high temperatures. However, this process is normally conducted at relatively high temperatures resulting in tempering, affecting temperature-sensitive microstructures and/or producing non-desirable equilibrium phases [4].

For example, these nitriding treatments of the Cr-containing alloy, such as the Inconel 625 which above 500 °C modifies the surface by the formation of chromium nitrides (CrN) and expanded austenitic phase, which degrades the corrosion resistance. Additionally, the main difficulty is the adherence problem that can occur due to the diffusion of the elements that form the coating during the thermal cycles. Based on this, the aim of this work is to study the mechanical properties (through tensile tests between 600 and 1000 °C) of plasma-nitrided Inconel 625 superalloy.

## 2 Experimental Procedure

Bars of the Inconel 625 superalloy (12 mm diameter) were rolled at high-temperatures at the Multialloy Company (São Paulo, Brazil). The nitriding process was performed at 520 °C for 12 h. The material was prepared following conventional metallographic techniques (mounting at 21 MPa and 150 °C, grinding with SiC sand paper, polishing with diamond paste and finally etching with 100 ml HCl + 3 ml HNO<sub>3</sub> + 100 ml ethylic alcohol for 5 min). The microstructure and depth of the samples was analysed with the aid of an optical microscopy Olympus BX51 M with Olympus UC30 camera.

Tensile tests were performed in a universal machine (Instron 4400) at temperatures between 600 and 1000 °C and deformation rate between 0.0002 and 0.002 s<sup>-1</sup>. The length and diameter of the specimen were 50 and 5 mm, respectively. X-ray diffraction (XRD) experiments were performed using a Rigaku Multiflex diffractometer with Cu-K $\alpha$  radiation, over the 2 $\theta$  range 20° to 90° at a scanning rate of 1° per minute. Thermodynamic simulations of the phases at each temperature of the mechanical tests were performed with the aid of the JMatPro software (Ni database).

## 3 Results and Discussion

The result of the chemical analysis of the main elements is as follows: (wt%): 21.5 Cr; 9 Mo; 3.6 Nb; 2.5 Fe; 0.25 Mn; 0.2 Ti; 0.2 Al; 0.05 C; Ni balance. This result is in agreement with ASTM B443-00(2009) [5, 6].

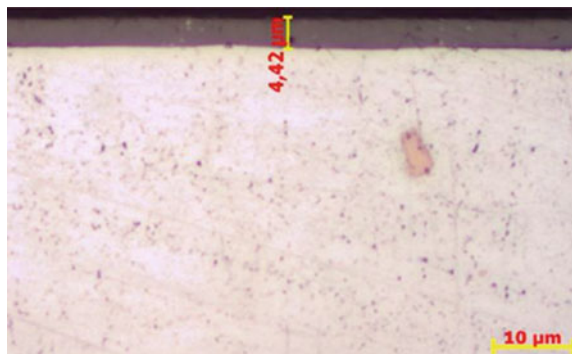
**Table 1** Phase fraction (wt %) as function of temperature of the tensile test for the Inconel 625 superalloy

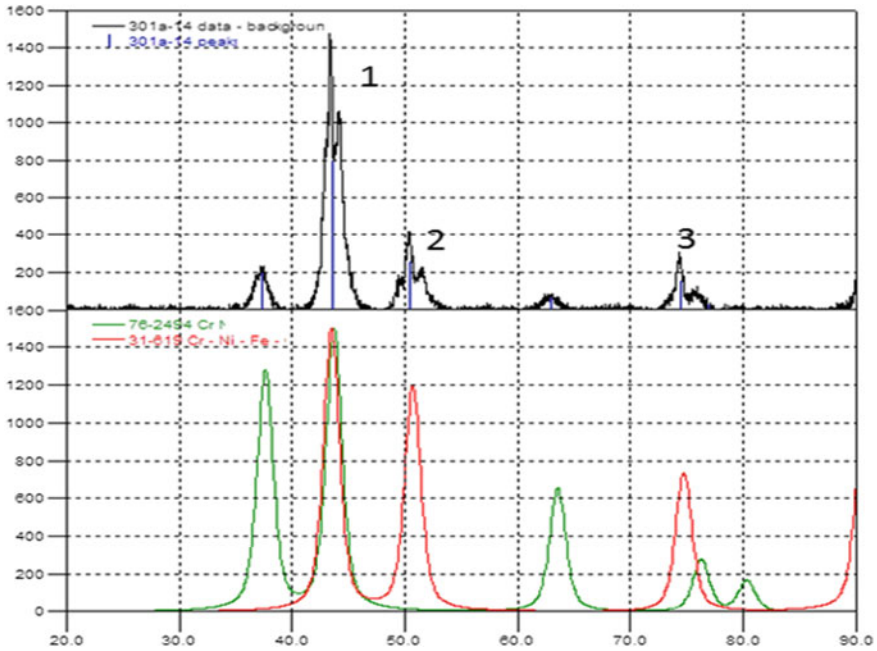
T (°C)	Phase fraction (wt%)						
	$\gamma$	$\mu$	$\delta$	$\gamma'$	$M_{23}C_6$	$M_6C$	MC
600	77.11	11.18	9.32	1.41	0.97		
700	83.78	6.99	8.25		0.97		
800	92.22	0.91	5.51		0.52	0.85	
900	97.70		0.52			1.78	
1000	99.10					0.64	0.26

Table 1 shows the percentage of the phases obtained by thermodynamic simulations with the JMatPro software. It can be seen that there is a high amount of  $\gamma$  phase at high temperatures and also the presence of 3 types of carbides: MC,  $M_6C$  and  $M_{23}C_6$ . The MC carbides are stable at high temperatures. During aging heat-treatments or service conditions, these particles can decompose slowly, generating carbon that can diffuse into the matrix and initiates important reactions such as  $MC + \gamma \rightarrow M_6C/M_{23}C_6 + \gamma'$  in order to form  $M_6C$  and  $M_{23}C_6$  carbides rich in Cr, Mo and W, which are stable at lower temperatures than MC carbides. The simulation also shows that  $M_6C$  carbides are stable at higher temperatures when compared with  $M_{23}C_6$  carbides.

Figure 1 shows the micrograph of the nitrided layer for the Inconel 625 superalloy. The depth of the layer is slightly above 4  $\mu\text{m}$ . Figure 2 shows the x-ray diffraction spectra of the nitride sample and the pattern for  $\gamma$  (red) and CrN (green) phases. Figure 3a–c show the zoom of positions 1, 2 and 3, respectively. It was noted that nitrided samples presented mainly two phases:  $\gamma$  fcc expanded phase (Fig. 3—region A) and chromium nitride CrN (Fig. 3—region B), which were evidenced by peaks at 37.5, 42.5, 63.3 and 76.2°. Additionally, the plasma nitriding of Inconel 625 shifts the (111) peak of the  $\gamma$  fcc phase from 43.6° to 43° and the

**Fig. 1** Micrograph of the nitrided layer for the Inconel 625 superalloy





**Fig. 2** X-ray diffraction spectra of the nitride sample and the pattern for  $\gamma$  (red) and CrN (green) phases

(200) peak from  $50.7^\circ$  to  $49.5^\circ$ . The different amount of shifting in peak position of (111) and (200) was attributed to the lower atomic density of the latter plane, resulting in larger lattice expansions. The expansion of the lattice in different crystallographic directions depends on the tension level and the elastic constant of the diffraction plane [4].

Figures 4 and 5 show the results of the tensile tests (deformation rate =  $0.0002 \text{ s}^{-1}$ ) between 600 and 1000 °C for non-nitrided and nitrided samples of the Inconel 625 superalloy, respectively. The values of yield strength, ultimate tensile strength and elongation are shown in Table 2. As expected, the yield and ultimate tensile strength decreases as the temperature of the test increases. On the contrary, the elongation increases with the increasing of the temperature. This behavior is similar for nitrided and non-nitrided alloys.

Figures 6, 7, 8, 9 and 10 show, in detail, the curves for non-nitrided and nitrided samples of the Inconel 625 superalloy at each temperature (600, 700, 800, 900 and 1000 °C). At 600 °C, it was not possible to verify significant differences between the curves of nitrided and non-nitrided samples. At 700 °C, the ultimate tensile

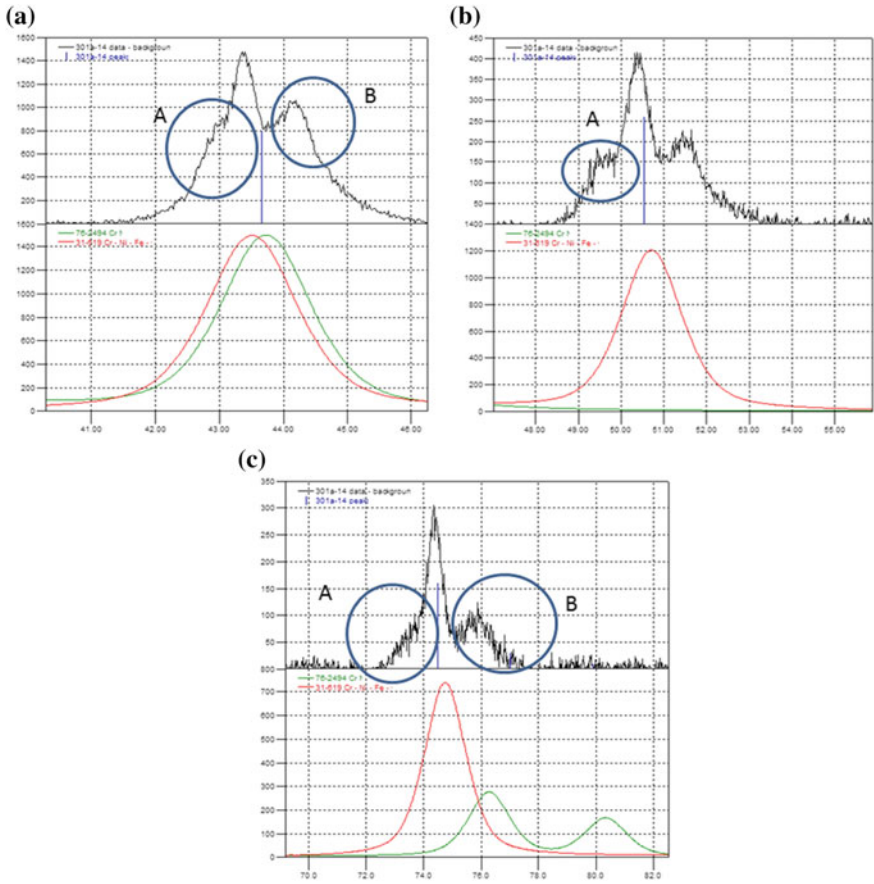
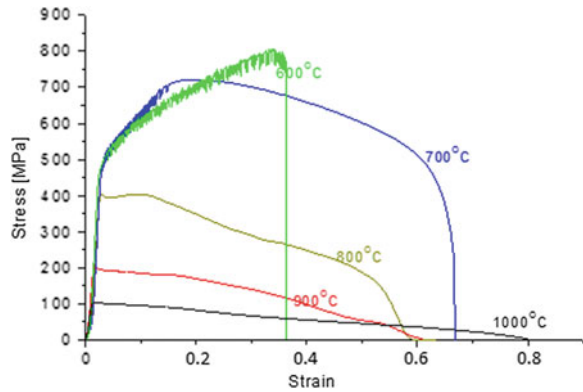
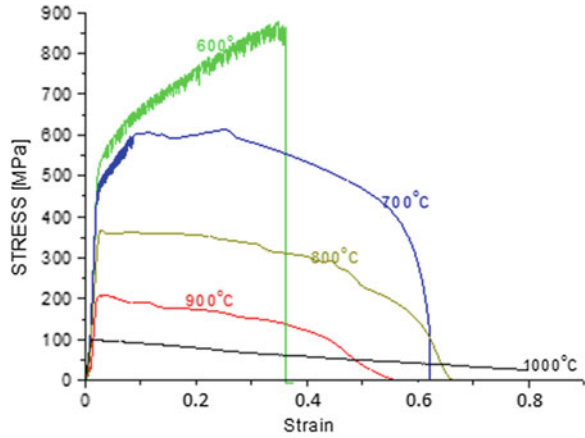


Fig. 3 Magnified picture of positions 1, 2 and 3 shown in Fig. 2

Fig. 4 Tensile curves (deformation rate =  $0.0002 \text{ s}^{-1}$ ) between 600 and 1000 °C for non-nitrided samples of the Inconel 625 superalloy



**Fig. 5** Tensile curves (deformation rate =  $0.0002 \text{ s}^{-1}$ ) between 600 and 1000 °C for nitrided samples of the Inconel 625 superalloy



**Table 2** Results of the tensile test (deformation rate =  $0.0002 \text{ s}^{-1}$ ) between 600 and 1000 °C for both non-nitrided and nitrided samples of the Inconel 625 superalloy

Tensile temperature test (°C)	Condition	Yield strength (MPa)	Ultimate tensile strength (MPa)	Elongation (%)
600	Non-nitrided	497	887	18
	Nitrided	495	879	19
700	Non-nitrided	512	722	33
	Nitrided	475	613	32
800	Non-nitrided	417	417	32
	Nitrided	357	357	34
900	Non-nitrided	199	199	30
	Nitrided	208	208	28
1000	Non-nitrided	103	103	40
	Nitrided	101	101	40

**Fig. 6** Tensile curves (deformation rate =  $0.0002 \text{ s}^{-1}$ ) at 600 °C for non-nitrided (black) and nitrided (green) samples of the Inconel 625 superalloy

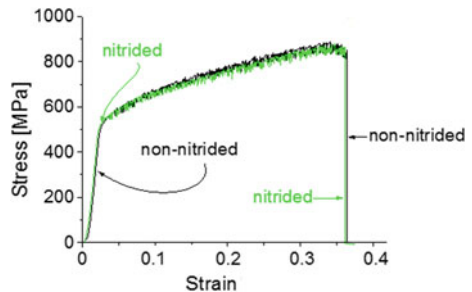




**Fig. 7** Tensile curves (deformation rate =  $0.0002 \text{ s}^{-1}$ ) at  $700 \text{ }^\circ\text{C}$  for non-nitrided (*black*) and nitrided (*blue*) samples of the Inconel 625 superalloy

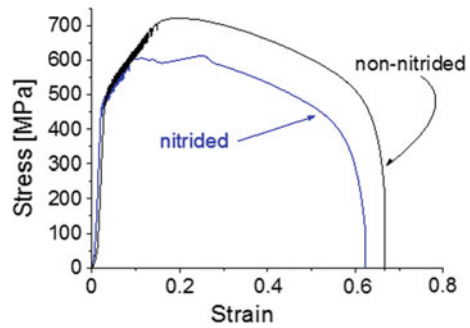


**Fig. 8** Tensile curves (deformation rate =  $0.0002 \text{ s}^{-1}$ ) at  $800 \text{ }^\circ\text{C}$  for non-nitrided (*black*) and nitrided (*brown*) samples of the Inconel 625 superalloy

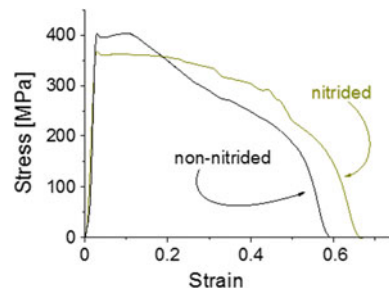
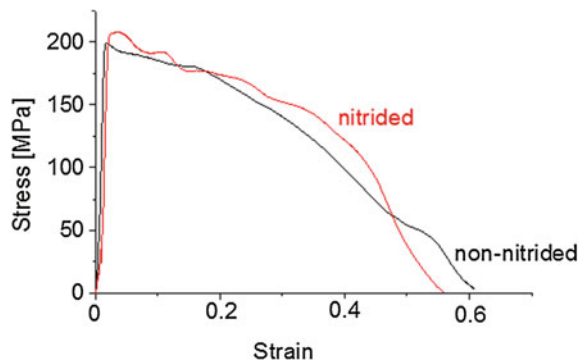


**Fig. 9** Tensile curves (deformation rate =  $0.0002 \text{ s}^{-1}$ ) at  $900 \text{ }^\circ\text{C}$  for non-nitrided (*black*) and nitrided (*red*) samples of the Inconel 625 superalloy



strength of non-nitrided samples was  $722 \text{ MPa}$  whilst for nitrided sample this value decreased to  $613 \text{ MPa}$ . The ultimate tensile strength values tend to be higher for the non-nitrided samples at temperatures higher than  $700 \text{ }^\circ\text{C}$ . However, the nitrided samples tend to keep high strength as the strain progress, as can be seen in Fig. 9 (at  $900 \text{ }^\circ\text{C}$ ). This tendency will be investigated in more detail with the creep tests in the future.

Figures 11, 12 and 13 show the results of the tensile tests for the non-nitrided Inconel 625 superalloy at  $600 \text{ }^\circ\text{C}$  and different deformation rates:  $0.0002 \text{ s}^{-1}$  (Fig. 11);  $0.001 \text{ s}^{-1}$  (Fig. 12);  $0.002 \text{ s}^{-1}$  (Fig. 13). The mechanical properties at

**Fig. 10** Tensile curves (deformation rate =  $0.0002\text{ s}^{-1}$ ) at  $1000\text{ }^{\circ}\text{C}$  for non-nitrided (*black*) and nitrided (*pink*) samples of the Inconel 625 superalloy

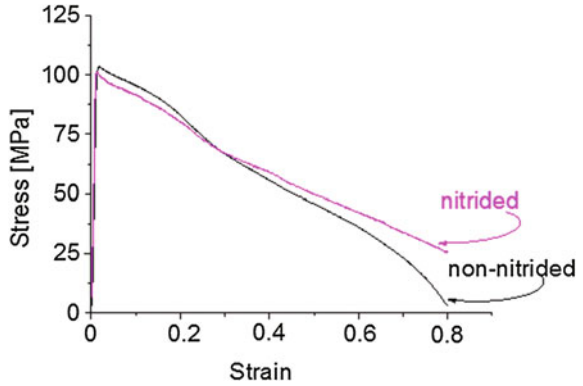


**Fig. 11** Tensile curves (deformation rate =  $0.0002\text{ s}^{-1}$ ) at  $600\text{ }^{\circ}\text{C}$  for non-nitrided sample of the Inconel 625 superalloy

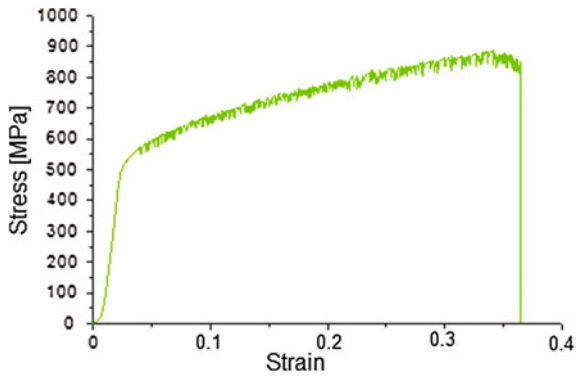
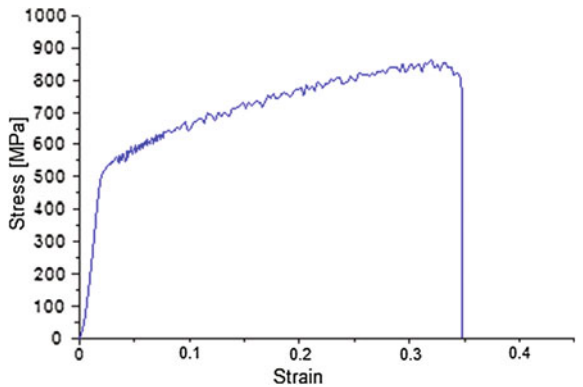
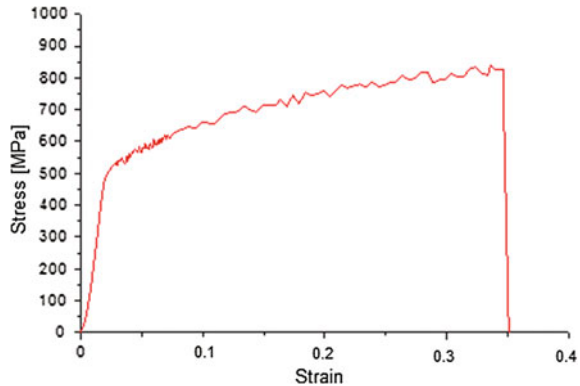


**Fig. 12** Tensile curves (deformation rate =  $0.001\text{ s}^{-1}$ ) at  $600\text{ }^{\circ}\text{C}$  for non-nitrided sample of the Inconel 625 superalloy



different deformation rates didn't present significant differences. It can also be seen as a serrated stress-strain behavior which was associated with a dynamic strain aging effect. The increasing in the strain rate promoted an increasing in the amplitude and oscillation frequency of the stress. Different mechanisms can

**Fig. 13** Tensile curves (deformation rate =  $0.002 \text{ s}^{-1}$ ) at  $600 \text{ }^\circ\text{C}$  for non-nitrided sample of the Inconel 625 superalloy



originate this oscillation process, such as dynamic aging and recrystallization, the last one more common at high temperatures [7, 8]. At low temperatures, such as  $600 \text{ }^\circ\text{C}$ , the main mechanism responsible for the oscillation frequency of the stress was attributed to the Portevin-Le Chatlierou effect [9]. However, it is difficult to determine the mechanisms responsible for this serrated behavior based only on the shape of the stress-strain curves.

## 4 Conclusions

The results have shown that the nitrided sample presented an expanded fcc and chromium nitride (CrN) phases. The presence of CrN was evident by the two peaks at  $37.5^\circ$  and  $42.5^\circ$ . It can be seen that plasma nitriding of Inconel 625 shifts the (111) peak from  $43.6^\circ$  to  $43^\circ$  and the (200) peak from  $50.7^\circ$  to  $49.5^\circ$ . The different amounts of shifting in peak position of (111) and (200) was attributed to the lower atomic density of the latter plane, resulting in larger lattice expansion. Tensile tests showed that there was no significant difference in the yield strength and elongation between non-nitrided and plasma-nitrided samples at the same temperature. Serrated stress–strain behavior was observed in the curves obtained at  $600$  and  $700 \text{ }^\circ\text{C}$ , which was associated with the dynamic strain aging effect. At  $600 \text{ }^\circ\text{C}$ , the increasing in the strain rate promoted an increase in the amplitude and oscillation frequency of the stress.

## References

1. Faria F, Hirschmann A, Moura Neto C, Reis D, Piorino Neto F (2009) Comportamento em Fluência a Temperatura de  $650 \text{ }^\circ\text{C}$  da Superliga Inconel 718. Anais XV ENCITA 2009, ITA, 19–22 Outubro 2009

2. Zavaglia C, Galdino A (2004) O Níquel e suas Ligas. EM833 - Seleção de Materiais. UNICAMP. Campinas, 2004. <ftp://ftp.fem.unicamp.br/pub/EM833/Parte%20II%201.3.b%20-%20Niquel%20e%20suas%20ligas.pdf>
3. ASM, American Society for Metals (1980) Metals handbook. Properties and selection tool materials and special purpose metals, vol 2
4. Singh V, Meletis E (2006) Synthesis, characterization and properties of intensified plasma-assisted nitrated superalloy Inconel 718. Surf Coat Technol 201:1093–1101
5. ASTM B443-00(2009) Standard Specification for nickel-chromium-molybdenum-columbium alloy (UNS N06625) and nickel-chromium-molybdenum-silicon alloy (UNS N06219) plate, sheet, and strip
6. American Society for Testing and Materials (2011) E8/E8M-11. Standard test method for tension testing of metallic materials. ASTM, Philadelphia, 28 p
7. Wang Y, Shao W, Zhen L, Yang C, Zhang X (2009) Tensile deformation behavior of superalloy 718 at elevated temperatures. J Alloy Compd 471:331–335
8. Wang Y, Shao W, Zhen L, Yang C, Zhang X (2008) Flow behavior and microstructures of superalloy 718 during high temperature deformation. Mater Sci Eng A 497:479–486
9. Rahman MS, Priyadarshan G, Raja K, Nesbitt C, Misra M (2009) Characterization of high temperature deformation behavior of Inconel 617. Mech Mater 41:261–270

# Thermal Properties of Sandwiches for Applications in Transportation

Pavel Košťal, Vladimír Rusnák, Svetozár Malinarič, Zora Jančíková,  
Jan Valíček and Marta Harničárová

**Abstract** Composite sandwich structures are often used in the transportation industry as floors, roofs or parts of internal or external skeletons of buses, trains or trams. Compared to a monolithic composite there are a number of advantages which are apparent. Especially the low weight, higher rigidity, faster installation, better thermal insulation and good acoustic properties make it such an advantageous material. It is especially lower weight higher rigidity, faster installation, better thermal insulation and good acoustic properties. The paper deals with the measurement of the specific heat capacity, diffusivity and thermal conductivity of sandwiches differing in “core” material and a lining “skin” materials. As a “core” material the PET foam Airex T90.100, honeycomb type CORMASTER and natural cork material under the trade name CORECORK NL10 was used. As a coating phenolic prepreg and a composite material based on polyester/glass was used. All sandwiches under investigation have very low thermal conductivity as well as diffusivity.

**Keywords** Sandwiches · Thermal properties · Mechanical properties

---

P. Košťal · V. Rusnák · Z. Jančíková (✉) · J. Valíček · M. Harničárová  
VŠB—TU Ostrava, 17. Listopadu 15, 708 33 Ostrava-Poruba, Czech Republic  
e-mail: zora.jancikova@vsb.cz

P. Košťal  
e-mail: pavel.kostial@vsb.cz

V. Rusnák  
e-mail: vladimir.rusnak@form-composite.sk

J. Valíček  
e-mail: jan.valicek@vsb.cz

M. Harničárová  
e-mail: marta.harnicarova@vsb.cz

S. Malinarič  
Constantine the Philosopher University, Trieda Andreja Hlinku 1,  
94974 Nitra, Slovak Republic  
e-mail: smalinaric@ukf.sk

## 1 Introduction

Low cost, high quality composites are currently being designed and implemented for primary and secondary load bearing structures such as foundations, deckhouses, hulls, propellers, and mast systems in surface ships and submarines all around the world. The use of composite materials aboard naval vessels is driven by the need to increase range, covertness, and stability while reducing weight, fuel consumption, and life-cycle costs.

Their particular disadvantage can be the difficult production, higher demands on space (the thickness is usually many times higher compared to monolithic), or a specific approach in the design of sandwich products.

Steel/polymer/steel sandwich materials with varying core thickness were produced using the roll bonding technology. At a constant skin thickness, the effect of the core thickness change on the mechanical properties, particularly their specific stiffness and strength, was investigated [1].

The work [2] deals with the problem of the optimum design of a sandwich panel. The design process is based on a general two-level optimisation strategy involving different scales: the meso-scale for both the unit cell of the core and the constitutive layer of the laminated skins and the macro-scale for the whole panel. Concerning the meso-scale of the honeycomb core, an appropriate model of the unit cell able to properly provide its effective elastic properties (to be used at the macro-scale) must be conceived. Numerical results show that shell-based models are no longer adapted to evaluate the core properties, mostly in the context of an optimisation procedure where the parameters of the unit cell can get values that go beyond the limits imposed by a 2D model.

The work [3] deals with the problem of the optimum design of a sandwich panel. The design strategy that we propose is a numerical optimisation procedure that does not make any simplifying assumptions to obtain a true global optimum configuration of the system. To face the design of the sandwich structure at both meso and macro scales, they use a two-level optimisation strategy: at the first level they determine the optimal geometry of the unit cell of the core together with the material and geometric parameters of the laminated skins, while at the second level determine the optimal skins lay-up giving the geometrical and material parameters issued from the first level.

The study [4] is focused on the fabrication and the evaluation of the acoustic properties of sandwich cover-ply-reinforced high-resilience thermal-bonding nonwoven hybrid composites. P-phenyleneterephthalamides and bicomponent high-resilience bonding polyester intra-ply hybrid nonwoven fabrics were compounded with glass plain fabric to produce the high strength sandwich structural cover ply by means of needle punching and thermal bonding to reinforce the whole composites and dissipate energy when being impacted. Acoustic absorption coefficients were promoted with increases in areal densities and the fibre blending ratio of 3D crimped hollow polyester, particularly at the low-mid frequency range. In

addition, needle punching depths and back air cavity thicknesses considerably affected the average absorption coefficients.

Effects of the stitching angle on the mechanical properties, thermal protection capabilities and induced thermal stress of the stitched sandwich laminate are numerically analysed by ABAQUS codes in [5].

A new analytical model has been proposed in the paper [6] for an accurate analysis of the through-the-thickness temperature variation in composites and sandwich laminates based on piecewise linear zig-zag thermal lamination theory. This theory assumes a piecewise linear through-the-thickness temperature distribution in terms of temperature at the reference plane and temperature slopes at the layer interfaces. The continuity of temperature at different layers is ensured by choosing a suitable temperature profile. For the purpose of identifying the acoustic characteristics of honeycomb sandwich panels, the finite element method, combined with the boundary element method, has been widely used in [7, 8]. In order to improve the acoustic performance of the honeycomb sandwich panel while satisfying weight and strength requirements, a new double core honeycomb sandwich panel is designed to have the same mass per unit area as the baseline single core panel but have a larger equivalent flexural stiffness than that of the baseline panel.

The flame behaviour of sandwiches was studied in [9]. Flame structure in wide-distribution ammonium-perchlorate (AP), hydroxyl-terminated-polybutadiene binder, aluminium (Al) composite propellants are studied using 2-D laminates with oxygenated binders was studied. Very fine AP (PAP) is used to produce a fuel-rich, matrix propellant with a FAP/binder ratio of 75/25. The flame structure is found to be similar to that previously described using UV and IR imaging for non-aluminized laminates with a split (diffusion) flame structure at high pressures (P) and low fuel thicknesses (L) and merged (partially premixed) flame structure for low P and L.

In this paper we deal with the study of thermal properties of sandwich constructions differing in “core” material and the lining “skin” materials to. As a “core” material PET foam Airex T90.100, honeycomb type CORMASTER and natural cork material under the trade name CORECORK NL10 was used.

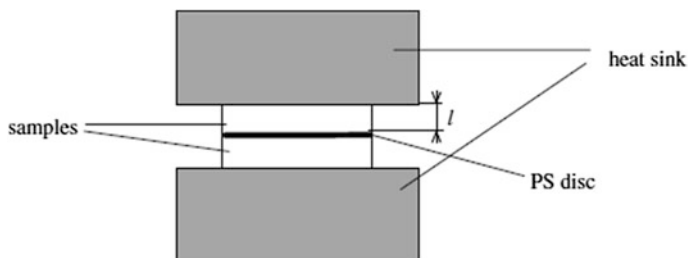
## 2 Experimental Part

Sample composition is described in Table 1.

The extended dynamic plane source (EDPS) method is arranged for one-dimensional heat flow into a finite sample (Fig. 1) [9]. The plane source (PS) disc, which simultaneously serves as the heat source and thermometer, is made of a nickel film covered from both sides with a kapton layer. The heat in the form of a step-wise function is produced by the passage of an electrical current through the PS disc. Two identical samples of cylindrical shape cause symmetrical division of the heat flow into a very good heat conducting material (heat sink), which provides isothermal boundary conditions of the experiment. This method appears to be

**Table 1** Sample composition

Sample number	Sandwich sample composition
1	2x phenolic prepreg PH840-300-42
	<b>1x honeycomb Cormaster C2-3,2-48 9 mm</b>
	1x phenolic prepreg PH840-300-42
2	2x phenolic prepreg PH840-300-42
	<b>1x AirexT90.1009 9 mm</b>
	1x phenolic prepreg PH840-300-42
3	Gelcoat Büfa S 250 V (Surface layer)
	1x glass matt 300 g/m <sup>2</sup>
	1x bidiagonal fabric Saertex 980 g/m <sup>2</sup>
	<b>1x Airex T90.100 10 mm</b>
	1x bidiagonal fabric Saertex 980 g/m <sup>2</sup>
	Matrix: polyester resin NORPOL 850-M850
4	2x phenolic prepreg PH840-300-42
	<b>1x Corecork NL10 10 mm</b>
	1x phenolic prepreg PH840-300-42
5	Gelcoat NGA HX3 RAL 9010 (surface layer)
	1x glass matt 300 g/m <sup>2</sup>
	1x bidiagonal fabric Saertex 980 g/m <sup>2</sup>
	<b>1x Corecork NL10 10 mm</b>
	1x bidiagonal fabric Saertex 980 g/m <sup>2</sup>
	Matrix: polyester resin NORPOL 850-M850

**Fig. 1** Schema of the method

useful for the simultaneous determination of thermal diffusivity and thermal conductivity of low thermally conducting materials. Results of thermal measurements are collected in Table 2.

Results of mechanical measurements are collected in Table 3.

As seen in Table 2 the greatest specific heat capacity and the lowest thermal conductivity are measured in the samples 2 and 3. Also, the thermal conductivities of these samples are relatively low, and so they are very good thermal insulators comparable with glass wool.



**Table 2** Thermal properties of sandwiches under investigation

Physical value	Sample 1	Sample 2	Sample 3	Sample 4	Sample 5
$k$ (W/m K)	0.086	0.033	0.074	0.083	0.124
$\alpha$ ( $m^2$ s)	$3.4 \times 10^{-7}$	$6 \times 10^{-8}$	$6 \times 10^{-8}$	$2.04 \times 10^{-7}$	$2.43 \times 10^{-7}$
$c_p$ (J/kg K)	1150	2037	2371.8	1369.9	936.3
$\rho$ ( $kg/m^3$ )	220	270	520	297	545

**Table 3** Mechanical properties of samples under investigation

Physical value	Sample 1	Sample 2	Sample 3	Sample 4	Sample 5
$E$ (GPa)	2.93	2.68	1.42	1.31	0.62
$\sigma_m$ (MPa)	4.26	3.50	5.57	7.63	8.37

On the other hand the lowest specific heat capacity is measured in sample 5, which has the highest thermal conductivity. Thermal conductivity and thermal diffusivity of samples 1, 3 and 4 are comparable. From the density measurements it is clearly seen that materials under investigation are light. On the other hand they must have sufficiently good mechanical parameters. From Table 3 we can see the highest value of  $\sigma_m$  for sample 5 and the highest Young's modulus is calculated for sample 1.

### 3 Conclusions

As we said, the mentioned sandwich materials are used for the production of internal parts of means of transport. In this work we focus on testing materials suitable for such applications. The tested sandwich materials have very good mechanical properties represented by values of  $\sigma_m$ , and  $E$ . Further they are light with very good thermal insulation properties. The selection of individual sandwich materials will therefore depend on the specific application.

### References

1. Harhash M, Sokolova O, Carrado A et al (2014) Mechanical properties and forming behaviour of laminated steel/polymer sandwich systems with local inlays—Part I. *Compos Struct* 118:112–120
2. Catapano A, Montemurro M (2014) A multi-scale approach for the optimum design of sandwich plates with honeycomb core. Part I: Homogenisation of core properties. *Compos Struct* 118:664–676

3. Catapano A, Montemurro M (2014) A multi-scale approach for the optimum design of sandwich plates with honeycomb core. Part II: The optimisation strategy. *Compos Struct* 118:677–690
4. Yan R, Wang R, Lou CW et al (2014) Manufacturing technique and acoustic evaluation of sandwich laminates reinforced high-resilience inter/intra-ply hybrid composites. *Fibers Polym* 15:2201–2210
5. Ai SG, Mao YQ, Pei YM et al (2013) Numerical analysis of thermodynamic behaviour of through-thickness stitched sandwich laminate. *Appl Compos Mater* 20:1161–1171
6. Khandelwal RP, Chakrabarti A, Mishra BK et al (2013) A new heat flux continuity model for thermal analysis of laminated plates. *J Compos Mater* 47:2053–2059
7. Kim YJ, Han JH (2013) Identification of acoustic characteristics of honeycomb sandwich composite panels using hybrid analytical/finite element method. *J Vib Acoust Trans ASME* 135
8. Brewster MQ, Mullen JC (2010) Flame structure in aluminized wide-distribution AP composite propellants. *Combust Flame* 157:2340–2347
9. Malinarič S (2004) Contribution to the sensitivity coefficients analysis in the extended dynamic plane source (EDPS) method. *Int J Thermophys* 25:1913–1919

# Evaluation of Creep Resistance and Superficial Study of Titanium Alloy Treated by PIII-N

S. Zepka, D.A.P. Reis, M.M. Silva, M. Ueda, A.A. Couto and A.G. Reis

**Abstract** The search for alloys with improved high-temperature specific strength and creep-resistance properties for aerospace applications has led in the last decades to sustained research activities to develop new alloys and/or improve existing ones. Titanium and its alloys are excellent for applications in structural components submitted to high temperatures owing to their high strength to weight ratio, good corrosion resistance and metallurgical stability. However, the high affinity to oxygen is one of the main factors that limit their application as a structural material

---

S. Zepka · D.A.P. Reis · M.M. Silva · A.G. Reis  
Instituto Tecnológico de Aeronáutica (ITA),  
12228-900 São José dos Campos, Brazil  
e-mail: susana@ita.br

D.A.P. Reis  
e-mail: danielireis@gmail.com

M.M. Silva  
e-mail: meg@ita.br

A.G. Reis  
e-mail: adriano.reis@ict.unesp.br

D.A.P. Reis  
Universidade Federal de São Paulo (UNIFESP),  
12231-280 São Paulo, Brazil

M. Ueda  
Instituto Nacional Pesquisas Espaciais (INPE),  
12227-010 São José dos Campos, Brazil  
e-mail: ueda@plasma.inpe.br

A.A. Couto (✉)  
Instituto de Pesquisas Energéticas e Nucleares (IPEN/CNEN-SP),  
05508-900 São Paulo, Brazil  
e-mail: acouto@ipen.br.br

A.A. Couto  
Universidade Presbiteriana Mackenzie (UPM), 05508-900 São Paulo, Brazil

at high temperatures. Materials with adequate behavior at high temperatures and in aggressive environments have become a scientific requirement for technological and economic reasons. The goal of this work is the roughness and creep studies of the Ti–6Al–4V alloy after treatment by the nitrogen Plasma Immersion Ion Implantation (PIII-N) process. The aim of this process is the improvement of the superficial mechanical properties of the Ti–6Al–4V alloy. The selected alloy after ionic implantation process by plasma immersion was submitted to creep tests in 600 °C at 250 and 319 MPa. The techniques used in this work were Auger spectroscopy, Atomic Force microscopy (AFM), X ray, Raman spectroscopy and creep testing. The results show the significant increase of material resistance, it can be used as protection of oxidation in high temperatures applications.

**Keywords** PIII-N · Creep · Ti–6Al–4V · Auger · AFM

## 1 Introduction

Titanium and its alloys have many attractive properties, including high specific strength and modulus, excellent corrosion resistance, and, in some cases, good cryogenic properties. They are widely used in aerospace applications and many corrosive environments. The Ti–6Al–4V alloy has also been used for orthopedic devices and other engineering components due to its beneficial properties, such as low density, low modulus of elasticity, excellent corrosion resistance and biocompatibility [1].

Many engineering components will operate under severe conditions such as elevated temperatures, complex loading conditions and harsh environments. Under such loading conditions, several damage mechanisms, including fatigue and creep, play an important role [2].

The fast developments in engineering demand the requirement of materials with better mechanical properties, resistance to frictional wear, resistance to corrosion and erosion, etc. These demands can be satisfied by applying various surface engineering techniques that allow modifying the microstructure, phase and chemical composition of the surface layers of the treated parts [2].

The plasma immersion ion implantation treatment is an emerging technology with potential for use in surface engineering of semiconductors, metals and dielectrics. This technique has received increased attention from researchers, because it allows the surface treatment of parts with complex three-dimensional geometries [3, 4]. Plasma immersion ion implantation is a method by which nitrogen atoms are introduced in the surface alloy using nitrogen containing plasma to form either nitrides or nitrogen in solid solution to increase the hardness [5–7].

## 2 Material and Methods

The Plasma Immersion Ion Implantation technique consisted in mounting the sample of Ti-6Al-4V in the sample holder device, inserted and fixed in the reactor. It is sealed to form the vacuum, targeting the surface treatment, with a mechanical pump and after using a diffusing pump until the pressure reaches  $5.3 \times 10^{-3}$  mbar, when the system is ready to begin the deployment implantation process. Nitrogen was injected (to implement of nitrogen ions in the sample) and to obtain the plasma, turn up the pulser RUP-4. The implantation of nitrogen treatments were performed at 250 °C, high voltage pulse of 8.5 kV, time average amplitude of 40  $\mu$ s, frequency of 400 Hz, working pressure of 0.21 Pa during 120 and 180 min [3, 4, 8, 9].

The determination of the atomic concentration as a function of depth for the samples with 2 and 3 h of immersion was studied by the technique of Auger electron spectroscopy using the spectrometer FISIONS Surface Science Instrument, Model F-310 MICROLAB, which performed the sputtering of the sample surfaces with argon.

Panalytical hallmark and X'Pert Powder model X-ray diffractometer was used in the  $\theta/\theta$  configuration for the identification of the crystalline phases present in the samples. The analysis parameters were: pitch of 0.002,  $2\theta$  ranging between 10° and 90°, and a step time of 10 s.

In this work were obtained the Raman scattering spectrum using Micro-Raman spectrometer from Renishaw, the System 2000 model, owned by LAS-INPE. The intension was to identify the characteristic bands of nitrides present in the samples treated superficially with Plasma Immersion ion Implantation with different times of implantation.

For observation of the microstructures on the samples surface, images were obtained by atomic force microscopy using a VEECO and model multimode V, in intermittent contact mode.

For the creep tests, it used the Ti-6Al-4V acquired in the form of cylindrical bars of 12.7 mm diameter and 1 m length in the provided wrought and annealed at 190 °C for 6 h and cooled in air, having an equiaxial structure.

Chemical analyses were performed by inductively coupled plasma optical emission spectrometry coupled in an ARL equipment model 3410 attending to composition for the league Ti-6Al-4V: Ti = 89.16 %; Al = 6.61 %; and V = 4.23 %, according norm ASTM B265-89 [10].

The creep samples were made in accordance with the specifications, gripper systems and gauges available. Figure 1 shows the shape and dimensions of the specimens used in creep tests in accordance with ASTM-E 139-83 [11].

Samples of Ti-6Al-4V for the remaining experiments were made into tablets of 10 mm diameter and 3 mm thickness.

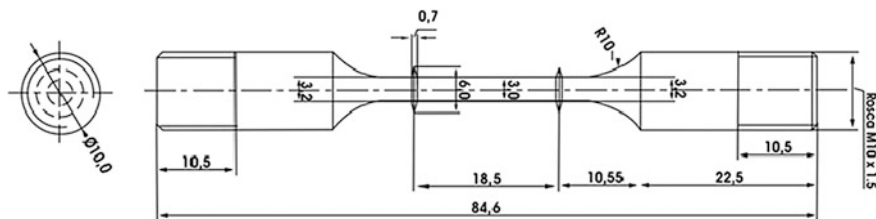


Fig. 1 Creep specimen

### 3 Results and Discussion

The results of the Auger spectroscopy presented in Fig. 2a, b, show that with the PIII treatment, the layer obtained is 18 nm thick for the sample immersed for 2 h, and a layer of 36 nm immersed for 3 h. It was also observed that in the sample immersed for 2 h, the nitrogen atoms measure up to a maximum concentration of 20 % to 6 nm and the sample immersed for 3 h, 32 % of the maximum concentration to 18 nm.

We observe the presence of the elements of the alloy (Ti, Al, V). The oxygen is found in the atmosphere and due to the strong affinity of titanium with oxygen, forming a passive oxide layer on its surface, which serves as a protective layer against corrosion. The thickness of this oxide layer may undergo some changes according to the ambient conditions and the treatment. In the sample treated for 3 h, oxygen is detected within 10 nm with an atomic concentration maximum of approximately 25 % near the surface. It is observed that the concentrations of the atomic elements aluminum and vanadium are lower near the surface due to the presence of oxygen and nitrogen. The presence of carbon at the surface is possibly due to the oil contamination of the PIII system vacuum pump [9, 12].

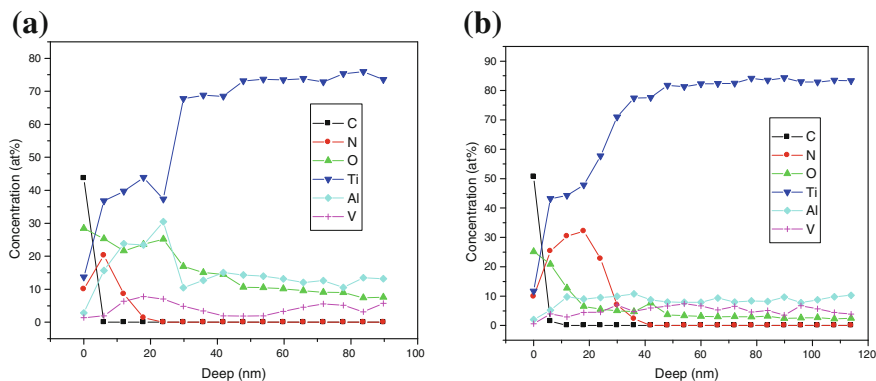
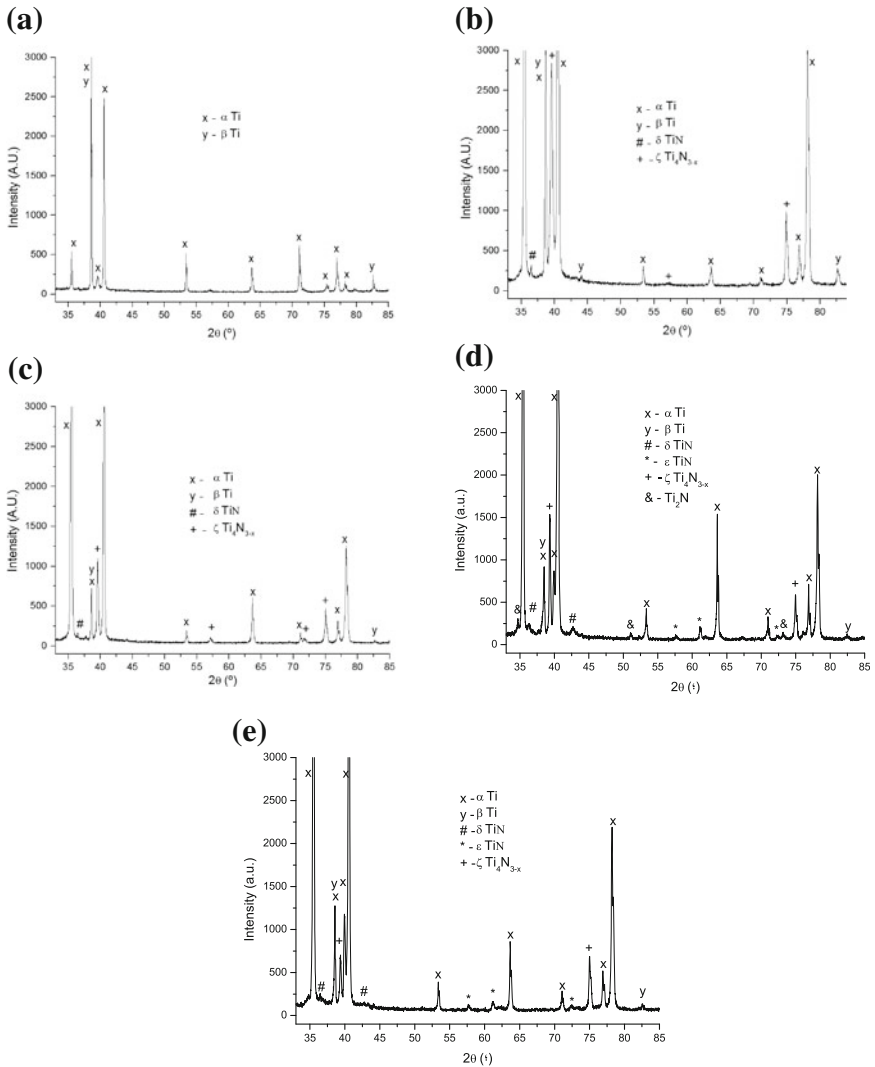


Fig. 2 Sample Auger spectroscopy with: **a** 2 h implantation and **b** 3 h implantation

The results of the X-ray diffraction presented in Fig. 3a, e, show the surface modification with formation of nitrides. In Fig. 3a, we have the untreated sample on which only is observed the presence of  $Ti\alpha$  and  $Ti\beta$ . In Fig. 3b the results of the sample, which underwent 120 min of implantation are shown, where nitride formation is observed. As well as in Fig. 3c, where there is increased nitride formation and decreased  $Ti\beta$ , since N is an aphagenic component [4, 13].



**Fig. 3** X-ray diffraction of the **a** untreated sample, **b** sample with 2 h immersion, **c** sample with 3 h immersion, **d** sample with 4 h and **e** sample with 8 h immersion

An analysis was made from the X-ray diffraction on samples without IIIIP treatment, and the samples treated with immersion time of 2, 3, 4 and 8 h. In Fig. 3a–e the spectra of the relative sample are displayed. In the untreated sample, it was observed that the titanium alloy is of type  $\alpha + \beta$  phase with a percentage of  $\alpha$ -phase much larger than  $\beta$ . In the sample with 2 h immersion time, the formation of different kinds of nitrides was noticed, as well as how the  $\zeta$   $\text{Ti}_4\text{N}_{3-x}$  nitride is unstable. The formation of nitride TiN was observed. The aluminum and nitrogen are  $\alpha$ -phase stabilizers and vanadium is a  $\beta$ -phase stabilizer [14, 15], it was also observed an increase in  $\alpha$ -phase Ti peaks, due the increasing of N.

In the 3-h immersion sample the decreasing of the Ti- $\beta$  peaks, and N is  $\alpha$ -phase stabilizer, increasing the peaks of Ti- $\alpha$  was observed. There is the increase in the nitride unstable formation, probably because there is more Ti present in the surface than N.

In the 4-h immersion sample, there is a formation of many types of nitrides, showing the surface saturation by N, which kept the levels of Ti- $\alpha$  and Ti- $\beta$  stable. The decreasing of the  $\zeta$   $\text{Ti}_4\text{N}_{3-x}$  nitride can be observed.

In the 8-h immersion sample the tendency of nitride type TiN stabilization in the surface was noted, suggesting that in the surface the connection between Ti and N is near 1:1, because the increase in the time necessary of the N ion implantation.

Observing the results obtained from the Raman spectroscopy analysis of the untreated sample, the absence of bands related to titanium nitride (TiN) can be noted, as it was confirmed by analysis to the X-ray diffraction (see Fig. 4a–d).

In Fig. 4b, after 2 h of implantation sample, good characteristics TiN bands can be seen on the sample, agreeing with the analysis by X-ray diffraction, which shows the presence of peaks relating to nitride formation.

Confirmation of the formation of the TiN on the 3 h implantation sample surface is shown in Fig. 4c, which has the same characteristic bands of nitride formation.

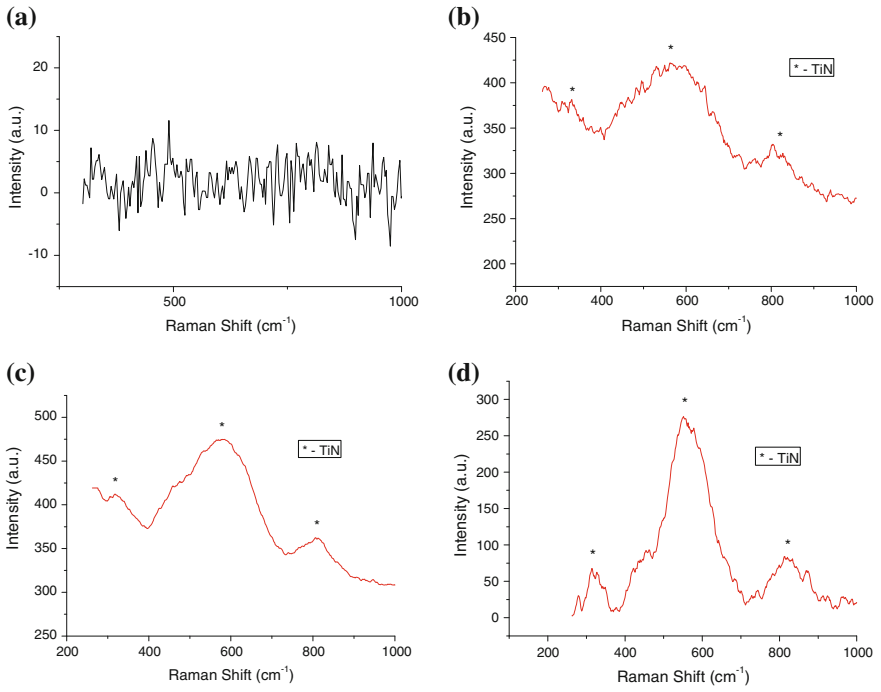
In Fig. 4d we can observe the same TiN bands, which can be verified by comparing the analysis of X-ray diffraction. It was observed that in the 4 h implantation sample there were various nitrides formed [16].

The samples analyzed by AFM are observed in Fig. 5a–e. Table 1 shows the values of average roughness for Ti-6Al-4V samples by AFM. The increase of the roughness of the sample surface was observed, due to formation of TiN, directly proportional with respect to increase the time of implantation the samples were submitted [17].

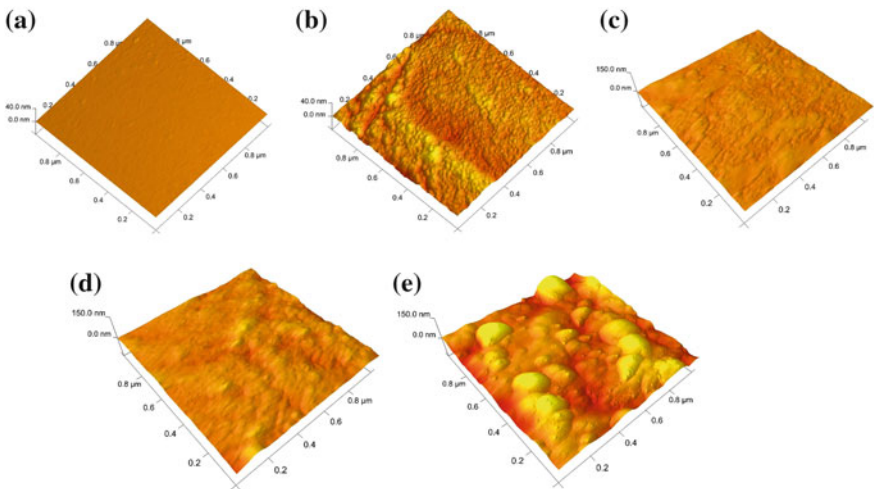
The results of creep tests are presented in Table 2. The main parameters named: primary creep time ( $t_p$ ), steady state creep rate ( $\dot{\epsilon}_s$ ), time and deformation to failure ( $t_f$  and  $\epsilon_f$ ) can describe further behavior of deformation regime. These values are calculated based on creep curves and distribution of primary, secondary and tertiary stages.

Figure 6 summarizes the creep curves for all tests performed in both conditions, which were obtained by following the Norton power creep law. The Ti-6Al-4V alloy shows a normal curve of creep stages consisting of primary, secondary and tertiary well defined. There is a relatively short initial period of decreasing primary





**Fig. 4** Analysis of Raman spectroscopy of the sample. **a** Untreated, **b** 2 h immersion, **c** 3 h immersion and **d** 4 h immersion, to identification of the TiN bands



**Fig. 5** AFM of de samples. **a** Untreated (reference), with implantation time of: **b** 2 h, **c** 3 h, **d** 4 h and **e** 8 h

**Table 1** Values of average roughness obtained by AFM

PIII treatment (h)	Average roughness (nm)
Without treatment	0.09
2	1.94
3	2.46
4	4.07
8	15.00

**Table 2** Creep parameters data

Treatment	T (°C)	$\sigma$ (MPa)	$t_p$ (h)	$\dot{\epsilon}_s$ (1/h)	$t_f$ (h)	$\epsilon_f$ (mm/mm)
Untreated	600	250	0.030	0.1906	0.620	0.1938
		319	0.010	0.5698	0.390	0.1742
PIII 2h	600	250	0.270	0.0615	1.830	0.1807
		319	0.110	0.1925	0.600	0.1964
PIII 3h	600	250	0.100	0.4026	0.267	0.1225
		319	0.017	1.3206	0.130	0.2544
PIII 8h	600	250	0.033	0.3413	0.480	0.3017

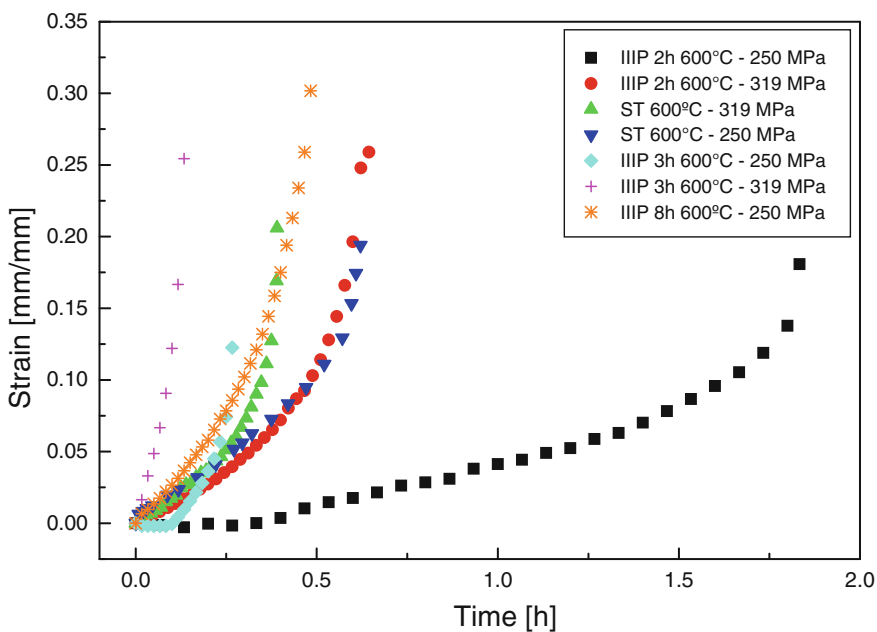


**Fig. 6** Creep curves

creep rate that is associated with hardening due to the accumulation of dislocations. However, most of the creep life is dominated by a constant creep rate that is thought to be associated with a stable dislocation configuration due to recovery and hardening processes.

The PIII 3 and 8 h samples showed lower creep resistance than those treatment samples. This lower creep resistance was verified by a higher stationary creep rate and the decreasing of fracture time, which can be related to TiN formation on surface of the material promoting a fragile behavior to the alloy, decreasing its creep resistance. In the samples with 2 h implantation time, the thin layer of TiN formed didn't change significantly the ductile behavior of the alloy, protecting against oxidation in high temperatures and in creep performance.

The effect of stress levels on creep deformation on the primary creep stage can be modeled like the previous model by Reis et al. [18] using the Norton power law creep, in the linearized format. The same approach has been applied to the secondary stage, with exception of the change, the parameters for steady state creep rate and stress value. Figures 7 and 8 show detailed value of  $n$ ,  $B$  and  $Q_c$ , where  $n$  is the stress exponent, where  $B$  is constant that depends on the microstructure of the material and  $Q_c$  is the activation energy necessary to creep process. The results indicate that, for the as received condition, the higher levels  $n$  correlate to a higher dependence of stress levels. The values of stress exponent for secondary stage and

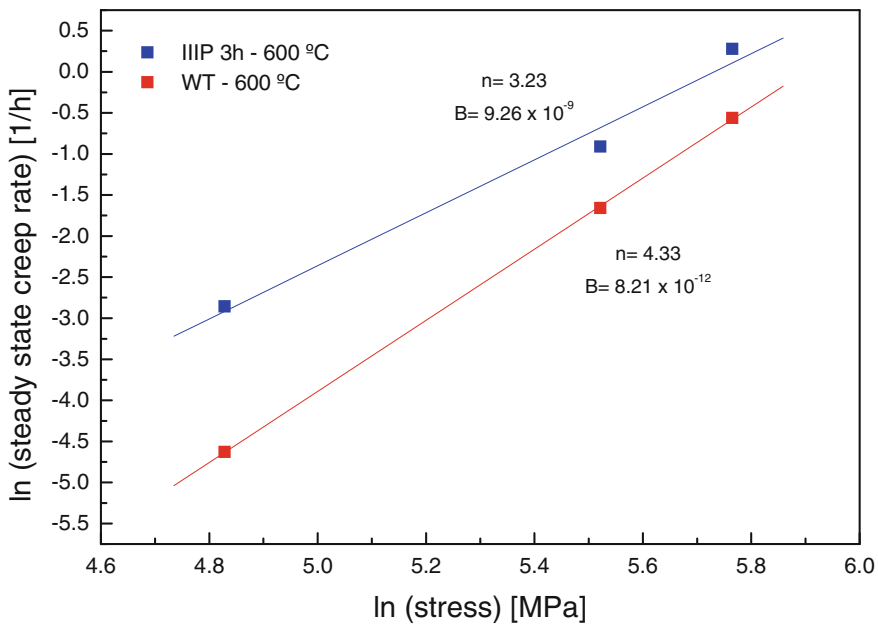


Fig. 7 Stress-creep rate correlation for secondary creep stage

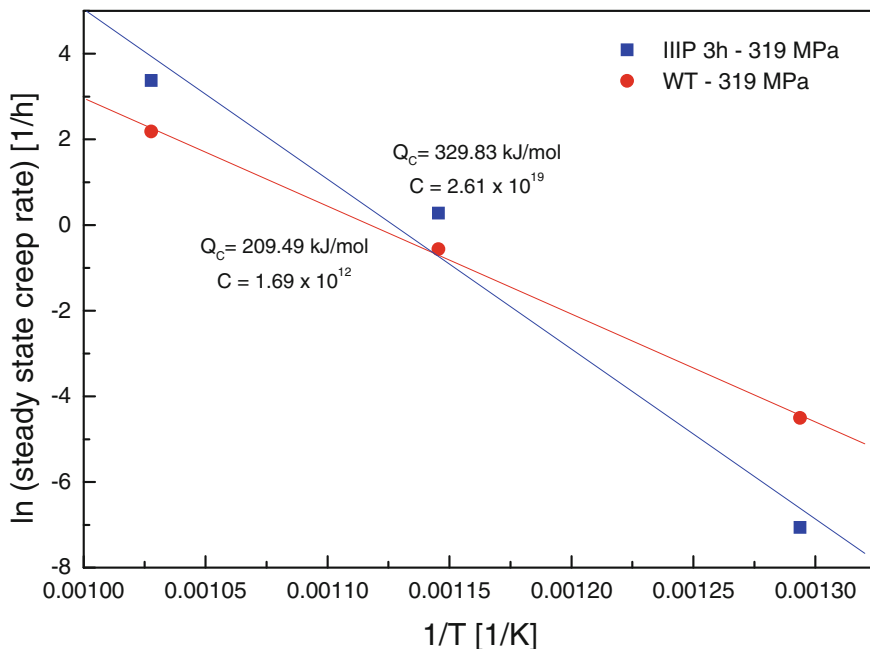


Fig. 8 Time-creep rate correlation for secondary creep stage

the activation energy, which is in accordance with a previous value reported by Lagneborg and Bergman [19], which indicate a mechanism of creep deformation controlled by the dislocation glide and climb.

## 4 Conclusions

The obtained results showed the nitrites superficial in the alloys. The roughness values increased accordingly implantation time, because the TiN formation. The PIII 3h samples showed lower creep resistance than without treatment samples. This lower creep resistance was verified by higher stationary creep rate and the decreasing of fracture time, it can be related to TiN formation on surface of the material promoting a fragile behavior to the alloy, decreasing its creep resistance. In the samples of 2 h implantation time, the thin layer of TiN formed didn't change significantly the ductile behavior of the alloy, protecting to oxidation in high temperatures and in creep performance. The values correlation of stress exponent and activation energy to stationary stage indicated that the creep mechanism to this work is associated to dislocation.

**Acknowledgments** FAPESP, CAPES and CNPq for financial support.

## References

1. Leyens C, Peters M (2003) Titanium and titanium alloys: fundamentals and applications. Wiley-VCH Verlag GmbH & Co. KGaA, Weinheim
2. Budinski KE (1991) Tribological properties of titanium alloys. *Wear* 151:203–217
3. Ueda M, Silva MM, Lepienski CM et al (2007) High temperature plasma immersion ion implantation of Ti6Al4V. *Surf Coat Tech* 201:4953–4956
4. Mello CB, Ueda M, Silva MM et al (2009) Tribological effects of plasma immersion ion implantation heating treatments on Ti–6Al–4 V alloy. *Wear* 267:867–873
5. Saillard P, Gicquel A, Amouroux J (1991) Plasma process for therm diffusional titanium nitriding. *Surf Coat Tech* 45:201–207
6. Johns SM, Bell T, Samandi M, Collins GA (1996) Wear resistance of plasma immersion ion implanted Ti6Al4V. *Surf Coat Tech* 85:7–14
7. Wang SY, Chu PK, Tang BY et al (1997) Radiofrequency plasma nitriding and nitrogen plasma immersion ion implantation of Ti-6Al-4V alloy. *Surf Coat Tech* 93:309–313
8. Silva MM, Ueda M, Pichon L et al (2007) Surface modification of Ti6Al4V alloy by PIII at high temperatures: effects of plasma potential. *Nucl Instrum Meth B* 257:722–726
9. Silva MM, Ueda M, Otani C et al (2005) Hybrid processing of Ti-6Al-4V using plasma immersion ion implantation combined with plasma nitriding. *Mater Res* 9:97–100
10. ASTM B265-15 (2015) Standard specification for titanium and titanium alloy strip, sheet, and plate, Philadelphia
11. ASTM E139-11 (2011) Standard test methods for conducting creep, creep-rupture, and stress-rupture tests of metallic materials, Philadelphia
12. Silva LIG, Ueda M, Silva MM et al (2004) Results from experiments on hybrid plasma immersion ion implantation/ nitriding processing of materials. *IEEE T Plasma Sci* 221:34–39
13. Baur K, Hornes J (1999) The formation of intermetallic compounds in ion implantation aluminium and Ti-6Al-4V observed by X-ray absorption spectroscopy. *Surf Sci* 436:141–148
14. Brun M, Anoshkin N, Shakhanova G (1998) Physical processes and regimes of thermomechanical processing controlling development of regulated structure in the  $\alpha+\beta$  titanium alloys. *Mat Sci Eng A-Struct* 243:77–81
15. Evans WJ (1998) Optimizing mechanical properties in alpha + beta titanium alloys. *Mat Sci Eng A-Struct* 243:89–96
16. Mandi S, Thorwarth G, Schreck M et al (2000) Raman study of titanium oxide layers produced with plasma immersion ion implantation. *Surf Coat Tech* 125:84–88
17. Sun Y, Luo N, Bell T (1994) Three-dimensional characterization of plasma nitrided surface topography. *Surface Eng* 10:279–286
18. Reis DAP, Silva CRM, Nono MCA et al (2005) Effect of environment on the creep behavior of the Ti-6Al-4V alloy. *Mat Sci Eng A-Struct* 399:276–280
19. Lagneborg R, Bergman B (1976) The stress/creep rate behaviour of precipitation-hardened alloys. *Met Sci* 10:20–28

# Properties of WE43 Metal Matrix Composites Reinforced with SiC Particles

B. Dybowski, T. Rzychoń, B. Chmiela and A. Gryc

**Abstract** It is well known that the properties of metal matrix composites depend upon the properties of the reinforcement phase, on the matrix and on the interface. A strong interface bonding without any degradation of the reinforcing phase is one of the prime objectives in the development of metal matrix composites. The objective of this work is to characterize the interface structure of WE43/SiC particles composite and their mechanical properties at ambient and elevated temperatures. Magnesium alloys containing yttrium and neodymium are known to have high specific strength, good creep and corrosion resistance up to 523 K. The addition of SiC ceramic particles strengthens the metal matrix composite resulting in better wear and creep resistance while maintaining good machinability. In the present study, WE43 magnesium matrix composite reinforced with SiC particulates was fabricated by stir casting. The SiC particles with 15, 45 and 250  $\mu\text{m}$  diameter were added to the WE43 alloy. Microstructure characterization of WE43 MMC with 45  $\mu\text{m}$  showed a relatively uniform reinforcement distribution and presence of inconsiderable porosity. Moreover, the Zr-rich particles at the particle/matrix interface were visible. The presence of SiC particles assisted in improving hardness and decreasing the tensile strength creep resistance.

**Keywords** WE43 MMC · Stir casting · Mechanical properties · Creep resistance · SiC reinforcement

---

B. Dybowski · T. Rzychoń (✉) · B. Chmiela · A. Gryc  
Faculty of Material Science and Metallurgy, Silesian University of Technology,  
Krajskiego Street 8, 40-019 Katowice, Poland  
e-mail: tomasz.rzychon@polsl.pl

B. Dybowski  
e-mail: bartlomiej.dybowski@polsl.pl

B. Chmiela  
e-mail: bartosz.chmiela@polsl.pl

A. Gryc  
e-mail: gryadam@wp.pl

## 1 Introduction

Magnesium alloys are a more and more widely applied material in automotive and aerospace industries. The combination of low density ( $\approx 1.8 \text{ g/cm}^3$ ) and good mechanical properties of aluminium containing magnesium alloys (AZ, AM types) led to the application of these materials in structural elements operating at ambient temperature in the automotive and aerospace industries [1–4]. The very low maximal working temperature of these alloys (about  $120 \text{ }^\circ\text{C}$ ) stopped the further application of these in elements of, for example, engine blocks. The addition of rare earth elements (RE) to the aluminium containing alloys or even replacing aluminium with them, causes formation of thermally stable Al-RE or Mg-RE phases, thus increasing operation temperature up to  $250 \text{ }^\circ\text{C}$  [5, 6].

Further increases in creep resistance of magnesium alloys may be achieved by an introduction of ceramic particles to the alloy structure. It has been revealed that the addition of 3 % of nanoscaled SiC particles to pure magnesium increases its creep resistance to the level of commercial Mg-RE alloys [7]. The majority of authors produce magnesium MMC reinforced with ceramic particles by means of milling and sintering [8–11]. This method, however, is difficult to apply in commercial production, mainly because of the difficulties in the production of more complicated elements. For this reason, stir casting seems to be an effective method to manufacture more complex structures [10]. The main drawback of this method is, the tendency of the particles to cluster. This leads to the formation of agglomerates, dramatically decreasing mechanical properties of the material [12]. To avoid agglomeration of the particles, a relatively long time of stirring at elevated temperature is needed, which in turn, may result in degradation of the ceramic particles. A too short stirring time, or stirring at too low a temperature may in turn lead to a not uniformly distributed reinforcing phase.

The following paper presents results of the investigations on the mechanical properties at ambient and elevated temperature of the stir cast WE43 MMC reinforced with SiC particulates.

## 2 Research Material and Methodology

The material used in this research was the WE43 metal matrix composite (MMC) reinforced with SiC particulates. The composite has been reinforced with particulates with mean diameter  $d = 15, 45 \text{ } \mu\text{m}$  as well as  $200 \text{ } \mu\text{m}$ . The volume fraction of the reinforcement was equal to 10 %. Additionally, composites with reinforced with the  $0 \div 6 \text{ } \%$  of  $45 \text{ } \mu\text{m}$  particulates were investigated. All composites were produced by means of stir casting. Commercial ingots of WE43 magnesium alloy were melted in a resistance furnace under the protective atmosphere of 99.999 % Ar. The melt was homogenised for about 20 min. at  $720$  and

780 °C. The Mg–Y, Mg–Zr and Mg–Nd hardeners were added to compensate the alloy's chemical composition. Particulates preheated up to 300 °C were added to the liquid alloy after the homogenisation. The suspension was then stirred for about 15 min. Immediately after the stirring process, the composite was poured into the graphite moulds, preheated up to 200 °C. The pouring process as well as composite solidification were also conducted under the Ar protective atmosphere. The researches were done on specimens in both as-cast as age hardened specimens. Solution treatment of the composites was conducted at 525 °C for 8 h, while aging at 250 °C for 16 h.

The microstructure observations of the composites were done on microsections prepared with the following procedure: cutting, grinding on the SiC abrasive papers with grades 120 ÷ 2400, polishing on the diamond suspensions with the mean grain size 6, 3 and 1 µm and final polishing on Struers OP-AN alumina suspension with a grain size 0.05 µm. The microstructure of the composite was investigated on un-etched specimens. Observations were done on an Olympus GX71 light microscope (LM) as well as a Hitachi S3400N scanning electron microscope (SEM). The investigations were also conducted by means of scanning-transmission electron microscopy (STEM) on a Hitachi HD2300A STEM. Specimens for the STEM investigations were prepared with a FIB 2100 focused ion beam microscope. Chemical composition of the phases was analysed by energy dispersive X-Ray spectroscopy (EDS).

Phase analysis were done by X-Ray diffraction (XRD) on a JEOL JDX-7S diffractometer with a copper anode. Registration of XRD patterns was performed by 0.02° stepwise regression for 2θ ranging from 10° to 90° 2θ. Phase identification was performed using the ICDD PDF-4+database.

The mechanical properties and the creep resistance of the composites were investigated on a Kappa 50DS tensile testing machine. Creep tests were conducted at 250 °C with a load of 90 MPa. The testing time was equal to 120 h. HV2 Vickers hardness was investigated on a Duramin A300 hardness tester.

## 3 Research Results

### 3.1 Composite Microstructure in the as Cast Condition

The microstructure of the composite's matrix in the as-cast state consists of α-Mg dendrites and the eutectic equilibrium β-Mg<sub>5</sub>RE phase [5]. The eutectic phase is distributed homogenously within the interdendritic regions (Fig. 1a). Sporadically, Y- and Zr- enriched non-metallic inclusions are observed in the WE43 matrix microstructure (Fig. 1b). Composites prepared with 45 µm particulates are characterized by a relatively homogenous distribution of the reinforcing phase (Fig. 2a). Composites reinforced with 15 µm particles also show a homogenous microstructure, however, only if stirred at 780 °C. After stirring at 720 °C such small particles



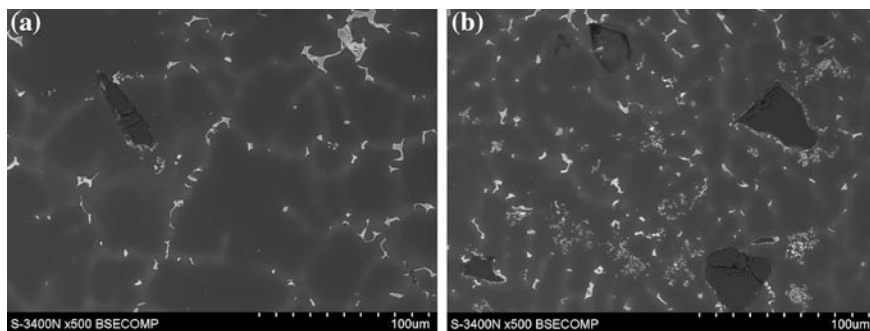


**Fig. 1** Microstructure of the WE43 MMC reinforced with SiC particulates, SEM

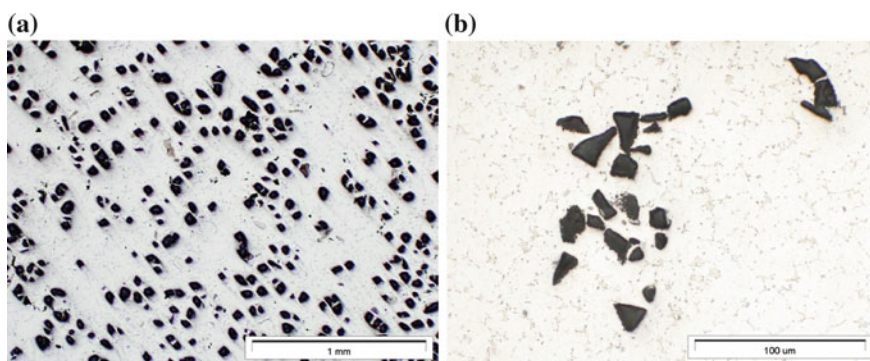


**Fig. 2** Reinforcement in the WE43 MMC, LM; **a** composite reinforced with 45  $\mu\text{m}$  SiC particulates; **b** composite reinforced with 15  $\mu\text{m}$  SiC particulates, stirred at 720  $^{\circ}\text{C}$

tend to form agglomerates (Fig. 2b). Composites reinforced with 250  $\mu\text{m}$  SiC particles exhibit homogenous distribution at the transverse section of the research cast. However, such big particles settle down both in the crucible and mould, forming an inhomogeneous distribution of the reinforcement at the longitudinal section of the cast.

The stirring of the melt at 780  $^{\circ}\text{C}$  leads to reactions between the reinforcement and liquid alloy. Massive YSi particles are formed at the SiC/matrix interface. Degradation of the SiC particles led to the dissolution of silicon within the alloy and formation of  $\text{Mg}_2\text{Si}$  phase within the composite matrix (Fig. 3a). Stirring and pouring of the composite at the 720  $^{\circ}\text{C}$  led to much smaller reactions between the liquid alloy and reinforcement. The SiC particles are covered with a thin, Zr enriched layer, consisting of fine Zr–Si (mainly  $\text{Zr}_2\text{Si}$ ) and  $\text{Y}_2\text{O}_3$  particles (Fig. 3b). The more detailed investigations on the composite microstructure will be published elsewhere.

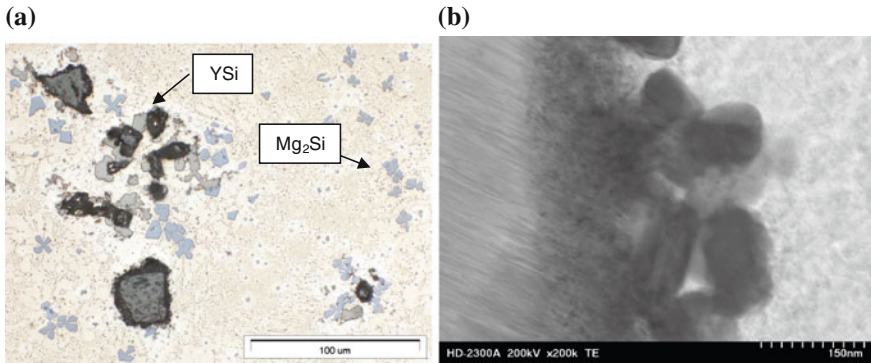


**Fig. 3** Interfaces between SiC particulates and WE43 matrix; **a** composite stirred at 780 °C, LM; **b** composite stirred at 720 °C, STEM

### 3.2 Composite Microstructure After the Heat Treatment

The solution treatment of the composites at 525 °C led to the complete dissolution of eutectic  $\beta$   $Mg_5RE$  phase within the  $\alpha$ -Mg dendrites (Fig. 4). In the composites stirred at 720 °C further reactions between the alloy and SiC have not been observed. It indicates that the fine Zr–Si layer effectively hinders alloying elements to diffuse at an elevated temperature.

Aging of the composite stirred at 780 °C did not lead to precipitation of reinforcing phase. Yttrium bonded in the YSi phases cannot take a part in age-hardening process, thus leading to a lack of composite age-hardening response.

Aging of the composites stirred at 720 °C led to the precipitation of strengthening phases. Aging at 250 °C for 16 h leads to the precipitation of both  $\beta''$  with a  $D0_{19}$  crystal structure and  $\beta'$  with orthorhombic crystal structure phases [13, 14]. These phases possess platelet-like morphology with a width of about 7–15 nm and lengths between 30 and 200 nm as well as a globular morphology with a diameter between 15 and 45 nm [15].

### 3.3 Mechanical Properties of the Composites in Ambient Temperature

The mechanical properties of the WE43 MMC reinforced with SiC particles in the as-cast state are shown in Table 1. Addition of SiC particulates significantly reduces the tensile strength of the WE43 alloy. It decreases both with the increasing size of the SiC particulates and their volume fraction. Yield strength and elongation of the composite also decrease after the addition of SiC particulates; however it

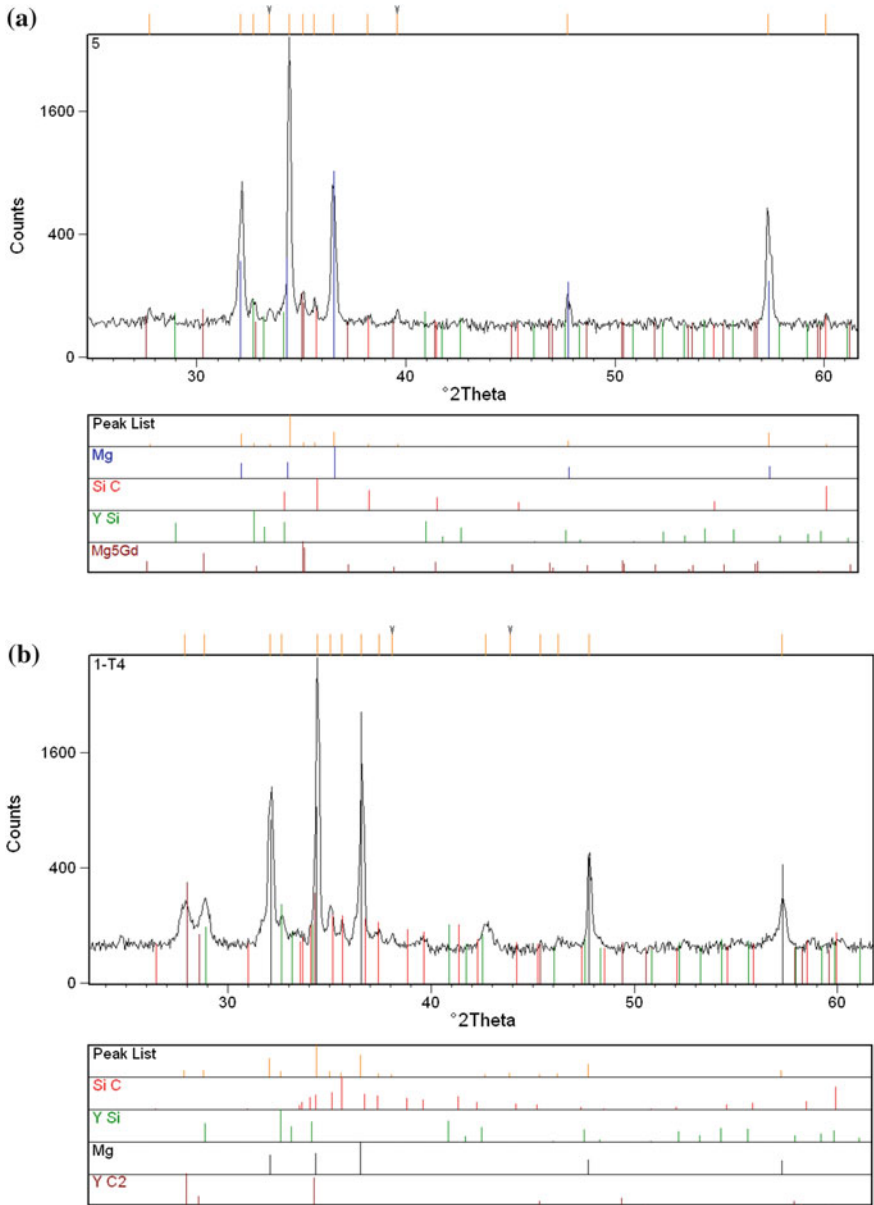


**Fig. 4** XRD analysis results for the composite stirred at 780 °C; **a** composite in the as-cast condition; **b** composite after solution treatment at 525 °C

does not exhibit a further decrease with increasing volume fraction of the reinforcement. Hardness of the composites increases with increasing volume fraction and mean diameter of SiC particles.

**Table 1** Mechanical properties of the WE43 MMC reinforced with SiC particulates in the as-cast condition

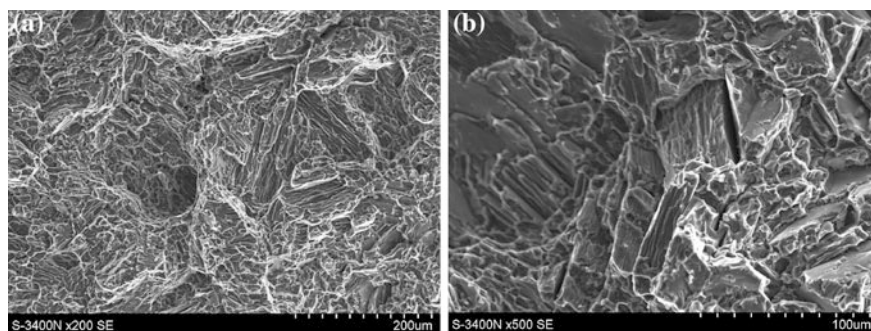
Material	Particle diameter (µm)	Stirring temperature (°C)	Stirring time (min)	Hardness HV2	R <sub>m</sub> (MPa)	R <sub>0,2</sub> (MPa)	A <sub>5</sub> (%)
WE43	–	–	–	59 ± 4	166 ± 18	113 ± 9	6.7 ± 1.5
WE43 + 10 % SiC	15	720	15	68 ± 5	142 ± 4	103 ± 6	2.9 ± 0.3
WE43 + 10 % SiC	15	780	15	66 ± 7	146 ± 9	111 ± 12	2.8 ± 0.2
WE43 + 0.3 % SiC	45	720	15	61 ± 5	150 ± 1	112 ± 10	2.2 ± 1.3
WE43 + 2 % SiC	45	720	15	64 ± 7	151 ± 13	116 ± 6	2.2 ± 1.3
WE43 + 5 % SiC	45	720	15	68 ± 5	146 ± 7	110 ± 6	1.3 ± 0.4
WE43 + 10 % SiC	45	720	15	71 ± 6	149 ± 16	125 ± 14	3.0 ± 0.1
WE43 + 10 % SiC	250	720	15	81 ± 4	112 ± 11	89 ± 6	1.1 ± 0.1

**Table 2** Mechanical properties of the WE43 MMC reinforced with 45  $\mu\text{m}$  SiC particulates after the heat treatment

Material	Particle diameter ( $\mu\text{m}$ )	Stirring temperature ( $^{\circ}\text{C}$ )	UTS (MPa)	YTS (MPa)	El. (%)
WE43 unreinforced	–	–	$222 \pm 4$	$153 \pm 6$	$7.7 \pm 1.3$
WE43 + 0.3 % SiC	45	720	$198 \pm 10$	$147 \pm 3$	$4.0 \pm 2.0$
WE43 + 2 % SiC	45	720	$181 \pm 20$	$146 \pm 6$	$2.0 \pm 1.5$
WE43 + 5 % SiC	45	720	$173 \pm 16$	$148 \pm 6$	$1.9 \pm 1.3$
WE43 + 10 % SiC	45	720	$142 \pm 24$	$115 \pm 2$	$1.4 \pm 2.2$

Heat treatment of composites stirred at 720  $^{\circ}\text{C}$  causes a significant increase of their mechanical and plastic properties (Table 2), however, they are still lower than those exhibited by an unreinforced alloy. The beneficial effect of heat treatment is hindered by the increase of the reinforcement volume fraction. In the case of composites reinforced with 10 % of SiC particulates, the properties are the same as in the as-cast state.

Typical fracture surfaces of heat-treated, unreinforced SiC alloys are shown in Fig. 5. The fracture has a mixed character, with brittle and ductile regions recognizable. Numerous cleavage steps and facets suggest hindered propagation of the fracture. Many secondary cracks are observed at its surface. Fractures of the reinforced alloy are rich in SiC particles (Fig. 6a). Many secondary cracks nucleate at the SiC particles or at the interface between the particle and WE43 alloy. These cracks then propagate within the matrix (Fig. 6b).

**Fig. 5** Fracture surface in the unreinforced WE43 alloy after the tensile tests in the ambient temperature, SEM

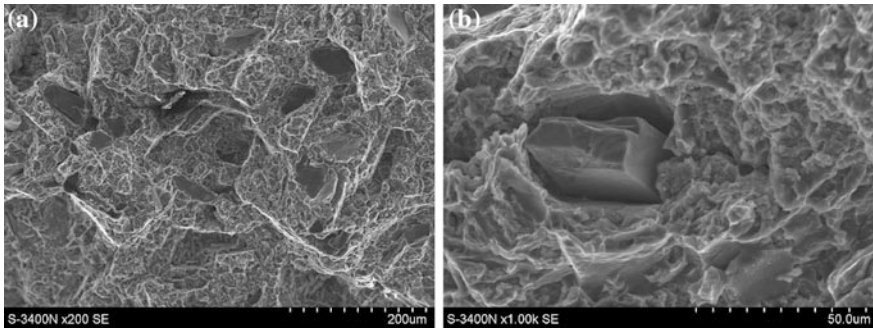


**Fig. 6** Fracture surface in the SiC reinforced WE43 alloy after the tensile tests in the ambient temperature, SEM

### 3.4 Creep Resistance of the Composites

The creep tests were conducted on the heat treated composites reinforced with 45 µm SiC particulates at a temperature of 250 °C and at an applied stress of 90 MPa. The 120 h creep curves for some MMC WE43 are shown in Fig. 7. From the gradient of the secondary stage in the creep curves, the steady-state creep rate can be calculated and the results are shown in Table 3. Creep rate in the investigated composites increases with an increasing volume fraction of the SiC particulates. Creep strain at the rupture of the composites varies from 2.0 % up to 9.0 %, and does not exhibit any tendency with increasing volume fraction of the

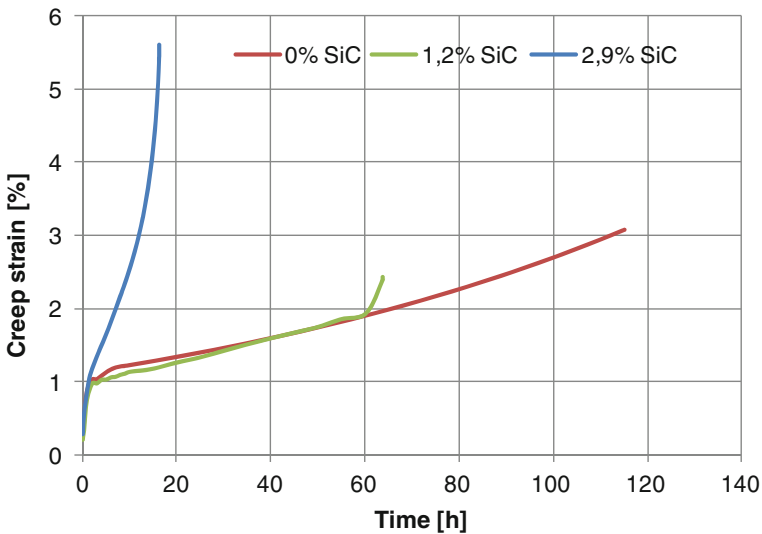


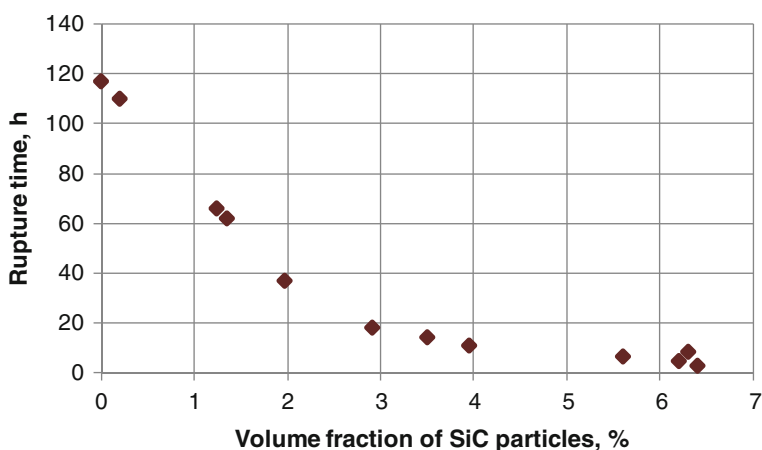
**Fig. 7** Exemplary creep curves for the unreinforced and SiC reinforced WE43 alloy

**Table 3** Creep properties of the WE43 MMC reinforced with 45  $\mu\text{m}$  SiC particulates after the heat treatment

SiC volume fraction (%)	Rupture time (h)	Creep strain (%)	Creep rate $\dot{\epsilon}$ (1/s)
0	–	3.2	$4.13 \times 10^{-8}$
0.2	110	9.0	$7.25 \times 10^{-8}$
1.2	66	2.4	$4.42 \times 10^{-8}$
1.4	62	2.0	$1.75 \times 10^{-8}$
2.0	37	2.4	$1.23 \times 10^{-7}$
2.9	18.2	5.6	$4.59 \times 10^{-7}$
3.5	14.3	5.7	$6.12 \times 10^{-7}$
4.0	11	4.6	$6.18 \times 10^{-7}$
5.6	6.6	3.3	$7.47 \times 10^{-7}$
6.2	4.8	3.5	$1.92 \times 10^{-6}$
6.3	8.5	3.4	$6.35 \times 10^{-7}$
6.4	2.9	2.3	$1.58 \times 10^{-6}$

reinforcement. It may be stated that, in majority it is similar to this, exhibited by an unreinforced WE43 alloy (3.2 %). The time to the rupture decreases with an increasing volume fraction of the SiC particulates (Fig. 8).

There are several creep mechanisms occurring within the composite matrix. First of all, strengthening fine  $\beta''$  and  $\beta'$  phases present in the heat treated alloy, undergo further transformations. Mengucci et al. [15] reports that precipitates in the WE43 alloy after heat treatment for 16 h at 250 °C are not bigger than 200 nm. The microstructure of the WE43 matrix alloy after the creep tests consist of much more coarse, precipitates of  $\beta$  phase (Fig. 9a) easily recognizable even with SEM microscopy (Fig. 9b). The length of these precipitates is usually higher than

**Fig. 8** Time to the rupture versus reinforcement volume fraction

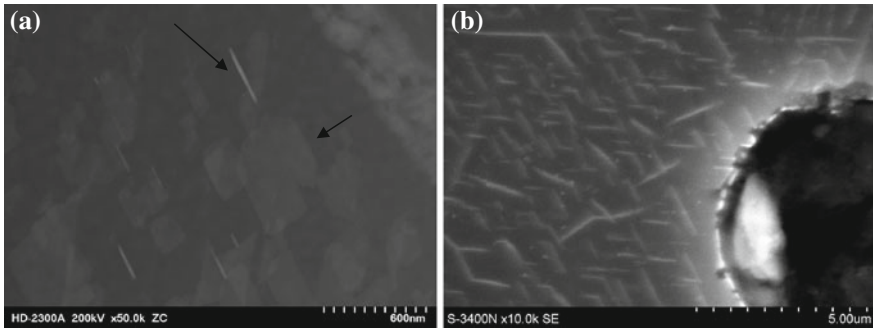


**Fig. 9** Strengthening phases in the WE43 matrix alloy after creep tests

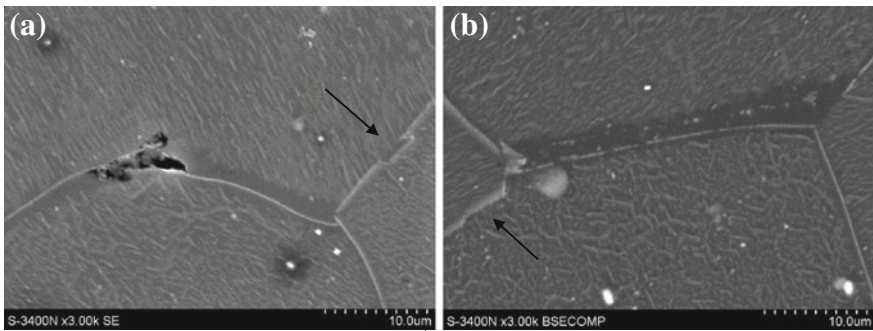


**Fig. 10** Grain boundaries migration and zones depleted in the solute elements, SEM

300 nm and their width is equal to about 200 nm. The biggest precipitates observed by SEM are even a few micrometers long.

Temperature activated diffusion leads to the migration of grain boundaries in the direction of the applied load. The migration effects in the formation of solute element depleted zones in the vicinity of the boundaries (Fig. 10). It can be seen, that these denuded zones are clearly the weakest point in the microstructure, as many cracks nucleate within them (Fig. 11). The grain boundary sliding can be blocked by fine primary phase particles present within the structure (Fig. 12).

The creep cavities found within the composites microstructure are observed at the grain boundaries triple junctions. Nearly perfectly circular cavities are also observed within the WE43 magnesium alloy dendrites (Fig. 13). All above mentioned phenomena were observed both in unreinforced WE43 alloy as well as in the SiC reinforced composites.

No further transformations are observed at the interfaces between SiC particulates and the composite’s matrix. The thin layer enriched in Zr and Si is still present, without significant thickening (Fig. 14a). At the layer, fine Zr–Si and  $Y_2O_3$  (Fig. 15) phases are observed. A thin zone depleted in alloying elements is visible



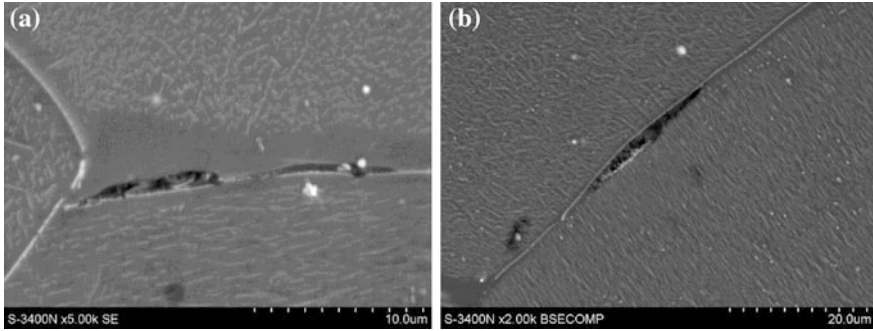


Fig. 11 Cracks in denuded zones at the grain boundaries, SEM

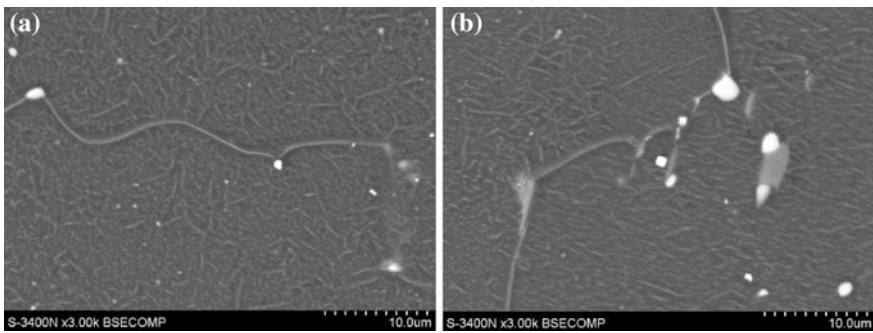


Fig. 12 Phases blocking grain boundaries sliding, SEM

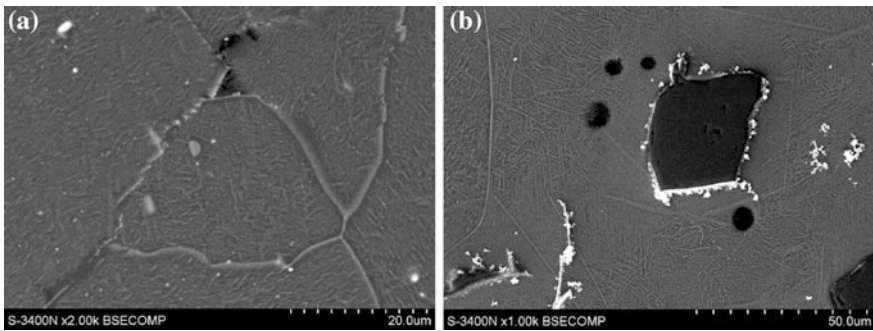
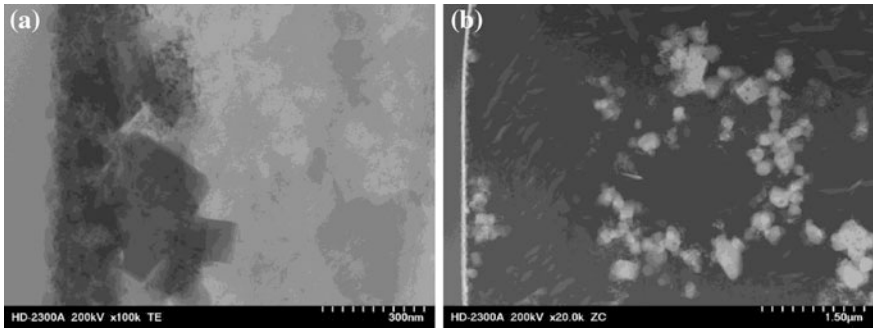
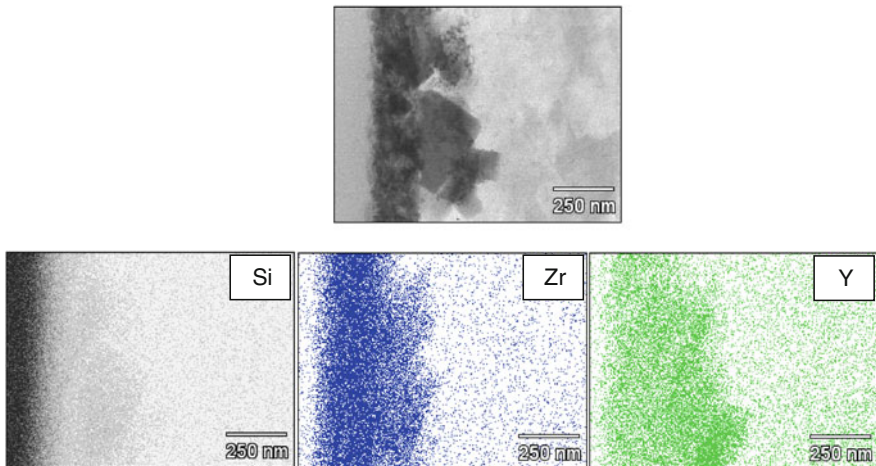


Fig. 13 Creep cavities in the WE43 alloy microstructure, SEM; **a** at the grain boundaries triple junctions; **b** within the  $\alpha$ -Mg dendrites

near the particles (Fig. 14b). Even though the SiC/WE43 matrix interface did not undergo any transformations during the creep, many cracks are observed at the interfaces perpendicular to the applied loads (Fig. 16).



**Fig. 14** SiC/WE43 interface, STEM; **a** Zr-Si layer and and Y<sub>2</sub>O<sub>3</sub> phase; **b** Yttrium depleted zone between the particle and matrix



**Fig. 15** Mapping of elements at the SiC/WE 43 matrix interface after the creep tests

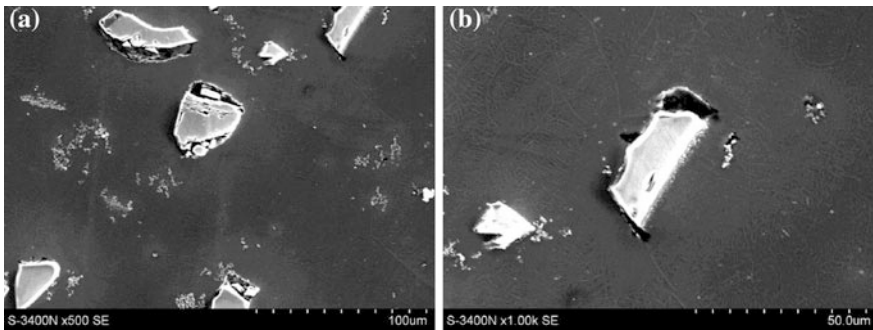


**Fig. 16** Cracks at the SiC/WE43 interfaces perpendicular to the applied loads, SEM

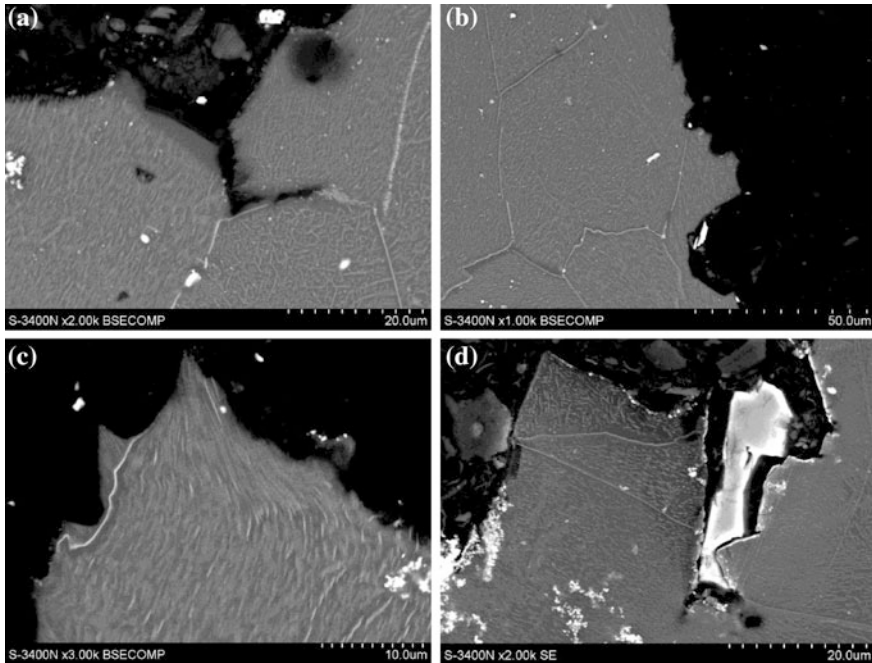


**Fig. 17** Fracture surface of the crept composites, SEM; **a** cracks propagating through the denuded zones; **b** intercrystalline fracture; **c** plastic deformation at the fracture profile; **d** broken SiC/WE43 interfaces

Secondary cracks are propagating through the denuded zones at the grain boundaries (Fig. 17a). This leads to the formation of intergranular fracture. The fracture often propagates also through the softened  $\alpha$ -Mg dendrites (Fig. 17b). Signs of plastic deformation (Fig. 17c) are observed at these places, which indicates a change from the brittle fracture at ambient temperature to the more ductile character of the fracture at the 250 °C. The SiC particles observed at the fracture surface are detached from the matrix, which indicates that fracture propagates preferentially through the SiC/WE43 interfaces (Fig. 17 c, d).

## 4 Discussion

The WE43 MMC reinforced with SiC particulates were prepared by means of stir casting. Investigations revealed that the application of SiC particulates with a mean diameter of 45  $\mu\text{m}$  enables achieving a relatively uniform distribution of reinforcement. The addition of larger particles causes the settling down of the reinforcement both in the crucible and mould. The introduction of smaller particles led to the formation of numerous agglomerates after stirring at 720 °C. The distribution

of the small particles is relatively homogenous after stirring the melt at 780 °C. However, at this temperature, significant reactions between the reinforcement and the liquid alloy take place. The reactions lead to formation of yttrium containing phases. Formation of these phases leads to the depletion of the composite matrix in yttrium, which causes the lack of age-hardening response.

Stirring at 720 °C seems to be a relatively good compromise between the homogenous distribution of 45 µm particles and the reasonably small reaction between the liquid alloy and SiC. Literature [16] suggests the mechanism of degradation of SiC particle with molten magnesium. In the first stage of reaction, magnesium reacts with the SiO<sub>2</sub> layer covering SiC particulates. As a result, MgO and elemental silicon are formed. In the next stage, molten magnesium reacts with SiC, leading to its dissolution. Elemental carbon may precipitate in the form of graphite, reacting in turn with the excess of Si and form fine β-SiC crystals. In the last stage, during cooling, as the solubility of Si in magnesium decreases, Mg<sub>2</sub>Si phases may form. However, this mechanism is true for pure magnesium reacting with SiC. In the investigated composite, the magnesium is alloyed with Zr and Y, which are more reactive than Mg, thus, changing the above mentioned mechanism. In the composite stirred at 720 °C the Zr and Si rich layer has been found to cover the SiC particles. Additionally Y<sub>2</sub>O<sub>3</sub> and Zr<sub>2</sub>Si phases have been found at the interface. The following mechanism is suggested for the dissolution of the reinforcing phase at 720 °C. In the first stage yttrium reacts with SiO<sub>2</sub> layer forming Y<sub>2</sub>O<sub>3</sub> in reaction (1).



The formation enthalpy of this reaction at the 720 °C is equal about -518 kJ mol<sup>-1</sup> of Y<sub>2</sub>O<sub>3</sub> and is about four times smaller than the enthalpy of the MgO formation in the analogical reaction (-128.5 kJ mol<sup>-1</sup>). This indicates that the yttrium reaction with SiO<sub>2</sub> is much more favourable. As the reaction (1) created zone depleted in yttrium near the SiC particle, elemental Si from this reaction may react only with Zr or Mg. As the main Zr-Si compound found within the structure of the composite is Zr<sub>2</sub>Si, the following reaction (2) is suggested for the second stage of particle degradation:



The enthalpy of this reaction is equal to about -209 kJ mol<sup>-1</sup> of Zr<sub>2</sub>Si. The reaction (2) is also more thermodynamically favourable than the similar reaction of Mg<sub>2</sub>Si formation, with the enthalpy of which is about -69 kJ mol<sup>-1</sup>. The reaction of Zr and Mg with SiC is also possible, however, their enthalpies are higher and are equal: -145 kJ mol<sup>-1</sup> for formation Zr<sub>2</sub>Si and -5.5 kJ mol<sup>-1</sup> for Mg<sub>2</sub>Si. Thin Zr-Si layers formed at the interface seems to be a quite effective barrier for the element's diffusion and further reactions. The lack of reactions significantly depleting the matrix in yttrium enables age-hardening of the composite cast at 720 °C.

Addition of SiC particles to the WE43 magnesium alloy led to the decrease of mechanical properties of the as-cast composite. The tensile strength decreased with increasing reinforcement size and its volume fraction. Yield strength, however, did not decrease significantly after the addition of SiC particles. Only in the case of the addition of large, 250  $\mu\text{m}$  particles, a decrease in yield strength was observed. Similar tendencies are observed in the case of the heat treated composite reinforced with 45  $\mu\text{m}$ . The tensile strength of the heat treated material decreases with increasing SiC volume fraction, while yield strength does not decrease. It can be stated that ultimate tensile strength is affected by the SiC addition, while yield strength of the composite depends only on the state of the WE43 matrix. Many authors present results of their investigations on the mechanical properties of SiC reinforced magnesium alloys. It can be stated that addition of the SiC particles may lead to an increase of material mechanical properties, which is not in agreement with our investigations. However, our research was conducted on composites reinforced with relatively big particulates, which may act as structural notches, decreasing materials' mechanical properties. On the other hand, applications of smaller SiC particulates during conventional stir casting of WE43 magnesium alloys with stirring conducted in the liquid state is difficult, due to the formation of SiC agglomerates and significant reaction between the reinforcement and liquid metal. Some research [10, 17] was done on the promising stir casting technique with stirring in the semi-solid state, slightly below the liquidus line of the alloy. Small particles may be successfully introduced to the alloy with this technique, ensuring an increase of material properties.

The creep strength of the composites is also decreasing with increasing particulates volume fraction. Cabbibo et al. [18] found that the main strengthening mechanisms at 250  $^{\circ}\text{C}$  for SiC reinforced Mg-RE alloys are, decreasingly: Hall-Petch matrix strengthening with grain and cells boundaries; Strengthening by mismatch in thermal expansion of SiC particles and the matrix; Orowan strengthening of the matrix; Load transfer between the particle and matrix and few more, less important. All these factors lead to an increase of creep resistance of the SiC strengthened WE43 alloy. However, it is again true for the particles smaller than 10  $\mu\text{m}$ . The presence of big particles probably does not ensure effective strengthening by mismatch in thermal expansion coefficients. Presence of the particles detached from the matrix on the fracture surface clearly indicates that SiC/WE43 interface in the investigated composite is not strong enough to transfer the loads to the particle.

## 5 Conclusions

1. WE43 MMC reinforced with 45  $\mu\text{m}$  SiC particulates were successfully produced by stir casting. Stirring of the melt at 720  $^{\circ}\text{C}$  leads to formation of uniform microstructure with SiC particles present at grain boundaries.

2. WE43 MMC reinforced with SiC particulates cast at 720 °C exhibit strong response to age hardening, which significantly increases mechanical properties of the composites.
3. Addition of SiC particulates causes an increase in hardness of the WE43 alloy. However it decreases the tensile strength of the material. With increasing volume fraction of the reinforcement, the tensile strength of the composite both in as-cast and heat treated condition decreases.
4. Addition of SiC particulates does not influence the yield strength of the material, the yield strength is rather dependent upon the WE43 matrix state.
5. Creep resistance of the composite decreases with increasing volume fraction of SiC reinforcement.

**Acknowledgments** The present work was supported by the National Centre for Research and Development under the project LIDER/29/198/L-3/11/NCBR/2012

## References

1. Friedrich H, Mordike BL (2006) Magnesium technology, metallurgy, design data, applications. Springer, Berlin
2. Luo AA (2004) Recent magnesium alloy development for elevated temperature applications. *Int Mater Rev* 49:13–30
3. Rzychoń T, Adamczyk-Cieślak B, Kielbus A et al (2012) The influence of hot-chamber die casting parameters on the microstructure and mechanical properties of magnesium-aluminum alloys containing alkaline elements. *Mat-wiss u Werkstofftech* 43:421–426
4. Dybowski B, Kielbus A, Jarosz R (2014) Effect of mould components on the cooling rate, microstructure, and quality of We43 Magnesium casting alloy. *Arch Metall Mater* 59:1527–1532
5. Kielbus A, Rzychoń T (2011) The intermetallic phases in sand casting Magnesium alloys for elevated temperature. *Mater Sci Forum* 690:214–217
6. Rzychoń T, Kielbus A, Lityńska-Dobrzyńska L (2013) Microstructure, microstructural stability and mechanical properties of sand-cast Mg-4Al-4RE alloy. *Mater Charact* 83:21–34
7. Ferkel H, Mordike BL (2001) Magnesium strengthened by SiC nanoparticles. *Mater Sci Eng A* 298:193–199
8. Rashad M, Pan F, Asif M et al (2014) Powder metallurgy of Mg-1 %Al-1 %Sn alloy reinforced with low content of graphene nanoplatelets (GNPs). *J Ind Eng Chem* 20:4250–4255
9. Shen MJ, Wang XJ, Zhang MF et al (2014) Fabrication of bimodal size SiCp reinforced AZ31B magnesium matrix composites. *Mater Sci Eng A* 601:58–64
10. Wang XJ, Wang NZ, Wang LY et al (2014) Processing, microstructure and mechanical properties of micro-SiC particles reinforced magnesium matrix composites fabricated by stir casting assisted by ultrasonic treatment processing. *Mater Des* 57:638–645
11. Lu L, Lim CYH, Yeong WM (2004) Effect of reinforcements on strength of Mg 9 %Al composites. *Compos Struct* 66:41–45
12. Tzamtzis S, Barekar NS, Hari Babu N et al (2009) Processing of advanced Al/SiC particulate metal matrix composites under intensive shearing—A novel Rheo-process. *Compos A* 40:144–151
13. Kielbus A, Rzychoń T (2011) Mechanical and creep properties of Mg-4Y-3RE and Mg-3Nd-1Gd magnesium alloys. *Procedia Eng* 10:1835–1840

14. Nie JF, Muddle BC (2000) Characterisation of strengthening precipitate phases in a Mg–Y–Nd alloy. *Acta Mater* 48:1691–1703
15. Mengucci P, Barucca G, Riontino G et al (2008) Structure evolution of a WE43 Mg alloy submitted to different thermal treatments. *Mater Sci Eng A* 479:37–44
16. Epicier T, Bosselet F, Viala JC (1994) Microstructure of interfaces between a magnesium matrix and preoxidized silicon carbide particles. *Interface Sci* 1:213–221
17. Aravindan S, Rao PV, Ponappa K (2015) Evaluation of physical and mechanical properties of AZ91D/SiC composites by two step stir casting process. *J Magnes Alloys* 3:52–62
18. Cabibbo M, Spigarelli S (2011) A TEM quantitative evaluation of strengthening in an Mg–RE alloy reinforced with SiC. *Mater Charact* 62:959–969

# Primary Dendrite ARM Spacing Effects upon Mechanical Properties of an AL-3Wt% CU-1Wt% LI Alloy

G.A. Santos, P.R. Goulart, A.A. Couto and A. Garcia

**Abstract** The imposition of a wide range of operational conditions in foundry and castings processes generates, as a direct consequence, a diversity of solidification structures. It is well known that mechanical properties depend on solidification structures. The literature presents relationships between yield strength and grain size, such as the Hall-Petch's equation, or ultimate tensile strength and dendrite arm spacing. In this work, an Al-3wt%Cu-1wt%Li alloy was solidified under upward unsteady state heat flow conditions. Heat was directionally extracted only through a water-cooled bottom made of steel (SAE 1020). The aim of the present study is to obtain correlations between the as-cast microstructure, solidification thermal variables and mechanical properties of an Al-3wt%Cu-1wt%Li alloy casting. The results include tip growth rate ( $V_L$ ), cooling rate ( $\dot{T}$ ), primary dendrite arm spacing ( $\lambda_1$ ), ultimate tensile strength ( $\sigma_{UTS}$ ) and yield strength ( $\sigma_y$ ) as a function of solidification conditions imposed by the metal/mold system. It is found that the primary dendrite arm spacing decreases with the increase in tip growth rate and cooling rate. In both cases ( $\sigma_{UTS}$  and  $\sigma_y = 0.2 \text{ \%}\epsilon$ ), the finer dendritic arrangement presents superior mechanical properties.

---

G.A. Santos (✉) · P.R. Goulart

Department of Mechanical, Federal Institute of São Paulo, IFSP, São Paulo, SP, Brazil  
e-mail: givanildo@ifsp.edu.br

P.R. Goulart

e-mail: pedrogoulart1951@yahoo.com.br

A.A. Couto

Department of Materials Engineering, Institute of Nuclear and Energy Research, IPEN, São Paulo, SP, Brazil  
e-mail: acouto@ipen.br

A.A. Couto

Department of Materials Engineering, Mackenzie Presbyterian University, UPM, São Paulo, SP, Brazil

A. Garcia

Department of Materials Engineering, State University of Campinas, UNICAMP, Campinas, SP, Brazil  
e-mail: amaurig@fem.unicamp.br



**Keywords** Al–3wt%Cu–1wt%Li alloy · Primary dendrite arm spacing · Solidification thermal variables · Mechanical properties

## 1 Introduction

The high specific properties of Al–Li alloys have led to tremendous development effort aimed in particular at aerospace applications. Al–Li castings and cast alloys that combine the good properties of Al–Li alloys with foundry technology have great potential in both the aircraft and automotive sectors [1]. To provide a basis for composition design of these alloys, a study on the solidification process, microstructure and mechanical properties of Al–Li cast alloys has been carried out.

Solidification of metals involves the transformation of the molten metal back into the solid state. The transformation of a liquid into solid is probably the most important phase transformation in applications of science and engineering materials. Casting of metals is an example of solidification process. The principle of casting seems simple: melt the metal, pour it into a mold, and let it cool and solidify; yet there are many factors and variables that must be considered in order to accomplish a successful casting operation. The physical mechanism of solidification that occurs during casting influences the structure and properties of metals [2].

The effects of microstructure on metallic alloys properties has been highlighted in various studies and particularly, the influence of grain size and dendrite arm spacing upon the mechanical properties has been reported [2–10]. Although the metallurgical and micromechanical aspects of the factors controlling microstructure, unsoundness, strength and ductility of as-cast alloys are complex, it is well known that solidification processing variables are of high importance. In the as-cast state an alloy may possess within individual grains, a dendritic network where solute concentration varies continuously, a complex dispersion of second phases and possibly porosity and inclusions [6]. In addition to the above obstacles to slip, the grain boundary is present at the grain perimeter. It is generally found that the grain size reduction increases the metal strength. The well known Hall-Petch equation shows that the yield strength is proportional to the reciprocal of the square root of the grain diameter [5].

For cast metals, however, it is not always true that the strength improves with decreasing grain size. Strength will increase with grain size reduction only if the production of small grains does not increase the amount of microporosity, the percentage volume of second phase or the dendrite spacing [6].

It is well known that there is a close correlation between thermal variables and the solidification structure and as a direct consequence, morphological structure parameters such as grain size and dendritic arm spacing also depend on solidification conditions imposed by the metal/mould system. Thus, the control of solidification thermal variables such as tip growth rate ( $V_L$ ) and cooling rate ( $\dot{T}$ ) permits

a range of microstructures to be obtained [11–19]. Reports can be found in the literature relating microstructural characteristics with mechanical properties (i.e., ultimate tensile strength, and yield strength) [2–10].

The present work focuses on the influence of heat transfer solidification variables on the microstructural formation of Al–3wt%Cu–1wt%Li alloy castings and on the development of correlations between dendritic spacing and mechanical properties. Experimental results include tip growth rate ( $V_L$ ) and cooling rate ( $\dot{T}$ ), primary dendrite arm spacing ( $\lambda_1$ ), ultimate tensile strength ( $\sigma_{UTS}$ ) and yield strength ( $\sigma_y$ ).

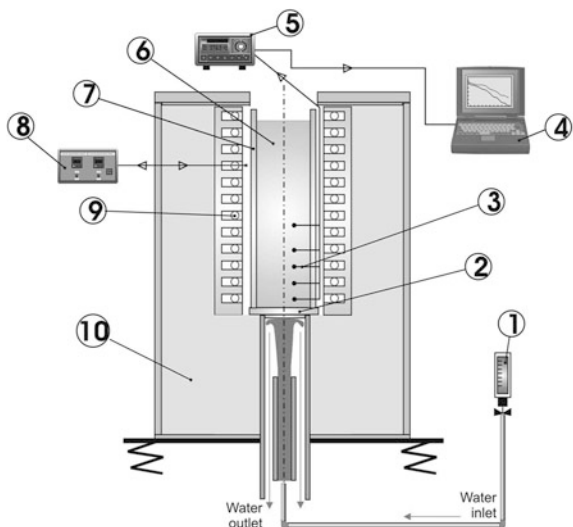
## 2 Materials and Methods

Figure 1 shows the casting assembly used in the experiments. It can be seen that heat is directionally extracted only through a water-cooled bottom made of steel, promoting vertical upward directional solidification. The use of bottoms made of low carbon steel (SAE 1020) permitted a wide range of solidification conditions to be analyzed. As a consequence, a wide range of dendritic spacings should be expected.

A stainless steel split mold was used having an internal diameter of 60 mm, height 157 mm and a 5 mm wall thickness. The lateral inner mold surface was covered with a layer of insulating alumina to minimize radial heat losses. The bottom part of the mold was closed with a thin (3 mm) steel sheet.

Experiments were performed with an Al–3wt%Cu–1wt%Li alloy. The mentioned chemistry was evaluated regarding to dendritic growth while tensile tests were performed with this aluminum alloy. The thermophysical properties of the aluminum and studied alloy are summarized in Table 1. Specific heats, latent heats

**Fig. 1** Schematic representation of the experimental setup: 1 rotameter; 2 heat-extracting bottom; 3 thermocouples; 4 computer and data acquisition software; 5 data logger; 6 casting; 7 mold; 8 temperature controller; 9 electric heaters; 10 insulating ceramic shielding

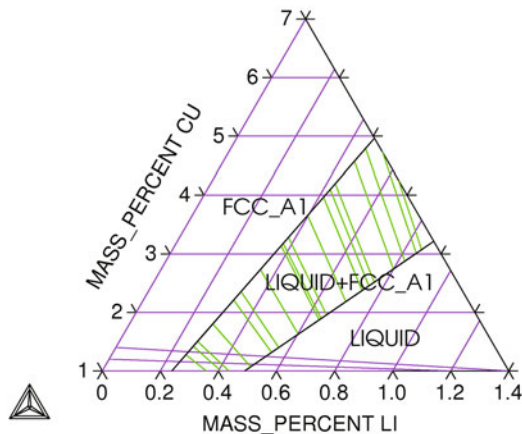


**Table 1** Casting material used for experimentation and the corresponding thermophysical properties

Properties	Symbol/units	Al (pure)	Al-3wt%Cu-1wt%Li
Thermal conductivity	$K_S$ [W m <sup>-1</sup> K <sup>-1</sup> ]	221.6	216
	$K_L$ [W m <sup>-1</sup> K <sup>-1</sup> ]	91.9	93
Specific heat	$c_S$ [J kg <sup>-1</sup> K <sup>-1</sup> ]	1255	1170
	$c_L$ [J kg <sup>-1</sup> K <sup>-1</sup> ]	1175	1140
Density	$\rho_S$ [kg m <sup>-3</sup> ]	2700	2887
	$\rho_L$ [kg m <sup>-3</sup> ]	2389	2554
Latent heat of fusion	$L$ [J kg <sup>-1</sup> ]	383,000	322,000
Melting temperature	$T_M$ [°C]	660	
Liquidus temperature	$T_{Liq}$ [°C]		655
Solidus temperature	$T_{Sol}$ [°C]		645

**Fig. 2** Al-Cu-Li partial phase diagram furnished by the software ThermoCalc AB, version N

THERMO-CALC (2009.06.04:13.44) :AL-CU-LI at T=930 K  
 DATABASE:PURE4  
 T=930, P=1E5, N=1;

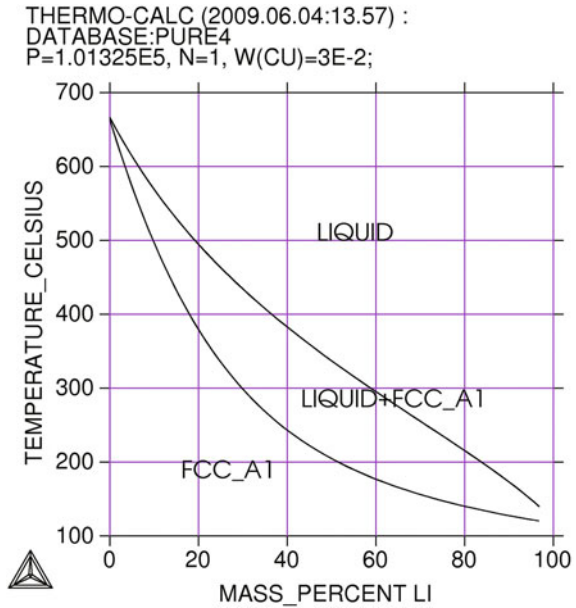


of fusion and *liquidus* temperatures were obtained by Thermo-Calc<sup>1</sup> computations. The Al-Cu-Li partial phase diagram and the Al-Cu-Li isomorph phase diagram with 3wt% Cu (constant) were also computed by Thermo-Calc and it is shown in Figs. 2 and 3, respectively.

The initial melt temperature ( $T_p$ ) was standardized at 10 °C above the *liquidus* temperature ( $T_{Liq}$ ) of the studied alloy. The thermal contact condition at the metal/mold interface was also standardized with the heat-extracting surface at the mold bottom being polished.

<sup>1</sup>Thermo-Calc software is an exclusive copyright property of the STT Foundation (Foundation of Computational Thermodynamics, Stockholm, Sweden).

**Fig. 3** Al-Cu-Li isomorph phase diagram with 3wt% Cu (constant) furnished by the software ThermoCalc AB, version N



Continuous temperature measurements in the casting were monitored during solidification via the output of a bank of fine type K thermocouples (made from 0.2 mm diameter wire) sheathed in 1.6 mm diameter steel tubes, and positioned at 4, 8, 12, 22, 52, 68 and 88 mm from the heat-extracting surface at the bottom. The thermocouples were calibrated at the melting point of aluminum exhibiting fluctuations of about 1 °C. All of the thermocouples were connected by coaxial cables to a data logger interfaced with a computer, and the temperature data, read at intervals of 0.1 s, were automatically acquired.

Each cylindrical ingot was subsequently sectioned along its vertical axis, ground and etched with an acid solution to reveal the macrostructure (Poulton’s reagent: 5 mL H<sub>2</sub>O; 5 mL HF—48 %; 30 mL HNO<sub>3</sub>; 60 mL HCl).

Selected transverse (perpendicular to the growth direction) sections of the directionally solidified specimens at different positions from the metal/mold interface were polished and etched with Tucker’s reagent (a solution of 45 mL HCl; 15 mL HNO<sub>3</sub>, 15 mL HF and 25 mL distilled water) for metallography. Image processing systems Neophot 32 (Carl Zeiss, Esslingen, Germany) and Leica Quantimet 500 MC (Leica Imaging Systems Ltd., Cambridge, England) were used to measure primary dendrite arm spacings,  $\lambda_1$ , (about 30 independent readings for each selected position, with the average taken to be the local spacing) and their distribution range. The method used for measuring the primary arm spacing on the transverse section was the triangle method [13].

Transverse specimens were cut from the castings, as indicated in Fig. 4, and prepared for tensile testing according to specifications of ASTM standard E 8M [20]. In order to ensure reproducibility of results, three specimens were tested for each

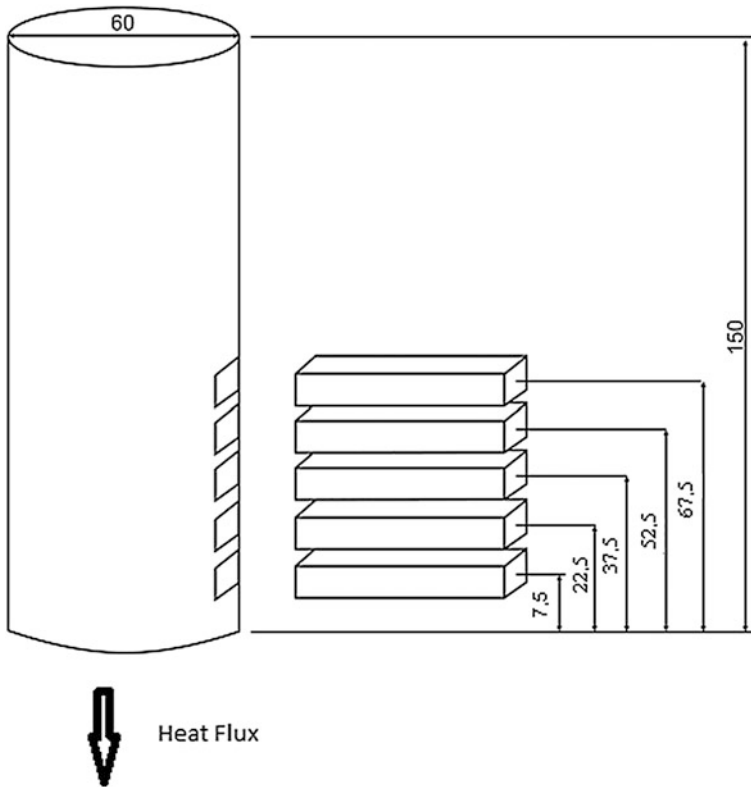


Fig. 4 Removal of specimens for tensile tests (dimensions in mm)

selected position, and mean values of yield tensile strength, ultimate tensile strength have been determined at different positions with respect to the casting surface.

### 3 Results and Discussion

Figure 5 shows cooling curves corresponding to the thermal responses of seven thermocouples inserted into the casting at different positions from the cooled surface. The data were acquired during the solidification of Al–3wt%Cu–1wt%Li alloy.

The thermocouples readings have been used to generate a plot of position from the metal/mold interface as a function of time corresponding to the *liquidus* ( $t_L$ ) front passing by each thermocouple. A curve fitting technique on these experimental points has generated a power function of position as a function of time (Fig. 6).

The derivative of this function with respect to time has yielded values for tip growth rate,  $V_L = dP/dt$ . Figure 7 shows the experiment performed with an Al–3wt% Cu–1wt%Li alloy. The line represents an empirical power function fit with the experimental points. A single experimental law represents the experimental scatter (Fig. 8).

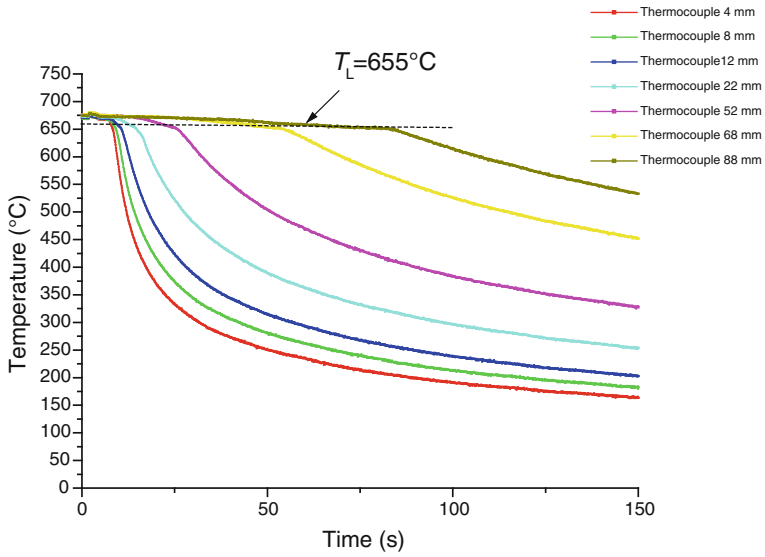


**Fig. 5** Experimental cooling curves for seven thermocouples inside the casting (Al-3wt%Cu-1wt%Li)

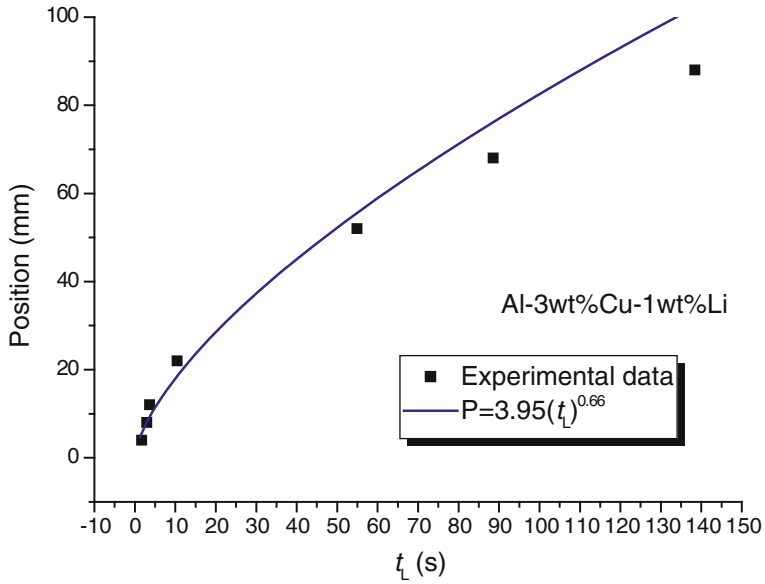


**Fig. 6** Position from the metal/mold interface as a function of time corresponding to the *liquidus* ( $t_L$ ) for thermocouples inside the casting (Al-3wt%Cu-1wt%Li)

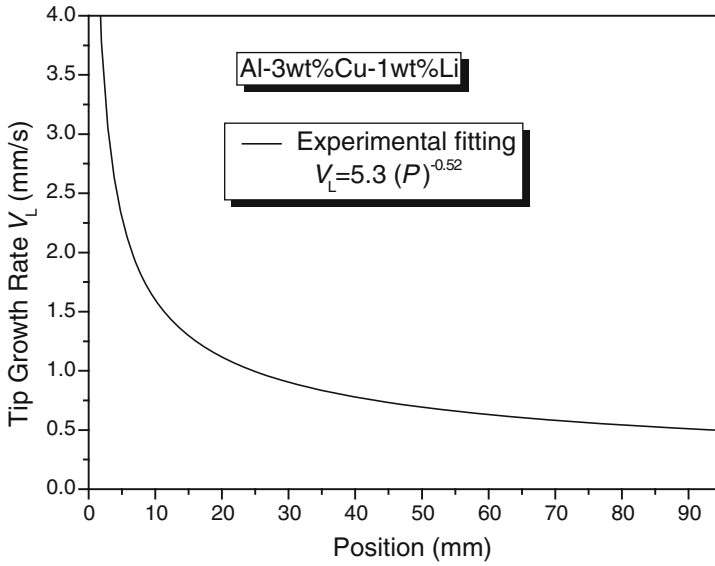


**Fig. 7** Tip growth rate as a function of position from the metal/mold interface for an Al-3wt% Cu-1wt%Li alloy

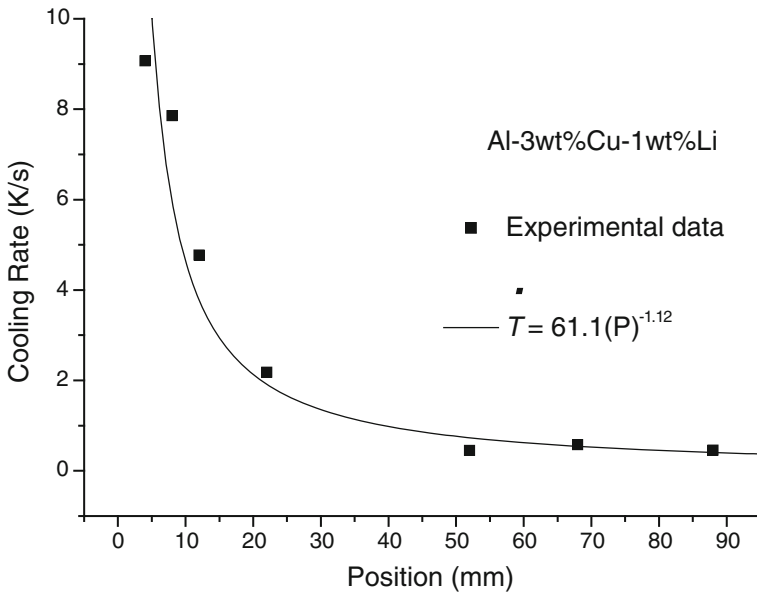


**Fig. 8** Cooling rate as a function of position from the metal/mold interface for an Al-3wt%Cu-1wt%Li alloy

**Fig. 9** Macrostructure of Al-3wt%Cu-1wt%Li alloy casting



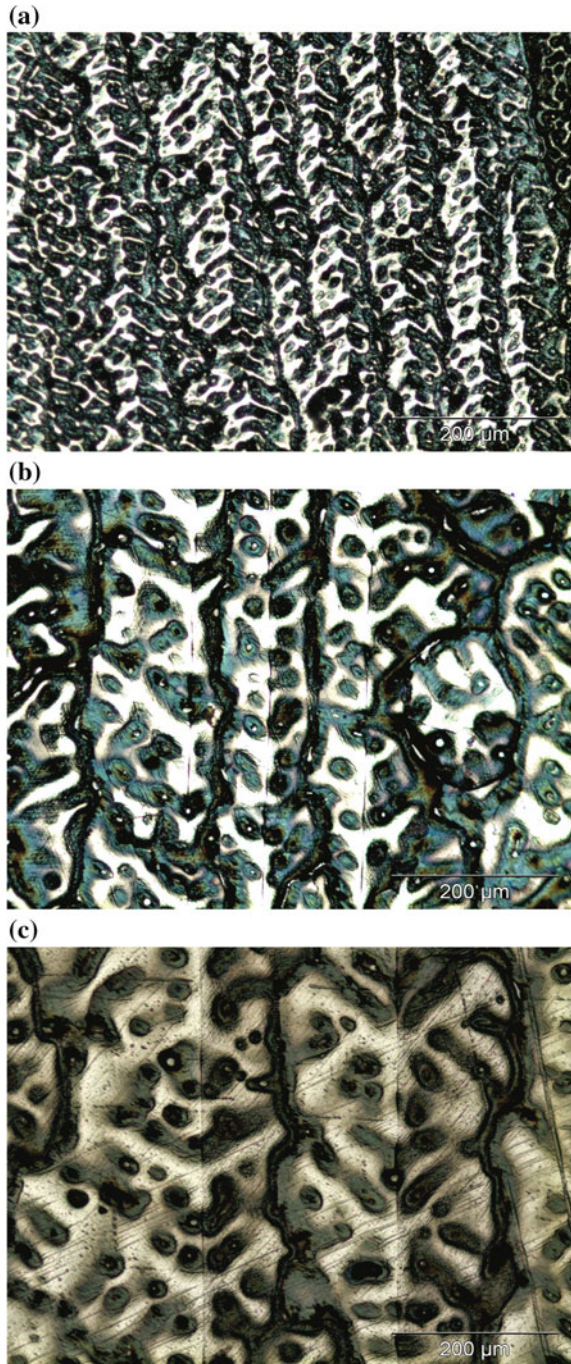
The data acquisition system, in which temperature readings are collected at a frequency of 0.5 s, permits accurate determination of the slope of the experimental cooling curves. The cooling rate was determined by considering the thermal data recorded immediately after the passing of the *liquidus* front by each thermocouple.

The macrostructure of the directionally solidified casting are shown in Fig. 9. Columnar growth has prevailed along the casting length for the alloy experimentally examined.

Typical microstructures on transverse sections of Al-3wt%Cu-1wt%Li alloy casting are shown in Fig. 10. The dendrite arm spacings were sufficiently distinct to permit accurate measurements along the casting length.



**Fig. 10** Experimental  $\lambda_1$  at different positions from the casting surface for the Al-3wt%Cu-1wt%Li alloy: 10 mm (a), 30 mm (b) and 60 mm (c)



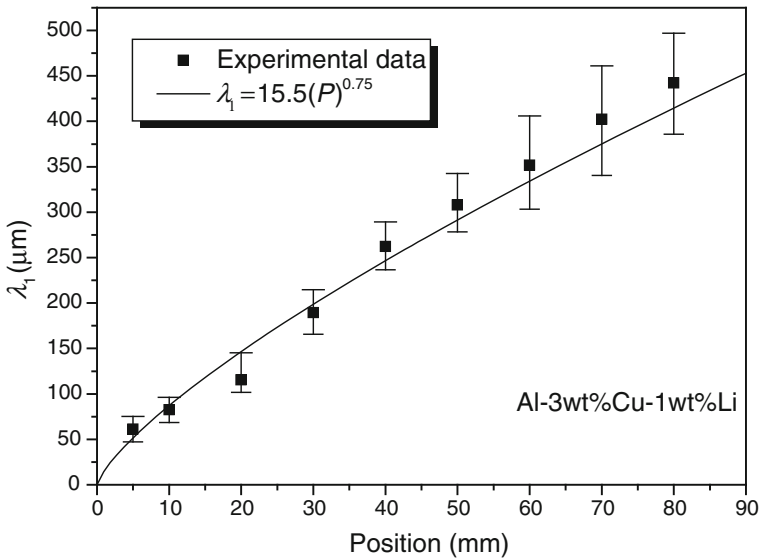


**Fig. 11** Primary dendrite arm spacing as a function of position from the metal/mold interface for an Al-3wt%Cu-1wt%Li alloy

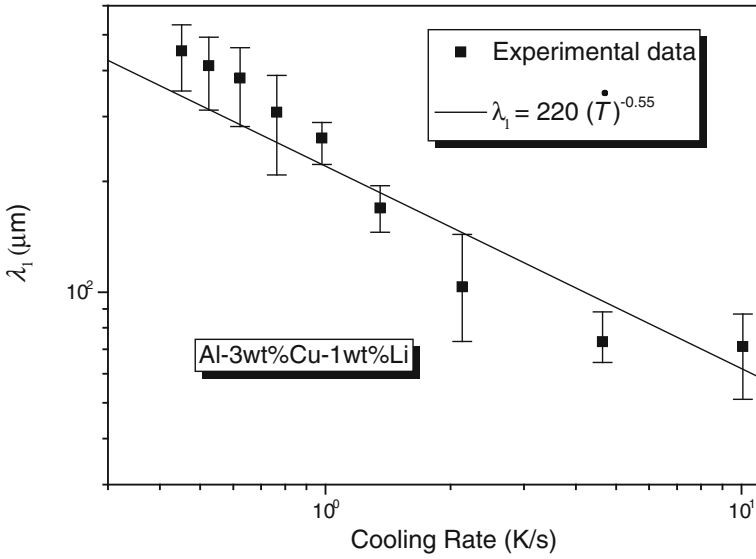
Figure 11 shows the measured primary dendrite arm spacing ( $\lambda_1$ ) expressed as a function of distance from the metal/mold interface. It can be observed that, as expected,  $\lambda_1$  increases with distance from casting surface due to the corresponding decrease in cooling rate and tip growth rate.

Figures 12 and 13 show the mean experimental values of primary dendrite arm spacings ( $\lambda_1$ ) as a function of cooling rate and tip growth rate, respectively, measured from the afore mentioned microstructures. Points are experimental results and lines represent an empirical fit of the experimental points, with dendritic spacings being expressed as a power function either of tip growth rate or of cooling rate.

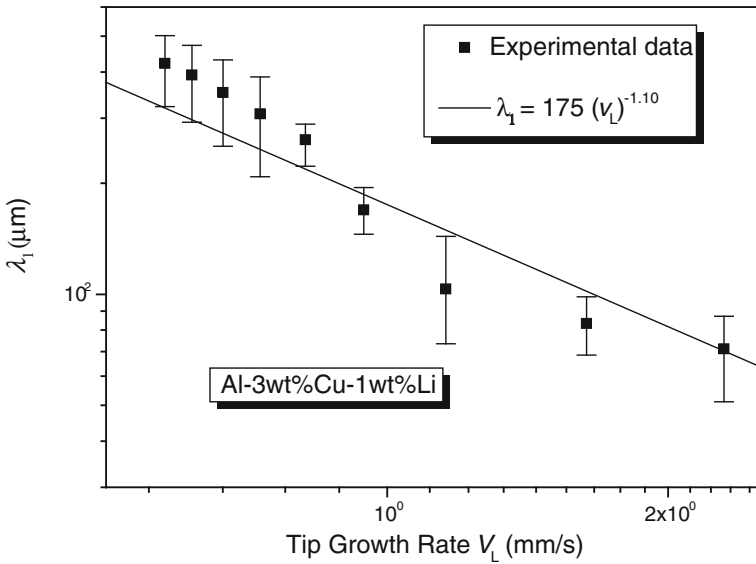
It can be seen that a  $-0.55$  power law characterizes the experimental variation of primary spacings with cooling rate (Fig. 12). This is in agreement with recent observations reported by Rocha et al. [13] that exponential relationships best generate the experimental variation of primary dendritic arms with cooling rate along the unsteady-state solidification of Sn-Pb and Al-Cu alloys. Peres and co-authors [21] have also found this type of relation as the best one regarding to unsteady-state directional solidification of Al-Si hypoeutectic alloys.

Figure 14 shows the primary dendrite stems have grown perpendicularly to the imposed loading in the tests, which probably becomes the primary dendrite an efficient barrier against the tensile forces. Because of that, the mechanical parameters determined through the tensile tests were correlated with primary dendrite arm spacing.

The results of the tensile tests are summarized in Fig. 15a, b, where the ultimate tensile strength ( $\sigma_{UTS}$ ) and the yield strength [ $\sigma_{y=0.2}$ ] (0.2 % proof stress) are related



**Fig. 12** Primary dendrite arm spacing as a function of cooling rate for an Al-3wt%Cu-1wt%Li alloy



**Fig. 13** Primary dendrite arm spacing as a function of tip growth rate for an Al-3wt%Cu-1wt%Li alloy

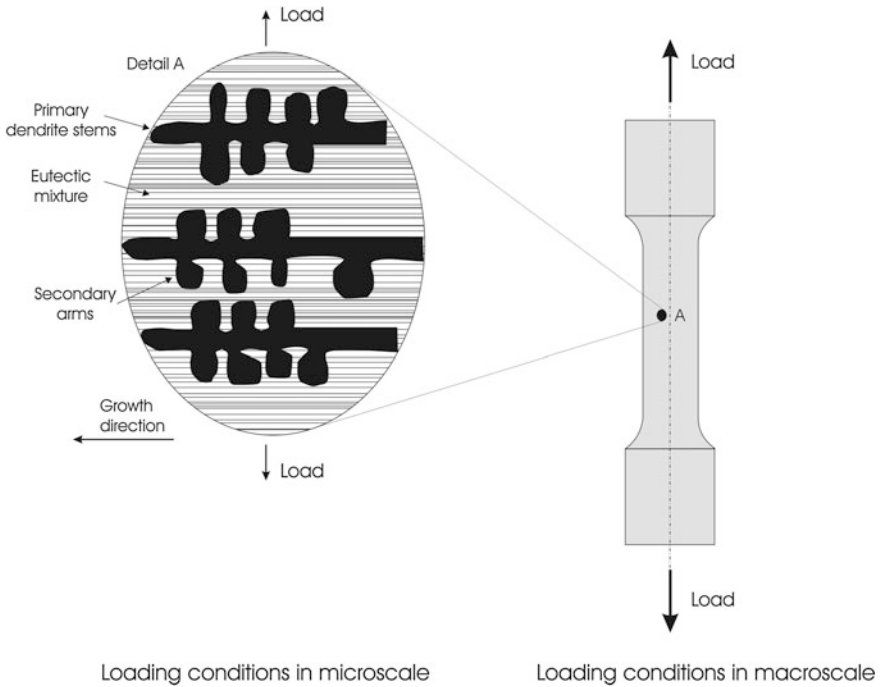


**Fig. 14** Aligned dendritic network dealing with the uniaxial loading of tensile tests

to the primary dendrite arm spacing, respectively. It can be seen that both  $\sigma_{UTS}$  and  $\sigma_y$  increase with decreasing dendrite arm spacing.

#### 4 Conclusions

In order to investigate the role of primary dendrite arm spacing on mechanical properties of the Al-3wt%Cu-1wt%Li alloy, solidification experiments and tensile tests were carried out. The following main conclusions can be drawn from the present experimental investigation:

- (1) The experimental expressions correlating the ultimate tensile strength and yield strength with primary dendrite arm spacing for an Al-3wt%Cu-1wt%Li alloy have shown that a finer structural dendritic morphology provides better mechanical properties than a coarser morphology; and
- (2) The control of as-cast microstructures, by manipulating solidification processing variables, such the cooling rate and tip growth rate can be used as an alternative way to produce components with better mechanical properties.

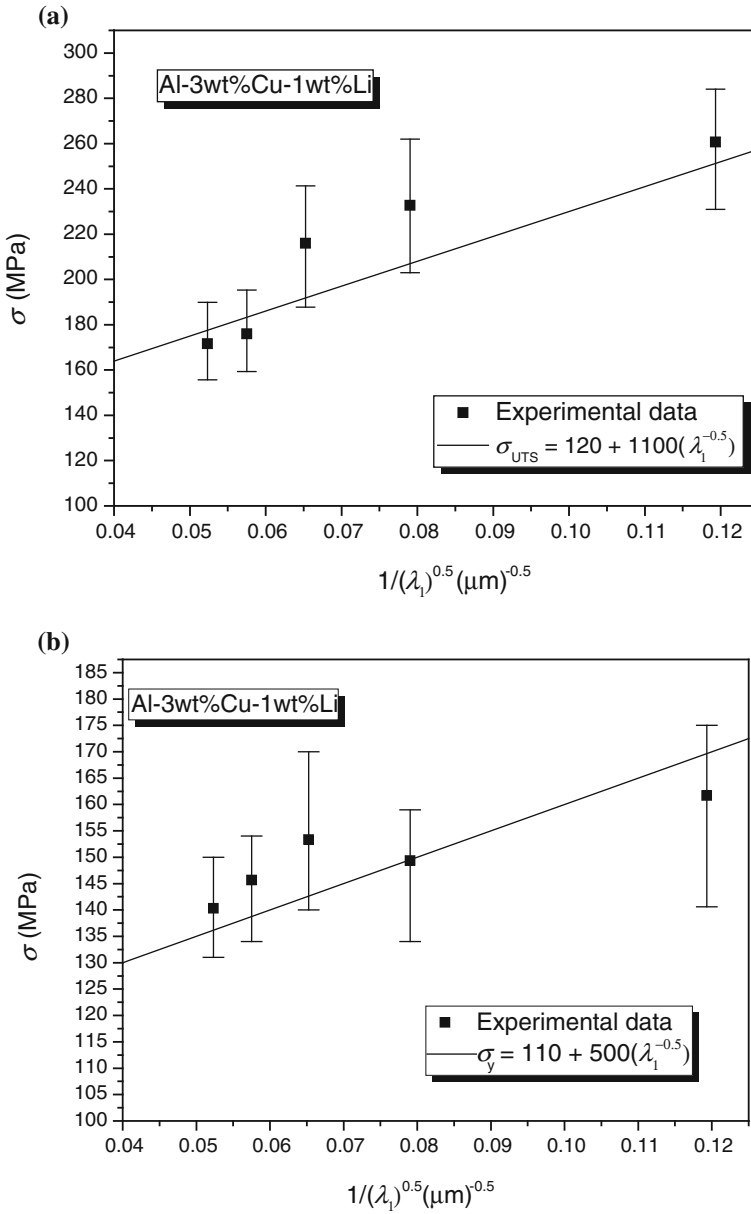


**Fig. 15** Relationships: **a** ultimate tensile strength  $\sigma_{UTS} = f(\lambda_1)$  and **b** yield strength  $\sigma_y = f(\lambda_1)$

## References

1. Wang C, Min G, Lu Q, Lu Z (2004) Solidification structure and mechanical properties of Al–Li–Cu–Zr cast alloys. *Int J Cast Metal Res* 17:264–266
2. Santos GA (2015) *Tecnologia dos materiais metálicos – propriedades, estruturas e processos de Obtenção*, 1st edn. Editora Érica Ltda, São Paulo
3. Garcia A (2007) *Solidificação: fundamentos e aplicações*, 2nd edn. Unicamp, Campinas
4. Park C, Kim S, Kwon Y, Lee Y, Lee J (2005) Mechanical and corrosion properties of rheocast and low-pressure cast A356-T6 alloy. *Mater Sci Eng* 391A:86–94
5. Petch NJ (1953) The cleavage strength of polycrystals. *J Iron Steel Inst* 174:25–28
6. Osório WRR, Garcia A (2002) Modeling dendritic structure and mechanical properties of Zn–Al alloys as a function of solidification conditions. *Mater Sci Eng* A325:103–111
7. Osório WRR, Leiva DR, Peixoto LC, Garcia LR, Garcia A (2013) Mechanical properties of Sn–Ag lead-free solder alloys based on the dendritic array and Ag<sub>3</sub>Sn morphology. *J Alloy Compd* 562:194–204
8. Osório WRR, Bortolozo AD, Peixoto LC, Garcia A (2014) Mechanical performance and microstructure array of as-cast lead–silver and lead–bismuth alloys. *J Power Sources (Print)* 271:124–133
9. Santos GA, Osório WRR, Garcia A, Neto CM, Goulart PR (2006) Effect of dendritic arm spacing on mechanical properties and corrosion resistance of Al 9wt pct Si and Zn 27wt pct Al alloys. *Metall Mater Trans A* 37:2525–2538
10. Santos GA, Neto CM, Osório WRR, Garcia A (2007) Design of mechanical properties of a Zn27Al alloy based on microstructure dendritic array spacing. *Mater Design* 28:2425–2430
11. Quaresma JMV, Santos CA, Garcia A (2000) Correlation between unsteady-state solidification conditions, dendrite spacings and mechanical properties of Al–Cu alloys. *Metall Mat Trans A* 31:3167–3178
12. Siqueira CA, Cheung N, Garcia A (2002) Solidification thermal parameters affecting the columnar-to-equiaxed transition. *Metall Mat Trans A* 33(7):2107–2118
13. Rocha OL, Siqueira CA, Garcia A (2003) Heat flow parameters affecting dendrite spacings during unsteady-state solidification of Sn–Pb and Al–Cu alloys. *Metall Mat Trans A* 34 (4):995–1006
14. Spinelli JE, Garcia A (2014) Development of solidification microstructure and tensile mechanical properties of Sn–0.7Cu and Sn–0.7Cu–2.0Ag solders. *J Mat Sci-Mat El* 25:478–486
15. Spinelli JE, Silva B, Garcia A (2014) Assessment of tertiary dendritic growth and its effects on mechanical properties of directionally solidified Sn–0.7Cu–xAg solder alloys. *J Electron Mater* 1347–1361
16. Brito C, Costa TA, Vida TA, Bertelli F, Cheung N, Spinelli JE, Garcia A (2015) Characterization of dendritic microstructure, intermetallic phases, and hardness of directionally solidified Al–Mg and Al–Mg–Si alloys. *Metall Mat Trans A* 3343–3355
17. Brito C, Reinhart G, Nguyen-Thi H, Mangelinck-Noel N, Cheung N, Spinelli JE, Garcia A (2015) High cooling rate cells, dendrites, microstructural spacings and microhardness in a directionally solidified Al–Mg–Si alloy. *J Alloy Compd* 145–149
18. Dias M, Costa TA, Rocha OFL, Spinelli JE, Garcia A (2015) Interconnection of thermal parameters, microstructure and mechanical properties in directionally solidified Sn–Sb lead-free solder alloys. *Mater Charact* 106:52–61
19. Silva B, Nguyen-Thi H, Reinhart G, Mangelinck-Noel N, Garcia A, Spinelli JE (2015) Microstructural development and mechanical properties of a near-eutectic directionally solidified Sn–Bi solder alloy. *Mater Charact* 107:43–53
20. ASTM E 8M (1995) Standard test methods for tension testing of metallic materials. ASTM
21. Peres MD, Siqueira CA, Garcia A (2004) Macrostructural and microstructural development in Al–Si alloys directionally solidified under unsteady-state conditions. *J Alloy Compd* 381:168–181

# The Influence of Heat Treatment on the Microstructure and Mechanical Properties of the Mg-7Sn-1Si Magnesium Alloy

T. Rzychoń and B. Dybowski

**Abstract** The influence of precipitation hardening on the microstructure and mechanical properties of the Mg-7Sn-1Si alloy is reported. It was found that the microstructure of the Mg-7Sn-1Si alloy consists of  $\alpha$ -Mg solid solution,  $Mg_2Sn$  and  $Mg_2Si$  compounds. The solution heat-treatment of the tested alloy at 520 °C for 24 h causes the  $Mg_2Sn$  phase to dissolve in the  $\alpha$ -Mg matrix and spheroidization of the Chinese script  $Mg_2Si$  compound. Rod-shaped and polygonal precipitates of equilibrium  $Mg_2Sn$  phase were found in the microstructure after ageing treatment at 200 and 250 °C. The peak hardness is around 58 HV after 120 h at 250 °C and the hardness increment is about 22 HV. The tensile strength of the peak aged alloy is about 120 MPa. The creep rate of the Mg-7Sn-1Si alloy is of order  $10^{-9}$  at a stress of 30 MPa and temperatures of 200 and 250 °C.

**Keywords** Magnesium alloys · Mg–Sn alloys · Microstructure · Precipitation hardening

## 1 Introduction

Magnesium alloys are interesting materials for application in the automotive and aircraft industries because of their low density, good specific strength and corrosion resistance in air atmosphere [1–3].

Commercial cast magnesium alloys (AZ91, AM50, AM60) have limited application because of their poor creep resistance and poor mechanical properties at an elevated temperature of 120 °C. The cause of this phenomenon is a low-melting point of the  $Mg_{17}Al_{12}$  phase which is located at the grain boundaries [4–6].

---

T. Rzychoń (✉) · B. Dybowski  
Faculty of Materials Engineering and Metallurgy, Silesian University of Technology,  
40-019 Katowice, ul Krasieńskiego 8, Poland  
e-mail: tomasz.rzychon@polsl.pl

B. Dybowski  
e-mail: bartlomiej.dybowski@polsl.pl

To increase the creep resistance of Mg–Al alloys, alloying elements are introduced, such as silicon [4], strontium [2, 7], calcium [2, 8] and rare earth metals [2, 9, 10]. In the last decade, Al-free magnesium-alloy grades with high creep resistance have been developed, which can be used for components working at a temperature of up to 300 °C. This group comprises the following alloys: Mg–Zn–RE [11], Mg–Y–Nd–Zr and Mg–Nd–Gd–Zr [12–14]. These alloys have a very good thermal stability of the main strengthening phase at up to 250 °C. However, the Mg–Y–Nd–Zr alloys have high associated costs due to the high cost of yttrium and the difficulties in casting. Therefore there is a need for an alternative alloy (Mg–Nd–Gd–Zr) which has similar properties to Mg–Y alloys, but with foundry handling and associated costs like non-yttrium containing alloys [12–15].

Mg–Sn system has shown some promising properties to replace Mg–RE systems since the phase diagram of this system shows similarity in several aspects compared with typical Mg–RE phase diagrams, such as Mg–Nd and Mg–Y systems [16]. The Mg–Sn system is known as a precipitation system, which has a relatively high solubility limit (3.35 at.%) at 561 °C and low solubility at ambient temperature [17]. In addition, since the main precipitate phase, Mg<sub>2</sub>Sn, has a high melting temperature of about 770 °C, a creep resistance superior to that of the AZ alloys is anticipated [18]. Generally, the hardening response of Mg–Sn alloys after solution treatment and ageing, despite the relatively large content of plate-like precipitates of Mg<sub>2</sub>Sn phase, is very low. Moreover, the peak hardness is obtained after long times of ageing. The low hardness increment of aged Mg–Sn alloys is related to an unfavorable crystallographic orientation of Mg<sub>2</sub>Sn precipitates and their large size [19]. Therefore, in recent years the studies have focused on improving the hardening response of Mg–Sn alloys. These studies concentrated on decreasing the size of precipitates, increasing their number density in the matrix and optimize the crystallographic orientation. The alloying elements which improve the hardening response include Zn, Al, Si and microalloying of Na, In, Li [18–22].

In this work the silicon to binary Mg–7Sn alloy was introduced in order to enhance the creep properties and to check the possibility to refine the Mg<sub>2</sub>Sn phase.

## 2 Experimental Procedure

The magnesium alloy containing silicon and tin was prepared, and its composition was analyzed by X-ray fluorescence spectroscopy (Table 1). Commercially pure Mg, Sn and Si were used. Melting of the alloys was performed by induction melting in an alumina crucible under the protection of an argon atmosphere. The melt was maintained at 730 °C for 3 min then poured into sand moulds.

**Table 1** Chemical composition of Mg-7Sn-1Si alloy

–	Mg	Sn	Si
wt%	Balance	7.1	0.8
at. %	Balance	1.5	0.7



Microstructural observations of the alloys were carried out by light microscopy (LM), scanning electron microscopy (SEM) and scanning transmission electron microscopy (STEM). The microanalysis of the intermetallic compounds was performed by energy-dispersive X-ray spectroscopy (EDS). The phase identification was carried out by X-ray diffraction analysis (XRD). The phase content was determined by the reference intensity ratio (RIR) method. The length of rod-like precipitates of the  $Mg_2Sn$  phase was measured by quantitative metallography on the images registered using SEM microscopy at  $10 \text{ k}\times$  magnification. Constant load creep tests were performed at 200 and 250 °C and 30 MPa. The creep strain was measured by extensometers, which were attached directly to the gauge section of the specimens. The length of the specimen was 100 mm, the gage length was 60 mm and the diameter of the reduced section was 6 mm. The hardness was measured by the Vickers method with a 2 kg load. Static tensile tests were performed in order determination of tensile properties. The heat treatment consist of two stages: solution treatment and ageing treatment. The solution treatment was performed at 520 °C for 24 h in argon atmosphere. The ageing treatment was performed at 200 and 250 °C in time range from 4 to 200 h.

### 3 Results and Discussion

#### 3.1 Microstructure of as-Cast Mg-7Sn-1Si Alloy

Figure 1 shows the LM micrographs of the Mg-7Sn-1Si alloy. It shows that the microstructure of this alloy consists of  $\alpha$ -Mg solid-solution and secondary solidification compounds distributed in the interdendritic regions. Moreover, the matrix is non-uniformly etched and darker areas are visible in the LM images. It is indicated on the microsegregation of alloying elements in the solid solution, what is a characteristic feature of cast alloys. As can be seen in Fig. 2, the interdendritic compounds show two morphologies: Chinese script (point 2) and irregular-shaped

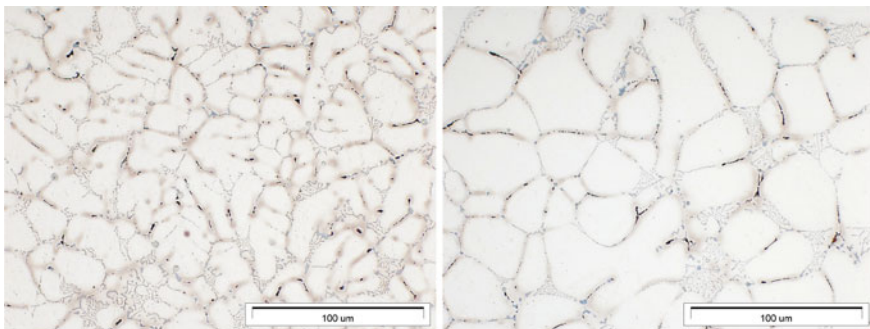
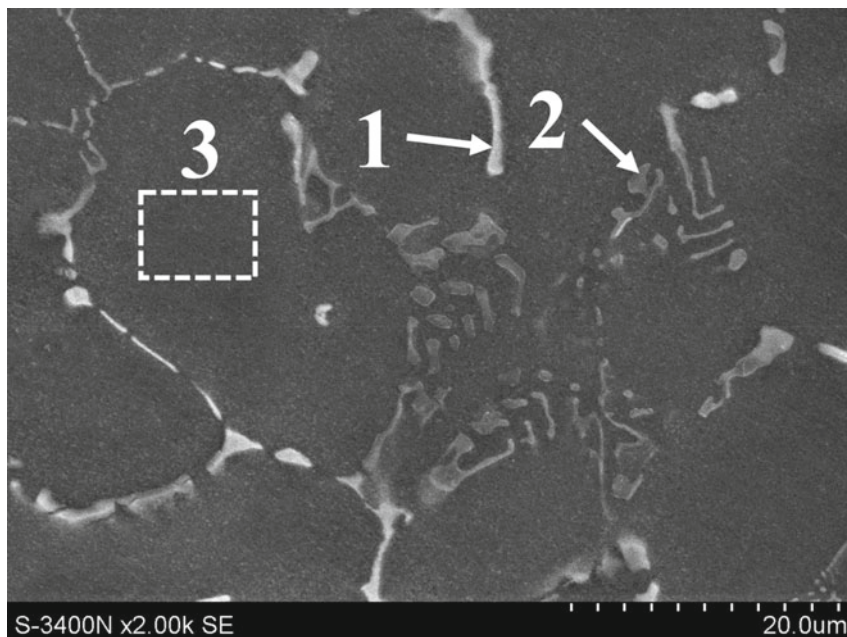


**Fig. 1** LM images of Mg-7Sn-1Si alloy



Point	Mg	Si	Sn
1	66.4	4.4	29.2
2	83.8	10.8	5.4
3	99.4	0.6	

**Fig. 2** SEM micrograph of Mg-7Sn-1Si alloy and results of EDS analysis (at.%) from points marked in SEM image

(point 1) eutectic. To identify the existing phases in the alloy, X-ray diffraction analysis was performed. Figure 3 shows the X-ray diffraction pattern of the Mg-7Sn-1Si alloy, in which the  $\alpha$ -Mg (hexagonal, P63/mmc,  $a = 32,094 \text{ \AA}$ ,  $c = 52,112 \text{ \AA}$ ),  $\text{Mg}_2\text{Si}$  (cubic, Fm-3 m,  $a = 6353 \text{ \AA}$ ) and  $\text{Mg}_2\text{Sn}$  (cubic, Fm-3 m,  $a = 6763 \text{ \AA}$ ) phases were clearly identified.

The energy-dispersive spectroscopy (EDS) analysis (Fig. 2) showed that the Chinese script eutectic phase (point 2) is enriched in silicon, indicating the  $\text{Mg}_2\text{Si}$  phase. Minor amounts of Sn can be dissolved in the  $\text{Mg}_2\text{Si}$  phase. The eutectic phase in point 3 (in the LM images this phase appears as dark irregular phase) is mainly composed of magnesium and tin. Thus it can be concluded that it is the cubic  $\text{Mg}_2\text{Sn}$  phase with solubility of silicon.

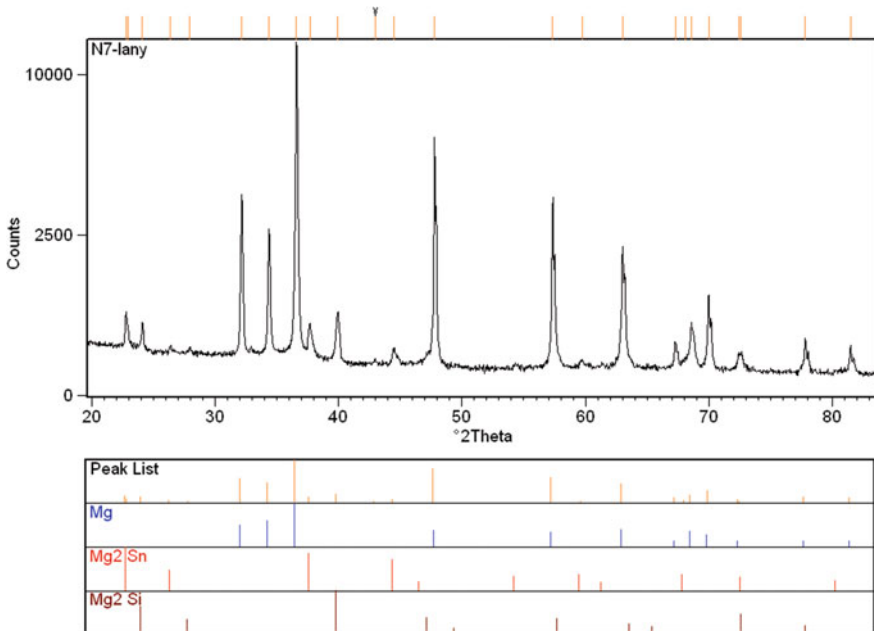
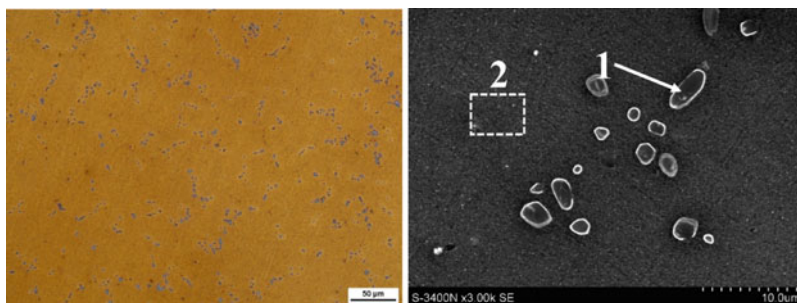


Fig. 3 X-ray diffraction pattern of Mg-7Sn-1Si alloy

### 3.2 Microstructure of Solution-Treated Mg-7Sn-1Si Alloy

Figure 4 shows a microstructure of the solution treated alloy at 520 °C for 24 h, from which it can be seen that the microstructure of Mg-7Sn-1Si is substantially altered. The  $Mg_2Sn$  compound has been dissolved in the magnesium matrix, due to high solubility of tin in magnesium (3.35 at.%, 14.5 wt%) [17]. Thus the content of tin significantly increased in the solid solution. The  $Mg_2Si$  phase with Chinese script morphology, which is formed as a result of eutectic reaction at ~640 °C, is not dissolved in the  $\alpha$ -Mg matrix due to the very low solubility of silicon in magnesium (0.005 at.%). However, the morphology of the  $Mg_2Si$  phase have been changed from the Chinese script to globular shape, thus the spheroidization of Chinese script particles is observed. It should be emphasized that not all particles of the  $Mg_2Si$  phase has been rounded and needle-like  $Mg_2Si$  phase are also observed after solution treatment. Because the solubility of Si in Mg is close to zero, the diffusion of atoms occurs at the Mg/ $Mg_2Si$  interface.

The results of microstructural observations are further confirmed by the X-ray diffraction analysis, which can be seen in the Fig. 5. The diffraction lines of  $\alpha$ -Mg are shifted towards higher angles compared to as-cast state. It indicates a change the lattice parameters of  $\alpha$ -Mg solid solution which is caused by the presence of tin atoms in the  $\alpha$ -Mg matrix. The diffraction lines of the  $Mg_2Sn$  compound are not



	Mg	Si	Sn
Point 1	88.0	10.3	1.7
Point 2	97.7	0.3	2.0

**Fig. 4** LM and SEM micrographs of Mg-7Sn-1Si alloy after solution treatment at 520 °C for 24 h in argon atmosphere and EDS results (at.%) from points marked in SEM image

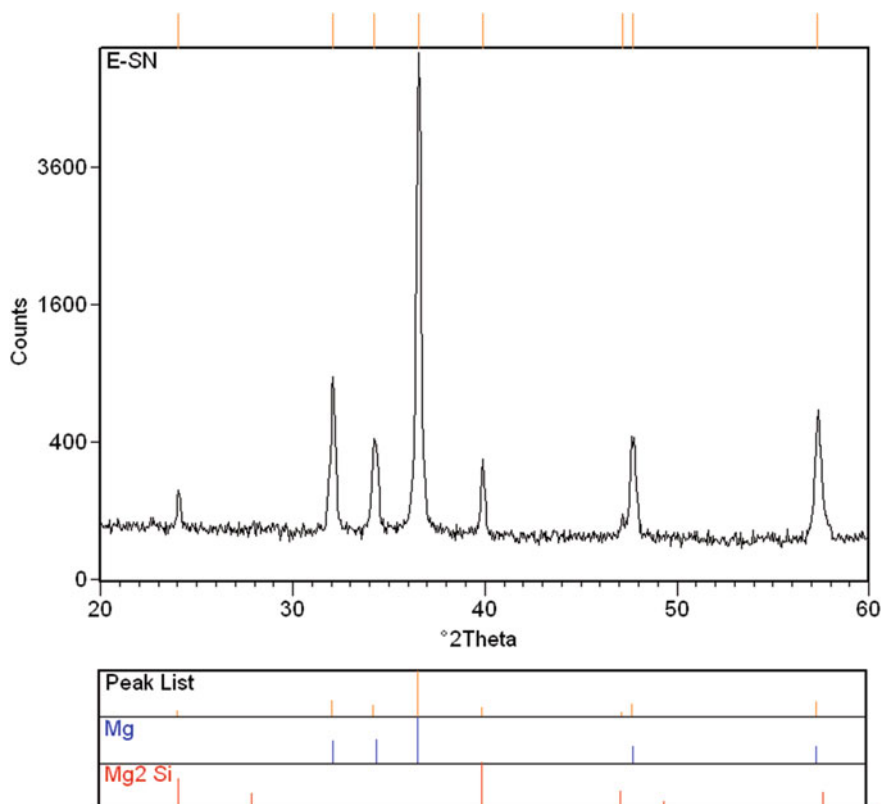


**Fig. 5** X-ray diffraction pattern of Mg-7Sn-1Si alloy after solution treatment at 520 °C for 24 h in argon atmosphere

observed due to the dissolution of  $Mg_2Sn$  phase in the solid solution. Because the  $Mg_2Si$  phase did not dissolve during the solution treatment at 520 °C, its diffraction peaks are still visible in the X-ray diffraction pattern.

### 3.3 Microstructure of Aged-Treated Mg-7Sn-1Si Alloy

Figures 6 and 7 show X-ray diffraction patterns of the Mg-7Sn-1Si alloy aged at 200 and 250 °C. From these results it can be seen that the precipitates of the  $Mg_2Sn$  phase are formed in early stages of ageing and the intensities of diffraction peaks of the  $Mg_2Sn$  phase increase with ageing time. In binary Mg–Sn alloys the formation of  $Mg_2Sn$  phase is not preceded by the formation of intermediate phases (G-P zones, non-equilibrium compounds) [19]. Also in our case non-equilibrium phases were not observed and the precipitation process begins with the equilibrium formation of the  $Mg_2Sn$  phase. Table 2 presents the volume fraction of phases after different stages of ageing which were determined by the RIR method. It can be seen that the content of the  $Mg_2Si$  phase is at a similar level due to the lack of solubility of this compound in the  $\alpha$ -Mg solid solution. The content of the  $Mg_2Sn$  phase increases with ageing duration. The kinetics of the precipitation of  $Mg_2Sn$  phase from supersaturated  $\alpha$ -Mg solid solution at a temperature of 200 °C is significantly lower than at 250 °C. The content of the  $Mg_2Sn$  phase in the alloy aged at 250 °C for 20 h is close to 3 vol.%, while after ageing at 200 °C the same content of the  $Mg_2Sn$  phase is achieved after 120 h. The maximum volume fraction of the  $Mg_2Sn$

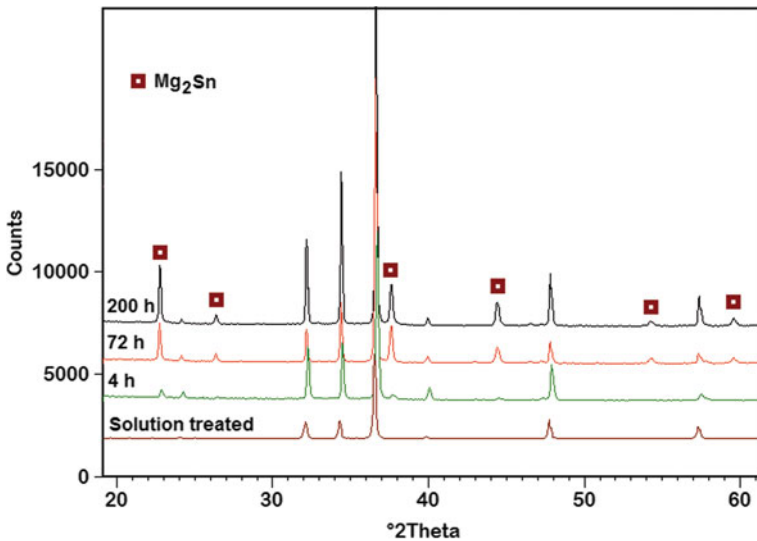


Fig. 6 X-ray diffraction patterns of Mg-7Sn-1Si alloy aged at 200 °C

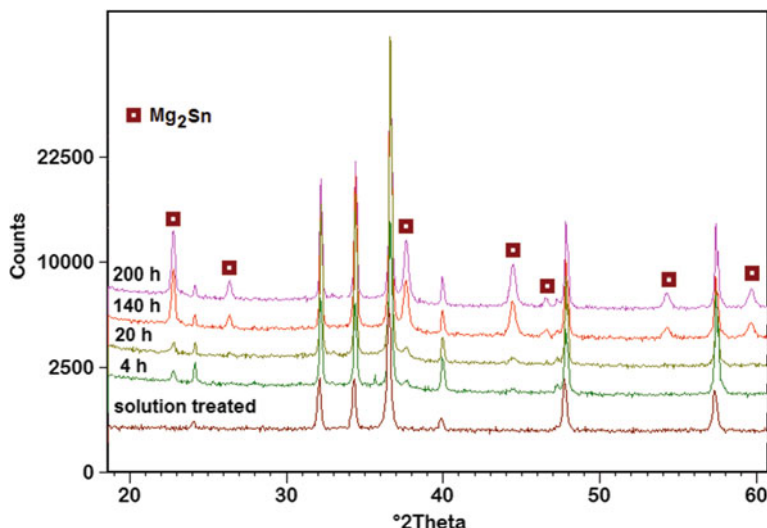


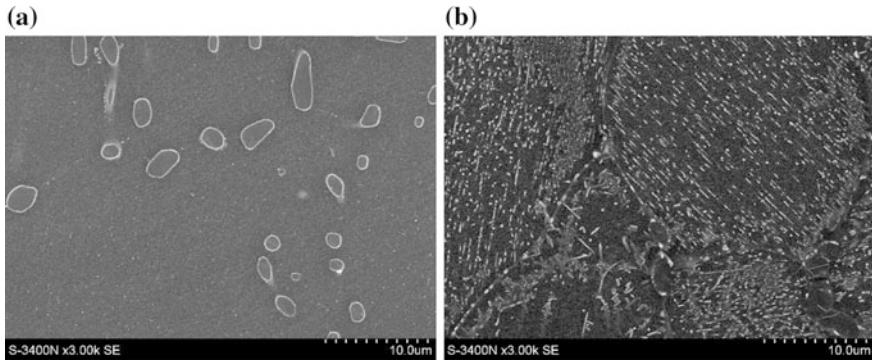
Fig. 7 X-ray diffraction patterns of Mg-7Sn-1Si alloy aged at 250 °C

Table 2 Contents of Mg<sub>2</sub>Si and Mg<sub>2</sub>Sn phases in the Mg-7Sn-1Si alloy and hardness HV2

Material condition	Ageing time, h	Ageing temperature, °C	Phase content, wt%			Phase content, vol.%			HV2
			Mg	Mg <sub>2</sub> Si	Mg <sub>2</sub> Sn	Mg	Mg <sub>2</sub> Si	Mg <sub>2</sub> Sn	
As-cast	0	–	96.7	2.3	1.0	97.4	2.1	0.5	52
Supersaturated	0	–	97.1	2.9	0.0	97.4	2.6	0.0	46
Aged	4	200	96.6	2.8	0.6	97.2	2.5	0.3	47
Aged	20	200	96.8	2.4	0.8	97.5	2.2	0.4	51
Aged	72	200	94.0	2.4	3.6	96.0	2.2	1.8	52
Aged	120	200	91.6	2.1	6.3	94.9	1.9	3.2	53
Aged	140	200	91.5	2.8	5.7	94.6	2.6	2.9	57
Aged	200	200	91.6	2.2	6.2	94.9	2.0	3.1	56
Aged	4	250	96.4	2.6	1.0	97.2	2.3	0.5	50
Aged	20	250	92.2	2.4	5.4	95.1	2.2	2.7	55
Aged	48	250	90.7	2.6	6.7	94.2	2.4	3.4	56
Aged	72	250	90.6	2.7	6.7	94.1	2.5	3.4	57
Aged	120	250	90.7	2.1	7.2	94.4	2.0	3.6	58
Aged	140	250	90.7	2.5	6.8	94.3	2.3	3.4	56
Aged	200	250	90.7	2.5	6.8	94.3	2.3	3.4	56

phase in the tested alloy is about 3.5 vol.% and is higher than in the as-cast alloy (0.5 vol.%) because the tin not only participates in the formation of the eutectic, but also dissolves in the  $\alpha$ -Mg crystals.

Figures 8 and 9 show the SEM images of a typical microstructure of the Mg-7Sn-1Si alloy aged at 200 and 250 °C, respectively. The Mg<sub>2</sub>Sn precipitates are characterized by a fine size after 4 h of ageing and are hardly visible in the SEM



**Fig. 8** Microstructure of Mg<sub>7</sub>Sn-1Si alloy aged at 200 °C for 4 h (a) and 200 h (b)

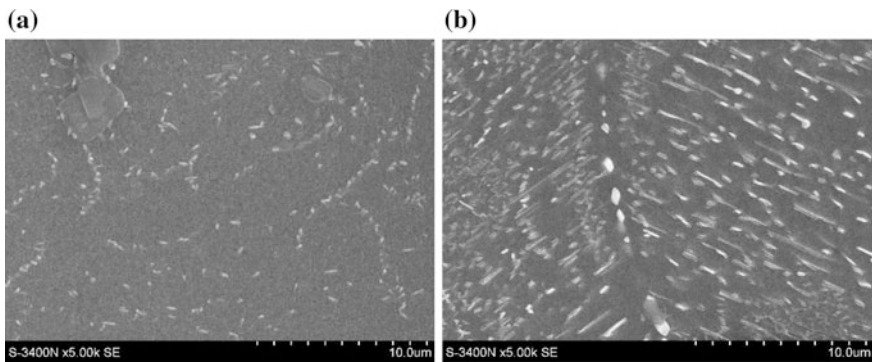


**Fig. 9** Microstructure of Mg<sub>7</sub>Sn-1Si alloy aged at 250 °C for 4 h (a) and 200 h (b)

image at magnification of  $3 \times$  (Fig. 8a), whereas in Figs. 8b and 9b it can be seen that the Mg<sub>2</sub>Sn precipitates are uniformly distributed in the  $\alpha$ -Mg matrix and have mainly a rod-shaped morphology. Moreover, the globular Mg<sub>2</sub>Si compound is visible in the microstructure. Generally, the size of Mg<sub>2</sub>Sn precipitates increases with duration and temperature of ageing. After ageing at a temperature of 200 °C, the maximum length of rod-shaped Mg<sub>2</sub>Sn precipitates does not exceed 1  $\mu$ m, while ageing at 250 °C their length can reach up to 5  $\mu$ m. Generally, the obtained results are in good agreement with general knowledge concerning the solution and ageing treatment of metallic alloys.

More detailed observations of the microstructure are shown in Fig. 10, in which the STEM images of a typical microstructure of Mg-7Sn-1Si alloy aged at 250 °C for 120 h are presented. It can be seen that the precipitates formed during ageing treatment have mainly rod-shaped and polygonal morphology. The size of rod-shaped precipitates does not exceed 1  $\mu$ m, whereas the size of polygonal precipitates is not greater than 0.4  $\mu$ m. EDS results from points 1 and 2 showed that these precipitates are composed of magnesium and tin. Silicon was not detected in



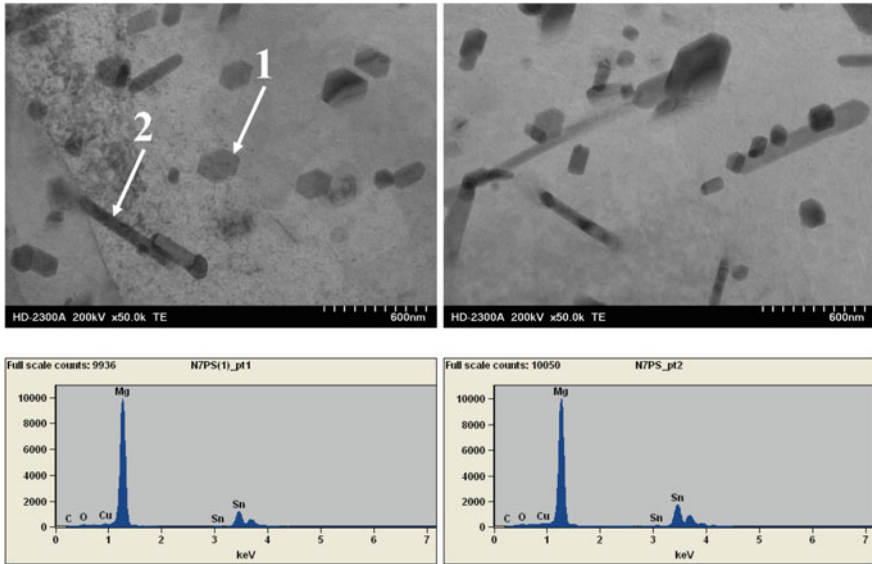


**Fig. 10** Rod-like and polygonal precipitates of  $Mg_2Sn$  phase in alloy aged at 250 °C for 120 h and EDS spectrum obtained from precipitates with the use of electron nano-beam

these precipitates, thus on the basis of XRD analysis, we suppose that these precipitates are the  $Mg_2Sn$  phase (detailed SAED analysis was not performed).

### 3.4 Mechanical Properties of Mg-7Sn-1Si Alloy

The hardness of the as-cast Mg-7Sn-1Si alloy is about 52 HV<sub>2</sub>. Solution treatment at 520 °C causes a reduction in hardness (46 HV<sub>2</sub>) due to the dissolution of the  $Mg_2Sn$  phase and  $\alpha$ -Mg grain growth. Figure 11 shows the variation in Vickers hardness as a function of aging time at 200 and 250 °C. It can be seen that the hardness of tested alloys increases with the increasing aging time. The peak hardness of the Mg-7Sn-1Si alloy aged at 250 °C is about 58 HV<sub>2</sub>, while during ageing at 200 °C the maximum hardness reaches about 57 HV<sub>2</sub>. The maximum hardness is achieved after 120 h at 250 °C and at 200 °C the peak hardness is obtained after 140 h.

The tensile properties including, ultimate tensile strength (UTS), 0.2 % yield strength (YTS), elongation (A<sub>5</sub>) and creep properties of the as-cast and heat-treated Mg-7Sn-1Si alloy, are listed in Table 3. The ultimate tensile strength of as-cast alloy is about 96 MPa. The heat treatment increases the mechanical properties, however the ultimate tensile strength increment is not significant (only 34 MPa). For comparison, the UTS of aged WE43 or AZ91 alloys can reach up to 280 MPa and the hardness increment is ~100 MPa [2].



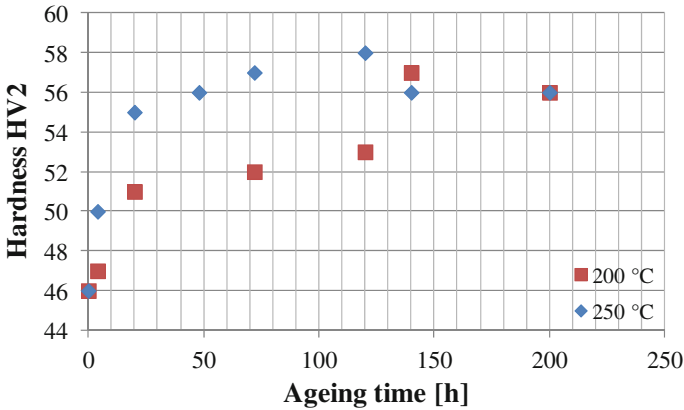


**Fig. 11** Age hardening behavior of Mg-7Sn-1Si alloy at 200 and 250 °C

**Table 3** Tensile properties at ambient temperature and creep properties at 200 and 250 °C of Mg-7Sn-1Si alloy

Material condition	UTS, MPa	YTS, MPa	A <sub>5</sub> , %	Temperature of creep tests	ε	ε̇, 1/s	Time of creep tests
As-cast	96 ± 12	73 ± 16	2.9 ± 0.2	–	–	–	–
Aged (250 °C/120 h)	120 ± 9	95 ± 10	3.1 ± 0.2	200 °C	0.50	1.1 × 10 <sup>-9</sup>	160
				250 °C	0.55	3.0 × 10 <sup>-9</sup>	160

Good creep properties are observed at a stress of 30 MPa and at temperatures of 200 and 250 °C. In this range of temperature and stress low creep strain and low creep rate were found. It must be emphasized that creep resistance at 60 MPa and 200 °C is very low (detailed results will be published elsewhere).

## 4 Discussion

In some papers [19, 20, 22] it was reported that hardness increment for the binary as-cast Mg–Sn alloy (~ 10 wt% of Sn) is about 10 HV, whereas Sasaki et al. [18] reported that the hardness increment of the Mg-10Sn alloy is around 16 HV. The addition of zinc or aluminum to the Mg–Sn alloy greatly increases the hardening response of the alloy and the increment of the peak hardness can achieve 35 HV. Addition of Na allows further increase in hardening response due to refinement of Mg<sub>2</sub>Sn precipitates and increasing the number of precipitates in unit volume as well as increasing the content of non-basal precipitates. In our case the hardening response of the Mg-7Sn-1Si alloy aged at 200 and 250 °C is approximately 22 HV. Thus it can be concluded that silicon addition slightly improves the hardness

increment of the Mg–Sn alloy. It should be stressed that the maximum hardness value of the aged Mg–7Sn–1Si alloy is only 58 HV and it is achieved only after 120 h ageing at 250 °C. Such long term ageing is not practical for industrial use. Moreover, the aged alloy has low tensile properties at ambient temperature, thus it cannot be recommended to applications in automotive or aerospace industry.

Elsayed et al. [20] reported that in the peak aged Mg–10Sn alloy (ageing at 200 °C) the average size of Mg<sub>2</sub>Sn precipitates is ~1.6 μm. Similar results were reported in Ref. [19]. In this work we obtained similar values for the peak-aged alloy, however in our case the peak hardness was obtained for an alloy aged for 120 h at 200 °C, meanwhile in Ref. [19, 20] the peak hardness was obtained after ~1000 h. The length of the rod-like Mg<sub>2</sub>Sn precipitates after ageing for 200 h is  $1.4 \pm 0.5$  μm, whereas in alloy aged for 120 h it is  $1.2 \pm 0.7$  μm, however our measurements were performed only in SEM micrographs and do not include small particles having size below SEM image resolution. These results suggests that the addition of silicon did not cause a significant refinement of rod-shaped Mg<sub>2</sub>Sn precipitates. One of the reasons why the hardness increment is slightly better may be fact that besides the rod-like precipitates, the numerous polygonal Mg<sub>2</sub>Sn precipitates with size of ~0.3 μm exist in the α-Mg matrix of the peak aged alloy. Zhang et al. [23] reported that polygonal Mg<sub>2</sub>Sn precipitates have a larger increment in the prismatic planes of hexagonal crystal lattice of α-Mg than lath- or plate-shaped precipitates lying mainly in the (0001)<sub>α</sub> plane. The shape and crystallographic orientation of the precipitates play an important role in plastic deformations that occur predominantly via the motion of dislocations gliding on the (0001)<sub>α</sub> slip plane. Thus the polygonal precipitates are a more effective barrier to gliding dislocations in Mg–Sn alloys than those on the slip plane. This may explain the higher hardness increment of the Mg–7Sn–1Si alloy in comparison to the binary Mg–Sn alloy. However, in this work we did not answer to the question: why silicon causes the increase volume fraction of polygonal precipitates.

Obviously, increasing the hardness of the Mg–7Sn–1Si alloy after ageing is related to increasing the volume fraction of the rod-like and polygonal Mg<sub>2</sub>Sn phase. The peak hardness is obtained when the content of the Mg<sub>2</sub>Sn phase is close to 3 vol.%. Longer ageing time causes reduction in hardness due to coarsening of Mg<sub>2</sub>Sn precipitates. It should be also noted that growth of α-Mg grains and spheroidization of Mg<sub>2</sub>Si phase, which is the results of solution treatment, promotes the reduction of hardness.

Silicon in this alloy was added in order to improve the creep resistance of this alloy. During solidification of Mg–Sn alloys, Si does not react with tin and participates in the formation of the Mg<sub>2</sub>Si phase. According to a Mg–Si equilibrium phase diagram [17], silicon forms the Mg<sub>2</sub>Si phase as a results of eutectic reaction, if its content in the Mg alloys is below 1.16 at.%. Therefore, in the as-cast Mg–7Sn–1Si alloy the eutectic consisting of Chinese script Mg<sub>2</sub>Si phase is observed in the microstructure. It is well known, that fine eutectic located in the interdendritic regions, which formed the continuous network in the Mg matrix improves the creep resistance of as-cast Mg alloys, especially when eutectic consist of thermally stable phases. It is related to retardation of grain boundary sliding. The Mg<sub>2</sub>Si compound

is characterized by high melting temperature, thus stability of this phase in typical range of creep temperatures of magnesium alloys (up to 350 °C) is high. The positive impact of Chinese script  $Mg_2Si$  phase on the creep resistance at 150 °C was reported in Ref. [24]. In this work the creep rate of the Mg-7Sn-1Si alloy at 200 and 250 °C is in order of  $10^{-9}$ , thus it can be stated that this alloy has good creep resistance at these temperatures and at a stress below 30 MPa. However, when stress will be greater, the creep rate increases rapidly and significant shortening of the time to rupture will be observed (only a few hours). Generally, creep properties of the Mg-7Sn-1Si alloy are better than those of typical Mg–Al alloys (AZ- and AM alloys). The superior creep resistance of the aged alloy can be attributed to the presence of  $Mg_2Sn$  precipitates that are distributed inside the  $\alpha$ -Mg grains as well as in the grain boundary and  $Mg_2Si$  phase. Thus,  $Mg_2Sn$  phase precipitates can enhance the strength of both the grain interiors and their boundaries [25]. On the other hand, the creep resistance could have been improved if the morphology of  $Mg_2Si$  phase did not changed from Chinese script to globular after solution heat treatment. The spheroidization process of Chinese script particles does not have a beneficial effect on inhibiting grain boundary sliding.

## 5 Conclusions

The microstructure of the as-cast Mg-5Si-7Sn alloy is composed of  $\alpha$ -Mg solid solution, Chinese script  $Mg_2Si$  phase and irregular  $Mg_2Sn$  phase.  $Mg_2Si$  and  $Mg_2Sn$  phases are formed as a result of eutectic reactions with magnesium. The solution heat-treatment of the tested alloy at 520 °C for 24 h causes the  $Mg_2Sn$  phase to dissolve in the  $\alpha$ -Mg matrix and spheroidization of Chinese script  $Mg_2Si$  compound. Rod-shaped and polygonal precipitates of equilibrium  $Mg_2Sn$  phase were found in the microstructure after ageing treatment at 200 and 250 °C. The length of rod-shaped precipitates is around 1.5  $\mu m$  and the size of polygonal below 0.5  $\mu m$  in the peak aged alloy. The peak hardness is around 58 HV after 120 h at 250 °C and the hardness increment is about 22 HV. Tensile strength of aged alloy is about 120 MPa. Creep rate of Mg-7Sn-1Si alloy is in the order of  $10^{-9}$  at 200 and 250 °C.

**Acknowledgments** The present work was supported by the National Science Centre under the project UMO-2011/03/D/ST8/03869.

## References

1. Suresh K, Rao KP, Prasad YVRK et al (2013) Microstructure and mechanical properties of as-cast Mg-Sn-Ca alloys and effect of alloying elements. *Trans Nonferrous Met Soc China* 23:3604–3610
2. Friedrich H, Mordike BL (2006) *Magnesium technology*. Springer, Berlin

3. Liu H, Chen Y, Tang Y, Wei S, Niu G (2007) The microstructure, tensile properties, and creep behavior of as-cast Mg-(1–10)%Sn alloys. *J Alloys Compd* 440:122–126
4. Luo AA (2003) Recent magnesium alloy development for elevated temperature applications. *Int Mater Rev* 49:13–30
5. Rzychoń T (2014) Characterization of Mg-rich clusters in the C36 phase of the Mg-5Al-3Ca-0.7Sr-0.2Mn alloy. *J Alloys Compd* 598:95–105
6. Homma T, Nakawaki S, Kamado S (2010) Improvement in creep property of a cast Mg-6Al-3Ca alloy by Mn addition. *Scr Mater* 63:1173–1176
7. Rzychoń T, Adamczyk-Cieślak B, Kielbus A, Mizera J (2012) The influence of hot-chamber die casting parameters on the microstructure and mechanical properties of magnesium-aluminum alloys containing alkaline elements. *Mat-wiss u Werkstofftech* 43:421–426
8. Rzychoń T, Adamczyk-Cieślak B (2014) Microstructure and creep resistance of Mg-Al-Ca-Sr alloys. *Arch Metall Mater* 59:329–334
9. Rzychoń T, Kielbus A, Lityńska-Dobrzyńska L (2013) Microstructure, microstructural stability and mechanical properties of sand-cast Mg-4Al-4RE alloy. *Mater Charact* 83:21–34
10. Bai J, Sun Y, Xue F, Qiang J (2012) Microstructures and creep properties of Mg-4Al-(1-4)La alloys produced by different casting techniques. *Mater Sci Eng A* 552:472–480
11. Rzychoń T, Szala J, Kielbus A (2012) Microstructure, castability, microstructural stability and mechanical properties of ZRE1 magnesium alloy. *Arch Metall Mater* 57:245–252
12. Tighiouaret S, Azzeddine H, Sam A, Sari A, Alili B, Bradai D (2012) On the precipitation behavior at 250 and 300 °C of WE54 supersaturated solid solution. *Adv Mater Research* 629:85–89
13. Dybowski B, Kielbus A, Jarosz R (2014) Effect of mould components on the cooling rate, microstructure, and quality of WE43 magnesium casting alloy. *Arch Metall Mater* 59:1527–1532
14. Dybowski B, Kielbus A, Jarosz R, Paśko J (2014) The microstructure of elektron21 and WE43 magnesium casting alloys after subsequent melting process operations. *Solid State Phenom* 211:65–70
15. Kielbus A, Rzychoń T (2011) Mechanical and creep properties of Mg-4Y-3RE and Mg-3Nd-1Gd magnesium alloy. *Procedia Eng* 10:1835–1840
16. Zhang M, Zhang WZ, Zhu GZ (2008) The morphology and orientation of  $Mn_5Si_3$  precipitates in an Mg–Sn–Mn–Si alloy. *Mater Lett* 62:4374–4376
17. Nayeb-Hashemi AA, Clark JB (1988) Phase diagrams of binary magnesium alloys. ASM International, Materials Park, OH
18. Sasaki TT, Oh-ishi K, Ohkubo T, Hono K (2006) Enhanced age hardening response by the addition of Zn in Mg–Sn alloys. *Scr Mater* 55:251–254
19. Mendis CL, Bettles CJ, Gibson MA, Hutchinson CR (2006) An enhanced age hardening response in Mg–Sn based alloys containing Zn. *Mater Sci Eng A* 435:163–171
20. Elsayed FR, Sasaki TT, Mendis CL, Ohkubo T, Hono K (2013) Compositional optimization of Mg–Sn–Al alloys for higher age hardening response. *Mater Sci Eng A* 566:22–29
21. Mendis CL, Bettles CJ, Gibson MA, Gorsse S, Hutchinson CR (2006) Refinement of precipitate distributions in an age-hardenable Mg–Sn alloy through microalloying. *Phil Mag Lett* 86(7):443–456
22. Elsayed FR, Sasaki TT, Mendis CL, Ohkubo T, Hono K (2013) Significant enhancement of the age-hardening response in Mg–10Sn–3Al–1Zn alloy by Na microalloying. *Scr Mater* 68:797–800
23. Zhang M, Zhang WZ, Zhu GZ (2008) The morphology and crystallography of polygonal  $Mg_2Sn$  precipitates in a Mg–Sn–Mn–Si alloy. *Scr Mater* 59:866–869
24. Poddar P, Sahoo KL, Mukherjee S, Ray AK (2012) Creep behaviour of Mg–8 % Sn and Mg–8 % Sn–3 % Al–1 % Si alloys. *Mater Sci Eng A* 545:103–110
25. Nayyeri G, Mahmudi R (2010) Enhanced creep properties of a cast Mg–5Sn alloy subjected to aging-treatment. *Mater Sci Eng A* 527:4613–4618

# Volume Changes of Cement Composite Based on Steel Slag During Thermal Load

V. Šimíček, V. Václavík, T. Kubín, T. Dvorský, A. Břenek, J. Valíček, M. Kušnerová, M. Harničárová and L. Gola

**Abstract** The use of natural sources of aggregate for production of cement composites with different physical and mechanical properties is common. From the viewpoint of saving natural sources of aggregate in the production of concretes, there is an effort to find alternative substitutes of natural sources. The use of secondary materials in the production of concretes in terms of sustainability represents a progressive way to meet the ever-increasing demand for environmentally friendly building materials with sufficient properties for high usage. One of the possibilities for this is steel slag. The article is devoted to the preparation and testing of cement composites based on steel slag as a 100 % substitute of natural aggregates. The produced test specimens (beams of 40 × 40 × 160 mm) are 28 days old

---

V. Šimíček · V. Václavík (✉) · T. Dvorský · A. Břenek  
Faculty of Mining and Geology, Institute of Environmental Engineering,  
VŠB—TU Ostrava, 17. Listopadu 15, 708 33 Ostrava-Poruba, Czech Republic  
e-mail: vojtech.vaclavik@vsb.cz

V. Šimíček  
e-mail: vojtech.simicek@vsb.cz

T. Dvorský  
e-mail: tomas.dvorsky@vsb.cz

A. Břenek  
e-mail: ales.brenek@vsb.cz

V. Šimíček · V. Václavík · A. Břenek · J. Valíček  
Faculty of Mining and Geology, Institute of Clean Technologies for Mining and Utilization  
of Raw Materials for Energy Use, VŠB—TU Ostrava, 17. Listopadu 15, 708 33  
Ostrava-Poruba, Czech Republic  
e-mail: jan.valicek@vsb.cz

T. Kubín  
Department of Production Machines and Design, Faculty of Mechanical Engineering,  
VŠB—TU Ostrava, 17 listopadu 15, 708 33 Ostrava-Poruba, Czech Republic  
e-mail: tomas.kubin@vsb.cz

J. Valíček · M. Kušnerová · M. Harničárová · L. Gola  
Institute of Physics, Faculty of Mining and Geology, VŠB—TU Ostrava,  
17. Listopadu 15, 708 33 Ostrava-Poruba, Czech Republic  
e-mail: milena.kusnerova@vsb.cz

and they are tested for volume changes and changes in their physical and mechanical properties with a thermal load of 200, 400, 600 and 800 °C. 3D scanning by means of the Handy Scan 700 device was used to determine the volume changes of these test specimens after thermal load, which, thanks to the latest TRUaccuracy technology, has a high precision scanning ability within the range of 0.030–0.050 mm, regardless of the work environment.

**Keywords** Steel slag · Concrete · Volume changes · 3D scanning · Thermal load · Strength characteristics

## 1 Introduction

The present time lays great value on the use of secondary raw materials in all industrial and technical fields, in particular in the building industry, that make up the global segment for the application and use of new building materials based on recycled secondary raw materials. This leads to the conservation of natural resources and to the quest for a new way of the utilization and processing of building and industrial waste materials. Effective management of secondary raw materials significantly extends the raw material base, and is also a way to reduce the energy and material intensity of production, which ultimately provides benefits in quality care for the environment [1].

Metallurgy is one of the important areas providing secondary raw materials for the purpose of their further use. There are results of an experimental research dealing with the use of alkali-activated blast furnace slag in combination with fly ash [2, 3], the use of finely ground blast furnace slag as a substitute of cement in production of concrete composite [4], processing of metalliferous wastes by means of plasma heating [5], but also by means of hydrocyclones, pyrometallurgical methods or microwave radiation [6]. Steel slag is another by-product of the metallurgical process used as a partial substitute of natural aggregates in the production of concrete composites resistant to thermal loads of up to 800 °C [7], or as a partial and/or total substitute of natural aggregates in the production of bitumen concrete

---

M. Harničárová  
e-mail: marta.harnicarova@vsb.cz

L. Gola  
e-mail: lukas.gola@vsb.cz

J. Valíček · M. Kušnerová  
RMTVC, Faculty of Metallurgy and Materials Engineering, VŠB—Technical University  
of Ostrava, 17. Listopadu 15/2172, 708 33 Ostrava, Czech Republic

M. Harničárová  
Nanotechnology Centre, VŠB—Technical University of Ostrava, 17. listopadu 15/2172, 708  
33 Ostrava-Poruba, Czech Republic

[8, 9]. The effect of steel slag on cement hydration has been examined as well, and it has been proven that the increasing share of steel slag results in a deceleration of the hydration process [10].

This article presents the results of an experimental research aimed at the verification of the possibility of identifying volume changes of concrete composites based on steel slag at different degrees of thermal load using a 3D scanner.

## 2 Materials and Methods

### 2.1 Concrete Composite Components

**Steel slag**—is an artificial aggregate produced during the metallurgical process, where adulterants are separated by means of active slag. The basic components of steel slag include the solutions of orthosilicates with the oxides of iron, manganese, aluminium and magnesium, which are chemically bound to the calcium oxide. The chemical composition of the arising slag varies considerably depending on the nature and progress of the technological process. Steel slag is a predominantly basic material with a different share of oxides, in particular the oxides of iron. It is not, however, a mixture of oxides, but a complex system in which we can indicate more than 100 components that cannot be mechanically separated. Figure 1 presents the world production of steel slag in the past 15 years, assuming that one ton of steel produces 0.172 t of steel slag. In 2009, there was a significant drop in production as a result of the economic crisis in 2008–2009. From 2010 to 2014, there is a

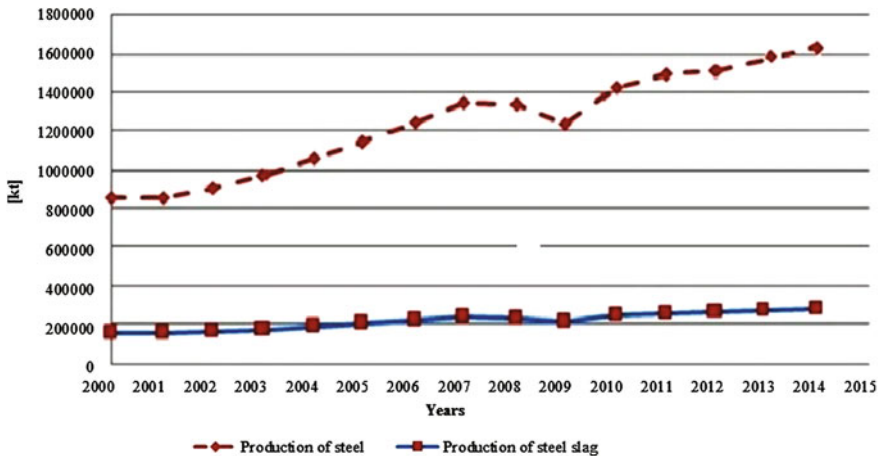


Fig. 1 World production of steel and steel slag

**Table 1** Properties of Portland cement CEM I 42,5 R

Monitored parameter	Unit	Value	Level required according to EN 197-1
Compressive strength after 2 days	N·mm <sup>-2</sup>	32.3	≥20.0
Compressive strength after 28 days	N·mm <sup>-2</sup>	54.2	≥42.5 ≤62.5
Flexural strength after 2 days	N·mm <sup>-2</sup>	6.28	–
Flexural strength after 28 days	N·mm <sup>-2</sup>	9.87	–
Initial setting	min	130	≥60
Stability of volume	mm	1.0	≤10
Specific weight	g·cm <sup>-3</sup>	3.06	–
Specific surface	cm <sup>2</sup> ·g <sup>-1</sup>	4180	–
Chemical analysis			
Sulphates content	% of weight	2.82	≤4.00
Annealing loss	% of weight	1.38	≤5.00
Insoluble residue	% of weight	0.40	≤5.00
Chlorides content	% of weight	0.020	≤0.100

significant increase in steel production, and hence the amount of steel slag. Cast converter steel slag with a fraction of 0/8 from Trinecké železářny, a.s. was used for the experimental research, and it was subjected to grain size analysis, density and absorption capacity tests.

**Cement**—Portland cement CEM I 42,5R from the Cement Hranice Company, a. s. was used as the binding component in the production of concrete composites based on steel slag. The tested cement properties according to EN 197-1 [11] are presented in Table 1.

**Mixture water**—water from the water-supply network was used as the mixture water. Exact criteria for the mixture water are defined in EN 1008 [12].

**Additives**—the following additives were used in order to improve the workability of the concrete mixture based on steel slag:

- The plasticizing additive Stachement 6358 in a dose of 1.15 % of the weight of cement. It is an additive based on polycarboxylates with high plasticizing effect which persists longer than commonly used do plasticizers.
- The retarding additive Retardal 540. It is a product which delays the initial setting of fresh concrete depending on the dose of cement, water-cement ratio and the ambient temperature. This additive has no more side-effects and does not increase the air content in the mixture. The dose in this case was 1 l per 1 m<sup>3</sup> of the mixture.



## 2.2 Methods

### 2.2.1 Determination of the Physical and Mechanical Properties of Concrete Composites

The preparation of an experimental concrete mixture required a determination of the grain size of steel slag with the fraction of 0/8 mm according to EN 933-2 [13] and a determination of the grain density and absorption capacity according to EN 1097-6 [14] using the pycnometric method. The determination of the strength characteristics (flexural and compressive strength) of the test specimens with the dimensions of 40 × 40 × 160 mm was performed according to EN 196-1 [15]. The strength characteristics were measured using an American laboratory press—MTS 816—Rocktest System. The load rate during the flexural strength test was 0.050 MPa/s. The load rate of the test specimens during the compressive strength test was 1.50 MPa·s<sup>-1</sup>. The density of fresh concrete mixture (FCM) was determined according to EN 12350-6 [16], the content of air in FCM according to EN 12350-7 [17], and the determination of the consistency of concrete mixture took advantage of the slump test according to EN 12350-2 [18].

### 2.2.2 Thermal Load

Thermal load of the tested concrete composites with the dimensions of 40 × 40 × 160 mm was carried out in a laboratory muffle furnace Elsklo with a T<sub>max.</sub> of 1100 °C, with an even temperature distribution. Figure 2 presents the individual curves of thermal load at temperatures of 200, 400, 600 and 800 °C.

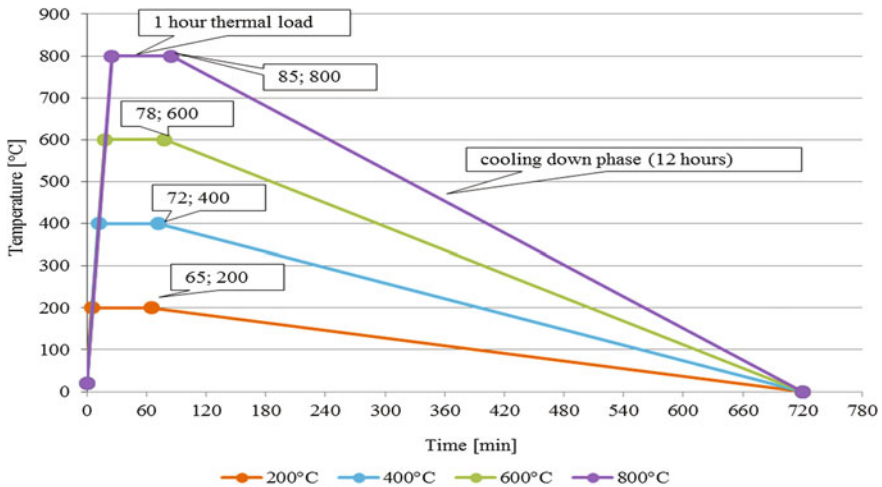


Fig. 2 Thermal load curves

**Table 2** Rise time to the thermal endurance temperature

Temperature (°C)	Rise time (min.)	Temperature (°C)	Rise time (min.)
200	5	600	18
400	12	800	25

The rise time to the aforementioned individual thermal endurance temperature is presented in Fig. 2. The thermal endurance at each temperature was 60 min. After the thermal load, the test specimens were transferred into a desiccator, where they were cooling naturally to the laboratory ambient temperature of 20 °C for 12 h (Table 2).

### 2.2.3 Determination of Volume Changes

The determination of the volume changes of concrete test specimens based on steel slag at different thermal loads was performed by means of an innovative scanning technology using the Handy Scan—Exascan 3D scanner. The test specimens were first scanned after 28 days in a water bath at 20 °C. After scanning, the specimens were subjected to a thermal load (see Fig. 2) and then they were re-scanned using the 3D scanning method in order to detect the volume changes of the test specimens. Volume measuring took advantage of a method comparing the datasets acquired by 3D scanning. The basic evaluation parameter was the volume change. The scanning of the volume changes was performed using the Handy Scan—Exascan 3D scanner. This is a hand-held laser scanner, which allows for mutual movement of the scanner and the body during scanning (see Fig. 3). The scanning is based on the principle of triangulation, where reflective marks used for orientation are placed on the scanned body or a pad (see Fig. 4). The marks are scanned by two cameras and, if both see at least three reflective marks at the same time, the system can automatically determine the position of the scanned body with respect to the scanner. If the position is known, the scanner starts projecting a laser cross on

**Fig. 3** Reference block scanning

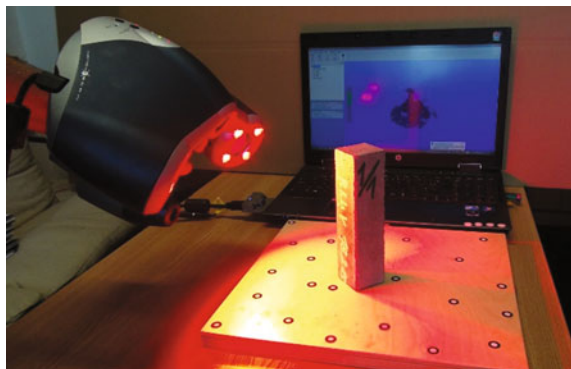


**Fig. 4** Triangulation principle

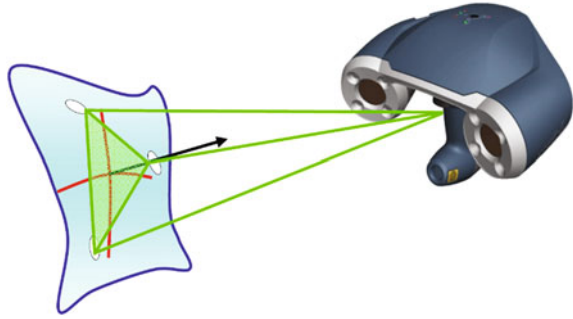


**Table 3** Parameters of the used HandyScan—ExaScan

Handyscan—Exascan		
Laser class	2	(-)
Number of measurements	18 000	(images·s <sup>-1</sup> )
<b>z</b> -resolution	0.05	(mm)
Accuracy	0.04	(mm)
Iso	0.02 + 0.1/m	(mm)
Number of cameras	3	(-)
Scanned surface distance	200–300	(mm)
Weight	1.25	(kg)
Dimensions	172 × 260 × 216	(mm)

the surface of the scanned area. This cross is scanned by cameras and the system receives information about the distance of the individual points from the scanner. The technical parameters of the used 3D scanner are shown in Table 3.

### 3 Measurement Results and Discussion

#### 3.1 Steel Slag

Figure 5 presents the results of the grain size analysis of the steel slag fr. 0/8 mm, which was used to design the compositions of the concrete experimental mixtures. The blue curve shows the graphic course of the oversize share and, on the contrary, the red curve shows the graphic course of undersize share in weight percentage. The intersection of these two curves defines the mean grain size of steel slag, which corresponds to the value 1.8 mm. The density of the used steel slag according to [14] was 3751 kg·m<sup>-3</sup> and the absorption capacity of the slag was 2.35 %.

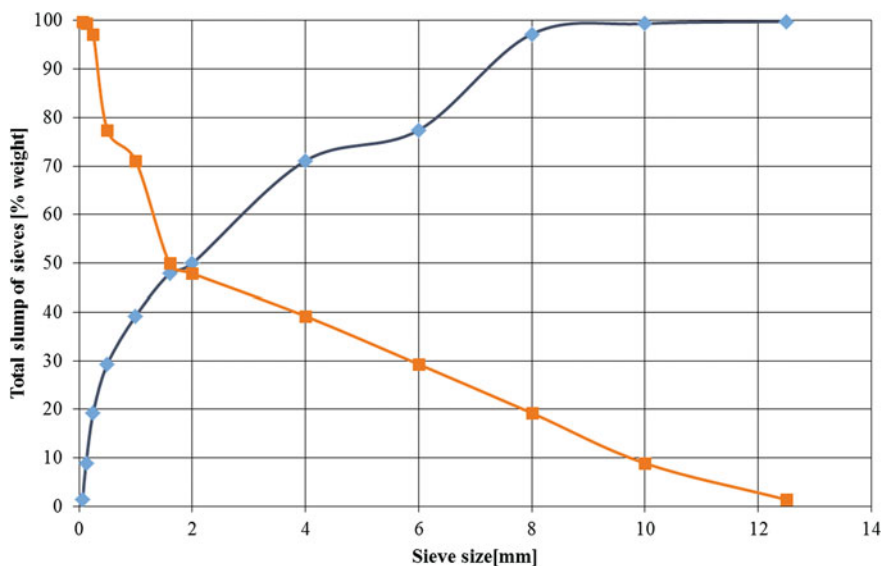


**Fig. 5** Graphic expression of the grain size curve of steel slag (*blue curve*—oversize share, *orange curve*—undersize share)

### 3.2 Preparation of Concrete Mixture from Steel Slag

The preparation of an experimental concrete mixture was conducted in laboratory conditions, in a cyclone mixer M80 from Fylamos Company. The mixing procedure was as follows:

1. Steel slag dosing and 1/3 of mixing water. Mixing time 3 min.
2. Cement dosing. Mixing time 1 min.
3. Dosing of 2/3 of mixing water with retarder. Mixing time 1 min.
4. Plasticizing additive dosing. Mixing time 3 min.

The total mixing time was 8 min.

A slump test was performed immediately after the mixing of the concrete mixture and after 30 min. in order to determine the consistency of the fresh concrete mixture according to [18]. The slump value immediately after mixing was 240 mm (degree S5) and after 30 min., it was 213 mm (degree S4).

The density of the fresh concrete mixture, which had been determined according to [16], reached the value of  $2814 \text{ kg}\cdot\text{m}^{-3}$ . The air content of the fresh concrete mixture, determined according to [17], was 5.1 %. The following activity was filling the moulds ready for the preparation of the test specimens with the dimensions of  $40 \times 40 \times 160 \text{ mm}$ . The filling was carried out in two layers, while each layer was compacted on a vibration table VSB 40 for 8 s. The specimens were demoulded the next day and they were kept in a water bath at  $20 \text{ }^\circ\text{C}$  for 28 days.

27 pieces of experimental specimens were prepared in total and they were subjected to testing. 12 pieces of the specimens were subjected to compressive and flexural load and the remaining 15 specimens were subjected to thermal load, followed by 3D scanning performed so as to detect the volume changes and strength characteristics.

### 3.3 Determination of Strength Characteristics

The tested strength characteristics of the test specimens included flexural strength and compressive strength. The strengths of the test specimens were tested after 7, 14, 21 and 28 days. The course of flexural strength is graphically shown in Figs. 6 and 7.

Figure 6 presents a graphic illustration of flexural strength. After 7 days, the specimens already had the flexural strength of 6.84 MPa. The largest increase in flexural strength was recorded after 7 and 14 days, during which the flexural strength increased by 0.48 to 7.32 MPa. During the following days, i.e. after 21 and 28 days, the changes were not so significant. The increase in strength after 21 days in comparison with 14 days was 0.07 Mpa and, after 28 days, it was 0.09 MPa.

Graphic illustration of compressive strength is clearly shown in Fig. 7. Compressive strength after 7 days in a water bath was 43.58 MPa. In this case, as in the case of flexural strength, the highest increase was recorded at intervals from the 7th to the 14th day. This increase reached 9.84 MPa (18.5 %) up to 53.42 MPa. The strength after 21 and 28 days witnessed only a gradual increase. The value after

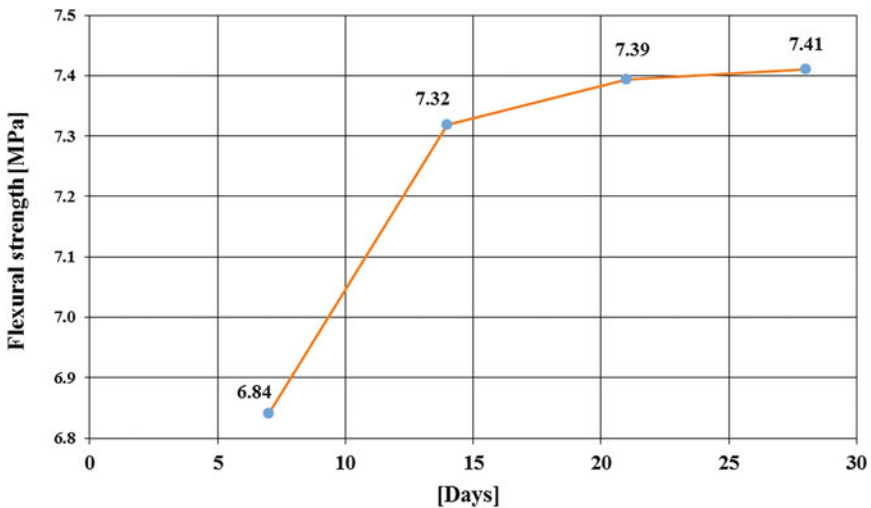


Fig. 6 Flexural strength

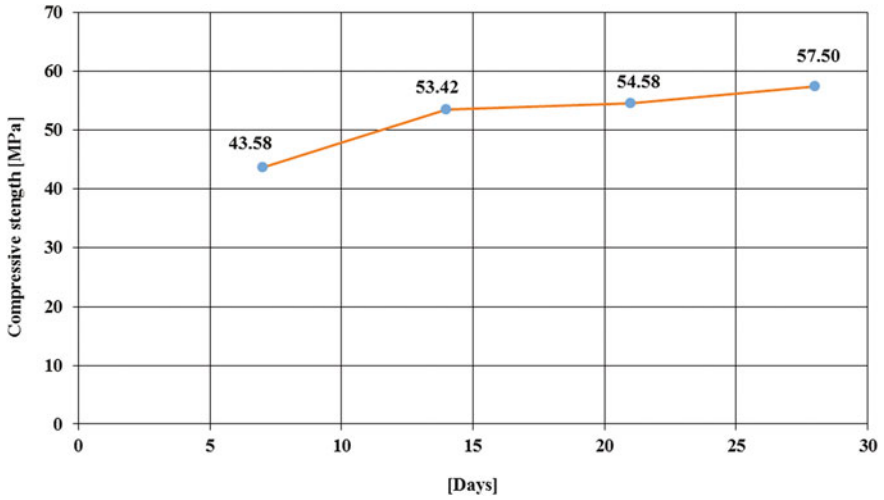


Fig. 7 Compressive strength

21 days was 54.58 MPa and, after 28 days, it was 57.50 MPa. The total increase between days 7 and 28 thus corresponded to 24.5 %.

The results of flexural strength after thermal load are presented in Fig. 8. It shows a comparison of the strengths with a reference body after 28 days in a water bath at 20 °C. There was only a slight decrease in strength in comparison with the

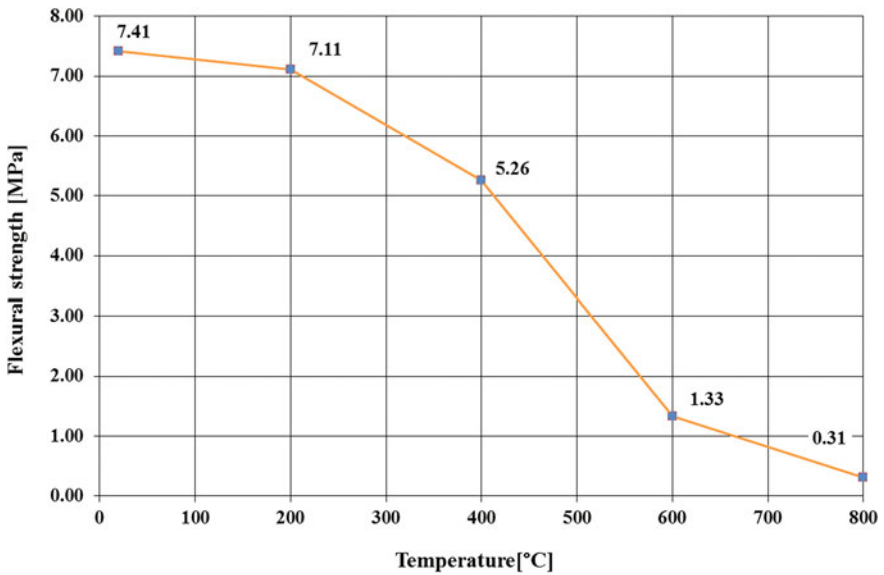


Fig. 8 Flexural strength after thermal load

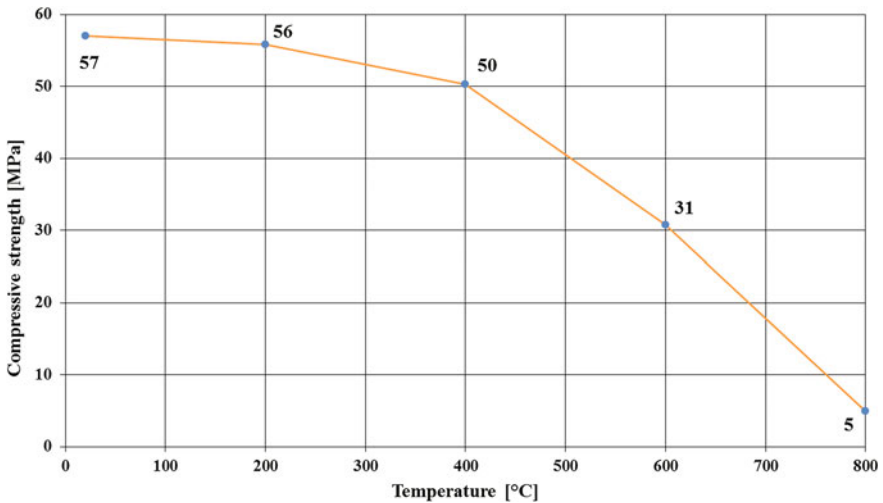


Fig. 9 Compressive strength after thermal load

reference body at 200 °C, namely by 0.3 MPa. Thermal load at 400 °C, however, caused a decrease by 2.15 to 5.26 MPa, which corresponds to 29.1 %. Load above 400 °C clearly shows that there was a significant decrease in strength. Flexural strengths of the bodies thermally loaded to 600 and 800 °C were lower when compared to the reference body by 6.07 and 7.10 MPa. It is a decrease by 82.1 % at 600 °C and by 95.9 % at 800 °C. It is therefore clear that bodies exposed to load exceeding 400 °C are degraded and lose their strength.

The graphic illustration of compressive strength in Fig. 9 shows a similar strength curve course as in Fig. 8. It is clearly visible that during thermal endurance at 200 °C, the compressive strength of composites only showed a minimal decrease by 1.15 MPa, which corresponds to 2 %. At a thermal load of 400 °C showed larger reductions in compressive strength when compared to the reference body, by 6.87 MPa (11.95 %). Thermal loads at 600 and 800 °C, however, show a significant degradation of strength. The value of compression strength in the case of 600 °C decreased by 26.18 MPa (45.74 %) and in case of 800 °C, it was 51.75 MPa (90 %) compared to the strength of the reference body.

Figures 10 and 11 illustrate the comparison of the individual flexural and compressive strengths with the reference body according to gradual thermal loading.

### 3.4 Determination of the Volume Changes of Bodies

The determination of the volume changes starts with the physical model surface test. The structure and colour of the surface was all right, so there was no need for

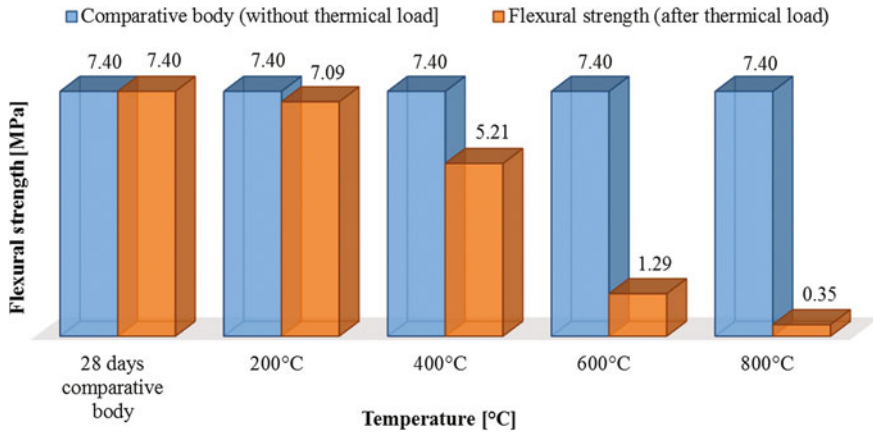


Fig. 10 Comparison of flexural strength of thermally loaded bodies with the reference body

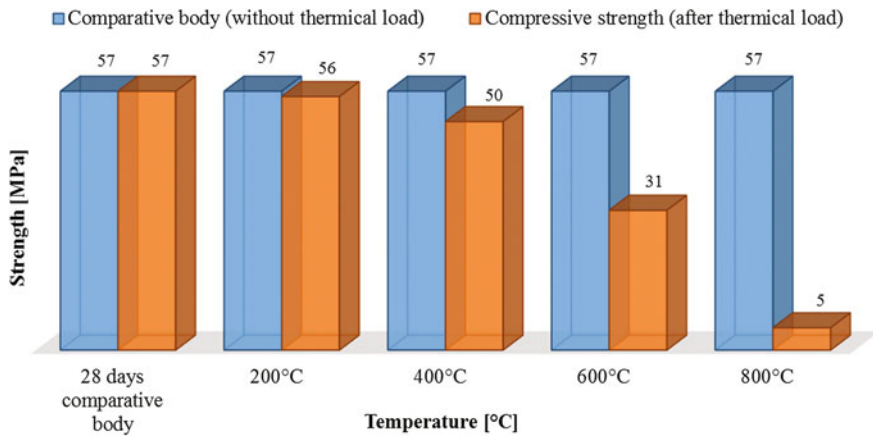
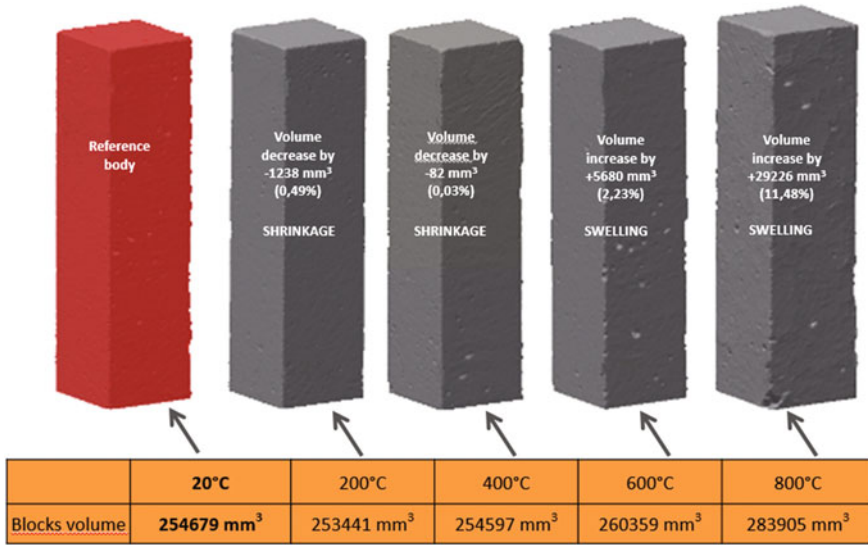


Fig. 11 Comparison of compressive strength of thermally loaded bodies with the reference body

additional surface treatment. The scanner resolution was set to 0.4 mm. Given the need to scan all areas of the model, the first step was to establish the method with the model positioned between spikes. The body was placed on a flat pad with the smallest possible area. The remaining five areas were scanned afterwards. The body was closed by means of a cutting plane positioned parallel to the pad plane, which was set off by two millimetres. The data file adjustment was limited to automatic functions only in order to keep the human factor entering the process at absolute minimum.

The volume changes of thermally loaded bodies were examined the same way as in the case of the strength changes. The loaded composites were also compared with the reference body with a volume of 254,679 mm<sup>3</sup>. Figure 12 shows the individual





**Fig. 12** Volume changes of concrete composites scanned by means of 3D Handy Scan

volume changes depending on temperature. At 200 °C, there was shrinkage by 1238 mm<sup>3</sup> (0.49 %). After being subjected to thermal load at 400 °C showed a negligible change by 82 mm<sup>3</sup> (0.03 %). Larger values of volume changes were observed at higher temperatures when the volume increased. The temperature of 600 °C increased the volume of the specimen by 5680 mm<sup>3</sup> (2.23 %). When the composites were loaded to the highest temperature, i.e. 800 °C, the volume increased by 29,226 mm<sup>3</sup>, corresponding to 11.48 %. This change was already visible by the naked eye.

#### 4 Conclusion

This article presents the results of an experimental research dealing with the volume changes of concrete composites based on steel slag during their thermal load. The monitored properties included particularly the flexural and compressive strengths before and after loading. The research has shown that concrete based on steel slag achieves high strength characteristics even after 7 days in a water bath. When subjected to thermal load, the strength of the specimens rapidly decreased during loading at temperatures over 400 °C, and the flexural and compressive strengths decreased almost by half. 3D scanning of the test specimens has shown volume changes in comparison with the reference body in the form of shrinkage or volume increase.

The largest volume increase has been recorded in the body loaded at 800 °C, when the volume increased by up to 11.48 % compared to the reference body. On the other hand, the largest shrinkage occurred in the body after subjecting it to thermal load of 200 °C, when the change was 0.49 % when compared to the reference body. The aim of this research was to verify the possibility of using 3D scanning technology to detect the volume changes of concrete composites based on steel slag, depending on their thermal load. Based on the presented results, it is clear that 3D scanning technology can be used to determine the volume changes of concrete composites.

**Acknowledgments** Article has been done in connection with the following projects:

- Student Grant Competition reg. no. SP2015/16
- Institute of Clean Technologies for Mining and Utilization of Raw Materials for Energy Use—Sustainability program, Reg. No. LO1406
- RMTVC No. LO1203 and the IT4 Innovations Centre of Excellence project, reg. no. CZ.1.05/1.1.00/02.0070

## References

1. Václavík V (2008) Effective utilization of steel-making slag in building industry. *Acta Metall Slovaca* 1:93–102
2. Tomkova V, Ovčačík P, Vlček J et al (2012) Potential modification of hydration of alkali activated mixtures from granulated blast furnace slag and fly ash. *Ceram-Silik* 56:168–176
3. Vlček J, Drongová L, Topinková M et al (2014) Identification of phase composition of binders from alkali-activated mixtures of granulated blast furnace slag and fly ash. *Ceram-Silik* 56:79–88
4. Václavík V, Dirner V, Dvorský T et al (2012) The use of blast furnace slag. *Metallurgy* 51:461–464
5. Brozova S, Jursová S (2012) Processing of Metal-bearings Oxides Wastes, Pet-bottles and worn tyres by plasma heating. *SGEM Albena* 4:745–752
6. Jursová S (2010) Metallurgical waste and possibilities of its processing. In: 19th international conference on metallurgy and materials. *Metal 2010*, pp 115–120
7. Neteringera I, Rukavina MJ, Mladenovič A (2013) Improvement of post-fire properties of concrete with steel slag aggregate. *Procedia Eng* 62:745–753
8. Asi IM, Qasrawi HY, Halabi FI (2007) Use of steel slag aggregate in asphalt concrete mixes. *Can J Civ Eng* 34:902–911
9. Wu S, Xue Y, Ye Q et al (2007) Utilization of steel slag as aggregates for stone mastic asphalt (SMA) mixtures. *Build Environ* 42:2580–2585
10. Wang Q, Yan PY, Han S (2011) The influence of steel slag on the hydration of cement during the hydration process of complex binder. *Sci China Technol Sci*. doi:[10.1007/s11431-010-4204-0](https://doi.org/10.1007/s11431-010-4204-0)
11. EN 197–1 (2012) Cement—Part 1: composition, specifications and conformity criteria for common cements
12. EN 1008 (2003) Mixing water for concrete—specification for sampling, testing and assessing the suitability of water, including water recovered from processes in the concrete industry, as mixing water for concrete
13. EN 933–2 (1999) Tests for geometrical properties of aggregates—Part 2: determination of particle size distribution—test sieves, nominal size of apertures

14. EN 1097-6 (2014) Tests for mechanical and physical properties of aggregates—Part 6: determination of particle density and water absorption
15. EN 196-1 (2005) Methods of testing cement—Part 1: determination of strength
16. EN 12350-6 (2009) Testing fresh concrete—Part 6: density
17. EN 12350-7 (2009) Testing fresh concrete—Part 7: air content—pressure methods
18. EN 12350-2 (2010) Testing fresh concrete—Part 2: slump-test

# Magnetic Alloys Design Using Multi-objective Optimization

R. Jha, G.S. Dulikravich, M.J. Colaço, M. Fan, J. Schwartz  
and C.C. Koch

**Abstract** This work presents a computational design of optimal chemical concentrations of chosen alloying elements in creating new magnetic alloys without rare earth elements that have their multiple desired macroscopic properties extremized. The design process is iterative and uses experimental data and a multi-objective evolutionary optimization algorithm combined with a robust response surface generation algorithm. Chemical concentrations of each of the alloying elements in the initial set of candidate alloys were created using a quasi-random sequence generation algorithm. The candidate alloys were then examined for phase equilibria and associated magnetic properties using a thermodynamic database. The most stable candidate alloys were manufactured and tested for macroscopic properties, which were then fitted with response surfaces. The desired magnetic properties were maximized simultaneously by using a multi-objective optimization algorithm. The best predicted Pareto-optimal alloy

---

R. Jha · G.S. Dulikravich

Department of Mechanical and Materials Engineering, Florida International University,  
Miami, FL 33174, USA  
e-mail: rjha001@fiu.edu

M.J. Colaço

Department of Mechanical Engineering, Federal University of Rio de Janeiro,  
UFRJ/COPPE, Rio de Janeiro, Brazil  
e-mail: colaco@asme.org

M. Fan · J. Schwartz · C.C. Koch

Department of Materials Science and Engineering, North Carolina State University,  
Raleigh, NC, USA  
e-mail: mfan3@ncsu.edu

J. Schwartz

e-mail: Justin\_Schwartz@ncsu.edu

C.C. Koch

e-mail: carl\_koch@ncsu.edu

G.S. Dulikravich (✉)

MAIDROC Laboratory, Florida International University,  
10555 West Flagler Street, EC 3462, Miami, FL 33174, USA  
e-mail: dulikrav@fiu.edu

© Springer Science+Business Media Singapore 2017

A. Öchsner and H. Altenbach (eds.), *Properties and Characterization of Modern Materials*, Advanced Structured Materials 33,  
DOI 10.1007/978-981-10-1602-8\_22

compositions were manufactured, synthesized and tested thus increasing a set of experimentally verified alloys. This design process converges in a few cycles resulting with alloy chemistries that produce significantly improved desired macroscopic properties, thus proving efficiency of this combined meta-modelling and experimental/computational alloy design method.

**Keywords** Alnico alloys · Response surface methodology · Multi-objective optimization · Pareto-optimal · Hierarchical clustering analysis

## 1 Introduction

Rare-earth elements (REE) are important for the development of high-intensity magnets. Recently, the rare-earth crisis has posed a challenging task in front of the materials research community. Basically, the task is to look for alternate options of synthesizing these magnets and prepare it for application as soon as possible. To address this, one may think of using computational tools to aid experimentalist in order to accelerate this process, [1]. From application point of view, it is important to address a few specific bulk properties: magnetic remanence ( $B_r$ ), magnetic coercivity ( $H_c$ ), magnetic energy density ( $(BH)_{max}$ ) and Curie temperature.  $H_c$  is the ability of a magnet to withstand strong external magnetic field without demagnetizing, [2].  $B_r$  corresponds to the amount of magnetic flux density left in the magnet without demagnetizing.  $(BH)_{max}$  is mathematically the area of the largest rectangle that can be inscribed in the second quadrant of the  $B$ - $H$  curve as shown in Fig. 1, [3]. A high  $(BH)_{max}$  means that one can synthesize smaller magnets while maintaining superior magnetic properties. Curie temperature is the temperature above which ferromagnetic behavior disappears as a result of thermal agitation of atoms. Hence, one has to deal with conflicting objectives in order to address the problem.

Magnetism is a result of the motion of electrons around the nucleus. The resultant magnetic moment is a result of orbital motion and spin motion. Atoms that have incomplete shells possess permanent magnetic moment. These moments interact with each other and align themselves parallel to each other. At Curie temperature, thermal energy exceeds exchange interaction. Thus, the material loses its magnetic properties and becomes paramagnetic. This phenomenon is observed predominantly in two groups of elements: 3d elements (Cr, Mn, Fe, Co, Ni) and 4f elements (Ce, Nd, Sm, Eu, Gd, Th, Dy, Ho, Er, Tm). 4f elements mentioned here belong to Lanthanides or are also known as rare-earth elements (REE). Ce, Nd, and Sm are light REEs, while Gd and Dy are heavy. Of these, Ce is the most abundant (less critical) while other REEs are critical in terms of supply. REEs have superior magnetic properties due to the presence of 4f electron, [2]. REE based magnets possess very high  $(BH)_{max}$ ,  $H_c$  and  $B_r$ , [2]. Hence, one can synthesize comparatively smaller magnets without compromising on the magnetic properties. Neodymium based magnets are the strongest available magnets in this family. Samarium–Cobalt based magnets are next to it. Gd and Dy are usually added in varying amounts in

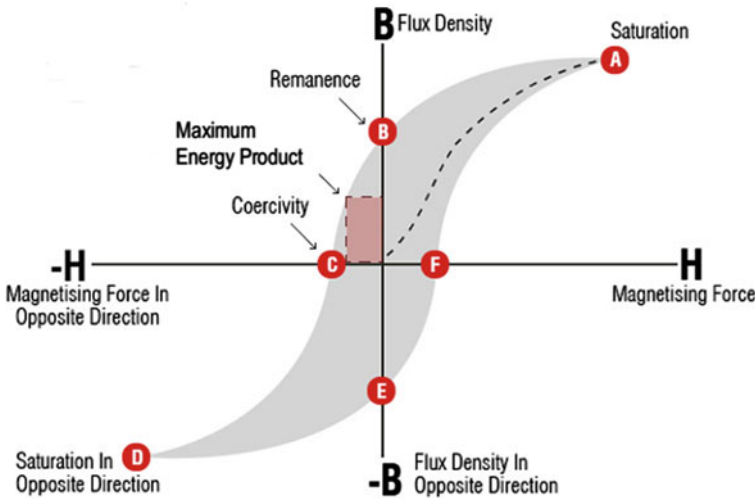


Fig. 1 B-H curve shows relation between  $H_c$ ,  $B_r$  and  $(BH)_{max}$  [3]

order to improve magnetic properties. However, performance of these magnets deteriorates significantly with the rise of temperature. For example, Nd-Fe-B (neodymium-iron-boron) magnets perform the best up to 150 °C [4]. For applications in the range of 150–350 °C, Sm-Co (samarium-cobalt) magnets are usually used. REE-based magnets are susceptible to corrosion and usually need a protective coating in order to prevent corrosion. REE-based magnetic materials are essential in electric cars, in wind turbine electric generators, and any high-efficiency electric devices requiring magnetic fields. Thus, REEs are strategic materials determining which national economies will survive and prosper in the post combustion-engine era. The problem is that deposits of most of the REEs used for synthesizing these magnets are concentrated in a relatively small geographic area. Due to depleting resources and stringent trade rules from the suppliers, it is important to look at other options to synthesize high performance permanent magnets.

Alnico magnets are permanent magnetic alloys predominantly based on the Fe-Co-Ni-Al system without REEs, [2]. Alnico magnets possess very high  $B_r$  values that are comparable to REE magnets. Alnico magnets have lower  $H_c$  values. However, low  $H_c$  also means that these magnets can be easily magnetized to saturation. A high  $B_r$  and low  $H_c$  value help to cast this material in complex shapes while magnetizing it in the production heat treatment stages. Alnico magnets offer excellent corrosion resistance and high-temperature stability and are the only magnets that can be used up to 800 °C. The excellent high-temperature stability combined with a comparatively higher temperature limits have been successfully exploited by researchers in the past. These properties make it a perfect choice for military and automotive sensor applications. Hence, any improvement in the existing properties of Alnico alloys will help in covering the gap between the

Alnico and REE based magnets. This will help in addressing a few important energy conversion applications.

In the present research work, a novel approach is presented for implementation of computational tools (various machine learning algorithms) in design and multi-objective optimization of permanent magnetic Alnico type alloys. The proposed research combines a number of numerical design optimization algorithms with several concepts from artificial intelligence and experimentally evaluated desired properties of an affordable set of candidate alloys. These alloys were further screened by various statistical tools in order to determine various patterns, or any specific trend in the data set. This information will be helpful to the research community in developing a material knowledge base for development of new alloys for targeted properties.

## 2 Background

At present, researchers around the globe are working on finding alternatives in order to design magnetic alloys that will be able to cover the gap between the properties achieved by Alnico magnets and the rare-earth magnets. An initiative in Europe, Replacement and Original Magnet Engineering Options (ROMEEO) program has laid down certain guidelines for researchers that will help to address this topic, [1]. It varies from recycling devices containing rare-earth metals to finding new mines outside China and Russian federation as well as designing magnets without rare-earth additions or with a minimal amount of those rare-earth elements that are less critical in the sense of supply. This will help in addressing a few important energy conversion applications. Sellmyer et al. worked on a few rare-earth free alloys and the properties were found to be in the vicinity of Alnico alloys, [5]. Zhou et al. demonstrated the scope of improvement of magnetic properties of Alnico alloys by theoretical modeling, [6]. However, the difference between the theoretically calculated and the measured properties were quite large for  $(BH)_{max}$  and  $H_c$ . Hence, random experimentation may be misleading in terms of improvement in alloy properties while being both expensive and time-consuming.

Development of new alloys or even improving the properties of existing alloys is a challenging task mainly due to limited experimental database. Over the years, there has been a growing trend of using machine learning algorithms in materials science, [7–9].

Machine learning algorithms that have been successfully used in materials science domain can be categorized as supervised learning and unsupervised learning algorithms.

- Supervised learning algorithms like neural networks, support vector machines, genetic programming has been successfully used in the past. These algorithms were used to predict processing-structure-property relationship, predict and classify crystal structures, develop model Hamiltonian.

- Unsupervised learning algorithms like principal component analysis (PCA), hierarchical cluster analysis (HCA), *K*-means clustering have been used to address a few important features regarding the dataset. These algorithms can be used to analyze composition spreads, analyze micrographs and noise reduction in the datasets.

A reliable knowledge base for design of new alloys, can be developed by focusing on determining various correlations (composition-property, property-property, composition-composition) from the available databases (simulated and experimental), [10]. This information can be coupled with the theoretical knowledge (atomistic and continuum based theories) to develop the knowledge base. In recent years, integrated computational materials engineering approach along with the materials genome initiative highlights the importance and growing application of computational tools in the development of new alloys, [11]. It aims at reducing a new alloy development cycle from currently 10 years to two years or even less. Various data-driven techniques combined with evolutionary approaches have been successfully implemented in alloy design and also in improving thermodynamic databases such as ThermoCalc for alloy development, [7, 8, 12–16]. Data mining approaches such as PCA and partial least square (PLS) regression have been successfully used in designing new alloys, [17], as well as determining properties of element Lutetium, [18]. These applications demonstrate the efficacy of application of computational tools for materials design. This acted as motivation for us in proceeding forward to design our own approach for design and optimization of magnetic alloys.

In this work, we will be using a number of machine learning algorithms. We will be using the response surface methodology approach to develop meta-models that will link the bulk properties to the chemical composition. Multi-objective optimization of targeted properties will be done in order to predict the next set of alloys, basically by using various algorithms based on evolutionary approaches. Data analysis will be performed to discover various patterns within the dataset by using various statistical tools.

## 2.1 *Alnico Magnets*

Alnico magnets were discovered in 1931 by Mishima in Japan [2, 3]. These magnets were based on the Fe–Co–Ni–Al system. Magnetic properties in these magnets were attributed to the presence of a two-phase system of body centered cubic (BCC),  $\alpha_1$  and  $\alpha_2$ . In later years, it was observed that separation of  $\alpha_1$  and  $\alpha_2$  is due to a metallurgical phenomenon popularly known as “Spinodal” decomposition.  $\alpha_1$  is Fe–Co rich ferromagnetic phase, while  $\alpha_2$  is Ni–Al rich phase. These phases are stable up to 850 °C (Curie temperature is about 860 °C). Above 850 °C, the face centered cubic (FCC) phase begins to appear. FCC phase is quite detrimental for magnetic properties. In the past, an FCC  $\gamma$  phase was observed in a few compositions [3]. In later years, various attempts were made to stabilize the



magnetic  $\alpha_1$  and  $\alpha_2$  phases, while at the same time eliminate or reduce the amount of FCC  $\gamma$  phase. These attempts include modification of heat treatment protocol and addition of other alloying elements to enhance various magnetic properties of these materials. Due to the discovery of powerful REE-based magnets, there has been limited research on Alnico magnets after 1980. The recent rise in prices of rare earth elements led to the search magnets that are free of REEs and has motivated researchers to work on improving magnetic properties of Alnico magnets. Due to their proven high-temperature stability and related properties, Alnico magnets are a popular choice for research.

Currently, Alnico alloys contain 8+ elements. Calphad approach can successfully handle ternary or at most quaternary systems [19]. This makes this work even more complicated. In our work, we used 8 alloying elements on the basis of available literature and mutual discussion. These elements include iron (Fe), cobalt (Co), nickel (Ni), aluminum (Al), titanium (Ti), hafnium (Hf), copper (Cu) and niobium (Nb). Variable bounds of these elements have been tabulated in Table 1. It is important to know the role of these alloying elements initially for the manufacture of alloys for targeted properties. Later, this information can be utilized to select a meta-model for a certain property. This is done with a purpose to develop a knowledge base for discovery of new materials while improving properties of existing materials.  $(BH)_{max}$  is mathematically the area of the largest rectangle that can be inscribed in the second quadrant of the  $B-H$  curve as shown in Fig. 1. Coercivity and remanence are conflicting that is one has to sacrifice on one of these properties to improve the other property. Therefore, in order to increase  $(BH)_{max}$ , one needs to optimize  $H_c$  and  $B_r$ . Hence, multi-objective optimization will prove to be an asset to address this problem.

Role of various alloying elements and their effects on  $H_c$  and  $B_r$  have been addressed by Dillon [3] and are summarized here.

1. Cobalt is a  $\gamma$  stabilizer. Hence, a solutionization anneal is needed to homogenize it to a single phase. It increases  $H_c$  and Curie temperature.
2. Nickel is also a  $\gamma$  stabilizer. Hence, a higher solutionization anneal temperature is needed to homogenize the gamma phase. It increases  $H_c$  (less than cobalt) but, at the expense of  $B_r$ .

**Table 1** Concentration bounds AlNiCo type alloys

Alloying elements	Variable bounds (wt%)		
	1–85	86–143	144–180
Cobalt (Co)	24–40	24–38	22.8–39.9
Nickel (Ni)	13–15	13–15	12.35–15.75
Aluminum (Al)	7–9	7–12	6.65–12.6
Titanium (Ti)	0.1–8	4–11	3.8–11.55
Hafnium (Hf)	0.1–8	0.1–3	0.095–3.15
Copper (Cu)	0–6	0–3	0–4.5
Niobium (Nb)	0–2	0–1	0–1.5
Iron (Fe)	Balance to 100		

3. Aluminum is an  $\alpha$  stabilizer. Hence, it will help in reducing the solutionization temperature. It affects  $H_c$  positively.
4. Copper is an  $\alpha$  stabilizer. It increases  $H_c$  and  $B_r$ . In Alnico 8 and 9 alloys, Cu precipitates out of the  $\alpha_2$  phases into particles and increases the magnetic separation between  $\alpha_1$  and  $\alpha_2$  phases. It results in an increase in  $H_c$ . In Alnico 5–7 alloys, Cu remains in  $\alpha_2$ . It leads to an increase in  $H_c$  while a decrease in Curie temperature.
5. Titanium is also an  $\alpha$  stabilizer. It is one of the most reactive elements. It reacts with impurities such as S and N and precipitates out thus purifying the magnet. It also eliminates carbon which is a strong  $\gamma$  stabilizer and needs to be eliminated at any cost. Titanium helps in grain refining and inhibits columnar grain growth. Due to columnar grain growth, majority of grains are aligned perpendicular to the chill plate. Large shape anisotropy can be achieved if spinodal decomposition occurs in this direction. Titanium increases  $H_c$  while it decreases  $B_r$ .
6. Niobium is also an  $\alpha$  stabilizer. It helps in neutralizing the effects of carbon. Like titanium, Nb inhibits columnar grain growth. Nb increases  $H_c$ , while it decreases  $B_r$ . However, the decrease in  $B_r$  due to Nb is less than that observed due to Ti.
7. Hafnium is used for enhancing high-temperature properties. Hf usually precipitates at the grain boundary and helps in improving creep properties. Recent studies related to Co–Hf magnets motivated us to use Hf in this work, [20].

### 3 Current Research

In this work, we used a set of computational tools to develop a novel approach for design and optimization of high-temperature, high-intensity magnetic alloys, [15]. The steps involved in the proposed approach can be listed as follows.

1. Initial dataset: From the open literature and our expertise, we defined the concentration bounds of 8 alloying elements that we used to create alloy. Within these bounds, we used a well-known quasi-random sequence generator [25], to generate chemical concentrations for each of the initial 80 candidate alloys (see Tables 1 and 2). The initial set of alloys was screened on the basis of limited knowledge of phase equilibrium and magnetic property from a commercial thermodynamic database, Factsage [21].
2. Manufacture and testing: The alloys were manufactured and tested for various properties of interest as shown in Table 3. This work was performed at North Carolina State University.
3. Response surface generation: From the available data, response surfaces were developed for the measured and calculated properties listed in Table 3. We used a commercial optimization package, modeFRONTIER for this purpose [22]. The response surfaces were developed using the following algorithms: Radial

**Table 2** Cycle and alloy number

Cycle number	Alloys designed	Best alloy (number)
1	1–80	30
2	81–85	84
3	86–90	86
4	91–110	95
5	111–120	117
6	120–138	124
7	139–143	139
8	144–150	150
9	151–160	157
10	161–165	162
11	166–173	169
12	174–180	180

**Table 3** Quantities to be simultaneously extremized using multi-objective optimization

	Properties	Units	Objective
1	Magnetic energy density ( $(BH)_{max}$ )	$\text{Kg m}^{-1} \text{s}^{-2}$	Maximize
2	Magnetic coercivity ( $H_c$ )	Oersted	Maximize
3	Magnetic remanence ( $B_r$ )	Tesla	Maximize
4	Saturation magnetization ( $M_s$ )	Emu/g	Maximize
5	Remanence magnetization ( $M_r$ )	Emu/g	Maximize
6	$((BH)_{max})/\text{mass}$	$\text{m}^{-1} \text{s}^{-2}$	Maximize
7	Magnetic permeability ( $\mu$ )	$\text{Kg m A}^{-2} \text{s}^{-2}$	Maximize
8	Cost of raw material ( <i>cost</i> )	USD/Kg	Minimize
9	Intrinsic coercive field ( $jH_c$ )	$\text{A m}^{-1}$	Maximize
10	Density( $\rho$ )	$\text{Kg m}^{-3}$	Minimize

basis functions (RBF), Kriging, Anisotropic Kriging and Evolutionary Design. Each response surface was tested using various accuracy measures and the most accurate one was chosen for further study.

- Multi-objective optimization: The most accurate response surfaces were used to extremize the various properties as per the objectives specified in Table 3. Several optimization runs were performed to get a diverse pool of results. The optimization algorithms used in modeFRONTIER were: Non-dominated Sorting Genetic Algorithm II (NSGA2), Multi-Objective Particle Swarm Optimization (MOPSO), Multi-Objective Simulated Annealing (MOSA) and FAST optimizer (FAST uses response surface models (meta-models) to speed up the optimization process using various algorithms like NSGA2, MOPSO, MOSA), [22]. Besides modeFRONTIER optimization software, we also used IOSO optimization software [7], an in-house hybrid response surface generation algorithm [23, 24] and a surrogate model selection algorithm [24]. Predictions from the

optimization packages were merged and a set of Pareto-optimized alloy concentrations were selected for manufacture and testing.

5. The computational-experimental work was performed in cycles to check upon improvements over the previous cycles. Steps 2–2 were repeated until the improvements of multiple macroscopic properties of such magnetic alloys become negligible in consecutive cycles.
6. Sensitivity analysis: Various statistical tools were used to determine composition-property relations. This was done in order to find the most and the least influential alloying element so as to make way for possible single affordable rare-earth element addition.
7. Hierarchical cluster analysis (HCA) was used to determine pattern in the dataset as a whole and in the clusters as well. This can be used to screen alloys before manufacture.

This work is aimed at developing a knowledge base that will motivate experimentalists to make modifications in standard manufacture protocols for improvements. This will also help the research community in designing new alloys for targeted properties. In data-driven material science, one needs to focus upon a few key factors that will help in developing knowledge base for designing new materials, [10]:

1. Data: Our database is a combination of experimentally verified data predicted by a well-known random number generator and data from Pareto-optimized predictions as discussed above.
2. Correlations: Dataset was examined by a set of statistical tools and various linear and non-linear correlation, hierarchical clustering analysis, and principal component analysis tool to discover various trends in the dataset.
3. Theory: This information can be coupled with theoretical knowledge to motivate the experimentalists to move forward with the manufacture of new alloys.

## 4 Results

At present, we have worked through 12 cycles of design and optimization followed by experimental validation. Table 2 lists the alloys manufactured in each of the cycles and the best alloy in each cycle ranked on the basis of  $(BH)_{max}$  values. Work done in all the cycles are described as follows:

1. Cycle 1 (Alloys 1–80): As discussed in Sect. 3, initial chemical compositions were predicted randomly by Sobol’s algorithm [25]. A set of 80 such candidate compositions was manufactured and macroscopic properties of each of these alloys measured.
2. Cycle 2 (Alloys 81–85): Using experimentally measured properties of these 80 initial alloys, response surfaces were created and multi-objective optimization

was performed resulting in 5 new Pareto-optimized chemical compositions. These 5 predicted compositions were manufactured and their macroscopic properties measured. It was observed that one of the predicted alloys (alloy 84) outperformed the initial set of alloys and the other Pareto-optimized alloys. This demonstrates the efficacy of the current approach in using computational tools in materials design. The bounds on chemical concentrations of alloying elements were modified (Table 1) to accelerate the design.

3. Cycle 3 (Alloys 86–90): Using experimentally measured properties of the 80 + 5 alloys, response surfaces were created and multi-objective optimization was performed resulting in 5 new Pareto-optimized chemical compositions. These 5 predicted chemical compositions were manufactured and their macroscopic properties measured. In this cycle, alloy 86 was the best candidate. It was observed that the measured properties of the new set (alloys 86–90) were in the vicinity of the previous set of alloys. This can be attributed to non-uniform distribution of some of alloying elements in the initial set of 80 candidate compositions which was due to an oversight on the part of users of the random sequence generator. This negatively affected the accuracy of the response surfaces resulting in no significant improvement over the previous cycle.
4. Cycle 4 (Alloys 91–110): Therefore, next set of 20 alloys were randomly predicted by Sobol's algorithm [25] specifically to improve the uniformity of distribution of concentrations of the 8 alloying elements. This provided response surfaces with more uniform support in the eight-dimensional variable space. These 20 random alloys were manufactured and their macroscopic properties measured. In this cycle, alloy 95 was the best performer. Alloy 95 had an  $H_c$  of 980 Oe (as compared to 750 Oe for the previous best alloy 84).
5. Cycle 5 (Alloys 111–120): Using measured values of the macroscopic properties of the 110 alloys, response surfaces were created and multi-objective optimization was performed resulting in 10 new Pareto-optimized alloys. These 10 chemical compositions were then manufactured and their properties measured. We observed significant improvements in the properties of the new alloys. Alloy 111 and 114 had  $H_c$  of 1050 Oe and alloy 117 reported 1000 Oe (as compared to 980 Oe for the previous best alloy 95). In this cycle, alloy 117 was the best alloy in terms of  $(BH)_{max}$ .
6. Cycle 6 (Alloys 121–138): Using measured values of the macroscopic properties of the 120 alloys, response surfaces were created and multi-objective optimization was performed resulting in 18 new Pareto-optimized alloys. These 18 alloys were then manufactured and their properties measured. In this cycle, alloy 124 was the best performer. We observed significant improvement in both  $(BH)_{max}$  and  $H_c$ .
7. Cycle 7 (Alloys 139–143): Using measured values of the macroscopic properties of the 138 alloys, response surfaces were created and multi-objective optimization was performed resulting in 5 new Pareto-optimized alloys. These 5 alloys were then manufactured and their properties measured. In this cycle, alloy 139 was the best performer, although its properties were in the vicinity of alloy 124. Since there was no significant improvement in the desired properties,

design and optimization task was halted at this point to minimize waste of resources and funding. There was a clear need to perform a sensitivity analysis of the variables and associated properties as well as to test a hybrid response surface [24]. Consequently, in cycles 8–11 (Alloys 144–180) bounds on concentrations of each of the alloying elements were relaxed by 5 %, while the overall methodology remained the same (as mentioned in Sect. 3).

8. Cycle 8 (Alloys 144–150): Using modeFRONTIER software there was a marginal improvement in  $H_c$ , with no improvement in other properties of new alloys.
9. Cycle 9 (Alloys 151–160): using surrogate model selection algorithm (SM), no significant improvement was observed in this cycle for any of the properties discussed in Table 3.
10. Cycle 10 (Alloys 161–165): Using modeFRONTIER software there was a marginal improvement in  $H_c$ .
11. Cycle 11 (Alloys 166–173): Using a hybrid response surface and modeFRONTIER software there was a marginal improvement in  $H_c$ , with no improvement in other properties.
12. Cycle 12 (Alloys 173–180): Using a hybrid response surface and modeFRONTIER software, there was a marginal improvement in  $H_c$ , with no improvement in other properties.

Figures 2, 3 and 4 show the comparison between various approaches for several macroscopic properties of alloys created in this work. These figures demonstrate that the alloys predicted by meta-modeling and multi-objective optimization dominate the ones predicted by random design approach either by Sobol’s algorithm or a human brain. The achieved properties improved in consecutive cycles:

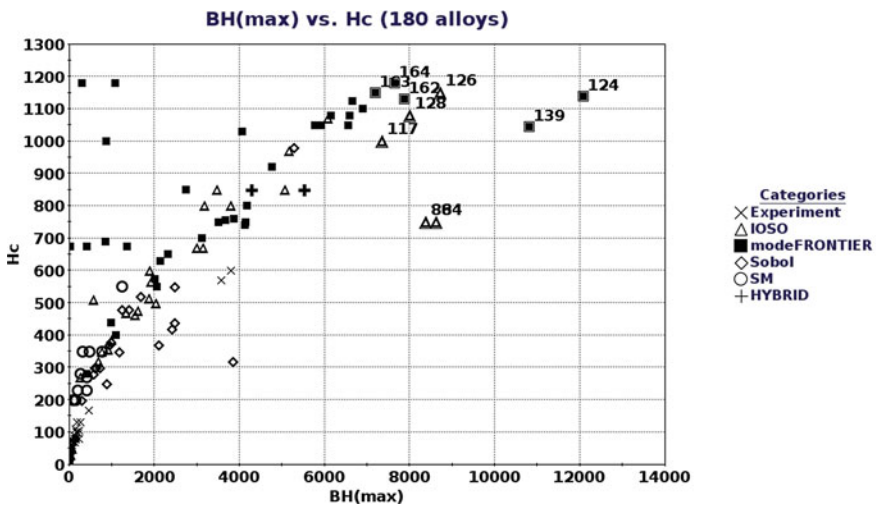


Fig. 2 Magnetic energy density versus magnetic coercivity

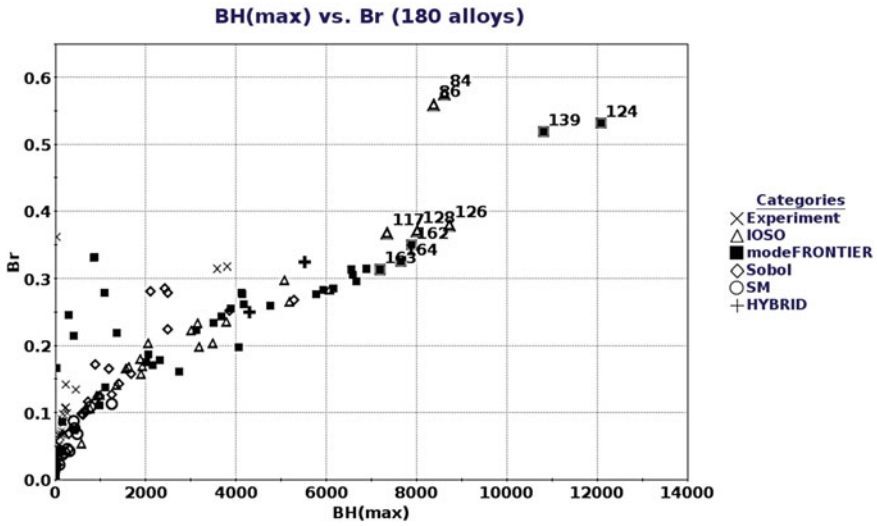


Fig. 3 Magnetic energy density versus magnetic remanence, comparison of solutions by various approaches

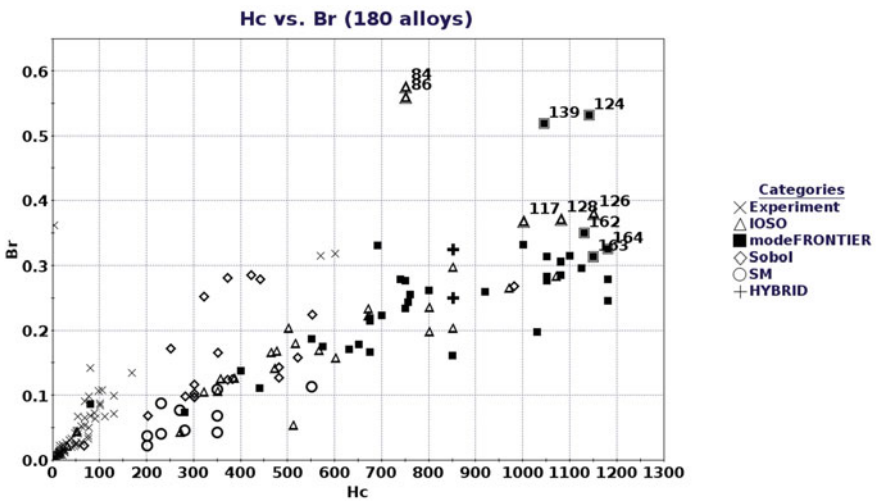


Fig. 4 Magnetic coercivity versus magnetic remanence, comparison of solutions by various approaches

$H_c$  values are at par with commercial alloys [6], while further improvements in  $(BH)_{max}$  and  $B_r$  values are expected in the next few cycles. Hence, sensitivity analysis of the response surfaces and pattern recognition in the dataset need to be performed at this point.

## 5 Sensitivity Analysis

This was done in order to establish/determine the composition-property relationship, find various trends and patterns within the dataset. Initially, Pearson's linear correlation method was used (not reported here), [15]. Coefficients were too low. This was expected as the dataset is quite noisy. A few other statistical measures used to address this issue are discussed below.

### 5.1 Single Variable Response (SVR)

SVR has been used in the past for qualitative analysis of the training results obtained from evolutionary neural network [26] and bi-objective genetic programming, [16, 27]. Here, a trend of variation is created by generating values between 0 and 1 on a time scale. The trend line is intentionally made irregular so that there are regions of constant values, sharp increases, and sharp decreases in the line. This is done to emulate non-linear behavior of the dataset. It has been referred to as an input signal in the following text. This input signal (a trend of variation) was used for one of the variables (concentration of one of the alloying chemical elements), while the other variables were kept constant at an average value. The various responses were tabulated in Table 4 for each of the models. Following terminologies were used for the responses:

- Direct: In this case, the model output increases by increasing the value of an input signal and decreases on decreasing the value.
- Inverse: In this case, a particular variable will affect the model output in an opposite manner.

**Table 4** Single variable response for various properties

Sl. no.	Single variable response (SVR)								
	Properties	Fe	Co	Ni	Al	Ti	Hf	Cu	Nb
1	$(BH)_{max}$	Nil	Nil	Mixed	Nil	Nil	Nil	Nil	Nil
2	$H_c$	Mixed	Mixed	Mixed	Inverse	Mixed	Direct	Direct	Mixed
3	$B_r$	Mixed	Mixed	Mixed	Inverse	Mixed	Direct	Direct	Inverse
4	$M_s$	Direct	Inverse	Direct	Mixed	Inverse	Direct	Mixed	Mixed
5	$M_r$	Nil	Nil	Nil	Nil	Nil	Nil	Nil	Nil
6	$(BH)_{max}/mass$	Nil	Nil	Nil	Nil	Nil	Nil	Nil	Nil
7	$\mu$	Mixed	Mixed	Mixed	Mixed	Inverse	Mixed	Mixed	Mixed
8	$cost$	Inverse	Inverse	Inverse	Direct	Direct	Direct	Inverse	Direct
9	$jH_c$	Mixed	Mixed	Mixed	Inverse	Inverse	Mixed	Direct	Mixed
10	$\rho$	Mixed	Direct	Mixed	Inverse	Inverse	Mixed	Mixed	Direct



- Nil: This means that the model was unable to find any correlation between that particular variable and the model output.
- Mixed: In this case, the model has a different response for a different set of data of any particular variable.

Since current experimental dataset is quite noisy, the SVR analysis resulted in many mixed responses. However, a few important findings can be listed as follows.

1. Copper shows a direct response for  $H_c$  and  $B_r$ , thus response surface predictions are at par with available literature, [3]. This has been discussed earlier in Sect. 2.1.
2. Hafnium shows a direct response for  $H_c$  and  $B_r$ . Hf has not been previously used in Alnico alloys. Hence, further data analysis is required before reaching a final conclusion.
3. Nickel shows mixed response with  $(BH)_{max}$ .

Thus, meta-modeling can prove to be an asset for developing alloys in future as well as in predicting the properties of alloys with a new composition. We moved forward to analyze the dataset by few other machine learning tools in order to cross check our findings.

## 5.2 Hierarchical Cluster Analysis (HCA)

Clustering analysis is usually performed to find a pattern in a dataset. A cluster consists of data points which are similar to the other data points within the same cluster, while dissimilar to data points in the other clusters. In most cases, the similarity criterion is the Euclidian distance between the data points.

In HCA, clustering begins with each data point within a cluster [9, 22]. These clusters are iteratively merged to form larger ones and finally merged into one large cluster. In this work, clustering was done by Ward's approach while there are several other alternatives for the same [22, 28]. The final result is a tree like structure referred to as "dendrogram", which shows the way the clusters are related. The user can specify a distance or number of clusters to view the dataset in disjoint groups. In this way, the user can eliminate a cluster that does not serve any purpose as per his expertise.

In this case, we used multivariate data analysis (MVA) node in optimization package: modeFRONTIER [22] and another statistical software known as IBM SPSS [28] for HCA analysis. The alloys were clustered on the basis of targeted properties. Dendrogram was cut in a manner so that it results in a total of 9 clusters (Cluster 0 to Cluster 8) as denoted by the numbers in the dendrogram plot. Figure 5 shows the dendrogram plot obtained from HCA analysis. Cluster 8 and cluster 7 were merged as one when analyzed by Ward's approach. Clustering parameters and the number of alloys included in each cluster have been tabulated in Table 5.

**Fig. 5** Dendrogram plot from HCA analysis

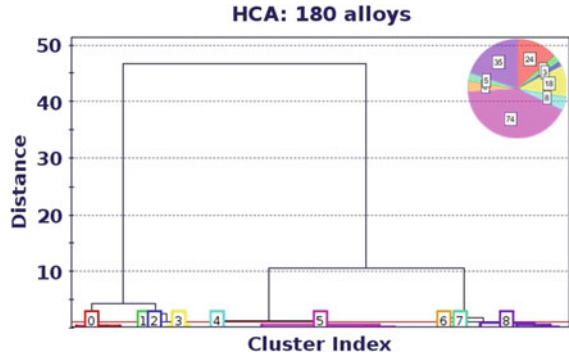


**Table 5** Clustering parameters in HCA analysis

Cluster number	Cluster size	ISim	ESim	Best alloy
0	24	2.5	1.1	175, 115
1	4	1.5	0.6	84, 86, 124, 139
2	3	1.5	0.7	145, 146, 147
3	18	3.2	0.8	117, 126, 128
4	8	4.5	1.3	
5	74	4.6	1.0	
6	6	1.7	1.0	
7	40	2.1	1.3	

Clusters are classified by the following measures [22].

1. Internal similarity (ISim): It reflects the compactness of the  $k$ th cluster. It must be higher.
2. External similarity (ESim): It reflects the uniqueness of  $k$ th cluster. It must be lower.
3. Descriptive variables: These are the most significant variables that help in identifying cluster elements that are similar to one another.
4. Discriminating variables: These are the most significant variables that help in identifying cluster elements that are dissimilar to other clusters.

From Table 5, we can see that cluster 1, cluster 2 and cluster 3 have higher Isim, while a lower Esim when compared to other clusters. Cluster 1 and cluster 3 contain top 10 alloys based on  $(BH)_{max}$  value, while alloys in cluster 2 possess high  $H_c$ .

HCA analysis can be used to cross-check the findings of SVR analysis mentioned above in the text. The following text includes cluster scatter plots for various elements versus  $(BH)_{max}$ ,  $H_c$  and  $B_r$  followed by relevant information extracted from them. In the following figures, confidence level for both the confidence interval and confidence ellipse is 0.9. These figures can be helpful in determining the variable bounds for targeted properties.

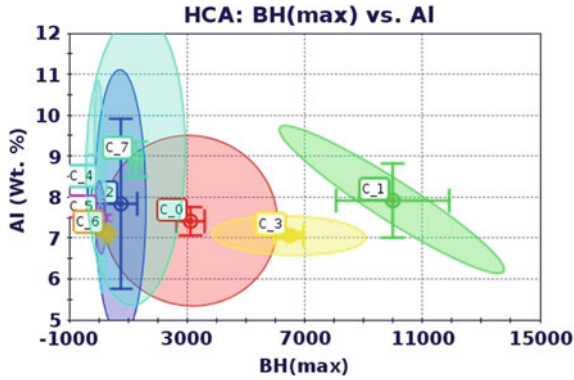


Fig. 6 Clusters scatter:  $(BH)_{max}$  versus aluminum concentration

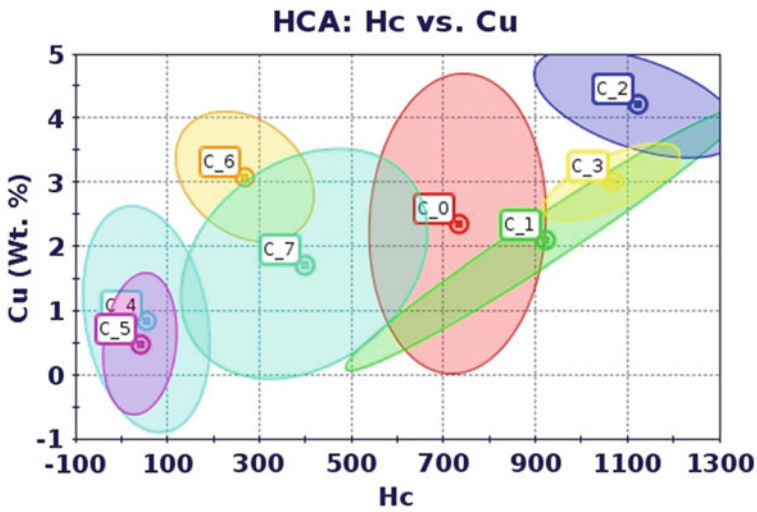


Fig. 7 Cluster scatter:  $H_c$  versus copper concentration

In Fig. 6, for cluster 1,  $(BH)_{max}$  increases with decrease in aluminum content in the range 6–10 wt%. Other clusters have mixed response for variation of aluminum.

It can be seen from Fig. 7 that  $H_c$  increases with an increase in Cu content in cluster 1 and cluster 3, while  $H_c$ , decreases with increasing Cu content in cluster 2 in a narrow composition range. Overall, copper affects  $H_c$  positively, and this is known from the literature (Sect. 2.1) as well as SVR analysis (Sect. 5.1).

From Fig. 8, it is difficult to determine the role of Cu addition on  $B_r$ . From literature (Sect. 2.1) as well as SVR analysis (Sect. 5.1, Cu tends to affect  $B_r$  positively. Hence, this needs further investigation.

**Fig. 8** Cluster scatter:  $B_r$  versus copper concentration

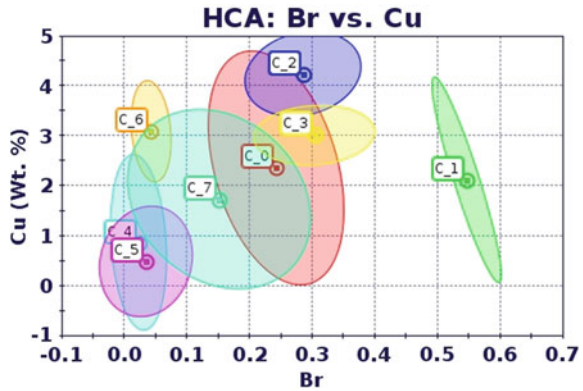


**Fig. 9** Clusters scatter:  $(BH)_{max}$  versus copper concentration

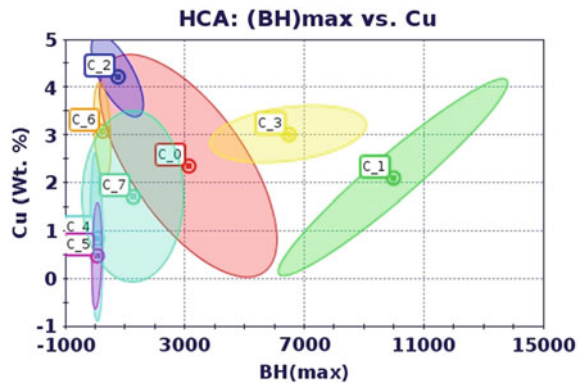


Figure 9 shows scatter plot for  $(BH)_{max}$  versus copper for various clusters. This behavior was expected as  $B_r$  and  $H_c$  are conflicting (see Figs. 1, 7 and 8). It is difficult to determine the role of Cu addition from  $(BH)_{max}$  versus Cu plot.

From Fig. 10, one can observe that in cluster 2 and cluster 7,  $H_c$  tends to increase with an increase in Ti content.

From Fig. 11, it can be seen that in order to increase  $(BH)_{max}$ , one needs to stay in a narrow concentration range for Fe.

Nickel showed a weak response for  $(BH)_{max}$  in SVR analysis (Sect. 5.1). Hence, we plotted scatter plots for Ni versus  $(BH)_{max}$ . From Fig. 12, it can be observed that in cluster 1,  $(BH)_{max}$  increases with decrease in Ni content. This can also be observed in cluster 2.

One can also use these plots for discarding a few alloying elements in order to make way for REE addition. We plotted scatter plots for niobium versus  $(BH)_{max}$ ,  $H_c$  and  $B_r$  with this objective in mind. From Figs. 13, 14 and 15, one can see that Nb is almost neutral to  $H_c$  and  $B_r$ . This was also observed in SVR analysis (Sect. 5.1). Additionally, Nb has the same effect as Ti (Sect. 2.1). Hence, one can think of manufacturing a few samples without Nb. Or, replacing Nb and with a REE.

**Fig. 10** Clusters scatter:  $H_c$  versus titanium concentration

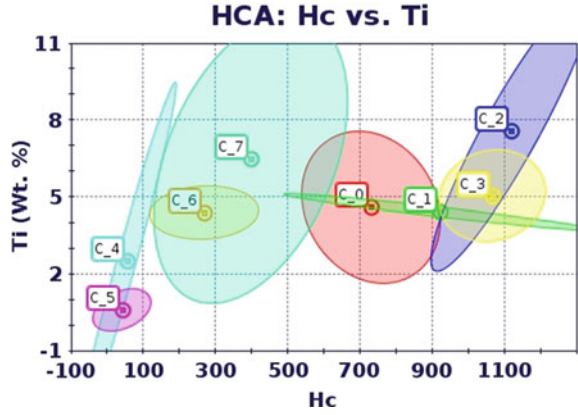


**Fig. 11** Clusters scatter:  $(BH)_{max}$  versus iron concentration

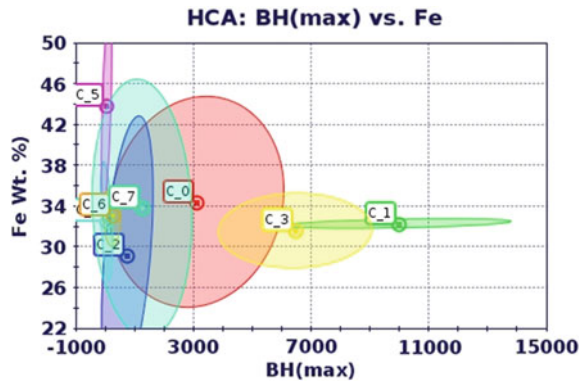


**Fig. 12** Clusters scatter:  $(BH)_{max}$  versus nickel concentration

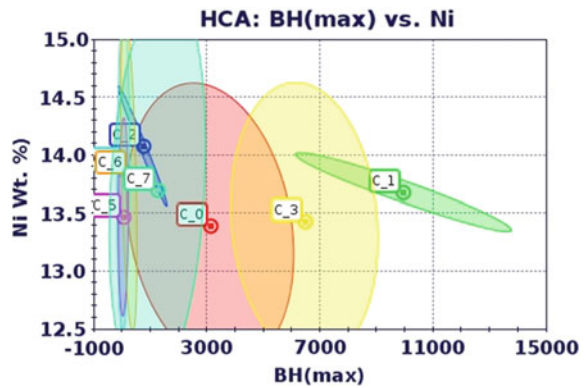


**Fig. 13** Clusters scatter:  $H_c$  versus niobium concentration

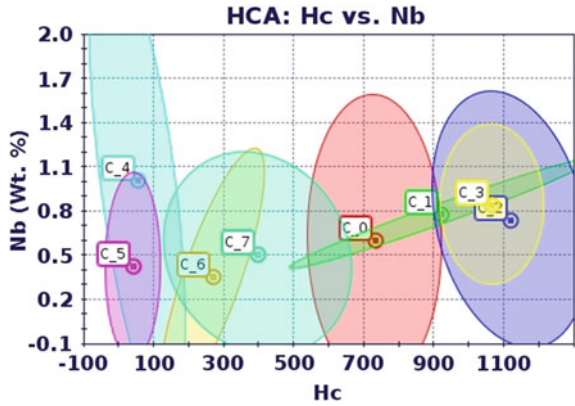


**Fig. 14** Clusters scatter:  $B_r$  versus niobium concentration

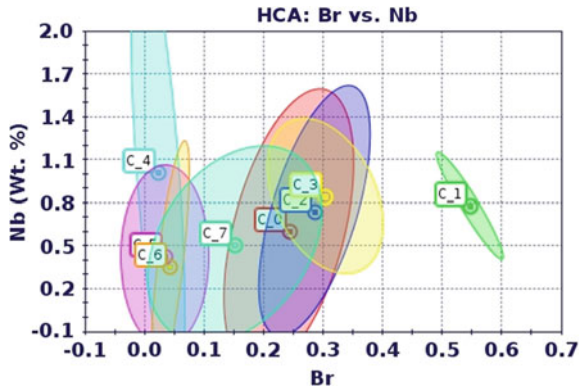
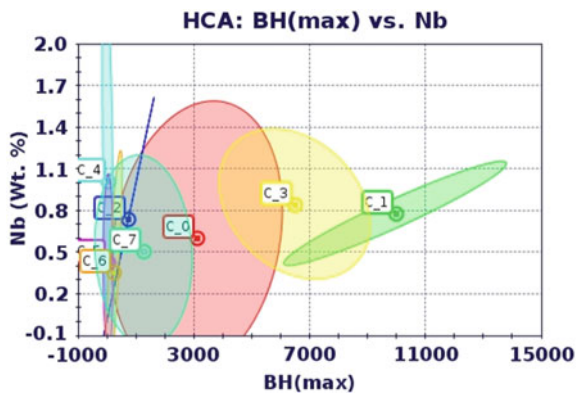


**Fig. 15** Clusters scatter:  $(BH)_{max}$  versus niobium concentration



### 5.3 Thermodynamic Analysis

In this research, we have been using 8 alloying elements. Hence, it will be helpful for the experimentalists to have some information regarding the stability of critical phases during manufacture and designing heat treatment protocols. In this work, we studied phase stability of a few Alnico type alloys from 0 to 1200 °C using Factsage software [21]. The resulting diagrams are based on equilibrium calculation, hence the final experimental results may be different. However, these diagrams can be used as a guideline for the experimentalists when selecting alloys prior to manufacture [16, 29].

From Fig. 16, it can be observed that alloy 124 is thermodynamically stable up to 800 °C, while in alloys 84, 86 and 126 transformation (BCC-FCC) starts at a lower temperature. Hence, the experimentalists can design a heat treatment protocol so they can avoid transformations that will have a detrimental effect on the magnetic properties. We extended this analysis by modifying the composition of alloy 124. We added Mn in various amounts and plotted the critical phases.

From Fig. 17, it can be seen that these additions had detrimental effect and BCC-FCC transformation starting well below 800 °C. Consequently, at this point we can say that Alnico type alloys should not have any Mn and B addition.

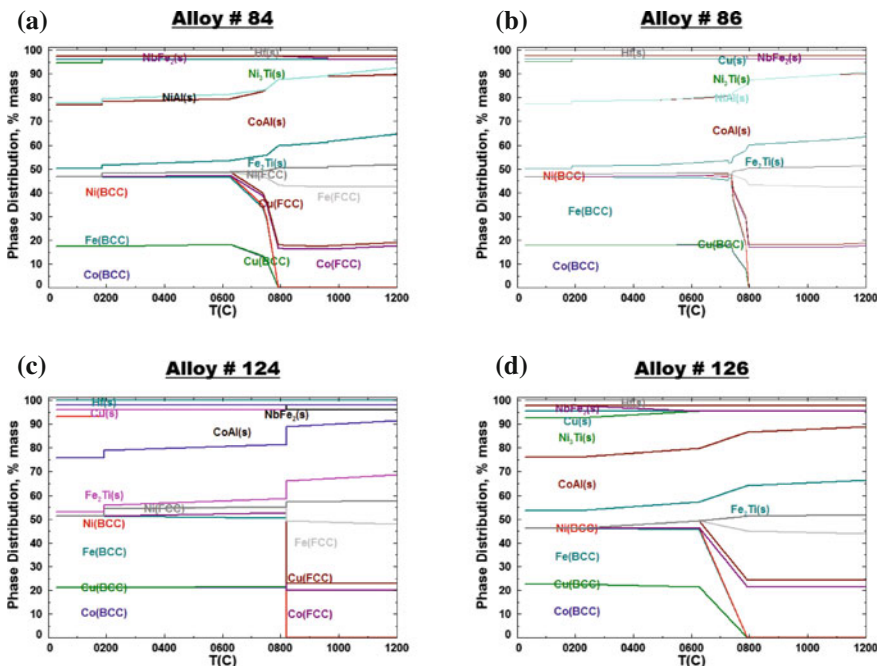
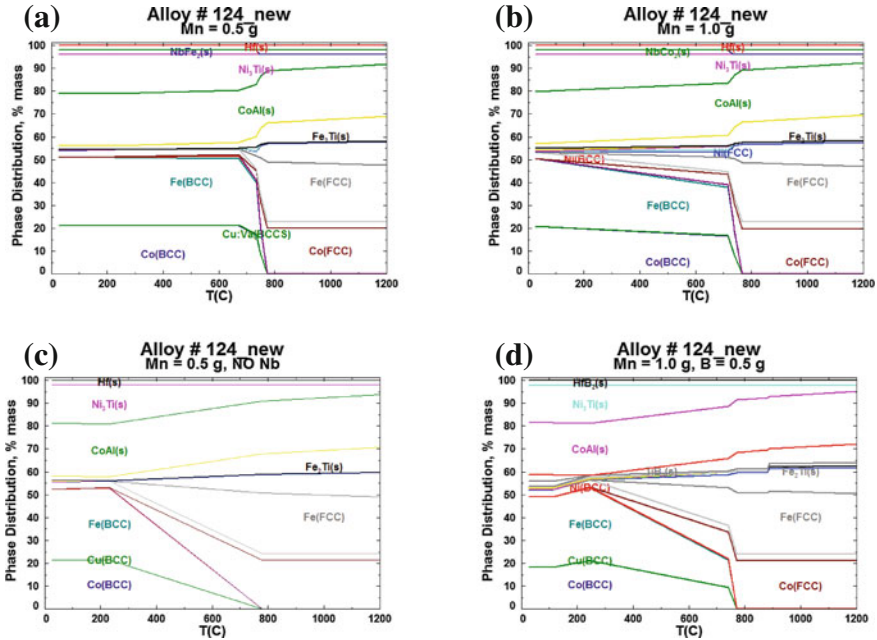


Fig. 16 Phase distribution diagrams for alloy a 84, b 86, c 124 and d 126





**Fig. 17** Phase distribution diagram obtained after modifying composition of alloy 124 **a** 0.5 g Mn added to alloy 124, **b** 1.0 g Mn added to alloy 124, **c** 0.5 g Mn added to alloy 124 and Nb removed, and **d** 1.0 g Mn and 0.5 g of B added to alloy 124

## 6 Discussions

Figures 2, 3 and 4 show the scatter plots of magnetic energy density versus magnetic coercivity and magnetic remanence. Top 10 alloys are marked on the figure. Alloys were ranked on the basis of  $(BH)_{max}$  values in Figs. 2, 3 and 4 and Table 2. So far, the best alloy is alloy 124 and its composition was predicted computationally in MAIDROC laboratory at Florida International University. Figures 2, 3 and 4 demonstrate the efficacy of the present approach. Pareto-optimized predictions (using modeFRONTIER, IOSO and HYBRID approach) dominate the initial 80 candidate alloys as well as most of those predicted by the random number generator Sobol’s algorithm in later stages. The present alloy development time was approximately one year which is significantly less than the time needed to design new alloys using standard procedures. In order to improve from the initial set of 80 alloys to the current best, the time frame was only 5 months. Moreover, our computational design approach was able to successfully recover from the initial flaws. This would have been impossible by random experimentation. One peculiar finding in this work is that we were able to achieve an increase in  $H_c$  without compromising on  $B_r$ .



Cu shows a direct correlation with  $H_c$  and  $B_r$ , which can be confirmed from the literature (Sect. 2.1). Hf seems to affect  $H_c$  and  $B_r$  positively.  $H_c$  increases with an increase in Cu content. This was observed in SVR analysis (Sect. 5.1), as well as from the literature (Sect. 2.1). Nickel shows mixed response for  $(BH)_{max}$  as observed in SVR analysis (Sect. 5.1). Titanium showed mixed response for  $H_c$  in SVR analysis. In HCA analysis, we observed an increase in  $H_c$  values with an increase in Ti content. From the above analysis, we can conclude that we can remove niobium in order to make way for the rare-earth addition.

Thermodynamic analysis can prove to be helpful in designing heat treatment protocols. Hence, an initial study shows promising results. There is scope for improvement in the accuracy of response surface predictions, equilibrium calculations and HCA which can be used to screen a few alloys prior to manufacture.

## 7 Conclusions

One of the main purposes of computational materials science is to motivate experimentalists to incorporate a few modifications in the standard alloy development protocols for improved results. In this work, we demonstrated that it is possible to start the alloy design optimization process without any expertise in the design of alloys and to rapidly develop/improve alloys during several design cycles requiring an affordable number of alloys to be manufactured and tested. Even though our first set of results were not per our expectations due to a human error in the design process, the interactive computational/experimental design procedure was able to rapidly recover from it. We were able to improve these properties by an order of magnitude by meta-modeling and multi-objective optimization. Obtained results were screened by using standard statistical tools and the entire design procedure utilized multiple concepts of machine learning to come at a meaningful conclusion. The experimental dataset was quite noisy at the same time we were dealing with a multi-component system. Hence, non-linear composition-property relation was expected. Several such correlations known from the open literature were also proven in this work. For other correlations, we need to do further experiments. Screening of alloys on the basis of thermodynamic analysis from a limited database is another positive outcome of this work. Other query from the experimentalists can be addressed by modifying our algorithms.

## 8 Future Work

Based on the experience learned while developing this computational/experimental alloy design optimization methodology, it can be recommended that future work include the following items.

1. Improve response surface accuracy.
2. Introduce uncertainty in response surface predictions.
3. Microstructure and texture study.
4. Design an optimal temperature versus time heat treatment protocol for simultaneously with the design of the optimal chemical composition of the alloy.

**Acknowledgements** Authors would like to express their gratitude to Prof. Carlo Poloni, founder and president of ESTECO, for providing modeFRONTIER software free of charge for this project. They would also like to express their gratitude to Prof. Igor N. Egorov, founder and president of IOSO Technologies, for providing IOSO software free of charge and for performing some of the preliminary calculations. This work was funded by the US Air Force Office of Scientific Research under grant FA9550-12-1-0440 monitored by Dr. Ali Sayir. The views and conclusions contained herein are those of the authors and should not be interpreted as necessarily representing the official policies or endorsements, either expressed or implied, of the US Air Force Office of Scientific Research or the U.S. Government. The U.S. Government is authorized to reproduce and distribute reprints for government purposes notwithstanding any copyright notation thereon.

## References

1. McGuinness P, Akdogan O, Asali A, Bance S, Bittner F, Coey JMD, Dempsey NM, Fidler J, Givord D, Gutfleisch O, Katter M, Le Roy D, Sanvito S, Schrefl T, Schultz L, Schwöbl C, Soderžnik M, Šturm S, Tozman P, Üstüner K, Venkatesan M, Woodcock TG, Žagar K, Kobe S (2015) Replacement and Original Magnet Engineering Options (ROMEOS): A European seventh framework project to develop advanced permanent magnets without, or with reduced use of, critical raw materials. *JOM* 67:1306
2. Cullity B, Graham C (2009) Hard magnetic materials. Chapter 14 in: *Introduction to magnetic materials*. Wiley-IEEE Press, New York
3. Dillon H (2014) Effects of heat treatment and processing modifications on microstructure in AlNiCo-8H permanent magnetic alloys for high temperature applications. Master thesis, Iowa State University, USA. <http://lib.dr.iastate.edu/etd/13867>
4. Kramer MJ, McCallum RW, Anderson IA, Constantinides S (2012) Prospects for non-rare earth permanent magnets for traction motors and generators. *JOM* 64:752
5. Sellmyer DJ, Balamurugan B, Zhang WY, Das B, Skomski R, Kharel P, Liu Y (2013) Advances in rare-earth-free permanent magnets. The 8th Pacific rim international congress on advanced materials and processing. John Wiley and Sons Inc., Hoboken, NJ, USA
6. Zhou L, Miller M, Lu P, Ke L, Skomski R, Dillon H, Xing Q, Palasyuk A, McCartney M, Smith D, Constantinides S, McCallum R, Anderson I (2014) Architecture and magnetism of AlNiCo, *Acta Mater* 74:224
7. Egorov-Yegorov IN, Dulikravich GS (2005) Chemical composition design of superalloys for maximum stress, temperature, and time-to-rupture using self-adapting response surface optimization. *Mater Manuf Processes* 20:569
8. Datta S, Zhang Q, Sultana N, Mahfouf M (2013) Optimal Design of Titanium Alloys for Prosthetic Applications Using a Multiobjective Evolutionary Algorithm. *Mater Manuf Processes* 28(7):741
9. Mueller T, Kusne AG, Ramprasad R (2016) Machine learning in materials science: Recent progress and emerging applications. *Rev Comput Chem* 29
10. Rajan K (2013) Materials informatics: An introduction. *Informatics for materials science and engineering: Data-driven discovery for accelerated experimentation and application*. Butterworth-Heinemann, Waltham, MA, USA

11. Horstemeyer MF (2012) Integrated computational materials engineering (icme) for metals: Using multiscale modeling to invigorate engineering design with science. TMS—The Minerals, Metals and Materials Society. John Wiley and Sons Inc., Hoboken, New Jersey
12. Thermocalc, <http://www.thermocalc.com/solutions/by-application/alloy-development/>, accessed on 3/1/2015
13. Jha R, Sen PK, Chakraborti N (2014) Multi-objective genetic algorithms and genetic programming models for minimizing input carbon rates in a blast furnace compared with a conventional analytic approach. *Steel Res Int* 85:219
14. Jha R, Dulikravich GS, Pettersson F, Saxen H, Chakraborti N (2014) A combined experimental-computational approach to design optimization of high temperature alloys. ASME symposium on elevated temperature application of materials for fossil, nuclear, and petrochemical industries, Seattle, WA, 25–27 March 2014, ETS2014-1008
15. Jha R, Dulikravich GS, Fan M, Shwartz J, Koch C, Egorov I, Poloni C (2014) A combined computational-experimental approach to design of high-intensity permanent magnetic alloys. CONEM 2014, Uberlandia, Brazil, 10–15 August 2014
16. Jha R, Pettersson F, Dulikravich GS, Saxen H, Chakraborti N (2015) Evolutionary design of nickel-based superalloys using data-driven genetic algorithms and related strategies. *Mater Manuf Processes* 30(4):488
17. Toda-Caraballo I, Rivera-Diaz-Del-Castillo P (2015) Modelling and design of magnesium and high entropy alloys through combining statistical and physical models. *JOM* 67:108
18. Settouti N, Aourag H (2015) A study of the physical and mechanical properties of lutetium compared with those of transition metals: A data mining approach. *JOM* 67:87
19. Spencer PJ (2008) A brief history of CALPHAD: Comput Coupling Phase Diagrams *Thermochem* 32(1):1
20. Balamurugan B, Das B, Zhang WY, Skomski R, Sellmyer DJ (2014) HfCo and ZrCo alloys for rare-earth-free permanent magnets. *J Phys: Condens Matter* 26(6):064204
21. Factsage, <http://www.factsage.com/>. Accessed on 3 Jan 2015
22. ESTECO:modeFRONTIER, <http://www.esteco.com/modefrontier>. Accessed on 3 Jan 2015
23. Colaço MJ, Orlande HRB, Dulikravich GS (2006) Inverse and optimization problems in heat transfer. *J Braz Soc Mech Sci Eng* 28(1):1
24. Dulikravich GS, Colaço MJ (2015) Hybrid optimization algorithms and hybrid response surfaces. In: *Advances in evolutionary and deterministic methods for design, optimization and control in engineering and sciences*. Springer, Heidelberg, p 19
25. Sobol IM (1967) Distribution of points in a cube and approximate evaluation of integrals. *USSR Comput. Maths Math Phys* 7:86
26. Pettersson F, Saxen H, Chakraborti N (2007) A genetic algorithms based multi-objective neural net applied to noisy blast furnace data. *Appl Soft Comput* 7(1):387
27. Giri BK, Pettersson F, Saxen H, Chakraborti N (2013) Genetic Programming Evolved through Bi-Objective Genetic Algorithms Applied to a Blast Furnace. *Mater Manuf Processes* 28(7):776
28. IBMSPSS: IBM corp. released 2013. IBM spss statistics for windows, version 22.0. armonk, ny: Ibm corp. <http://www-01.ibm.com/software/analytics/spss/>. Accessed on 3 Jan 2015
29. Rettig R, Ritter NC, Helmer HE, Neumeier S, Singer RF (2015) Single-crystal nickel-based superalloys developed by numerical multi-criteria optimization techniques: design based on thermodynamic calculations and experimental validation. *Modell Simul Mater Sci Eng* 23(3):035004

# Basic Evaluation Technology Development of Battery Installation Safety for Electric Vehicles

Kee Joo Kim, Young-Cheol Lee and Jun-Hyub Park

**Abstract** A common feature of electric vehicles is that they do not emit exhaust gases, such as CO<sub>2</sub> or Nox, have low noise and vibration harshness (NVH), and are silent as a result of their using secondary electric energy, i.e. alternatives to petroleum. The case of an electric vehicle, where a motor system can be substituted for a combustion engine comprises a very fascinating power source which is environmentally sustainable. However, due to the low power performance of the motor and battery source, the weight reduction of the electric vehicle is necessary to increase its efficiency. To research this new vehicle, the benchmarking performed by leading companies of electric vehicles was thoroughly investigated. The reinforcement degree can differ as a consequence of the motor and the battery position in the vehicle in order to satisfy the vehicle safety and it can induce the weight variation of the vehicle. Therefore, the CAE (computer aided engineering) simulation of the full vehicle (Metro by Geo Co.) model was performed. Through the battery mounts modeled by the Hyper-Mesh program and the benchmarking of the battery installation placed in the vehicle location (on front engine room, center floor or rear trunk position), the optimized position of the power train system considering weight balancing of the electric vehicle was suggested in the present study. In addition, the best mounting position and mounting method of the battery to suggest the design guidelines in order to make up a safe electric vehicle were evaluated.

**Keywords** Electric vehicle · Motor · Battery installation · Safety

---

K.J. Kim (✉) · J.-H. Park  
Department of Mechatronics Engineering, Tongmyong University,  
Busan 608-711, Republic of Korea  
e-mail: kjkim@tu.ac.kr

J.-H. Park  
e-mail: jhpark@tu.ac.kr

Y.-C. Lee  
Korea Institute of Industrial Technology, 30 Goahakdan 1-Ro, 60 Beon-Gil,  
Gangseo-Gu, Busan 618-230, Republic of Korea  
e-mail: yclee87@kitech.re.kr

## 1 Background and Purpose of Study Aim

The case of an EV (electric vehicle), where a motor and a battery system can be substituted for an engine system, comprises a very economic power source. Concerning fuel expenses, it is very economic because the electrical bills are a small fraction of the average petroleum ones. This economic feasibility has a tendency to expand in accordance with the rise in the value of oil price. On the other hand, there are still a number of problems for the EV that need to be solved, such as that the driving range on a full battery charge is too short and that the price of high performance batteries is very high, and the batteries' lifecycles are very short. Furthermore, because of the large battery the electrical vehicle in accordance with the battery performance is very heavy. Therefore, design guidelines considering these safety, performance and weight issues will have to be presented.

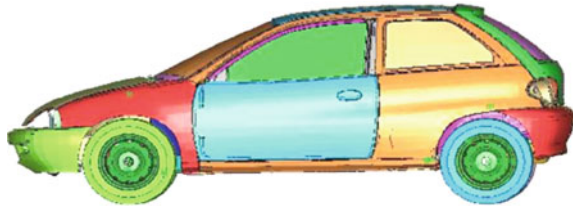
In the present study, the design guidelines suggest to consider the high stiffness and strength of the battery mount, the optimum layout of the power train system and the lightweight design considering the mounting positions of the driveline batteries. For the research of the new electric vehicle, the benchmarking of developments from leading companies about the electric vehicle was considerably investigated first. Then the CAE (computer aided engineering) simulation of the full vehicle (Metro by Geo Co.) model was performed by using the commercially available Hyper-Mesh and MSC Nastran program. Through the battery mount modeling using commercially available programs and by benchmarking the battery installation place in the vehicle location (on front engine room, center floor or rear trunk position), the optimized position of the power train system considering weight balancing of the electric vehicle was suggested in the present study. From these results, the optimum battery location and the design guidelines were proposed considering the weight balance and the safety of the electric vehicle.

## 2 Benchmarking and Simulation Procedure

For the benchmarking, 24 electrical vehicles from 11 countries around the world which are being produced or are under development were surveyed. The investigated EV developing countries are Japan, USA, Canada, Norway, Germany, Austria, Italy, France, Spain, India and China. The surveyed EV developing companies were Mitsubishi Motors, Fuji Heavy Industries, Showa Airplane Industry, Tesla, EV Innovation, Coda Auto., Chrysler, Ford, Zenn, Elbil, Think Nordic, Daimler, BMW, Seat, Renault, Reva, Tata, BYD and Cherry Motor Co. and others. All the surveyed data were provided from the electric vehicle companies' internet homepages.

The CAE computer modeling was executed by using the Hyper-Mesh program and the CAE simulation was performed by using a commercial program (Nastran Sol. 101 and Sol. 111). The simulation model was composed of 306,399 numbers

**Fig. 1** The type of vehicle (Metro made by Geo Company)



of solid and shell elements plus 202,591 welding entities. Figure 1 shows the vehicle type based on the CAE model. All components were composed and mounted with 1-D welding elements [1, 2].

### 3 Results and Discussion

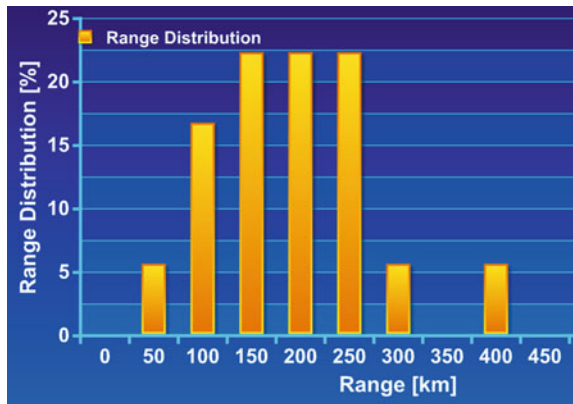
Figure 2 shows the results of the EV mileage range per charge analysis. The mileage ranges of over 70 % of the surveyed vehicles varied between 100 and 250 km as shown in Fig. 2.

Figure 3 shows the results of the EV maximum speed analysis. The high frequency level of maximum speeds was 140 km/h except for NEVs (neighborhood electric vehicle) and sport sedans as shown in Fig. 3.

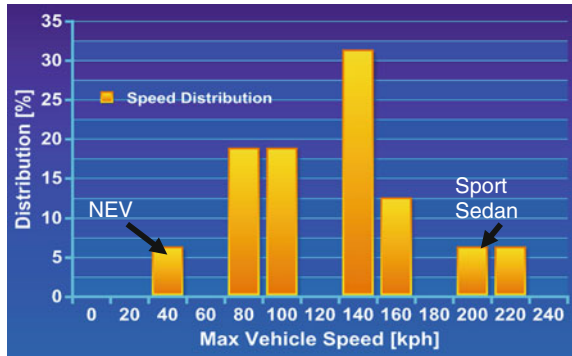
Figure 4 shows the results of the EV motor power analysis. The motor power of the 20–80 kW class shows the most visible frequency. Among these, the class with the highest frequency was served to be the 60 kW one.

Figure 5 shows the results of the EV motor power and battery capacity analysis. The motor power and the battery capacity are as factors that directly affect the performance and mileage (range) of the vehicle per one charge. As shown in this figure, these show a linearly proportional trend. The appropriate motor and battery capacity setting is important for the countries having many slope terrains.

**Fig. 2** Range distribution of the EV mileage per charge [3]



**Fig. 3** Max. Vehicle speed distribution of EV [3]



**Fig. 4** Motor power distribution of EV [3]

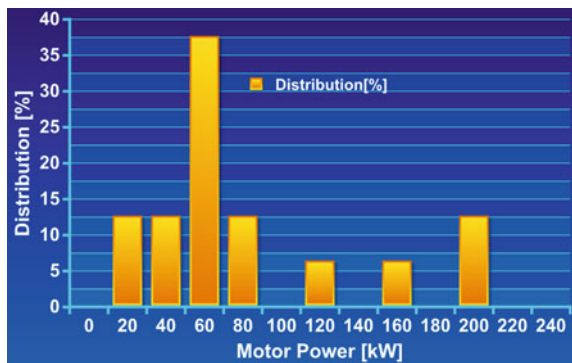


**Fig. 5** Motor and battery capacity distribution of EV

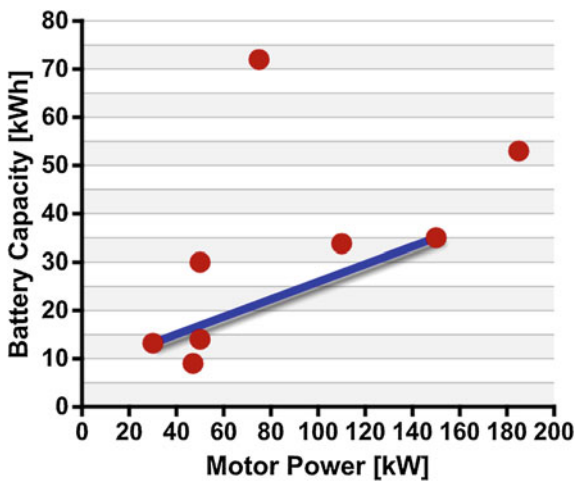


Figure 6 shows the results of the EV battery voltage analysis. Battery Voltage is 360 V class under investigation by the looks of the dominant frequency as shown in Fig. 6.

Furthermore, all analyzed vehicles, with the exception of two, were used a Lithium-ion battery and its weight varied between 250 and 350 kg. The battery mounting position of the general sedan type vehicle was on the center of the floor. The motor mounting position should be determined in accordance with the power train type (front wheel drive, rear wheel drive, all wheel drive, etc.). The process of benchmarking as outlined above, by analyzing the battery type and size, the battery and motor mounting position, power performance which has been adopted by most of the electric vehicle manufacturers, will reduce trial-and-error procedures in initial engineering.

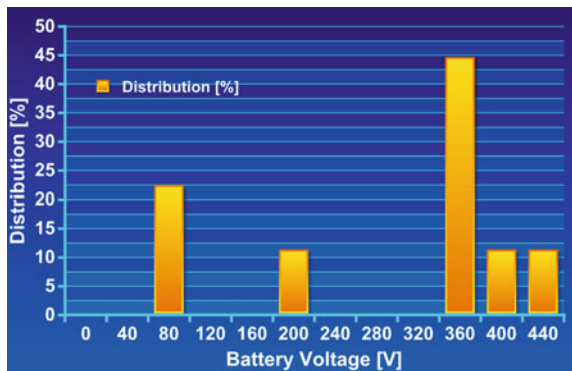
Figure 7 shows the CAE model including boundary and load condition for the strength analysis for a weight of 752.5 kg because of battery weight increase when the batteries are located in the engine room.

Figure 8 shows the design of the mounting position for the batteries and the stacked position when the batteries are located in the engine room in order to suggest the best design method in present study. The vertically stacked structure of upper and lower batteries is shown in this figure. The upper stacked batteries are mounted with 2-points position and the lower stacked batteries are mounted with 4-points position as shown in this figure.

Figure 9 shows the stress contour after the strength analysis of the model with batteries which are vertically stacked and located in the engine room with the loading condition  $z = -4$  g. In the model, the maximum stress was shown to be 696 MPa in this case.

Figure 10 shows the stress contour after the strength analysis of the model with batteries which are arranged in parallel with structure and located in the engine room with the loading condition  $x = -20$  g (=case 2). In this model, the maximum stress was shown to be 853 MPa. The loading condition with  $z = -4$  g case (=case 1) was lighter than the  $x = -20$  g case. Therefore, the loading condition with  $x = -20$  g was comparably important and strong condition than that with the

Fig. 6 Battery voltage distribution of EV





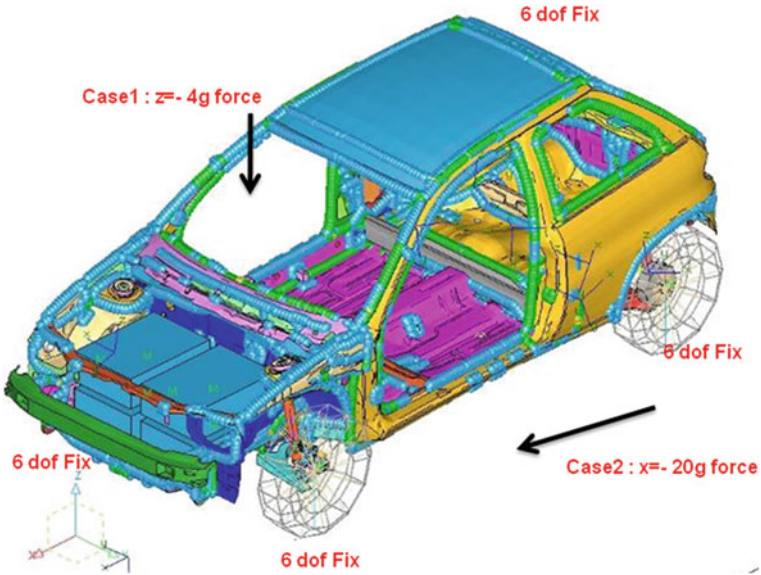


Fig. 7 CAE model for strength analysis when the batteries are located in the engine room (Metro by Geo Company)

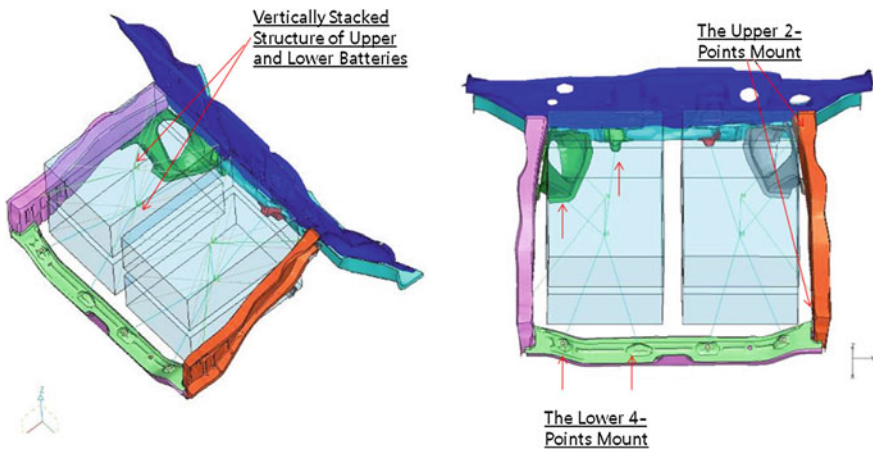
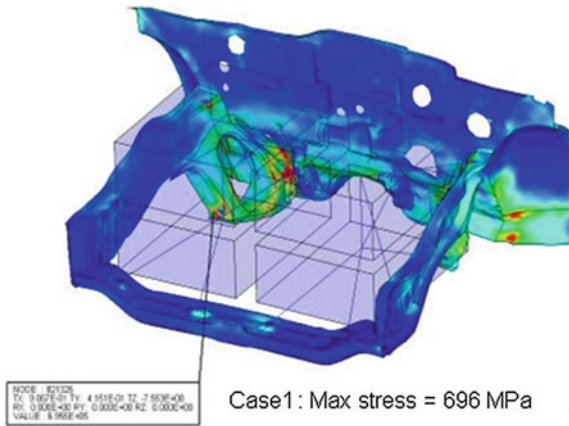


Fig. 8 Batteries mounting position and stacked position in engine room

$z = -4$  g condition. Therefore, the remaining analysis was performed only for the  $x = -20$  g case.

From these analyses, it was found that the number of battery mount can be reduced by using a battery mounted not with floor panel but with a cross member and section.

**Fig. 9** Strength analysis results with batteries which are vertically stacked structure with the loading condition  $z = -4 \text{ g}$



**Fig. 10** Strength analysis results with batteries which are arranged in parallel with structure with the loading condition  $x = -20 \text{ g}$

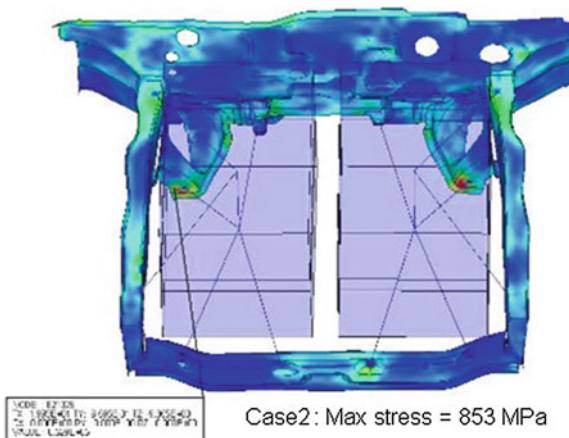
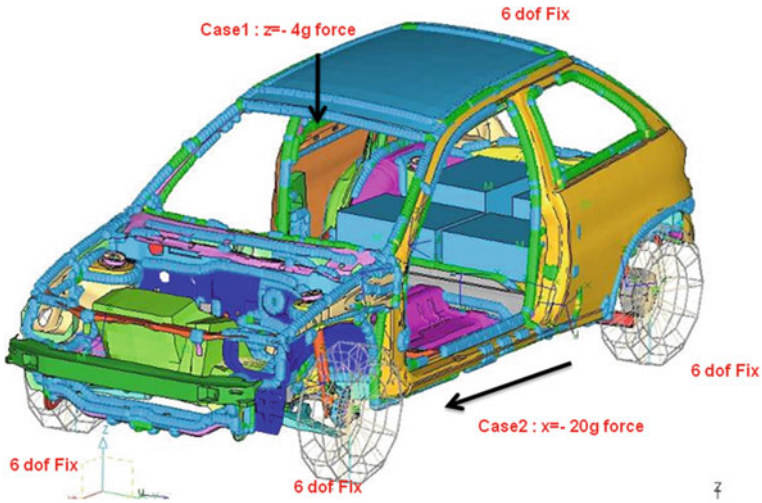


Figure 11 shows the CAE model including boundary and load condition for the strength analysis when the batteries are located in the rear floor.

Figure 12 shows the stress contour after the strength analysis of the model with batteries which are arranged in parallel with structure and located in the rear of the floor with the loading condition  $x = -20 \text{ g}$ . In this model, the maximum stress was shown to be 1132 MPa in this case and its value are comparably higher and better than the model with batteries located in engine room. Therefore, the modification or design change in order to make up a safe vehicle is required in the case.

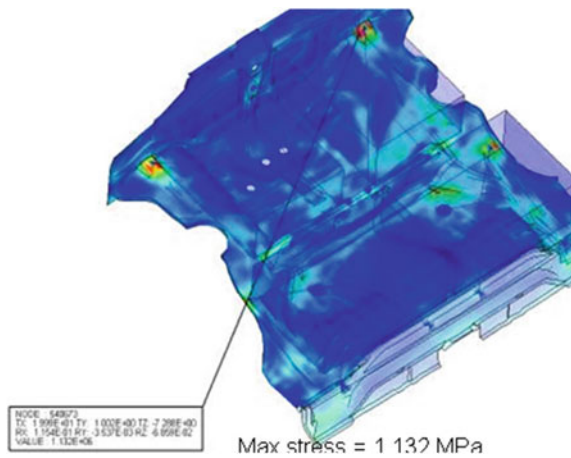
Figure 13 shows the CAE model including boundary and load conditions for the strength analysis when the batteries are located in the center of the floor.

Figure 14 shows the stress contour after the strength analysis of the model with batteries which are arranged in parallel with structure and located in center floor. In this model, the maximum stress was shown to be 1034 MPa. Therefore, the design changes such as the application of reinforcements should be required in this case.



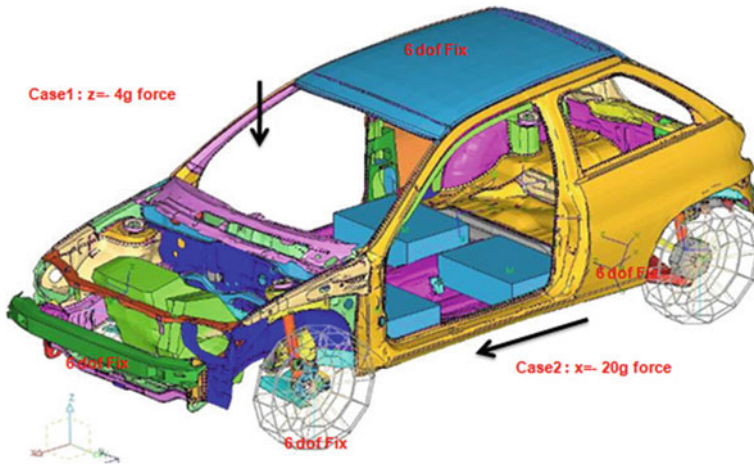
**Fig. 11** CAE model for strength analysis when the batteries are located in the engine room (Metro by Geo Company)

**Fig. 12** Strength analysis results with batteries which are arranged in parallel with structure in the rear of the floor with the loading condition at  $x = -20\text{ g}$



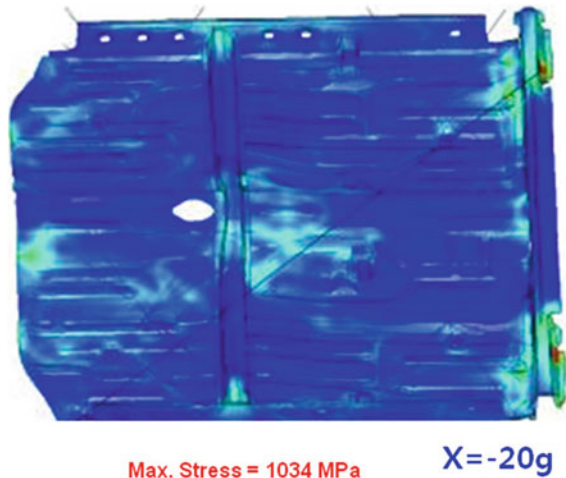
The reinforcement is needed in the floor and battery mounting area with batteries. Therefore, the design of the battery mounting bracket requires considering the location of the battery in the initial design stage in order to make up a lighter vehicle.

Figure 15 shows the comparison of the reaction force analysis results when the battery pack was placed in the center floor (model 10), engine room (model 11) and rear trunk (model 12). There was an increase of front axis load of more than 50 % when the batteries were mounted in the engine room (model 11), however, the rear axis load was decreased. Therefore, in this case, the stiffness of the front suspension



**Fig. 13** CAE model for strength analysis when the batteries are located in the center floor (Metro by Geo Company)

**Fig. 14** Maximum stress analysis results after the strength analysis with batteries which are arranged in the center of the floor



must be increased and the body reinforcements and stiffness distribution should be improved following the load concentration. In addition, there was no variation of the front axis load when the batteries were mounted in the rear trunk (model 12), however, the rear axis load increased more than 115 %. Therefore, in this case, the stiffness of the front suspension must be increased and the body reinforcements and stiffness distribution should be improved following the load concentration. In addition, it was found that it is possible to suppress the increase in thickness to increase the strength of the suspension parts that can be expected to remove a concentrated load applied to the tire by placing the battery in front floor.

**Conclusion : Reaction Force Table  
(Vertical 1g)**

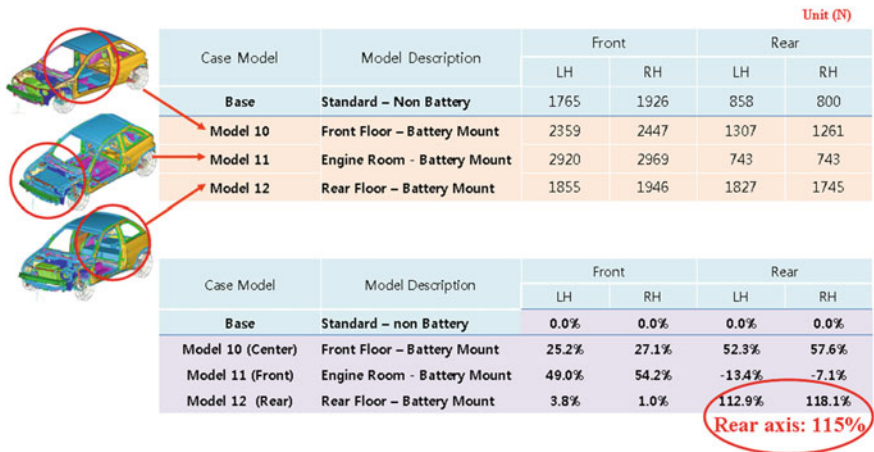


**Fig. 15** Results of the reaction force analysis in various models when the batteries were placed in the engine room, rear trunk and center floor

### 4 Conclusions

In the benchmarking investigation, the mileage ranges of over 70 % of the surveyed EV vehicles varied between 100 and 250 km. The high frequency level of maximum speeds of the EVs was 140 km/h. The motor power of the 20–80 kW class shows the most visible frequency. Among these, the class with the highest frequency was shown to be the 60 kW one. The motor power and the battery capacity are factors that directly affect the performance and mileage (range) of the vehicle per one charge. These show a linearly proportional trend. The appropriate motor and battery capacity setting should be required for countries having many slope terrains. Battery Voltage is of the 360 V class under investigation by the looks of the dominant frequency.

It was found that number of battery mounts can be reduced by using a battery mounted not with a floor panel but with cross member and section.

By using CAE simulation, the reaction forces were calculated when the batteries were placed in the floor center, engine room and rear trunk. From these results, the position of center floor exhibited excellent and predictable load distribution. Therefore, the optimum battery location is found to be the center floor from the view point of the vehicle weight balance. Additionally, this kind of approach could be useful for EV design engineers. In addition, it was found that it is possible to suppress the increase in thickness to increase the strength of the suspension parts that can be expected to remove a concentrated load applied to the tire by placing the battery in the front part of the floor from the perspective of weight balance.

**Acknowledgments** We would like to acknowledge the financial support from the R&D convergence program of MSIP (Ministry of Science, ICT and Future Planning) and ISTK (Korea Research Council for Industrial Science and Technology) of the Republic of Korea (Grant B551179-13-02-08).

In addition, this work (Grants No. C0185249) was supported by Business for Cooperative R&D between Industry, Academy, and Research Institute funded Korea Small and Medium Business Administration in 2014.

## References

1. Kim KJ, Won ST (2008) Effect of structural variables on automotive body bumper impact beam. *Inter J Auto Tech* 9:713–720
2. Kim KJ, Sung CW, Baik YN, Lee YH, Bae DS, Kim K-H, Won ST (2008) Development of an automotive rear subframe by the tube hydroforming process. *Inter J Prec Eng Manuf* 9:55–60
3. Kim KJ, Lee Y-C, Park J-H (2015) Fundamental research on power train systems for electric vehicles. *Mat-wiss Werkstofftech* 46:414–419



# Study of the Electrochemical Properties of 316LVM Steel with TiO<sub>2</sub> Layer Deposited by Means of the ALD Method

M. Basiaga, W. Walke, M. Staszuk and W. Kajzer

**Abstract** ALD is a variation of CVD, which, for example, found application in depositing two-component compounds, such as SiO<sub>2</sub> or TiO<sub>2</sub>. In the case of layers applied to the surfaces of products intended for contact with blood, important determinants include, aside from chemical composition, achieving an appropriate thickness and adequate sealing. A secure layer of the right thickness forms an effective barrier that protects the metal nanomaterial from the effects of corrosive environments (Shan et al. in *Surf Coat Technol* 202:2399–2402, 2008 [1]). Thin oxide layers based on such elements such as Ti or Si (up to 250 nm) are more hemocompatible, which significantly reduces the risk of complications related to the disseminated intravascular coagulation (DIC) process, for example. Aside from improved hemocompatibility, another important issue related to creating surface layers is the ability to achieve an appropriate set of electrochemical parameters. For this reason, tests were performed concerning the electrochemical properties of the TiO<sub>2</sub> layers deposited on the surfaces of AISI 316LVM steel samples using ALD under varied process parameters. First, potentiodynamic and potentiostatic measurements were taken, which enabled pitting and crevice corrosion resistance to be assessed. Secondly, impedance measurements were performed to enable interpretation of the processes and phenomena

---

M. Basiaga (✉) · W. Walke · W. Kajzer  
Faculty of Biomedical Engineering, Department of Biomaterials  
and Medical Engineering Devices, Silesian University of Technology,  
Zabrze, Poland  
e-mail: marcin.basiaga@polsl.pl

W. Walke  
e-mail: witold.walke@polsl.pl

W. Kajzer  
e-mail: wojciech.kajzer@polsl.pl

M. Staszuk  
Faculty of Mechanical Engineering, Institute of Engineering Materials  
and Biomaterials, Silesian University of Technology, Gliwice, Poland  
e-mail: marcin.staszuk@polsl.pl

occurring at the TiO<sub>2</sub> layer—electrolyte (synthetic plasma) interface. Complementary examination of surface topography was performed using a scanning electron microscope (SEM).

**Keywords** AISI 316LVM · TiO<sub>2</sub> · ALD · SEM · EIS · Potentiodynamic test

## 1 Introduction

Preventing blood clots from forming on the surface of biomaterials and understanding their causes are the main problems associated with surface modification of materials intended for cardiovascular implants. Metallic materials used in the cardiovascular system, in addition to having appropriate mechanical properties, must meet very strict requirements for biocompatibility [1–3]. In particular, such materials cannot cause the destruction of the cellular components of blood, interact with the surrounding tissues or release harmful substances to the bloodstream. An especially important parameter is the ability to minimize the potential for platelet clotting since clots formed during implant functioning reduce its functionality and can be very dangerous to the health and life of the patient [4, 5]. Moreover, biomaterials intended for contact with blood should have good mechanical properties and hemocompatibility, which is greatly influenced by the method of surface preparation [6, 7]. 316LVM steel is a known and widely used metal as a biomaterial, intended for the production of implants for reconstructive and interventional surgery. Such implants are mainly used in orthopaedic and trauma surgery, thoracic surgery and interventional cardiology. This steel meets the requirements concerning mechanical properties, corrosion resistance and biocompatibility in tissues and body fluids, is not toxic and does not trigger immune and allergic reactions [8–10].

Many years of experience in the use of implants made of metallic biomaterials have shown that, unfortunately, implants always undergo some degree of interaction with cellular components of blood and affect blood coagulation [11]. Therefore, an appropriate modification is necessary to improve biocompatibility, which will be aimed at changing the physicochemical properties of the surface layers of materials, preserving very good mechanical properties of the base material. Such modifications are made, for example, by creating oxide films in the process of chemical passivation and anodic oxidation, in order to prevent protein adsorption and platelet aggregation—key processes for the formation of blood clots on the surface of the material. In recent years, oxide films deposited by means of the sol-gel and ALD methods have increasingly been the subject of interest of researchers involved in the modification of Cr–Ni–Mo steel for biomedical applications [12–14]. Therefore, the aim of this study was to choose the optimum



parameters for producing a titanium-based oxide film using the ALD technology in order to obtain a surface film with improved corrosion resistance that allows its use for implants intended for contact with blood.

## 2 Materials and Methods

The Cr–Ni–Mo (316LVM) steel in the form of discs with a diameter of  $d = 14$  mm was selected for testing. Samples were subjected to surface treatment involving the following processes: mechanical polishing, electrochemical polishing and chemical passivation. Mechanical polishing was carried out with the use of the tumbling process, using suitable ceramic blocks. In turn, the process of electrochemical polishing was performed in a phosphate-sulphate acid based bath. Both polishing processes were performed until the surface roughness  $R_a < 0.16$   $\mu\text{m}$  recommended for implants was achieved. Next, the samples were subjected to chemical passivation in 40 %  $\text{HNO}_3$  acid. These are the basic steps of forming the properties of functional metallic biomaterials used for implants of miniaturized geometrical features. Next, a  $\text{TiO}_2$  film was deposited on the prepared samples using the Atomic Layer Deposition (ALD) method.  $\text{TiO}_2$  films studied in this work were grown from  $\text{TiCl}_4$  and  $\text{H}_2\text{O}$  in a low type low-pressure ALD reactor [12]. The deposition process consisted of repeated ALD cycles. Each cycle included a  $\text{TiCl}_4$  pulse, purge time,  $\text{H}_2\text{O}$  pulse and another purge time. The deposition process was carried out at a variable number of cycles of 500–2500, at a constant temperature of 200 °C.

### 2.1 Potentiodynamic Tests

Two groups of samples of AISI 316LVM steel after mechanical and electrolytic polishing, with  $\text{TiO}_2$  films deposited using the ALD technology, underwent potentiodynamic tests for pitting corrosion resistance in accordance with ASTM F2129 [15]. The measuring station consisted of the VoltaLab PGP201 potentiostat, reference electrode (saturated calomel electrode SCE, KP-113type), auxiliary electrode (platinum electrode, PtP-201 type), anode (tested sample) and PC computer with VoltaMaster 4 software. Corrosion tests started with determination of the opening potential ( $E_{OCP}$ ) in electroless conditions. Polarization curves were recorded from the baseline potential  $E_{start} = E_{OCP} - 100$  mV. The voltage change progressed towards the anode at 3 mV/s. The polarity was reversed each time the anodic current reached 1 mA/cm<sup>2</sup>. Based on the obtained curves, the corrosion potential  $E_{corr}$ , breakdown potential  $E_b$ , repassivation potential  $E_{cp}$ , and transpassivation potential  $E_{tr}$  were determined; polarization resistance  $R_p$  was determined using the Stern method. Tests of pitting corrosion resistance were carried out in the artificial plasma with the chemical composition in accordance with the recommendations of ISO 10993-15 [16] at  $T = 37 \pm 1$  °C, pH  $7 \pm 0.2$ .

## 2.2 EIS Study

In order to obtain additional information about the physicochemical surface properties of the AISI 316LVM samples, tests using electrochemical impedance spectroscopy were carried out. Measurements were performed using the Auto Lab PGSTAT 302 N measurement system, equipped with the FRA2 module (Frequency Response Analyser). The used measurement system enabled conducting studies in the frequency range of  $10^4$ – $10^{-3}$  Hz.

In the studies, impedance spectra of the circuit were determined and the obtained measurement data was matched to the equivalent circuit. On this basis, numerical values of resistance (R) and capacity (C) of analyzed circuits were determined. The impedance spectra of the studied circuit were presented as Nyquist diagrams for different frequency values, and as Bode diagrams. The resulting EIS spectra were interpreted after matching to the equivalent electrical circuit with the least squares method. Both potentiodynamic and impedance studies were carried out using artificial plasma [16] at  $T = 37 \pm 1$  °C and  $\text{pH} = 7.0 \pm 0.2$ .

## 2.3 SEM Study

Tests of the surface were performed using the scanning electron microscope ZEISS SUPRA 35 (ZEISS) with SE detector (Secondary Electrons) for secondary electrons, in magnification range of 1000–70,000 $\times$ .

# 3 Results

## 3.1 Potentiodynamic Tests Results

The results of potentiodynamic tests of pitting corrosion resistance are shown in Table 1 and Figs. 1 and 2. The results indicated that the corrosion potential  $E_{corr}$  of the baseline samples with the mechanically polished surface ranged from  $-167$  to  $-208$  mV, while for electrochemically polished samples these values were in the range of  $-166$  to  $-256$  mV. Furthermore, for the baseline samples average transpassivation potentials were  $E_{tr} = +1203$  mV for the mechanically polished surface and  $E_{tr} = +1198$  mV for the electrochemically polished surface. For baseline samples, the average polarization resistance was  $R_p = 411$  k $\Omega$  cm<sup>2</sup> and  $R_p = 211$  k $\Omega$  cm<sup>2</sup>. Next, samples with TiO<sub>2</sub> films formed by means of the ALD technique were tested. The films were characterized by different thickness, depending on the number of cycles of deposition. The analysis involved 500, 1250 and 2500-cycle processes. Irrespective of the number of cycles, the presence of

**Table 1** Results of potentiodynamic tests—mean values

Lp.	Surface	$E_{corr}$ , mV	STD	$E_b$ , mV	STD	$E_{cp}$ , mV	STD	$E_{tr}$ , mV	STD	$R_p$ , $k \Omega \text{ cm}^2$	STD
Samples with mechanical polishing base											
1	Initial state	-188	±28	-	-	-	-	+1203	±5	411	±301
2	500 cycles	-201	±13	+1578	±13	+1385	±46	-	-	1056	±481
3	1250 cycles	-206	±19	+1573	±60	+1379	±4	-	-	502	±105
4	2500 cycles	-171	±1	+1482	±44	+1338	±5	-	-	479	±42
Samples with electrochemical polishing base											
5	Initial state	-211	±63	-	-	-	-	+1198	±12	221	±79
6	500 cycles	-214	±60	+1584	±48	+1389	±5	-	-	415	±83
7	1250 cycles	-209	±37	+1609	±8	+1385	±3	-	-	384	±171
8	2500 cycles	-255	±86	+1585	±20	+1345	±28	-	-	276	±1715

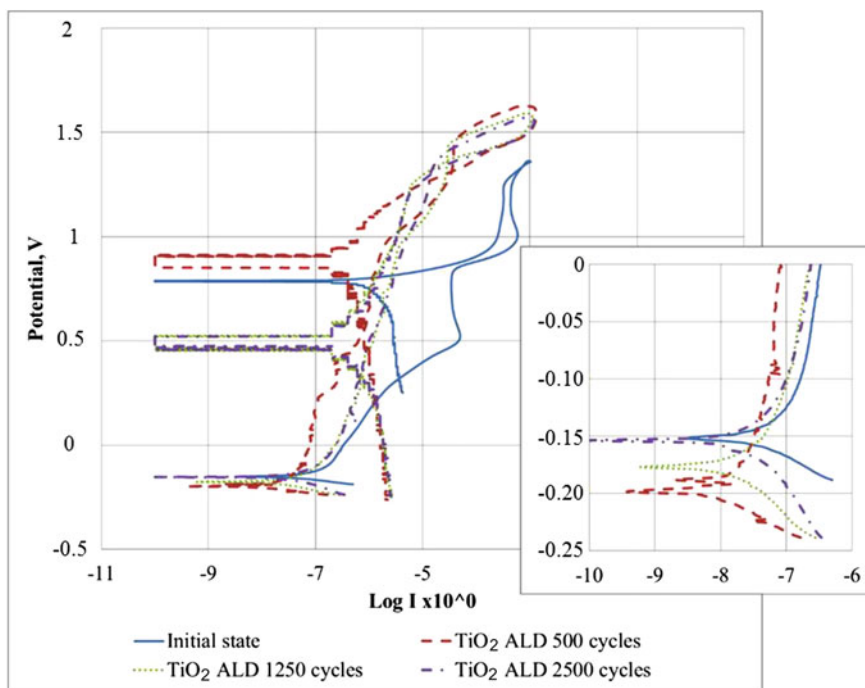


**Fig. 1** Polarisation curves regarding AISI 316LVM after mechanical polishing at initial condition and after TiO<sub>2</sub> ALD surface modification. Area of corrosion potentials

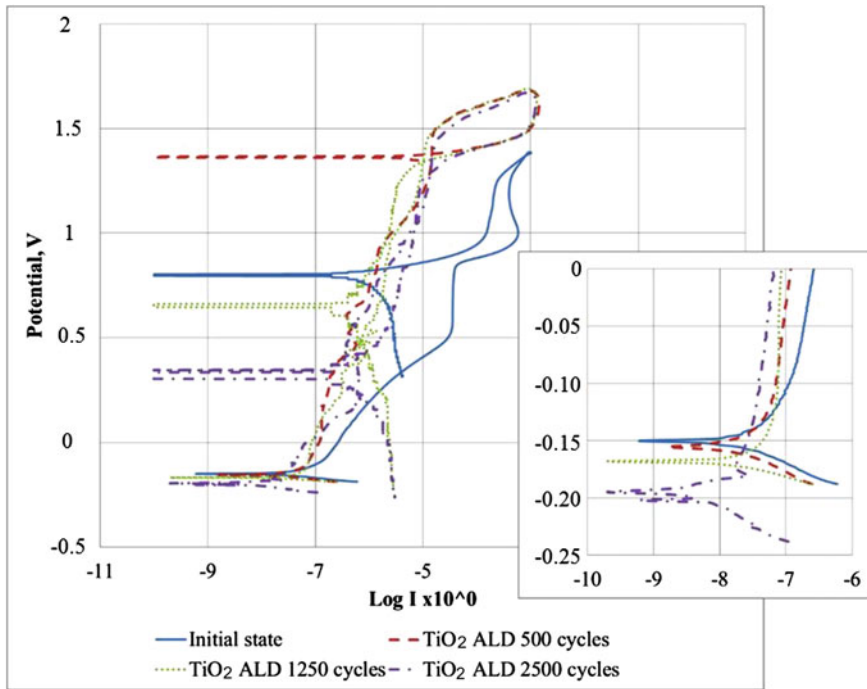


**Fig. 2** Polarisation curves regarding AISI 316LVM after electrochemical polishing at initial condition and after TiO<sub>2</sub> ALD surface modification. Area of corrosion potentials

breakdown  $E_b$  and repassivation  $E_{np}$  potentials was observed for the tested samples, which indicated a possible occurrence and development of pitting corrosion. The average values of breakdown potential for the analyzed variants were greater than the values of transpassivation potential  $E_{tr}$ , measured for the baseline status, and ranged from  $E_b = 1482$  mV to  $E_b = 1578$  mV for samples with the mechanically polished base area, and from  $E_b = 1584$  mV to  $E_b = 1609$  mV for samples with the electrochemically polished base area. In addition, all registered repassivation potential  $E_{cp}$  values were also higher than baseline transpassivation potential, and were approx.  $E_{cp} = 1380$  mV for all examined variants. This demonstrates the increased corrosion resistance of samples with the surface modified with titanium oxide in the ALD process compared to the baseline status, in spite of the occurrence of breakdown potentials. An increase in polarization resistance was also observed for samples subjected to surface modification in the ALD process (Table 1 and Fig. 3) with respect to the baseline values. Based on the study and taking into account the obtained results and their similarity, it was concluded that the most stable TiO<sub>2</sub> films were on samples, where the oxide coatings were applied in the 500-cycle process (Table 1).

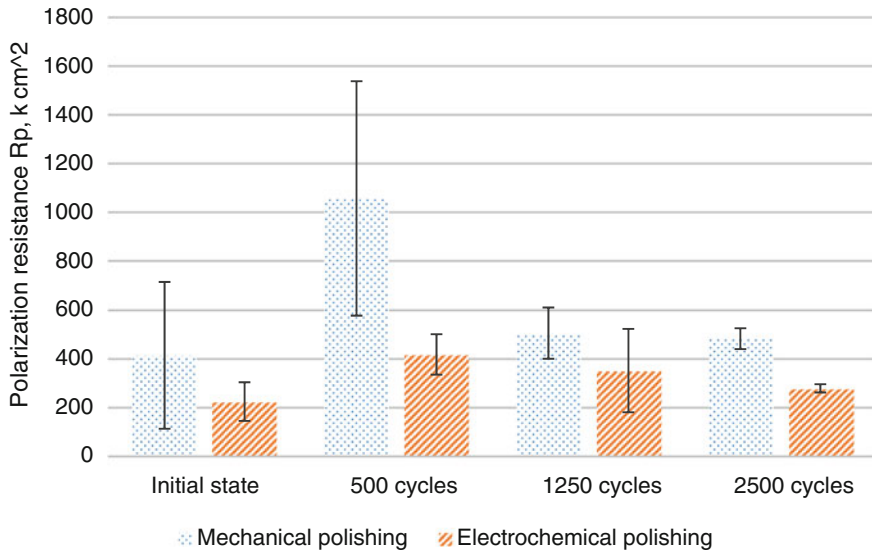


Fig. 3 Comparison of polarization resistance Rp for initial state and after surface modification

### 3.2 EIS Results

Figures 4 and 5 show the impedance spectra of AISI 316L steel at baseline and with a TiO<sub>2</sub> film, in the assumed technological conditions. For the analysis of experimentally determined impedance spectra of the corrosive AISI 316 steel systems the equivalent circuits were used, as shown in Fig. 6. Impedance spectra obtained for the test samples were interpreted by comparison with the equivalent electrical circuit, which indicates the existence of the double film (two time constants in the graphs), where  $R_s$  is the resistance of the artificial plasma,  $R_{pore}$ —resistance of the

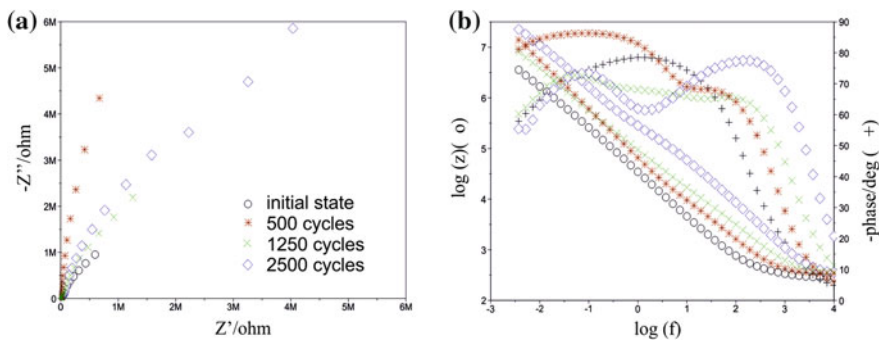
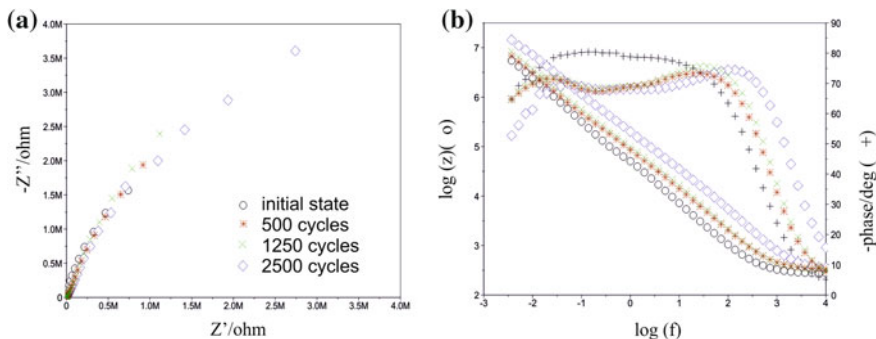
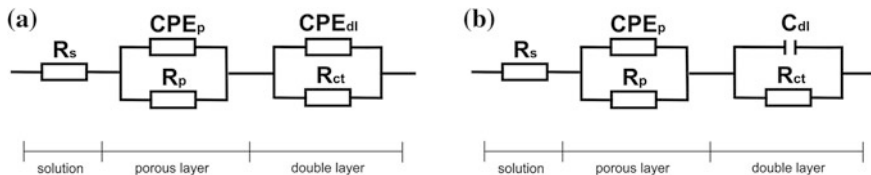


Fig. 4 Impedance spectrums for AISI 316LVM steel (electrochemical polishing): **a** Nyquist diagram, **b** Bode diagram



**Fig. 5** Impedance spectra for AISI 316LVM steel (mechanical polishing): **a** Nyquist diagram, **b** Bode diagram



**Fig. 6** Electrical model of equivalent circuit for AISI 316LVM—TiO<sub>2</sub> layer—artificial plasma

electrolyte in the pores, and  $CPE_{pore}$ —the capacity of a double film (porous, surface), while  $R_{ct}$  and  $CPE_{dl}/C_{dl}$ —resistance and capacity of the oxide film. The use of two constant phase elements ( $CPE$ ) in the equivalent electrical circuit positively influenced the quality of matching curves that were determined experimentally (Table 2).

**Table 2** Results of EIS

$R_s, \Omega \text{ cm}^2$	$R_{ct}, M \Omega \text{ cm}^2$	$C_{dl}, \mu F \text{ cm}^{-2}$	$CPE_{dl}$		$R_{pore}, k \Omega \text{ cm}^2$	$CPE_{pore}$		$E_{OCP}, \text{mV}$
			$Y_0, \Omega^{-1} \text{ cm}^{-2} \text{ s}^{-n}$	$n$		$Y_0, \Omega^{-1} \text{ cm}^{-2} \text{ s}^{-n}$	$n$	
Samples with electrochemical polishing base								
17	2.5	–	0.1887E-4	0.87	0.2	0.2621E-4	0.87	–198
17	43.5	–	0.2002E-4	0.81	1.5	0.8268E-5	0.96	–268
18	11.0	–	0.1852E-4	0.80	2.7	0.7943E-5	0.82	–214
17	15.8	–	0.1958E-5	0.93	27.4	0.2892E-5	0.86	–191
Samples with mechanical polishing base								
18	6.6	–	0.1493E-4	0.90	5.0	0.5747E-4	0.81	–239
16	5.1	17	–	–	111.0	0.1117E-4	0.80	–220
18	5.6	13	–	–	119.0	0.9193E-5	0.82	–214
18	6.3	6	–	–	193.0	0.4449E-4	0.80	–198

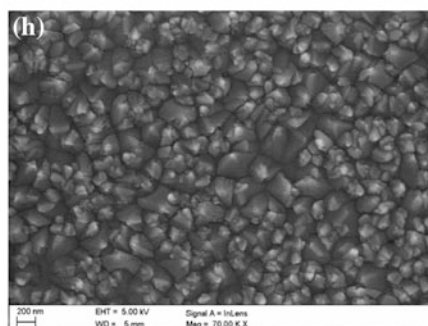
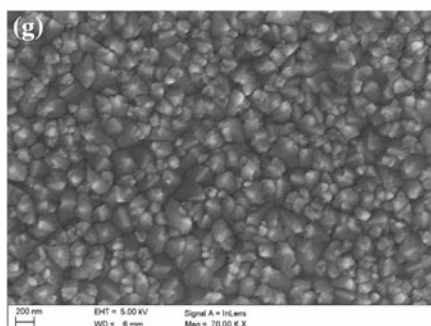
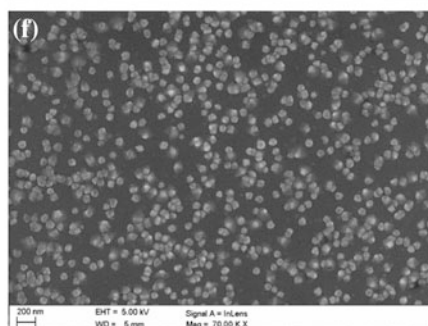
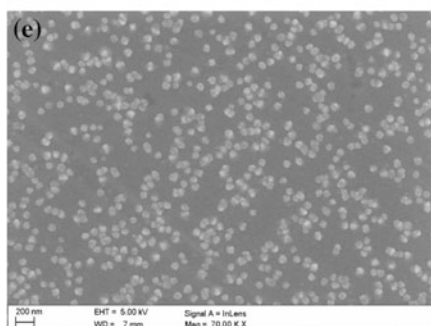
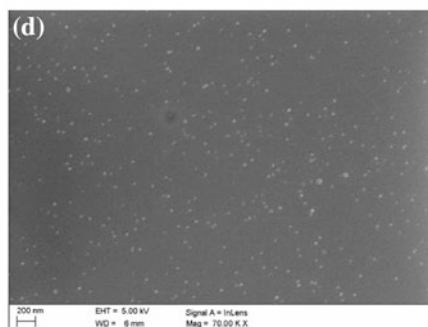
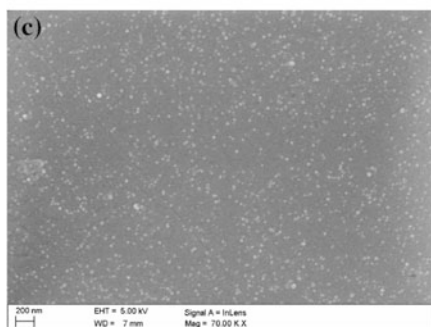
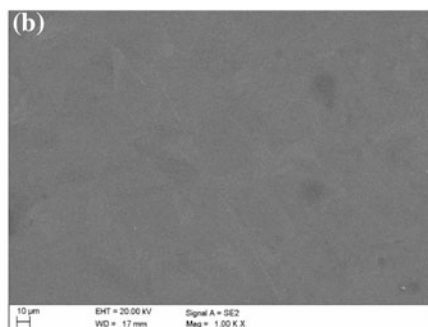
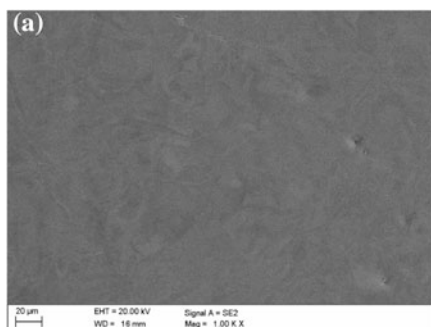
In summary, the results of impedance measurements confirm the significant impact of the  $\text{TiO}_2$  film on the corrosion resistance of AISI 316LVM steel. It was found that in all cases, the impedance module of investigated corrosion systems decreased with increasing frequency, and the phase angle also changed with the frequency. The impedance spectra measured for all samples indicate a high electrochemical stability of the resultant oxide coating deposited on the surface of the prepared steel. For samples after electrochemical polishing, the ion passage resistance  $R_{ct}$  is much higher than for mechanically polished samples. The additional presence of a porous film on the surface of the oxide coating with a large surface development forms a kind of protective barrier for morphotic blood elements. Such a structure of the surface film provides steel with a good protection against the effects of a corrosive environment such as human blood.

### 3.3 SEM Results

The results of the observation with a scanning electron microscope are shown in Fig. 7. The observation of the surface showed differences in its topography, depending on the number of cycles of  $\text{TiO}_2$  film deposition. It was found that increasing the number of cycles, and thus film thickness, resulted in more porous films. The sample surface with a film formed after 2500 cycles was characterized by the highest porosity—Fig. 7h. Nanopores formed during the application process can be used as capsules for controlled drug release. There were no marked differences between the films applied on the substrate after the process of mechanical or electrochemical polishing—Fig. 7.

## 4 Discussion

Modification of the 316LVM steel surface with different forms of titanium is of interest to researchers studying issues related to improving the biocompatibility of this material in the tissue environment. Sarafbidabad described the process of synthesis of Ti-based metallic glass film under high vacuum pressure on 316L stainless steel using the HVPLD method (High Vacuum Pulse Laser Deposition). This method allowed obtaining a single amorphous film of a suitable chemical composition by controlling the process parameters, including the rotational speed of the sample and vacuum pressure in the chamber. The aim of the study was to achieve a high quality top film on the steel surface to improve its biocompatibility [17]. Bou-Saleh et al. [18] confirmed the positive impact of another surface modification using the method of cyclic potentiodynamic polarization to improve the corrosion resistance of 316LVM steel used for implants. Another attempt to increase the biocompatibility of this metal biomaterial was made by Wang et al. This surface modification involved the application of zirconium carbonitride ( $\text{ZrCN}$ ). The





◀ **Fig. 7** SEM surface images of as-deposited films: (a) initial state after mechanical polishing, (b) initial state after electrochemical polishing, (c) 500 cycles (mechanical polishing), (d) 500 cycles (electrochemical polishing), (e) 1250 cycles (mechanical polishing), (f) 1250 cycles (electrochemical polishing), (g) 2500 cycles (mechanical polishing), (h) 2500 (electrochemical polishing)

researchers used the magnetron sputtering method with radio frequency. This increased the corrosion resistance of the material and improved its mechanical properties and hemocompatibility [19]. Kheirkhah, Fathi, Salimijazi and Razavi decided to cover 316L steel with the forsterite  $Mg_2SiO_4$  film. The coating, deposited using the sol-gel method, also improved corrosion resistance when tested in simulated body fluid. Biological tests also confirmed the bioactivity of samples coated with forsterite [20]. However, surface modification of miniaturized forms of implants requires a method that enables precise control of the thickness during film deposition, and especially, maintains a constant thickness over the entire surface. Currently, the ALD method creates such opportunities. Therefore, the authors applied this method to form  $TiO_2$  films on the surface of 316LVM steel used to produce vascular stents, and analyzed the impact of the number of cycles on their physicochemical properties. The research showed that an increased number of cycles was associated with increased porosity of the film, which was demonstrated in EIS and SEM studies. The number of cycles, and thus film thickness had no significant effect on corrosion resistance in the artificial plasma. All film-covered samples were characterized by a better resistance compared to the baseline samples. The method of preparing a metal substrate (mechanical and electrochemical polishing) did not affect corrosion resistance. In addition, the impedance studies have shown improved barrier properties (higher  $R_{ct}$  value) of a film deposited on the surface after the electrochemical polishing process. This may be attributed to a higher susceptibility to self-passivation of the surface after electrochemical polishing, and thus, an increased amount of oxygen forming  $TiO$ ,  $TiO_2$  or  $Ti_2O_3$  during the process of film deposition. This is particularly evident in the case of  $TiO_2$  films formed during 500 cycles. To sum up, the obtained results are promising and indicate a prospective use of the ALD method for the surface modification of metal implants intended for the human cardiovascular system.

**Acknowledgments** The project was funded by the National Science Centre allocated on the basis of the decision No. 2014/13/D/ST8/03230

## References

1. Shan CX, Hou X, Choy K (2008) Corrosion resistance of  $TiO_2$  films grown on stainless steel by atomic layer deposition. *Surf Coat Technol* 202:2399–2402
2. Walke W, Paszenda Z, Basiaga M, Karasiński P (2013) The silica-titania layer deposited by sol-gel method on the AISI 316L for contact with blood. *J Achievements Mater Manuf Eng* 56:75–82

3. Marciniak J, Szweczenko J, Kajzer W (2015) Surface modification of implants for bone surgery. *Arch Metall Mater* 60(3B):13–19
4. Nair K, Muraleedharan CV, Bhuvaneshwar GS (2003) Developments in mechanical heart valve prosthesis. *SADHANA—Acad Proc Eng Sci* 28:575–587
5. Kostrzewa B, Rybak Z (2013) Historical background, present and future of biomaterials used in artificial heart valves. *Polym Med* 43:183–189 (in Polish)
6. Walke W, Paszenda Z, Basiaga M, Karasiński P, Kaczmarek M (2014) EIS study of SiO<sub>2</sub> oxide film on 316L stainless steel for cardiac implants. *Inf Technol Biomed* 284:403–410 (*Advances in Intelligent Systems and Computing*, Springer)
7. Basiaga M, Paszenda Z, Walke W, Karasiński P, Marciniak J (2014) Electrochemical impedance spectroscopy and corrosion resistance of SiO<sub>2</sub> coated cpTi and Ti-6Al-7Nb alloy. *Inf Technol Biomed* 284:411–420 (*Advances in Intelligent Systems and Computing*, Springer)
8. Krauze A, Ziębowicz A, Marciniak J (2005) Corrosion resistance of intramedullary nails used in elastic osteosynthesis of children. *J Mater Process Technol* 162–163:209–214
9. Basiaga M, Jendruś R, Walke W, Paszenda Z, Kaczmarek M, Popczyk M (2015) Influence of surface modification on properties of stainless steel used for implants. *Arch Metall Mater* 60(4):2965–2969
10. Kajzer A, Kajzer W, Dzieliński J, Matejczyk D (2015) The study of physicochemical properties of stabilizing plates removed from the body after treatment of pectus excavatum. *Acta Bioeng Biomech* 2:35–44. doi:10.52777/ABB-00140
11. Basiaga M, Staszuk M, Walke W, Opilski Z (2016) Mechanical properties of ALD TiO<sub>2</sub> layers on stainless steel substrate. *Materialwiss. Werkstofftech* 47(5):1–9
12. Kumagai H, Masuda Y, Shinagawa T (2011) Self-limiting nature in atomic-layer epitaxy of rutile thin films from TiCl<sub>4</sub> and H<sub>2</sub>O on sapphire substrates. *J Cryst Growth* 314:146–150
13. Saleem MR, Silfsten P, Honkanen S, Turunen J (2012) Thermal properties of TiO<sub>2</sub> films grown by atomic layer deposition. *Thin Solid Films* 520:5442–5446
14. Leskela M, Ritala M (2003) Atomic layer deposition chemistry: recent developments and future challenges. *Angew Chem Int Ed* 42:5548
15. Standard: ASTM F2129—Electrochemical corrosion testing of surgical implants (Standard test method for conducting cyclic potentiodynamic polarization measurements to determine the corrosion susceptibility of small implant devices)
16. Standard: ISO 10993-15 (2005) Biological evaluation of medical devices—Part 15: identification and quantification of degradation products from metals and alloys
17. Sarafbidabad M (2015) Synthesis of Ti-based metallic glass thin film in high vacuum pressure on 316L stainless steel. *Thin Solid Films* 574:189–195
18. Bou-Saleh Z, Shahryari A, Omanovic S (2007) Enhancement of corrosion resistance of a biomedical grade 316LVM stainless steel by potentiodynamic cyclic polarization. *Thin Solid Films* 515:4727–4737
19. Wang L, Zhao X, Ding MH, Zheng H et al (2015) Surface modification of biomedical AISI 316L stainless steel with zirconium carbonitride coating. *Appl Surf Sci* 340:113–119
20. Kheirkhah M, Fathi M, Salimijazi HR, Razavi M (2015) Surface modification of stainless steel implants using nanostructured forsterite (Mg<sub>2</sub>SiO<sub>4</sub>) coating for biomaterial applications. *Surf Coat Technol* 276:580–586

# Design and Development of a Simplified Wear Simulator for Total Knee Replacement (TKR) Based on Pin-Disc Machine

R. Rodríguez-Martínez, G. Urriolagoitia-Sosa, C. Torres San Miguel,  
L.H. Hernández-Gómez, J.A. Beltrán-Fernández and  
B. Romero-Ángeles

**Abstract** The failure of polyethylene inserts in the prostheses of diverse members is the main cause for total replacement of the articulation. In this study, the most influential conditions for the different types of failures for a total knee replacement (TKR) causing the main wear or rupture were analyzed. Mexico, little research has been done on total knee prostheses (Rodríguez in *Int J Phys Sci* 7(43): 5779–5786, 2012, [1]), this being one of the main problems of national health. In the previous publications a few studies were conducted concerning the gait cycle in Mexican patients were made. One of the cases involved the TKR *Scorpio™ II Stryker™* (Rodríguez in *Revista Colombiana de Biotecnología* XV(1): 28–41, 2013, [2]) where axial and shear stresses have been analyzed and the way this functions in the gait cycle considering this type of prosthesis (Rodríguez in *Revista Colombiana de Biotecnología* XV(1): 28–41, 2013, [2]). Due to the scarce resources with which it had to operate, the design of the components of the machine had to be improvised or modified, which is quite useful in two different cases. In present case, a

---

R. Rodríguez-Martínez (✉) · G. Urriolagoitia-Sosa · C. Torres San Miguel ·  
L.H. Hernández-Gómez · J.A. Beltrán-Fernández · B. Romero-Ángeles  
“Adolfo López Mateos” Unit, without number, Section of Postgraduate  
and Research Studies, Mechanical Electrical Engineering Superior School,  
2th floor, Col. Lindavista, Del. G.A.M, México City, Mexico  
e-mail: rafarm68@hotmail.com

G. Urriolagoitia-Sosa  
e-mail: guiurri@hotmail.com

C. Torres San Miguel  
e-mail: napor@hotmail.com

L.H. Hernández-Gómez  
e-mail: luishector56@hotmail.com

J.A. Beltrán-Fernández  
e-mail: jbeltranf@hotmail.com

B. Romero-Ángeles  
e-mail: urrio332@hotmail.com

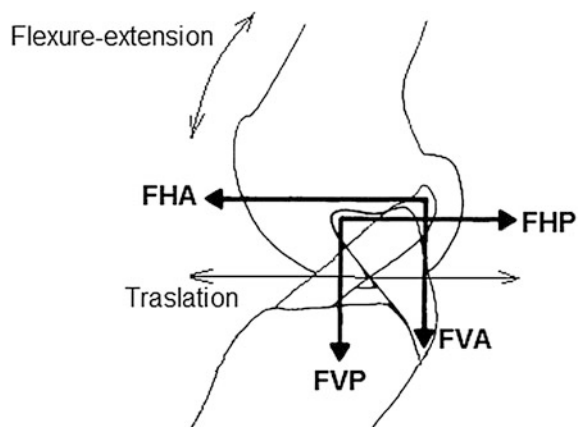
hybrid-machine was developed, adapting new mechanical components on the pin-disk machine modified. The results of effects the wear of UHMWPE inserts are not involved in this research, only those related to the design and adaptation of the new components to the wear of the pin-disk machine are presented as results of this work.

## 1 Introduction

In this research a model of design based on a pin-disk machine was proposed, which was adjusted several times to improve the efficiency of operation and diminish its cost, since we do not have enough financial resources to acquire mark simulators. It is necessary to indicate that this simulator is called simplified since alone it reproduces two types of movements of the articulation that are: the flexo-extension and the translation of the condyles when the first of these movements is made, which are carried out simultaneously. Figure 1 shows the acting forces in the articulation.

Any knee wear simulator which has been made this way, produces a considerable innovation percentage and savings in expenses of having to buy or to design a simplified a wear simulator of TKR. On the other hand, it is necessary to take into account that other phenomena are presented in the wear of the UHMWPE insert. The debris particle generation of UHMWPE remains a clinical issue in total joint replacements such as knee and hip replacements. Significant advances in modeling and understanding the origin of wear debris liberation in total hip replacements have been made over the past decade. One recently discovered aspect is the importance of the sliding direction on wear in UHMWPE. From the perspective of an individual material element on the UHMWPE surface, variations in sliding direction appear as transverse crossing motion in equivalent pinon-disk experiments. The order of magnitude changes the wear rate with increasing degrees of

**Fig. 1** Movements and forces acting in the articulation



crossing motion, as reported in [3–6]. Consequently, we need to increase the capacities to observe the contact phenomenon and to attack to the most severe conditions that provoke the wear and rupture.

## 2 Simplified Wear Simulator

Based on the experimental development reported in [7, 8] which make reference to experimentally proven fastener-disk, the conceptual design for a simplified wear simulator exclusively for TKR was carried out, which goes mounted on a pin-disk prove experimental fastener-disk, it was carried out the conceptual design for a simplified wear simulator of exclusive for TKR, which goes mounted on a pin-disk experimental machine, and has the particularity of using the same femoral insert as in TKR as a rigid member.

### 2.1 Operation Principle

The simulator consists of several parts as indicated in Fig. 2, which can complete diverse works. The operation on the whole consists of transmitting the axial load on

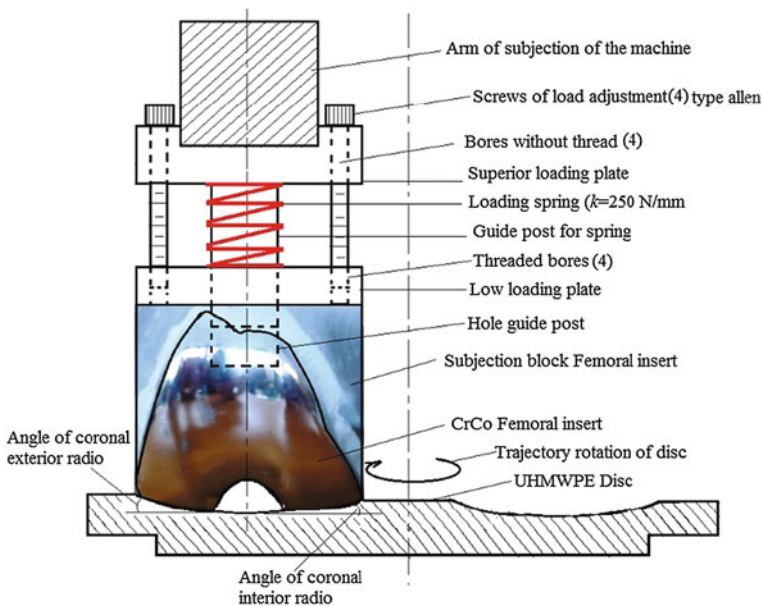


Fig. 2 Simplified wear simulator for TKR

the articulation by means of the fixed arm of the pin-dick machine. The test conditions are obtained by precharging a spring calculated for a load axial maximum of 2250 N, This is made by putting four screws, through the both top and low plates are screwed. The necessary spring constant to produce 2250 N of load is obtained from *Hooke's Law* for springs.

$$F = kL \quad (1)$$

where  $F$  is the compression force applied by the spring in (N),  $k$  is the spring constant in (N/mm) and  $L$  is the distance that the spring has to be compressed to produce the required load (m). For the specific case of this experiment a maximum distance of compression of 10 mm was chosen, with a

$$k = \frac{F}{L} = \frac{2250}{10} = 225 \text{ N/mm} \quad (2)$$

This condition makes sure that the device will exercise 225 N (aprox. 22.5 kg) for each millimeter that is compressed. This is in agreement with the smallest load applied to the insert of polyethylene, that corresponds to several positions of the gait cycle, specifically to 60–100 % of the gait cycle. When it is adjusted to the wanted load, the device is placed between the arm and the disk of UHMWPE and the spring retiring the four load screws are liberated. In this condition one has the contact couple with the geometric conditions and a very similar operational load to those of a prosthesis working inside a patient. Finally, the polyethylene couple consists of a disk with a 140 mm diameter (see Fig. 2), the one which manufactured with a geometry of congruency very similar to the original insert in the coronal plane, and it becoming subject to the lower circle of the UHMWPE specimen (see Fig. 2) with a chuck of machine.

### 3 Materials and Methods

For the realization of the wear tests, the disks of polyethylene of 140 mm diameter and a thickness of 19.1 mm were used. It also used the original CrCo femoral insert of a right prosthesis *Scorpio-II<sup>®</sup> Striker<sup>®</sup>* of size 7. As main equipment a conventional wear pin-disc was used (Fig. 3).

In Fig. 4, one can observe that the half radius  $R$  of the contact area is 50 mm, by means of the one which the tangential speed  $V_t$  of the half line is determined.

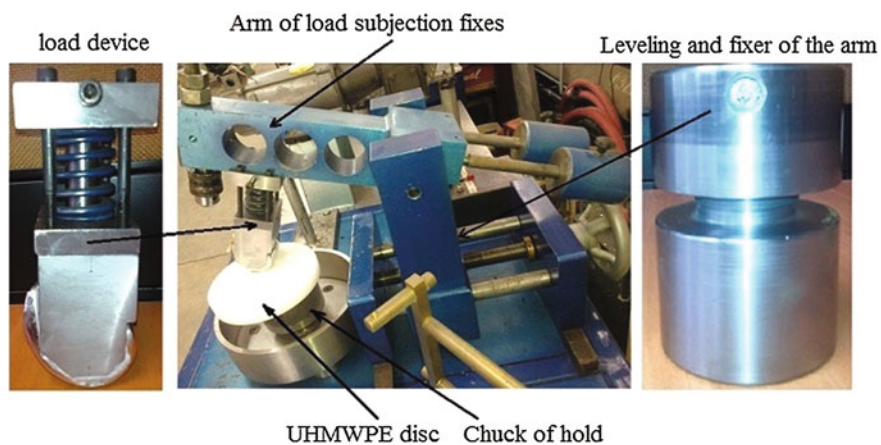
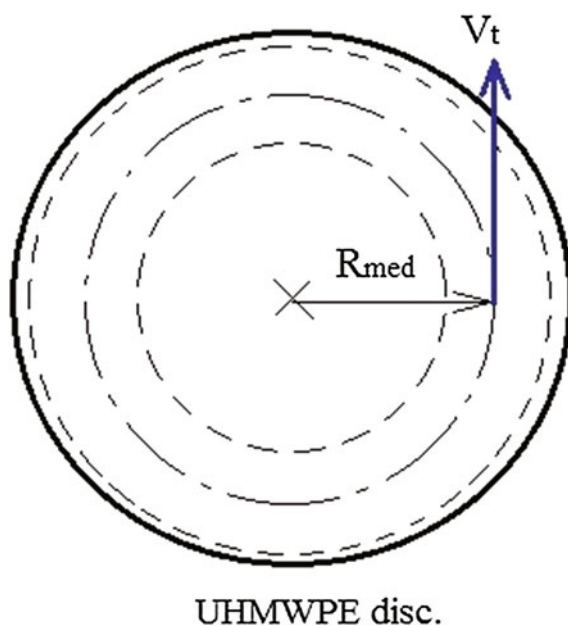


**Fig. 3** General arrangement of the machine pin-disc, adapted with the load devices of own development for wear test in TKR

**Fig. 4** Polyethylene disc for wear test



## 4 Results

In the present research the follow results were obtained:

1. Starting from a pre-existing machine already made, it was possible to make a test of wear of TKR, by means of implement a group of the devices of more reliable.
2. The investment expenses went smaller to develop a complete machine
3. It was proven that the Mexican scientists have the capacity to implement solutions to problems like the machinery acquisition.

## 5 Conclusions

The most favorable conclusion, was that could be proven that making the adaptations of elements to other machines satisfactory results can be obtained, since is not had the equipment acquisition.

**Acknowledgment** The author's knowledge to the support provided by Instituto Politécnico Nacional.

## References

1. Rodríguez MR (2012) Development of an experimental apparatus for testing a total knee prostheses focused on Mexican phenotype. *Int J Phys Sci* 7(43):5779–5786
2. Rodríguez MR (2013) Numerical analysis on stresses and contact areas in a TKR Scorpio II™ Stryker™ in accordance to Mexican phenotype. *Revista Colombiana de Biotecnología* XV (1):28–41
3. Bragdon CR, O'Conner DO, Lowenstein JD, Jasty M, Syniuta WD (1996) The importance of multidirectional motion on the wear of polyethylene. *IMEchE Part H: J Eng Med* 210:157–165
4. Muratoglu OK, Bragdon CR, O'Connor DO, Jasty M, Harris WH, Gul R, McGarry F (1999) Unified wear model for highly crosslinked ultra-high molecular weight polyethylenes (UHMWPE). *Biomaterials* 20:1463–1470
5. Burroughs BR, Blanchet TA (2001) Factors affecting the wear of irradiated UHMWPE. *Tribol Trans* 44:215–223
6. Wang A (2001) A unified theory of wear for ultra-high molecular weight polyethylene in multi-directional sliding. *Wear* 248:38–47
7. Urriolagoitia-Calderón G, Urriolagoitia-Sosa G, Hernández-Gómez LH, Merchán-Cruz EA, Vite-Torres M, Fera-Reyes CV, Beltrán-Fernández JA (2008) Análisis del desgaste de la articulación cabeza femoral-copa acetabular mediante simulación experimental con máquina pernodisco. *Revista Colombiana de Biotecnología* X(1):94–110
8. Rodríguez-Cañizo RG, García-García LA, Vite-Torres LA, Merchán-Cruz EA, Sandoval-Pineda JM (2010) Análisis experimental del desgaste entre UHMWPE y acero inoxidable 316L empleados en la manufactura de prótesis coxofemorales. *Revista Colombiana de Biotecnología* XII(2):67–85



# Elaboration and Modeling of Water Molecule Sensitive Layers Deposited from Hexamethyldisiloxane

Noubeil Guermat

**Abstract** This paper reports the simulation study of humidity-sensitive and electrical properties of plasma polymerized hexamethyldisiloxane (pp-HMDSO) thin film based sensors. The humidity sensitive film was deposited by glow discharge at low frequency power (19 kHz) in a capacitively coupled parallel plate plasma reactor. The sensor design comprises the interdigitated electrodes and the absorbing layer. The sensor was calibrated in terms of impedance as a function of relative humidity (10–95 %), using a frequency response analyzer. The used frequency signal was fixed at 1 kHz with a signal amplitude of 3 V. The hexamethyldisiloxane thin film is investigated as humidity sensor. The elaborated sensor exhibited a small hysteresis (2 % RH) and fast response (8 and 34 s when the adsorption and desorption occur between 35 % of RH and 95 % of RH, respectively). The simulations results showed an increase in time characteristic of diffusion with the increase of sensitive layers thickness, which confirms the reduction in the sensitivity for thicker films. The performance of the films and the results of the model simulations are presented and discussed. The HMDSO film showed promising characteristics for humidity sensor development.

**Keywords** HMDSO · Thin film · Humidity sensors · Electrical characterization · Modeling

---

N. Guermat

Département d'Electronique, Faculté de Technologie, Université Mohamed Boudiaf de M'sila, BP.166, Route Ichebilia, 28000 M'sila, Algeria

N. Guermat (✉)

Laboratoire des Etudes de Matériaux d'Electronique Pour Applications Médicales (LEMEAMED), Faculté des Sciences de l'Ingénieur, Université de Constantine 1, 25000 Constantine, Algeria  
e-mail: g\_noubeil@yahoo.fr

## 1 Introduction

Thin film humidity sensors are widely used in many measurement and control applications, including those in domestic appliances, meteorology, automated process control, agriculture, and medical equipment [1]. They can be categorized into capacitive, resistive, mechanical, oscillating and thermoelemental type based on the used sensing principle [2]. Among these, the resistive devices are often preferred since they can offer high sensitivity, fast response, low cost and son on [3]. For resistive type humidity sensors, the resistance or impedance of the sensing material decreases with increasing relative humidity, whereas, the mechanism for capacitive-type sensors is the dielectric constant change of the sensing layer with relative humidity (RH). Important parameters for humidity sensors include the response time, sensitivity, long-term stability and hysteresis.

Various materials such as porous ceramics [4], organic polymers [5], and electrolytes [6, 7] are used as humidity-sensitive materials. Organic polymers are advantageous because they usually have low fabrication costs, high thermal and chemical stability and adhere to various substrates. Typical hygroscopic organic polymers include hexamethyldisiloxane (HMDSO) [8] and tetraethoxysilane (TEOS) [9].

The aim of this study it is to elaborate a mathematical model based on Fick's law that governs the evolution of water molecules concentration as a function of time inside the bulk of the sensitive layer using initial and limit conditions provided by experimental results.

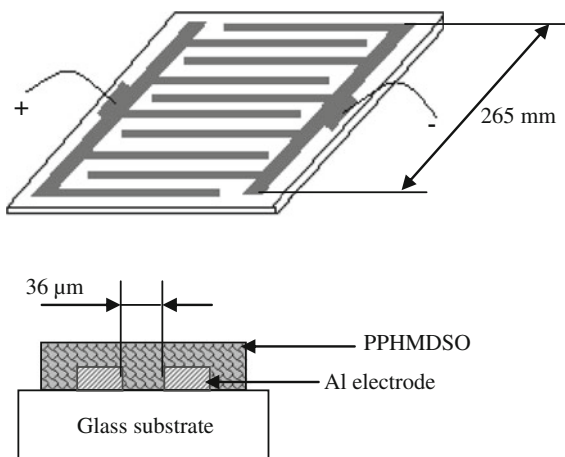
## 2 Experimental

### 2.1 Sensing Material Fabrication

The device concept consists of a resistive-type humidity sensor based on a thin polymerized HMDSO film deposited on clean glass substrate with a com-shape aluminum electrodes (interdigitated structure IDS). A schematic top view of the sensor is depicted in Fig. 1. The Al electrodes with spaces of 36  $\mu\text{m}$  between tracks were evaporated on clean glass substrates. The advantage of sensors based on the IDS structure is the simple and cheap fabrication process and the ability to use the sensor in a wide range of applications without crucial changes to the sensor design.

Films were deposited using plasma enhanced chemical vapor deposition (PECVD) at low frequency (19 kHz) power in a homemade and capacitively coupled parallel plate plasma reactor. The substrate was horizontally placed on the lower electrode and the reactor chamber was pumped down to  $10^{-2}$  mbar. During deposition the discharge power and pressure were fixed to 8 Watts and 0.4 mbar, respectively. The chemical structure of the elaborated layers has been studied using a Fourier Transform Infrared spectrometer (Nicolet Avatar 360 in the 400–4000  $\text{cm}^{-1}$  range).

**Fig. 1** Schematic top view and cross section of the sensor design



## 2.2 Sensor Test

Response behaviors at different humidity level of plasma polymerization of hexamethyldisiloxane (pp-HMDSO) based humidity sensor were evaluated in a humidity chamber system shown in Fig. 2. Measurements have been performed at atmospheric pressure with controlled humidity and temperature. The humidity chamber volume is about  $3526 \text{ cm}^3$ . The relative humidity value is obtained by bubbling dry air in the humidifier containing distilled water that can be heated to  $50 \text{ }^\circ\text{C}$  by means of a resistor. The relative humidity percentage inside the measurement chamber is controlled by two inlet valves. A temperature and humidity sensor (commercial Testo 610) was used to evaluate the relative humidity (RH) and to measure temperature stability in the testing cell. The evacuation of the chamber is performed by a mechanical pump. The electrical sensing properties were carried out by recording the impedance values of the sensors at different humidity level using a HP impedance analyzer (4284 LCZ meter).

## 3 Results

### 3.1 Electrical Sensing Properties

The plasma polymerized HMDSO thin films deposited on two-interdigitated aluminum electrodes were used as sensor element and evaluated for humidity detection under an applied voltage of 3 V and signal frequency of 1 kHz. Figure 3 shows the measured impedance responses over the thin pp-HMDSO film in the range of relative humidity (RH) of 10–95 % at temperature of approximately  $27 \text{ }^\circ\text{C}$ .

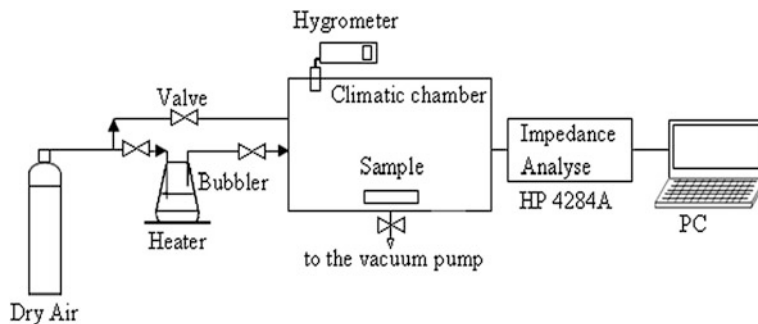


Fig. 2 Schematic view of the experimental set up

The impedance of the sensor decreased two orders of magnitude when the relative humidity decreased from 30 to 95 % on a semi-logarithmic scale. Between 10 and 30 % of RH, the deposited films were found to be insensitive to water vapor. The pp-HMDSO film sensor did not show a visible change of the electrical impedance, the value of this later was in order of about  $10^6 \Omega$ . Increasing RH beyond 30 % gives rise to an abrupt impedance decrease. The value of the electrical impedance decrease significantly until reaching the value of  $10^4 \Omega$ . At lower RH, the electrical response is caused by proton hopping between chemisorbed hydroxyl groups. Afterwards, when the amount of physisorbed water molecules starts to increase, the hydronium ion,  $H_3O^+$ , is most likely the charge carrier. Furthermore, the pp-HMDSO-based sensor showed small hysteresis (2 %), excellent sensitivity to humidity and wide scale of impedance (Fig. 3), which indicated that the reversible absorption/desorption is easily achieved in this case [10].

Response and recovery behavior is one of the significant features for estimating the performance of the humidity sensors. The response time was measured by quickly moving the humidity sensor from relatively dry environment (35 % RH) to the other chamber in equilibrium at 90 % RH and the recovery time was recorded in the opposite way. The time taken by the sensor to achieve 90 % of the total impedance change is defined as the response time for humidification and the recovery time for desiccation. Figure 4 shows the response recovery property of the pp-HMDSO humidity sensor. It is found that the sensor exhibits a fast response and recovery time, the response and recovery times were in the order of 8 and 34 s, respectively, which are among the best results reported for resistive type humidity sensor [11, 12]. The faster response time to humidity of the pp-HMDSO sensor might be due to a regular morphology and suitable thickness of the sensing layer. Films deposited by low frequency plasma from pure HMDSO have been reported to be homogeneous, without pinholes and defects [13]. This is convenient for efficient absorbing and desorbing of water molecules. The response time associated with the absorption process is shorter than that associated with the desorption process. This asymmetry in diffusion of water inside the polymer film is a characteristic property of most humidity sensors, where kinetics of desorption of water molecules from the pores are slower than their absorption [14].

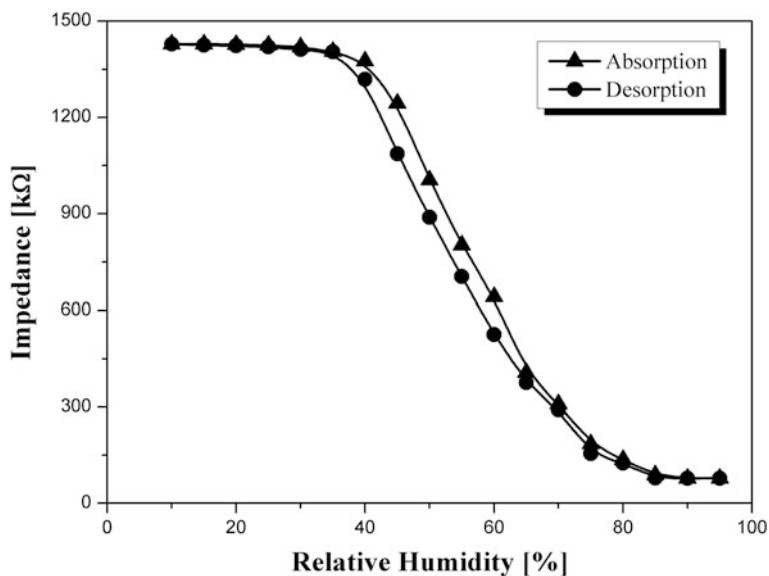


Fig. 3 Typical impedance response of pp-HMDSO based humidity sensor

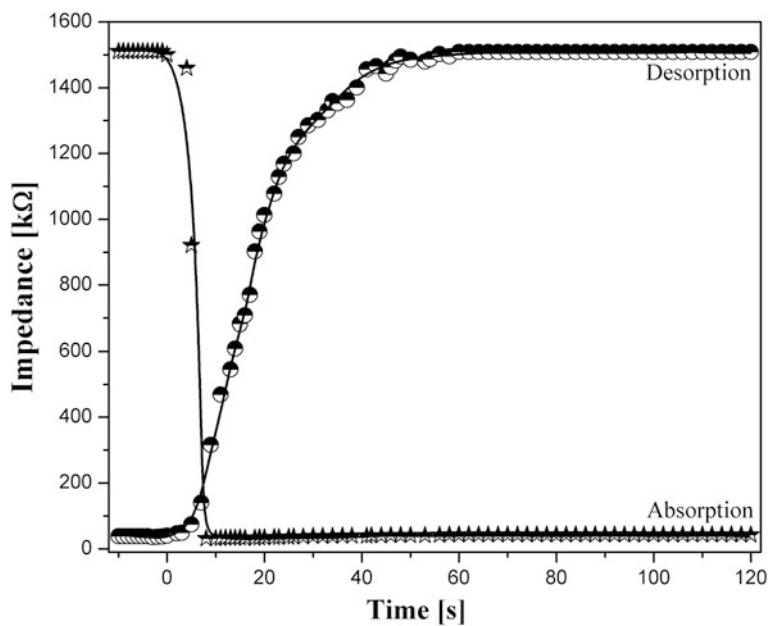


Fig. 4 Response-recovery properties of pp-HMDSO sensor

## 4 Modeling

### 4.1 Moisture Diffusion Modeling in HMDSO Films

The device concept consists of a resistive-type humidity sensor based on a thin polymerized HMDSO film deposited on two-interdigitated aluminum electrodes. A sketch of the top view and the cross section of the sensor are depicted in Fig. 5.

In order to compare the impedance of the conventional and the high-speed structures, equations governing the transient capacitance for each structure have been derived. In this analysis, it has been assumed that no moisture is present inside the film in its initial state and that the diffusion constant is independent of moisture concentration. The diffusion kinetics is assumed to obey to Fick's law [15]. Assuming that the upper electrode is transparent to moisture, the transient moisture concentration distribution inside the film is derived by solving the one-dimensional diffusion equation.

$$\frac{\partial C(x, t)}{\partial t} = D \frac{\partial^2 C(x, t)}{\partial x^2} \quad (1)$$

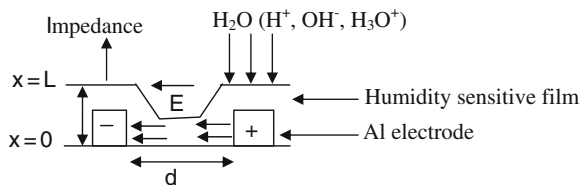
With the initial condition of  $C(x, 0) = 0$  and the boundary condition of  $C(L, t) = C_s$ , where  $C$  is the moisture concentration,  $C_s$  is the surface moisture concentration, and  $D$  is the diffusion constant of moisture. The solution to this equation is formulated as [16]:

$$C(x, t) = C_s + \sum_{n=1}^{\infty} \left[ \frac{1}{n} C_s (\cos(n\pi) - 1) \sin\left(\frac{n\pi(x-L)}{2L}\right) \exp\left(-\frac{n^2\pi^2}{4L^2}Dt\right) \right] \quad (2)$$

### 4.2 Time Comparison

The response time of a humidity sensor can be improved either by selecting a hygroscopic material with a high moisture diffusion coefficient or by changing the dimensions of the moisture sensing film. However, once the material has been specified, the response can only be enhanced by modifying the geometry of the film. The moisture diffusion modeling presented in this section assumes the

**Fig. 5** Schematic of the theoretical model



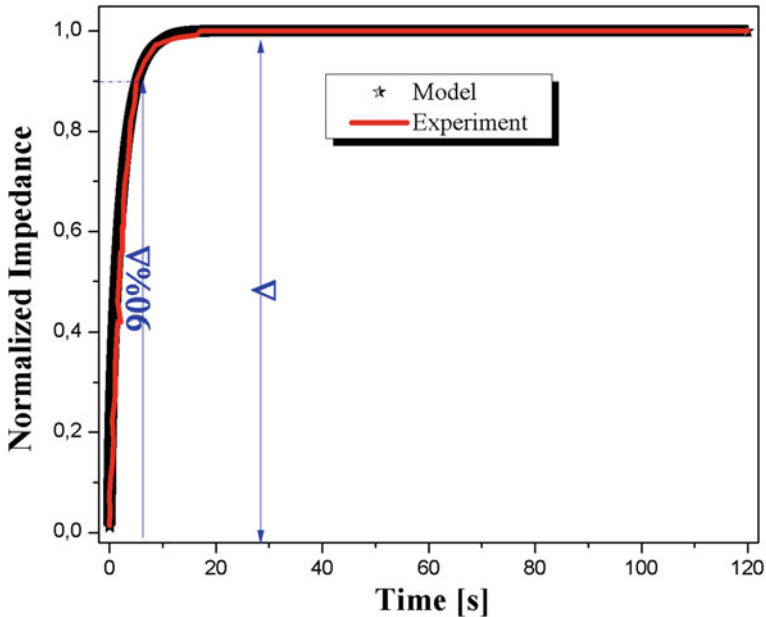


**Fig. 6** Analytical comparison of response times for diffusion into a thin film (pp-HMDSO)

hygroscopic material to be HMDSO and specifies a diffusion coefficient of  $0.15 \times 10^{-9} \text{ cm}^2/\text{sec}$  (Fig. 6).

The simulation results show an excellent agreement with measured data [5], and the model features offer a deeper knowledge of either the device behaviour or the changes that may be operated to improve the sensor's response.

In order to determine whether there is a relationship between the thickness of the absorbent layer and the diffusion time of the humidity sensor, we have studied the variation of the concentration of water molecules released versus time for different values of the sensitive layer thickness.

Figure 7 shows the variations of absorption kinetics for different values of the test body thickness. Note that the greater sensitive layer thickness of the humidity sensor the slower absorption kinetics (see Table 1). This behavior is probably due to the films densification. In other words, the reduction of pores in the sensitive layers reduces the sensor sensitivity.

Figure 8 shows of the absorption kinetics curves for four layer thickness (150, 215, 400 and 740 nm). Note that for small thicknesses (150 and 215 nm) sensitive layers have a large absorption kinetics speed of water molecules with respect to the other layers (400 and 740 nm). This behavior is probably due to the distribution and size of the ports that provide good absorption of water molecules.

According to the work of Yang et al. [17], humidity sensors based sensitive layers of nano-pores can detect the change in resistance and/or capacitance with a high sensitivity due to the absorption of molecules water (capillary condensation)

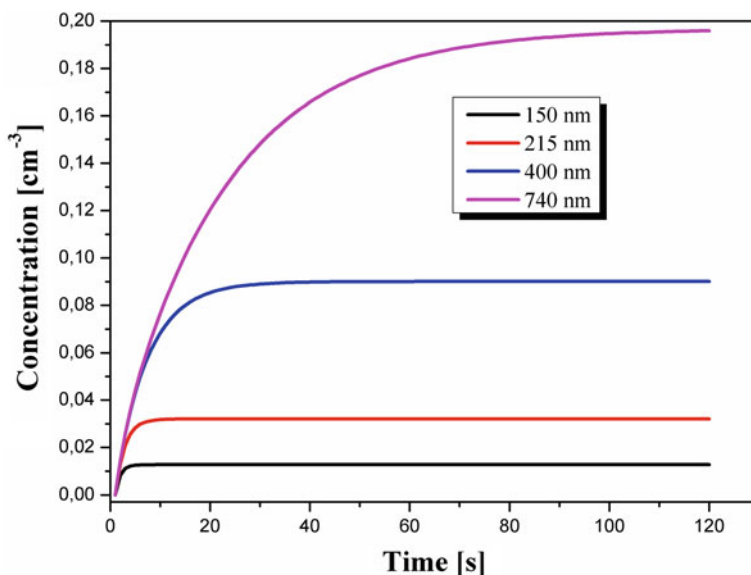


**Fig. 7** Effect of the sensitive layer thickness on the absorption kinetics

**Table 1** The values of the characteristic diffusion time

Thickness [nm]	Diffusion coefficient [ $\text{cm}^{-2}/\text{s}$ ]	Response times [s]
150	$0.15 \times 10^{-9}$	5
215	$0.15 \times 10^{-9}$	8
400	$0.15 \times 10^{-9}$	16
740	$0.15 \times 10^{-9}$	49

inside the nano-pores of the sensitive layer. Against by, thicknesses greater than 400 nm show a slow absorption kinetics which can be attributed to the densification of the deposited film due to the reduction in the proportion and/or the section of the pores through which water molecules can diffuse.

Table 1 summarizes the different values of the diffusion constant for different the sensitive layer thicknesses. From Table 1, we see an increase in the characteristic diffusion time with increasing the sensitive layer thickness on the one hand. On the other hand, the results show that for a thickness of about 215 nm, we obtained a characteristic diffusion time equal to 8 s. This value is in same order as the experimental value for the response time of the sensor (8 s). So we can conclude that the sorption kinetics of the humidity sensor is based on the diffusion of water molecules that follows Fick's law.



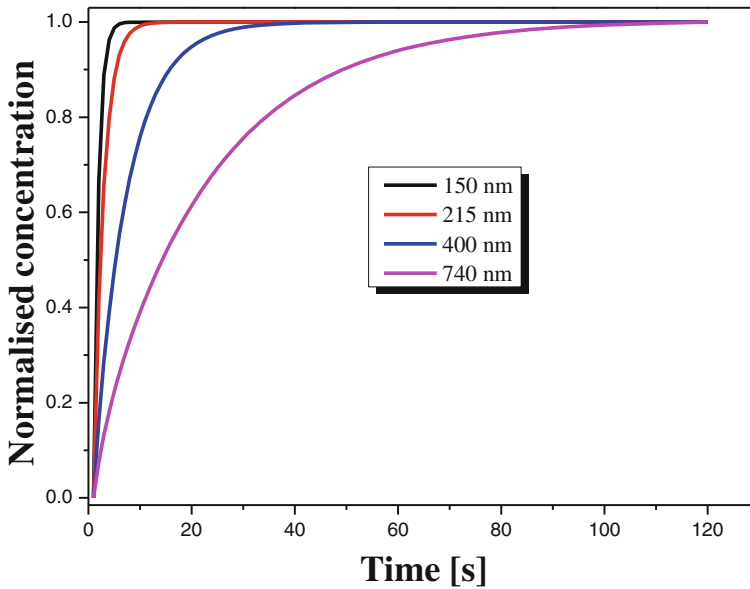


Fig. 8 Absorption kinetics for different sensitive layer thickness

## 5 Conclusions

Due to the great interest in humidity sensors for their applications in electronic control systems, we have developed and investigated HMDSO thin films. The humidity sensor based on pp-HMDSO thin film exhibited good electrical response to relative humidities from the range of 10 to 95 % of RH with small hysteresis of about 2 %. In addition, it also shows a fast response and recovery times. The simulation results show an excellent agreement with measured data and the model features offer a deeper knowledge of either the device behavior or the changes that may be operated to improve the sensor's response.

## References

1. Huang JR, Li MQ, Huang ZY, Liu JH (2007) A novel conductive humidity sensor based on field ionization from carbon nanotubes. *J Sen Act A* 133(467):467–471. doi:[10.1016/j.sna.2006.04.020](https://doi.org/10.1016/j.sna.2006.04.020)
2. Gu L, Huang QA, Qin M (2004) A novel capacitive-type humidity sensor using CMOS fabrication technology. *J Sen Act B* 99(491):491–498. doi:[10.1016/j.snb.2003.12.060](https://doi.org/10.1016/j.snb.2003.12.060)
3. Lv X, Li Y, Li P, Yang M (2009) A resistive-type humidity sensor based on crosslinked polyelectrolyte prepared by UV irradiation. *J Sen Act B* 135(581):581–586. doi:[10.1016/j.snb.2008.10.008](https://doi.org/10.1016/j.snb.2008.10.008)

4. Tailoka F, Fray DJ, Kumar RV (2003) Application of nafion electrolytes for the detection of humidity in a corrosive atmosphere. *J Sol Sta Ion* 161(267):267–277. doi:[10.1016/S0167-2738\(03\)00145-0](https://doi.org/10.1016/S0167-2738(03)00145-0)
5. Guermat N, Bellel A, Sahli S, Segui Y, Raynaud P (2009) Thin plasma-polymerized layers of hexamethyldisiloxane for humidity sensor development. *J Thi Sol Fil* 517:4455–4460. doi:[10.1016/j.tsf.2009.01.084](https://doi.org/10.1016/j.tsf.2009.01.084)
6. Casalbore-Miceli G, Camaioni N, Li Y, Martelli A, Yang MJ, Zanelli A (2005) Water sorption in polymer electrolytes: kinetics of the conductance variation. *J Sen Act B* 105(351):351–359. doi:[10.1016/j.snb.2004.04.123](https://doi.org/10.1016/j.snb.2004.04.123)
7. Li LY, Dong YF, Jiang WF, Ji HF, Li XJ (2008) High-performance capacitive humidity sensor based on silicon nanoporous pillar array. *J Thi Sol Fil* 517(948):948–951. doi:[10.1016/j.tsf.2008.07.016](https://doi.org/10.1016/j.tsf.2008.07.016)
8. Guermat N, Bellel A, Sahli S, Segui Y, Raynaud P (2014) Plasma polymerization of hexamethyldisiloxane and tetraethoxysilane thin films for humidity sensing application. *J Def Dif For* 354:41–47. doi:[10.4028/www.scientific.net/DDF.354.41](https://doi.org/10.4028/www.scientific.net/DDF.354.41)
9. Guermat N, Bellel A, Sahli S, Segui Y, Raynaud P (2010) Electrical and structural characterisation of plasma-polymerized TEOS thin films as humidity sensors. *MJ Con Mat* 12. <http://www.fsr.ac.ma/MJCM/>
10. Maiboroda A, Fechner A, Zahn D, Hietschold M, Lang H (2001) Humidity sensing behaviour of mono- and dinuclear osmium (IV) chloro complexes. *J Sen Act B* 75:188–191. <http://www.elsevier.nl/locate/sensorb>
11. Yun SW, Cha JR (2014) Gong MS (2014) Water-resistive humidity sensor prepared from new polyelectrolyte containing both photo-curable 4-styrylpyridinium function and thiol anchor. *J Sen Act B* 202:1109–1116. doi:[10.1016/j.snb.06.065](https://doi.org/10.1016/j.snb.06.065)
12. Redava EI, Avramov IV (2000) High-resolution humidity measurements with surface transverse wave based resonant devices: application to wireless remote sensing. *J Mat Sci Eng C* 12:71–76. <http://www.elsevier.com/locate/msec>
13. Martins CR, De Paoli MA, Rubinger RM (2007) Sulfonated polystyrene polymer humidity sensor: synthesis and characterization. *J Sen Act B* 123:42–49. doi:[10.1016/j.snb.2006.07.019](https://doi.org/10.1016/j.snb.2006.07.019)
14. Biju KP, Jain MK (2008) Effect of crystallization on humidity sensing properties of sol-gel derived nanocrystalline TiO<sub>2</sub> thin films. *J Thi Sol Fil* 516(2179):2175–2180. doi:[10.1016/j.tsf.2007.06.147](https://doi.org/10.1016/j.tsf.2007.06.147)
15. Tételin A, Pellet C, Laville C, N’Kaoua G (2003) Fast response humidity sensors for a medical microsystem. *J Sen Act B* 91(212):211–218. doi:[10.1016/S0925-4005\(03\)00090-X](https://doi.org/10.1016/S0925-4005(03)00090-X)
16. Crank J (1975) *The mathematics of diffusion*. Oxford university, London, U.K
17. Yang B, Aksak B, Lin Q, Sitti M (2006) Compliant and low-cost humidity nanosensors using nanoporous polymer membranes. *J Sen Act B* 114(260):254–262. doi:[10.1016/j.snb.2005.05.017](https://doi.org/10.1016/j.snb.2005.05.017)

# Synthesis and Characterization of $\text{Cu}_2\text{ZnSnS}_4$ Absorber Layers by Ultrasonic Spray Pyrolysis

W. Daranféd, M.S. Aida, N. Attaf, J. Bougdira and H. Rinnert

**Abstract** The influence of substrate temperature on the properties of  $\text{Cu}_2\text{ZnSnS}_4$  thin films elaborated by spray ultrasonic method has been investigated. Samples are deposited at various substrate temperature ranged from 280 to 360 °C about 75 min. The results of X-ray diffraction analyses indicated that  $\text{Cu}_2\text{ZnSnS}_4$  films have a nanocrystalline structure with (112) preferential orientation and reveals the formation of  $\text{ZnSnO}_3$  and  $\text{Cu}_2\text{ZnSnS}_4$  phases. The crystalline size is varied from 28 to 52 nm with increasing substrate temperature. The optical films characterization was carried out by the measurement of UV-visible transmission. The optical band gap of films deposited at various substrate temperatures is found to lie between 1.40 and 1.6 eV. Electrical conductivity of the films is found to lie in the range  $0.9\text{--}10 \Omega \text{ cm}^{-1}$ .

**Keywords** CZTS · Spray technique · Thin films · Transmission · XRD

## 1 Introduction

$\text{Cu}_2\text{ZnSnS}_4$  (CZTS) is one of the most promising materials for absorber layer in thin film solar cells because of the suitable optical band gap of about 1.5 eV, a high absorption coefficient greater than  $10^4 \text{ cm}^{-1}$  [1], and the p-type conductivity is a promising characteristic for absorber layers in thin film solar cells. It is known that the electrical, optical, morphological and structural properties of this material are

---

W. Daranféd (✉) · M.S. Aida  
Laboratory of Thin Films and Interface, Department of Physics,  
Exact Faculty of Science, University Constantine 1, 25000 Constantine, Algeria  
e-mail: daranfadouarda@hotmail.com

M.S. Aida  
e-mail: aida\_salah2@yahoo.f

N. Attaf · J. Bougdira · H. Rinnert  
Institute Jean Lamour UMR, Department CP2S University of Nancy,  
7198 Nancy, France  
e-mail: nattaf1@yahoo.fr

strongly influenced by the used deposition technique and by the related experimental parameters. Several techniques have been employed for preparing CZTS thin films: sputtering [1, 2], thermal evaporation [3], electrodeposition [4], etc. Among these techniques, spray ultrasonic appears as an interesting technique for preparing  $\text{Cu}_2\text{ZnSnS}_4$  thin films [5]. This technique is very attractive because it is inexpensive, easy and allows obtaining optically smooth, uniform and homogeneous layers. In this work, the effect of substrate temperature on both of the structure, chemical composition, optical and electrical properties of  $\text{Cu}_2\text{ZnSnS}_4$  thin films, deposited by ultrasonic spray, has been investigated.

## 2 Experimental Procedure

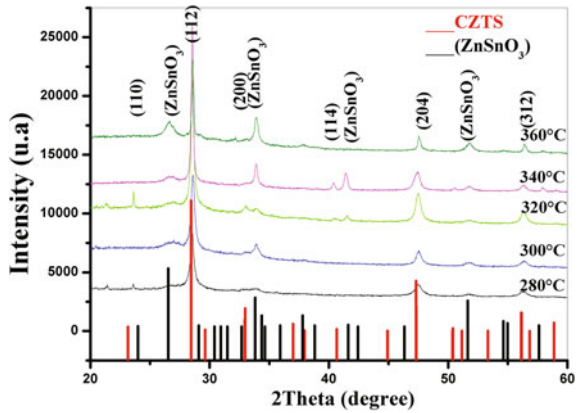
The initial solution is prepared from copper chloride  $\text{CuCl}_2$  (0.01 M), zinc acetate (0.005 M), tin chloride  $\text{SnCl}_2$  (0.005 M) and thiourea SC  $(\text{NH}_2)_2$  (0.04 M). These salts used as sources of different elements (Cu, Zn, Sn and S) are diluted in methanol. In order to optimize the temperature deposition, the substrate temperature was changed from  $T = 280\text{--}360$  °C with a step of 20 °C and the spraying duration was fixed at 75 min. The structural properties were determined by XRD using a Philips X'Pert system with  $\text{CuK}\alpha$  radiation ( $\text{CuK}\alpha = 1.5418$  Å). The films morphology and composition were analyzed using a microscopic scanning SEM equipped with an EDX analysis system. The optical transmissions in the UV-visible range (300–2400 nm) measurements were used with a Shimadzu UV-3101 PC spectrophotometer. Finally, the electrical properties were measured in dark with a coplanar structure with two evaporated golden electrodes.

## 3 Results and Discussion

### 3.1 Structural Properties

The X-ray diffraction patterns of the CZTS thin films synthesized at various substrate temperatures are shown in Fig. 1. The diffraction angles vary from 20° to 60°. For all of the as-deposited films, peaks assigned to the (112), (200), (204) and (312) planes of CZTS are present in the whole diffraction patterns. However, preferential (112) orientation was observed for all deposited films [6]. Peaks are assigned to the kesterite phase (according to the card JCPDS 26-0575). On the other hand, one observes with the growth of the substrate temperature the presence of the secondary phase of the  $\text{ZnSnO}_3$  that has been identified thanks to the peaks next one 26.46°, 33.93° and 51.77°. In addition, we note the emergence of new peaks of the orientation (200), (114) and (111) of CZTS which are seen in Fig. 1. The individual

**Fig. 1** XRD diffraction patterns of CZTS thin films deposited at various substrate temperatures



crystalline size ( $D$ ) in the films has been determined from the (112) peak by using the Scherrer's formula.

$$D = \frac{K\lambda}{\beta \cos \theta}$$

where  $K$  is the Scherrer constant value corresponding to the quality factor of the apparatus measured with a reference single crystal,  $\lambda$  is the wavelength of the X-ray used;  $\beta$  is the full width at half maximum of the peak and  $\theta$  is the Bragg angle. The crystalline size in films of different thicknesses is of the order 28–52 nm and is in good agreement with the reported values [7].

### 3.2 Optical Properties

Optical properties of the deposited  $\text{Cu}_2\text{ZnSnS}_4$  films are studied by the analysis of the spectroscopic optical transmittance in the visible range. In Fig. 2, it is reported the transmittance spectra of films deposited with various substrate temperatures. From the solid band theory, the relation between the absorption coefficient  $\alpha$  and the energy of the incident light ( $h\nu$ ) is given by:

$$(\alpha h\nu)^n = B (h\nu - E_g)$$

where  $B$  is a constant,  $E_g$  the band gap energy and  $n = 2$  or  $1/2$  for crystalline (direct transition) or amorphous CZTS, respectively.

The variation of the deduced optical gap of films with substrate temperature is reported in Fig. 3, as seen, at substrate temperature of 280, 300 and 320 °C the values of the optical gap are 1.6, 1.5 and 1.47 eV respectively. These values are in good agreement with  $\text{Cu}_2\text{ZnSnS}_4$  band gap values reported by other authors [8, 9].

**Fig. 2** Optical transmission spectra of CZTS thin films prepared at various substrate temperatures

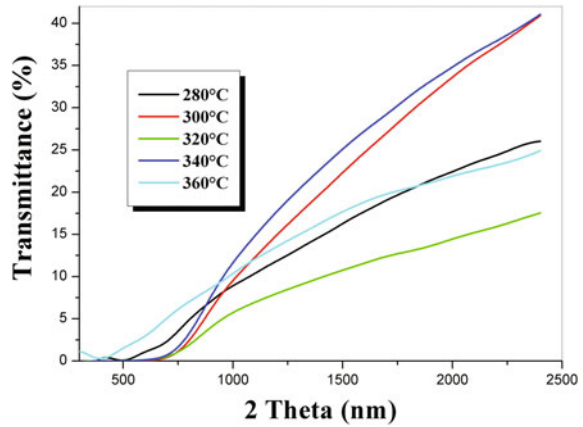
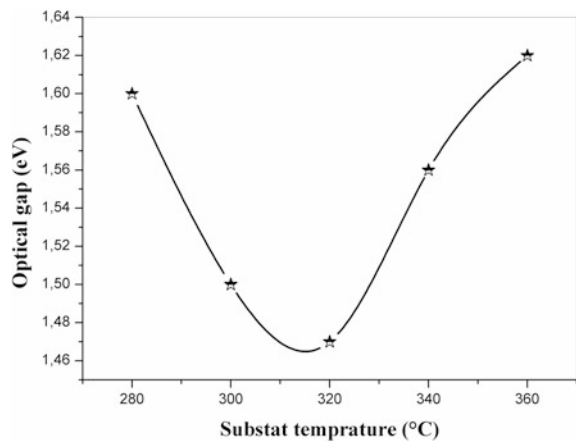


**Fig. 3** Variation of the optical gap as a function of the substrate temperature



Higher substrate temperatures 340 and 360 °C yielded to 1.56 and 1.62 eV optical gaps. The increase in optical gap with increasing substrate temperature can be due to improvement in the films crystallinity as shown in Fig. 1. Such a band gap shift can be related to the formation of different Zn-content according to the DRX diffractograms and EDX (Zn-riche, Cu-poor) analysis. The incorporation of ZnS (with a gap above 3.5 eV) has resulted in a large shift of the band gap of other materials such as CuInS<sub>2</sub> [10]. In another work, Torodov et al. [11] fabricated CZTS thin films by the soft-chemistry method and they reported that the optical gap varies from 1.33 to 1.86 eV where the films are Zn-riche and Cu-poor. On the other hand the presence of ZnSnO<sub>3</sub> phase causes the enlargement of the optical band gap since this phase has a large band gap of 2.42 eV.

### 3.3 Morphological and Composition

As shown in Fig. 4 the elemental composition of  $\text{Cu}_2\text{ZnSnS}_4$  thin films deposited at 360 °C of substrate temperatures is determined from EDS analysis. From this analysis we conclude that CZTS films are Zn-rich, Cu-poor and sulphur deficient. Sulphur deficiency is significantly higher with increasing substrate temperatures; this is due to the sulphur volatility. Sundra et al. [7] have also noticed the sulfur deficiency in CZTS thin films prepared by RF magnetron sputtering [8].

Spray-deposited CZTS films obtained from pure aqueous solution by Nakayama et al. [9] in the substrate temperature range 553–633 K are also sulphur-deficient (28–38 at.%). Previous works suggests that a slightly Zn-rich and Cu-poor composition gives good optoelectronic properties [9, 12].

Figure 5a, b presents the surface morphology images by SEM observation at substrate temperature 320 and 360 °C. It can be seen that the surface of the films

**Fig. 4** EDX characterizations of as-synthesized CZTS thin films

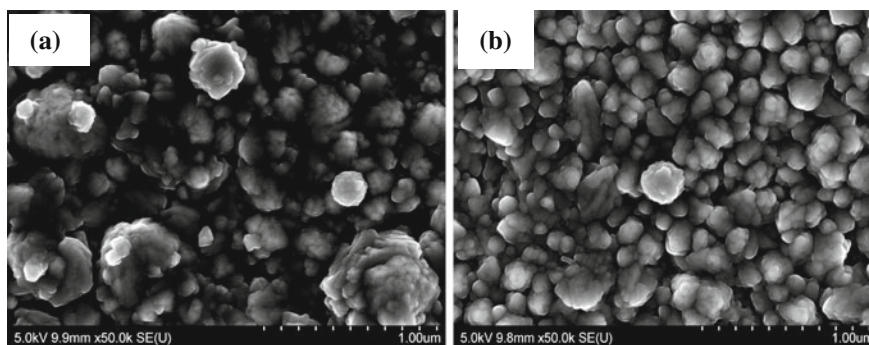
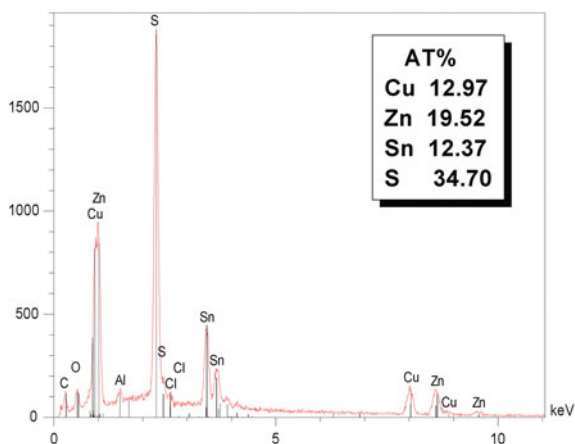
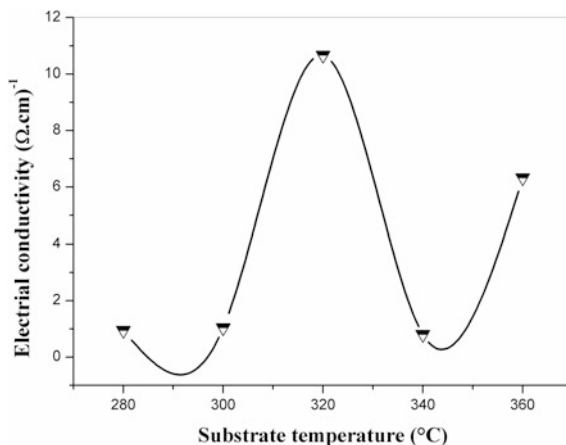


**Fig. 5** SEM images of CZTS thin films prepared at substrate temperature: **a** 320 °C and **b** 360 °C

**Fig. 6** Electrical conductivity and optical gap as various substrates temperatures



deposited at low temperature have a rough aspect. Its shape of non-regular agglomeration of grains with a middle size of the order of 33 nm. With the increase of the substrate temperature, the size of the grains decreases, it varies about from 20 to 10 nm, and the surface of the film becomes more homogeneous and less rough. It is well known that the efficiency of polycrystalline solar cells increases with increasing grain size in the absorber layer, hence larger grains are required for the fabrication of high efficiency solar cells [13].

### 3.4 Electrical Proprieties

In Fig. 6 we have reported the variation of CZTS dark conductivity as a function of substrate temperature. The obtained films have a large conductivity, it varies from 0.9 to 10 Ω cm<sup>-1</sup>. Few works have been devoted to the electrical conductivity measurement in CZTS films. Our films conductivities are relatively higher than the reported ones in the literature by Nakayama and Ito [9]. The relatively high conductivity measured in our film may originate from their Cu-poor composition.

## 4 Conclusion

Cu<sub>2</sub>ZnSnS<sub>4</sub> thin films have been successfully deposited by the spray ultrasonic technique. The effect of substrate temperature on the growth of spray-deposited Cu<sub>2</sub>ZnSnS<sub>4</sub> thin films was investigated. In conclusion, Kieserite structured CZTS with satisfactory nearly stoichiometry and the crystalline sizes in the range of 28–52 nm were obtained. The band gap of the obtained CZTS films ranged from 1.4 to 1.6 eV and the electrical conductivity change from 0.9 to 10 Ω cm<sup>-1</sup> indicating that



the deposited films have suitable optical properties for efficient solar energy conversion. The substrate temperature of 320 °C proves to be a critical temperature; to this temperature we found optimal features of the movies of CZTS indeed.

## References

1. Zhou Z, Wang Y, Xu D, Zhang Y (2010) Fabrication of  $\text{Cu}_2\text{ZnSnS}_4$  screen printed layers for solar cells. *J Sol Energy Mater Sol Cells* 94(2042):2042–2045. doi:[10.1016/j.solmat.2010.06.010](https://doi.org/10.1016/j.solmat.2010.06.010)
2. Katagiri H, Kotoe S, Washio T, Shinohara H, Kurumadani T, Miyajima S (2001) Development of thin film solar cell based on  $\text{Cu}_2\text{ZnSnS}_4$  thin films. *J Sol Energy Mater Sol Cells* 65:141–148. PII: S0927-0248(00)00088-X
3. Liu F, Li Y, Zhang K, Wang B, Yan C, Lai Y, Zhang Z, Li J, Liu Y (2010) In situ growth of  $\text{Cu}_2\text{ZnSnS}_4$  thin films by reactive magnetron co-sputtering. *J Sol Energy Mater Sol Cells* 94:2431–2434. doi:[10.1016/j.solmat.2010.08.003](https://doi.org/10.1016/j.solmat.2010.08.003)
4. Chan CP, Lam H, Surya C (2010) Preparation of  $\text{Cu}_2\text{ZnSnS}_4$  films by electro deposition using ionic liquids. *J Sol Energy Mater Sol Cells* 94:207–211. doi:[10.1016/j.solmat.2009.09.003](https://doi.org/10.1016/j.solmat.2009.09.003)
5. Kamoun N, Bouzouita H, Rezig B (2007) Fabrication and characterization of  $\text{Cu}_2\text{ZnSnS}_4$  thin films deposited by spray pyrolysis technique. *J Thin Solid Films* 515:5949–5952. doi:[10.1016/j.tsf.2006.12.144](https://doi.org/10.1016/j.tsf.2006.12.144)
6. Tanaka T, Yoshida A, Saiki D, Saito K, Guo Q, Nishio M (2010) Influence of composition ratio on properties of  $\text{Cu}_2\text{ZnSnS}_4$  thin films fabricated by co-evaporation. *J Thin Solid Films* 518:S29–S33. doi:[10.1016/j.tsf.2010.03.026](https://doi.org/10.1016/j.tsf.2010.03.026)
7. Kishore Kumar YB, Suresh Babu G, Uday Bhaskar P, Sundara Raja V (2009) Preparation and characterization of spray-deposited  $\text{Cu}_2\text{ZnSnS}_4$  thin films. *J Sol Energy Mater Sol Cells* 93:1230–1237. doi:[10.1016/j.solmat.2009.01.011](https://doi.org/10.1016/j.solmat.2009.01.011)
8. Katagiri H (2005)  $\text{Cu}_2\text{ZnSnS}_4$  thin film solar cells. *J Thin Solid Films* 480–481:426–432. doi:[10.1016/j.tsf.2004.11.024](https://doi.org/10.1016/j.tsf.2004.11.024)
9. Nakayama N, Ito K (1996) Sprayed films of stannite  $\text{Cu}_2\text{ZnSnS}_4$ . *J Appl Surf Sci* 92:171–175. SSI: 0169-4332(95)00225-1
10. Schorr S (2011) The crystal structure of kesterite type compounds: a neutron and X-ray diffraction study. *J Sol Energy Mater Sol Cells* 95:1482–1488. doi:[10.1016/j.solmat.2011.01.002](https://doi.org/10.1016/j.solmat.2011.01.002)
11. Todorov T, Kita M, Carda J, Escribano P (2009)  $\text{Cu}_2\text{ZnSnS}_4$  films deposited by a soft-chemistry method. *J Thin Solid Films* 517:2541–2544. doi:[10.1016/j.tsf.2008.11.035](https://doi.org/10.1016/j.tsf.2008.11.035)
12. Scragg JJ, Dale PJ, Peter LM (2008) Towards sustainable materials for solar energy conversion: preparation and photo electrochemical characterization of  $\text{Cu}_2\text{ZnSnS}_4$ . *J Electrochem Commun* 10:639–642. doi:[10.1016/j.elecom.2008.02.008Z](https://doi.org/10.1016/j.elecom.2008.02.008Z)
13. Seung Seola J, Yul Leea S, Choon Leea J, Duk Namb H, Ho Kima K (2003) Electrical and optical properties of  $\text{Cu}_2\text{ZnSnS}_4$  thin films prepared by rf magnetron sputtering process. *J Sol Energy Mater Sol Cells* 75:155–162. PII: S0927-0248(02)00127-7

# Fault Tolerance Methodology for Micro-volume Deposit System

Luis Yépez-Pérez, Rogelio Bustamante-Bello,  
Ricardo A. Ramírez-Mendoza and Jorge de J. Lozoya-Santos

**Abstract** This work presents a method and an algorithm for implementing the control of two micro-pumps with tolerance to sensors faults. These micro-pumps are used in a micro-volume deposit system, which is intended to help with biomedical and laboratory tests that involve the use of medical samples. This deposit system performs the suction or deposit of the required volumes of fluid. A requirement for this system is to protect the samples and reagents used in the process for the cost associated with gathering the samples. In this way, the idea is to have a fault tolerant system, which can ensure the integrity of the samples. The method and algorithm are implemented using a technique called analytic redundancy Muenchhof et al. (Eur J Control 15, 2009 [1]), which allows reducing the number of physical redundant sensors in a system. For this implementation, we propose the use of a physical sensor and an analytic sensor, using the model of suction-expulsion of the micro-pump from a previous work.

**Keywords** Kalman filter · FDI · Fault tolerant · Deposit system · Micro-pump

## 1 Introduction

Biomedical and laboratory tests involve the use of medical samples, which are typically analyzed using various reagents. A micro-volume fluid deposit system is being developed at Microsystems Research and Biodesign Center in Mexico City.

---

L. Yépez-Pérez · R. Bustamante-Bello (✉) · R.A. Ramírez-Mendoza  
Departamento de Mecatrónica, Tecnológico de Monterrey, Campus Ciudad de México,  
Centro de Investigación en Microsistemas y Biodiseño (CIMB), Calle del Puente 222,  
Tlalpan, 14380 Mexico, D.F., Mexico  
e-mail: rbustama@itesm.mx

J.d.J. Lozoya-Santos  
Dirección de Investigación, División de extensión, consultoría e investigación,  
Universidad de Monterrey, Av. I. Morones Prieto 4500 Pte., Col. Jesús M. Garza,  
San Pedro Garza García 66238, NL, Mexico

This system can move along X and Y axes, has suction and expulsion functions for fluids to deposit samples or reagents. This system uses a novel distributor module powered by MEMS micro-pumps, which are small in size and consume little power. A previous work [2] shows the implementation to use the micro-pumps in an open-loop mode. As higher precision is needed, an additional sensor is being added. Test results are shown in this work with this sensor operating in the system.

The main contribution of this paper is in identifying a suitable fault tolerant method to ensure the integrity of the samples. This method considers two cases: the first one, a quasi-fault tolerant method, using just one sensor and human intervention. For this method, an external operator can check if the fault is on the sensor or the actuator, and the operator can make a decision. The second method uses two sensors, and in case of a faulty sensor, an automatic switch is performed for the sensor. In both cases, only sensor fault tolerance is considered. In contrast to market devices, which commonly use multiple physical redundancy in sensors, this system has less complexity and is therefore cheaper.

Traditionally fault tolerance implementation has three steps: fault detection, fault identification and fault correction [1, 2]. The simplest method for sensors is, for several devices to be added, and the faulty sensor to be detected using a voting scheme. However, system model techniques [2, 3] as analytic redundancy, allow the reduction of devices, and for the simplest implementation [1], two sensors allow the correct detection, identification and correction of the fault.

## 2 Materials and Methods

The micro-volume fluid deposit system has several components (Fig. 1). Two components allow the movement of the fluid distributor in the horizontal and vertical axis.

For the horizontal axis sensors, a fault-tolerant subsystem was proposed and implemented [4]. A fault-tolerant subsystem for the fluid distributor sensors is proposed. A previous work [5] tested the micro-pumps, and it generated the conceptual model in an open loop manner; also, in this work, it designed and constructed the distributor for using eight pipettes at a time. The fluid distributor system is shown in Fig. 2.

The distributor should load eight pipettes, which will move along four modules. In the first module, the eight pipettes are loaded by pressure. In the second one, a liquid is sucked, generally a reagent. In the third one, the liquid is deposited in wells, where commonly a biologic or chemical sample resides; and in the fourth one, the pipettes are thrown away, because the samples may contain DNA residues.

The principal objective for the distributor is sucking-up the correct volume of liquid. For the distribution of fluids two micro-pumps are empowering the distributor: one for suction and the other for expulsion. The micro-pumps are controlled by pulses in a specific frequency and work cycle. The volume to be distributed is about 100  $\mu\text{L}$ , but this may vary for several applications from 50 to

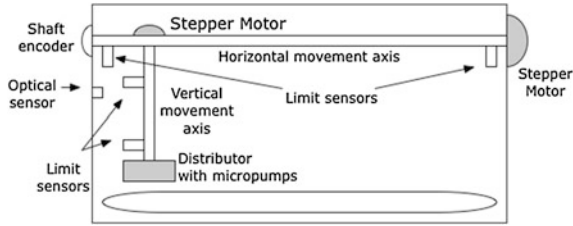


Fig. 1 Micro-volume fluid deposit system

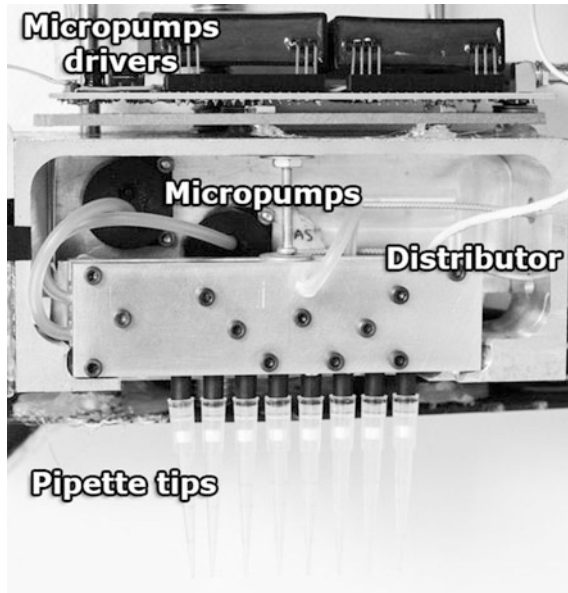


Fig. 2 Distributor system

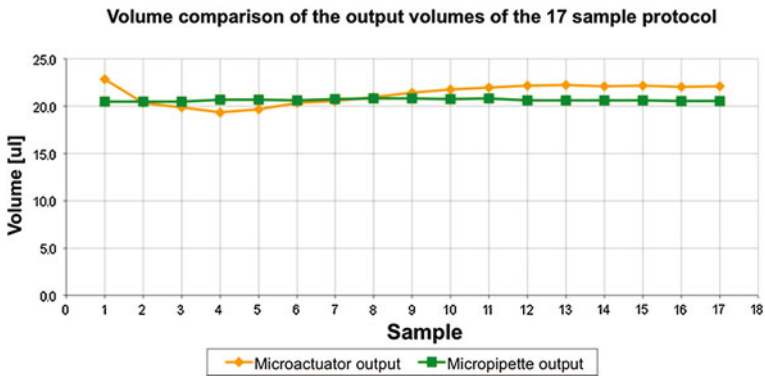


Fig. 3 Micropipette versus micropump [5]

200  $\mu\text{L}$ . From the previous work, using an open-loop control, 100  $\mu\text{L}$  can be reached for one pipette with about 80–100 pulses sent to the micro-pumps. The results for these tests are shown in Fig. 3.

To improve the precision and accuracy for the loaded volume, a pressure sensor was added to the distributor, which can determine if the sucked volume is what was expected. This sensor was added in the main distributor's conduct in order to obtain a general measure of the pressure inside. The added sensor is an air pressure sensor that works with positive and negative differential pressure. When the micro-pump is sucking up, the differential pressure is negative. Otherwise, when the micro-pump is expelling, a positive pressure is measured. The quantities for the measurements are shown and explained in the next section. As expected, the pressure measured depends on the volume of liquid; however, small differences may exist. In any case, combining the open-loop control with the pressure sensor allows for better measurements to be obtained.

## 2.1 Fault Tolerance Background

As the system's objective is to work with sensitive samples, a fault tolerance system is preferred. Fault tolerance has three steps to be implemented [1, 6], which are fault detection, fault isolation or identification, and reconfiguration. Commonly, replicated sensors may help to achieve fault tolerance, and mathematical techniques allow reducing the number of replicated sensor, as an analytic redundancy [2] (Fig. 4).

Analytic redundancy [2] (Fig. 4) is used in this work, using a model of the system that allows decreasing the number of sensors.

The system already uses a fault tolerance implementation on the horizontal axis for faulty sensors. These sensors are dissimilar; one of them is accurate and precise. On the other hand, the second is not precise and has some noise associated. Having noise associated, and being recognized as Gaussian noise, a Kalman filter was proposed to obtain a better sensor measurement and a prediction, in our case, for the analytic redundancy proposed. So, the implementation of the fault tolerance for the horizontal axis uses the diagram as indicated in Fig. 5 [4].

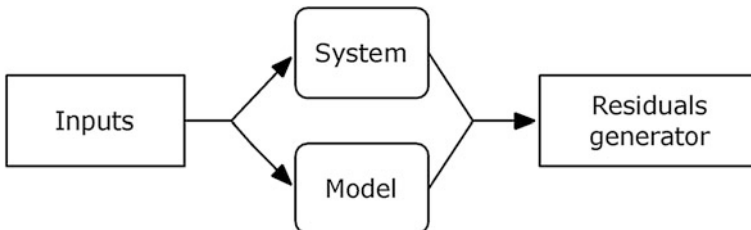


Fig. 4 Analytic redundancy [2]

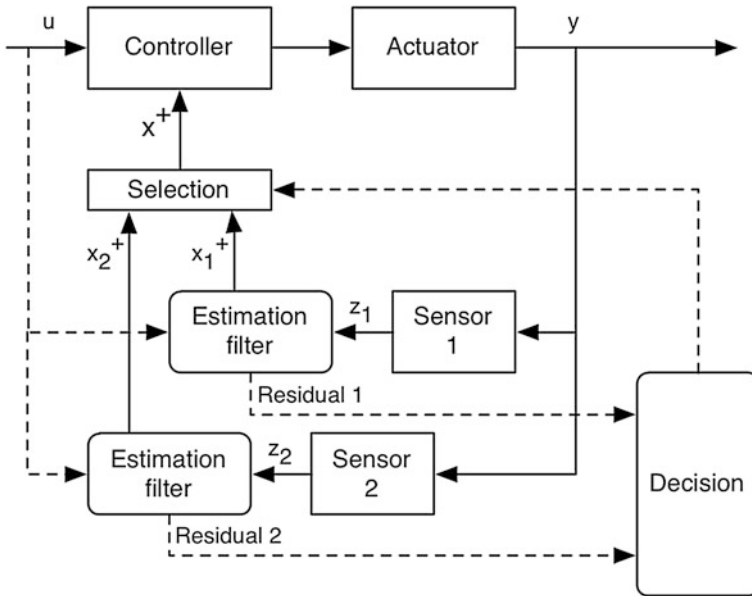


Fig. 5 Fault tolerance implementation for previous system [4]

The estimation filter contains a Kalman filter for each sensor, each one with their own parameters. Using the prediction against the sensor measurement, a residual is generated, which should maintain it within the necessary range to assure a correct operation. Since the system uses a better sensor than the other, the first one is used as primary sensor, while the second one is used as a backup sensor.

When the residual for any of the sensors exceeds the parameters, a discrepancy exists. Here a fault detection is declared. Depending on the discrepancies encountered, a fault is identified. Table 1 shows the possible faults. When the fault has been identified, an action can be taken. In a simpler method, the system can simply stop their operation and report the faulty component. Having a backup sensor, the operation can continue, while the system reports the identified fault.

Table 1 Faults and action taken [4]

Encoder	Optical sensor	Result
OK	OK	All OK
Error	OK	Encoder error
OK	Error	Optical sensor error
Error	Error	Actuator error

### 3 Fault Tolerance Implementation

#### 3.1 Quasi Fault Tolerance Implementation

For the current implementation, with just one sensor, it is not possible to achieve fault tolerance because for the identification of a fault at least three measurements are needed. This condition allows the discrimination of the faulty component. Although it is possible to use analytic redundancy, one more measurement is needed. Hence, a quasi-fault tolerance method is proposed. The main idea is to allow for human intervention to identify where the fault occurs.

As a first task, what is needed is a model to be compared against the measurements. Due to previous observations it was noted that the more fluid there is in the pipette, the more difficult it is to suck up (the water's adhesion to the pipette's wall), so the first approximation was done using an inverse method, with three constants to be determined. These constants could be determined using three average points on the measurements. The formula is showed in Eq. 1.

$$y = \frac{A}{x+B} + C \quad (1)$$

After having a good model of the system, a forecast is needed, which will serve to generate the residuals. As a first approximation, a simpler model will be used, that is:

$$x(k+1) = x(k) + u(k) \quad (2)$$

$$y(k) = f(x(k)) \quad (3)$$

As mentioned, the approximation was done using an inverse method, so,  $y(k)$  will be obtained using the function constructed. This  $y(k)$  will be compared with the measurement  $z(k)$ :

$$r = z(k) - y(k) \quad (4)$$

This residue will be the responsible for knowing if a discrepancy exists; this method is implemented as shown in Fig. 6.

For this implementation, if a discrepancy exists, two options are possible: the sensor is faulty or the distributor is faulty. But the distributor can be faulty for several reasons: the micro-pump broke down, any one of the conducts is obstructed, or there may be an air leak. Even if one or some of the pipettes did not fit properly, leaks will exist and will cause a discrepancy. For this case, if the sensor is faulty an external observation may conclude what the problem is.

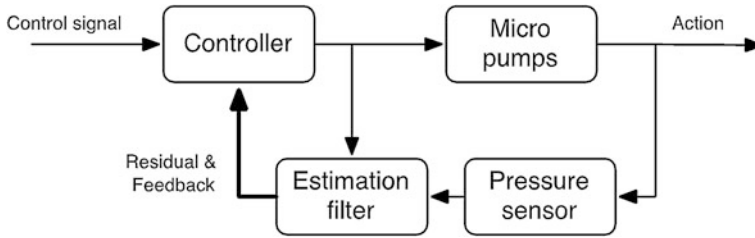


**Fig. 6** Quasi fault tolerance implementation

To implement this method, the next steps that should be considered when suction is in progress are:

1. In case of a discrepancy between the model and the measurement, an alarm should be raised. The operation is suspended momentarily, and a request should be sent to the operator. The operator should verify if the pipettes are fitted correctly and if there is no other apparent leak in the system. A common problem could be that the pipettes are not fitted correctly. After fitting the pipettes, the operation should be restarted.
2. If for the second time there is a discrepancy, the problem could be in the micro-pumps or even in the sensor. To verify this, the operator should look if the pipettes are filling enough and if there is the characteristic pulse sound of the micro-pumps. A sensor fault will be identified when the pipettes are filling up correctly in the estimated pulse count, but the pressure measurement is not correct. An algorithm for this implementation is shown in Fig. 7.

### 3.2 Sensor Fault Tolerance Implementation

As previously stated, to achieve fault tolerance at least two devices are needed; so, if one fails the other will replace the operation. Despite the second pressure sensor not having been yet installed physically, we propose an alternative approach. Such an approach is based on previous experiences of fault-tolerance following the horizontal component.

The method will assume that the second sensor is measuring the main connection to the distributor, and being very close to the first sensor, hence, it should measure almost the same values. The method of implementation is shown in Fig. 8.

As each sensor has its own estimation, any sensor or both can read a discrepancy. So, it is possible to have three options:



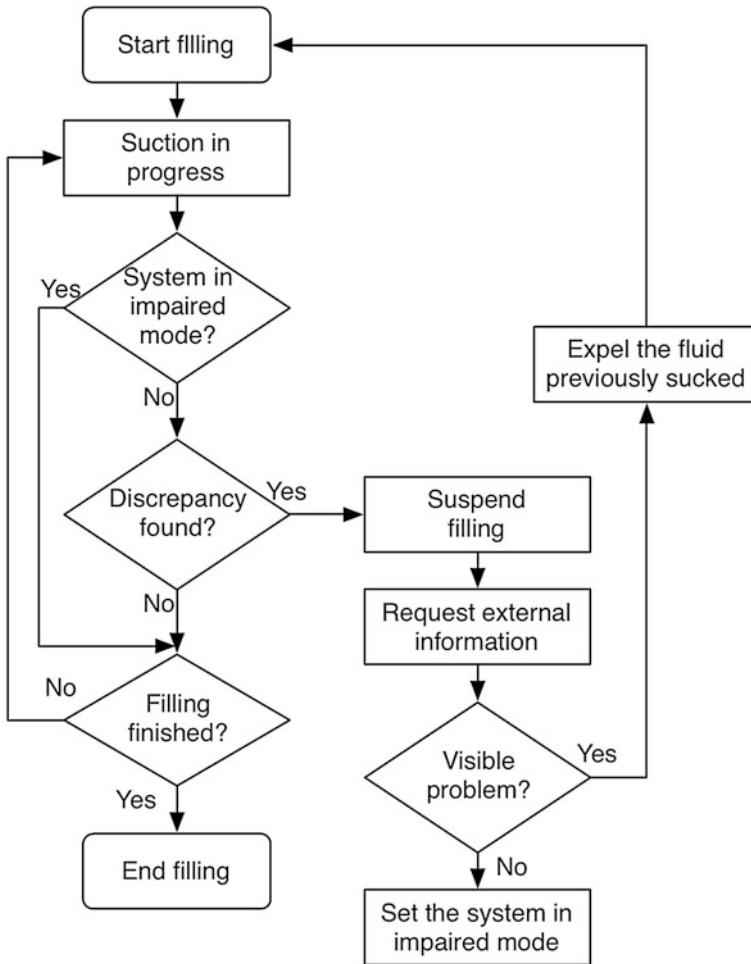


**Fig. 7** Algorithm for quasi fault implementation

1. Both sensors are working inside parameters
2. One sensor has a discrepancy
3. Both sensors have a discrepancy

For the first option, it means the system is working correctly, inside the parameters. For the second option, if just one sensor has a discrepancy, the most likely cause is that the sensor has a problem. For the third option, if both sensors have any discrepancy, then the problem leads to the implementation with just one

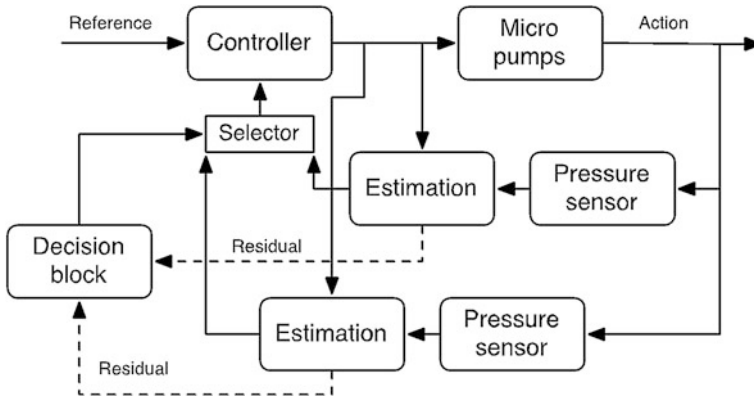


Fig. 8 Method proposed for fault tolerance

sensor, but with the assurance that the problem comes from the distributor, and not from the sensors. Although the solutions can be similar, the differences are explained below.

For the case where just one sensor detects a discrepancy, as both sensors are being verified against the model, we can be sure that the sensor is having difficulties. It will be very unlikely than the model and the measurement were incorrect at the same time. Thus, in a voting scheme, the sensor with the discrepancy will be marked as faulty. Having identified the fault correctly, a decision can be taken for this case, which will be the use of the second sensor as a feedback sensor. Also, it is necessary to raise an alarm in order to verify the faulty sensor. The system (as was implemented and proved in the horizontal component) can continue its operation without interruptions. Here is where the fault tolerance arises for the sensors. Figure 9 shows the algorithm for this implementation.

For the case where both sensors detect a discrepancy, which means that the model does not agreed with the measurement, the distributor has an issue. Similarly, the problem can be that some pipettes are not fitted correctly, there is a leak in the system, or a micro-pump is not working accurately. However, in this case, it is not necessary to check the sensors because both are detected with the same discrepancy. Thus, the trouble has been isolated and more probably easy to find out.

Both implementations improve the operation of the distributor micro-pumps, not just having a feedback signal but also by trying to discover more easily any trouble in the system. In certain cases, the system would be fault tolerant, in this case to a sensor fault.

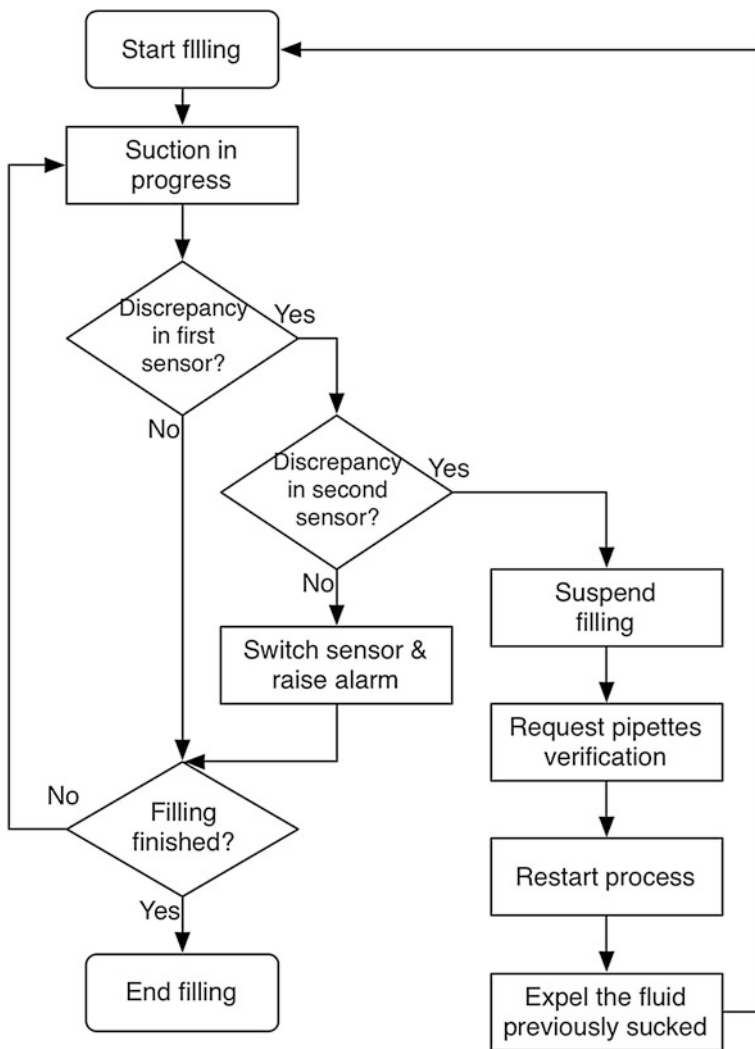
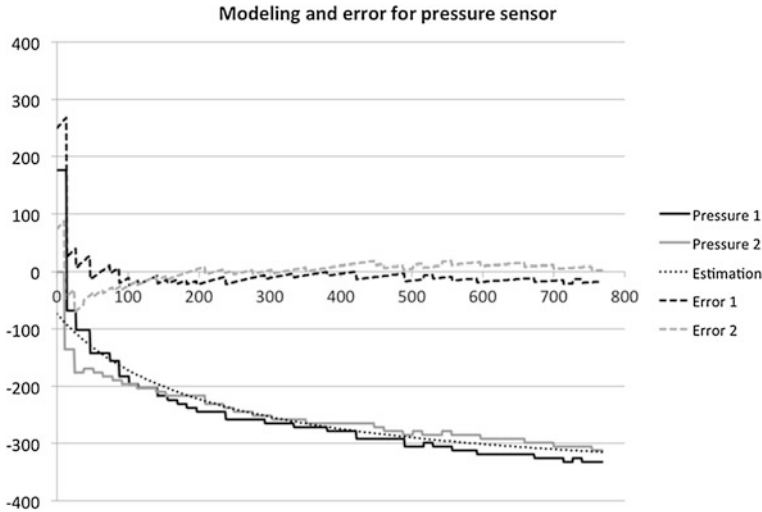


Fig. 9 Algorithm for fault tolerance

### 4 Results and Discussion

As a result of this work, a model and a method have been presented for the pressure sensors from using the pulses to the micro-pumps. This model just works for suction, since it is the main task. Here, an error was obtained at about 11 pulses after the first 50 pulses, and a maximum error about 18 pulses. Before the first 50 pulses there is a lot of instability because a negative pressure sucks in an instant from zero (Fig. 10).



**Fig. 10** Error for pressure sensors

At first sight, we can see how important it is to have a very good model for following the sensed signal; linear and n-order methods were explored, but for the characteristics of the sensors (pressure sensor for the actual system and light sensor for the system explained before) an inverse approximation works in a very good manner, having errors between a controlled parameter. Extensive tests are needed to encounter the best approximation.

However, for creating the model, just three constants were needed to approximate the curve, and these constants can be calculated from three points from the real sensed values. So, it could be useful to program this calculus in the controller in addition to having a calibration sequence before each operation of the system to avoid small variations due to temperature, humidity or atmospheric pressure; in this manner, more precise values will be obtained.

A previous work gives us with certainty information on how these kinds of systems work. Although the first system uses dissimilar sensors, the switching method and the detection method are the same. For this work the model proposed used just one sensor, but allowing for human intervention since for this kind of application supervision is frequently mandatory.

## 5 Conclusions

In the market there are already commercial systems for the deposit of micro-volumes of biomedical samples, but they are generally very complex and costly; using innovative methods in these systems, its complexity can be decreased,

thus reducing the costs and improving the performance of systems. Using a method as analytic redundancy allows having fault detection or fault tolerance without adding replicated sensors.

That is why this paper analyzes one innovative process that allows to improve the measurements made in a micro-volume deposit system, in order to detect some possible failure and, additionally, be fault tolerant to the suction component in that system; moreover, a method and a model are proposed, and experiments conducted to show the feasibility of them. Thus a complete implementation can be added to construct a more robust system.

**Acknowledgments** This work was possible thanks to the Microsystems Research and Biodesign Center (CIMB) from the *Instituto Tecnológico y de Estudios Superiores de Monterrey*, Mexico City campus.

## References

1. Muenchhof M, Beck M, Isermann R (2009) Fault diagnosis and fault tolerance of drive systems: status and research. *Eur J Control* 15
2. Paton RJ (1991) Fault detection and diagnosis in aerospace systems using analytical redundancy. *Comput Control Eng J* 2
3. Zhang Y, Jiang J (2008) Bibliographical review on reconfigurable fault-tolerant control systems. *Ann Rev Control* 32
4. Luis Yépez-Pérez, “Diseño, Desarrollo y Evaluación de un Algoritmo Tolerante a Fallas para un Sistema de Depósito de Fluidos en Microvolúmenes Variables,” Escuela de Graduados en Ingeniería y Arquitectura, Instituto Tecnológico y de Estudios Superiores de Monterrey, Campus Ciudad de México, México, Thesis 2013
5. Quintanar-Melendez AL et al (2009) Concept validation of a MEMS powered, automatic multichannel pipetting device. In: Symposium on circuits and systems, 2009. MWSCAS '09. 52nd IEEE international midwest, Cancun, pp 325–328
6. Paton RJ (1997) Fault-tolerant control systems: the 1997 situation.: IFAC symposium on fault detection supervision and safety for technical processes

# Electromagnetic Compatibility Aspects of Wind Turbine Analysis and Design

D. Poljak and D. Čavka

**Abstract** The paper reviews numerical modeling of arbitrarily shaped wire antennas pertaining to some Electromagnetic Compatibility (EMC) issues in wind turbine (WT) analysis and design. The formulation is undertaken in the frequency domain and based on the related Electric Field Integral Equations—EFIE (Pocklington integro-differential equations for arbitrary wire structures in the presence of a lossy half-space). The influence of a dissipative half-space is taken into account via the rigorous Sommerfeld integral approach. The numerical solution of corresponding EFIE is carried out by means of the Galerkin-Bubnov Indirect Boundary Element Method (GB-IBEM) featuring the use of isoparametric elements while the Sommerfeld integrals are evaluated numerically. The corresponding transient response is obtained via the Inverse Fourier Transform (IFT). The computational examples are related to the transient response of WTs struck by lightning and the transient behaviour of the realistic grounding systems for WTs. The WTs are energized by either an ideal voltage or a current source, respectively. WT is represented by a corresponding multiple wire configuration, while the lightning channel is modelled as an equivalent lossy vertical wire attached to the wind turbine. Furthermore, the grounding system is composed from rings, horizontal and vertical electrodes, respectively.

## 1 Introduction

Wind turbines (WT) are extremely vulnerable to lightning strikes due to their special shape and isolated locations mainly in high altitude areas. Lightning strikes may cause serious damages to WTs and available relevant statistical data indicate that between 4 and 8 % of wind power systems in Europe suffers damages due to

---

D. Poljak (✉) · D. Čavka  
Faculty of Electrical Engineering, Mechanical Engineering and Naval Architecture,  
University of Split, R. Boskovicica 32, 21000 Split, Croatia  
e-mail: dpoljak@fesb.hr

D. Čavka  
e-mail: dcavka@fesb.hr

lightning strikes each year [1]. This situation is even worse in the southern parts of Europe, due to the increased number of thunder storms and relatively low soil conductivities. Thus, the development and installation of integral lightning protection system for wind turbines (WT) is of particular interest [1–8]. Though the methodology for WT lightning protection has been already proposed in [1], a number of issues pertaining to transient behaviour of grounding system, in the case of lightning strike, are still open for researching.

Note that the grounding methodology described in IEC 61400-24:2010 [1] is completely subjected to the IEC 62305-3:2006 [9], which handles lightning protection for general structures including houses and buildings. The foundation and grounding system of a WT are generally much smaller compared to the grounding systems for buildings of the same height.

Therefore, there are two rather important electromagnetic compatibility (EMC) issues to be addressed:

- a study on WT's transient behaviour due to a direct lightning strike which involves the assessment of the transient current distribution along WT configuration
- analysis and design of an efficient low-impedance grounding system as a major prerequisite for an effective protection of WT from lightning strikes.

The first issue, an impact of lightning discharge to WT, particularly lightning strike to tall structures, has generally focused the attention of many prominent researchers in last few decades (e.g. [10]). Several models have been proposed for the assessment of the current distribution along the structure and lightning channel. Usually, the representations are based on the extension of certain return stroke models initially developed for the case of return stroke initiated at the ground level. The presence of a tall structure has been included in two classes of return stroke models: engineering models and antenna theory (AT) models [11]. The presence of a tall object within engineering models has been considered by representing the object as a uniform, lossless transmission line [12, 13]. The AT models [14–19], have been mostly applied in the analysis of lightning strikes to CN tower in Toronto, e.g. [18] or similar towers, e.g. [19]. The formulation can be posed in either the time [14, 19] or the frequency domain [15–18], respectively. Within the framework of the frequency domain formulation a Numerical Electromagnetic Code (NEC) is commonly used for current distribution calculation assuming the ground to be perfectly conducting (PEC) [14].

On the other hand, grounding systems, such as buried vertical or horizontal electrodes and large grounding grids are important not only for safety of personnel but, also for the protection of electrical equipment in industrial and power plants. The principal task of such grounding systems is to suppress the values of transient step and touch voltages, respectively, under the level that could cause adverse health effects. The secondary purpose of grounding systems is to provide common reference voltage for all connected electrical and electronic systems.

Therefore, a low-impedance, proper grounding for the protection of the WT should be designed to reach the grounding resistance of preferably less than  $10 \Omega$

(for an isolated WT, without taking into account the entire grounding system of a wind farm [1]. This requirement is rather difficult to meet in the case of the high specific resistance of the soil. It is worth noting that the standards for grounding systems [11] are based on the steady state or low frequency analysis. Consequently, almost all practical aspects of grounding systems design rely on the steady state analysis. However, such studies do not account for a transient behavior of a grounding system during lightning strikes.

On the other hand, the transient analysis is of great importance as impulse currents increase the grounding system potential related to zero ground during the transient state, which represents great danger to humans, installations and equipment.

One of the most important parameters arising from the transient analysis of a grounding system is the transient impedance. Generally, grounding systems can be modeled using the simple electric circuit methods [20, 21], the transmission line model (TLM) [22–24] or the antenna (full-wave) model (AM) [25–28]. While the circuit approximations are often considered to be oversimplified, the TL models have advantage of simplicity and relatively low computational cost. However, though valid for long horizontal conductors, a simplified TL approach is not convenient for vertical and interconnected conductors. In general, the TL based solutions are limited to a certain upper frequency, depending on the electrical properties of the ground and configuration of particular grounding system [29]. On the other hand, the rigorous electromagnetic models based on the antenna theory are regarded as the most accurate. The AT approach is based on the solution of the Pocklington's integro differential equation for the half space problems [30, 31].

In the last decade several researchers have raised important questions about WT grounding. Some papers on the subject [32–35] are referred to the use of commercial software packages (EMPT and CEDGS) for WT grounding analysis. There are also papers reporting the use of MoM (Method of Moments) [36, 37], the FDTD (Finite Difference Time Domain) [38], the FEM (Finite Element Method) [39], EMPT [40] and CEDGS [41, 42].

The present paper reviews not only a direct lightning strike to the WT, but also transient analysis and design of realistic WT grounding systems. WT is represented by a simple perfectly conducting wire configuration, consisting of tower and three blades, while the lightning channel is represented by a lossy vertical wire attached to WT. The lightning return stroke current is injected by an ideal voltage source at the tip of the WT blade. The current distribution along the WT and lightning channel is obtained by solving the set of Pocklington integro-differential equations in the frequency domain by means of the Galerkin-Bubnov variant of Indirect Boundary Element Method (GB-IBEM) [30].

Furthermore, in the present work the transient impedance of a typical WT grounding system placed in a low conductivity soil is determined. Since the standard [9] provides a very few information about installation and influence of additional electrodes attached to the original grounding system a special attention is focused to the influence of additional vertical and horizontal electrodes, respectively. The influence of a grounding wire placed in a cable trench on the transient behavior is also studied.



Contrary to the analyses reported in [32–42] this work deals with the antenna model presented in [31]. The model is based on the set of homogeneous integro-differential equations of Pocklington type, with ground-air interface effects being taken into account via the exact Sommerfeld integral formulation. Furthermore, instead of applying the usual approach featuring the Moment Method [27, 28] (also implemented in CEDGS), the current distribution along the grounding system is obtained by solving the set of the Pocklington integro-differential equations in the frequency domain via the Galerkin-Bubnov indirect Boundary Element Method (GB-IBEM) [30] featuring the linear isoparametric elements. Finally, the corresponding transient response is obtained by the means of the Inverse Fast Fourier Transform (IFFT) algorithm.

## 2 Formulation

Modeling of arbitrarily shaped wires in the presence of a lossy media is rather important task in many studies pertaining to antenna design and electromagnetic compatibility (EMC) issues [31, 43].

This section deals with a rigorous integral equation formulation for the frequency response of the multiple wire configurations located above or below a lossy ground, respectively. Once the currents along the multiple wire configuration are determined, other parameters of interest could be calculated. The wire of arbitrary shape radiating above or below ground is treated by means of the image theory, as depicted by Fig. 1, and Sommerfeld integral approach.

The set of Pocklington equations for a configuration of multiple wires in the presence of a two media configuration is obtained as an extension of the Pocklington integro-differential equation for a single wire of arbitrary shape which can be derived by enforcing the continuity conditions for the tangential components of the electric field along the perfectly conducting (PEC) wire surface.

First, a single wire of an arbitrary shape, insulated in an unbounded medium, as shown in Fig. 2, is considered.

For the PEC wire the total field composed from the excitation field  $\vec{E}^{exc}$  and scattered field  $\vec{E}^{sct}$  vanishes [31, 44]:

$$\vec{e}_x \cdot (\vec{E}^{exc} + \vec{E}^{sct}) = 0 \quad \text{on the wire surface} \quad (1)$$

Combining Maxwell's equations and Lorentz gauge the scattered electric field can be expressed in terms of the vector potential  $\vec{A}$ :

$$\vec{E}^{sct} = -j\omega\vec{A} + \frac{1}{j\omega\mu\epsilon} \nabla(\nabla\vec{A}) \quad (2)$$

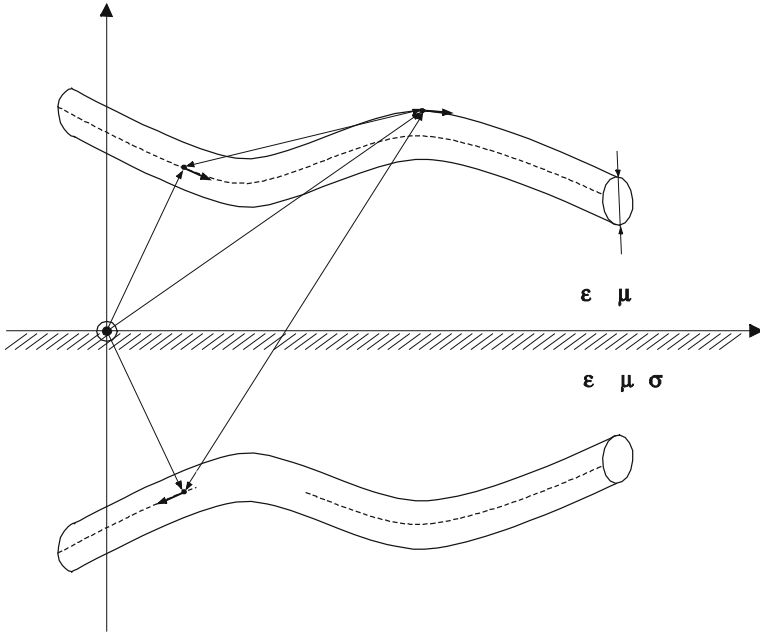


Fig. 1 The wire of arbitrary shape and its image

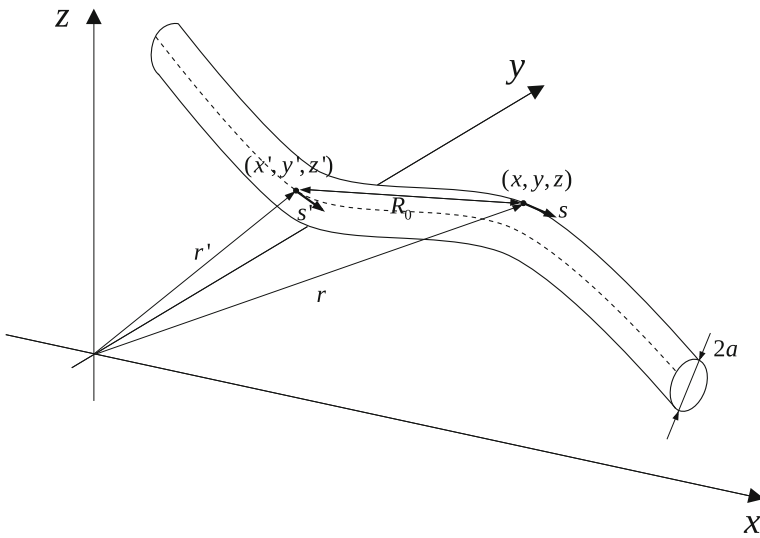


Fig. 2 Single wire of an arbitrary shape in a homogeneous medium

The vector potential is defined by the particular integral along a conducting wire structure of interest:

$$\vec{A}(s) = \frac{\mu}{4\pi} \int_C I(s') g_0(s, s', s^*) \vec{s}' ds' \quad (3)$$

where  $I(s')$  is the current distribution along the wire, and  $g_0(s, s')$  denotes the homogeneous medium Green function:

$$g_0(s, s') = \frac{e^{-jkR}}{R} \quad (4)$$

where  $R$  is the distance from the source point to the observation point, respectively, while  $k$  stands for the propagation constant of the homogeneous medium (lossless or lossy medium, respectively).

Inserting (3) into (2) yields the integral relation for the scattered electric field:

$$\vec{E}^{sct} = \frac{1}{j4\pi\omega\epsilon_0} \int_C I(s') \cdot \vec{s}' \cdot [k^2 + \nabla\nabla] g_0(s, s') ds' \quad (5)$$

Combining (5) and (1) results in the Pocklington integral equation for the unknown current distribution along the wire of an arbitrary shape insulated in free space:

$$E_{\tan}^{exc}(s) = -\frac{1}{j4\pi\omega\epsilon_0} \int_C I(s') \cdot \vec{s} \cdot \vec{s}' \cdot [k^2 + \nabla\nabla] g_0(s, s') ds' \quad (6)$$

where  $E_{\tan}^{exc}$  denotes the tangential component of the electric field illuminating the wire.

The analysis to follow is related to the case of wires above and below ground, respectively.

## 2.1 Integral Equation Formulation for Multiple Overhead Wires

For the case of a wire configuration above a lossy half-space the excitation function  $E^{exc}$  is composed from the incident and reflected field, respectively:

$$E^{exc} = E^{inc} + E^{ref} \quad (7)$$

The corresponding set of integral equations is derived by extending the expression (6) to a multiple wire configuration and is given by:

$$\begin{aligned}
 E_{sm}^{exc}(s) = & -\frac{1}{j4\pi\omega\epsilon_0} \\
 & \sum_{n=1}^{N_w} \left[ \int_{C'_n} I_n(s') \cdot \vec{s} \cdot \vec{s}' \cdot [k_0^2 + \nabla\nabla] g_{0n}(s_m, s'_n) ds' \right. \\
 & + \frac{k_g^2 - k_0^2}{k_g^2 + k_0^2} \int_{C'_n} I_n(s'_n) \cdot \vec{s} \cdot \vec{s}^* \cdot [k_0^2 + \nabla\nabla] g_{in}(s_m, s_n^*) ds' \\
 & \left. + \int_{C'_n} I_n(s') \cdot \vec{s} \cdot \vec{G}_s(s_m, s'_n) ds' \right] \\
 & + Z_S \cdot I_m(s) \\
 m = & 1, 2, \dots, N_w;
 \end{aligned} \tag{8}$$

where  $N_w$  is the total number of wires and  $I_n(s'_n)$  is the unknown current distribution induced on the  $n$ th wire.

Furthermore,  $g_{0mn}(x, x')$  and  $g_{imn}(s, s')$  are the Green functions of the form:

$$g_{0mn}(s_m, s'_n) = \frac{e^{-jkR_{1mn}}}{R_{1mn}}, \quad g_{imn}(s_m, s'_n) = \frac{e^{-jkR_{2mn}}}{R_{2mn}} \tag{9}$$

where  $R_{1mn}$  and  $R_{2mn}$  are distances from the source point and from the corresponding image, respectively to the observation point of interest.

Furthermore,  $k_0$  and  $k_g$  are propagation constants of air and lossy ground:

$$k_0^2 = \omega^2 \mu_0 \epsilon_0 \tag{10}$$

$$k_g^2 = \omega^2 \mu_0 \epsilon_{efec} = \omega^2 \mu_0 \left( \epsilon_0 \epsilon_{rg} - j \frac{\sigma_g}{\omega} \right) \tag{11}$$

where  $\epsilon_{rg}$  and  $\sigma_g$  are relative permittivity and conductivity of the ground, respectively, and  $\omega$  is operating frequency.

The term  $\vec{G}_s(s, s')$  contains the Sommerfeld integrals and is constructed from the vector components for horizontal and vertical dipoles [45]:

$$\begin{aligned}
 \vec{G}_s(s, s') = & (\hat{x} \cdot \hat{s}') \cdot \left( G_\rho^H \cdot \vec{\rho} + G_\phi^H \cdot \vec{\phi} + G_z^H \cdot \vec{z} \right) + (\hat{z} \cdot \hat{s}') \\
 & \cdot \left( G_\rho^V \cdot \vec{\rho} + G_z^V \cdot \vec{z} \right)
 \end{aligned} \tag{12}$$

where:

$$G_\rho^V = \frac{\partial^2}{\partial \rho \partial z} k_g^2 V^R \tag{13}$$

$$G_z^V = \left( \frac{\partial^2}{\partial z^2} + k_0^2 \right) k_g^2 V^R \quad (14)$$

$$G_\rho^H = \cos \phi \left( \frac{\partial^2}{\partial \rho^2} k_0^2 V^R + k_0^2 U^R \right) \quad (15)$$

$$G_\phi^H = -\sin \phi \left( \frac{1}{\rho} \frac{\partial}{\partial \rho} k_0^2 V^R + k_0^2 U^R \right) \quad (16)$$

$$G_z^H = -j4\pi\omega\epsilon_0 \cos \phi G_\rho^V \quad (17)$$

$$U^R = \int_0^\infty D_1(\lambda) e^{-\gamma_0|z+z'|} J_0(\lambda\rho) \lambda d\lambda \quad (18)$$

$$V^R = \int_0^\infty D_2(\lambda) e^{-\gamma_0|z+z'|} J_0(\lambda\rho) \lambda d\lambda \quad (19)$$

$$D_1(\lambda) = \frac{2}{\gamma_0 + \gamma_g} - \frac{2k_0^2}{\gamma_0(k_0^2 + k_g^2)} \quad (20)$$

$$D_2(\lambda) = \frac{2}{k_g^2\gamma_0 + k_0^2\gamma_g} - \frac{2}{\gamma_0(k_0^2 + k_g^2)} \quad (21)$$

$$\gamma_0 = \sqrt{\lambda^2 - k_0^2}; \quad \gamma_g = \sqrt{\lambda^2 - k_g^2} \quad (22)$$

$$\phi = \arctg \frac{\rho}{z+z'} \quad (23)$$

## 2.2 Numerical Solution of Integral Equation Set for Overhead Wires

The set of Pocklington integro-differential Eqs. (8) is numerically handled via the Galerkin-Bubnov variant of the Indirect Boundary Element Method (GB-IBEM). The Boundary Element solution technique used in this work is an extension of the method applied to single wire cases and presented elsewhere, e.g. in [30, 31, 43].

As a first step, at a wire segment the current is expressed in terms of linear combination of shape functions:

$$I_n^e(s') = \sum_{i=1}^n I_{ni} f_{ni}(s') = \{f\}_n^T \{I\}_n \tag{24}$$

and the implementation of the isoparametric parameters yields:

$$I_n^e(\zeta) = \sum_{i=1}^n I_{ni} f_{ni}(\zeta) = \{f\}_n^T \{I\}_n \tag{25}$$

where  $n$  is the number of local nodes per element.

Furthermore, applying the weighted residual approach and utilizing the Galekin-Bubnov procedure the set of Pocklington integro-differential equations is transformed into a system of algebraic equations which matrix form is given by:

$$\sum_{n=1}^{N_w} \sum_{i=1}^{N_n} [Z]_{ji}^e \{I\}_i^e = \{V\}_j^e, \quad m = 1, 2, \dots, N_w; \quad j = 1, 2, \dots, N_m \tag{26}$$

where  $[Z]_{ji}^e$  is the mutual impedance matrix for the  $j$ th observation segment on the  $m$ th wire and  $i$ th source segment on the  $n$ th antenna:

$$\begin{aligned} [Z]_{ij}^e = & - \int_{-1}^1 \int_{-1}^1 \{D\}_j \{D'\}_i^T g_{0nm}(s_n, s'_m) \frac{ds'_m}{d\xi'} d\xi' \frac{ds_n}{d\xi} d\xi \\ & + k_0^2 \vec{s}_n \cdot \vec{s}'_m \int_{-1}^1 \int_{-1}^1 \{f\}_j \{f'\}_i^T g_{0nm}(s_n, s'_m) \frac{ds'_m}{d\xi'} d\xi' \frac{ds_n}{d\xi} d\xi \\ & - \frac{k_g^2 - k_0^2}{k_g^2 + k_0^2} \int_{-1}^1 \int_{-1}^1 \{D\}_j \{D'\}_i^T g_{imm}(s_n, s_m^*) \frac{ds'_m}{d\xi'} d\xi' \frac{ds_n}{d\xi} d\xi \\ & + \frac{k_g^2 - k_0^2}{k_g^2 + k_0^2} k_0^2 \vec{s}_n \cdot \vec{s}'_m \int_{-1}^1 \int_{-1}^1 \{f\}_j \{f'\}_i^T g_{imm}(s_n, s_m^*) \frac{ds'_m}{d\xi'} d\xi' \frac{ds_n}{d\xi} d\xi \\ & + \vec{s}'_m \int_{-1}^1 \int_{-1}^1 \{f\}_j \{f'\}_i^T \vec{G}_{smm}(s_n, s_m^*) \frac{ds'_m}{d\xi'} d\xi' \frac{ds_n}{d\xi} d\xi \\ & + \frac{j}{4\pi\omega\epsilon_0} \int_{-1}^1 Z'_T \{f\}_j \{f'\}_j^T \frac{ds_n}{d\xi} d\xi \end{aligned} \tag{27}$$

Note that matrices  $\{f\}$  and  $\{f'\}$  contain the shape functions while  $\{D\}$  and  $\{D'\}$  contain their derivatives.

The voltage vector is given by:

$$\{V\}_j^m = -j4\pi\omega\epsilon_{eff} \int_{-1}^1 E_{s_m}^{inc}(s_m) f_{jm}(s_m) \frac{ds_m}{d\xi} d\xi_m \quad (28)$$

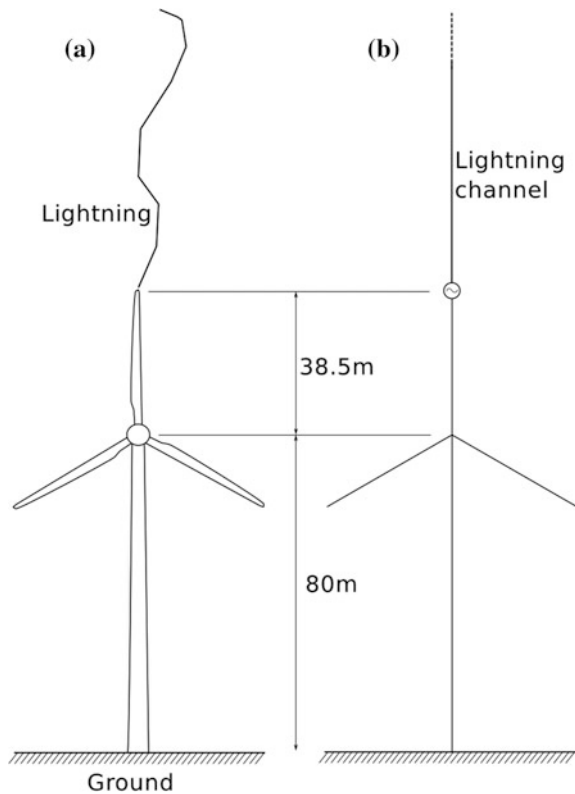
$$m = 1, 2, \dots, N_W; j = 1, 2, \dots, N_m$$

and can be evaluated in the close form [43].

### 2.3 Computational Example: Transient Response of a WT Lightning Strike

WT struck by lightning is depicted in Fig. 3a, while the corresponding wire antenna representation is shown in Fig. 3b. WT configuration is modeled by a simple configuration of four perfectly conducting wires representing the tower and three blades. Furthermore, the lightning channel is represented by a lossy vertical wire

**Fig. 3** Wind turbine struck by lightning and related wire antenna model



antenna, neglecting the corona effect. Note that the resistance per unit channel length is assumed to be  $0.07 \Omega/m$ , as in [19], the wire radius is  $a = 10$  cm. For the sake of simplicity the current wave along the channel is assumed to propagate at the velocity of light although the realistic current propagation velocity is by the factor of two or three less than in the model used in this work. Nevertheless, no significant effects on the distribution of the current wave along the WT are noticed. The lightning return-stroke current is injected by using the equivalent voltage source on the tip of the WT blade.

The channel base current shown in Fig. 4 is given in terms of the Heidler's function with the current and current derivative peaks are assumed to be  $4.7$  kA and  $25$  kA/ $\mu s$ , respectively [19]. The simulations are carried out for the different ground conductivities; PEC ground,  $0.01$ ,  $0.001$  S/m,  $0.1$  m S/m and  $\epsilon_r = 10$ . The grounding wires are not taken into account, as it was shown that they do not significantly affect the current distribution [17, 44].

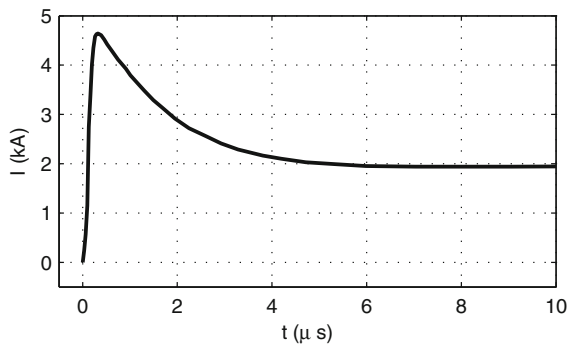
The transient current is analyzed at the characteristic points along the WT; strike blade tip, middle of strike blade, middle of side blade, WT base as it is shown in Fig. 5.

Figure 6 shows the transient current induced at different points along the WT (strike blade tip, middle of strike blade, middle of side blade, WT base) for the case of PEC ground. All major reflections are clearly visible, e.g. the maximum value of the transient current at the side blades is five times less than at the strike blade.

It can also be seen that the transient at the side blade is of significantly shorter duration than in other WT points.

Figures 7, 8, 9 and 10 show transient current waveforms induced at different points along the WT: strike blade tip, middle of strike blade, middle of side blade and WT base obtained for different values of ground conductivity. In all cases the permittivity is assumed to be  $\epsilon_r = 10$ . Analyzing rather small differences between current waveforms for different ground conductivities, which is consistent with the results published in [16] for the CN tower, it can be considered that the influence of a finite ground conductivity to the transient current induced along the WT is rather negligible.

**Fig. 4** The source current waveform





**Fig. 5** Characteristic points along the WT

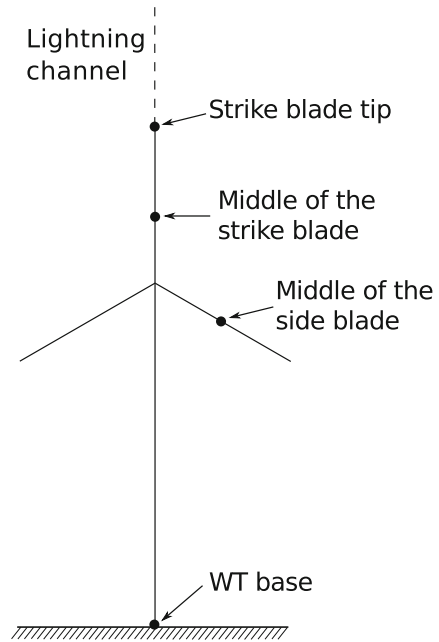


**Fig. 6** Transient induced at different points along WT for the case of PEC ground

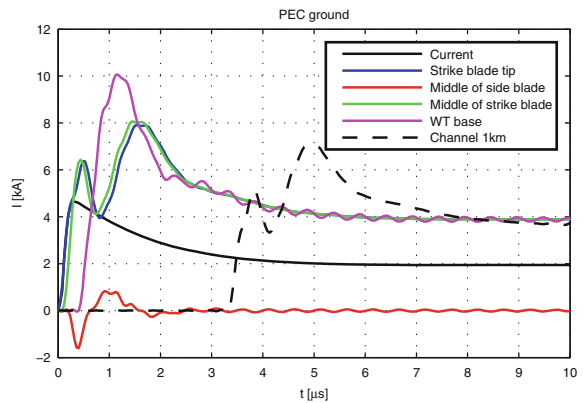
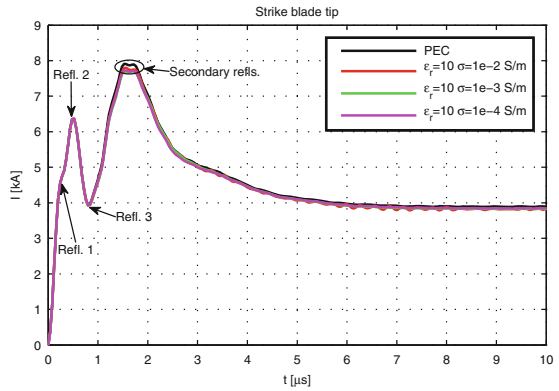
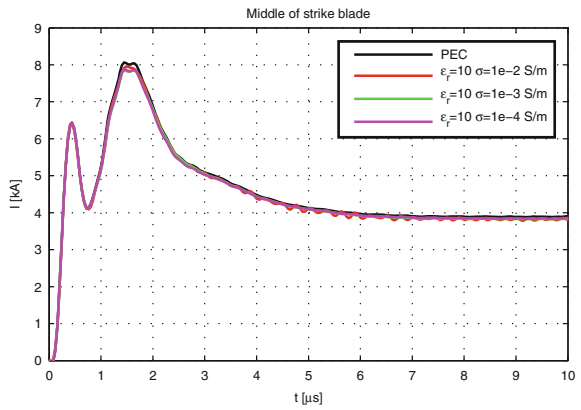


Figure 7 shows all major reflection. Thus, the curve assigned as Refl.1 represents the first reflection of the transient current from the wire junction occurring after 0.253  $\mu$ s. Furthermore, Refl. 2 represents the reflection from the ends of the side blades. This reflection occurs after 0.507  $\mu$ s. The reflection from the ground appears after after 0.78  $\mu$ s and it is assigned as Refl. 3. Finally, due to secondary reflections, the transient current reaches maximum around 1.6  $\mu$ s due to secondary reflections which is followed by the small oscillations.

**Fig. 7** Transient current induced at the strike blade tip



**Fig. 8** Transient current induced at the middle of the strike blade



**Fig. 9** Transient current induced at the middle of side blade

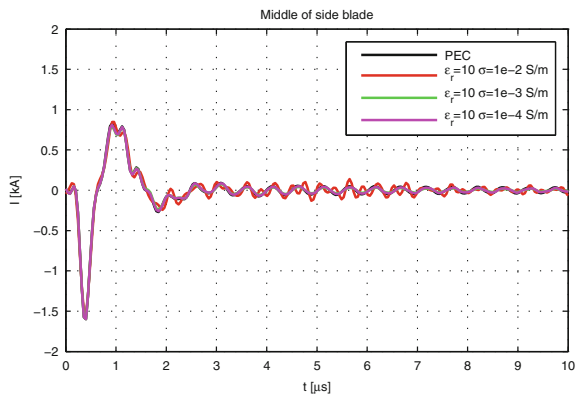
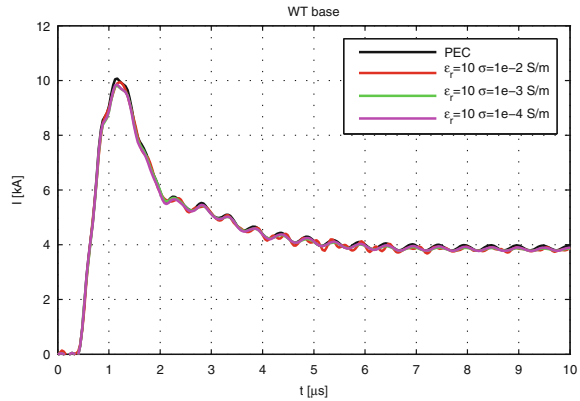


**Fig. 10** Transient current induced at WT base



### 2.4 Integral Equation Formulation for Complex Grounding Systems

The space time current distribution induced along the grounding grid can be obtained as a solution of the set of coupled homogeneous Pocklington integro-differential equations for wires of an arbitrary shape given by [31]:

$$\sum_{n=1}^{N_W} \left[ \begin{aligned} & \int_{C'_n} I_n(s'_n) \cdot \vec{s}_m \cdot \vec{s}'_n \cdot [k_1^2 + \nabla \nabla] g_{0n}(s_m, s'_n) ds'_n \\ & + \frac{k_0^2 - k_1^2}{k_0^2 + k_1^2} \int_{C'_n} I_n(s'_n) \cdot \vec{s}_m \cdot \vec{s}_n^* \cdot [k_1^2 + \nabla \nabla] g_{inn}(s_m, s_n^*) ds'_n \\ & + \int_{C'_n} I_n(s'_n) \cdot \vec{s}_m \cdot \vec{s}_n^* \cdot G_s(s_m, s'_n) ds'_n \end{aligned} \right] = 0 \quad (29)$$

$m = 1, 2, \dots, N_W$

where  $N_w$  is the total number of wires and  $I_n(s'_n)$  is the unknown current distribution along the  $n$ th wire, while  $g_{0mn}(x, x')$  and  $g_{imn}(s, s')$  are the corresponding Green functions:

$$g_{0mn}(s_m, s'_n) = \frac{e^{-jkR_{1mn}}}{R_{1mn}}, \quad g_{imn}(s_m, s'_n) = \frac{e^{-jkR_{2mn}}}{R_{2mn}} \quad (30)$$

where  $R_{1mn}$  and  $R_{2mn}$  are distances from the source point and from the corresponding image, respectively to the observation point of interest.

The current source excitation is incorporated into the integral equation formulation in terms of the forcing condition [15]:

$$I_1 = I_g \tag{31}$$

where  $I_g$  is the current generator while  $I_1$  represents the current at the injection point.

Furthermore, at a given wire junction the continuity conditions for the electric field have to be satisfied [31], which is ensured through the the Kirchhoff current law:

$$\sum_{k=1}^n I_k = 0 \tag{32}$$

and the following form of the continuity equation:

$$\left[ \frac{\partial I_1}{\partial s'_1} \right] \Big|_{at\ junction} = \left[ \frac{\partial I_2}{\partial s'_2} \right] \Big|_{at\ junction} = \dots = \left[ \frac{\partial I_n}{\partial s'_n} \right] \Big|_{at\ junction} \tag{33}$$

The condition (33) provides the discontinuities in charge density to be ruled out in passing from one conductor to another across the junction. At the conductor free ends, on the other hand, the total current vanishes.

The input impedance of the grounding system is defined by the ratio:

$$Z_{in} = \frac{V_g}{I_g} \tag{34}$$

where  $V_g$  and  $I_g$  are the values of the voltage and the current at the injection point.

Once obtaining the current distribution, an injection point voltage is calculated by integrating the normal electric field component from remote soil to the electrode surface:

$$V_g = - \int_{\infty}^r \vec{E} d\vec{l} \tag{35}$$

The direct calculation of (34) is rather time consuming. Nevertheless, by carefully choosing an integration path, the computational cost can be significantly reduced. Thus, for horizontal arrangement of wires, the most appropriate path is vertical, i.e. over  $z$  axis.

The frequency response of grounding system is obtained by multiplying the input impedance spectrum with the actual current spectrum. Finally, the transient response is evaluated by means of the Inverse Fourier Transform (IFT).

### 2.5 Numerical Solution of the Integral Equation Set for Buried Wires

The set of Pocklington integro-differential Eqs. (29) is solved by using the Galerkin-Bubnov variant of the Indirect Boundary Element Method (GB-IBEM).

Undertaking the procedure already presented in Sect. 2.2 the set of Pocklington Eqs. (29) is transferred to the system of equations [31]:

$$\sum_{n=1}^{N_w} \sum_{i=1}^{N_n} [Z]_{ji}^e \{I_n\}_i = 0, \quad m = 1, 2, \dots, N_w; \quad j = 1, 2, \dots, N_m \quad (36)$$

where  $N_w$  is the total number of wires,  $N_m$  is number of elements on the  $m$ th conductor and  $N_n$  is number of segments on the  $n$ th conductor.

Provided the implementation of isoparametric elements the mutual impedance matrix  $[Z]_{ji}$  becomes:

$$\begin{aligned} [Z]_{ji}^e = & - \int_{-1}^1 \int_{-1}^1 \{D\}_j \{D'\}_i^T g_{0nm}(s_m, s'_n) \frac{ds_n}{d\zeta'} d\zeta' \frac{ds_m}{d\zeta} d\zeta \\ & + k_1^2 \cdot \widehat{s}_m \cdot \widehat{s}_n' \int_{-1}^1 \int_{-1}^1 \{f\}_j \{f'\}_i^T g_{0nm}(s_m, s'_n) \frac{ds_n}{d\zeta'} d\zeta' \frac{ds_m}{d\zeta} d\zeta \\ & + \frac{k_0^2 - k_1^2}{k_0^2 + k_1^2} \left[ - \int_{-1}^1 \int_{-1}^1 \{D\}_j \{D'\}_i^T g_{inm}(s_m, s_n^*) \frac{ds_n}{d\zeta'} d\zeta' \frac{ds_m}{d\zeta} d\zeta \right. \\ & \left. + k_1^2 \cdot \widehat{s}_m \cdot \widehat{s}_n^* \int_{-1}^1 \int_{-1}^1 \{f\}_j \{f'\}_i^T g_{inm}(s_m, s_n^*) \frac{ds_n}{d\zeta'} d\zeta' \frac{ds_m}{d\zeta} d\zeta \right] \\ & + \widehat{s}_m \cdot \widehat{s}_n' \int_{-1}^1 \int_{-1}^1 \{f\}_j \{f'\}_i^T G_{snm}(s_m, s'_n) \frac{ds_n}{d\zeta'} d\zeta' \frac{ds_m}{d\zeta} d\zeta \end{aligned} \quad (37)$$

Matrices  $\{f\}$  and  $\{f'\}$  contain the shape functions while  $\{D\}$  and  $\{D'\}$  contain their derivatives.

### 2.6 Computational Example: Transient Behaviour of a WT Grounding System

The problem of interest, i.e. WT connected to a corresponding grounding system is shown in Fig. 11. The WT grounding system is subjected to a transient current due the direct lighting strike at a certain point. Note that the influence of WT itself (tower, blades etc.) is neglected.

The practical grounding system is shown in Fig. 12.

The grounding system consists of a square of galvanized steel flanges (Fe/Zn  $30 \times 3.5$  mm—gray line in Fig. 2) at the 2 m depth, two copper ring wires (Cu  $70 \text{ mm}^2$ —black line in Fig. 2) at different levels (smaller one of 3.25 m radius at 5 cm depth and the larger with 6.8 m radius buried at 55 cm depth) and additional four copper wires connecting rhombus with the tower. All this parts of the grounding system are connected by aluminothermy welding.

The grounding system is buried in a homogenous soil of relatively high specific resistance of  $\rho = 1200 \text{ } \Omega/\text{m}$ . The relative dielectric constant is assumed to be  $\epsilon_r = 9$ .

**Fig. 11** WT subjected to a lightning strike

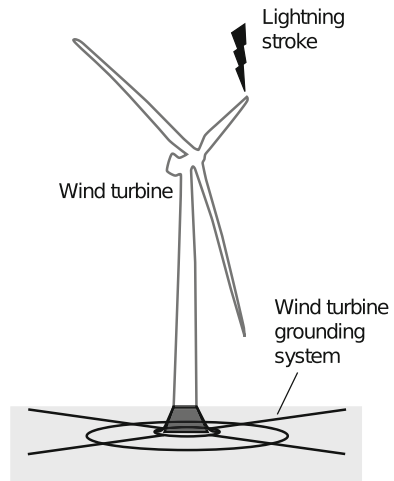
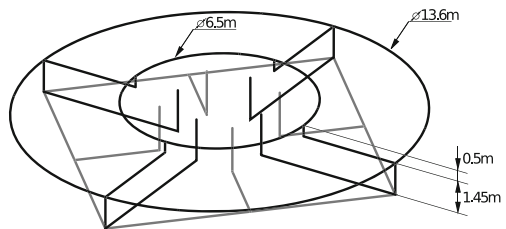


**Fig. 12** Typical WT grounding system arrangement



In all computational examples the lightning current is expressed by the double exponential function:

$$i(t) = I_0(e^{-\alpha t} - e^{-\beta t}) \tag{38}$$

where:  $I_0 = 1.1043 \text{ A}$ ,  $\alpha = 0.07924 \times 10^6 \text{ s}^{-1}$ ,  $\beta = 0.07924 \times 10^6 \text{ s}^{-1}$  (so called 1/10  $\mu\text{s}$  impulse).

Figure 13 shows the transient response of the basic grounding system. Dashed line represents a ten times higher input current waveform for comparison reasons.

The maximal value of voltage is about 37 V and it is reached slightly after current peak value. Transient impedance continuously increases from zero to the maximal value of 40  $\Omega$  witch is equivalent to the steady state condition.

Given that the value of the transient impedance is relatively high, i.e. four times higher then required by the standards in the steady state, this grounding system does not satisfy required safety standards.

The original grounding system can be improved by adding horizontal and/or vertical electrodes.

To investigate the influence of additional horizontal electrodes, the wind turbine grounding system has been upgraded with four 5 or 15 m long horizontal electrodes, Fig. 14, placed at 2 m depth.

Figures 15 and 16 show transient voltage induced at the injection point and the transient impedance, respectively, for different lengths of additional horizontal

**Fig. 13** Transient behavior of the basic grounding system

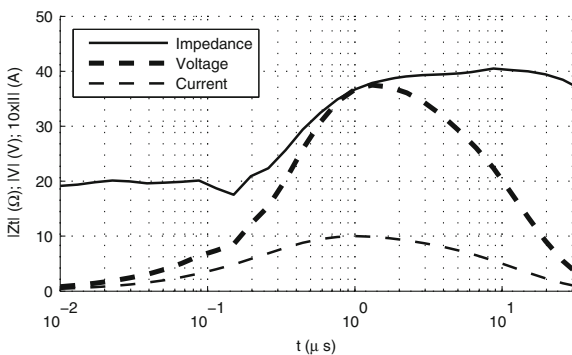


**Fig. 14** Additional horizontal electrodes on WT grounding system

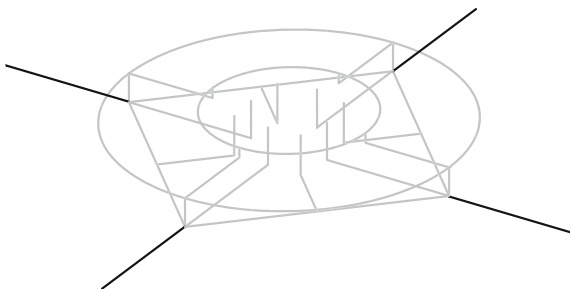


**Fig. 15** Induced feeding point transient voltage for different lengths of additional horizontal electrodes

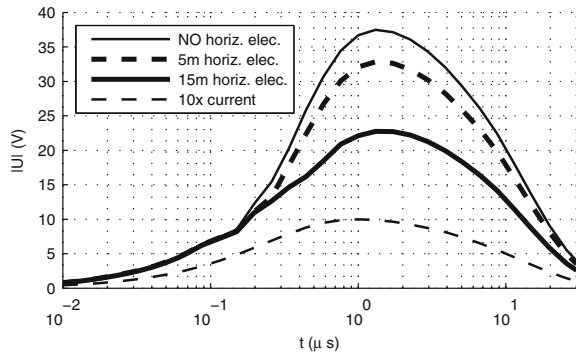
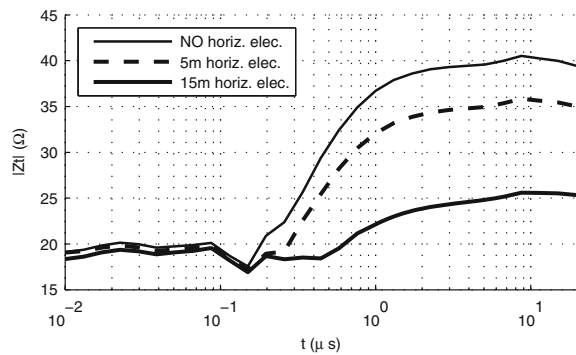


**Fig. 16** Transient impedance for different lengths of additional horizontal electrodes



electrodes. A significant reduction in the value of the maximal induced voltage and consequently the transient impedance can be observed with the increase of the horizontal electrodes length. Compared to the configuration without horizontal electrodes, additional four 5 m horizontal electrodes reduce maximal transient voltage by 13 % while four 15 m electrodes reduce it by 40%. A similar behavior can be noticed for the transient impedance in Fig. 16. Note that no difference in transient behavior until 0.15 μs occurs, therefore the additional horizontal electrodes do not affect very early time behavior.

The influence of vertical electrodes on WT grounding system have been analyzed by investigating vertical electrodes of various length (3, 5.5 and 15 m) were examined. Placement of the vertical electrodes is shown on Fig. 17.

Results given in Figs. 18 and 19 show the influence of additional vertical electrodes of various lengths on transient behavior of the wind turbine grounding system. It is clear that additional, relatively short, vertical electrodes do not significantly decrease the value of the transient impedance with respect to the case without vertical electrodes (5 % with four 3 m electrodes, and 12 % with four 5.5 m electrodes). On the other hand, in the case of long vertical electrodes such influence is significant (around 40 % with respect to the case without vertical electrodes).



**Fig. 17** Additional vertical electrodes on WT grounding system

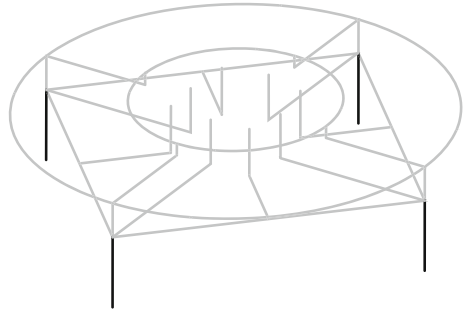


**Fig. 18** Induced feeding point transient voltage for different lengths of additional vertical electrodes

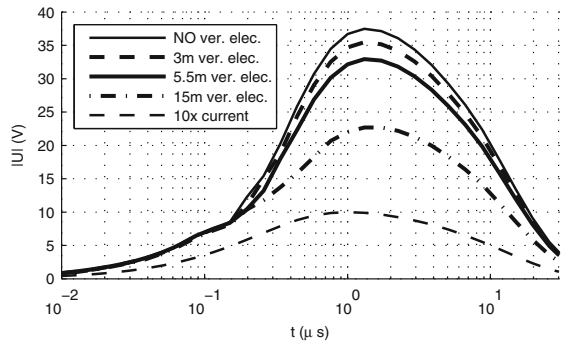
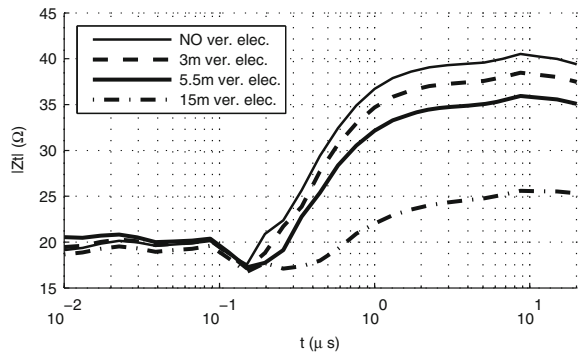


**Fig. 19** Transient impedance for different lengths of additional vertical electrodes



Figures 20 and 21 show the transient behavior of the grounding system with added four 15 m horizontal or vertical electrodes, respectively.

Comparing those two cases no significant difference can be found. This conclusion is important as installation of horizontal electrodes is appreciably cheaper than placing vertical ones, especially in a rocky terrain.

Therefore, the principal parameter which determines the overall grounding system performance is the electrode length. On the other hand, the installation of

**Fig. 20** Comparison of the induced feeding point transient voltage in the case of added 15 m horizontal or vertical electrodes, respectively

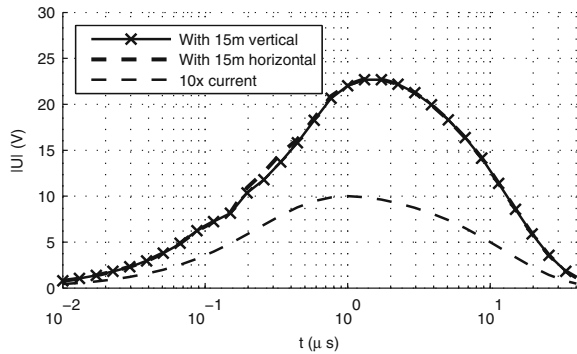
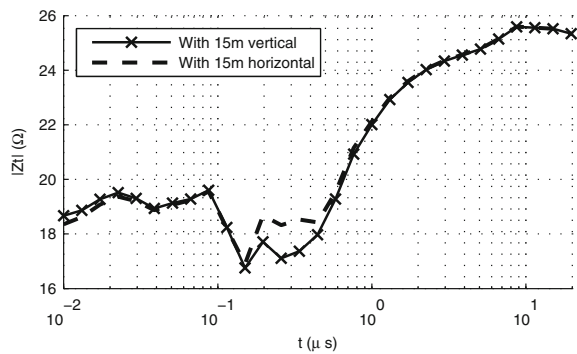


**Fig. 21** Comparison of transient in the case of added 15 m horizontal or vertical electrodes, respectively



the vertical electrodes is plausible in the case of highly conductive earth layer under the main grounding system, which is rarely the case in the rocky terrain.

It is also important to analyze the impact of the grounding wire in cable trench to the behavior of grounding system in the impulse mode. Results are compared (Figs. 22 and 23) for three different configurations:

- grounding system with additional four 15 m horizontal electrodes without grounding wire in cable trench (config 1);

**Fig. 22** Influence of grounding wire in a cable trench on the induced feeding point transient voltage

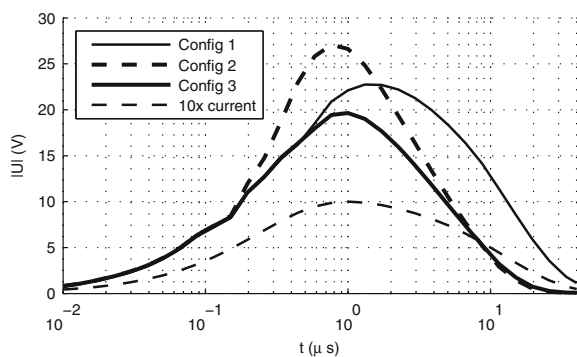
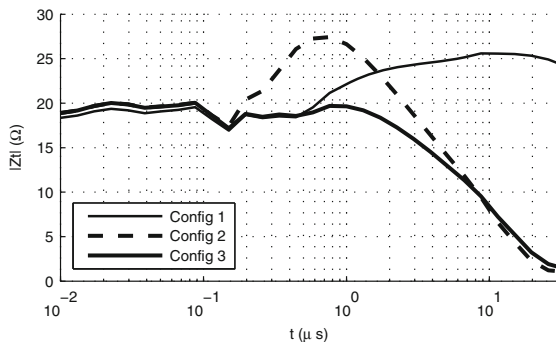


**Fig. 23** Influence of the grounding wire in a cable trench on the transient impedance



- grounding system without additional horizontal electrodes with 200 m grounding wire in cable trench (config 2);
- grounding system with additional three 15 m horizontal electrodes with 200 m grounding wire in cable trench (config 3).

All configurations do not contain vertical electrodes. The grounding wire is modeled as a 200 m-horizontal electrode.

It is clear from the obtained numerical results that the adding of grounding wire in a cable trench reduces the grounding impedance in steady state. A significant increase in maximal induced voltage and related transient impedance is also evident in the case of configuration without additional horizontal electrodes.

Consequently, added long grounding wire in a cable trench significantly influences only the steady state behavior. Therefore, the configuration with both horizontal electrodes and grounding wire in cable trench seems to be optimal.

### 3 Closure

The paper addresses two EMC aspects pertaining to the analysis and design of wind turbines (WT); a study on WT's transient behaviour due to a direct lightning strike which involves the assessment of the transient current distribution along WT configuration; analysis and design of an efficient low-impedance grounding system as a major prerequisite for an effective protection of WT from lightning strikes.

The WT struck by lightning, in accordance to the antenna theory model, is represented by a simple wire structure while the channel is represented by a lossy vertical antenna energized by a voltage source placed on the tip of the blade. The current distribution along the structure is governed by the set of the coupled Pocklington integro-differential equations. The effects of the ground-air interface are taken into account via the Sommerfeld integral approach. The corresponding set of equations in the frequency domain is solved using the Galerkin-Bubnov scheme of the indirect Boundary Element Method (GB-IBEM). Transient response is computed via the Inverse Fast Fourier Transform (IFFT).

The presented results clearly demonstrate the finite ground conductivity to have a minor effect on the current distribution along the struck WT, which is in accordance to the previously published works pertaining to CN tower.

The transient behaviour of wind turbine grounding system has been analyzed using the thin wire antenna theory, as well. The formulation is based on the corresponding set of homogeneous Pocklington integro-differential equation. Transient behaviour of a typical WT grounding system is analysed by using the GB-IBEM. Finally, the corresponding transient response is obtained by means of the IFFT algorithm.

The influence of the horizontal and vertical electrodes of various lengths same as grounding wire in a cable trench on transient behaviour has been analyzed. It is shown that short vertical electrodes do not appreciably reduce the transient impedance values. In the case of long vertical electrodes the influence is significant but almost the same when using horizontal electrodes of the same length. This is important fact, particularly when grounding is performed in rocky terrain, where drilling is rather expensive. Thus, configuration with certain number of additional, long enough, horizontal electrodes and grounding wire in a cable trench has shown to be optimal.

## References

1. IEC INTERNATIONAL STANDARD (2010) Wind turbine generation system—24: Lightning protection, IEC 61400-24. International Electro-technical Commission, Geneva
2. IEA (1997) Recommended practices for wind turbine testing and evaluation, 9. Lightning protection for wind turbine installations. ed. (1997)
3. IEE Professional Group S1 (1997) (New concepts in the generation, distribution and use of electrical energy): Half-day colloquium on “Lightning protection of wind turbines”, (1997, 11)
4. Sorensen T, Sorensen JT, Nielsen H (1998) Lightning damages to power generating wind turbines. In: Proceedings of 24th international conference on lightning protection (ICLP98):176–179
5. McNiff B (2002) Wind turbine lightning protection project 1999–2001. NREL Subcontractor report, SR-500-31115
6. Rachidi F, Rubinstein M, Montanya J et al (2008) A review of current issues in lightning protection of new-generation wind turbine blades. IEEE Trans Industr Electron 55(6):2489–2496
7. Yoh Y, Toshiaki F, Toshiaki U (2007) How does ring earth electrode effect to wind turbine? Universities power engineering conference, UPEC 2007. 42nd international: pp 796–799
8. Glushakow B (2007) Effective lightning protection for windturbine generators. IEEE Trans Energy Convers 22(1):214–222
9. IEC INTERNATIONAL STANDARD (2006) Protection against lightning—Part 3: physical damage to structures and life hazard. IEC 62305-3. International Electro-technical Commission, Geneva
10. Rakov VA (2001) Transient response of a tall object to lightning. IEEE Trans Electromagn Compat 43:654–661
11. Rakov VA, Uman MA (1998) Review and evaluation of lightning return stroke models including some aspects of their application. IEEE Trans Electromagn Compat 40:403–426

12. Rachidi F, Rakov VA, Nucci CA, Bermudez JL (2002) The effect of vertically-extended strike object on the distribution of current along the lightning channel. *J Geophys Res* 107 (D23):4699
13. Pavanello D, Rachidi F, Rakov VA, Nucci CA, Bermudez JL (2007) Return stroke current profiles and electromagnetic fields associated with lightning strikes to tall towers: comparison of engineering models. *J Electrostat* 65:316–321
14. Podgorski S, Landt JA (1987) Three dimensional time domain modeling of lightning. *IEEE Trans Power Deliv* 2:931–938
15. Petrache E, Rachidi F, Pavanello D et al (2005) Lightning strikes to elevated structures: influence of grounding conditions on currents and electromagnetic fields. In: Presented at IEEE international symposium on electromagnetic compatibility. Chicago
16. Petrache E, Rachidi F, Pavanello D et al (2005) Influence of the finite ground conductivity on the transient response to lightning of a tower and its grounding. In: Presented at 28th general assembly of international union of radio science (URSI), New Delhi, India
17. Podgorski S, Landt JA (1985) Numerical analysis of the lightning-CN tower interaction. In: Presented at 6th symposium and technical exhibition on electromagnetic compatibility, Zurich, Switzerland
18. Baba Y, Ishii M (2001) Numerical electromagnetic field analysis of lightning current in tall structures. *IEEE Trans Power Delivery* 16:324–328
19. Kordi B, Moini R, Janischewskyj W et al (2003) Application of the antenna theory model to a tall tower struck by lightning. *J Geophys Res* 108
20. Meliopoulos AP, Moharam MG (1983) Transient analysis of grounding systems. *IEEE Trans Power Appar Syst* 102(2):389–399
21. Ramamoorthy M, Narayanan MMB, Parameswaran S, Mukhedkar D (1989) Transient performance of grounding grids. *IEEE Trans Power Deliv* 4(4):2053–2059
22. Liu Y, Zitnik M, Thottappillil R (2001) An improved transmission line model of grounding system. *IEEE Trans EMC* 43(3):348–355
23. Lorentzou MI, Hatzargyriou ND, Papadias BC (2003) Time domain analysis of grounding electrodes impulse response. *IEEE Trans Power Deliv* 2:517–524
24. Liu Y, Theethayi N, Thottappillil R (2005) An engineering model for transient analysis of grounding system under lightning strikes: nonuniform transmission-line approach. *IEEE Trans Power Deliv* 20(2):722–730
25. Poljak D, Doric V (2006) Wire antenna model for transient analysis of simple grounding systems. Part I: the vertical grounding electrode. *Prog Electromagnet Res* 64:149–166
26. Poljak D, Doric V (2006) Wire antenna model for transient analysis of simple grounding systems. Part II: the horizontal grounding electrode. *Prog Electromagnet Res* 64:167–189
27. Grcev L, Dawalibi F (1990) An electromagnetic model for transients in grounding systems. *IEEE Trans Power Deliv* 5(4):1773–1781
28. Grcev L, Heimbach M (1997) Frequency dependent and transient characteristics of substation grounding systems. *IEEE Trans Power Deliv* 12(1):172–178
29. Cavka D, Harrat B, Poljak D, Nekhoul B, Kerroum K, Drissi KEK (2011) Wire antenna versus modified transmission line approach to the transient analysis of grounding grid. *Eng Anal Bound Elem* 3:1101–1108
30. Poljak D (2007) *Advanced modeling in computational EMC*. Wiley, New York
31. Poljak D, Drissi KEK, Nekhoul B (2013) Electromagnetic field coupling to arbitrary wire configurations buried in a lossy ground: a review of antenna model and transmission line approach. *Int J Comput Methods Exp Meas* 1(2):142–163
32. Hatzargyriou N, Lorentzou M, Cotton I, Jenkins N (1997) Wind farm earthing. In: *Proceedings of IEE half-day colloquium on lightning protection of wind turbines*, no. 6
33. Cotton I, Jenkins N (1997) The effects of lightning on structures and establishing the level of risk. In: *Proceedings of IEE half-day colloquium on lightning protection of wind turbines*, no. 3
34. Cotton I, Jenkins N (1999) Windfarm earthing. In: *Proceedings of European wind energy conference (EWEC1999)*, pp 725–728

35. Lorentzou M, Hatzigiorgiou N, Papadias BC (2000) Analysis of wind turbine grounding systems. In: Proceeding of 10th mediterranean electrotechnical conference (MELECON2000). Cyprus, pp 936–939
36. Lewke B, Krug F, Kindersberger J (2006) Risk of lightning strike to wind turbines for maintenance personnel inside the hub. In: Proceedings of 28th international conference on lightning protection (ICLP2006), no. XI-9, Kanazawa
37. Ukar O, Zamora I (2011) Wind farm grounding system design for transient currents. *Renew Energy* 36:2004–2010. doi:[10.1016/j.renene.2010.12.026](https://doi.org/10.1016/j.renene.2010.12.026)
38. Yasuda Y, Fuji T, Ueda T (2007) Transient analysis of ring earth electrode for wind turbine. In: Proceedings of European wind energy conference (EWEC2007), no. BL3.212, Milan
39. Muto A, Suzuki J, Ueda T (2010) Performance comparison of wind turbine blade receptor for lightning protection. In: Proceedings of 30th international conference on lightning protection (ICLP2010), no. 9A-1263, Cagliari
40. Yasuda Y, Uno N, Kobayashi H, Funabashi T (2008) Surge analysis on wind farm when winter lightning strikes. *IEEE Trans Energy Convers* 23(1):257–262
41. Kontargyri VT, Gonos IF, Stathopoulos IA (2005) Frequency response of grounding systems for wind turbine generators. In: Proceedings of the 14th international symposium on high-voltage engineering (ISH 2005) no. B-13, Beijing
42. Elmghairbi A, Haddad A, Griffiths H (2009) Potential rise and safety voltages of wind turbine earthing systems under transient conditions. In: Proceedings of 20th international conference on electricity distribution (CIRED2009), pp 8–11
43. Poljak D, Drissi KEK (2012) Electromagnetic field coupling to overhead wire configurations: antenna model versus transmission line approach. *Int J Antennas Propag*, pp 1–18
44. Rachidi F (2005) Modeling lightning return strokes to tall structures: recent development. In: VIII international symposium on lightning protection. Sao Paulo, Brazil
45. Burke GJ, Miller EK (1984) Modeling antennas near to and penetrating a lossy interface. *IEEE Trans Antenna Propag* 32(10):1040–1049

# Customization and Numerical Simulation of a Cranial Distractor Using Computed Axial Tomography (CAT)

J.A. Beltrán-Fernández, J. Martínez-Paredes, M. González-Rebattú,  
L.H. Hernández-Gómez and O. Ruíz-Muñoz

**Abstract** The main objective of this research is to obtain a useful computational model to know the mechanical response of a cranial distractor which is widely used in patients who have been affected by osteogenesis in craniosynostosis. As a part of an optimization of this model, the parametric parts and the assembly will be modified in order to adjust the system to the Mexican anthropometry. The research considers the influencing of the osteogenesis and the cranial deformation in childrens and adults, trying to recover the best shape from the cranial affected zone. Therefore, an engineering approach will be applied and the analysis of each one of the assembled parts, considering the specific geometry and mechanical properties of the commercial models. It will be reported in the context of numerical tests. It will allow the evaluation of the structural integrity and the customization. It aims to develop the design and finite element analysis of an adjustable vertical, horizontal, sagittal and occlusal vectors external distractor system. Two proposals that arise design by performing a device made in materials and manufacturing cost economize, but which in turn is reliable and meets the general requirements for patient treatment.

**Keywords** Osteotomy · Distraction · Maxillar · Distractor system · Osteogenic distraction · Stereolithography

---

J.A. Beltrán-Fernández (✉) · J. Martínez-Paredes · L.H. Hernández-Gómez · O. Ruíz-Muñoz  
Instituto Politécnico Nacional, Escuela Superior Ingeniería Mecánica y Eléctrica - SEPI,  
Av. IPN s/n, 07738 Ciudad de México, Mexico  
e-mail: jbeltranf@hotmail.com

J. Martínez-Paredes  
e-mail: jon6101@hotmail.com

L.H. Hernández-Gómez  
e-mail: luishector56@hotmail.com

O. Ruíz-Muñoz  
e-mail: omarrolandocv@hotmail.com

M. González-Rebattú  
Hospital Regional 1°. de Octubre, ISSSTE, Cirugía maxilofacial y cirugía plástica,  
Av. Politécnico Nacional Col. Lindavista #1669, C.P. 07730 Ciudad de México, México  
e-mail: mauriciorebattu@yahoo.com.mx

# 1 Introduction

The osteogenic distraction is a biological complex process that allows the bony regeneration by means of the gradual separation of two bony fragments. This technology has spread since, if in a beginning it was in use for the elongation of long bones, the results obtained with this technology have been satisfactory when it was applied in the craniofacial and pertaining to the jaw bones. The osteogenic distraction is a method developed to prolong or to reconstruct the bone that takes as a base the regenerative natural mechanism of the human body.

The use of the distracting systems allows generating the relative displacements in the bone at the same time as it supports the stability of the same one. Due to this, the design of the distracting bony has evolved together with the external fasteners for treatment of fractures; both devices share to a great extent the biomechanic principles of the external fixation and are based in the beginning of bony regeneration.

## 1.1 Generalities

The osteogenic distraction is an unleashed process originated from the evolution of technologies of bony fixation for the application of a load of traction in a controlled form on a corticotomy or osteotomy (defined as a surgical process that consists of the incision of the bone), to install an instrument or tool able of separating the segments of (distracting) bone, in order to promote a bony apposition in the remaining space, allowing the regeneration of bone and hereby to increase the length or extent of the bone on the one that one is working. This elongation is transmitted to the soft tissues and introduces a growth of the same ones of gradual and constant form [1].

The process of distraction is realized through the fixing of both parts of the bone to two ends in a mechanical sufficiently rigid system to control the traction/compression between the parts and able to produce the gradual separation of the surfaces of the bony fracture, as in the Fig. 1 is shown.

## 1.2 Current State of the Osteogenic Distraction

In the last 50 years the osteogenic distraction has acquired an important role in the treatment of dimensional deficiencies of bony material, demonstrating to be effective in the extension and affecting to the jaw stretching in comparison with the ortognatic conventional surgery which presents diverse complications (Fig. 2). This technology has become popular since, if in a beginning it was in use for the elongation of long bones, the results obtained with this technology have been satisfactory when they were applied in the craniofacial and jaw bones.



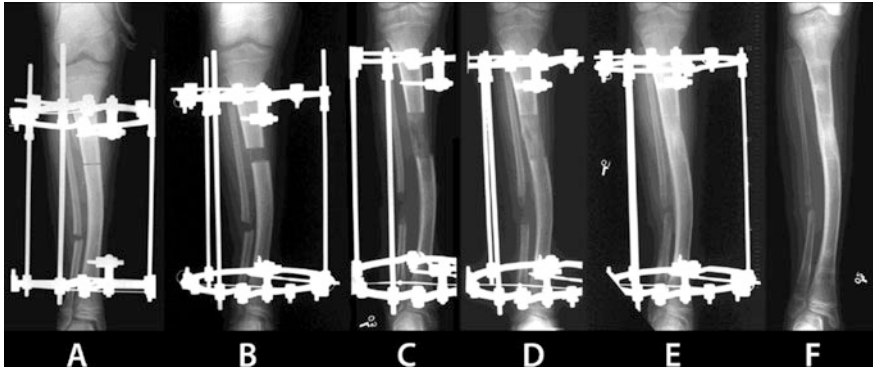
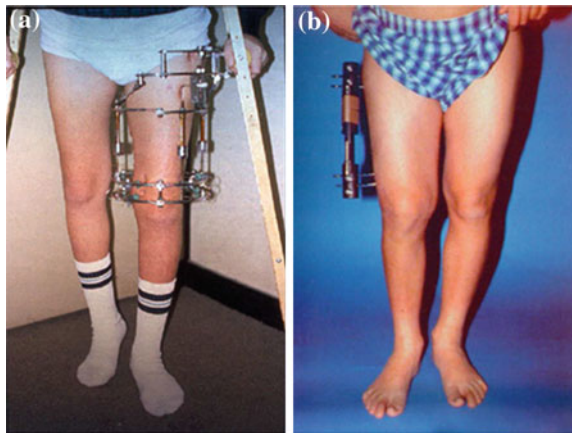


**Fig. 1** Elongation of the tibia showing the different phases of the process of distraction. **a** Osteotomy of the tibia and application of the fixator; **b** Beginning of the distraction; **c** Finished distraction; **d** and **e** Consolidation stage, without any distraction until the fracture of the bone is consolidated; **f** Removal of the fixator [2]

**Fig. 2** External fixators.

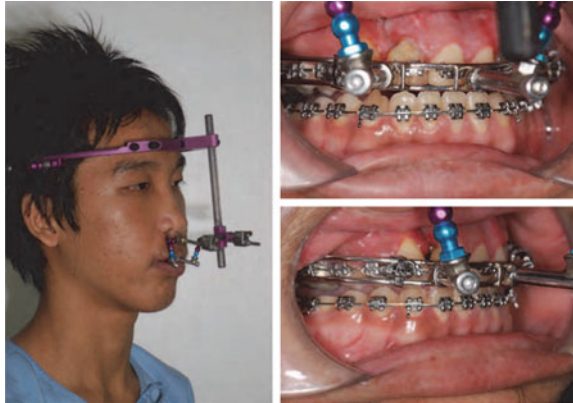
**a** Circular; **b** Monolateral [2]



Since then, the scientific production in the biomechanics sector applied to the osteogenic has been very important, because of it has helped to the manufacture and design of new distracting systems, especially in oral surgery and maxillofacial areas. In the Fig. 3, a RED device system is shown, which represents one of the most sophisticated systems nowadays. Its implementation has been parallel to the development and design of new fixators applied to the immobilization and reduction of the bony fractures, within the scope of the orthopaedic surgery and human and animal orthopedic surgery.

Nowadays, many authors insure that the internat distracting systems are better than the external systems for the patients, however, this type of distracting are difficult to place and its vector of distraction cannot change as in the external devices. The internal systems present some advantages as: the aesthetics, since they

**Fig. 3** RED system mixing the distractor system “Twin-Track” [8]



are less well-known and hinder less during the hours of dream. Its principal disadvantage is that they impede the mouth function on having eaten and to speak, having supported the hygiene also becomes more complicated.

Kebler et al. reported, in 2001, the use of internal maxillary distracting in four patients with maxillary retrusion. The used system was the Zurich pediatric ramus distracting, which has accessories reels for the activation, which were placed behind the lips, causing wounds and inconvenience. The obtained results were advances of between 7 and 14 mm without influence in the control of the postdistracting. There is highlighted the need of an excellent hygiene on the part of the patient to avoid infections and there is mentioned that the retirement of the devices is sometimes more complicated than its placement, also one refers to the need to ensure the distracting at to the moment of its placement [3].

Because of the problems for the placement and adjustment of the vectors of distraction, Yamayi et al. in 2004 designed in Houston an internal distracting maxillary placed on the maxillary sinus, which facilitated the procedure to obtain parallelism with the axis of distraction, nevertheless, it was necessary a second surgery for remove the distractor system. In his report, [4] it is mentioned an advance of 15.5 mm and nonappearance of relapse.

In the same line of research, Van Sickels in 2007, reported the use of a design of internal distracting and its placement in 10 patients, and even though it was the same design, some of the distracting systems were made of titanium and others of stainless steel. Van Sickels reported a specific case where there was lack of union of the bony segments and two cases with occlusals unacceptable results. Some minor complications were reported as the loosening of the systems and pain. It is reported in his conclusions that the manufacture of stereolithographic models helped to reduce the time of surgery, facilitated the placement of the systems and helped to determine the vectors of the distraction with higher precision. Finally, he stated that would be preferable to find some changes on the original design of the devices of distraction, this would help to make more comfortable the use of the distracting systems [5]. Likewise, diverse authors [6, 7] have applied the technology of quick

prototype by means of stereolithography to reduce the times, costs and mistakes in the design of the distracting systems.

### 1.3 Considerations of the Osteogenic Distraction System

Several types of distracting systems are known, which can be classified as internal or external, multidirectional or unidirectional or alveolar. The type of distracting will depend on the zone to being relaxing and of the size of the bony fault.

Five stages are recognized in the osteogenic distraction (Fig. 4);

1. **Osteotomy.** It is realized the disc of distraction (surgical fracture) which must be 2 cm of healthy bone.
2. **Stage of latency.** It is the later stage to the osteotomy and up to the activation of the distracting, generally between five and seven days.
3. **Stage of distraction.** It will depend on the size of the fault and the speed of distraction; generally it is considered of 1 mm for day, even though there can exist variations of 0.5 mm up to 2 mm a day.

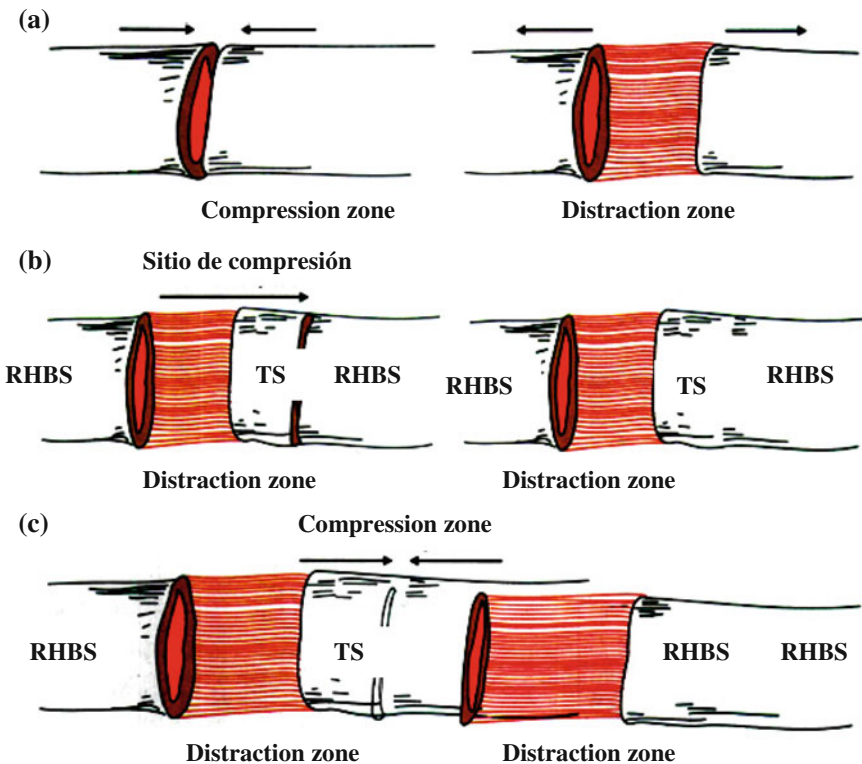


Fig. 4 a Monofocus osteosynthesis; b Bifocus distraction; c Trifocus distracción

4. **Stage of consolidation.** It includes the later stage to the distraction, generally it is considered from eight to 12 weeks, even though it can change in a relation the from three to one with regard to the time of distraction.
5. **Stage of bony remodeling.** This is a phase of variable period later to the bony consolidation, which can last some years after the consolidation and bony mineralization.

Several techniques of distraction by bony transport have been described and included on the classification of distraction compression of Ilizarov, in agreement with these techniques they have been divided in three groups: monofocus, bifocus and trifocus.

The monofocus osteosynthesis (monofocus distraction) is used in small faults of several millimeters, in which the ends of the bone are not normal and result in the retraction. The bifocus distraction is used for segments of some centimeters; it consists of taking a bony disc of one of the segments and of taking it towards extreme other one where ultimately the forces of compression will be applied.

The trifocus distraction is used in huge faults. In this technique two discs are taken, one of every end, and are taken towards the opposite side until they do contact. Finally, the compression forces are applied to create the bony union of the fragments.

## 1.4 Cases of Use of the Distraction

The distraction osteogenesis is indicated in the following cases:

- Severe Retrogenia with a syndrome (Pierre Robin, Treacher-Collins, Goldenhar) especially in children who are not candidates to osteotomies traditional.
- Patients with hypoplasia unilateral of the jaw (Microsomy hemifacial)
- Pertaining to the jaw Hypoplasia not associated with syndromes with malocclusion dental (especially if the advance exceeds the capacity of the traditional osteotomy) ó if the patient is unable to surrender to carved of grafts with associate morbidity.
- Pertaining to the jaw transverse Deficiency associated to malocclusion dental ó overcrowding.
- Patients with severe OSA (respiratory disturbances index major of 60) and obese patients (corporal mass major of 28).
- Pertaining to the jaw Hypoplasia due to trauma and/or ATM's ankylosis.
- Pertaining to the jaw Faults like result of excision of tumors and/or aggressive cysts of development.
- Decrease of the height of the alveolar bone (the destruction of an alveolar segment) can carry out to increase the vertical height in preparation for the placement of implants, In patients that supported pertaining to the jaw

reconstruction by means of grafts of fibula, the segment of fibula can be distracted vertically for the placement of implants.

- Pertaining to the jaw Deformity of the angle (the correction includes a component rotational and a component of distraction). The component of distraction for the angular deformity consists of rod of distraction with two connectors pivots of both ends. The type of hinge can be identified in its placement as follows: (1) the opening of the edge of the hinge, (2) the edge of the closing of the hinge and (3) the hinge of adjournment.
- Congenital malformations of maxillary or jaw, alveolar atrophy, sequels of lip or split palate, tumors, traumatism with bony loss and faults oncology.

The distraction must be realized in a range of 1.0 mm/day in two increases, preserving an interval of activation of 12 h.

The average maximum force across the distracting one in a period was of 34.7 N (range between 21.2 and 46.0 N) with increases Immediate after the activation of 6.7 N (range between 3.4 and 11.7 N). It has been observed a significant correlation (0.738) between the maximum applied (hardworking) force and the quantity of maxillary displacement.

The maximum average force of 34.7 N necessary for the distraction of the maxillary one is important for the design of the device, the miniaturization of the device is possible, so much as the safety factor it is incorporated in the design (Fig. 5). Simultaneously, it is necessary to readjust the angle of traction to allow the control on the bone of the maxillary one in three dimensions [8]. The evaluations of the forces of distraction allow the adjustment of the same for the process of distraction in the same levels of distances, avoiding the loss of forces. Other one of the advantages of the evaluations of the forces is the possibility of fitting individually the forces of traction in segments of the maxillary one in patients with split palate, optimizing the distraction and reducing the symptoms of inconvenience in the patient.

## 1.5 Distraction Vectors

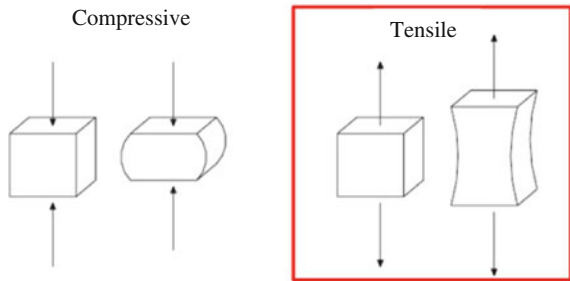
In order to achieve a osteogenic distraction after the osteotomy, the formation of new bony tissue between both surfaces of a bone cut is induced. This process is achieved through the application of incremental forces of traction, slow and gradual by means of a distracting mechanism. When the distracting forces are applied on the bony corn, it is created a bony neoformación parallel to the vector of distraction, which represents the direction, magnitude and sense of the obtained distraction. They are used normally for tension or also compression of the bony tissue, as in the Fig. 6 is shown [9].

The vector depends on the position of the distracting one and the direction of the osteotomy, and it can presented some cases, such as: parallel axis to the occlusal plane, vertical axis in stretching branch (opened later graft), the bilateral cases

**Fig. 5** Light sensor developed to identify the average force necessary for the distraction in the maxillary [8]



**Fig. 6** Representation of the vectors in compressive and tensile loading



where the symmetry of the vector depends on the symmetry on distracting both and it is possible to present a case of diversion of the planned vector that can be corrected by asymmetric activation of devices or with inter-maxillary rubbers (gums) (Fig. 7).

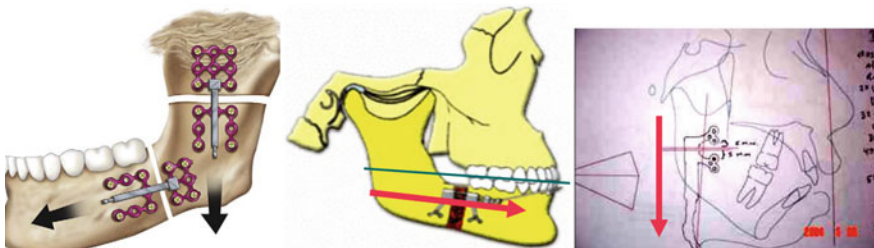


**Fig. 7** Example of the applied vectors to specific cases [10]

## ***1.6 Age of the Patient for the Use of Distracting***

In the year 2001 there was initiated a market study known as the study of distraction Eurocran. This consisted of two parts; the first one of them was based on a web survey, on which the professionals had to answer questions on the treatment to realizing in 4 clinical surgical cases: hypoplasia pertaining to the jaw unilateral, hypoplasia pertaining to the jaw severe, maxillary deficiency and facial deficiency bimaxilar (Crouzon's Syndrome).

For the period of latency, the study Eurocran showed that the majority of the participants considered to wait to be suitable of between 3–7 days (82–88 %) after the placement of the distracting one. Before initiating the distraction itself.

In relation to the variant age, inside the results obtained in this study, the majority selected as “the ideal age to realize the osteogenic distraction.” Between 7 and 14 years for the pertaining to the jaw distractions. On the other hand, in case of maxillary distractions, the majority of the polled preferred a major rather age, on 15 years.

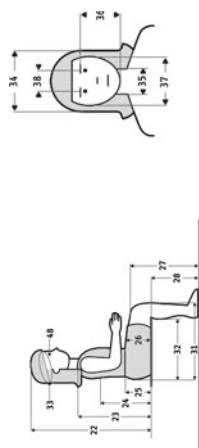
In a meta-analysis published on osteogenic distraction pertaining to the jaw for Ow and Cheung [11] that it included 1185 patients treated with bony distraction for pertaining to the jaw stretching, it showed that the patients treated with pertaining to the jaw unilateral distraction were presenting more commonly between 6 and 10 years (28.2 %). In case of the patients treated with pertaining to the jaw bilateral distraction, these they were commonly 2-year-old minors (21.4 %), followed by them of between 2 and 5 years of age (19.3 %).

As for the osteogenic distraction to maxillary level, another review published by Cheung and Chua in 2006 showed that 70.65 % of the documented patients was presenting between (among) 11–15 years of age to the moment to realize the distraction [12]. The speed variable and frequency of distraction in the study more used Eurocran is 1 mm/day (88–92 %).

## ***1.7 Anthropometry Mexican Phenotype***

To be able to obtain the measures of the links that shape the distracting maxillary external system, it is important keep in mind the dimensions of the cranium both of the masculine kind and of the female in a range of age of between 6 and 17 years, to be able in this way to assign the range of values of variation of the adjustable and adjustable system to the measures of the user with Mexican phenotype.

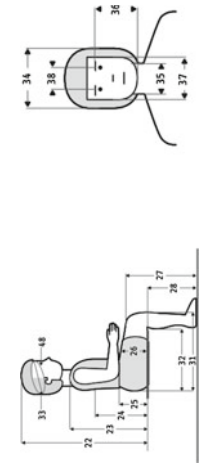
According to a study by the Universidad Autónoma de Guadalajara [13], the anthropometric dimensions of a sample of the population of school children and youth in the metropolitan area of Guadalajara, taking a total sample of 4758 as the basis of the study, in which 2387 were the female gender (Tables 1 and 3) and 2371 (Tables 2 and 4) of the male gender, as shown:

**Table 1** Anthropometric measures of the cranium of the female students from 6 to 8 years for the design of the distracting maxillary external systems [13]Scholars  
Female  
6-8 years

Dimensions	6 years (n = 369)						7 years (n = 406)						8 years (n = 402)					
	Percentiles			Percentiles			Percentiles			Percentiles			Percentiles					
	$\bar{X}$	D.E.	5	50	95	$\bar{X}$	D.E.	5	50	95	$\bar{X}$	D.E.	5	50	95			
Diameter a-p head	173	8	160	172	186	174	7	162	175	185	176	8	163	175	189			
Head perimeter	505	16	479	505	531	508	14	485	510	531	514	13	490	512	540			
Head width	141	6	131	141	151	142	7	130	143	153	143	7	131	143	154			
Neck width	84	7	72	83	95	86	8	73	85	97	88	7	76	87	99			
Face height	106	8	93	106	119	108	7	96	109	119	111	7	99	110	122			
Face width	115	8	101	115	128	116	9	101	116	131	118	9	103	118	133			
Interpupilar diameter	47	6	37	47	56	47	5	39	48	55	49	5	41	49	57			



**Table 2** Anthropometric measures of the cranium of the male students from 6 to 8 years for the design of the distracting maxillary external systems [13]



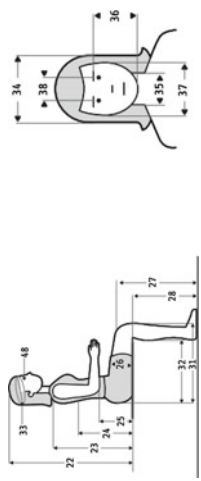
Scholars  
Male  
6 – 8 years

Dimensions	6 years (n = 384)						7 years (n = 405)						8 years (n = 375)						
	D.E.		50		95		D.E.		50		95		D.E.		50		95		
	$\bar{X}$						$\bar{X}$						$\bar{X}$						
33	175	8	162	176	188	188	177	7	165	177	188	188	178	7	166	179	189	189	189
48	514	18	484	515	544	544	518	15	493	520	543	543	522	16	496	520	548	548	548
34	145	6	135	145	155	155	146	7	134	146	157	157	146	6	136	147	160	160	160
35	85	7	73	85	96	96	88	7	76	88	99	99	91	8	78	91	104	104	104
36	108	8	95	108	121	121	111	8	98	110	124	124	112	7	101	112	126	126	126
37	116	8	103	116	129	129	117	8	104	117	130	130	120	8	107	120	133	133	133
38	47	6	37	47	57	57	48	6	38	49	58	58	50	5	42	50	58	58	58

**Table 3** Anthropometric measures of the cranium of the female students from 15 to 17 years for the design of the distracting maxillary external systems [13]

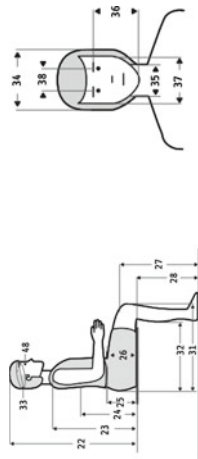
Dimensions	15 years (n = 91)					16 years (n = 121)					17 years (n = 138)				
	D.E.		Percentiles			D.E.		Percentiles			D.E.		Percentiles		
	$\bar{X}$		5	50	95	$\bar{X}$		5	50	95	$\bar{X}$		5	50	95
33 Diameter a-p head	184	7	172	184	196	184	9	169	184	199	185	10	168	185	202
48 Head perimeter	540	13	519	540	561	542	17	514	540	570	547	21	512	545	582
34 Head width	152	7	140	152	163	152	6	142	151	162	153	7	141	153	164
35 Neck width	100	8	87	99	113	100	6	90	100	110	100	7	88	100	112
36 Face height	122	7	110	122	134	121	7	109	121	133	123	7	113	123	135
37 Face width	130	7	118	130	142	128	8	115	128	141	129	7	117	130	141
38 Interpupilar diameter	53	4	46	53	60	53	5	45	54	61	52	5	44	54	60

Female  
15 – 17 years



**Table 4** Anthropometric measures of the cranium of the male students from 15 to 17 years for the design of the distracting maxillary external systems [13]

Dimensions	15 years (n = 74)					16 years (n = 120)					17 years (n = 151)				
	$\bar{X}$	D.E.	Percentiles			$\bar{X}$	D.E.	Percentiles			$\bar{X}$	D.E.	Percentiles		
			5	50	95			5	50	95			5	50	95
33 Diameter a-p head	190	8	177	190	203	292	7	180	191	204	192	7	180	192	205
48 Head perimeter	557	19	526	560	588	558	17	530	558	586	561	18	531	560	591
34 Head width	156	7	146	156	167	156	7	144	156	168	156	6	146	156	166
35 Neck width	109	8	96	109	122	112	8	99	110	125	113	8	100	112	126
36 Face height	130	7	118	130	142	130	8	117	130	143	129	7	119	130	141
37 Face width	134	10	118	135	150	135	9	122	135	150	135	8	122	135	148
38 Interpupilar diameter	54	5	46	55	62	55	3	50	56	60	55	5	47	56	63



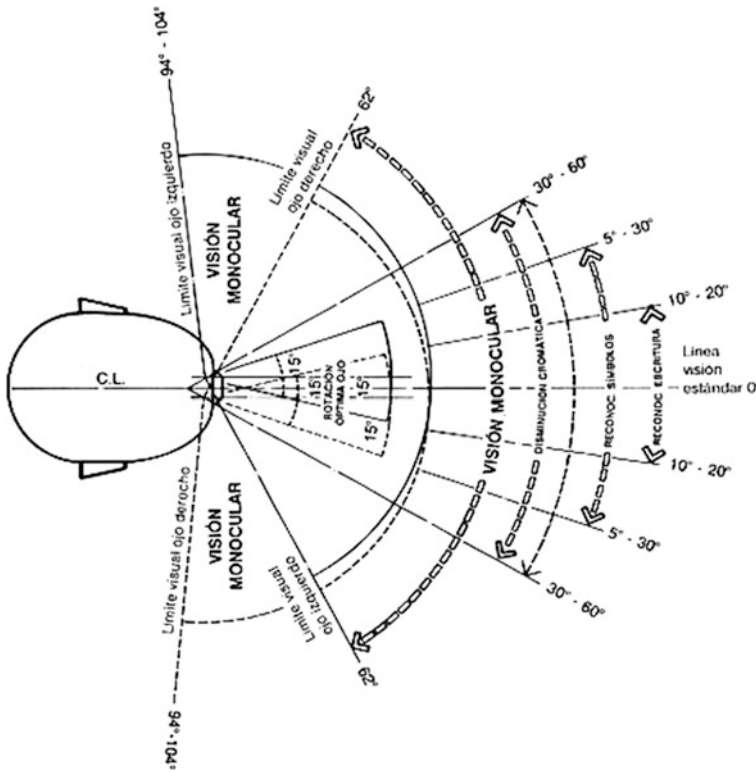


Fig. 8 Range of normal vision in the transverse plane

The ranges of normal vision of a person are considered for the design of the distracting system in order to avoid an obstruction of the sight of the user, taking into account 62° in his limits right and left-handed measured from the line of standard vision, as in the Fig. 8 is shown.

## 2 Statement of the Problem

The osteogenesis by distraction using some extraoral devices is often the only solution in cases of anatomical complicated conditions. The multidirectional systems offer the advantage of being able to modify the vectors during the process of distraction. In addition, in comparison with the simple intraoral systems, major methods of distraction can be reached. In spite of there have been designed different types of external distracting for the different vectors, such as: vertical, horizontal, sagittal and occlusal, the majority of the existing ones on the domestic market do not present suitable adjustment for the Mexican phenotype. Besides being devices

of high costs, in this work two proposals of systems for the optimization of the distracting maxillary external system are shown. It is fundamental to consider as a base of study a commercial system known as *\_ RED DEVICE SYSTEM ©*.

### 3 Materials and Methods

Based on the state of the art that introduced this research, the topic of maxillary distracting allowed considering the importance of the anthropometric measures of the Mexican population in a range of age between 6 and 17 years. It was considered male and female gender in order to design two distracting systems.

The process of modelling of some of the most complex pieces of the Distracting Maxillary External System were realized in the program CATIA V5 R19 ©. For it, it was necessary to keep in mind that the assemblies is completely composed by the left and the right pieces.

As example of the initial descriptive case is illustrated the piece: *Arch support*.

A sketch is generated by the basic form of the piece by the pertinent measures. It is proceeded with the extrusion, in CATIA © is called *Pad* (Fig. 9). Since the piece is not regular in its dimensions, another extrusion has to be generated as alternative of the original sketch on the top face of the piece.

It was necessary to realize the corresponding drilled holes with the command Hole, which allows defining the necessary parameters of the drilled hole, which can be for dimensions of the user, drilled holes standard and with different types of thread. In this case, it is a simple drilled hole without thread and it is placed in the respective levels with the icon Positioning Sketch. The drilled hole has to be done where the oppressive base that serves to fit the device to the user will be placed (Fig. 10).

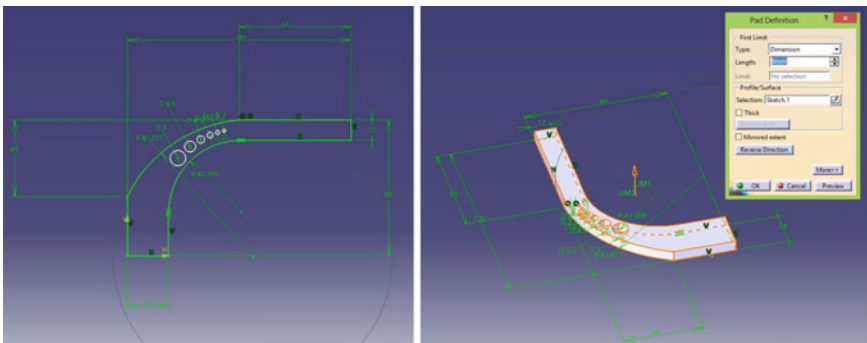
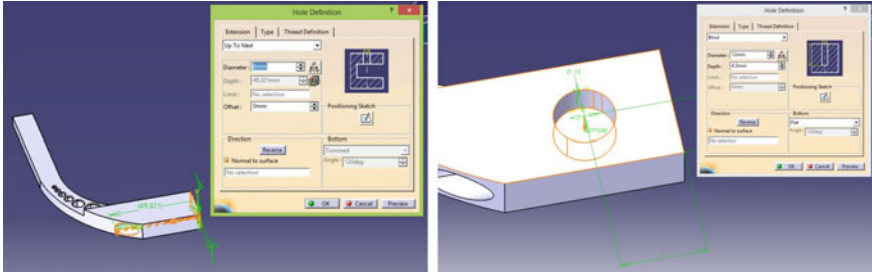
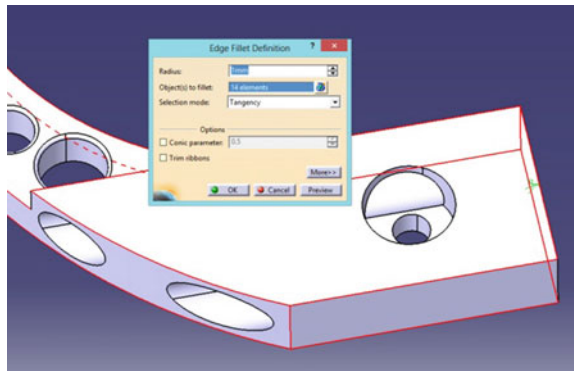


Fig. 9 Definition of *Sketch* and application of *Pad*



**Fig. 10** Drilling of pieces

**Fig. 11** Rounded of the edges



All the edges sharpened are rounded using the command *Edge Fillet* which allows some options; in this case the tangency was used in the selected edge (Fig. 11).

The final part is present on the Fig. 12.

The pieces are modeled and assembled in the module *Product* in order to obtain the complete three-dimensional model and to be able to be fixed in a three-dimensional model of the cranium of the user (Fig. 13).

As soon as the three-dimensional models are finished, there is proceeded to save each of the pieces that compose it in format .stl. Even though it is possible to export it directly of the three-dimensional model (file.stl) to the printer 3D, it is preferable to realize some operations to refine the piece before sending it to the printer, since the polygons generated automatically by the program are very big and the printing would go out with many ruggedness. To fulfil the correction of the polygons, the triangulation is generated by the command *Tessellation* by a value of pitch and crack sag depending on the size of the piece in order to obtain a thinner cloud of points (Fig. 14).

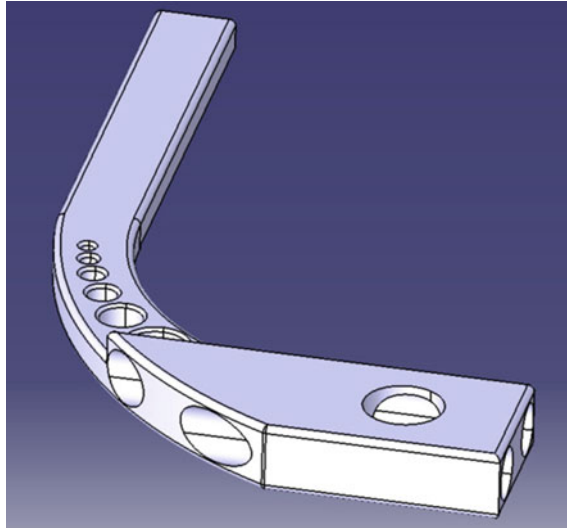


**Fig. 12** Finished part

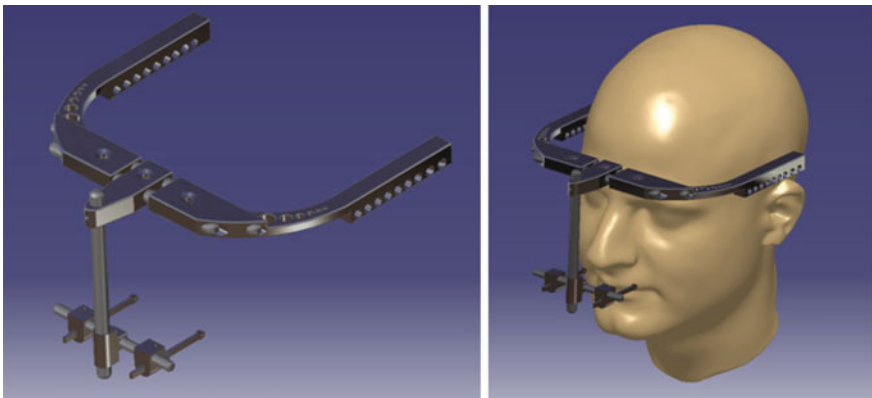


**Fig. 13** Assembly of the model of the system over a human head (User)

In the visual properties, the options *free edges* and *flat* are activated to have a visible mesh (Fig. 15).

Once the mesh was created it was necessary to export the file with extension *.stl* in order to be printed for stereolithography (Fig. 16).

To carry out the three-dimensional printing of the proposed models of distracting for stereolithography, there is needed the model of the pieces in format *.stl* in order

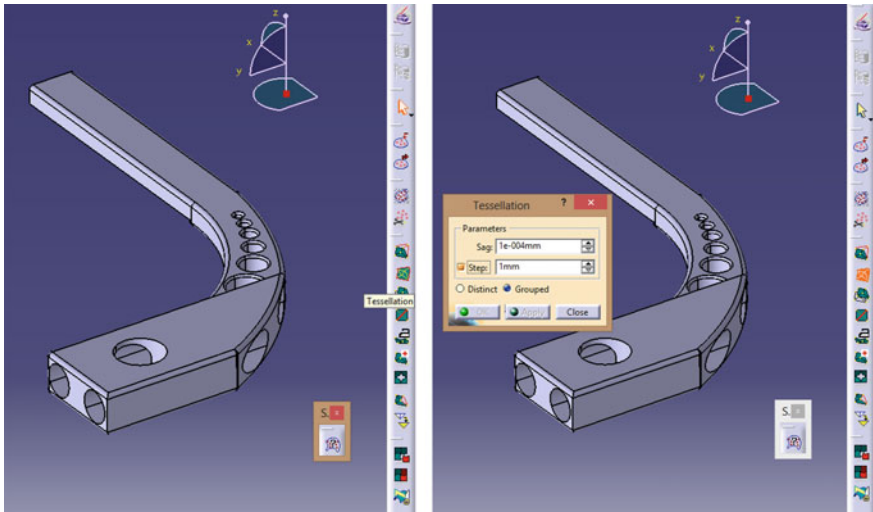


Fig. 14 Set up of tessellation

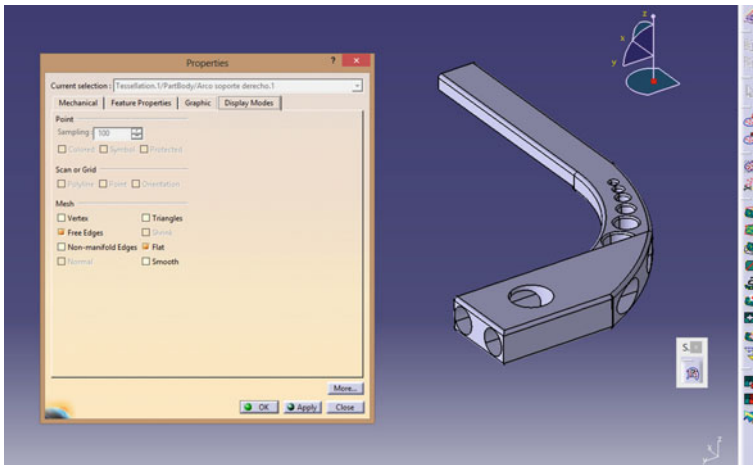


Fig. 15 Set up of the display modes

to be used in the program Catalyst ex-3.0. It serves as interface with the printer 3d dimension SST 1200 © in order to obtain the additive printing in plastic ABS and to generate the rapid prototype to discuss with the surgeons the possible changes or improvements in the device, as some works of the area of biomechanics reports [14, 15] (Fig. 17).



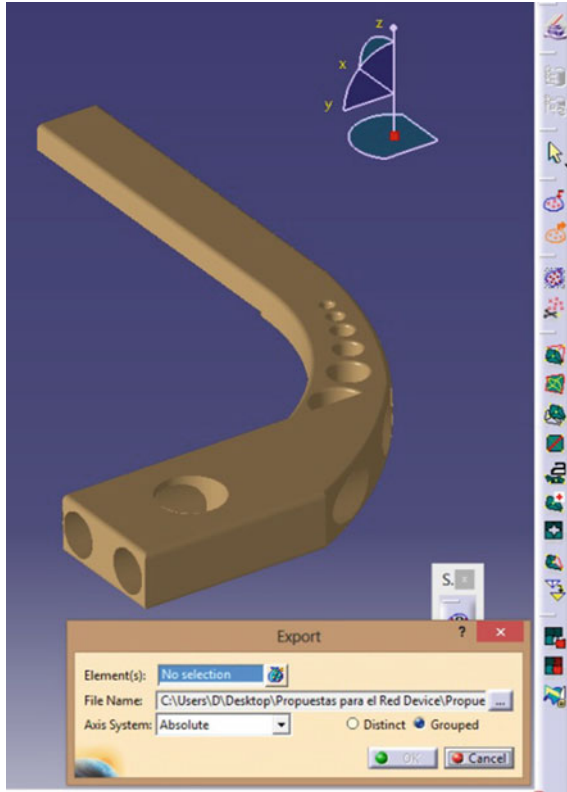


Fig. 16 Exportation of the meshing as .STL file



Fig. 17 Example of the printing of one piece using ABS polymer

**Fig. 18** Cleaning of the printed link



**Fig. 19** Links of each one of the distractors (printed by Stereolithography)



As soon as the pieces were printed, it is proceeded to clean and remove the residual resin of support from each one, using a special solvent (Fig. 18).

The same procedure is followed for each one of the pieces before being printed, remembering that depending on the size of the volume of printing is the number of pieces that can be printed on an alone package of printing, as in the Fig. 19 is shown.

## 4 Numerical Testings and Discussion of the Results

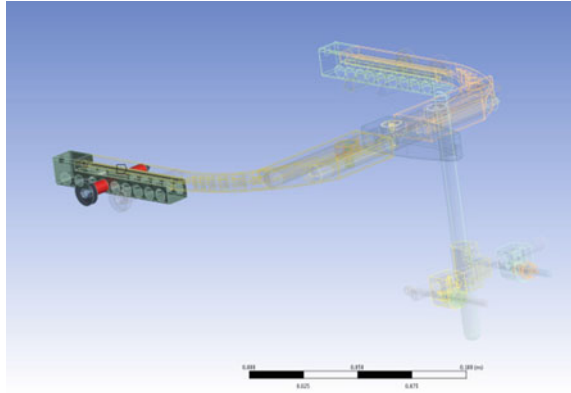
Once the three-dimensional models were generated in CATIA ©, to realize each one of the analyses in finite element, they are exported as files .step in order to be imported in ANSYS Workbench 14.0 ©. It is necessary to have the conditions of border and the type of element with which the device wants to be analyzed. A solid element in use is the number 185, which is defined by eight nodes and is considered to be as an orthotropic material used to shape solid in three dimensions.

In these first proposals, it was taken as a material base the Titanium. In the Table 5 the properties of the material used in the RED device system are shown. It

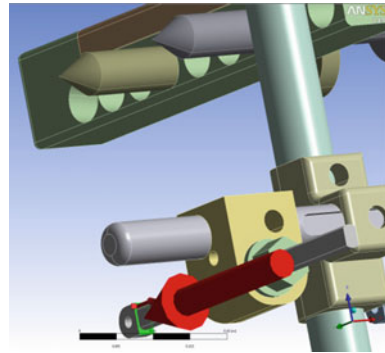
**Table 5** Mechanical properties of alloy of the materials proposed to be considered in the numerical analyses of the devices

<b>Mechanical properties for titanium alloy</b>	
Modulus of elasticity	96 GPa
Yielding strength	930 MPa (tensile)
Ultimate strength	1.07 GPa (tensile)
Poisson ratio	0.36
Thermic expansion constant	$9.4 \times 10^{-6}/^{\circ}\text{C}$
Density	4620 kg/m <sup>3</sup>
<b>Mechanical properties for aluminium 6061-T6</b>	
Modulus of elasticity	70 GPa
Yielding strength	240 MPa (tensile)
Ultimate strength	260 MPa (tensile)
Poisson ratio	0.346
Thermic expansion constant	$23.6 \times 10^{-6}/^{\circ}\text{C}$
Density	2710 kg/m <sup>3</sup>
<b>Mechanical properties for stainless steel 316L</b>	
Modulus of elasticity	193 GPa
Yielding strength	207 MPa (tensile)
Ultimate strength	586 Mpa (tensile)
Poisson ratio	0.31
Thermic expansion constant	$1.7 \times 10^{-5}/^{\circ}\text{C}$
Density	7750 kg/m <sup>3</sup>

**Fig. 20** Boundary and contact constraint

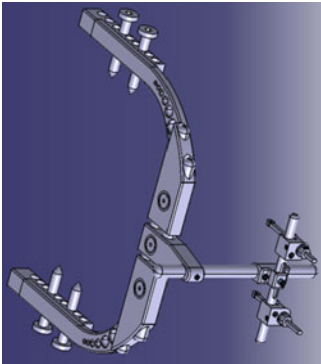
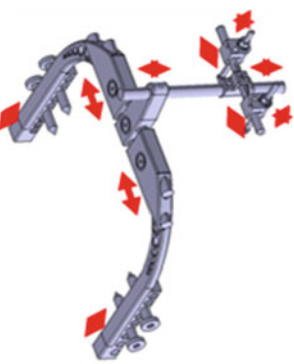
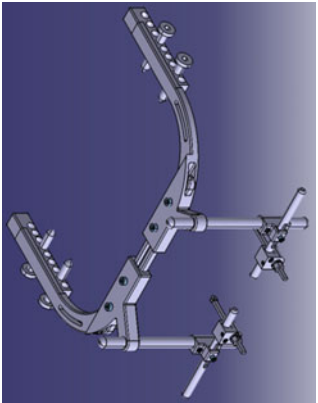
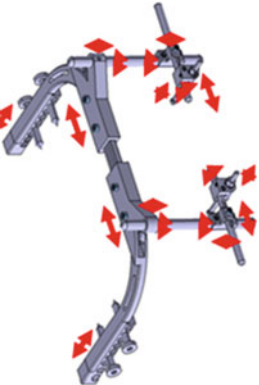
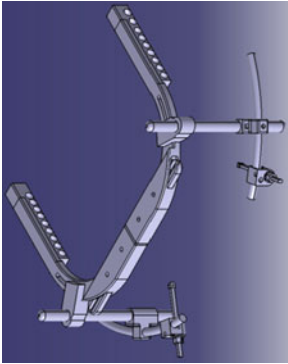
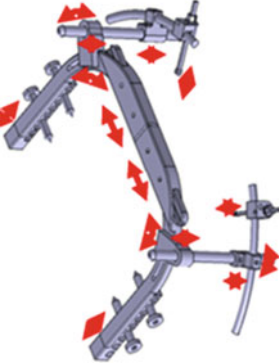


**Fig. 21** Force applications



was necessary in order to be able to do the assessments for the stresses in each of the links of the device according to the proposal of geometry and it is verified that the yielding strength was not exceeded.

The coincidences are respected and the types of restrictions “bonded contact” are added for the assembly. The supports are inserted to restrict the movement. The top of the screws for the cranium are placed in order to simulate they were fixed to the same one (Fig. 20). The force in the tensile used is of 34.7 N, according to the consulted references (Fig. 21).

<p><b>RED Device</b></p> 	<p>It is an external multi-vectorial system of distraction, designed for the correction of bony facial faults, where the patients can be benefited from an alternative of top distraction. It considers 14 DOF (Degrees of Freedom)</p> 
<p><b>Proposal 1</b></p> 	<p>The benefit that offers this proposal is that on having had two bars for the support of the mechanism for the tensile, the visibility of the patient is not affected since there is not included the central bar that has the RED Device and considers 18 DOF</p> 
<p><b>Proposal 2</b></p> 	<p>In this second proposal, besides relying on two bars for the support of the mechanism for the tensile and do not interrupting of drastic form the visibility of the patient, it is included a mechanism of angular displacement and curved bars for a better adjustment to the patient. It considers 22 DOF</p> 

(continued)

(continued)

**Numerical analysis for the RED device**

It was generated a meshing with 45354 nodes and 23009 elements



The results obtained for the first simulation of the RED device for Von Mises stress are the as follows:

**For alloy of titanium**

Max.: 79.54 MPa  
Min.: 29.367 Pa

**For aluminium 6061-T6**

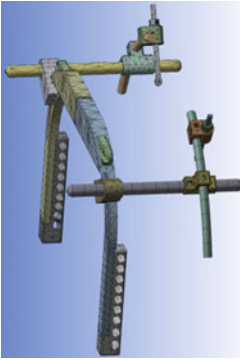
Max.: 122.88Mpa  
Min.: 26.22 Pa

**For stainless steel 316L**

Max.: 64.52Mpa  
Min.: 28.21 Pa

**Numerical analysis for the proposal 1**

It was generated a meshing with 42670 nodes and 21370 elements



The results obtained for the first simulation of the proposal 1 for Von Mises stress are the as follows:

**For alloy of titanium**

Max.: 82.5 MPa  
Min.: 4.16 Pa

**For aluminium 6061-T6**

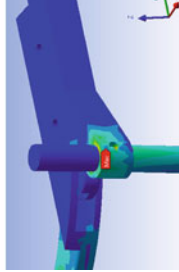
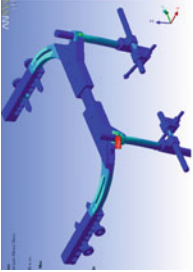
Max.: 163.5Mpa  
Min.: 3.5 Pa

**For stainless steel 316L**

Max.: 60.5 MPa  
Min.: 3.66 Pa

**Numerical analysis for the proposal 2**

It was generated a meshing with 38139 nodes and 18873 elements



The results obtained for the first simulation of the proposal 2 for Von Mises stress are the as follows:

**For alloy of titanium**

Max.: 124 MPa  
Min.: 4.012 Pa

**For aluminium 6061-T6**

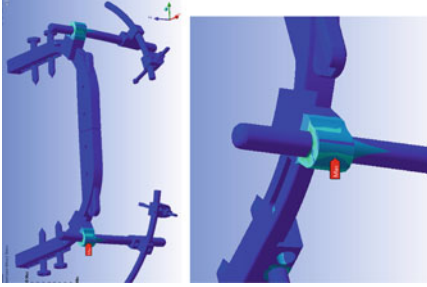
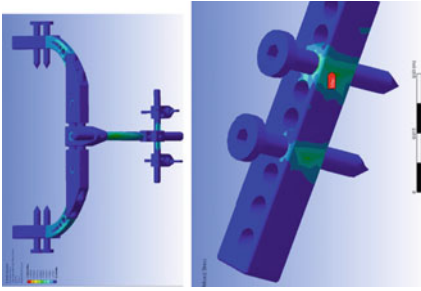
Max.: 281.24 MPa  
Min.: 2.8 Pa

**For stainless steel 316L**

Max.: 104.95 MPa  
Min.: 3.255 Pa

(continued)

(continued)



(continued)

(continued)

The printing of the model tridimensional of the RED device by the method of stereolithography was carried out in plastic ABS and later assembled and placed the necessary screw as it is shown



The printing of the model tridimensional of the proposal 1 by the method of stereolithography was carried out in plastic ABS and later assembled and placed the necessary screw as it is shown



The printing of the model tridimensional of the proposal 2 by the method of stereolithography was carried out in plastic ABS and later assembled and placed the necessary screw as it is shown





## 5 Conclusions

The suggestions of the distracting maxillary external systems showed in the present work were exposed to improvements and new modifications, and were in line with the expectations of the surgeons to achieve a osteogenic distraction of the maxillary adapted for persons of between 7 and 15 years principally.

Since the osteogenesis for distraction is often the only one remedy in cases of anatomical difficult conditions, the distracting external systems proposed have the characteristic of being adjustable of more versatile form to the vectors vertically, horizontally, sagittal, occlusal as well as for the not linear sections in case of being needed that the commercial systems on the market, since they rely on major number of degrees of freedom.

The analysis of finite element shows as conclusion that the device can be made by material of minor cost to the Titanium, since the efforts generated in the principal pieces diminished almost 50 %. This gives guideline to offers of materials and processes that economize its cost and improve its manufacture, but that in turn the device is reliable and expires with the general requirements for the treatment of the patient.

**Grants** To the Instituto Politécnico Nacional, to the Consejo Nacional de Ciencia y Tecnología and to the team of surgeons of the Hospital Regional 1° de Octubre of the ISSSTE, which thanks to the support was achieved to realize this research.

## References

1. Leiva N, Vergara C, Corsini R (2010). Distracción Osteogénica Craneofacial (D.O.C): antecedentes. *Revista Dental de Chile* 101(3):10–16
2. Hamdy RC, Rendon JS, Tabrizian M (2012) Distraction osteogenesis and its challenges in bone regeneration, bone regeneration. In: Tal H (ed) *InTech*, ISBN: 978-953-51-0487-2. doi:[10.5772/32229](https://doi.org/10.5772/32229)
3. Kebler P, Wiltfang S, Schultze U, Hirschfelder N (2001) Distraction osteogenesis of the maxilla and midface using a subcutaneous device: report of four cases. *British J Oral Maxillofac Surg* 39:13–21
4. Yamaji K, Gateno J, Xia J, Teichgraber J (2004) New internal le fort I distractor for the treatment of midface hypoplasia. *J Craniofac Surg* 15:124–127
5. Van Sikels J, Madsen M, Cunningham L, Bird D (2006) The use of internal maxillary distraction for maxillary hypoplasia: a preliminary report. *J Oral Maxillofac Surg* 64: 1715–1720
6. Beltrán-Fernández JA, Moreno-Garibaldi P, López-Saucedo F, Romo-Escalante E, Hernández-Gómez LH, Urriolagoitia-Calderón G, Camacho-Tapia N (2015) Design and manufacturing of prosthesis of a jaw for a young patient with articular ankylosis. In: *Applications of computational tools in biosciences and medical engineering. Advanced structured materials*, vol 71. pp 73–87
7. Camacho-Tapia N, Beltrán-Fernández JA, Gonzalez MGRY, Hernández-Gómez LH, Moreno-Garibaldi P, Urriolagoitia-Calderón G, López-Lievano D (2015) Numerical study in biomodels of maxillofacial prosthesis (Cancer and osteonecrosis cases). In: *Design and*

- computation of modern engineering materials. *Advanced structured materials*, vol 54, pp 59–72
8. Suzuki EY, Suzuki B (2011) Assessment of maxillary distraction forces in cleft lip and palate patients. Klika V (ed) *Biomechanics in applications*, InTech, ISBN: 978-953-307-969-1. doi:[10.5772/21685](https://doi.org/10.5772/21685)
  9. Marnie M (2008) The influence of mechanical environment on bone healing and distraction osteogenesis. *Atlas Oral Maxillofacial Surg Clin N Am* 16:147–158
  10. Nocini PF, Albanese M, Buttura da Prato E, D'Agostino A (2004) Vertical distraction osteogenesis of the mandible applied to an iliac crest graft: report of a case. *Clin Oral Implants Res* 15:366–370
  11. Ow AT, Cheung LK (2008) Meta-analysis of mandibular distraction osteogenesis: clinical applications and functional outcomes. *Plast Reconstr Surg* 121(3):54–69
  12. Chua HDP, y Cheung LK (2006) A meta-analysis of cleft maxillary osteotomy and distraction osteogenesis. *Int J Oral Maxillofac Surg* 35(1):14–24
  13. Ávila R, Prado LR, González EL (2001) Dimensiones antropométricas, Población Latinoamericana, ed. Universidad de Guadalajara, Centro Universitario de Arte, Arquitectura y Diseño, pp 24–123
  14. Beltrán-Fernández JA, Romo-Escalante E, López-Saucedo F, Moreno-Garibaldi P, Hernández-Gómez LH, Urriolagoitia-Calderón, G, Camacho-Tapia N (2014) Biomechanical assembled prosthesis of a temporo mandibular joint disorder using biocompatible materials. In: *Design and computation of modern engineering materials. Advanced structured materials*, Springer, vol 54, pp 135–146
  15. Beltrán-Fernández JA, González-Rebattú M, Hernández-Gómez LH, González-Rebatú M, Urriolagoitia-Calderón, (2013) Biomechanical prosthesis design of an orbicular cranial cavity. In: *Advances in bio-mechanicals systems and materials. Advanced structured materials*, Springer, vol 40, pp 87–94

# Prediction of In-Service NBR Properties by TG-IR After Storage in Mineral Oil

Tobias Förster

**Abstract** Compatibility tests of elastomers with unpolar liquids usually afford long time intervals to simulate applications and high experimental effort to determine mechanical properties. This paper describes the influence of short term storage in mineral oil on the composition of in-service acrylonitrile butadiene elastomer (NBR) and correlates it to its mechanical strength. Hardness and tensile strength at break are related to the fraction of volatile components determined by thermogravimetry coupled with IR spectroscopy (TG-IR). It is shown that the change of mechanical properties predominantly depends on the fraction of soluble/volatile components and barely on their detailed composition, as long as elastomers do not undergo chemical aging. TG-IR offers a new method of predicting mechanical performance based on chemical analysis applicable for in-service NBR independent of the acrylonitrile content.

**Keywords** Acrylonitrile butadiene elastomer · Swelling · Mineral oil · Thermogravimetry · Infrared spectroscopy

## 1 Introduction

In many applications as sealing, tank or hose line material elastomers are in contact to unpolar liquids, e.g. fuels or lubricants. Because of their polar character, acrylonitrile butadiene elastomers (NBR) are resistant to unpolar liquids and are frequently used for these applications [1, 2]. In-service elastomers regularly suffer from modifications of mechanical properties by immersion of surrounding liquids. These changes might result in malfunction or failure and cause high costs in the worst case. Therefore, it is highly interesting to have tools for the prediction of in-service properties of elastomers.

---

T. Förster (✉)

Bundeswehr Research Institute for Materials, Fuels and Lubricants (WIWeB),  
Institutsweg 1, 85435 Erding, Germany  
e-mail: Tobias.Foerster@Bundeswehr.org

In principle, physical and chemical phenomena of elastomer modifications can be distinguished. Physical modifications of an elastomer, which mainly include interactions of elastomers and surrounding media, lead to an exchange of soluble elastomer ingredients by the surrounding liquid driven by diffusion [3–8]. If the net uptake exceeds the loss of original elastomer additives, swelling is observed [9–11]. Altering the amount of these soluble components, i.e. elastomer additives or absorbed species, usually affects mechanical properties [12–14]. Physical effects usually are reversible, if mechanical damage of an elastomer is excluded. Chemical interactions resulting e.g. in oxidation of the polymer or an additional crosslinking are irreversible processes resulting in more severe changes of elastomer properties.

In this paper it is shown that a change of the NBR composition and also of mechanical properties takes place already in the first hours of storage in mineral oil at elevated temperature. Thermogravimetry coupled with IR spectroscopy (TG-IR) is applied as a method to detect changes of the in-service NBR composition. The determination of the material composition allows the prediction of the mechanical performance applicable for all NBR types independent of the acrylonitrile content. TG-IR offers the possibility of a very fast prediction of mechanical NBR properties after storage in mineral oil with one experiment.

## 2 Experimental

Three NBR materials with different acrylonitrile content 18 % (NBR 1846), 28 % (NBR 2845) and 39 % (NBR 3945) were used in this study (see Table 1). Further typical ingredients are carbon black (N550), bis-2-ethylhexyl phthalate (diethylhexyl phthalate, DEHP), *N*-(1,3-dimethylbutyl)-*N'*-phenyl-*p*-phenylenediamine (6-PPD), sulfur, zinc oxide, stearic acid, *N*-cyclohexyl benzothiazol-2-sulfenamide (CBS) and tetramethylthiuram monosulfide (TMTM). The in-service elastomers were purchased from the German Institute of Rubber Technology (DIK). Samples were partly extracted with acetone under Soxhlet conditions for 16 h.

**Table 1** Formulations of the NBR samples (values in phr, parts per hundred rubber)

	NBR 18	NBR 28	NBR 39
NBR 1846	100		
NBR 2845		100	
NBR 3945			100
Carbon black	60		
DEHP	20		
6-PPD	2		
Zinc oxide	5		
Stearic acid	1		
Sulfur	2		
CBS	1.5		
TMTM	0.5		

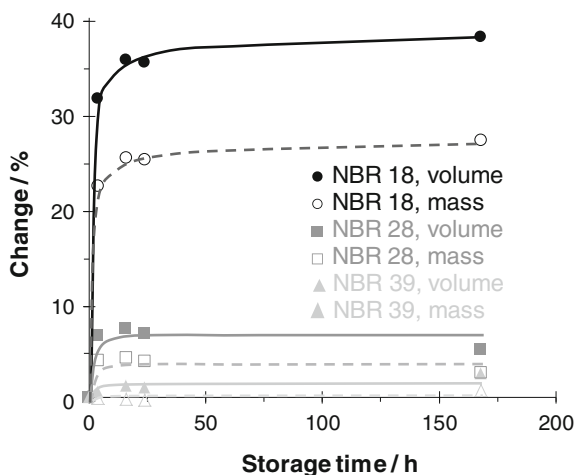
NBR materials were stored in a mineral oil based hydraulic fluid (NATO code H-515 according to MIL-PRF-5606H [15]) at 100 °C for time intervals in the range from 4 to 168 h. H-515 contains hydrocarbons with comparably low boiling temperatures and up to 20 % of polymeric viscosity coefficient improver. Volume and mass change of the NBR was determined according to DIN ISO 1817 [16] and Shore A hardness with a micro Shore A unit according to DIN ISO 7619-1 [17] using a Bareiss digi test II hardness tester. Thermogravimetry coupled with infrared spectroscopy (TG-IR) of the NBR was performed on a Netzsch TG209 F1 Iris thermo balance connected to a Bruker Tensor 27 spectrometer to analyze evolved gases. Typically 5–15 mg NBR was analyzed. Samples were heated with 10 °C min<sup>-1</sup> at a constant gas flow of 100 mL min<sup>-1</sup>. Below 500 °C nitrogen was used as carrier gas and synthetic air above 500 °C.

### 3 Results and Discussion

#### 3.1 Macroscopic Examination of Materials

Storage of NBR in mineral oil at 100 °C causes swelling of the materials even after only several hours (see Fig. 1). Volume increase of 38 % can be observed after 16 h when NBR 18 is stored in mineral oil followed by no significant change up to 168 h. After 168 h NBR 28 and NBR 39 also show a volume increase of ca. 6 and 3 %, respectively. The degree of swelling strongly depends on the intensity of the interaction between mineral oil and elastomer which can be derived from the polarity of NBR [18]. Higher acrylonitrile content of the polymer is equivalent to higher polarity and thus uptake of mineral oil is less favored. For that reason NBR 39 shows the smallest volume swell upon the investigated materials. All tested

**Fig. 1** Volume and mass change of NBR 18, 28 and 39 after storage in mineral oil at 100 °C



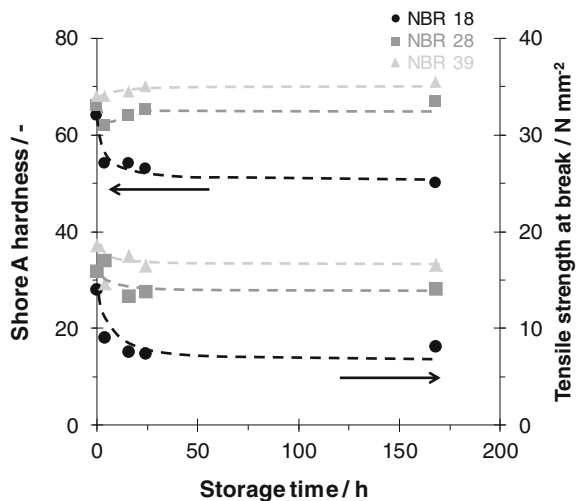
materials also show a rapid increase of mass after storage in mineral oil. The increase of mass and volume is the result of a net uptake of mineral oil components. However, a parallel loss of original NBR ingredients is likely but can not be detected by merely determining the volume/mass change.

Uptake of mineral oil components affects the mechanical properties of NBR demonstrated by a change of Shore A hardness (see Fig. 2). While the Shore A hardness of NBR 39 slightly increases from 68 to 71, the hardness of NBR 28 does not significantly change. NBR 18 shows a pronounced decrease of hardness from 64 to 50 after 168 h of storage in mineral oil at 100 °C. Note that the hardness of NBR 28 seems to decrease after storage intervals below 16 h while after longer storage durations the hardness increases. This indicates that the mineral oil uptake rate is higher compared to the one of plasticizer extraction at the beginning of storage, resulting in a (partial) replacement of original plasticizer by mineral oil having different plasticizing properties.

Uptake of mineral oil also affects the tensile strength at break (see Fig. 2). A reduction of the mechanical strength after storage in mineral oil can be observed for all tested materials. Note that the fluctuation for very short storing durations probably results from experimental inaccuracy. The most prominent decrease of ca. 42 % after 168 h can be found for NBR 18, followed by NBR 28 (ca. 12 %) and NBR 39 (ca. 11 %). As lower acrylonitrile content results in higher uptake of mineral oil (see above) it can clearly be demonstrated that the amount of absorbed mineral oil also affects tensile strength at break.

From the observed correlation between swelling and mechanical properties, it is assumed that the change of hardness and tensile strength at break is provoked by the total amount of soluble/volatile components in the NBR. Soluble/volatile components are the original NBR components namely plasticizer DEHP and anti aging

**Fig. 2** Shore A hardness and tensile strength at break of NBR 18, 28 and 39 after storage in mineral oil at 100 °C

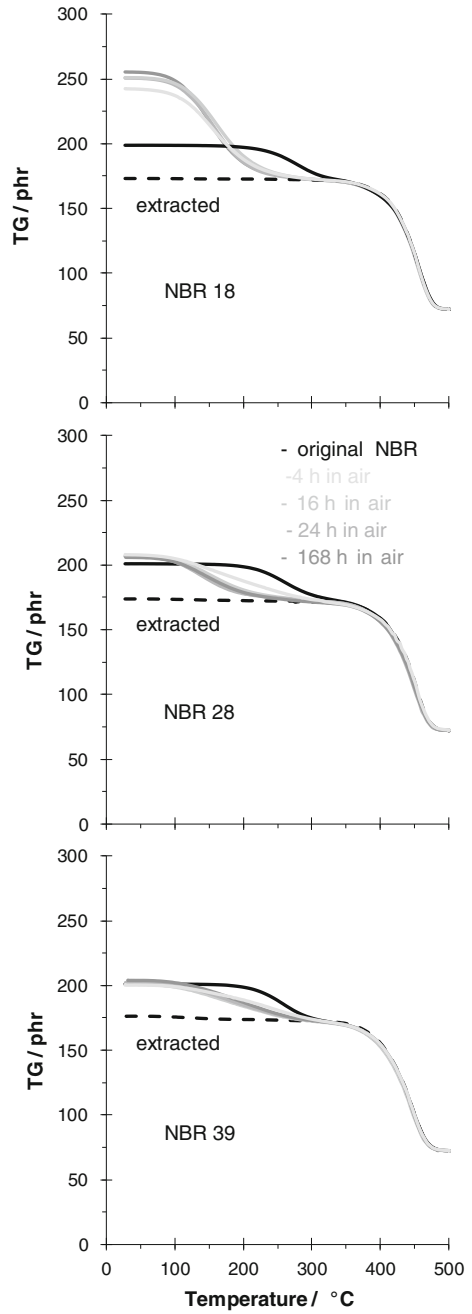


agent 6-PPD and also absorbed mineral oil components. Certainly the acrylonitrile content has an effect on hardness and tensile strength at break of the original NBR (NBR 18: 64 Shore A, NBR 28: 66 Shore A, NBR 39: 68 Shore A). However, the plasticizer, which is present in equal concentrations in every unstored NBR, is supposed to have the major influence on the hardness. And therefore, the substitution of plasticizer by mineral oil and/or addition of mineral oil results in a shift of mechanical NBR properties.

### 3.2 *Instrumental Analysis of Materials*

Volatile components are quantitatively detected by thermogravimetry. Here volatile compounds are defined as components evolved below 350 °C. Figure 3 shows TG curves of NBR 18, 28 and 39 before and after storage in mineral oil normalized to the acrylonitrile butadiene polymer content of the NBR (the polymer content is set to 100 phr). The dashed curves correspond to the extracted NBR proving that soluble and volatile components are equal for the investigated materials. The normalization allows a direct comparison of material changes after storage in mineral oil. From these TG curves it can be seen that the fraction of volatiles in NBR 18 markedly increases with storage time. NBR 28 also shows increased fraction of volatile components after mineral oil treatment, however, this trend is less pronounced. NBR 39 shows the smallest effect on the fraction of volatile components. Yet, a change of the shape of its TG curves can be observed, which is explained by the exchange of plasticizer by mineral oil. The original NBR materials only contain plasticizer as volatile components (except the negligible amount of anti aging agent). Thus, the mass loss temperature, determined from the inflection point of the TG curve, is observed at ca. 270 °C which is typical for DEHP containing NBR. When mineral oil is absorbed during storage, the relative concentration of DEHP decreases resulting in a lower amount of volatiles evolved at 270 °C. In parallel the uptake of mineral oil is responsible for the evolution of volatile components at a temperature of ca. 160 °C. During thermogravimetry the evolution of plasticizer and absorbed mineral oil can not be fully distinguished resulting in a change of the TG curve shape. The change of curve shape can be seen most clearly in the diagram of NBR 28. After very short storing the presence of DEHP can still be recognized very clearly, decreasing steadily with increasing storage time. At the same time the uptake of mineral oil takes place. From the curve shape it is interpreted that the uptake rate of mineral oil in the beginning stage of storing exceeds the extraction rate of DEHP. The curve shape of NBR 18 stored for 168 h indicates that DEHP is completely exchanged by mineral oil components.

**Fig. 3** Thermogravimetry curves of NBR 18, 28 and 39 compared to the extracted samples and to materials after different storage times in mineral oil at 100 °C



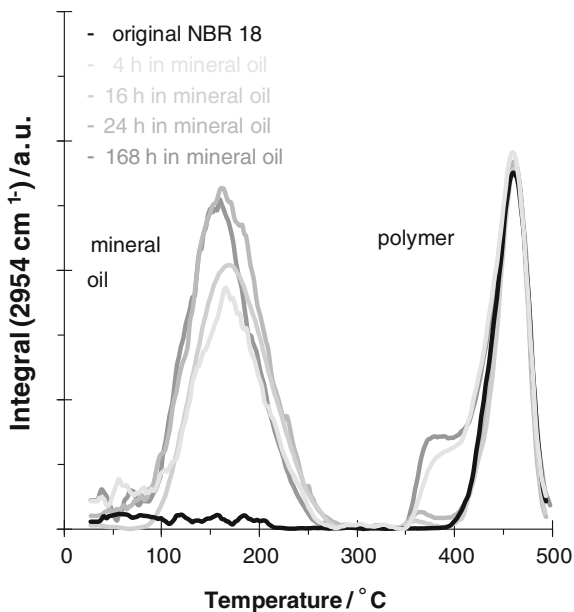


### 3.3 Differentiation of Evolved Components by TG-IR

The volume or hardness change represent the sum of processes, i.e. the uptake of mineral oil components and the dissolution of NBR constituents. In several cases a differentiation of all NBR components is necessary, e.g. in the field of failure analysis. By TG-IR evolved components can be identified via IR spectroscopy. Figure 4 shows the relative intensity of the  $2954\text{ cm}^{-1}$  band during thermo-gravimetry of NBR 18 stored in mineral oil for different intervals compared to the untreated sample. This band corresponds to C–H bond vibrations and can be used to detect organic molecules, e.g. acrylonitrile butadiene polymer fragments or mineral oil. The intensity is normalized to the amount of evolved gases during the decomposition of the acrylonitrile butadiene polymer (ca.  $460\text{ }^{\circ}\text{C}$ ) to allow a direct comparison of the mineral oil concentration (peak at ca.  $160\text{ }^{\circ}\text{C}$ ) of each NBR before and after storage.

An increase of the intensity of the  $160\text{ }^{\circ}\text{C}$  peak with storing time can be correlated to the detected degree of swelling of the stored materials. The combination of TG analysis and IR spectroscopy allows differentiation of the original elastomer additives and absorbed mineral oil as the plasticizer does not give a signal at  $160\text{ }^{\circ}\text{C}$  (see black line in Fig. 4). A peak in the  $2954\text{ cm}^{-1}$  trace would be expected at ca.  $270\text{ }^{\circ}\text{C}$  if neat DEHP is investigated under equal experimental conditions. However, an evolution of DEHP can not be observed here because evolved DEHP fragments condensate in the transfer line of the instrument and do not reach the IR spectrometer.

**Fig. 4** Temperature dependent relative intensity of the  $2954\text{ cm}^{-1}$  IR-band during TG analysis of NBR 18 before and after storage in mineral oil at  $100\text{ }^{\circ}\text{C}$



### 3.4 Correlation of NBR Composition and Mechanical Properties

The fraction of volatile components in NBR affects macroscopic material properties. To demonstrate this, the volume change after contact to mineral oil is directly correlated to the amount of volatiles determined by TG (see Fig. 5). The correlation proves that volatile components are responsible for the swelling of NBR. In a first approximation it can be derived that the detailed composition of soluble/volatile components does not play a role concerning the volume change for an NBR system. For the investigated NBR the composition of volatile components surely varies as the fractions of plasticizer, anti aging agent and mineral oil change during the storage in mineral oil. Additionally, the acrylonitrile content of NBR only plays a role concerning the interaction intensity between mineral oil and elastomer and, therefore, the amount of absorbed mineral oil. Thus, the acrylonitrile content is assumed to have a minor direct influence on the shift of mechanical properties by affecting the uptake of mineral oil. This can be derived from the fact that all tested NBR follow the same straight line. Under the experimental conditions an accumulation of values in the low swelling range (<10 %) and high swelling range (>30 %) is observed which is accompanied by an experimental uncertainty, especially provoked by missing data points in the medium swelling range (10–20 %). In future work this gap should be filled although it is not a straight forward procedure as the storage temperature and the material composition should not be altered because of comparability of results. Despite this uncertainty, the following hypothesis can be derived: Under the test conditions the volume change only depends on the absolute uptake of mineral oil components and the loss of original NBR additives.

The effect of a changed fraction of volatile components on the hardness and tensile strength at break of NBR can be seen in Fig. 6. It is not surprising that the hardness and the tensile strength at break of a swollen NBR are lower compared to

**Fig. 5** Correlation of volume change due to storage in mineral oil at 100°C and fraction of volatile components of NBR 18, 28 and 39

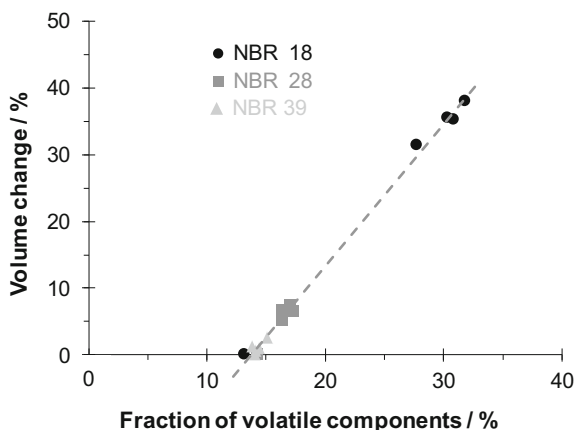
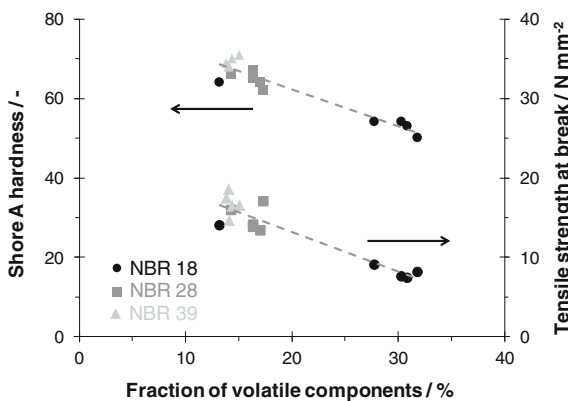


**Fig. 6** Correlation of the Shore A hardness, the tensile strength at break and the fraction of volatile components of NBR 18, 28 and 39 due to storage in mineral oil at 100 °C



the original. However, it is worth noticing that both, the Shore A hardness and the tensile strength at break, seem to linearly depend on the fraction of volatile components determined by thermogravimetry, taking into account the experimental boundaries described above. In analogy to the volume change, all NBR materials follow the same trend independent of their acrylonitrile content. This leads to the conclusion that the change of important NBR properties due to the contact to mineral oil, namely the volume change, the hardness and the tensile strength at break, only depend on the fraction of volatile components in the material. This linear correlation makes TG-IR capable of predicting mechanical properties after/during the use of in-service NBR.

Storing NBR 18, 28 and 39 in air at 100 °C does not result in distinct changes of the shape of the TG curve up to storage durations of 24 h (see Fig. 7). For all investigated materials only a very small decrease of the fraction of volatile components is observed. The change of mass and volume is relatively little compared to the mass and volume change after mineral oil contact at storage durations of 168 h (data not depicted). Additionally, a change of the curve shape during evolution of volatile components can not be observed after storage under air. Yet, for the relatively short storage times at 100 °C a pronounced loss of NBR additives is not expected and absorption of external compounds is excluded.

The Shore A hardness on the other hand increases for NBR 18, 28 and 39 after storage in air (see Fig. 8). After storing in air for 168 h NBR 39 undergoes an increase from 68 to 83, NBR 28 from 66 to 80, and NBR 18 shows an increase from 64 to 76. The increase of Shore A hardness is in the range of 12–15 and, therefore, approximately equal for all materials. Thus no significant effect of the acrylonitrile content can be derived. One possibility for an increase in hardness might be the loss of plasticizer. However, nearly no change of the fraction of volatile components determined by TG is observed after storage in air as diffusion processes are less pronounced during storage under air compared to storage in mineral oil. Yet, the effect of acrylonitrile butadiene polymer aging must not be excluded under these conditions [19]. Oxidation or additional crosslinking for example are processes

**Fig. 7** Thermogravimetry curves of NBR 18, 28 and 39 compared to the extracted samples and to materials after different storage times under air at 100 °C

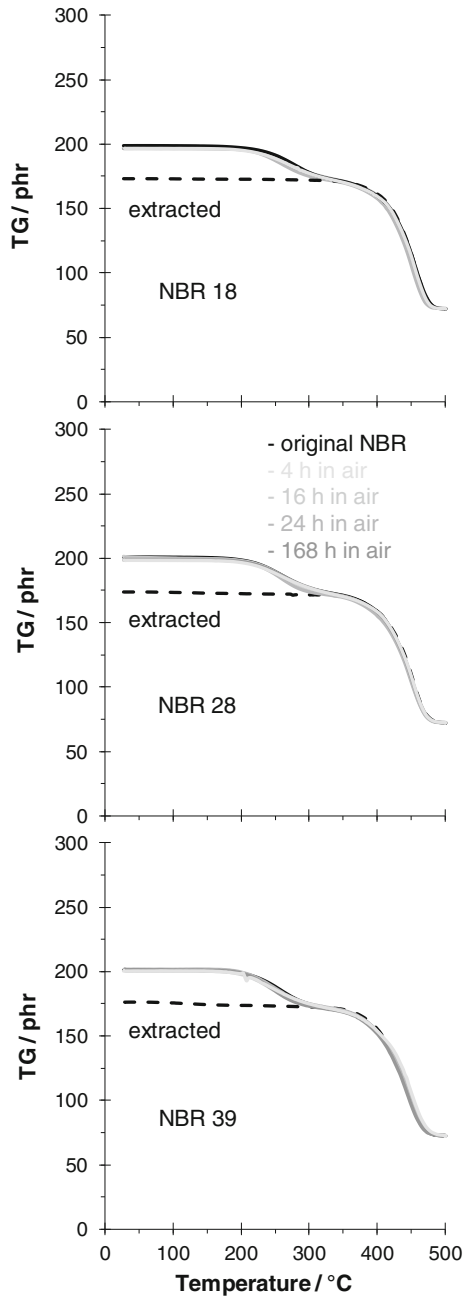
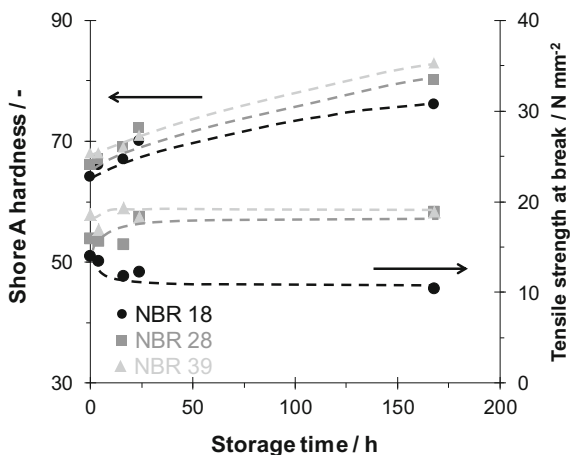


**Fig. 8** Shore A hardness and tensile strength at break of NBR 18, 28 and 39 after storage in air at 100 °C



resulting in embrittlement and thus an increase in hardness. In Fig. 7 a slight shift of the acrylonitrile butadiene polymer decomposition temperature towards lower temperatures can be observed. Although this is not a clear trend, depending on the storage duration, it nevertheless indicates a chemical modification of the acrylonitrile butadiene polymer. In this study no further analytical techniques were applied to explicitly detect chemical aging of the acrylonitrile butadiene network. However, aging effects of the acrylonitrile butadiene network are likely during air storage and TG results indicate changes of the polymer.

The fact that the NBR hardness increases after aging under air and at the same time the fraction of volatile components stays constant shows, that the above described correlation between soluble/volatile components and mechanical properties is only valid, if a modification of the acrylonitrile butadiene polymer, can be excluded. If NBR is stored in mineral oil or liquids having a similar conserving effect, the change of mechanical properties is only provoked by volatile/soluble components. The reason is that physical changes of the material are predominant and chemical attacks of the acrylonitrile butadiene network can be neglected.

A significant influence on the mechanical strength after storage under air at 100 °C can only be observed for NBR 18 (see Fig. 8). A decrease can be found for NBR 18, the mechanical strength of NBR 28 and NBR 39 are hardly affected, i.e. a slight increase can be observed within measurement tolerance. A reduction of the mechanical strength in combination with an increase of hardness after aging in air is supposed to correspond to a change of the acrylonitrile butadiene network, e.g. oxidation, or crosslinking. In contrary, the distinct reduction of hardness and mechanical strength after storage in mineral oil, is explained by the absorption of oil components. Furthermore, it is derived that storage in mineral oil has a more pronounced effect on the mechanical strength of the tested NBR.

## 4 Conclusion

Thermogravimetry coupled with IR spectroscopy is very well capable of detecting even small changes of NBR composition and it can also be applied to distinguish types of volatile components. The change of shape of the TG curve is a very precise indicator for the successive exchange of NBR additives by mineral oil. Furthermore, mineral oil can be detected by IR spectroscopy. It is demonstrated that already in the beginning phase of storage a distinct exchange of NBR additives and surrounding medium occurs strongly dependent on the acrylonitrile content and, therefore, on the interaction intensity between NBR and the mineral oil. The swelling behavior and the change of mechanical properties were shown to depend on the fraction of volatile components of NBR. It does not play a role whether NBR additives or mineral oil components are present in the material. The correlation of mechanical properties with the fraction of volatiles needs to be substantiated with more data in future work, e.g. storage at different temperatures.

The limitation of this observation is a chemical attack of the acrylonitrile butadiene polymer network. This modification of the acrylonitrile butadiene polymer can occur by oxidation, cross linking or also by reduction of crosslink density frequently observed after aging under air at high temperatures. As TG-IR can not give direct evidence for oxidation or additional crosslinking and other analytical techniques investigating polymer aging phenomena were not applied in this study, this should be investigated in future work. During storing in air an exchange of NBR additives by external liquids, e.g. mineral oil, can be excluded. In consequence, a change of mechanical NBR properties, i.e. increase of hardness, is observed. These changes are not correlated to the volatile/soluble components but to acrylonitrile butadiene polymer network aging. Under typical application conditions the conserving effect of surrounding liquids frequently prevents the acrylonitrile butadiene polymer from chemical changes.

With TG-IR a new method to predict mechanical properties of in-service NBR from chemical analysis is presented. The prediction of mechanical properties by TG-IR is a very promising application to analyze failure mechanisms of in-service NBR.

**Acknowledgments** The author wants to thank Niclas Kroll for his experimental effort during his studies.

## References

1. Konrad E, Tschunkur E (1930) Process for the preparation of polymerization products. Patent DE 658172
2. Röthemeyer F, Sommer F (2006) Kautschuk Technologie – Werkstoffe – Verarbeitung – Produkte, 2nd edn. Carl Hanser Verlag, Munich
3. Graham JL, Striebich RC, Myers KJ, Minus DK, Harrison WEIII (2006) Swelling of nitrile rubber by selected aromatics blended in a synthetic jet fuel. *Eng Fuel* 20:759–765

4. Rosca C, Giese U, Schuster R H (2006) Investigation of diffusion of phthalates in nitrile rubber by means of FT-IR-spectroscopy. *Kaut Gummi Kunstst* 86–92
5. Koenhen DM, Smolders CA (1975) The determination of solubility parameters of solvents and polymers by means of correlations with other physical quantities. *J Appl Polym Sci* 19:1163–1179
6. Harogopad SB, Aminabhavi TM (1991) Diffusion and sorption of organic liquids through polymer membranes. II. Neoprene, SBR, EPDM, NBR and natural rubber versus n-alkanes. *J Appl Polym Sci* 42:2329–2336
7. Mathai AE, Thomas SJ (1996) Transport of aromatic hydrocarbons through crosslinked nitrile rubber membranes. *J Macromol Sci, Phys B35*:229–253
8. Ogorodnikova GF, Sinitsyn VV (1982) Mechanism of rubber swelling in oils and grease. *Chem Tech Fuels Oils* 18:306–308
9. Starmer PH (1993) Swelling of nitrile vulcanizates by polar and non-polar liquids—part 1: review of parameters. *J Elastom Plast* 25:59–73
10. Starmer PH (1993) Swelling of nitrile vulcanizates by polar and non-polar liquids—part 2: swelling curves. *J Elastom Plast* 25:120–142
11. Starmer PH (1993) Swelling of nitrile vulcanizates—part 3: factors affecting maximum swelling. *J Elastom Plast* 25:188–215
12. Uedelhoven W (1990) Testing the elastomer compatibility of aviation turbine oils. *J Synthetic Lubric* 7:105–121
13. Neppel A (1986) Prediction of equilibrium swelling in fuel and lubricant ingredients. *Rubber Chem Technol* 59:46–69
14. Ehrenstein GW, Pongratz S (2013) Resistance and stability of polymers. Hanser Publishers, Munich
15. MIL-PRF-5606H (2002) Performance specifications hydraulic fluid, petroleum base; aircraft, missile and ordnance
16. DIN ISO 1817 (2005) Rubber, vulcanized—determination of the effect of liquids
17. DIN ISO 7619-1 (2010) Rubber, vulcanized or thermoplastic—determination of indentation hardness—part 1 durometer method (Shore hardness)
18. Salomon G (1948) Influence of structure on polymer-liquid interaction. II. Influence of nitrile groups. *Rubber Chem Technol* 21:805–813
19. Li X, Zhang Y, Yang M (2013) Study on thermal oxidative aging of nitrile rubber. *Appl Mech Mater* 299:199–202

# Structural Integrity Analysis of a BWR Core Shroud with an Irregular Distribution of Cracks: Limit Load Analysis

**Pablo Ruiz-López, Luis H. Hernández-Gómez,  
Guillermo Urriolagoitia-Calderón, María L. Serrano-Ramírez,  
Arturo Ocampo-Ramírez, Juan A. Beltrán-Fernández  
and Guillermo Urriolagoitia-Sosa**

**Abstract** Mexico has a nuclear power plant with two BWR reactors. Their internal components were manufactured with type 304 stainless steel. Since the initiation of their commercial operation, some relevant cracks have been detected through the periodic inspections of their internal components. Specifically, there have been cracks found at the core shroud and jet pumps. The causes of such cracks have been: excessive vibration, wear, stress corrosion cracking and residual stresses, acting alone or simultaneously. There are several aspects that have to be considered in the evaluation of the structural integrity of the core shroud, for instance: its shape is a

---

P. Ruiz-López · M.L. Serrano-Ramírez  
National Commission for Nuclear Safety and Safeguards, Dr. José Ma. Barragán No. 779,  
Colonia Narvarte. Delegación Benito Juárez, 03020 México D.F., Mexico  
e-mail: pruiiz1959@hotmail.com

M.L. Serrano-Ramírez  
e-mail: mlherrano@cnsns.gob.mx

L.H. Hernández-Gómez (✉) · G. Urriolagoitia-Calderón · A. Ocampo-Ramírez ·  
J.A. Beltrán-Fernández · G. Urriolagoitia-Sosa  
National Polytechnic Institute. ESIME-Zacatenco. Section of Postgraduate Studies  
and Research. “Adolfo López Mateos,” 5, 3rd Floor, Lindavista. Gustavo A. Madero,  
07738 México D.F., Mexico  
e-mail: luishector56@hotmail.com

G. Urriolagoitia-Calderón  
e-mail: urrio332@hotmail.com

A. Ocampo-Ramírez  
e-mail: ingaor@hotmail.com

J.A. Beltrán-Fernández  
e-mail: jbeltranf@hotmail.com

G. Urriolagoitia-Sosa  
e-mail: guirri@hotmail.com



cylinder and its  $R/t$  ratio is in the range between 60 and 100, as well as the water environment and the neutron irradiation. The last one has modified the mechanical properties of the material. Besides, each circumferential weld has a different non-symmetrical and irregular distribution of cracks with various depths. These cracks are monitored every 18 months, only during the plant shutdowns. Furthermore, the potential unstable cracking of the lower circumferential welds could induce important safety consequences if a loss of coolant accident and an earthquake event are postulated. Due to these reasons, it is very important to apply or develop adequate analytical procedures that can provide fast and reliable results. These procedures must cover elastic-plastic fracture analysis and plastic limit load analysis. In this paper, a methodology for the plastic limit load analysis was developed. The critical limit load for any crack distribution was calculated with a great degree of confidence. Operating conditions were considered. The shape of the cracks varies and the evaluation depends on the geometry of the cracked cylinder. In the problem at hand, the neutral axis varies, as it translates and rotates simultaneously at every cracked cross section, depending on the loading condition. This situation was also taken into account.

**Keywords** Through-wall thickness crack · Part through-wall thickness crack · Plastic hinge · Aging · License renewal

## 1 Introduction

Mexico has two nuclear power Boiling Water Reactors (BWR) in a plant, which is called Laguna Verde. Their internal components, such as jet pumps, core shroud, steam separators and steam dryers, etc., were manufactured with stainless steel type 304. The commercial operation of the first unit started in 1990 and the second unit began its operation in 1995. During its commercial operation, some relevant cracks have been detected at the internals components through the in-service inspection. In specific, such cracks have been located at the core shroud and jet pumps [1, 2]. A schematic view of the internals of a BWR is shown in Fig. 1.

The causes of these cracking events have been: excessive vibration, wear, stress corrosion cracking and residual stresses, acting alone or simultaneously producing synergistic effects [2].

The core shroud separates the descending flow of water, which is suctioned by the external part of the Reactor Recirculation Core (RRC) system. Afterwards, through the heating of the nuclear core, the water ascends. The safety related function is to provide enough flooding to the nuclear core in case of an accident. The designation of the welds of the core shroud for a generic BWR are illustrated in Fig. 2.

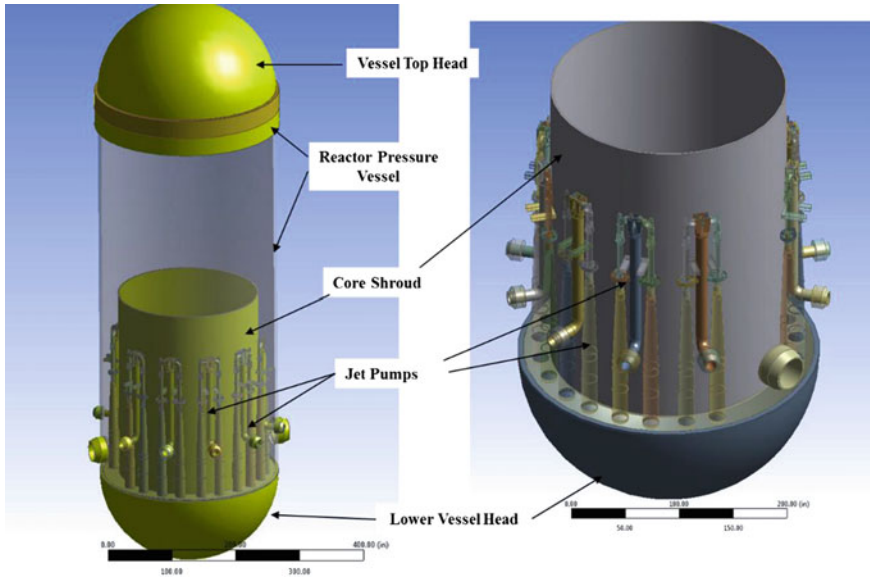


**Fig. 1** Localization of the core shroud and other relevant internals inside a BWR

The core shroud is a low pressure vessel. Its vertical welds are subjected to low circumferential stresses. However, from the safety point of view, the structural integrity of the circumferential welds should be analyzed when these are subjected to axial and bending stresses. They can be critical under seismic loads and/or the loads resulting from piping breaks of the Main Steam (MS) or the RRC system. In the last case, a loss of coolant accident is induced. Therefore, the structural integrity can be compromised under the presence of defects like cracks [3, 4].

In this paper, the structural integrity of the core shroud was evaluated with a limit load analysis, because stainless steel has a ductile behavior with a high fracture toughness. However, after a long term of operation, its mechanical properties have been modified. This has been caused by the water environment and the neutron irradiation coming from the nuclear reaction of fission at the core [5–8]. This is of importance to ensure the extended operation of a commercial nuclear power plant through the renewal of the current license.

## 2 Statement of the Problem

The structural integrity analysis of the core shroud has various aspects that must be considered. For instance, the cylindrical shape has a high  $R/t$  ratio. As it is a thin annulus, the range of its values is between 60 and 100. The crack monitoring is done only during the plant shutdowns for refueling. They take place every 18 months, when the reactor vessel top head is opened. If aging has been

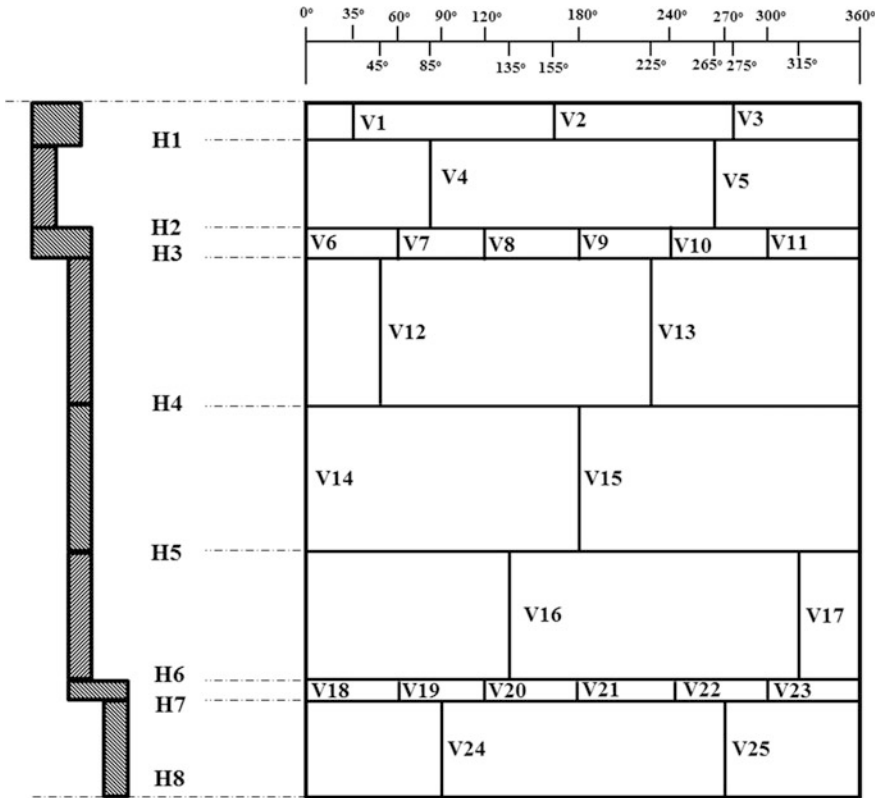
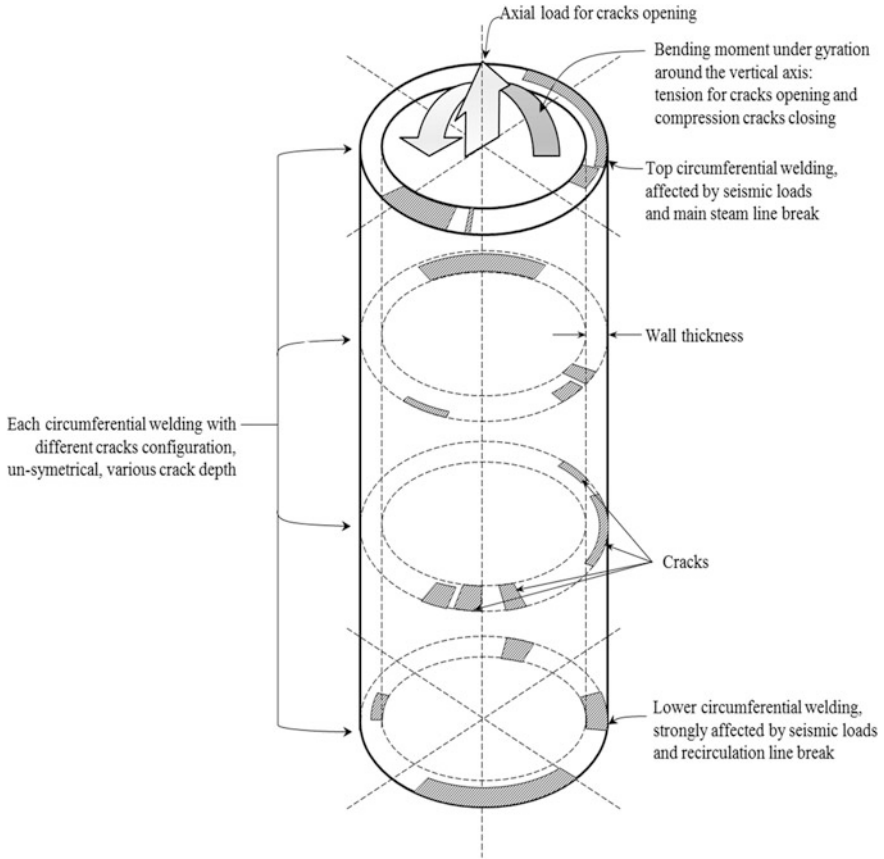


Fig. 2 Designation of a core shroud welds of a generic BWR

developed, the mechanical properties have been modified by the environment and neutron irradiation. Furthermore, the potential unstable cracking of the lower circumferential welds could induce important safety consequences if a loss of coolant accident and a design basis earthquake take place [3, 4].

The core shroud has eight circumferential welds as shown in Fig. 2, so the analysis of this component must be done under the two following considerations (see Fig. 3): (1) In accordance with the operating experience of Nuclear Power Plants (NPPs), it is very common to find that each weld has a very particular non-symmetrical and irregular distribution of cracks with various depths; (2) The seismic loads can take place from any direction. Therefore, the biggest crack is not always loaded under critical conditions, because in certain situation, the crack could be under tension (opening) or compression (closing) and in intermediate states, one part of the crack may be closed and its other part will be subjected to opening situations.

The owner of the plant (licensee) and the nuclear regulatory authority with jurisdiction at the nuclear plant could be involved in long and complicated discussions on the decision to repair, reinforce or substitute the core shroud, when the cracks have reached critical values. It must be kept in mind, that any possible



**Fig. 3** Non-uniform distribution of cracks for each circumferential weld, under a complex loading conditions (opening-closing of cracks)

activity like reinforcements or modifications of this component implies a high cost, time consuming, underwater activities and remote works with radiation. Small or reduced hardware has to be installed due to the reduced space inside the reactor, etc. Each day without a final resolution on repairing or “use as is” of the cracked component, implies high pressure for all the involved organizations. The owner loses high quantities of money every day because the energy is not produced and the regulatory authority is requesting is continuously requesting to preserve the safety to avoid critical events or accidents.

Therefore, all the people involved in the structural integrity evaluation must develop and apply analytical criteria. They have to be precise with a high degree of confidence. Besides, such criteria have to be low time consuming. In certain circumstances, the nuclear components operate at uprated power and the NPP’s owners are capable to operate the plants for a long term after of the original license validity. Therefore, the required nuclear safety margins must be maintained at every moment.

### 3 Available Methodologies for the Solution

Due to the complexities mentioned above, it is very important to apply or develop adequate analytical procedures that can provide reliable results in short periods of time. Such procedures must cover elastic-plastic fracture analysis—when the fragile behavior is dominating due to the long-term neutron irradiation during a long term—and plastic limit load analysis due to the inherent characteristics of ductility of stainless steel [9]. In this paper, a solution for the plastic limit load analysis will be developed.

As shown in Fig. 3, the core shroud has a non-uniform distribution of cracks in the circumferential welds, under complex loading, in which the cracks open and close. In order to perform a plastic limit load analysis, the available methodologies found in the open literature have to be analyzed [10–12].

The available methodologies for this purpose are illustrated in Fig. 4. It was considered that the one proposed by Rao et al. [12] of the Companion Guide to the ASME Boiler and Pressure Vessel Code is appropriate to obtain the solution for the plastic limit load analysis of a non-uniform cracked core shroud of a BWR. It has the following steps and is shown graphically in Fig. 5.

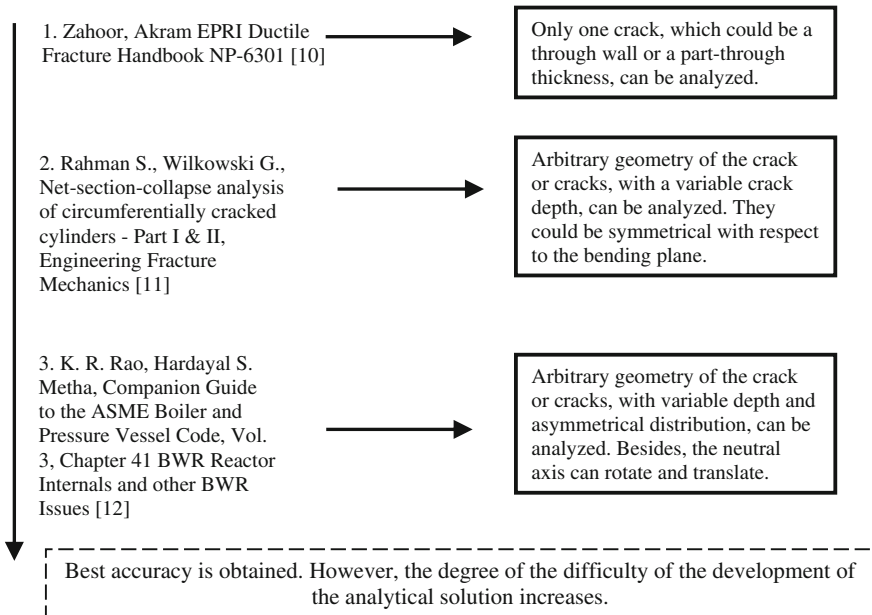


**Fig. 4** Methodologies available for solution of the plastic limit load analysis for a cracked core shroud



$$\frac{M_{\alpha}}{Z} + P_m \geq SF (P_m + P_b) \tag{3}$$

This methodology has been implemented in the DLL (Distributed Ligament Length) code, version 3.1. It was developed by the Electric Power Research Institute (EPRI). It evaluates cylindrical components of a BWR with the limit load, elastic plastic and linear elastic fracture mechanic analyses for [13, 14].

As an alternative, an analytical tool has been developed in this paper. It can provide solutions with a good degree of confidence. The technical basis and fundamentals of the proposed methodology are described below.

### 4 Theoretical Basis of the Limit Analysis

The structural response of a simple supported beam made of steel with a cross section symmetrical about a horizontal axis under an increasing load applied at its midspan is shown in Fig. 6. The general stress and strain variations at the cross section, from an elastic state to the fully plastic state, is illustrated. The extra

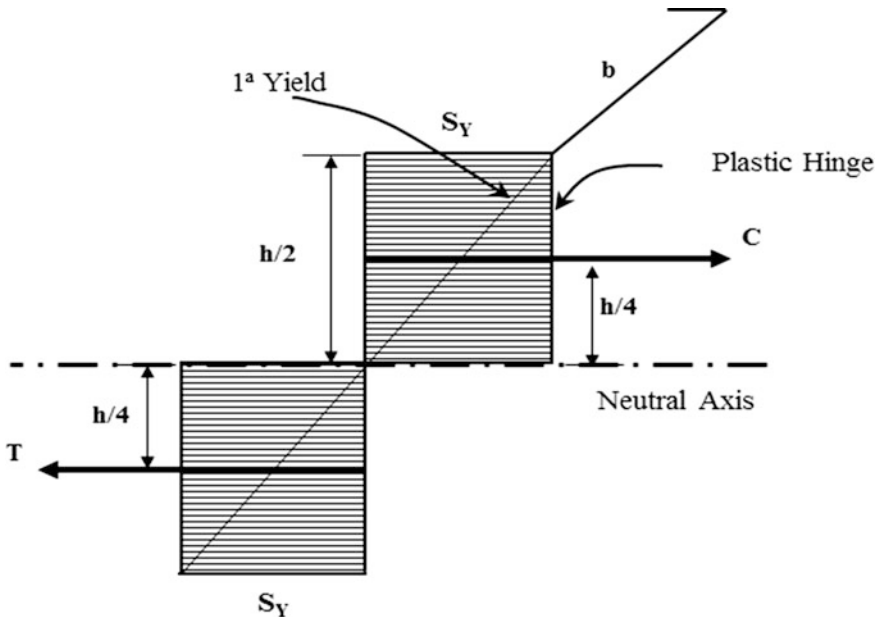
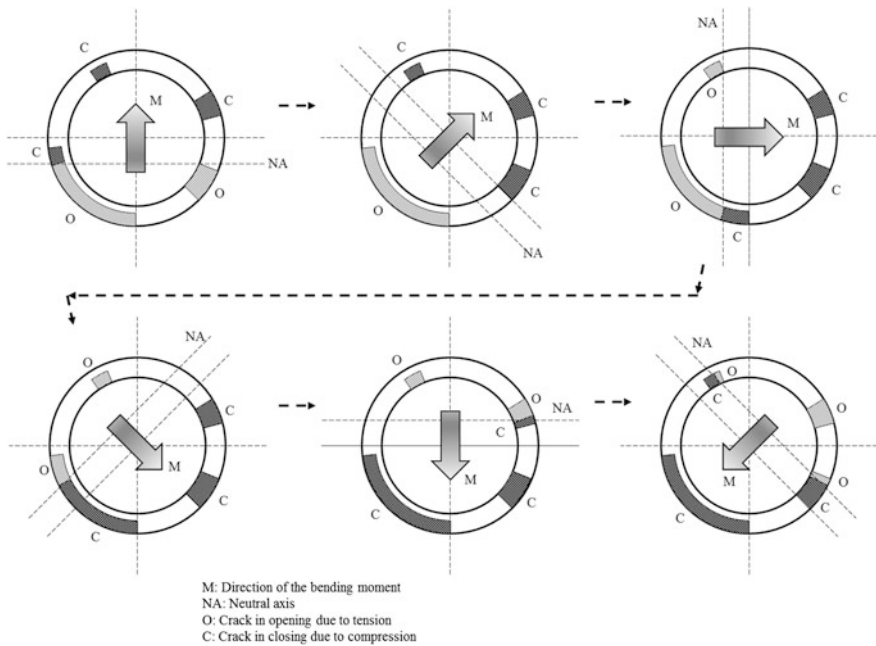


Fig. 6 Plastic state of the symmetrical cross section of a beam

strength provided by the strain hardening is ignored. In this case, the plastic moment is obtained when there is an equilibrium between the total forces of compression and tension under the yield stress  $S_y$  or a flow stress  $\sigma_f$ . Once that all the fibers are in a plastic state, there is a small rotation at this point that is called the “plastic hinge” [15, 16].

The part NB-3213.27 of the ASME Code Section III indicates that a limit analysis is a special case of plastic analysis in which the material is assumed to be ideally plastic (disregarding strain-hardening). The part NB-3213.30 says that a plastic hinge is an idealized concept used in limit analysis. In a beam or a frame, a plastic hinge is generated at the point where the moment, shear, and axial force lie on the yield interaction surface. So, the theoretical basis can be directed to the case of the core shroud of a BWR nuclear reactor with a non-uniform distribution of cracks [17].

However, in a beam with an un-symmetrical cross section, the mechanical-structural analyst must determine the small plastic moment between the X-axis and the Y-axis. This small value will be critical for safety purposes, because of seismic events, where the loads can arrive from any direction and the core shroud will be bent in a random pattern. Therefore, the core shroud of a BWR with a non-uniform distribution of cracks for each circumferential weld must be analyzed with respect to multiples axis in order to determine the critical value of the plastic moment  $M_p$ . Figure 7 shows how the axes must be rotated to diverse angles, in



**Fig. 7** Analysis of a crack configuration of a particular circumferential weld in which the bending moment is rotated around the vertical axis



order to obtain the critical orientation in which the cracks will open or close. In this way, the critical plastic hinge is calculated.

## 5 Methodology Proposed in this Paper

In a simplified solution for a cracked core shroud, the analytical method can be more useful than the Finite Element Method [14]. Based on the theoretical fundamentals of the limit load analysis and taking in consideration the notes on the methodology contained in the Companion Guide to the ASME Boiler and Pressure Vessel Code, Vol. 3, Chapter 41 BWR Reactor Internals and other BWR Issues, the following steps were followed.

1. Location of the Neutral Axis ( $\alpha + \beta$ ).

$$\frac{1}{2} \left\{ \sum_{n=1}^N \text{arc}_n t_n \right\} \text{arc}_i = R_m (\theta_{i1} - \theta_{i2}) \quad (4)$$

$N$  Number of segments of arcs which compose the complete cross section of the weld under analysis

$n$  Segments of arcs  $\theta_1 \rightarrow \theta_2$

$t_n$  Thickness of the segment of arc  $\theta_1 \rightarrow \theta_2$ , which can have values from 0 up to  $t_{nominal}$

Various iterations must be performed to obtain the critical position of the neutral axis.

2. Plastic Moment.

$$M_p = \sum_{n=1}^N \text{arc}_n t_n \left\{ R_m \sin \left( \alpha - \theta - \frac{\text{arc}}{2} \right) + R_m \sin (\beta) \right\} \quad (3)$$

The angle  $\alpha + \beta$  is determined with several iterations until the critical  $M_p$  is obtained. A fast way to find this angle and to minimize the iterations is to visualize the angle that obtains the highest cumulative length of cracks under tension.

Figure 8 provides the graphical representation of the methodology proposed. As is described in the next section of this paper, these expressions can be incorporated in a spreadsheet like Excel (Microsoft Windows<sup>®</sup>) or Numbers (Apple OS<sup>®</sup>) for portability of the mechanical-structural analysts.

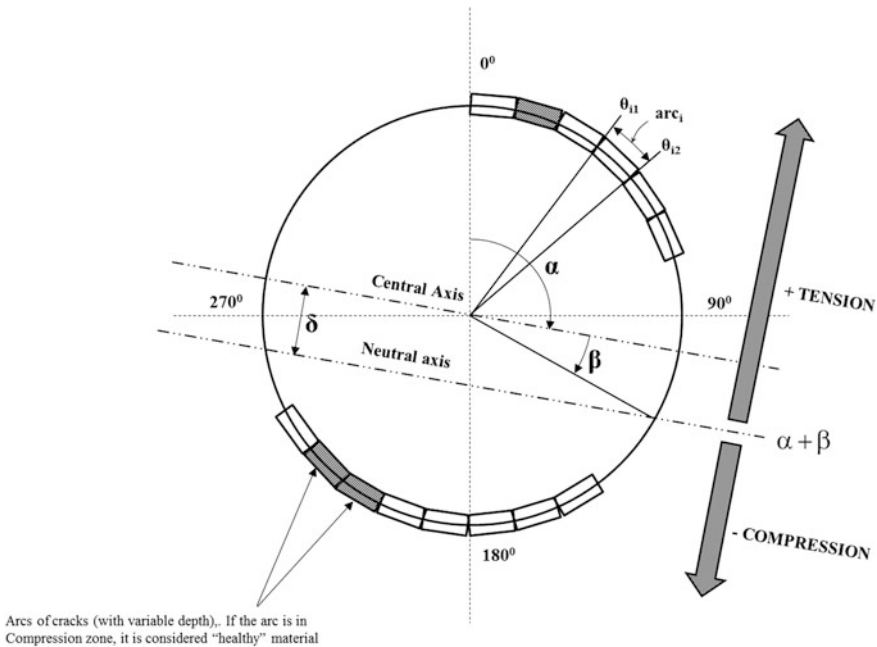


Fig. 8 Graphical representation of the methodology developed

## 6 Numerical Analysis Considering Aging Effects

Based on the methodology developed and implemented in spreadsheet, the next step was to perform the analysis.

This calculation is part of a Time-Limited Aging Analysis (TLAA), has to be submitted for license renewal. It is in accordance with the rules of 10 CFR 54 for a BWR nuclear power plant. It started its commercial operation in 1990. In this case, the owner of the plant has planned to operate for an extended period after the date of expiration of the original license until 2050. It has been requested that the applicant demonstrates the capability of the core shroud to perform its intended function up to the year 2050.

Also, it was assumed that the core shroud has three cracks at the time of analysis: two are part-through wall and the last one is a through thickness. The BWRVIP-76 NP Appendix K [14] indicates that a crack growth rate greater than  $3.5278 \times 10^{-10}$  m/s has to be considered. Accordingly, a conservative prediction for 60 years of operation shows that all the cracks will be through wall and the cracks lengths will have incremented 0.399034 m to both sides.

Another conservative assumption is that the Flow Stress  $\sigma_F$  is maintained, although the Yield Strength  $S_y$  can be incremented maybe up to 100 % by the neutron fluence impact from 1990 to 2050 due to the changes in the lattice of the

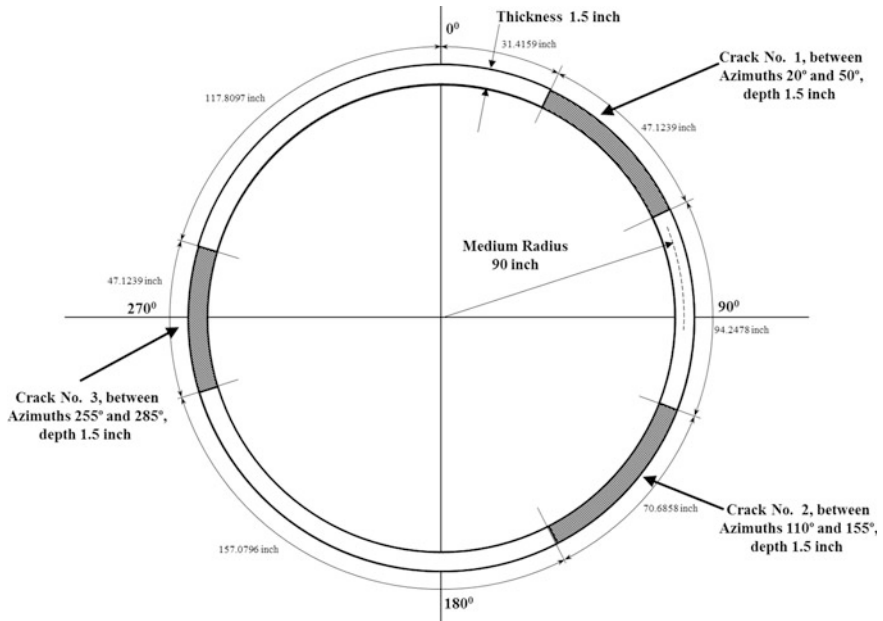


**Fig. 9** Crack configuration predicted of a core shroud of a generic BWR at the circumferential H8 weld after 60 years of operation

material of the core shroud [5–8]. Therefore, aging effects have been considered and the final cracked configuration is shown in Fig. 9.

Looking to the spreadsheet, the material was deleted in those places in which there are cracks under tension, because there is any contribution in the calculation of the Plastic Moment  $M_p$ . Regarding the cracks under compression or closing, the material was not deleted and acts as “health material” for the calculation of the plastic moment. Various iterations were performed to obtain the critical position of the neutral axis. From the experience of the authors of this work, the angle of each segments could be 5 % of the perimeter in order to reduce the calculations and obtain a useful and reliable result.

The data for the problem at hand was the following:

- Material: Stainless Steel Type 304
- Radius:  $R_m = 2.286$  m, Wall thickness:  $t = 0.0381$  m, ASME Stress Intensity:  $S_m = 99284505$  Pa, Flow Stress  $\sigma_f = 3S_m = 2.97854 \text{ e}+8$  Pa
- Stresses at failure conditions at the cross section of weld under study: primary membrane stress  $P_m = 1.0342 \text{ e}+7$  Pa and primary bending stress  $P_b = 2.4132 \text{ e}+7$  Pa
- Minimum Safety Factor requested: 1.5 (As a reference ASME Section IX requires 1.414)

## 7 Results

From the calculation, the angles  $\alpha$  and  $\beta$  determined the position of the critical neutral axis. The following results were obtained:

Plastic Moment ( $M_p$ ) = 10133.36 e+9 Pa (minimum value)

Bending stress ( $Pb'$ ) = 2.67668 e+8 Pa

Safety Factor calculated = 8.064 > 1.5 (minimum required for Accident Condition). This Safety Factor was determined by using the expression (3).

## 8 Discussion of the Results and Advantages of the Proposed Methodology

The Safety Factor calculated is greater than the minimum required, so it has been demonstrated that the structural integrity of the core shroud, with this cracked configuration, is safe. It is considered that the core shroud will perform its intended function up to 2050, even in faulty conditions (in case of a loss of coolant accident and the design basis earthquake).

Regarding the proposed methodology, the results were compared with those obtained with the DLL code. The convergence of the estimated parameters were in the following ranges:

- -2 % in the calculation of the Plastic Moment
- -1 % in the calculation of the Bending Stress
- -1 % in the calculation of the Safety Factor

The proposed methodology developed in this paper can be a useful and it is a simplified alternative for the limit load analysis of cracked core shrouds of a BWR.

## 9 Conclusions

In this paper, a useful methodology has been developed for the plastic limit load analysis of a core shroud of a BWR. A good degree of confidence has been obtained. It is useful for the determination of the critical limit load for any crack distribution on the circumferential welds, which are under diverse loading conditions. It can be easily implemented in a spreadsheet. However, several iterations are required in order to make a complete evaluation of the structural integrity.

This methodology also can be applied for the Time-Limited Aging Analysis (TLAA) which is a part of the submission for a license renewal according the rules of 10 CFR 54 for a nuclear power plant.

**Acknowledgments** The authors kindly acknowledge the support given by CONACyT through the Project No. 211704, the National Polytechnic Institute and the National Commission on Nuclear Safety and Safeguards (Mexican Nuclear Regulatory Body) from Mexico.

### Statement

The conclusions and opinions stated in this paper do not represent the position of the National Commission on Nuclear Safety and Safeguards, where the authors P. Ruiz-López and M.L. Serrano-Ramírez are working as employees. Although special care has been taken to maintain the accuracy of the information and results, all the authors do not assume any responsibility on the consequences of its use. The use of particular mentions of countries, territories, companies, associations, products or methodologies does not imply any judgment or promotion by all the authors.

### References

1. Secretariat of Energy (2013) National report that presents Mexico to meet the requirements of the convention on nuclear safety. International Atomic Energy Agency (IAEA), Period 2010–2012
2. Ruiz P (2014) Structural integrity of the BWR jet pumps under the presence of relevant defects. Thesis to obtain the Degree of Master in Sciences, National Polytechnic Institute, Mexico
3. United States Nuclear Regulatory Commission, NUREG-1544 (1996) Status report: Intergranular stress corrosion cracking of BWR core shrouds and other internal components
4. United States Nuclear Regulatory Commission (1994) Intergranular stress corrosion cracking of core shrouds in boiling water reactors (Generic Letter 94-03), Office of Nuclear Reactor Regulation
5. Serrano M, Hernández M (2007) Programas de investigación sobre fragilización por irradiación de los aceros de la vasija. *Anales de Mecánica y Electricidad, España*
6. Gary S (2007) *Fundamentals of radiation materials science, metals and alloys*. Springer, Berlin
7. United States Nuclear Regulatory Commission, NUREG/CR-6826 (2003) Fracture toughness of irradiated stainless steel
8. United States Nuclear Regulatory Commission, NUREG/CR-7027 (2010) Degradation of LWR core internal materials due to neutron irradiation
9. Hernández LH, Urriolagoitia GM, Urriolagoitia G et al (2009) Assessment of the structural integrity of cracked cylindrical geometries applying the EVTUBAG program. *Rev Téc Ing Univ Zulia* 32:190–199
10. Zahoor A (1999) Ductile fracture handbook. Electric Power Research Institute Report NP-6301
11. Rahman S, Wilkowski G (1998) Net-section-collapse analysis of circumferentially cracked cylinders—Part I & II. *Engineering fracture mechanics* 61, Pergamon
12. Rao KR, Hardayal S (2009) Companion guide to the asme boiler and pressure vessel code, vol. 3. Chapter 41:bwr reactor internals and other BWR issues
13. <http://www.epri.com/abstracts/Pages/ProductAbstract.aspx?ProductId=00000000001018251> (Internet consult made in June 20, 2015)
14. BWR Vessel and Internals Project, BWR Core Shroud Inspection and Flaw (2000) Evaluation guidelines (BWRVIP-76NP), TR-1 14232NP, Final report, Non-proprietary information, Appendix K guidelines for inspection of BWR core shrouds: demonstration of compliance

- with the technical information requirements of the license renewal rule (10 CFR 54.21), Electric Power Research Institute
15. Warren C et al (2002) *Formulas for stress and strain*. 7th edn. McGraw-Hill
  16. Wong M (2009) *Plastic analysis and design of steel structures*. Elsevier
  17. The American Society of Mechanical Engineers (2007) *Section III rules for construction of nuclear facility components, Division 1—Subsection NB class 1 components, ASME boiler & pressure vessel code*, 2007 edn

# Numerical Evaluation of the Structural Integrity Exhibited by a TiO<sub>2</sub> Thin Solid Film Doped with Au

D. Fernández-Valdés, L.H. Hernández-Gómez, M. Trejo-Valdéz,  
C. Torres-Torres, J.A. Beltrán-Fernández, N.M. León-Lugo  
and G. Urriolagoitia-Calderón

**Abstract** Some metal implants fail to generate natural bonding with living tissue. As a result, external fixation is required. Surface modification, with nanostructured coatings, has been used to improve their performance. The release of ions is limited and promotes the fixation of the implant to the tissues. In the field of biomechanics, gold nanoparticles exhibit good properties in some cases that are intrinsic to their nanometer size. Also, they have low toxicity and have a great potential for application in internal prostheses. In this paper, the mechanical behavior of the two coatings was studied with the Finite Element Method. The first was a TiO<sub>2</sub> thin film and the other one was a TiO<sub>2</sub> thin film doped with Au. Both coatings exhibited a thickness of approximately 250 nm. The objective of this analysis was to evaluate the structural integrity of each film. The stress field of each film was obtained. The

---

D. Fernández-Valdés · L.H. Hernández-Gómez (✉) · C. Torres-Torres ·  
J.A. Beltrán-Fernández · N.M. León-Lugo · G. Urriolagoitia-Calderón  
Instituto Politécnico Nacional. ESIME-Zacatenco. Section of Postgraduate Studies  
and Research, Adolfo López Mateos, 5, 3rd Floor, Lindavista. Gustavo A. Madero,  
07738 México, D.F., Mexico  
e-mail: luishector56@hotmail.com

D. Fernández-Valdés  
e-mail: dayvis86@hotmail.com

C. Torres-Torres  
e-mail: ctorrest@ipn.mx

J.A. Beltrán-Fernández  
e-mail: jbeltranf@hotmail.com

N.M. León-Lugo  
e-mail: nleon@ipn.mx

G. Urriolagoitia-Calderón  
e-mail: urrio332@hotmail.com

M. Trejo-Valdéz  
Instituto Politécnico Nacional. ESIQIE, Adolfo López Mateos, 8, 3rd Floor, Lindavista.  
Gustavo A. Madero, 07738 México, D.F., Mexico  
e-mail: martin.trejo@laposte.net

hardness values were obtained. The film of TiO<sub>2</sub> doped with Au showed the highest hardness.

**Keywords** Nano-indenter · Finite element · Thin films · TiO<sub>2</sub> · Gold

## 1 Introduction

The manufacturing of materials for specific uses has been fundamental in the progress of humanity throughout the ages. Obtaining new materials with specific functionality is possible nowadays. This is achievable through the modification and manipulation of atoms and molecules. Thanks to recent technological advances, the production of nanoparticles (1–100 nm) can be carried out in an industrial scale. This is a new source of innovation in the field of materials [1]. Obtaining products with improved mechanical properties for application in health is a priority [2].

Nanostructured coatings for prostheses' have shown good performance. They enable protection against erosion and corrosion, besides incorporating bioactive particles that can generate scaffolding within the existing bone [3]. In the field of biomechanics, gold nanoparticles exhibit good properties which are related to their shape and morphology. Besides, they seem to show biocompatibility [4], which makes them of great potential for developing prostheses coatings [5].

Characterization of the mechanical properties [6] is crucial for a fundamental understanding of the deformation behavior of materials under different loading rates, which is important for long term use [7]. With this motivation, the structural integrity of the TiO<sub>2</sub> thin films and the TiO<sub>2</sub> thin film doped with Au was studied with the finite element method. The mechanical properties of the films were obtained experimentally.

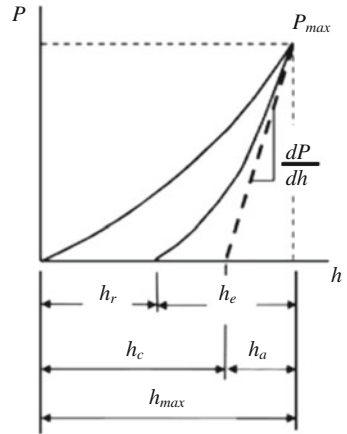
## 2 Theoretical Concepts

**Hardness evaluation.** A widely accepted method for the evaluation of hardness and elastic modulus in nanostructured thin films has been proposed by Oliver and Pahr in 1992 [8]. This takes into account the nonlinear unload curve obtained in most indentations and provides a physically justifiable process to determine the depth of indentation achieved by plastic deformation. When the indenter is pressed into the sample, elastic and plastic deformation occurs, forming an impression of the shape of the indenter. When removing the indenter, it recovers only the elastic displacement, [8]. The load-displacement curve (Fig. 1) can be employed to determine hardness [9] and the elastic modulus of the material [10].

The hardness  $H$  is defined as [8]:



**Fig. 1** Typical nanoindentation loading and unloading curve



$$H = \frac{P_{max}}{A} \tag{1}$$

where  $P_{max}$  is the maximum load and  $A$  is the projected area of contact.

For a Berkovich indenter geometry,  $h_f$  is the depth of residual print sample,  $h_s$  is the elastic sinking of the surface around the contact area and  $a$  is the radius of the circle of real contact [11] (Fig. 2). The projected area  $A$ , the contact area, can be determined from the depth  $h_c$  where:

$$A = 3\sqrt{3}h_c^2 \tan^2 \theta \tag{2}$$

In the case of a Berkovich indenter [11],  $\theta = 65.27^\circ$ , then:

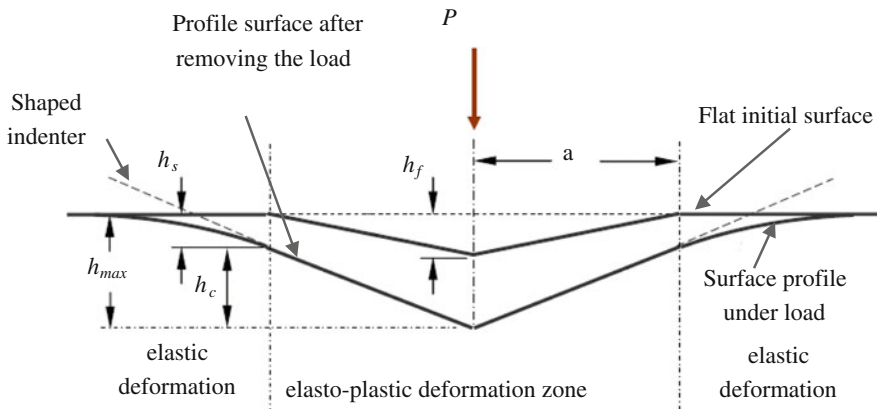


**Fig. 2** Schematic deformation of an ideal indenter under maximum load

$$A = 24.5h_c^2 \quad (3)$$

In the load versus displacement curve, the contact depth  $h_c$ , is different from maximum indentation depth  $h_{max}$  at the maximum load due to the elastic deformation of the area around the indenter tip. The contact depth is given in (Eq. 4), [8].

$$h_c = h_{max} - \varepsilon \frac{P_{max}}{S} \quad (4)$$

where,  $S$  represents the stiffness that can be calculated from the slope of the unloading curve at the maximum load. The value of  $\varepsilon$  is 0.75 for the pyramidal indenter [8].

The contact stiffness,  $S$ , at maximum depth is:

$$S = \left. \frac{dP}{dh} \right|_{h=h_{max}} \quad (5)$$

The effective elastic modulus [12] is expressed as

$$E_{eff} = \frac{1}{\beta} \frac{\sqrt{\pi}}{2} \frac{S}{\sqrt{A(h_c)}} \quad (6)$$

where  $\beta = 1.034$ , is a constant that depends on the geometry of the tip. For the problem at hand, this constant considers the absence of symmetry in a Berkovich tip [12]. In the evaluation of the elastic modulus, the effective elastic modulus of the material has to be considered:

$$\frac{1}{E_{eff}} = \frac{1 - \nu^2}{E} + \frac{1 - \nu_i^2}{E_i} \quad (7)$$

$E_i$  and  $\nu_i$  are the Young's modulus and the Poisson's ratio, respectively.

### 3 Methodology

The films were analyzed with the finite element method, in order to determine their structural integrity. For this purpose, the load vs displacement curve was vital for determining the hardness. The method of Oliver-Pahr was followed. The methodology used in this paper is schematized in Fig. 3. It shows the steps followed in the comparison of the mechanical characterization of each film.

Figure 4 shows the characteristics of the specimens that were analyzed. The TiO<sub>2</sub> thin film and TiO<sub>2</sub> thin film doped with Au were employed as coatings over

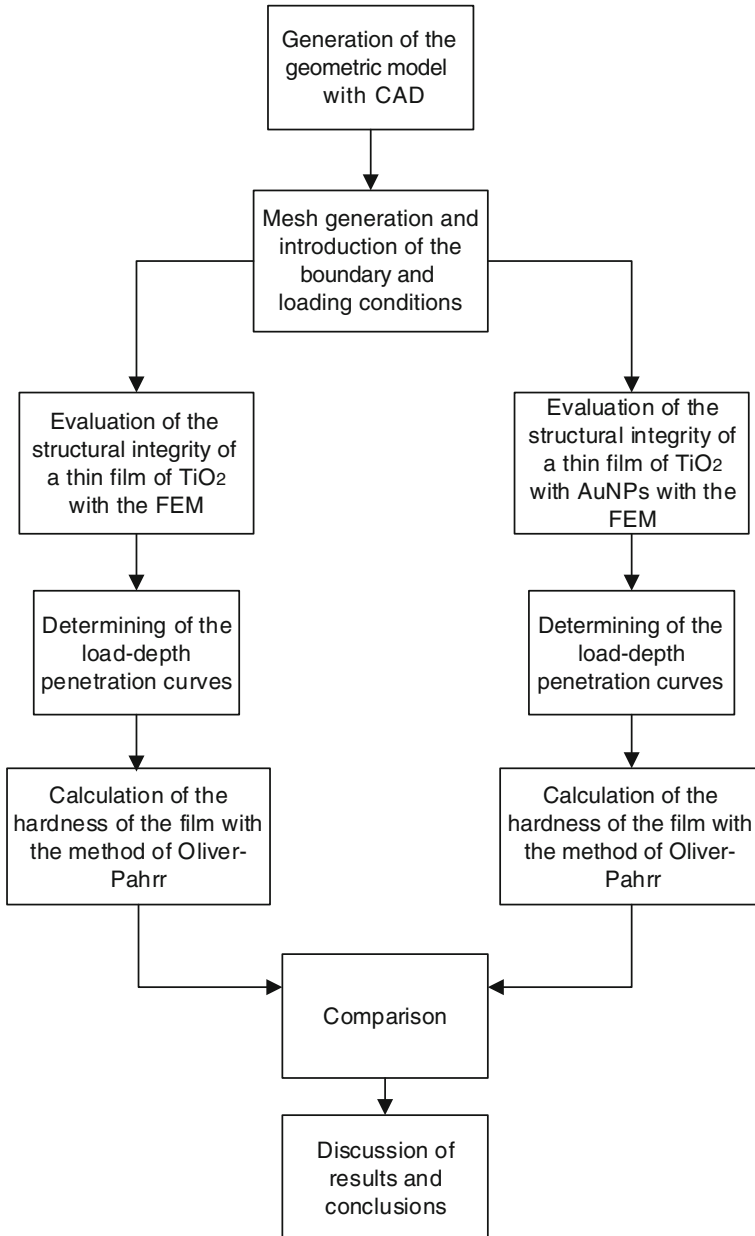
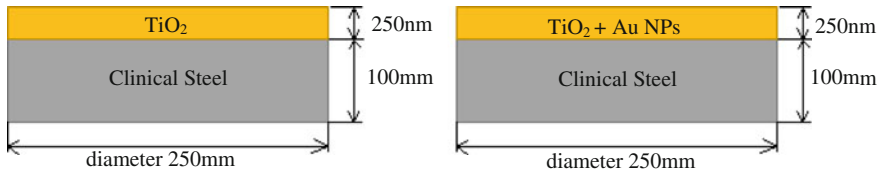


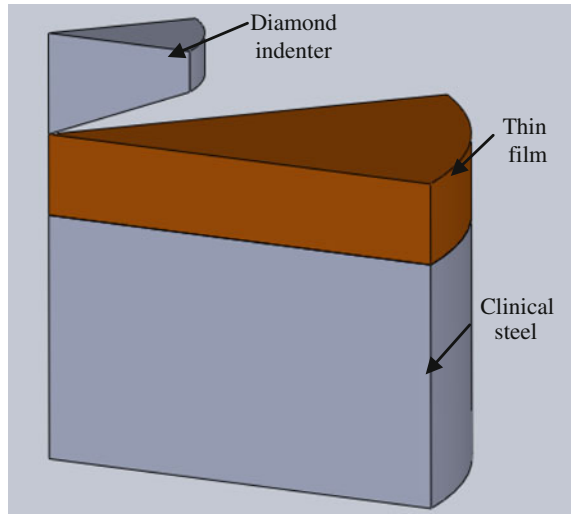
Fig. 3 Methodology

316L stainless steel substrates. It is worth noting that this metal is widely used in orthopedics considering its biocompatibility features, low cost and excellent corrosion resistance.



**Fig. 4** Dimensions of the samples

**Fig. 5** Scheme of the indenter and the sample under compression



In order to correctly simulate the indentation phenomena, a penetrator with  $65.27^\circ$  angle was considered. The measurement was contemplated to be conducted from the vertical axis by using contact elements (see Fig. 5). The film was considered to have elasto-plastic behavior, while the indenter and substrate were considered to be elastic. The three types of elements used were: (1) 59 contact elements, (2) 59 target elements and (3) 3016 solid elements. The clinical steel substrate was represented by a mesh with 299 solid elements. The thin film was modelled with a mesh of 1600 solid elements. The mesh of the diamond indenter had 999 solid elements.

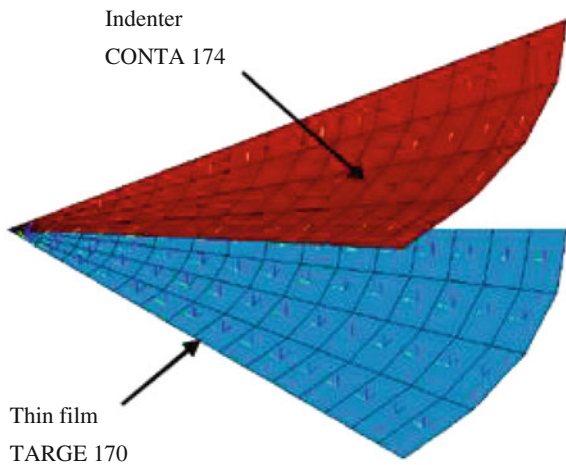
The mechanical properties of the materials involved in the simulation are shown in Table 1. These parameters were reported elsewhere [7]. In the literature [13], the mechanical properties and Poisson's ratio for similar coatings are in line with the experimental results.

For this purpose, contact elements (CONTA174) were placed along the lower surface of the penetrator and target elements (TARGE170) were localized along the upper surface of the film (Fig. 6). The indentation was simulated by applying displacements in the  $y$  direction. The lower surface of the penetrator was pressed against the upper surface of the film, thus a compressive load was exerted between

**Table 1** Mechanical properties of materials for simulation

Materials	Modulus of elasticity (GPa)	Poisson's ratio	Material behavior	Yield stress (MPa)
TiO <sub>2</sub> coating doped with Au	76	0.43	Elasto-plastic	205
TiO <sub>2</sub> coating	13.3	0.27	Elasto-plastic	140
Clinical steel substrate [14]	200	0.33	Elastic	
Indenter Berkovich [14]	1140	0.07	Elastic	

**Fig. 6** Mesh of the contact elements



the contact elements against the target elements. The contact was supposed to be without friction. The indentation was performed by multi-step shift. Then, loading and unloading were simulated. Since the problem has symmetry with respect to the y-axis, only one octant (1/8) geometry was analyzed.

## 4 Results

The stress field is shown in Fig. 7. The maximum von Mises stress was located at the point of indentation. For this analysis, 114 steps simulated the loading process, and 74 steps were required for unloading. The displacement was increased by 1.486 nm alongside the y direction in each step.

For the TiO<sub>2</sub> thin film (Fig. 8), the maximum value of the von Mises stress was 140 MPa and it was located at the point of indentation. The yield stress of the thin film was not exceeded. These results were consistent with other comparative studies reported in the literature [13].

**Fig. 7** Stress field of the sample with TiO<sub>2</sub> thin film

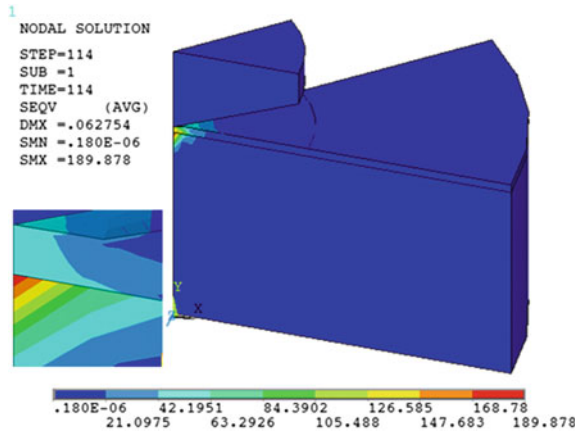


**Fig. 8** Von Mises stress for TiO<sub>2</sub> thin film

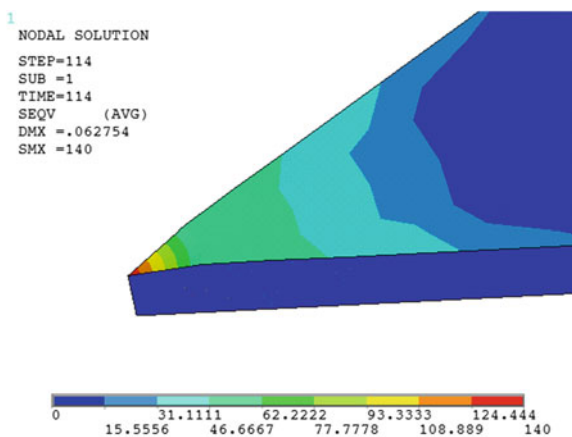
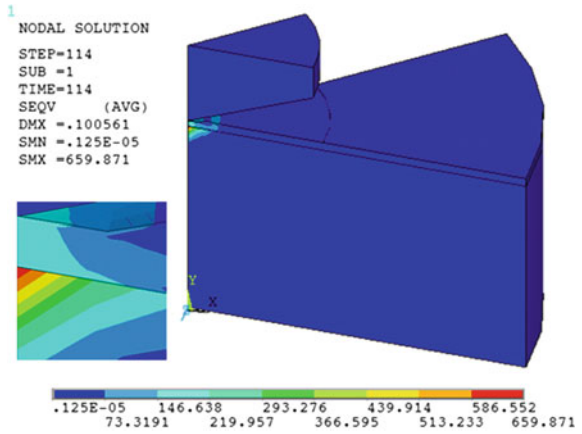


Figure 9 shows the results of the numerical analysis of the sample TiO<sub>2</sub> doped with Au. The stress field for the studied system was recorded at the point of indentation.

For the TiO<sub>2</sub> thin film doped with Au (Fig. 10), the maximum value of the von Mises stress is 205 MPa and it is located at the point of indentation. The thin film did not exceed its yield stress. Through this numerical analysis, noticeable differences between the films were observed. Remarkably, the resistance achieved in the TiO<sub>2</sub> thin film doped with Au was bigger because higher von Mises stresses took place.

Through the numerical analysis with the finite element method, the load vs displacement curve (see Fig. 11) could also be obtained. This curve represents the loading and unloading steps. Also, it is possible to see the indentation depth reached at the maximum load applied for the TiO<sub>2</sub> thin film. It can be stated that the

**Fig. 9** Stress field of the sample with TiO<sub>2</sub> thin film doped with Au



**Fig. 10** Von Mises stress for TiO<sub>2</sub> film with Au nanoparticles

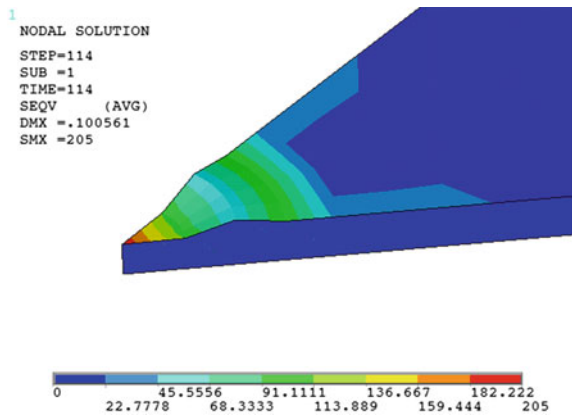


**Fig. 11** Load versus displacement curve of the TiO<sub>2</sub> thin film

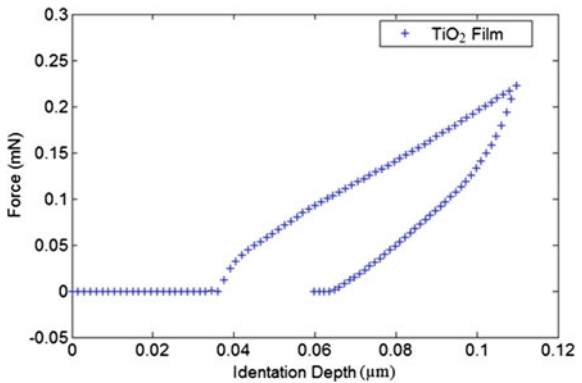
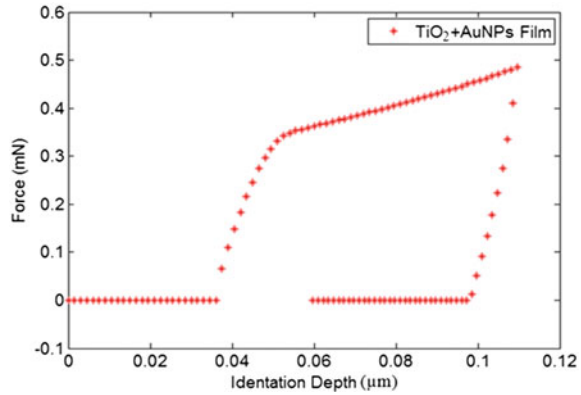


**Fig. 12** Load versus displacement curve of the  $\text{TiO}_2$  thin film doped with Au



differences in the load and unloaded path is due to the elasto-plastic behavior of the thin film.

In the case of the  $\text{TiO}_2$  thin film doped with Au, the displacement vs. load curve (see Fig. 12) has a different behavior in comparison to the results shown in Fig. 13. This is a consequence of the Au doping that modifies the film properties.

Comparing the load versus displacement curves of the studied films shown in Fig. 13, it is possible to see that the doped film can withstand higher loads. The maximum load applied in this analysis was 0.48 mN.

The mechanical behavior of the films was also analyzed by determining their hardness obtained by the Oliver-Pharr method. Based on the load vs displacement curve (see Fig. 1), it was possible to obtain the hardness values for the films which are reported in Table 2.

The hardness of the two films is shown in Table 2. The doping process seems to improve the mechanical characteristics of dielectric materials as has been previously reported [14]. This result constitutes a high potential for developing coatings, which increase the durability and performance of the prosthetic components.

**Fig. 13** Load versus displacement curve

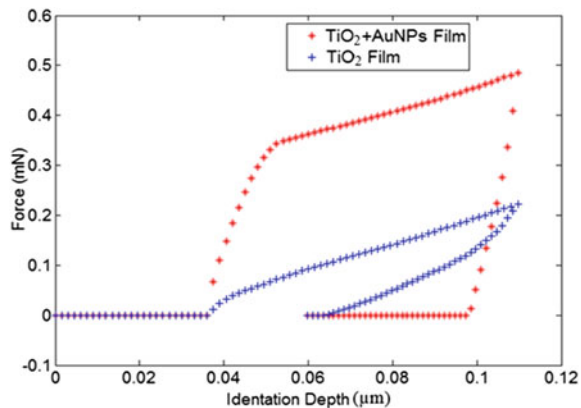




**Table 2** Hardness value for the thin films

	TiO <sub>2</sub> film	TiO <sub>2</sub> film with Au
P <sub>max</sub> (mN)	0.22	0.48
h <sub>c</sub> (nm)	85	98
H (GPa)	1.24	2.04

Doping processes in thin films can cause nanoparticle formation, and it could result in the creation of nanostructured materials with engineered properties sensitive to vectorial excitations [15]. As it is well known, controlling the size, shape and morphology of the nanoparticles allows tailoring the mechanical properties of nanosystems. Then, it seems to be feasible to propose designing tensorial mechanical functions; like for example energy transference by mechanical operations. Our results are in good agreement with those reported in [16], where similar studies were explored for other purposes.

## 5 Conclusions

An outstanding enhancement in the mechanical properties exhibited by a thin solid film of TiO<sub>2</sub> was obtained by a gold doping process. Nanoparticle formation seems to be responsible for the phenomena observed. The structural integrity of the film was evaluated with the Finite Element Method. The stress field and von Mises stress values were compared before and after the doping processing route. Potential applications for coating fabrication are proposed. The Au doping process can be considered as a good candidate to improve biocompatible materials.

**Acknowledgments** We kindly acknowledge the financial support of the Instituto Politécnico Nacional and the Consejo Nacional de Ciencia y Tecnología.

## References

1. Gutiérrez C (2005) Nanoparticles: small structures with great potential. *Contact Nucl* 39:24–29
2. Hernández LH, Pava J, Trejo M et al (2014) Strain measurements exhibited by a steel prosthesis protected with Au nanoparticles. *Des Comput Mod Eng Mater* 54:107–120
3. Shukla R, Bansal V, Chaudhary M et al (2005) Biocompatibility of gold nanoparticles and their endocytotic fate inside the cellular compartment: a microscopic overview. *Langmuir* 21:10644–10654
4. Connor EE, Mwamuka J, Gole A et al (2005) Gold nanoparticles are taken up by human cells but do not cause acute cytotoxicity. *Small* 1:325–327
5. Pan Y, Neuss S, Leifert A et al (2007) Size-dependent cytotoxicity of gold nanoparticles. *Small* 3:1941–1949

6. Morales S, Torres C, Trejo M et al (2013) Engineering the optical and mechanical properties exhibited by a titanium dioxide thin film with gold nanoparticles. *Optica Appl* 43:651–661
7. Maharaj D, Bhushan B (2014) Scale effects of nanomechanical properties and deformation behavior of Au nanoparticle and thin film using depth sensing nanoindentation. *Beilstein J Nanotechnol* 5:822–836
8. Oliver WC, Pharr GM (1992) An improved technique for determining hardness and elastic modulus using load and displacement sensing indentation experiments. *J Mater Res* 7:1564–1583
9. Tabor D (1951) *The hardness of metal*. Oxford University
10. Bhushan B (1999) *Handbook of micro/nanotribology*, 2nd edn. CRC Press, Boca Raton
11. Berkovich ES (1951) Three-faceted diamond pyramid for micro-hardness testing. *Ind Diam Rev* 11:129–133
12. Holmes D, Heuer A, Pirouz P (1993) Dislocation structures around Vickers indents in 9.4 mol%  $Y_2O_3$ -stabilized cubic  $ZrO_2$  single crystals. *Philos Mag A* 67:325–342
13. Biplab R, Guangneng Z, Junghyun C (2012) Titanium oxide nanoparticles precipitated from low-temperature aqueous solutions: III. Thin film properties. *J Am Ceram Soc* 95:676–683
14. Torres D, Torres C, Vega O et al (2015) Structured strengthening by two-wave optical ablation in silica with gold nanoparticles. *Optica Laser Technol* 75:115–122
15. Carrillo C, Torres D, Trejo M et al (2015) Bidirectional optical Kerr transmittance in a bilayer nanocomposite with Au nanoparticles and carbon nanotubes. *Phys Scr* 90:085804
16. Vera E, Arroyo R et al (2001) Simulación de prueba de nanoindentación para UHMW-PE con recubrimiento de  $SiO_2$ . In: *Multidisciplinary research symposium*

# State of the Art Thermal Barrier Coating (TBC) Materials and TBC Failure Mechanisms

Abdullah Cahit Karaoglanli, Kadir Mert Doleker  
and Yasin Ozgurluk

**Abstract** Thermal barrier coatings (TBCs) are widely used in the aviation industry to improve the service life of components being exposed to high temperatures. Providing a higher resistance compared to conventional coatings, TBCs also improve the performance and lifetime of materials through their thermal insulating characteristic. Resistance of gas turbine components, particularly turbine blades, vanes and combustion chambers, is required to be improved against failures such as corrosion, oxidation and thermal shock as well, since turbine inlet temperatures should be increased to improve the performance of gas turbine engines. Accordingly, it is aimed to obtain a better resistance and durability against the failure mechanisms through enhancement of the methods and materials used in thermal barrier coatings. In this study, thermal barrier coatings used in gas turbines as well as their structure, also the relevant failure mechanisms and the new material groups used in TBCs are discussed.

**Keywords** Thermal barrier coating (TBC) · Gas turbine · Failure mechanism · Advanced materials

## 1 Introduction to TBCs

TBCs are commonly used in high-temperature applications of aircrafts, gas turbines and advanced aero engine components like turbine pales, combustion chambers and nozzle vanes in order to increase efficiency and durability properties of these

---

A.C. Karaoglanli (✉) · K.M. Doleker · Y. Ozgurluk  
Metallurgical and Materials Engineering Department, Bartin University,  
74100 Bartin, Turkey  
e-mail: cahitkaraoglanli@gmail.com

K.M. Doleker  
e-mail: kmdoleker@bartin.edu.tr

Y. Ozgurluk  
e-mail: yozgurluk@bartin.edu.tr

components [1–4]. The most important goal in using of TBCs is to reach a higher turbine inlet temperature and providing better propulsion [5, 6]. The aircraft turbine blade temperature, which is uncoated, goes up to approximately 1300 °C during running. Most of the metals do not remain at stable structure in this temperature range although air cooling systems are used [7]. Inconel alloys belonging to a type of the Ni based superalloys with respect to their superior mechanical properties are most suitable materials against high temperature conditions. However, they cannot preserve their structures under working conditions of gas turbines. Therefore, thermal barrier coated superalloys are using in this field [8]. A typical TBC consists of four diverse layers (i) a Ni based single crystal superalloy as substrate material, (ii) a metallic inner layer (bond coat) as MCrAlY (M=Ni,Co or both of them along with Fe), (iii) thermally grown oxide (TGO), (iv) a ceramic top coat [9–11].

The bond coat has the most critical role in TBC systems. MCrAlY coated above substrate material as bond coat provides a good adherence between the substrate material and top coat as well as oxidation resistance and tolerating thermal expansion mismatch [12]. Bond coats can be produced a in variety of methods such as atmospheric plasma spray (APS), vacuum plasma spray (VPS) or low pressure plasma spray (LPPS), cold gas dynamic spray (CGDS), high velocity oxy-fuel (HVOF) and electro-beam physical vapour deposition (EB-PVD). VPS is the best method to produce low oxide scales but it is more expensive compared to other methods [13]. HVOF and CGDS have optimum properties as characteristic and almost similar compared with one another while the APS method is the most economic production method, including higher oxide scale and porosity due to open air atmospheric production [14].

TGO is formed during the deposition, approximately 0.5–1  $\mu\text{m}$  sizes but starting to grow due to high temperature oxidation and leading to spallation of the top coat from the bond coat. In TBCs, spallation arising from TGO is observed as the most common failure. Thus, a great amount of studies are done about this phenomenon [15–17]. Top coats used as ceramic based material are the last layer of the TBC system. The top coat provides thermal barrier due to being a ceramic based material which insulates the system against thermal effects and preserving stability. Thus, turbine inlet temperatures can be decreased in the range of 100 and 300 °C [7]. There are two types of methods; APS and EB-PVD are used in the production of TBCs. APS coatings grow as laminar while EB-PVD coatings grow as columnar [18]. Representations of coatings produced by APS and EB-PVD techniques are given in Fig. 1.

A splat-rich and porous structure is obtained through deposition on the substrate material by the PS coating method. Due to the high porosity content, the coatings produced by this method have a lower thermal conductivity. Columnar and granular structures are obtained in vertical direction on the substrate material through the EB-PVD method. In this coating method, porous structures form between the columns [19, 20]. Therefore, less porous structures compared to the PS method are obtained resulting in higher thermal conductivity values. However, since the TBCs produced with EB-PVD method allow higher expansion tolerances compared to those produced with the PS method, they exhibit a superior resistance [21].

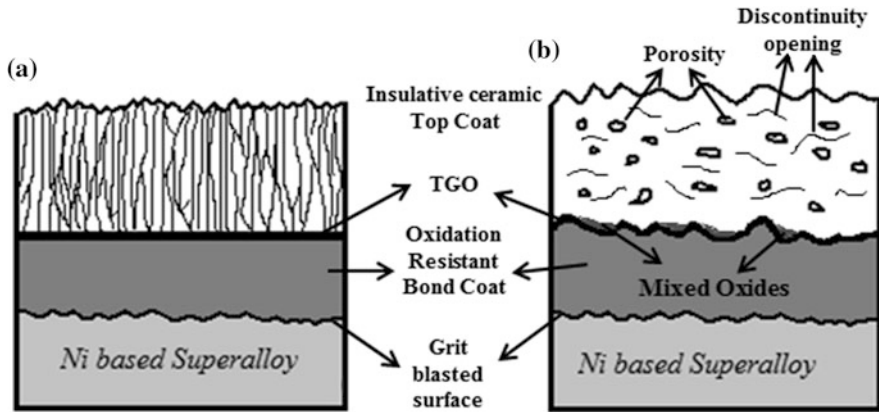


Fig. 1 TBC structures: **a** produced by EB-PVD method, **b** produced by APS method

## 2 Failure Mechanisms in TBCs

TBCs are exposed to various environmental effects causing occurrence of failures under service conditions. Failures occur as a result of one of these effects or combination of a number of effects. The main factors constituting the environmental effects occurring during service are: oxidation, hot corrosion, thermal shock/cycles, thermo-mechanic stresses, erosion and CMAS ( $\text{CaO-MgO-Al}_2\text{O}_3\text{-SiO}_2$ ) failures [18]. The most effective failure mechanisms occurring as a result of mentioned failure factors include TGO-related failures such as the impairment of the integrity of TGO structure and TGO growth.

### 2.1 Oxidation

Since vibration and diffusion of the atoms are facilitated through temperature rise, diffusion of the oxygen is facilitated at high temperatures and accordingly the coating is oxidized at higher rates. Top YSZ coatings used in TBCs exhibit high oxygen permeability rates. Therefore, TGO formation is observed between the bond coat and top coat in TBCs. On the other hand bond coat production is also crucial in terms of oxidation resistance. The production of a porous bond coat similarly promotes TGO growth at high temperatures [16].

Since the oxidation increases in time, diffusion of aluminium towards the interface also increases due to its high affinity against oxygen, leading to the formation of a TGO having a higher aluminium thickness. In connection with the aluminium concentration within the coating, after a while aluminium will be completely oxidized and depleted resulting in mixed oxide formations. Due to the

mechanical properties of mixed oxide formations, local stresses will increase in the coating interface, resulting in a failure through spallation of the coating from the interface [22].

## 2.2 *Hot Corrosion*

Another failure caused by the top coating is hot corrosion. This type of failure occurs as a result of the infiltration of molten salts from the micro cracks at the top layer [23]. It forms under service conditions as a result of modifications in the structure of elements such as sodium, vanadium and lead. Such elements, emitted due to fuel pollution, react with the  $Y_2O_3$  phase during their presence within the structure. In the absence of the  $Y_2O_3$  phase, tetragonal-monoclinic phase transformation occurs due to improbability of the stabilization of the tetragonal  $ZrO_2$  phase. This transformation may impair the integrity of the top layer through a modification in the volume [23]. In the latter case, this occurs due to the presence of phosphor and sodium caused by fuel pollution and through its reaction with zirconia. Occurrence of abovementioned corrosion mechanisms as a result of usage of low quality fuel or the service conditions impairs the integrity of the top coating and consequently result in the occurrence of failures [23, 24].

## 2.3 *Thermal Shock*

Thermal shock occurs via sudden temperature alteration whereas oxidation comes about chemical reactions at high temperatures. Thermal shock resistance is associated with various variables in the material. These are the thermal expansion coefficient, elastic module values, fracture resistance values of the material and the phase transformations occurring in the structure of some materials. The material group with the lowest resistance against thermal shock is the ceramics [25].

The top coating structure is desired to be compatible with the metallic bond coat to have a high thermal expansion coefficient and low elastic module, and exhibit a stable phase structure at high temperatures [26, 27]. Tensile stresses occur due to the thermal expansion growth coefficient mismatch between the substrate material and the top coat at high temperatures. During the heating process previously existing stresses are removed whereas compressive stresses occur following rapid cooling. Since the compressive stresses lead to further growth of the cracks, occurrence of failures in the coating will be observed over time.

There are three reasons for the spallation of the coating after thermal shock:

- (i) Spallation failure resulting from the increase in stresses due to the growth of the oxide layer.
- (ii) Expansions resulting from the thermal gradient within the oxide layer.

- (iii) Mismatch between the thermal expansion coefficient of oxide layer and the coating [18, 28].

While tensile stresses occur in the oxide layer due to rapid heating, the tensile stresses forming between the coating and oxide interface result in deformation. As widely known, YSZ is the most preferred top ceramic coating material for TBC production. YSZ is subjected to a number of adverse effects following the loadings with thermal cycles. One is the decrease in the coating life due to increasing stresses as a result of limited expansion tolerance due to sintering effects, and the other is phase transformation of the t-tetragonal phase during coating life. At high temperatures t-tetragonal phase transforms into tetragonal and cubic phase, while during cooling it undergoes volumetric change and transforms into a monoclinic phase [18].

## 2.4 Thermo-Mechanical Failure

Formation mechanism of thermo-mechanical stresses vary based on the thermal condition to which the TBC is exposed. If the thermal condition is isothermal, then the mechanism is rather associated with TGO growth, whereas the mechanism for TBCs exposed to thermal cycle is associated with the shrinkage of TGO during cooling. It should be noted that both of these mechanisms may be effective, whereas one of them may be the dominant mechanism. For instance TBCs operating at high temperatures for long operating hours are used in the gas turbines used for energy production purposes. In this case isothermal mechanisms become effective and cooling-related expansion or shrinkage occurs when the turbine operation stops. As a result, in such turbines, limited number of thermal cycles and long duration isothermal heating occur and accordingly failure formation occurs as the TGO reaches an average thickness of 5–15  $\mu\text{m}$ . In turbine components, TGO-related thermal expansion mismatch and TGO-growth-related failures become effective. However in the turbines used in aerospace industry in which the number of thermal cycles is the dominating factor, isothermal heating is not dominant, and failure occurs when the average TGO thickness is 1–5  $\mu\text{m}$ , and this failure mainly arises from thermal cycles [11, 29].

## 2.5 $\text{CaO-MgO-Al}_2\text{O}_3\text{-SiO}_2$ (CMAS) Effect

CMAS is an environmental deposition form of the particles such as dust, rock, etc. and these type of particles frequently cause failure during service in applications related with the hot region components of the turbines. CMAS effect occurs as a result of melting of cations such as Ca, Mg, Al, Si TBCs at high temperatures. By interaction of CMAS and YSZ soda-silicate glass phase forms and it infiltrates into

TBC through open gaps. The CMAS effect in TBCs is closely related with the deposition methods. EB-PVD coatings are more vulnerable against CMAS attack due to their columnar microstructures. As a result of the thermal expansion difference between this phase and YSZ and the decrease in the expansion tolerance the cracks, thus the failure occurs [30–32].

## 2.6 Erosion Failure

TBCs are exposed to impurity and erosion failure after being exposed to particle impacts at burning tracks. Due to the vast number of micro cracks included by their microstructure, the TBCs are more susceptible to erosion failures compared to a highly dense ceramic structure. The erosion rate is higher in the TBCs compared to bulk ceramic materials. Additionally, TBC production methods are essential in terms of development of erosion failures in aerospace and industrial gas turbine engine components such as high pressure turbine blades [30, 33–35].

## 3 New Material Types in TBCs

The main purpose of TBCs is to decrease the heat conducted to the metallic substrate by use of a ceramic top coating with a low thermal conductivity. Mostly, yttria stabilized zirconia (YSZ) is used as the top coating material for its superior mechanical, chemical and thermal characteristics [36–40].

In YSZ coatings, serious decreases may occur in the service life of YSZ coatings over 1200 °C by the effect of phase transformation and sintering [41–43]. Therefore, several studies are carried out for enhancement of YSZ and its service life. These are implemented through chemical modification of YSZ, use of a material with lower thermal conductivity or modifications in the microstructures [44–48].

The main characteristic expected from the ceramic top coatings that provide thermal insulation, is a low thermal conductivity. By use of a proper dopant, host atoms with varying valence numbers fill the gaps and cause the lattice to stretch. These two phenomena decrease the mean free path of scattered phonons, also decreasing the thermal conductivity. Zirconia based materials have low thermal conductivity. A more effective phonon dispersion is enabled through the formation of significant amounts of oxygen gaps by addition of a stabilizer, on the other hand transformation into monoclinic phase from tetragonal phase is prevented [49, 50]. For YSZ coating, if two or more dopants (instead of Y) add like rare earth elements, a lower thermal conductivity can be obtained due to more phonons scattering [51].

Oxides and zirconates of rare earth elements were found to have low thermal conductivity values [47, 52–54]. However, they have weak thermal cycle properties since their thermal expansion coefficients (CTE) are significantly lower compared



to metallic bond coats. This issue was resolved by the production of double layer coatings [47, 55, 56].

Even after a long period of use,  $\text{La}_2\text{Ce}_2\text{O}_7$  does not exhibit a phase transformation at 1400 °C. Also having a high thermal expansion coefficient,  $\text{La}_2\text{Ce}_2\text{O}_7$ 's thermal cycle life increases after being coated with single and double ( $\text{La}_2\text{Ce}_2\text{O}_7$ /YSZ) layer [57–59]. Xu et al. observed that LZ/YSZ resisted a cycle 30 % longer than YSZ when they applied a thermal cycle test at 1373 K. LZ top coat was found to have undergone a significantly lower cycle failure compared to both [60].

$\text{ZrO}_2$ —25 %  $\text{CeO}_2$ —2.5 %  $\text{Y}_2\text{O}_3$  (CeSZ) produced by the EB-PVD method was observed to have a more stable phase structure with lower thermal conductivity and better corrosion resistance compared to YSZ. During the thermal cycle tests carried out a 1100 °C, TBCs with higher thermal cycle resistance and a longer service life, were obtained [61, 62].

At 700 °C, YSZ had a thermal conductivity value of 2.3 W/mK, while  $\text{Gd}_2\text{Zr}_2\text{O}_7$ ,  $\text{Nd}_2\text{Zr}_2\text{O}_7$  and  $\text{Sm}_2\text{Zr}_2\text{O}_7$  had thermal conductivity values of 1.6, 1.6 and 1.5 W/mK, respectively [63]. The reason of the decline is the phonon dispersion caused by point flaws. These materials exhibit two types of point flaws. These are the oxygen gaps formed due to substitution of rare-earth cations with Zr and substitution of trivalent rare-earth elements with quadrivalent Zr. Dispersion intensity of the oxygen gaps is higher than the dispersion intensity of substitutional solid melts. Consequently the reason for having a lower conductivity compared to YSZ, is the higher oxygen gap concentration and a more effective phonon dispersion with dissolved cations due to the atomic mass difference between Zr and the cations [64].

A flawed cluster system is composed using more than one dopant. After addition of two cations one being smaller (as Yb, Sc) and one being larger (as Sm, Nd, Gd) to Y, a decrease in the thermal conductivity, compared to YSZ, was observed. Additionally, the total dopant concentration was also found to effect the conductivity. The TBCs produced by the PS method exhibited a decreased conductivity with 6–15 % molar addition, whereas lower thermal conductivity values were observed with 10 % molar addition in the TBCs produced by EB-PVD method. Multi-component oxide-based coatings were found to have a longer service life compared to YSZ after thermal cycle tests. Due to thermodynamically more stable and flawed lattice structure of added oxidized dopants, thermal conductivity decreased and sintering resistance increased [65, 66].

A significant decrease in the thermal conductivity values was obtained between 25 and 800 °C by addition of 6 wt% Niobia co-dopant to 8YSZ. The mean thermal conductivity value between 25 and 800 °C was measured as 1.171 W/mK for YSZ, whereas the mean value after Nb addition was measured as 0.542 W/mK [67].

Liu et al. [52] investigated the phase stability, sintering and thermal conductivity characteristics of 8 mol%  $\text{Sc}_2\text{O}_3$ , 0.6 mol%  $\text{Y}_2\text{O}_3$  stabilized  $\text{ZrO}_2$  (ScYSZ) prepared using a chemical co-precipitation method, and compared them with YSZ. The ScYSZ heated at 1500 °C for 300 h was found to be stable in  $t'$  phase, while the YSZ's 49.4 % was found to be in monolithic phase. The volume shrinkage of the samples reaches more than 26 % for 8YSZ whereas only 18 % for ScYSZ after heat treated up to

1500 °C. During the thermal conductivity measurements carried out between 30 and 700 °C ScYSZ was found to have a two times lower thermal conductivity compared to 8YSZ.

When the additions of NiO, Nd<sub>2</sub>O<sub>3</sub>, Gd<sub>2</sub>O<sub>3</sub>, Er<sub>2</sub>O<sub>3</sub> and Yb<sub>2</sub>O<sub>3</sub> oxides were examined, 4 % molar addition of all oxides except NiO resulted in a decrease in thermal conductivity. On the other hand addition of NiO resulted in a negligible decline in conductivity. Addition of 4 % mole of Er<sub>2</sub>O<sub>3</sub> resulted in a 25 % decline, addition of 4 % mole of Nd<sub>2</sub>O<sub>3</sub> resulted in a 42 % decline, while addition of Gd<sub>2</sub>O<sub>3</sub> resulted in an average decline of 47 % in the conductivity. At each addition the crystal structure remained in tetragonal phase structure [68–70].

HfO<sub>2</sub>, CeO<sub>2</sub> and ThO<sub>2</sub> TBCs constitute the oxide groups being used. CeO<sub>2</sub> is added to the system as Ce<sub>2</sub>O<sub>3</sub> due to its volatility. Despite its adverse effect on sintering when compared with YSZ, it has the advantages of high thermal expansion coefficient and low thermal conductivity [71–73].

The minimum thermal conductivity value of HfO<sub>2</sub> doped YSZ is measured as 1.1 W m<sup>-1</sup> K<sup>-1</sup> at 1316 °C. Additionally, it was found to have a superior sintering resistance compared to YSZ [74].

As a magnetic ceramic material, lanthanum hexaluminate's (LaMgAl<sub>11</sub>O<sub>9</sub>) low thermal conductivity characteristic and low shrinkage characteristic renders it an alternative to YSZ. Most of La<sup>+3</sup> cations are located on oxygen regions. Since the ion diffusion applies a vertical pressure to the c axis it has an inhibiting effect on sintering [75–77].

In Vassen et al.'s study [47] SrZrO<sub>3</sub>, BaZrO<sub>3</sub>, and La<sub>2</sub>Zr<sub>2</sub>O<sub>7</sub> powder's porosity content was reduced after being synthesised. Thermal expansion coefficients of SrZrO<sub>3</sub> and BaZrO<sub>3</sub>'s were found to be lower than that of YSZ. SrZrO<sub>3</sub> did not prove to be a suitable TBC material since it underwent a phase transformation around 700–800 °C. Thermal conductivity of La<sub>2</sub>Zr<sub>2</sub>O<sub>7</sub> and BaZrO<sub>3</sub> sintered at 1000 °C are 1.6 and 3.4 W/mK respectively while YSZ has a thermal conductivity value of 2.2 W/mK. As for the hardness values, these two materials are observed to have a 15 % lower value compared to YSZ. Plasma sprayed La<sub>2</sub>Zr<sub>2</sub>O<sub>7</sub> was found to have a better thermal cycle life than BaZrO<sub>3</sub>, but lower than YSZ.

## 4 Summary and Outlook

A wide range of current applications, production methods, failure mechanisms, and current uses of alternative materials in TBCs are reviewed in this study. High efficiency and performance increase constitute the main aspects of gas turbine engines during their development process. The increase in power and efficiency can be obtained only through increasing turbine inlet temperatures. The temperatures that the gas turbines are exposed to, are very close to or at the level of melting point of the super-alloy materials. Accordingly, complex cooling systems or TBCs are used as an attempt to protect super-alloy substrate materials against thermal failures and the adverse effects of hot gases.

Oxidation, hot corrosion effects, thermo-mechanical failures, chemical failures, erosion failures, sintering of top coating, thermal shock and CMAS ( $\text{CaO-MgO-Al}_2\text{O}_3\text{-SiO}_2$ ) attack, constitute the primary failure mechanisms restricting the service life of TBCs. As a result of failure mechanisms arising from high temperature effects, thermal conductivity coefficient mismatches, changes in thermal conductivity coefficients as well as chemical interactions occur and as a result, TBCs undergo rapidly developing failures. A thorough analysis of these failure mechanisms that the TBCs undergo under service conditions, and implementation of failure prevention measures are essential in terms of providing a long-term and secure protection.

The efforts to increase the aimed turbine performance and efficiency for the new generation gas turbine engines necessitate higher turbine inlet temperatures as well as the development of TBC materials with long-term resistance against failures under such high temperatures. Thus, future investigations in TBCs with emphasis on surface engineering promise to reveal new high temperature materials and new insights in the years to come.

**Acknowledgments** This work was partially supported by The Scientific and Technological Research Council of Turkey (TUBITAK, 113R049).

## References

1. Heveran CM, Xu JP, Sarin VK et al (2013) Simulation of stresses in TBC–EBC coating systems for ceramic components in gas turbines. *Surf Coat Tech* 235:354–360
2. Keyvani A, Saremi M, Sohi MH (2011) Oxidation resistance of YSZ-alumina composites compared to normal YSZ TBC coatings at 1100 °C. *J Alloy Compd* 509:8370–8377
3. Davis JR (1997) Protective coatings for superalloys, heat-resistance materials. ASM International, Ohio
4. Lu Z, Myoung SW, Kim EH et al (2014) Microstructure evolution and thermal durability with coating thickness in APS thermal barrier coatings. *Mater Today: Proc* 1:35–43
5. Pujol G, Ansart F, Bonino JP et al (2013) Step-by-step investigation of degradation mechanisms induced by CMAS attack on YSZ materials for TBC applications. *Surf Coat Tech* 237:71–78
6. Schulz U, Fritscher K, Leyens C (2000) Two-source jumping beam evaporation for advanced EB-PVD TBC systems. *Surf Coat Tech* 40:133–134
7. Padture NP, Gell M, Jordan EH (2002) Thermal barrier coatings for gas-turbine engine applications. *Science* 296:280–284
8. Bahadori E, Javadpour S, Shariat MH et al (2013) Preparation and properties of ceramic  $\text{Al}_2\text{O}_3$  coating as TBCs on MCrAlY layer applied on Inconel alloy by cathodic plasma electrolytic deposition. *Surf Coat Tech* 228:611–614
9. Ma K, Schoenung JM (2011) Isothermal oxidation behavior of cryomilled NiCrAlY bond coat: homogeneity and growth rate of TGO. *Surf Coat Tech* 205:5178–5185
10. Evans HE (2011) Oxidation failure of TBC systems: an assessment of mechanisms. *Surf Coat Tech* 206:1512–1521
11. Evans AG, Mumm DR, Hutchinson JW et al (2001) Mechanisms controlling the durability of thermal barrier coatings. *Prog Mater Sci* 46:505–553

12. Taylor TA, Walsh PN (2004) Thermal expansion of MCrAlY alloys. *Surf Coat Tech* 177:24–31
13. Zhang Q, Li CJ, Li CX et al (2008) Study of oxidation behavior of nanostructured NiCrAlY bond coatings deposited by cold spraying. *Surf Coat Tech* 202:3378–3384
14. Richer P, Yandouzi M, Beauvais L et al (2010) Oxidation behaviour of CoNiCrAlY bond coats produced by plasma, HVOF and cold gas dynamic spraying. *Surf Coat Tech* 204:3962–3974
15. Su L, Zhang W, Sun Y et al (2014) Effect of TGO creep on top-coat cracking induced by cyclic displacement instability in a thermal barrier coating system. *Surf Coat Tech* 254:410–417
16. Chen WR, Wu X, Marple BR et al (2008) Pre-oxidation and TGO growth behaviour of an air-plasma-sprayed thermal barrier coating. *Surf Coat Tech* 202:3787–3796
17. Karaoglanli AC, Altuncu E, Ozdemir I et al (2011) Structure and durability evaluation of YSZ + Al<sub>2</sub>O<sub>3</sub> composite TBCs with APS and HVOF bond coats under thermal cycling conditions. *Surf Coat Tech* 205:369–373
18. Karaoglanli AC, Ogawa K, Turk A et al (2013) Progress in gas turbine performance. *Intech, Croatia*
19. Peng H, Wang L, Guo L et al (2012) Degradation of EB-PVD thermal barrier coatings caused by CMAS deposits. *Prog Nat Sci Mater Int* 22:461–467
20. Rätzer-Scheibe HJ, Schulz U (2007) The effects of heat treatment and gas atmosphere on the thermal conductivity of APS and EB-PVD PYSZ thermal barrier coatings. *Surf Coat Tech* 201:7880–7888
21. Sampath S, Schulz U, Jarligo MO, Kuroda S (2012) Processing science of advanced thermal-barrier systems. *MRS Bull Mater Res Soc* 37:903–910
22. Xu H, Guo H (2011) Thermal barrier coatings. Woodhead Publishing, Cambridge
23. Saremi M, Afrasiabi A, Kobayashi A (2007) Bond coat oxidation and hot corrosion behavior of plasma sprayed YSZ coating on Ni superalloy *Trans JWRI* 36:41–45
24. Jones RL (1997) Some aspects of the hot corrosion of thermal barrier coatings. *J Therm Spray Technol* 6:77–84
25. Ghosh S (2014) Thermal behavior of glass–ceramic bond coat in a TBC system. *Vacuum* 101:367–370
26. Karger M, Vaßen R, Stöver D (2011) Atmospheric plasma sprayed thermal barrier coatings with high segmentation crack densities: spraying process, microstructure and thermal cycling behavior. *Surf Coat Tech* 206:16–23
27. Guo HB, Vaßen R, Stöver D (2004) Atmospheric plasma sprayed thick thermal barrier coatings with high segmentation crack density. *Surf Coat Tech* 186:353–363
28. Sun J, Fu QG, Liu GN et al (2015) Thermal shock resistance of thermal barrier coatings for nickel-based superalloy by supersonic plasma spraying. *Ceram Int* 41:9972–9979
29. Wright PK, Evans AG (1999) Mechanisms governing the performance of thermal barrier coatings. *Curr Opin Solid St M* 4:255–265
30. Aygun A (2008) Novel Thermal Barrier Coatings (TBCs) that are resistant to high temperature attack by CaO-MgO-Al<sub>2</sub>O<sub>3</sub>-SiO<sub>2</sub> (CMAS) glassy deposits, PhD thesis, The Ohio State University
31. Steinke T, Sebold D, Mack DE et al (2010) A novel test approach for plasma-sprayed coatings tested simultaneously under CMAS and thermal gradient cycling conditions. *Surf Coat Tech* 205:2287–2295
32. Li L, Hitchman N, Knapp J (2010) Failure of thermal barrier coatings subjected to CMAS attack. *J Therm Spray Technol* 19:148–155
33. Clarke DR, Levi CG (2003) Materials design for the next generation thermal barrier coating. *Ann Rev Mater Res* 33:383–417
34. Strangman T, Raybould D, Jameel A et al (2007) Damage mechanisms, life prediction, and development of EB-PVD thermal barrier coatings for turbine airfoils. *Surf Coat Tech* 202:658–664

35. Nicholls JR, Deakinand MJ, Rickerby DS (1999) A Comparison between the erosion behaviour of thermal spray and electron physical beam vapour deposition thermal barrier coatings. *Wear* 352:233–235
36. Bose S, Demasi J (1997) Thermal barrier coating experience in gas turbine engines. *J Therm Spray Technol* 6:99–104
37. Han M, Zhou G, Huang J, Chen S (2014) Optimization selection of the thermal conductivity of the top ceramic layer in the double-ceramic-layer thermal barrier coatings based on the finite element analysis of thermal insulation. *Surf Coat Tech* 240:320–326
38. Hass DD, Slifka AJ, Wadley HNG (2001) Low thermal conductivity vapor deposited zirconia microstructures. *Acta Mater* 49:973–983
39. Ferdinando MD, Fossati A, Lavacchi A et al (2010) Isothermal oxidation resistance comparison between air plasma sprayed, vacuum plasma sprayed and high velocity oxygen fuel sprayed CoNiCrAlY bond coats. *Surf Coat Tech* 204:2499–2503
40. Richer P, Yandouzi M, Beauvais L et al (2010) Oxidation behaviour of CoNiCrAlY bond coats produced by plasma, HVOF and cold gas dynamic spraying. *Surf Coat Tech* 204:3962–3974
41. Ma W, Jarligo MO, Mack DE, Pitzer D et al (2008) New generation perovskite thermal barrier coating materials. *J Therm Spray Technol* 17:5–6
42. Clarke DR, Levi CG (2003) Materials design for the next generation thermal barrier coatings. *Ann Rev Mater Res* 33:383–417
43. Habibi MH, Wang L, Liang J et al (2013) An investigation on hot corrosion behavior of YSZ-Ta<sub>2</sub>O<sub>5</sub> in Na<sub>2</sub>SO<sub>4</sub> + V<sub>2</sub>O<sub>5</sub> salt at 1100 °C. *Corr Sci* 75:409–414
44. Nicholls JR (2003) Advances in coating design for high-performance gas turbines. *MRS Bull* 28:659–670
45. Levi CG (2004) Emerging materials and processes for thermal barrier systems. *Curr Opin Solid State Mater Sci* 8(1):77–91
46. Ning XJ, Li CX, Li CJ, Yang GJ (2006) Modification of microstructure and electrical conductivity of plasma-sprayed YSZ deposit through postdensification process. *Mater Sci Eng* 428(1–2):98–105
47. Vassen R, Cao X, Tietz F, Basu D, Stöver D (1999) Zirconates as new materials for thermal barrier coatings. *J Am Ceram Soc* 83:2023–2028
48. Stöver D, Funke C (1999) Directions of the development of thermal barrier coatings in energy applications. *J Mater Process Tech* 195:92–93
49. Schulz U, Fritscher K, Leyens C (2000) Two-source jumping beam evaporation for advanced EB-PVD system. *Surf Coat Tech* 40:133–134
50. Guo X, Wang Z (1998) Effect of niobia on the defect structure of yttria-stabilized zirconia. *J Euro Ceram Soc* 18:237–240
51. Xu H, Wu J (2011) *Thermal barrier coatings*. Woodhead Publishing, Cambridge
52. Liu H, Li S, Li Q et al (2010) Investigation on the phase stability, sintering and thermal conductivity of Sc<sub>2</sub>O<sub>3</sub>-Y<sub>2</sub>O<sub>3</sub>-ZrO<sub>2</sub> for thermal barrier coating application. *Mater Design* 31:2972–2977
53. Suresh G, Seenivasan G, Krishnaiah MV, Murti PS (1997) Investigation of the thermal conductivity of selected compounds of gadolinium and lanthanum. *J Nucl Mater* 249:259–261
54. Saruhan B, Francois P, Kritscher K et al (2004) EB-PVD processing of pyrochlore-structured La<sub>2</sub>Zr<sub>2</sub>O<sub>7</sub>-based TBCs. *Surf Coat Tech* 182:175–183
55. Stöver D, Pracht G, Lehmann H et al (2004) New material concepts for the next generation of plasma-sprayed thermal barrier coatings. *J Therm Spray Technol* 13:76–83
56. Vassen R, Traeger F, Stöver D (2004) New thermal barrier coatings based on pyrochlore/YSZ double layer systems. *Int J Appl Ceram Technl* 1:351–356
57. Cao X, Vassen R, Fischer W et al (2003) Lanthanum-cerium oxide as a thermal barrier-coating material for high-temperature applications. *Adv Mater* 15:1438–1442
58. Ma W, Gong SK, Xu HB et al (2006) On improving the phase stability and thermal expansion coefficients of lanthanum cerium oxide solid solutions. *Scripta Mater* 54:1505–1508

59. Ma W, Gong SK, Xu HB et al (2006) The thermal cycling behavior of lanthanum-cerium oxide thermal barrier coating prepared by EB-PVD. *Surf Coat Tech* 200:5113–5118
60. Xu Z, He L, Mu R et al (2009) Double-ceramic-layer thermal barrier coatings of  $\text{La}_2\text{Zr}_2\text{O}_7/\text{YSZ}$  deposited by electron beam-physical vapor deposition. *J Alloy Compd* 473:509–515
61. Schulz U, Fritscher K, Peters M (1996) EB-PVD  $\text{Y}_2\text{O}_3$ - and  $\text{CeO}_2\text{Y}_2\text{O}_3$ -stabilized zirconia thermal barrier coatings—crystal habit and phase composition. *Surf Coat Tech* 82:259–269
62. Leyens C, Schulz U, Fritscher K (2003) Oxidation and lifetime of PYSZ and CeSZ coated Ni-base substrates with MCrAlY bond layers. *Mater High Temp* 20:475–480
63. Wu J, Wei X, Padture NP et al (2002) Low thermal conductivity rare-earth zirconates for possible thermal-barrier coatings application. *J Am Ceram Soc* 85:3031–3035
64. Lee KN (2006) In the gas turbine handbook. NETL, Cleveland
65. Zhu DM, Miller RA (2002) In: Lin HT, Singh M (eds) Thermal conductivity and sintering behavior of advanced thermal barrier coatings, 4th edn. The American Ceramic Society, Florida
66. Zhu DM, Chen YL, Miller RA (2003) Defect clustering and nano-phase structure characterization of multi-component rare earth oxide doped zirconia-yttria thermal barrier coatings. *Ceram Eng Sci Proc* 24:525–534
67. Almeida DS, Silva CRM, Nono MCA et al (2007) Thermal conductivity investigation of zirconia co-doped with yttria and niobia EB-PVD TBCs. *Mater Sci Eng, A* 443:60–65
68. Tamarin YA, Kachanov EB, Zherzdev SV (1997) Thermophysical properties of ceramic layers in TBC-EB. *Mater Sci Forum* 251–254:949–956
69. Nicholls JR, Lawson KJ, Johnstone A et al (2001) Low thermal conductivity EB-PVD thermal barrier coatings. *Mater Sci Forum* 369:595–606
70. Nicholls JR, Lawson KJ, Johnstone A et al (2002) Methods to reduce the thermal conductivity of EB-PVD TBCs. *Surf Coat Tech* 151–152:383–391
71. Gao W, Li Z (2008) Developments in high temperature corrosion and protection of materials. Woodhead Publishing, Cambridge
72. Thornton J, Majumdar A, Mcadam G (1997) Enhanced cerium migration in ceria-stabilised zirconia. *Surf Coat Tech* 94(95):112–117
73. Agarwal AK, Pandey A, Gupta AK et al (2014) Novel combustion concepts for sustainable energy development. Springer, India
74. Singh J, Wolfe DE, Miller RA et al (2004) Tailored Microstructure of zirconia and hafnia-based thermal barrier coatings with low thermal conductivity and high hemispherical reflectance by EB-PVD. *J Mater Sci* 39:1975–1985
75. Gadow R, Lischka M (2002) Lanthanum hexaaluminate—novel thermal barrier coatings for gas turbine applications—materials and process development. *Surf Coat Tech* 151:392–399
76. Cao XQ, Vassen R, Stöver D (2004) Ceramic materials for thermal barrier coatings. *J Euro Ceram Soc* 24:1–10
77. Cao XQ, Zhang YF, Zhang JF (2008) Failure of the plasma-sprayed coating of lanthanum hexaaluminate. *J Euro Ceram Soc* 28:1979–1986